12-2009

Polymeric Carbon Nanocomposites - Preparation, Characterization, and Properties

Lucia Veca
Clemson University, mvecaro@yahoo.fr

POLYMERIC CARBON NANOCOMPOSITES – PREPARATION, CHARACTERIZATION, AND PROPERTIES

A Dissertation
Presented to
the Graduate School of
Clemson University

In Partial Fulfillment
of the Requirements for the Degree
Doctor of Philosophy
Chemistry

---

by
Lucia Monica Veca
December 2009

Accepted by:
Dr. Ya-Ping Sun, Committee Chair
Dr. Gautam Bhattacharyya
Dr. Brian Dominy
Dr. Douglas E. Hirt

ABSTRACT

Excellent thermal properties of carbon nanomaterials such as carbon nanotubes and newly discovered graphene make them the filler of choice for the development of thermal management materials. Graphene has been viewed as “unrolled single-walled carbon nanotube and as a wonder material with many superlatives to its name” thus there is an excessive interest in developing new synthetic routes towards large scale production of high quality graphene nanosheets.

In this dissertation, we report different methods that could further exfoliate the commercially available expanded graphite to nanometer sized carbon structures, “carbon nanosheets” for their use in highly thermal conductive polymeric nanocomposites. Initially, an overview of recent advances in the development of thermal conductive polymeric/carbon nanocomposites is provided. Then, the “carbon nanosheets” from the specific processes will be carefully characterized by spectroscopic techniques and the effectiveness of the processing methods is demonstrated in terms of polymeric carbon nanocomposites thermal diffusivity. While the focus of this manuscript will be on the enhancement of thermal diffusivity we will also discuss the chemical modification and functionalization of these “carbon nanosheets” with matrix polymer. Finally, the critical research opportunities and challenges in the development of functional graphene nanocomposites for thermal management materials will be discussed.

ACKNOWLEDGMENTS

There are many fellows, here at Clemson as well as back home in Romania, that have been contributed to my achievements in Graduate School and I am very grateful to all of them. However, my advisor, Prof. Ya-Ping Sun, had the most significant influence on my career path. He was never hesitating to lend me his hand when I needed it the most. Moreover, his support, mentorship, understanding in my less inspired moments, as well as his exigency during the completion of my studies is greatly appreciated. I would also like to acknowledge the other committee members, Prof. Gautam Bhattacharyya, Prof. Brian Dominy, and Prof. Douglas E. Hirt for their suggestions and corrections as completing this manuscript. As a student, is always very encouraging to know that your committee members will be there to help you in case you will need them, thank you to all of you for this.

There is not a secret that the Graduate School has its ups and downs and you will always need friends and colleagues to assist you. Therefore a special tanks is also paid to the former and present group members: Dr. Yi Lin, Dr. Liangwei Qu, Dr. Pankaj Pathak, and Dr. Wei Wang for their help to smoothly integrate within the group and get on my own feet; Dr. Fushen Lu, Dr. Mohammed J. Meziani, Dr. Bing Zhou, Dr. Sk. Anwarul Haque, and Dr. Muhammet E. Kose for their very kind and constructive scientific discussions; Dr. Li Cao, Mr. Xin Wang, Mrs. Barbara Harruff , Dr. Pengju G. Luo, Dr. Heting Li, Dr. Huaping Li, Dr. Lingrong Gu, , Dr. K. A. Shiral Fernando, Dr. Bailin Chen, Dr. Haifang Wang, Dr. Puyu Zhang, Dr. Jinping Cheng, and Mr. Sheng-tao Yang, for their assistance with some of the characterization experiments and friendship.

TABLE OF CONTENTS

Page

Table of Contents (Continued)

Page

Table of Contents (Continued)

Page

LIST OF SCHEMES

LIST OF FIGURES

List of Figures (Continued)

Figure Page

List of Figures (Continued)

Figure Page

List of Figures (Continued)

Figure Page

List of Figures (Continued)

Figure Page

List of Figures (Continued)

Figure Page

CHAPTER ONE

ADVANCES IN THE DEVELOPMENT OF THERMAL CONDUCTIVE POLYMERIC/CARBON NANOCOMPOSITES

Polymeric nanocomposites are important materials with applications that include technological fields such as nanoelectronics,[1] sensors,[2] and actuators,[3] batteries,[4] supercapacitors,[5] and hydrogen storage.[6] In addition to the traditional benefits of polymers, such as design flexibility, light weight, and manufacturing cost reductions, thermally conductive polymeric composites have a low coefficient of thermal expansion, therefore suitable in printed circuit boards, connectors, thermal interface materials, heat sinks and many others.

1.1 INTRODUCTION

In recent years, scientists and engineers alike have shown an increased interest in the field of nanocomposites. The driving force for their research comes form the simple hypothesis that using building blocks with dimensions in the nanometer range would allow the creation of new materials with unique or/and improved physical properties. In other words, components with dimensions in the nanometer range may be used to develop materials with customized properties. For example – highly conductive but brittle carbon nanomaterials are incorporated into insulating polymers to create light weight conductive composites. Unlike the traditional micro-scale composites, small

nanoparticles do not scatter light significantly; therefore development of nanocomposites with improved electrical or mechanical properties that keep their optical clarity is possible. In addition, the small size will produce a lower stress concentration than their micron size counterparts; therefore will not compromise the ductility of the polymer.

Among the most studied carbon nano-materials in the filed of polymeric composites are carbon nanotubes and recently carbon nanosheets/graphene due to their favorable geometry and remarkable properties. Although carbon based materials, such as diamond and graphite, represent the most thermal conductive materials,[7] with their room temperature thermal conductivity being 2-5 times higher than that of the most conductive metals, thermal conductivity of carbon nanomaterials in general and of carbon nanotubes in particular, as well as their composites have yet to be fully exploited, for several reasons. It is worth pointing out that thermal conductivity/diffusivity of carbon nanotubes is even higher than that of diamond or graphite.

First is the difficulty to produce impurities and defects free carbon nanotubes. The predicted, 6600 W/mK [8] thermal conductivity of an individual, perfect, metallic nanotube would be very difficult to be translated to the bulk nanocomposites as long as all the synthetic methods produce a mixture of nanotube chiralities, diameters, and lengths beside different amount and type of impurities. This heterogeneity would definitely have a large impact on the polymeric-carbon nanocomposite properties.

Second reason would be the mechanism of thermal conductivity- efficient transport of heat is relatively marginal in these polymeric nanocomposies. Large reductions in thermal conductivity, in comparison to bulk materials, have been observed

in materials structured at the nanoscale level. These reductions are attributed to a combination of classical and quantum size effects that manifest when the characteristic length scales in the nanostructured material become comparable to, or shorter than, the mean free path of the heat carriers in the bulk material.[9] That is, at the nanoscale level phonons scattering due to the interaction with the boundary of nanostructure will be higher than in the bulk material (there are more boundaries in the nanomaterials). Moreover, in semiconductors and insulators (such as polymers) the primary heat carriers are the lattice vibrations (i.e. phonons) and most of the heat is carried by phonons with mean free path in the range of 1 – 100 nm at room temperature.[10] Thus, size effects on heat transport become important in nanostructured materials. In addition, the absence of thermal conductivity contrast, the difference in thermal conductivity between the CNTs and polymeric matrix is only 10^4W/mK,[11] would probably favor the phonons transport through the matrix, unlike the electrons which are carried out through the tube network since the electrical conductivity contrast between the nanotubes and polymer is about 10^{15}-10^{19} S/m. [12] Another important factor in the effectiveness of heat transport is the interfacial thermal resistance. In order to achieve superior thermal conductivity in the bulk composite, the thermal conductance of nanotube-polymer interface should be relatively high (small interfacial thermal resistance).

Third reason could be due to the chemical processing of nanocomposites. To implement the novel properties of nanocomposites, processing methods that lead to controlled particle size distribution, dispersion, and interfacial interaction are critical.

In the following sections of this chapter we will highlight the most representative research in the field of thermal conductivity of carbon nanotubes and their polymeric composites as well as the limitations in developing the polymeric/carbon nanocomposites with superior thermal conductive properties. Finally, the future of polymer/carbon nanocomposites with superior thermal conductivity will be discussed.

1.2 CARBON NANOTUBES

There are some theoretical and experimental results suggesting that an individual, perfect (defect free) carbon nanotube could achieve extraordinary high heat flow[8,13,16]. Because the current synthetic methods produce a mixture of carbon nanotubes with different morphologies, tremendous research has been carried out in order to understand their structure – properties relationship. Thus, this section reviews the key research work on the thermal conductivity of carbon nanotubes and the dependence on their purity, diameter, chirality, length, defects concentration and orientation.

1.2.1 THERMAL CONDUCTIVITY OF INDIVIDUAL CARBON NANOTUBES

It has been almost a decade since the first theoretical computation (from the combination of equilibrium and non-equilibrium molecular dynamics simulations) predicted the room-temperature thermal conductivity of an isolated (10,10) SWNT to be

around 6600 W/mK.[8] The unusually high value of thermal conductivity was associated with the long phonon mean free path in the nanotubes.

One year later, Kim et al.[13] was able to develop a micro-device to measure the thermal conductivity of a single MWNT. The observed room-temperature thermal conductivity for the 14 nm diameter MWNT was more than 3000 W/mK, even higher than that of diamonds. The thermal conductivity was much higher than that of both MWNT mat (20 W/mK)[14] and aligned SWNTs (250 W/mK)[15] reported earlier but was comparable to the theoretical values for SWNTs (3000-6000 W/mK).[16-18] In addition to high thermal conductivity at room-temperature, the thermal conductivity dependence on changes in temperature, presented in Figure 1.1, showed remarkable differences from the previously reported values on bulk samples. As shown in the inset of Figure 1.1, there was a maximum in thermal conductivity at 320 K, a feature that was absent in bulk measurements. In order to understand the phenomenon the authors measured the thermal conductivity of MWNT bundles, and found that as the diameter of the MWNT bundle increased, thermal conductivity quickly became similar to the result from bulk measurement on a mat sample.

Due to their difficulty on handling it took much longer time until the thermal conductivity of a SWNT was measured. In 2005 Yu et al.[19] reported that the intrinsic thermal conductivity of a SWNT measured with a device similar to the one used for MWNT was very close to the calculated ballistic thermal conductivity of a 1-nm diameter SWNT (Figure 1.2). Moreover, the signatures of the phonon-phonon Umklapp scattering were not observed in the measured temperature range (110 to 300 K), which is consistent

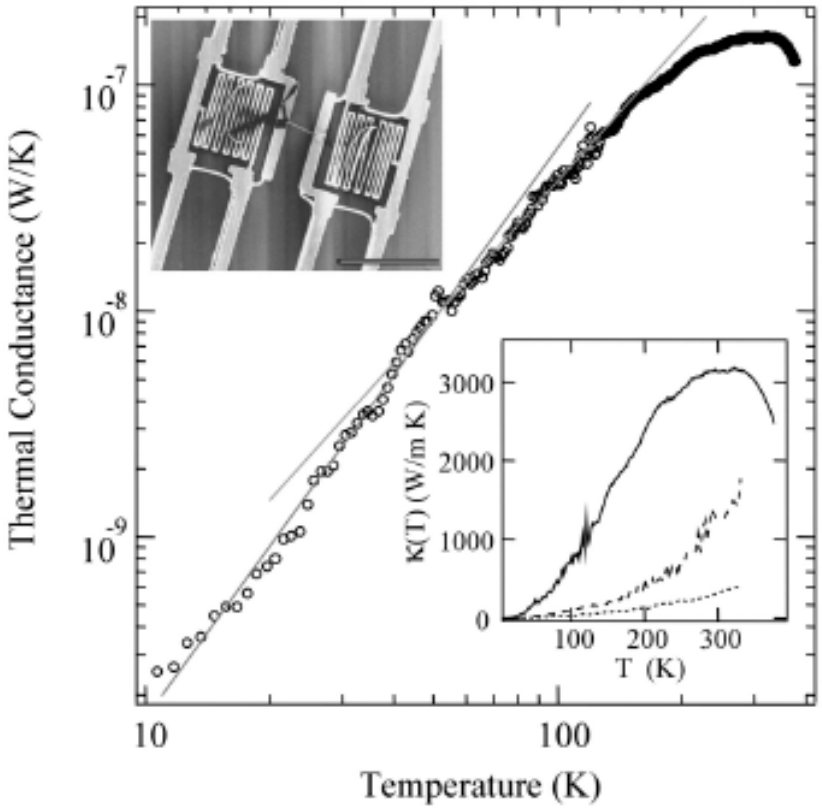

Figure 1.1 Temperature dependent thermal conductivity measurement for an individual 14 nm diameter MWNT. The solid lines represent linear fits of the data in a logarithmic scale at different temperature ranges. Lower inset: Solid line represents κ(T) of an individual MWNT (d = 14 nm). Broken and dotted lines represent small (d = 80 nm) and large bundles (d = 200 nm) of MWNTs, respectively. Upper inset: SEM image of the suspended islands with the individual MWNT. The scale bar is 10 μm (From Ref. [13]).

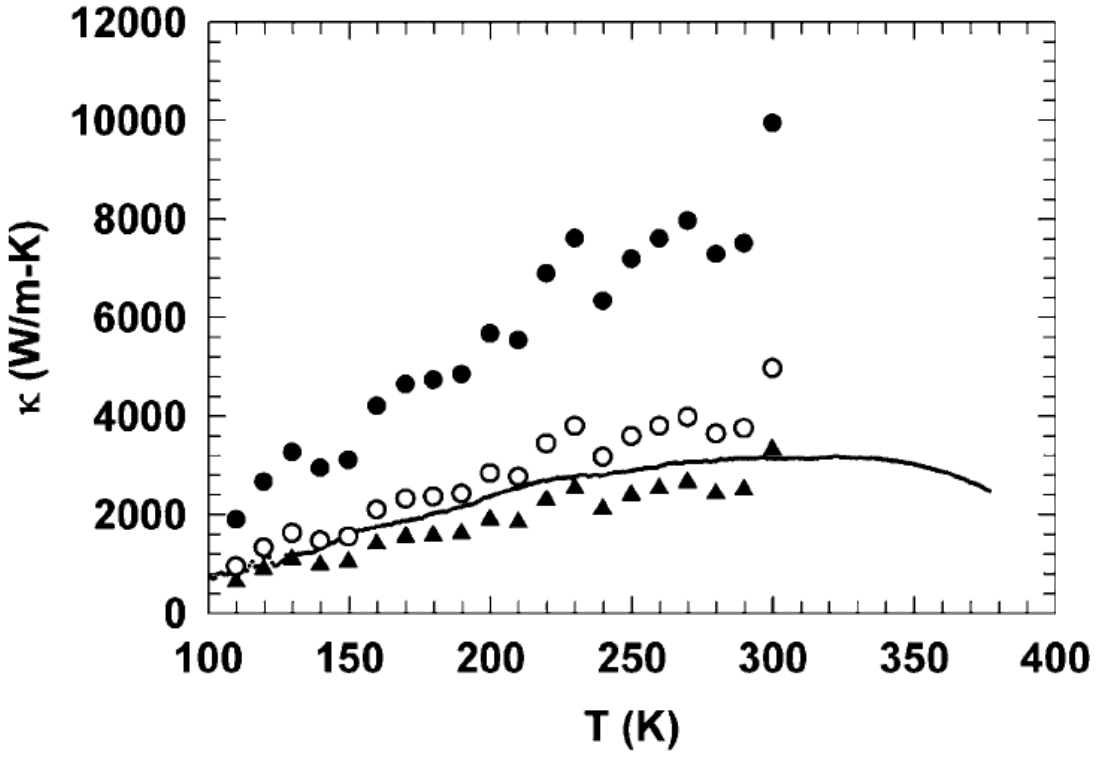

Figure 1.2 Thermal conductivity of the SWNT if the diameter was 1nm (filled circles), 2 nm (open circles), and 3 nm (filled triangles). The line is the measurement result of an individual MWNT -from Ref. [13] (From Ref. [19]).

with the small crystallite size (Umklapp scattering should be suppressed in one dimensional system because of unavailability of states into which to scatter).

Soon after that report, Dai and coworkers[20] extracted the thermal conductance of an individual SWNT above room-temperature (300-800 K) from high bias electrical measurements by reverse fitting using an existing electrothermal transport model. Thermal conductivity of a 2.6 μm long and 1.7 nm in diameter SWNT was around 3500 W/mK at room-temperature but decreased to 1000 W/mK near the upper end of the temperature range, a phenomenon ascribed to the second order three phonon scattering.

These theoretical and experimental results suggest that smaller diameter carbon tubes, especially SWNTs, would have the potential to achieve higher thermal conductivity since their small diameter would quantize phonons. In other words, exfoliation of carbon nanotubes could be the milestone in the development of the thermally conductive polymeric composites. We should also point out that in these experiments and simulations the heat loss to the surrounding environment was not considered, therefore these results could have been overestimated.

1.2.2 THERMAL CONDUCTIVITY OF BULK CARBON NANOTUBES

The advances in large scale carbon nanotubes synthesis in the late 90's allowed scientists to further explore the physical properties of these materials, including their thermal conductivity. This section will present the current state of the art on the thermal

conductivity of CNTs at the bulk level as well as the parameters that may have a detrimental effect on the thermal conductivity.

Thermal conductivity of MWNT arrays and films from CVD[14] and microwave plasma CVD,[21] respectively, have been reported to be relatively low in comparison to what was expected. In the former, the room-temperature thermal conductivity of 1-2 millimeters long and few tens of nanometers in diameter MWNT bundles, measured by self heating 3ω technique (steady-state method) was around 25 W/mK. The films obtained by microwave plasma CVD with the thickness (also the length of the MWNT) of 10-50 μm and the diameter of 40-100 nm exhibited thermal conductivity of 15 W/mK at room-temperature. In this experiment the thermal conductivity was investigated by using a pulsed photothermal reflectance technique (noncontact method). While the radiative heat loss in a steady–state measurement could lead to uncertainties in the measured thermal conductivity, a negligible heat loss due to the short time of measurement is present in the more advanced noncontact method. Regardless of the difference in measurements and final results, both authors concluded that the thermal conductivity was dominated by the phonon contribution and ascribed its lower value to the presence of defects as well as of intergraphene layers and intertube coupling, which could reduce the phonon mean free path. It was also speculated that, in addition to the phonon scattering in the presence of defects, a much longer length than the phonon mean free path could converge the thermal conductivity, therefore a decrease in thermal conductivity was observed.

Yi et el.[14] also measured the variation in thermal conductivity with decreasing temperature of the bundled MWNTs (1-2 mm in length and few tens of nm in diameter) extracted from the CVD grown arrays. It was found that the thermal conductivity of the MWNT bundles monotonically decreased with decreasing the temperature, being linear above 120 K but becoming quadratic at temperatures below thermal conductivity (κ) α $T^{1.98\pm0.03}$, as depicted in Figure 1.3.

A valuable contribution to the field of SWNTs thermal conductivity has been brought by Hone et al.[22,15] The authors used a comparative method to measure the thermal conductivity of both random "mats" and aligned films of SWNTs produced by arc-discharge. When tangled (random) nanotube bundles mats of as-produced SWNTs were used, the thermal conductivity at room-temperature was around 35 W/mK[22], while the thermal conductivity of purified SWNT films that were aligned by filtration in a high magnetic field was greater than 200 W/mK[15] in the direction parallel to the alignment. As expected, the alignment of SWNTs had an important effect on the thermal conductivity, which was almost 7 fold higher than the unaligned sample. However the temperature dependence of thermal conductivity was almost the same for unaligned and aligned samples (Figure 1.4).

As better illustrated in Figure 1.5, the thermal conductivity of a random SWNT mat decreases smoothly with decreasing temperature and shows a change in slop near 30 K. Below this temperature, thermal conductivity is strictly linear with temperature and extrapolates to zero at T = 0 K. Although this linear behavior is usually associated with thermal conductivity dominated by electrons contribution, the measurement of Lorenz

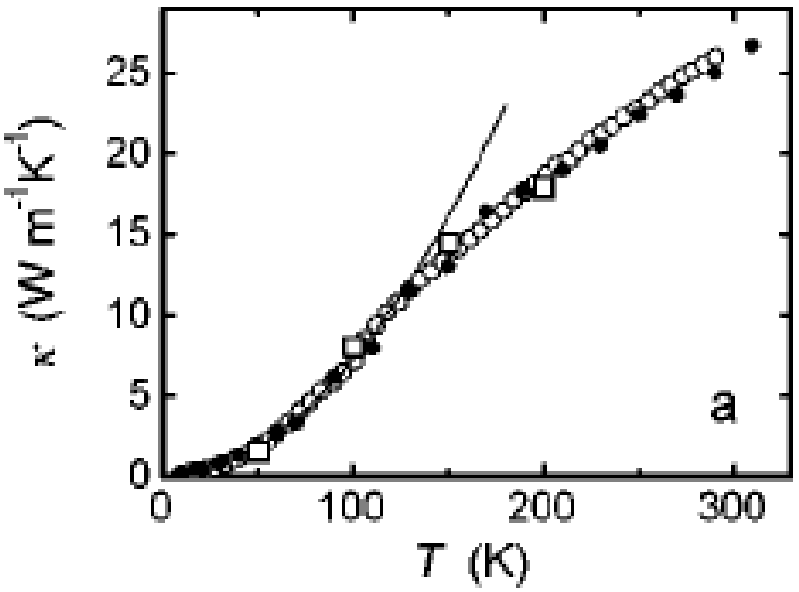

Figure 1.3 Temperature dependence of the thermal conductivity of three MWNTs samples (From Ref. [14])

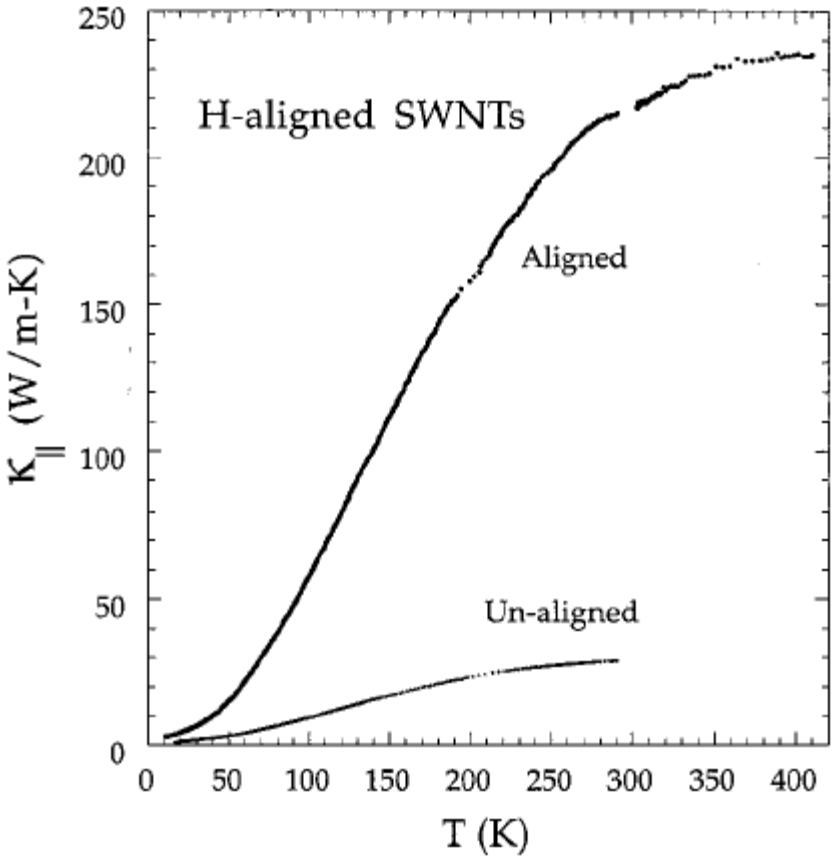

Figure 1.4 Temperature dependent thermal conductivity measurement of H-aligned SWNTs (From Ref. [15]).

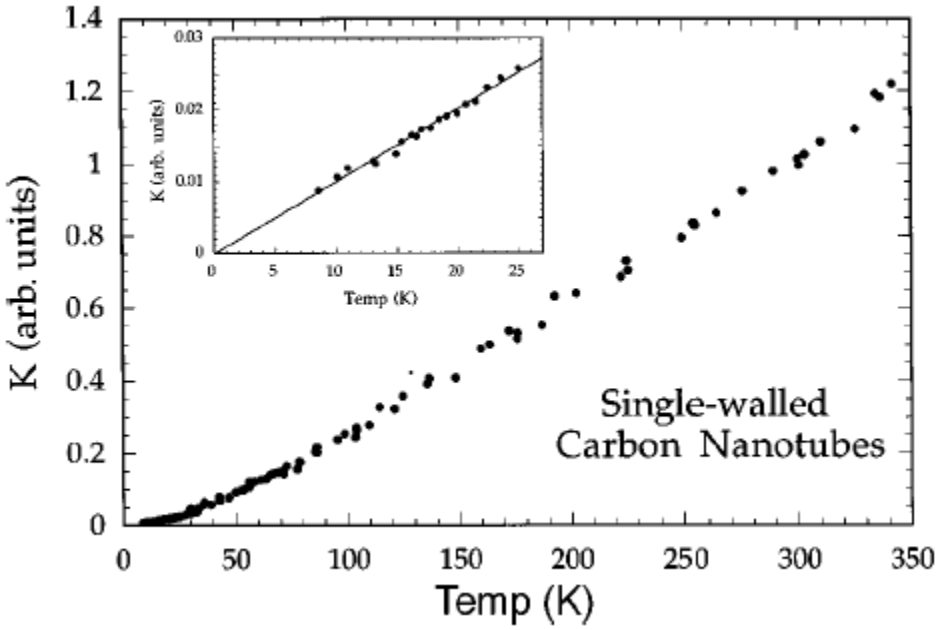

Figure 1.5 Temperature dependence of the thermal conductivity of arc SWNTs (From Ref. [22])

ratio ($\kappa/\sigma xT$) indicated that thermal conductivity is indeed dominated by phonons at all temperatures. Therefore, the linear temperature dependence of thermal conductivity likely reflects the one dimensional band-structure of individual SWNTs, with linear acoustic bands contributing to thermal transport at the lowest temperature and optical sub-bands entering at higher temperatures.[23, 24]

In order to more definitely determine whether the linear thermal conductivity is due to one dimensional quantization, the $\kappa(T)$ of SWNT samples with different diameters was measured.[25] It was observed that the linear $\kappa(T)$ extended to higher temperatures in SWNT samples with a smaller average tube diameter. For instance, $\kappa(T)/T$ begins to increase at about 35 K or 40 K when the diameter of SWNTs was 1.4 or 1.2 nm, respectively. The experimental results were consistent with the theory, since the phonon sub-band splitting increases with decreasing tube diameter.

A more systematic study on the purity and inter-tube coupling has been carried out in our group[26]. Thermal conductivity on pressed disks of both as-supplied and purified SWNTs has shown similar results. Because the purification of the SWNTs was performed in the presence of strong oxidizing reagents, the purified SWNTs would have defects that could also be phonons scattering paths. Therefore annealing for 30 minutes at 1200°C under inert atmosphere (Ar) was used to overcome this limitation. The interface barrier between the tubes is another issue in the phonon transport; therefore the as-supplied and purified SWNT powder was coated with about 100 nm layer of platinum. Indeed the thermal conductivity increased with annealing and coating, with the highest impact coming from the annealed sample (26 % increase; $\kappa(25) = 0.388$ W/mK) followed

by the coated specimens (11% increase). The relatively modest improvement in the sample after platinum coating could be due to the processing difficulty encountered after metal coating.

In order to further improve the thermal conductivity of SWNT pellets, the as-supplied sample was first mixed with graphite and then pressed into a pellet. The role of graphite (with well known lubricating properties and very high thermal conductivity) was to favor the tube-tube interaction and the formation of heat flow networks. The first, somewhat surprising observation was that the thermal conductivity of as-supplied SWNTs showed a 56 % increase from the experiment presented above, suggesting that it is very difficult to produce SWNTs with reproducible properties even when the same supplier is used. Besides this striking observation, the graphite had a positive impact on the thermal conductivity. There was a relatively large increase in thermal conductivity (about 68 % compare to that of the as-supplied SWNTs) when only 10 wt% graphite was added. As shown in Figure 1.6, there is an increase in the thermal conductivity with increasing the content of graphite but does not follow the more expected linear rule of mixture behavior.

In conclusion, thermal conductivity of carbon nanotubes is very sensitive to the nanotubes' orientation, purity, defects, temperature, compactness of the specimen used in the measurement, and the measurement setup.

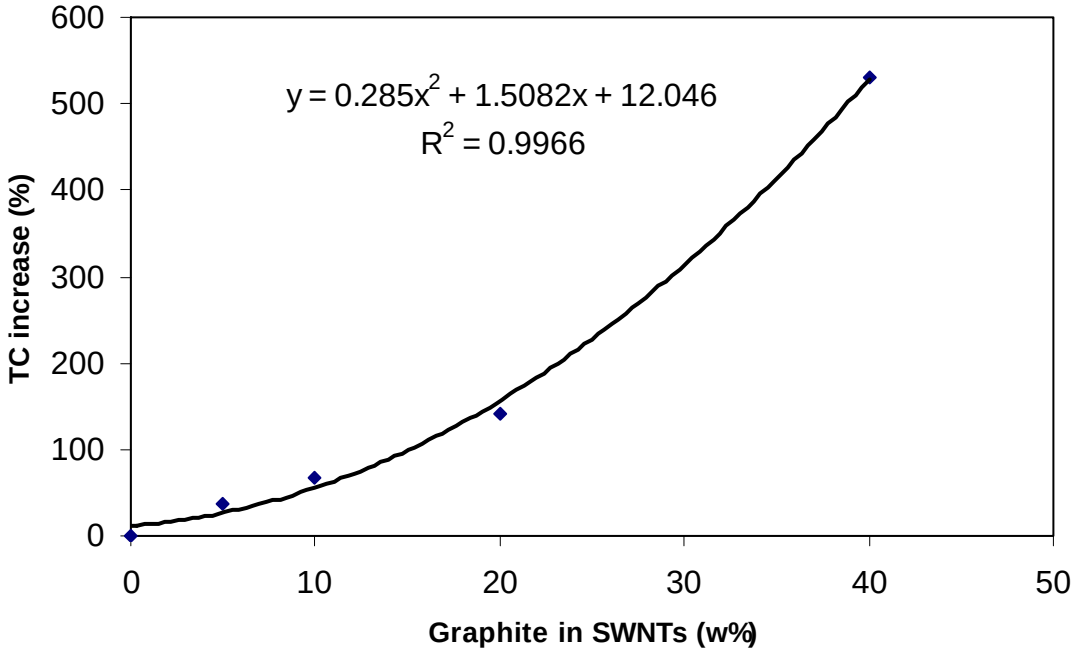

Figure 1.6 Increase in thermal conductivity as a function of graphite loading

1.2.3 DEPENDENCE ON NANOTUBE DIAMETERS AND CHIRALITY

SWNTs, conceptually formed by rolling up a graphene sheet (Scheme 1)[27], could be classified into zigzag (n, 0) or (0,m), armchair (n, n), and chiral (n, m), depending upon the relationship between the axial direction of rolling and the unit vector describing the hexagonal lattice. While armchair tubes show true metallic properties, the other two show semiconductive properties. Statistically, one-third of as-produced SWNTs are metallic and two-thirds are semiconductive. So it is important from both scientific and technological point of view to investigate the difference in thermal conductivity of SWNTs as a function of chirality.

Thermal conductivities of the three types of SWNTs, (11, 11), (20, 0) and (10, 13) with nearly equal radii were studied using homogeneous non-equilibrium Green-Kubo method based on Brenner potential.[28] The results, presented in Figure 1.7, suggest that the thermal conductivity of SWNTs is not related only to the temperature, but also to their chirality. From these calculations the highest thermal conductivity was obtained for the zigzag nanotube, while the armchair and chiral nanotube gave a lower value. The explanation of this behavior was based on the presence of excess strain along the circumference of armchair and chiral nanotubes that could limit the phonon mean free path and therefore lead to lower thermal conductivity.

On the other hand, the results of Cao et al.[29] on thermal conductivity of a perfect isolated zigzag SWNT (6,0) considering three-phonon Umklapp process suggest that the thermal conductivity is higher for SWNTs with smaller diameters as compared to the

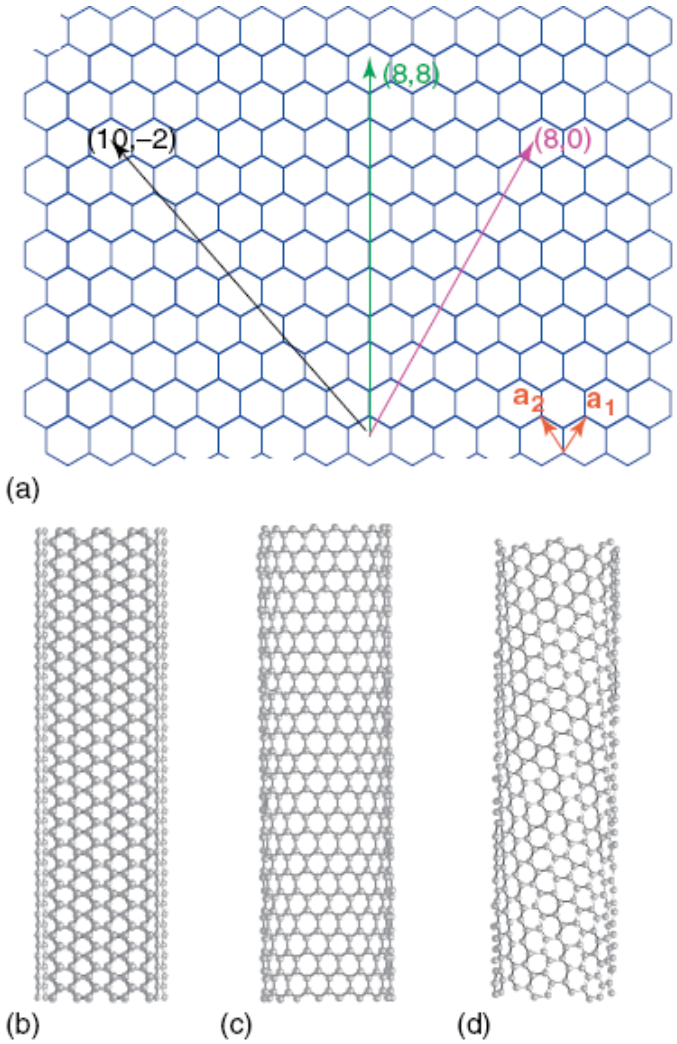

Scheme 1.1 (a) The two chiral vectors a_1 and a_2 on a graphene sheet; (b) an armchair SWNT (8,8); (c) a zigzag (8,0); and (d) a chiral SWNT (10,-2). (From Ref. [27])

tubes with larger diameters. In addition, their resuls show that the thermal conductivity at 300 K is approximately inversely proportional to the SWNT diameter. This phenomenon is considered to be caused by the phonon group velocity and the Umklapp process. The average phonon group velocity would decrease as the SWNT's diameters increase. Furthermore, at a given temperature, the probability of the Umklapp process is higher in a SWNT of a larger diameter.

As these studies suggest, a relatively small differences in the diameter and configuration of CNTs could lead to a significant change in their thermal conductivity. Therefore, synthesis of uniform CNTs or separation of metallic from semiconductive tubes is highly desirable in order to achieve higher performances at the bulk level.

1.2.4 DEPENDENCE ON NANOTUBE LENGTH AND DEFECTS

Using the empirical bond order dependent force field, Che et al.[30] studied the dependence of nanotubes thermal conductivity on length, conformational defects and vacancies. They demonstrated that the phonon mean free path was the limiting factor for the thermal conductivity of carbon nanotubes. For a (10, 10) SWNT, five different system sizes with 400, 800, 1600, 3200 and 6400 atoms were investigated. The results, presented in Figure 1.8, show that, as the simulation system size gets larger, the theoretically predicted value approaches 2980 W/mK along the tube axis at around 10 nm. Above this value thermal conductivity is independent of system size.

In addition to the different length, all of the synthetic methods produce carbon

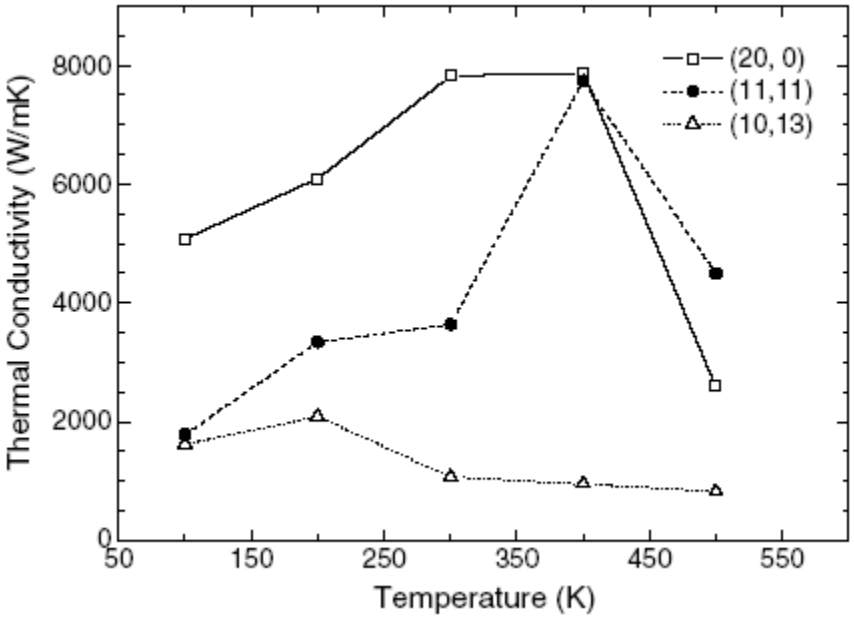

Figure 1.7 Thermal conductivities of three types of SWNTs with equal radii, zigzag – open square; armchair – solid circles; chiral – open triangles (From Ref. [28])

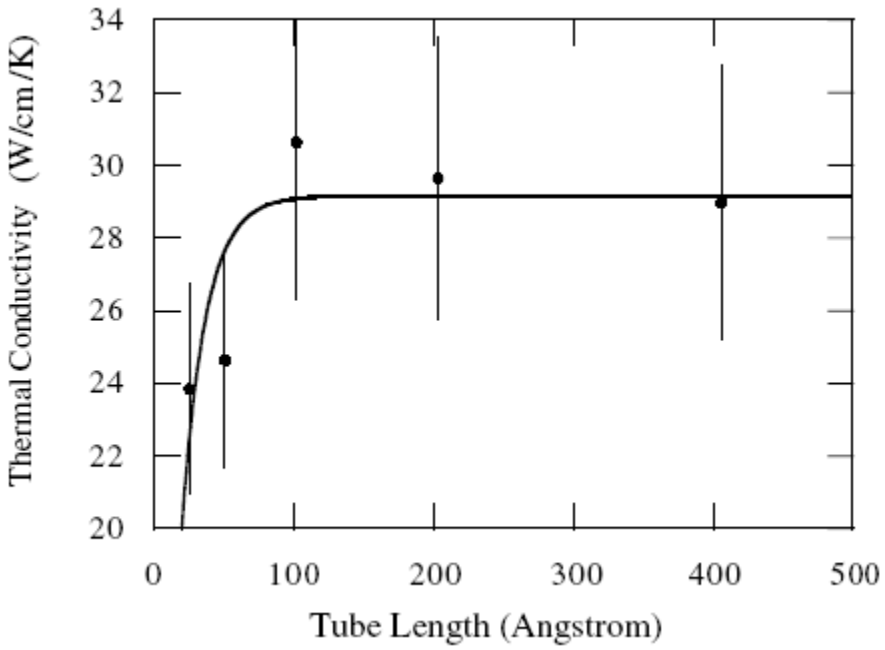

Figure 1.8 Thermal conductivity of nanotubes dependence on length (From Ref. [30])

nanotubes with various conformational defects (those where four hexagons change into two pentagons and two hexagons) and vacancies. The dependence of thermal conductivity on the concentration of these defects is presented in Figure 1.9 (a) and (b). The calculations show that the thermal conductivity decreases as the vacancy concentration increases. However, surprisingly the vacancies in carbon nanotubes are not much more influential than in diamond. This is probably due to the fact that the strong valence double bond network in carbon nanotubes provides effective additional channels for phonon to bypass the vacancy sites.

Similarly, conformational defects can also reduce the thermal conductivity of carbon nanotubes significantly, Figure 1.9(b). Compared with vacancies, the conformational defect is a milder form of point defect, since it does not change the basic bonding characteristics and causes much less overall structural deformation. Thus, both the rate and absolute amount of decrease in thermal conductivity of carbon nanotubes are less than those in the case of vacancies.

1.2.5 THERMAL CONDUCTIVITY OF NANOTUBES IN SUSPENSIONS

Carbon nanotubes have attracted interest not only in the solid state, but in their predicted application in nanofluids as well. Choi et al.[31] reported that the thermal conductivity enhancement for a suspension with 1.0 vol% MWNT in olefin oil (0.1448 W/mK) was 160%. Compared with other nanostructured materials, such as copper nanoparticles, the nanotubes show the highest enhancement at the same volume ratio.

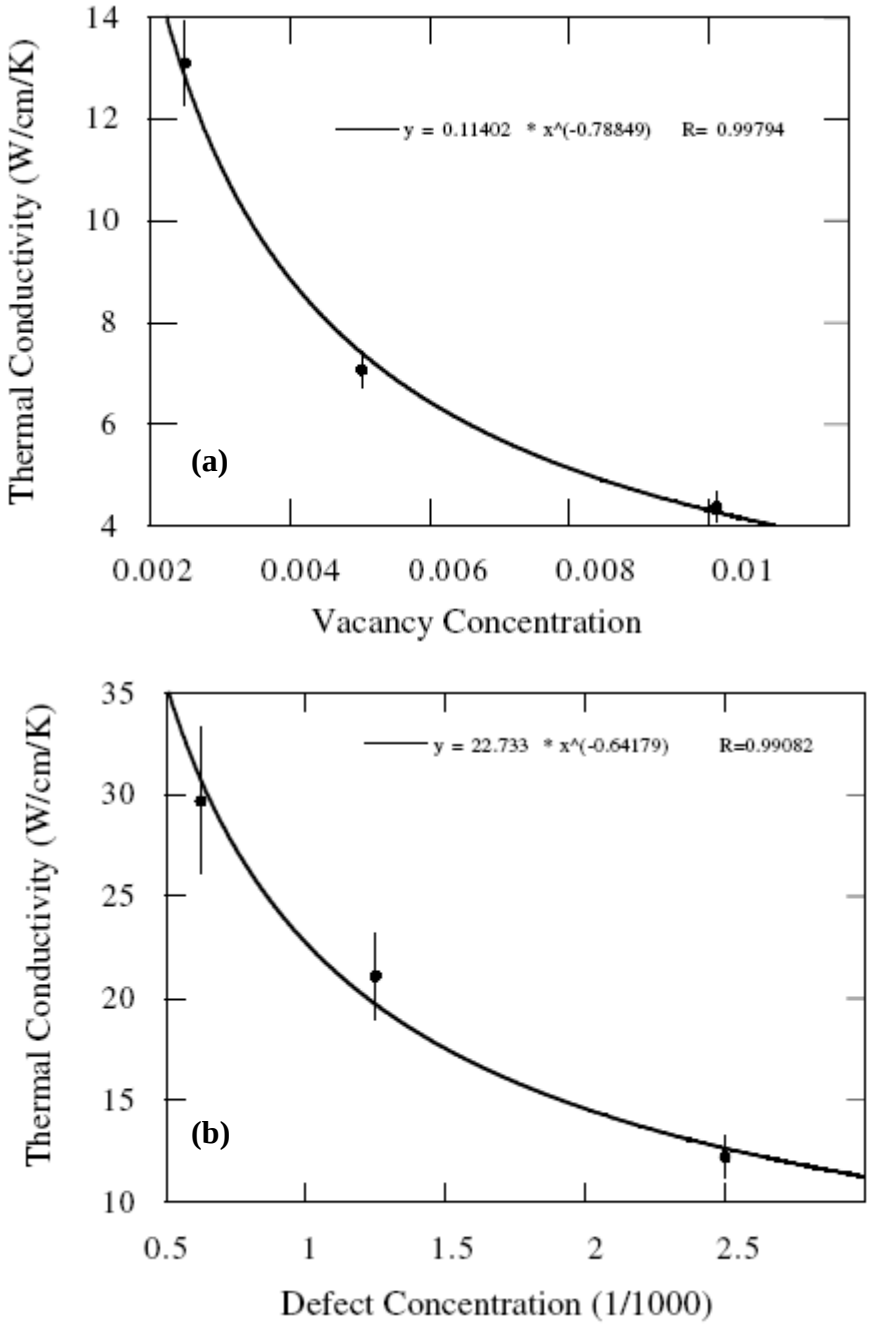

Figure 1.9 Thermal conductivity of nanotubes dependence on (a) vacancy concentration and (b) conformational defect concentration (From Ref. [30])

This suggests that carbon nanotubes in suspension could have a strong potential application as heat transfer medium. Unlike the previous authors, Xie et al.[32] observed a moderate enhancement (19.6%) for the suspension of 1.0 vol% MWNT in decene.

These relatively low thermal conductivities are the result of the very high interfacial thermal resistance. Picosecond transient measurements of CNT-surfactant micelles in water did indicate a very small interface conductance (12 MW/m^2K).[33]

In summary, simultaneous measurements of electrical and thermal conductivity showed that the electronic contribution to the thermal conductivity is negligible, thus the phonons are the major heat carriers at all temperatures. In addition, we have learned that, higher thermal conductivities of carbon nanotube could be achieved with high-quality carbon nanotunbes (without defects and impurities), and with the tube axis aligned in the direction of the heat flow.

1.3 THERMAL CONDUCTIVITY OF POLYMERIC/NANOTUBE COMPOSITES

Although thermal conductivity of CNTs has been proven to be very sensitive to their purity and morphology, such as length, diameter, defects and chirality, their relatively high experimental values at the bulk level have attracted attention for their being used in polymeric nanocomposites for different applications.

Similar to those for CNTs, different theoretical models have been used to predict the thermal conductivity of carbon nanotube based polymeric composites. For instance, according to the estimate based on 3-D potential theory and hybrid boundary node

method, the thermal conductivity of SWNT-composites cannot be higher than 0.8 W/mK. Moreover, it was suggested that this value could be achieve if and only if the difference between the thermal conductivity of CNTs and the polymeric matrix is equal or larger than 2000.[34]

On the other hand, boundary integral equation (BIE) method, based on a rigid-line inclusion model[35] was used to demonstrate that even with only 100 rigid-lines (carbon nanotubes), the effective thermal conductivity can be enhanced by 57% compared with that of blank polymer matrix and can reach 343% for 1000 rigid-lines. In addition to the relatively large enhancement, there was a non-linear relationship between the thermal conductivity of nanocomposites and the CNT loading, which is in good agreement with the experimental results. The length of CNTs was also found to be an important parameter in achieving highly conductive nanocomposites, implying that the longer the nanotubes the higher the thermal conductivity.

However, most of the experimental results on polymeric/nanotube composites showed much lower thermal conductivity than that predicted by theoretical calculations. It was suggested that this discrepancy could be attributed to defects, the interfacial resistance between nanotubes, and surrounding polymer matrix, as well as to the structure of regions close to the tube surface.[36] Molecular dynamics simulations on (5,5) armchair CNT-octane predicted an interfacial thermal resistance equivalent to the resistance of approximately 5 – 15 nm thick layer of low thermal conductivity matrix material. To minimize this resistance, the authors suggested either increasing the filler aspect ratio or

covalently attaching the polymer chains to the nanotubes in an optimum degree of covalent link density.

A more complex evaluation of the interface effect on the thermal conductivity enhancement in CNT-composites was carried out by Nan et al.[37] with the help of effective medium approach (EMA). This model takes into consideration the tube diameter, aspect ratio and volume fraction, the interfacial thermal resistance, as well as the differences in filler-polymer thermal conductivity. The results indicated that the thermal conductivity of polymer-carbon nanotube composites decreased dramatically due to the interfacial thermal resistance, which was close to, or larger than 8×10^{-8} m^2K/W. Another important observation from these simulations was that as filler, SWNTs might be worse than MWNTs as their smaller diameter could cause larger interfacial thermal resistance.

Although theoretical simulations have their own limitations they did not predict impressive improvements in the thermal conductivity of polymeric/carbon nanocomposites. However, several groups have developed carbon nanotube-based polymer composites to investigate their thermal properties. Different types of CNTs (SWNTs and MWNTs) from different synthetic methods, with different purities and morphology were incorporated into different polymeric matrices (from thermoplastic to elastomers, and thermosets). In order to improve the heat transfer in the nanocomposites the modification of the tube-matrix interface was also intensively investigated. In addition to all these variables, different methods have been used to measure thermal

conductivity of these composites. In these circumstances, it seems difficult to directly compare the results.

In order to present an overall picture on what has been achieved thus far in the field, we use here the following formula to estimate the enhancement in thermal conductivity relative to the blank polymer:

$$\%\text{enhancement} = 100x\ \Delta\kappa(T)/\kappa_0(T),$$

where $\Delta\kappa(T) = \kappa_c(T) - \kappa_0(T)$ with κ_c and κ_0 denoting the thermal conductivity of composite and matrix, respectively.

Thermoplastic nanocomposites - Kashiwagi et al.[38] used a line-source method to study thermal conductivity of a MWNT-polypropylene composite prepared by melt blending, and found that the thermal conductivity at room temperature for the composite with 5% MWNT by weight was only 0.3 W/mK (about 25% enhancement from the blank polymer). A much more significant enhancement was observed when the MWNT (10-20 nm in diameter and 5-20 μm in length) were homogeneously dispersed into the polystyrene matrix with the help of a surfactant (polyethylene glycol).[39] In that case, the room-temperature thermal conductivity of the 5 wt% MWNT-polystyrene film prepared by solution spraying and measured through transmission thermal inspection – flash was enhanced almost 120%, or about 202% (~0.43 W/mK) when the MWNT loading was 10% by weight. These authors considered the large enhancement in thermal conductivity a direct result of both surfactant-assisted dispersion and solution spray methods, which

have the advantage of producing uniform dispersion of the MWNTs in the matrix and uniform films due to the fast solvent evaporation (thus less sedimentation and aggregation of CNTs). It is also important to point out that the increase in thermal conductivity with increasing nanotube loading was not as dramatic as the increase in electrical conductivity. Moreover, as shown in Figure 1.10, unlike the electrical conductivity the percolation threshold in thermal conductivity was not observed, a behavior seen by other researchers as well. The lack of thermal percolation in carbon nanotube composites is related to the relatively small thermal conductivity contrast between filler and matrix (the matrix being the dominant path of thermal flow), to the contact resistance between fillers, and to the interfacial thermal resistance between fillers and matrix.

As described earlier, the purity of CNTs plays an important role in the physical properties of carbon nanotubes. In order to overcome this limitation, purified MWNTs, instead of as-produced MWNTs have been used to develop polymeric composites. Wang et al.[40] used purified MWNTs (30 nm in diameter and 50 μm in length) to prepare MWNT-palmitic acid (PA) composites by melting technique. And it was found a 36% enhancement in thermal conductivity, at a loading of 5% MWNT by weight.

Similarly, Kim et al.[41] used a biodegradable synthetic aliphatic polyester (poly(L-lactide) – PLLA) to prepare carbon-nanocomposites. A direct comparison between the nanocomposites prepared by melt compounding and covalent functionalization of the tube surface with PLLA matrix showed a thermal conductivity of 0.42 and 0.41 W/mK,

respectively. This represents about 160% enhancement at 1.2 wt% MWNT loading, which is by far the best result obtained for MWNTs dispersed in thermoplastic matrices. SWNTs produced by different methods, such as HiPCO, CoMoCAT or arc-discharge, have also been investigated in different thermoplastic matrices. For instance, Guthy et al.[42] took advantage of the coagulation method to develop a SWNT poly(methylmethacrylate) composite with random SWNT orientation. There were two aspects found in this study: first was a gradual increase in thermal conductivity with increasing carbon nanotube loading, and the second was a saturation level of the thermal conductivity at 0.45 W/mK (125% enhancement) when the composition reached 9% SWNT by volume. The saturation was ascribed to the poorly dispersed nanotubes at higher loading, while the relatively low thermal conductivity was explained by a reduction in the aspect ratio of SWNT during the composite processing. Using the same polymeric matrix, poly(methylmethacrylate), Bonnet et al.[43] studied thermal conductivity of SWNT-PMMA composites using a double guarded plate technique. Their room temperature conductivity of thick films (100 μm) obtained from solution casting was 0.35 W/mK (75% enhancement) for the composite with 7 vol% SWNTs.

It was assumed that the reduced values in thermal conductivity were a result of poor dispersion. Thus, Peters et al.[44] used the surfactant SDBS-4-dodecylbenzenesulfonic acid to disperse SWNTs into the polystyrene. Although they were not able to fully remove the surfactant from the final composite, the composite with 30% SWNTs by weight exhibited 360% enhancement in the room-temperature thermal conductivity. In addition to the relatively large increase in thermal conductivity it was also observed a

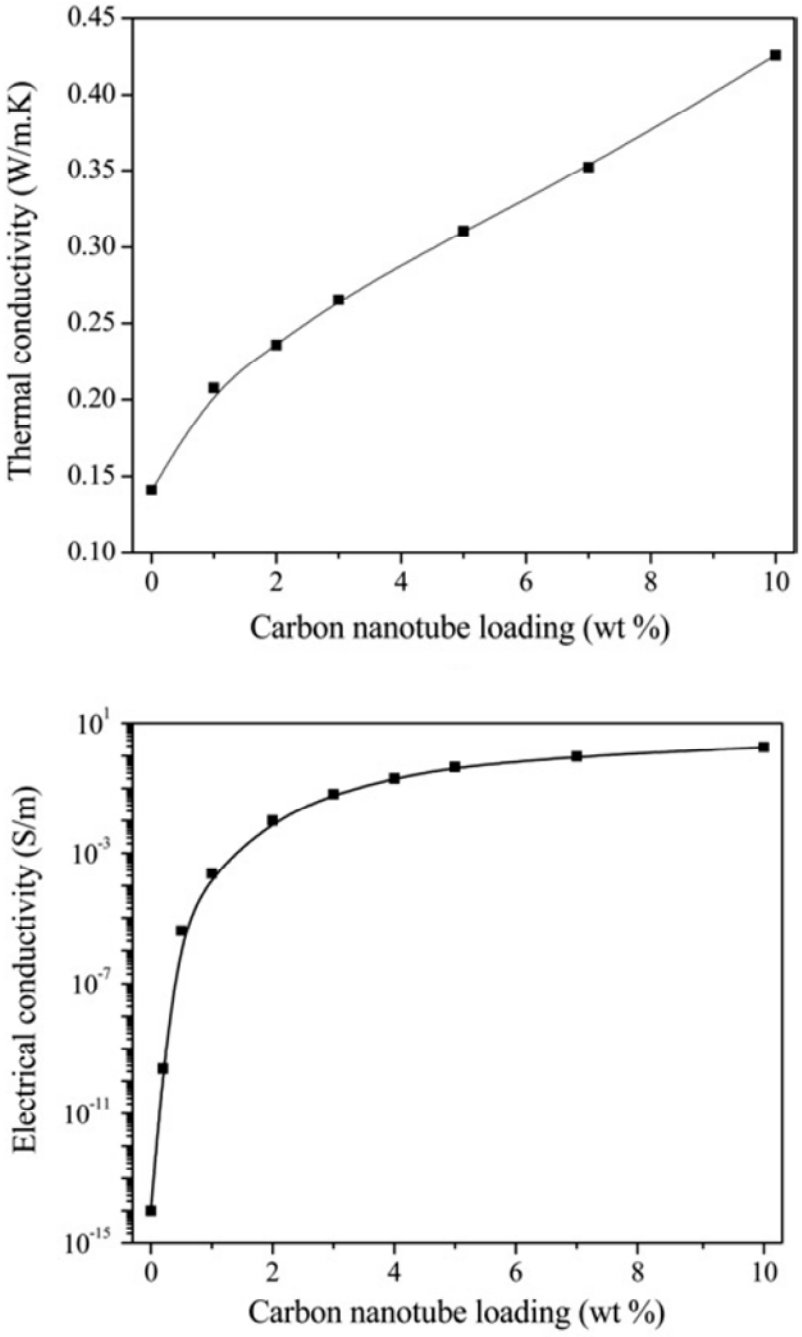

Figure 1.10 Variation of thermal conductivity and electrical conductivity of nanocomposites as a function of nanotube loading (From Ref. [39])

maximum in thermal conductivity at the glass transition temperature (Figure 1.11), a phenomenon ascribed to the increase in Kapitza resistance. In other words, the modulus of a molten polymer is orders of magnitude lower than the modulus of glassy polymer, and hence a decrease in thermal conductivity as the polymer goes through its glass transition temperature. A lower enhancement was observed by Chen et al.[26], who dispersed SWNT in polystyrene with any dispersing agent. The room-temperature thermal conductivity measured by the flesh method has increased with increasing SWNT loading, reaching 0.25 W/mK at 10wt % SWNTs (73% enhancement).

To reduce the interfacial phonon scattering Haggenmueller et al.[45] incorporated SWNTs into the crystalline high density polyethylene matrix. The 600% enhancement in thermal conductivity for the composite with 20 vol% SWNT was ascribed to the crystallites nucleating at SWNT-polyethylene interface, which reduced the interfacial phonon scattering.

Elastomers nanocomposites – owing to their flexibility, elastomers like polyurethanes have been used in carbon nanotube composites. Abdullah et al.[46] studied the thermal conductivity of MWNT thermoplastic elastomer (polyurethane) composite and found that it could reach 0.26 W/mK (86% enhancement) with only 3% MWNTs by weight. A much higher conductivity was obtained when the host matrix was silicon elastomer of high thermal conductivity.[47] As shown in Figure 1.12, at a loading of 3.8 wt% carbon nanotubes (a mixture of SWNTs and MWNTs) thermal conductivity was around 1.8 W/mK (65% enhancement), just slightly higher than carbon black.

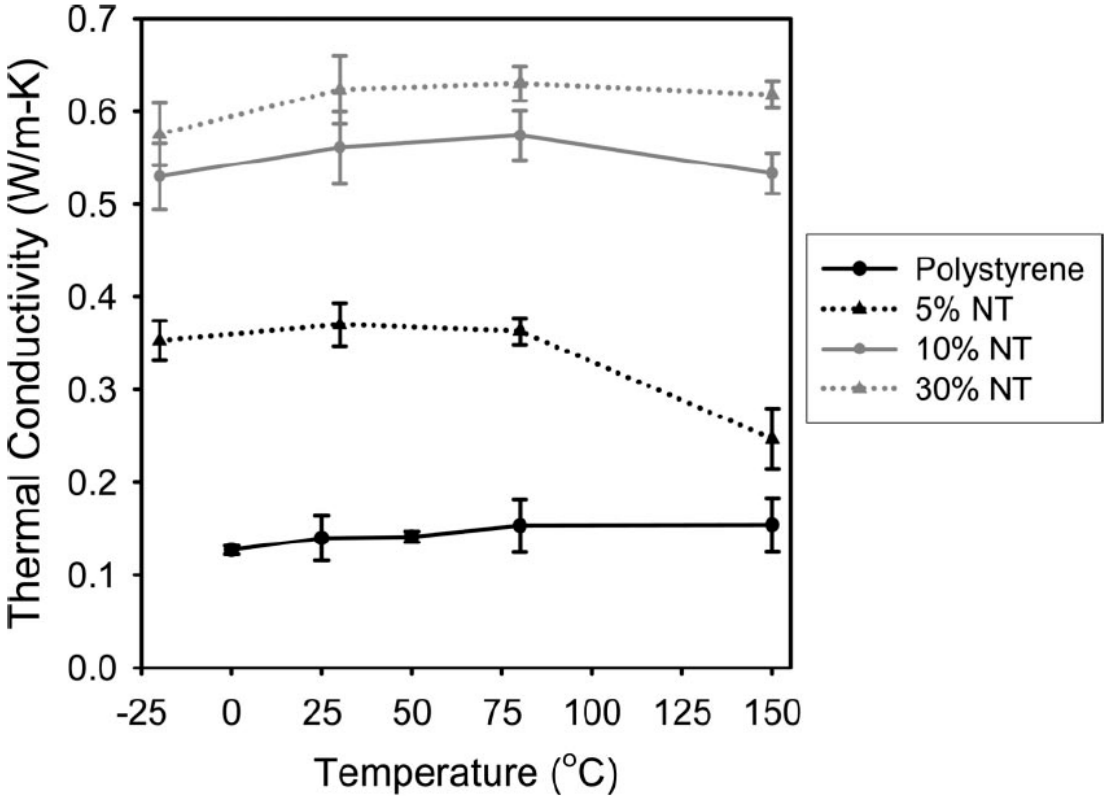

Figure 1.11 Thermal conductivities as measured using modulating temperature cycle around a single temperature (From Ref. [44])

It has been considered that the marginal enhancement in thermal conductivity of carbon nanotube composites is a result of the tube-tube interfacial thermal resistance. In order to overcome this limitation, Huang et al.[48] developed a method in which all CNTs are aligned from one surface to the other with all of the CNT tips revealed on both surfaces. A typical SEM image of these 0.3 mm long arrays is shown in Figure 1.13a. Once obtained, these well-aligned CNT arrays were immersed into both thermally conductive and low thermal conductive silicone elastomer solutions to prepare the final nanocomposite with 0.4 vol% CNTs, whose alignment was maintained (Figure 1.13b). According to a direct comparison between the thermal conductivity of aligned and dispersed CNTs in highly conductive silicone elastomer, the aligned composites were more conductive (1.21 W/mK and only 0.59 W/mK for the dispersed one at the same loading of nanotubes). On the other hand, when a low thermal conductive elastomer was used, the enhancement was about 280% compared to just 120% in the case of high conductive elastomer (Figure 1.14 - inset). Figure 1.14 showing both aligned and dispersed CNTs illustrates that with only a very small fraction of aligned CNTs the enhancement in thermal conductivity is relatively high, much higher than those loaded with dispersed CNTs. The method is very promising and the thermal conductivity can be further improved if ways to increase the volume fraction of CNTs as well as the arrays/composite density will be developed.

With the same goal, of reducing the interfacial phonon scattering, which is considered to be the bottleneck in developing carbon nanocomposites with superior thermal conductivity, Cai el al.[49] elaborated a latex technology. In this method the

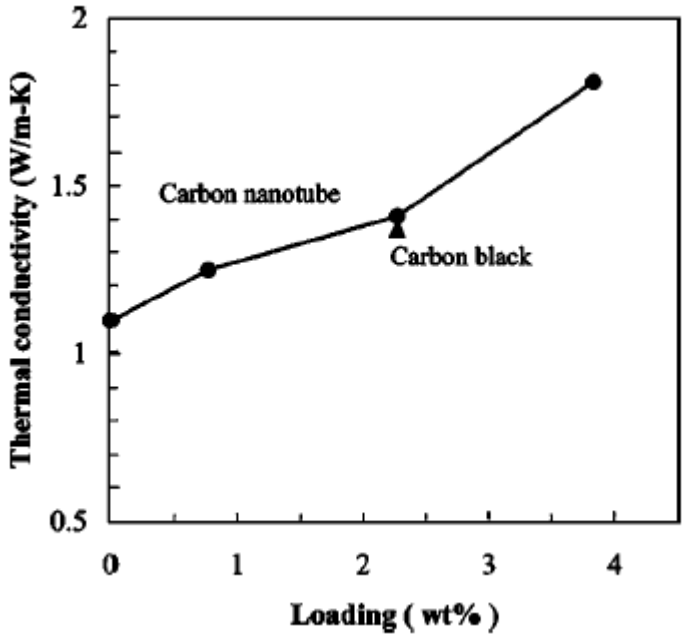

Figure 1.12 Measured thermal conductivity of the silicone elastomer/carbon nanotubes composites at 45°C as a function of nanotube loading (From Ref. [47])

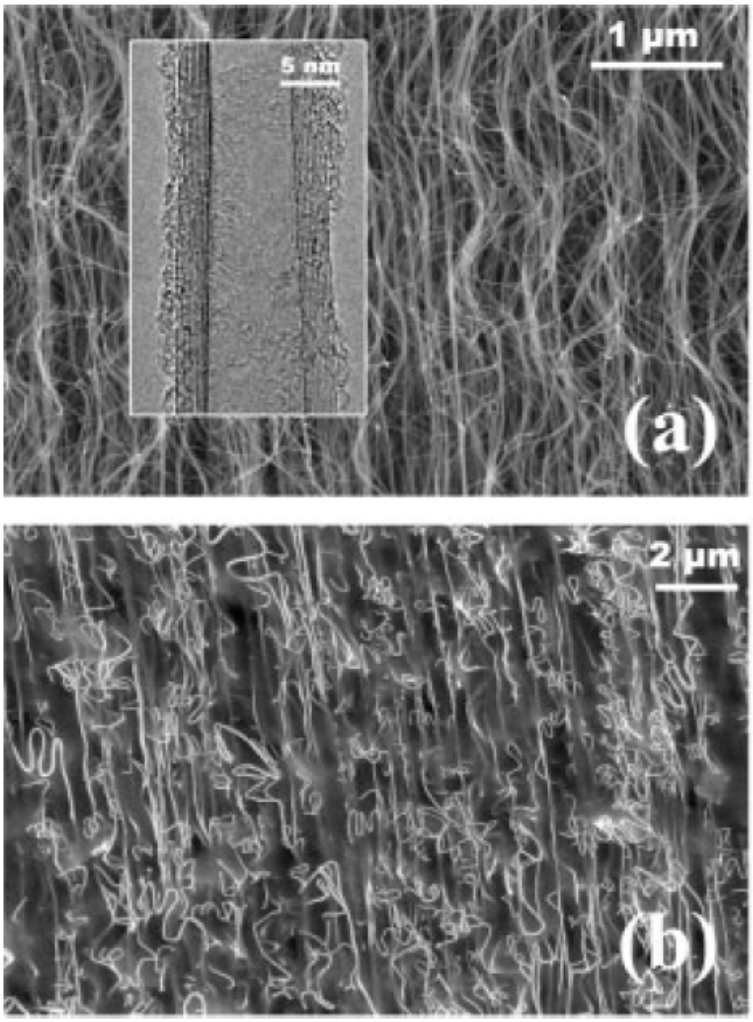

Figure 1.13 SEM images of a CNT array and a CNT array composite. a) Side view of an aligned CNT array. The inset is a HRTEM image of a typical CNT showing eight layers. b) Side view of the aligned CNT composite film, showing that the CNTs still remain aligned in the composite (From Ref. [48])

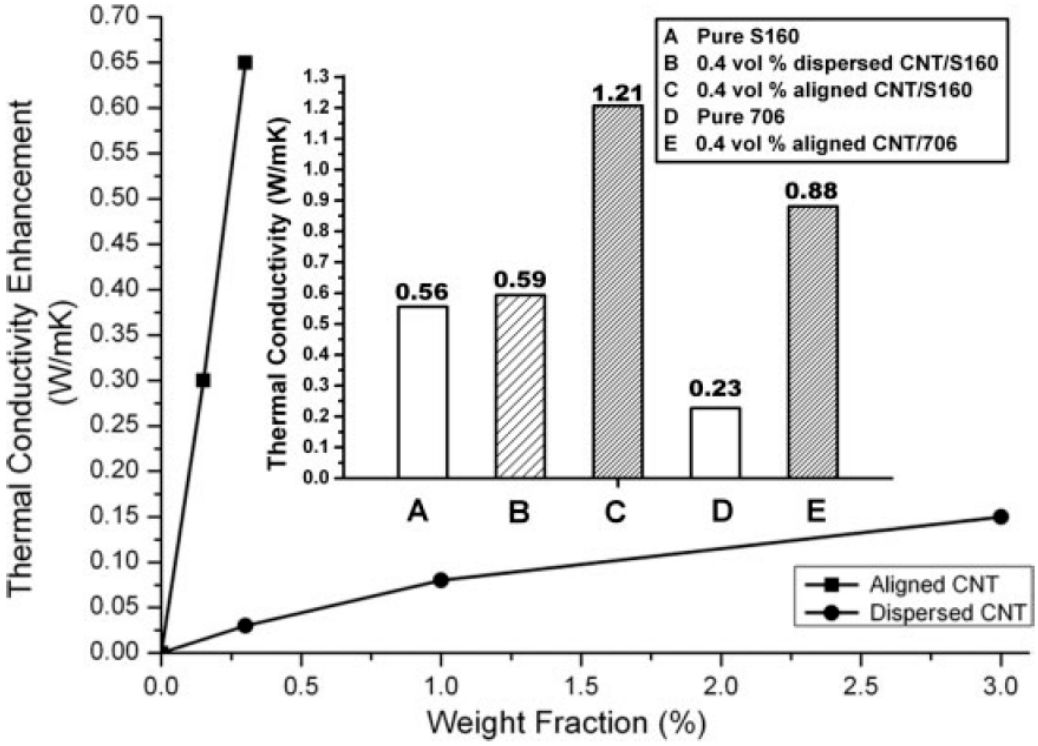

Figure 1.14 The enhanced values of thermal conductivity κ vs. weight fractions of the CNTs. The aligned CNT array composites have an enhancement of 0.65 W/mK with only a 0.3 wt% loading. Comparably, the enhanced κ of the dispersed CNTs at the same loading of 0.3 wt% was only 4.6 % of that of aligned CNTs. The inset is a comparison of measured κ values of different samples. S160 – thermally conductive silicone elastomer, 706 low conductive silicone elastomer (From Ref. [48])

aqueous colloidal suspension of MWNT-SDS (sodium dodecyl sulphate) was mixed with the solution of semicrystalline polycaprolactone-base polyurethane. The relatively large increase in thermal conductivity (210%) for a 3 wt% MWNT based composite was considered to be the result of the continuous CNT-rich phase existing in the interstitial space among the latex particles and the crystallites nucleation at the CNT-polymer interface. Compared to the polyurethane-MWNT, an amorphous polymer presented earlier by Abdullah[46], here the thermal conductivity was much higher due to the formation of the crystallite at the interface which is going to reduce the interfacial thermal resistance.

Thermosets nanocomposites – one of the most intensive studied polymeric matrixes is epoxy resin, perhaps due to its wide application in the electronics industry. Biercuk et al.[50] used pristine SWNTs (1.1 nm in diameter and lengths from hundreds of nm to microns) to increase the thermal conductivity of industrial epoxy. They obtained thermal conductivity value of ~0.5 W/mK (150% enhancement) for the SWNT-epoxy composite with only 1 wt% SWNT loading at room-temperature using comparative method. In contrast to SWNTs a much lower enhancement (45%) was observed when the filler was vapor grown carbon fibers (VGCFs). To further enhance the thermal conductivity of carbon nanotube-polymer composite, Choi et al.[51] used a high magnetic field to align the purified SWNTs in the SWNT-epoxy resin composite. When the composite was processed under 25T magnetic field, room-temperature thermal conductivity was ~6.4 W/mK for the composite with 3 wt% SWNTs. Comparing with the thermal conductivity of ~2.2 W/mK for the pure epoxy resin obtained under the same

conditions, the enhancement was up to ~200% (Figure 15). However, this value was only 10% higher than the one obtained for the same composite before the alignment under the magnetic field. These experiments show that magnetic field had a marginal effect on the thermal conductivity of carbon nanotube composites, unlike nanotube mat samples, in which thermal conductivities for magnetic aligned samples were five to eight times higher than that without alignment.[15,52] This might be due to the formation of SWNT bundles during the alignment processing, which would lead to a less efficient phonons transfer compared with that in nanotube mats.

Another parameter that has been considered to have a detrimental effect on the thermal conductivity of carbon nanotubes at the macroscopic level was the presence of impurities. A direct comparison was carried out by Haddon and coworkers[53], who used as-prepared SWNTs (AP-SWNT, 60% relative purity) and purified SWNTs (P-SWNT, 150 % relative purity) to prepare epoxy-nanocomposites. Thermal conductivity of these composites was measured at room-temperature by using steady-state method (FOX50 laser flash) and the thermal conductivity results of these nanotube-epoxy composites are presented in Figure 1.16. Firstly, it is observed that the maximum loading in the P-SWNT composites was twice higher than in AP-SWNT composites due to their better dispersion in the polymeric matrix. In addition to the improved processing, the P-SWNT composite displayed superior enhancement in thermal conductivity compare to its counterpart AP-SWNT composite.

Novel nanotechnologies have been explored to minimize the thermal resistance at the nanotube junctions. For instance, Du et al.[54] used a nitrogen gasification method to

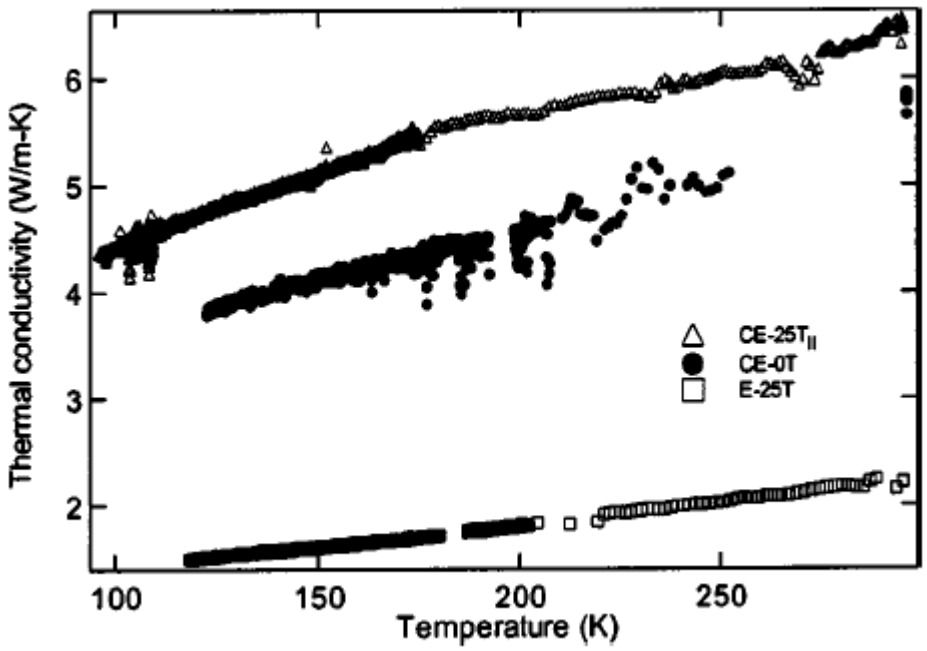

Figure 1.15 Thermal conductivity of carbon nanotubes-epoxy composites magnetically processed at 0 and 25T, compared with the epoxy control sample (also processed at 25T) (From Ref. [51])

develop a freestanding nanotube framework by removing the PMMA from a SWNT-PMMA composite. The framework thus obtained was infiltrated with a mixture of epoxy polymer and curing agent to obtain the final SWNT-epoxy composite with 2.3% SWNT by weight, whose room-temperature thermal conductivity was 0.61 W/mK (200% enhancement). It was suggested that the SWNT framework produced a bicontinuous structure with nanotube-rich phase, which favored the heat transport. The microscopic structure of these composites is presented in Figure 1.17. As shown in the optical micrograph (Figure 1.17 a) the nanotube-rich pathways connect opposite sides of the sample, while a closer inspection (Figure 1.17 b) reveals that the nanotubes are in close contact with one another within these pathways.

Another method used to minimize the thermal resistance at the nanotube junctions was developed by Ivanov et al.,[55] who fabricated millimeter long, vertically aligned carbon nanotube arrays (VANTAs) containing mixtures of single and few-walled carbon nanotubes. Then, the arrays were vacuum impregnated with epoxy resin to obtain a VANTAs-epoxy composite with 8 vol% VANTAs. The thermal conductivity of this nanocomposite was ~5.5 W/mK (more than 2600% enhancement from the neat polymer 0.2 W/mK), a value that exceeds the thermal conductivity of those phase-changing thermal interface materials used in microelectronics.

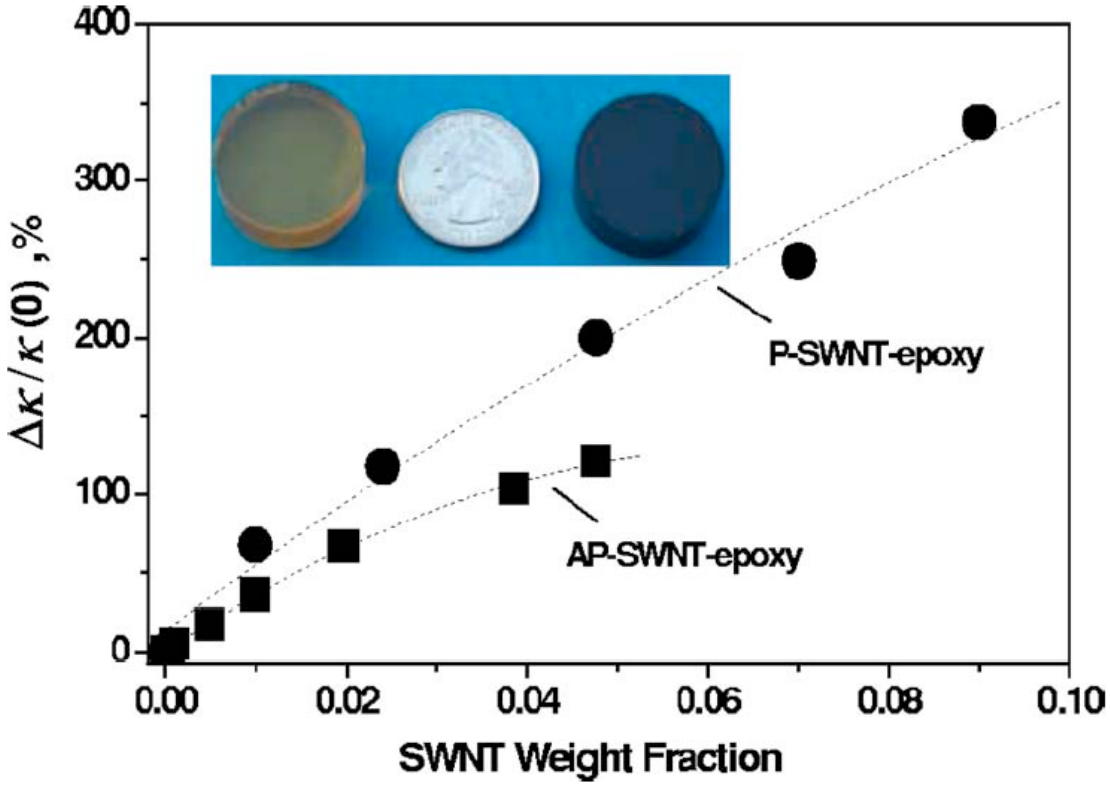

Figure 1.16 Thermal conductivity enhancement of SWNT-epoxy composites as a function of AP and P-SWNT loading. The inset shows 1 in diameter disk samples of neat epoxy and SWNT-epoxy composites (From Ref. [53])

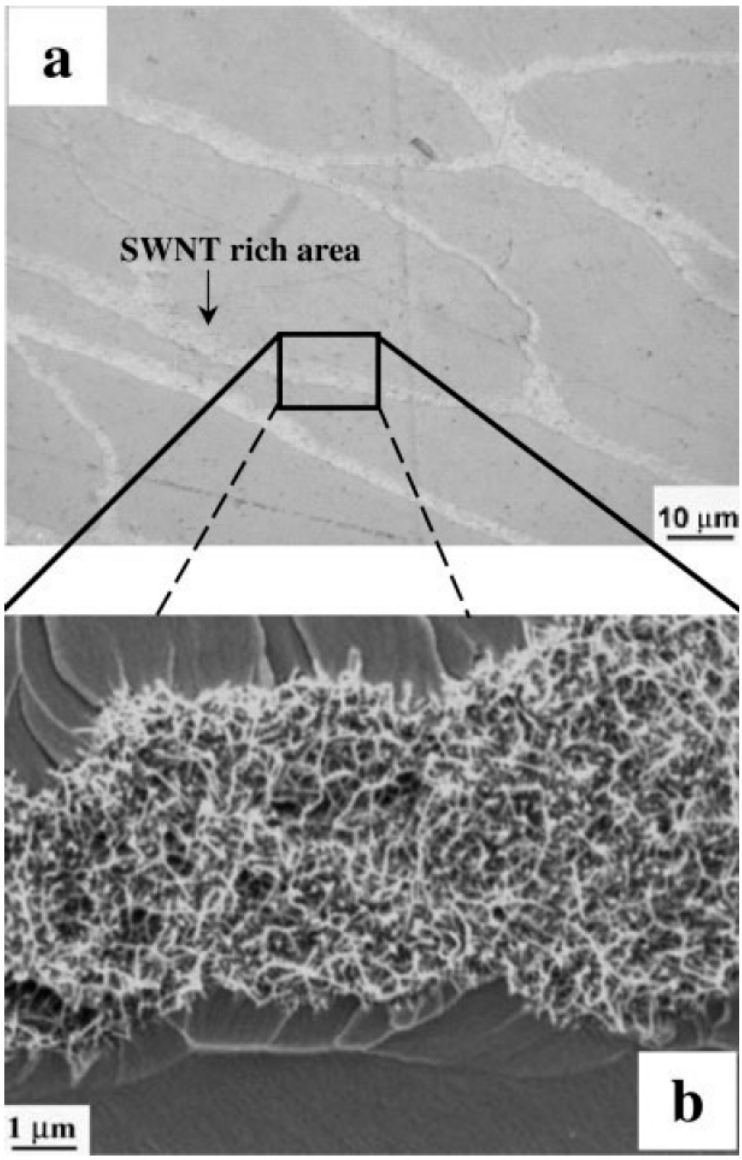

Figure 1.17 (a) Optical and (b) SEM image of the SWNT/epoxy composite fabricated by the infiltration method (From Ref. [54])

In conclusion, extensive effort has been made in order to take advantage of the large thermal conductivity of CNTs. As presented in this section, there are two examples of CNT-composites that have reached thermal conductivities close to those materials currently used in electronics industry. One is the epoxy composite with 3% SWNT by weight and a thermal conductivity of 6.4 W/mK and the other one is the VANTA-epoxy composite with 8 vol% VANTA (5.5 W/mK). Therefore, we could say that even most of the composites are still far away from real applications, present studies are very important, suggesting that the ultimate realistic assembly of CNTs for high thermal conductive materials would be made of long, continuous CNTs to minimize the thermal resistance at the nanotube junctions; of highly packed CNTs with minimized bundling and with few defects and high graphitic order for long-range phonon transport.[55]

1.4 EFFECTS OF NANOTUBE FUNCTIONALIZATION

It was deemed that the bending of carbon nanotubes inside the matrix, due to the presence of defects, and the acoustic phonon mismatch which are considered to be the primary cause for only modest increase in thermal conductivity, can be addressed by introducing a better interfacial bonding between the CNTs and the polymer matrix, such as chemical functionalization. Perhaps this could be engineered by matching the functional groups on the surface of CNTs with the chemical structure of the polymer.

Chemical functionalization is a technique frequently employed to disperse carbon nanotubes in various solvents. The functionalization changes the carbon atom bond from

sp^2 to sp^3 hybridization. Subsequently the geometry of these atom changes, where the bonded carbon atoms are "raised" away from the nanotube surface, which may be seen as a defect that could be a phonon scattering path.

Theoretical investigations carried out by Padgett et al.[56] showed that random chemical functionalization of phenyl groups to as little as 1.0% of the carbon atoms on a carbon nanotube reduces the thermal conductivity by more than a factor of 3 (Figure 1.18). Moreover, the faster convergence suggests a shorter phonon scattering length with increasing the degree of functionalization. Therefore, these results indicate that reducing the interfacial resistance by chemical functionalization may severely compromise the intrinsic thermal properties of the carbon nanotubes. Similar results have been reported by Shenogin et al.[57], who simulated the impact of chemical bonding between carbon nanotubes and the polymer matrix on thermal conductivity using molecular dynamics simulation method. It was shown that the thermal conductivity of carbon nanotubes remains nearly constant at ~1700 W/mK once the carbon atoms are functionalized more than 1%. The authors have also observed that the functionalized carbon atoms on the tubes were different from those unfunctionalized carbon atoms in terms of bonding strength and geometry. Differences which will probably act as phonon scattering centers and lead to reductions in thermal conductivity.

However, Clancy et al.[58] used a multi-scale modeling approach to predict that end-grafting linear hydrocarbon chains onto SWNTs via covalent bonds will lead to an increase in thermal conductivity of the nanocomposite due to the decrease of interfacial thermal resistance (Kapiza resistance). The interfacial thermal resistance has been shown

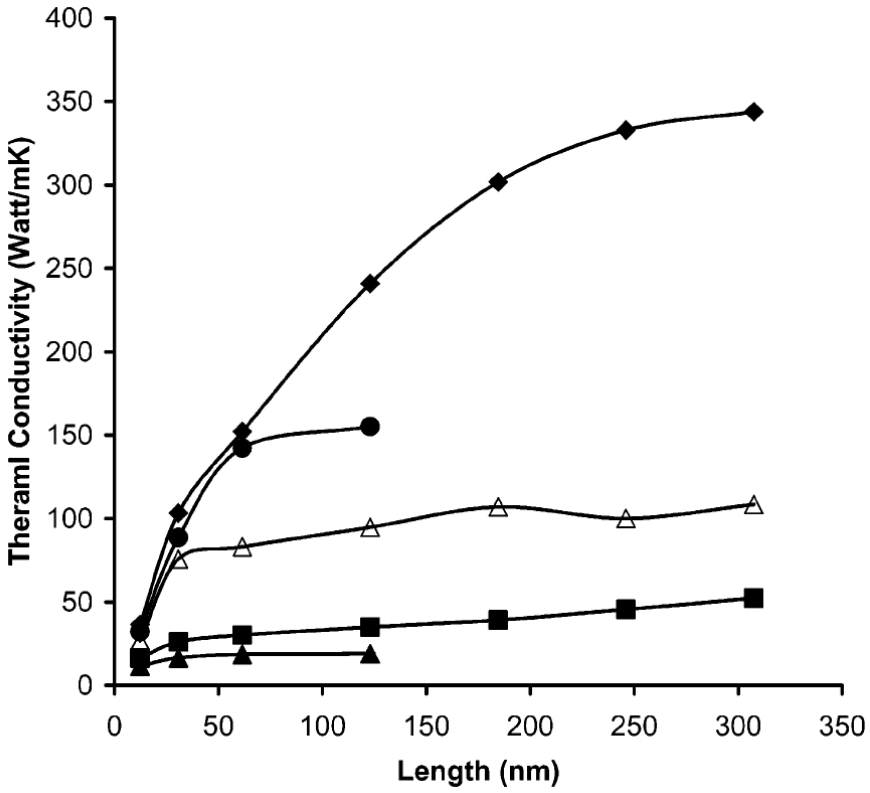

Figure 1.18 Thermal conductivity versus nanotube length for various degrees of functionalization. Diamonds 0%, circles 0.25%, open triangles 1%, squares 5%, and triangles 10% functionalized (From Ref. [56])

to decrease with increasing the grafting density and the hydrocarbon chain length covalently bonded to the nanotube surface

In a good agreement with the theoretical prediction[56,57], experimental studies have shown that the non-functionalized CNTs have a greater impact on the composite thermal conductivity compare to the functionalzed CNTs. For example, Gojny et al.[59] found that the amino-functionalized CNTs did not significantly affect the thermal conductivity of the epoxy at the low filler contents, while non-functionalized nanotube composites showed a better properties. Moreover, the thermal conductivity was different for different type of CNT with the lowest enhancement for SWNTs due to their largest specific surface area (SSA), followed by DWNTs (intermediate SSA), and then MWNTs with the smallest SSA.

Similar results have been obtained in our group.[26] The thermal conductivity of SWNT-functionalized polyimide showed a consistent decrease in thermal conductivity with increasing functionalization density. The highest increase was for the 0.02 wt% SWNTs (32% enhancement) and the lowest for the 2 wt% (25% enhancement).

Although most of the simulation research indicated that the thermal conductivity of carbon nanotubes is comparable to graphite and diamond, or even higher, experimentally observed enhancements have been nearly negligible considering the large thermal conductivity of an individual SWNT (~10^3 W/mK). These unimpressive improvements are in part due to the random orientation of CNTs in the matrix (conductivity in nanotubes is directional, being much better down their long axis) and in part to the purity/morphology of the CNTs. The presence of impurities reduces not only

the phonon mean free path but also the effective concentration of CNTs in the polymeric matrix. Additionally, many other problems must be solved before CNTs can be successfully incorporated into composites. The biggest issues are due to the fact that CNTs tend to bundle together during processing, reducing their aspect ratio and increasing the interfacial resistance; to the difficulty of controlling their morphology (chirality, diameter, length) and of achieving high filling ratio (carbon nanotubes significantly increase the composite viscosity, thus not possible to process it above certain loadings); to the acoustic mismatch at the nanotube-polymer interface; to the difficulty to evaluate and compare the results from different sources; and to the high cost of their production.

1.5 BEYOND CARBON NANOTUBES

The lack in high purity and uniformity in the properties of SWNTs are the primary reasons why SWNTs are rarely used in commercial applications. Once nanotubes can be efficiently purified, separated (metallic from semiconductive) and assembled on a macroscopic scale they could become serious competition for the present materials used in the engineering industries.

Alternatively, scientists turned their attention to the more effective 2D nanomaterials such as graphene. Graphene, one-atom-thick layer of sp^2 bonded carbons, have been predicted and to a certain extent proven to exhibit unusual properties. Owing to their plate-like structure with lateral size ranging from hundreds of nanometers to

microns and thickness below 10 nm, these materials have incredibly large aspect ratio. Therefore, polymer composites containing adequately-dispersed graphene (or carbon nanosheets) may exhibit enhanced properties.

Because these materials are at their early stage of development most of the recent research activities have been focused on their production and electrical properties, therefore not much is known about their thermal properties. Recently, Balandin et al.[60] measured the thermal conductivity of a suspended single-layer graphene using confocal micro-Raman spectroscopy. The extremely high value of the thermal conductivity (up to 5300 W/mK) suggests that graphene can outperform carbon nanotubes in heat conduction.

These "graphite nanoplateles" or "carbon nanosheets" polymeric composites have already exhibited higher thermal conductivity than their pseudo-1D counterparts. For instance, Drzal et al.[61] found that the thermal conductivity of nylon-6 expanded graphite with 20 vol% filler was 4.1 W/mK, which is more than 1500% enhancement in the polymer thermal conductivity. Similarly, Haddon and coworkers[62] showed that the thermal conductivity of a "graphite nanoplatelets"-epoxy composite could reach 6.44 W/mK at 25 vol% loading, corresponding to an enhancement of more than 3000%. Figure 1.19 (a) shows the thermal conductivity enhancement of different fillers at different loadings, confirming that thermal conductivity of "graphite nanoplateles"-epoxy composites has increased with increasing the degree of exfoliation and outperforms both carbon black and SWNT. As presented in Figure 1.19 (b) the increase in thermal

conductivity was directly related to the increase in the aspect ratio of the "graphite nanoplateles".

Even higher increase in thermal conductivity was achieved by Connell and coworkers[63] in the Ulthem 1000 resin nanocomposites. As shown in Figure 1.20 the expanded graphite was found to be the most effective among various fillers, with the in-plane thermal conductivity reaching 6.7 W/mK (>3200% enhancement) in the composites containing 40 wt% graphite. Additionally, Lafdi et al.[64] studied the dependence of thermal conductivity on the size of exfoliated graphite. As presented in figure 1.21 (a) the thermal conductivity increases with the increasing graphite content, with graphite of larger size showing higher conductivity. Then, the authors have compared the results from the larger graphite size, which were the best in terms of thermal conductivity, to the carbon nanofiber composites and high heated-treated nanofiber composites (Figure 1.21 (b)). The exfoliated graphite composite proved to be superior to the both carbon fibers.

Based on these few studies we can conclude that, although at its early stage, this material has been shown much better performance at lower price than CNTs. The main challenge in this field is to exfoliate the graphite to the level of one/few graphene layers.

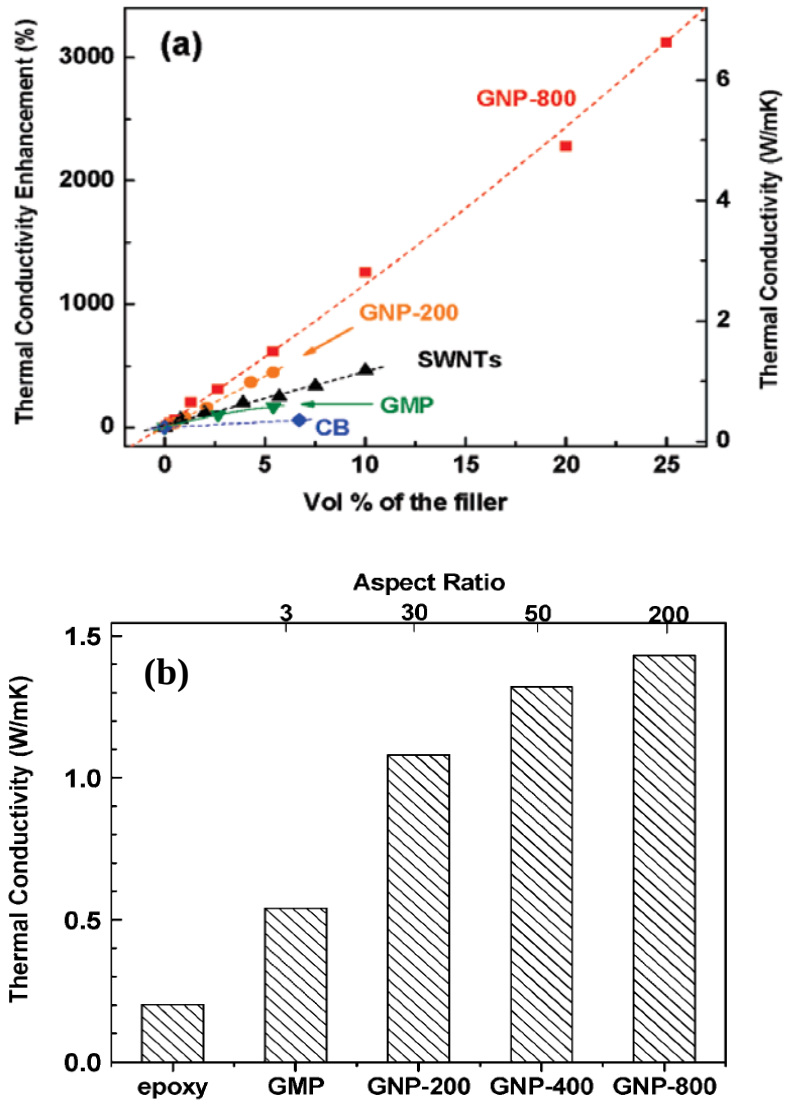

Figure 1.19 (a) Thermal conductivity enhancement of epoxy-based composites at 30°C. (b) Thermal conductivities of epoxy composites at 30°C prepared with 5.4 vol % loading. Top scale shows the average aspect ratios of the graphite micro- and nano-filler particles. Graphitic microparticles (GMP), GNPs exfoliated at 200°C (GNP-200), 400°C (GNP-400) and 800°C (GNP- 800), carbon black (CB), and purified SWNTs. (From Ref. [62])

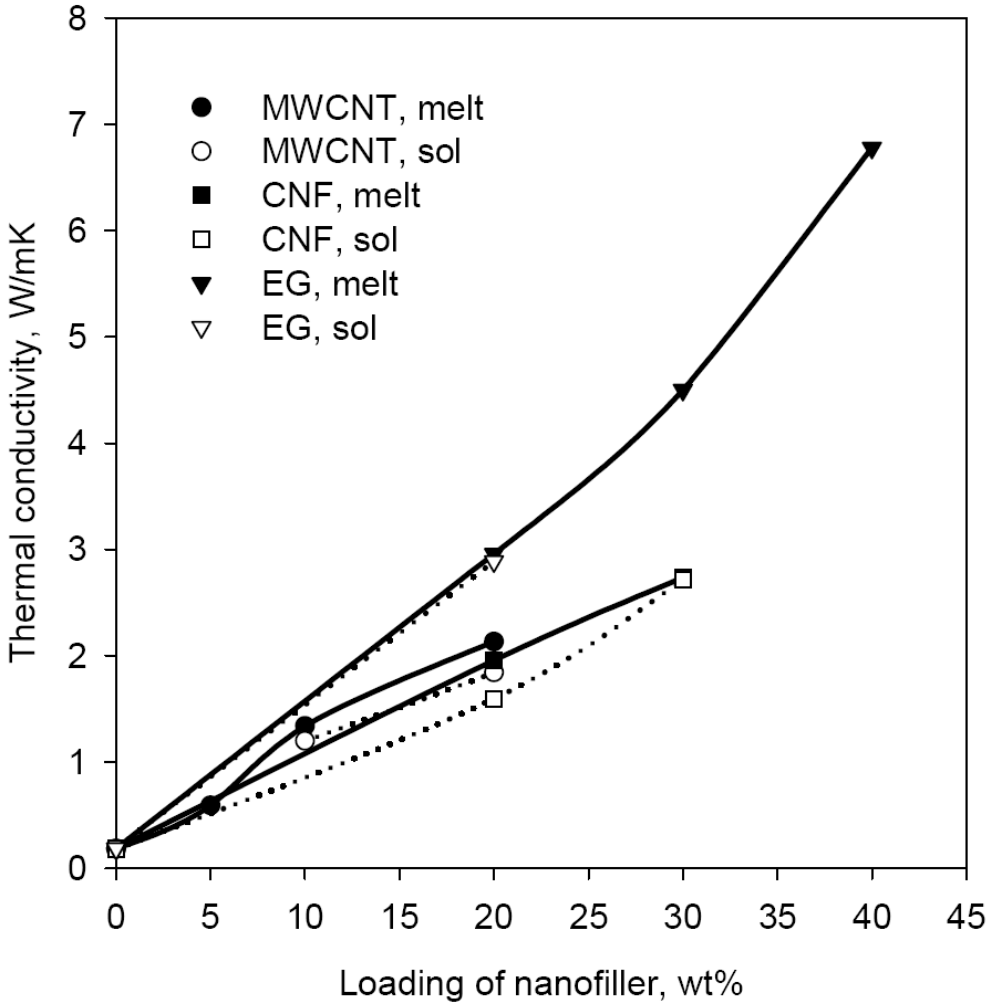

Figure 1.20 Thermal conductivity at room-temperature of molded Ultem™/nanofiller samples; measurement along direction of alignment (From Ref. [63])

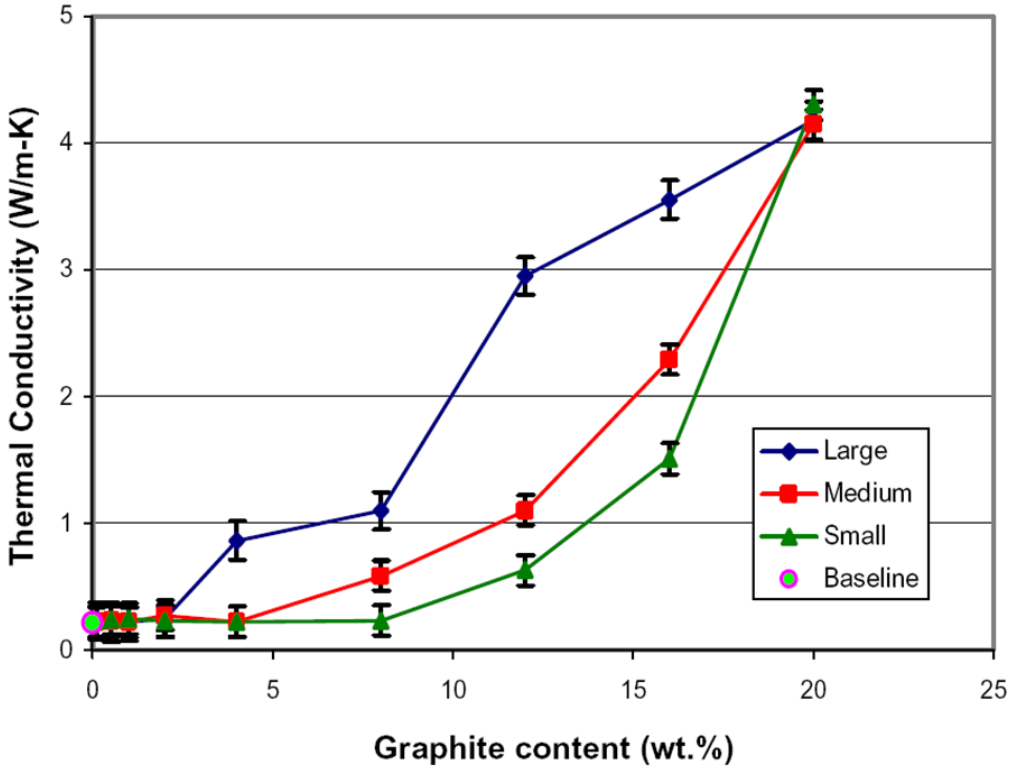

Figure 1.21 (a) Thermal conductivity of exfoliated graphite filled polymers with different graphite flake sizes as a function of the graphite content (From Ref. [64])

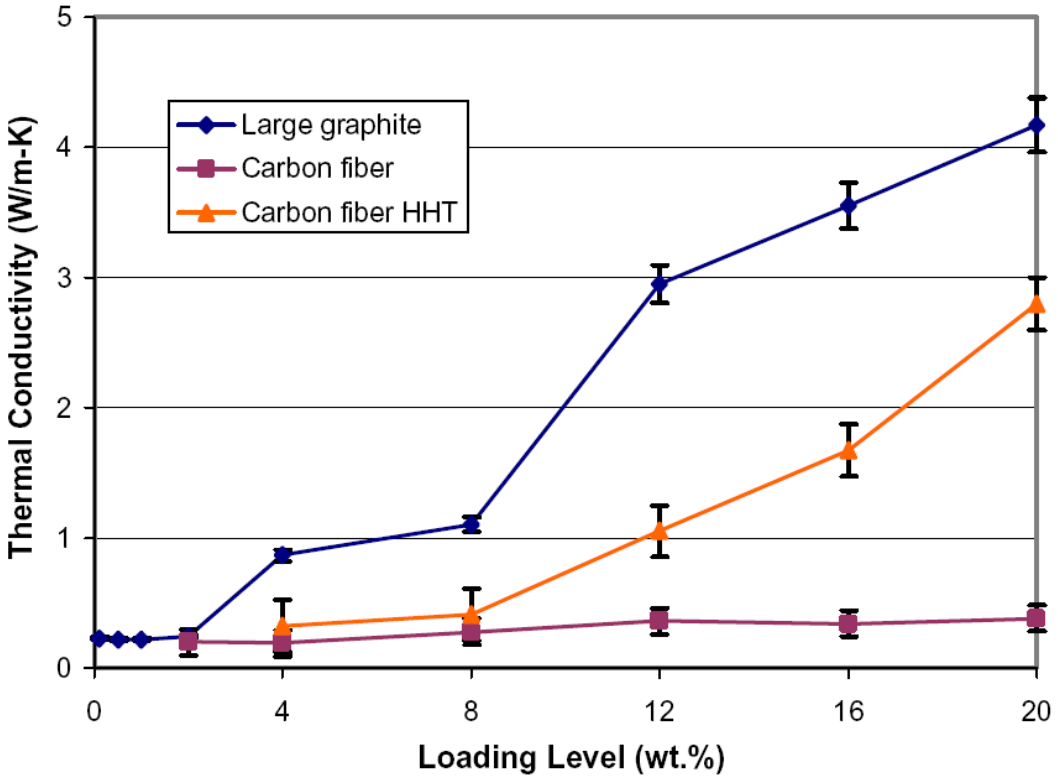

Figure 1.21 (b) Thermal conductivity comparison of graphite flake filled polymers versus carbon nanofiber and HHT carbon nanofiber composites (From Ref [64])

References

1. Avouris, P. *Acc. Chem. Res.* **2002**, *35*, 1026-1034.

2. Wei, C.; Dai, L. M.; Roy, A.; Tolle, T. B. *J. Am. Chem. Soc.* **2006**, *128*, 1412-1413

3. Tahhan, M.; Truong, V. T.; Spinks, G. M.; Wallace, G. G. *Smart Mater. Struct*. **2003**, *12*, 626-632

4. Chen, J. H..; Huang, Z. P.; Wang, D. Z.; Yang, S. X.; Li, W. Z.; Wen, J. G.; Ren, Z. F. *Synth. Met*. **2001**, *125*, 289-294

5. Frackowiak, E.; Beguin, F. *Carbon* **2002**, *40*, 1775-1787

6. Jurczyk, M. U.; Kumar, A.; Sriniasan, S.; Stefanakos, E. *Int. J. Hydrogen Energ.* **2007**, *32*, 1010-1015.

7. Pierson, H. O. *Handbook of carbon, graphite, diamond, and fullerenes, Noyes Publications*, **1993**.

8. Berber, S.; Kwon, Y. K.; Tomanek, D. *Phys. Rev. Lett.* **2000**, *84*, 4613-4616.

9. Chen, G. *Int. J. Therm. Sci.* **2000**, *39*, 471

10. Cahill, D. G.; Ford, W. K.; Goodson, K. E.; Mahan, G.D.; Majumdar, A.; Maris, H. J.; Merlin, R.; Phillpot, S.R. *J. Appl. Phys.* **2003**, *93* 793-818

11. Hone, J.; Batlogg, B.; Benes, Z,; Llaguno, M. C.; Nemes, N. M.; Johnson, A. T.; Fisher, J. E. *Mater. Res. Soc. Symp. Proc.* **2001**, *633*, A17.1.1-A17.1.12

12. Moniruzzaman, M.; Winey, K. I. *Macromolecules* **2006**, *39*, 5194-5205

13. Kim, P.; Shi, L.; Majumdar, A.; McEuen, P. L. *Phys. Rev. Lett.* **2001,** *87,* 215502-1-4

14. Yi, W.; Lu, L.; Zhang, D-L. ; Pan, Z. W.; Xie, S. S. *Phys. Rev. B* **1999**, *59*, R9015-9018.

15. Hone. J.; Llaguno, M. C.; Nemes, N. M.; Johnson, A. T.; Fischer, J. E.; Walters, D. A.; Casavant, M. J.; Schmidt, J.; Smalley, R. E. *Appl. Phys. Lett.* **2000**, *77*, 666-668.

16. Berber, S.; Kwon, Y. K.; Tomanek, D. *Phys. Rev. Lett.* **2000,** *84*, 4613-4616

17. Che, J.; Cagin, T.; Goddard, W. A. *Nanotechnology* **2000**, *11*, 65-69

18. M. Osman, M.; Srivastava, D. *Nanotechnology* **2001**, *12*, 21-24

19. Yu, C.; Shi, L.; Yao, Z.; Li, D.; Majumdar, A. *Nano Lett*., **2005**, *5*, 1842-1846

20. Pop, E.; Mann, D.; Wang, Q.; Goodson, K.; Dai, H. *Nano Lett*., **2006**, *6*, 96-100

21. Yang, D. J.; Zhang, Q.; Chen, G.; Yoon, S. F.; Ahn, J.; Wang, S. G.; Zhou, Q.; Wang, Q.; Li, J. Q. *Phys. Rev. B* **2002**, *66*, 165440-1-165440-6.

22. Hone, J.; Whitney, M.; Piskoti, C.; Zettl, A. *Phys. Rev. B* **1999**, *59*, R2514-2516.

23. Yamamoto, T.; Watanabe, S.; Watanabe, K. *Phys. Rev. Lett*. **2004**, *92*, 075502-1

24. Hone, J.; Batlogg, B.; Benes, Z.; Johnson, A. T.; Fischer, J. E. *Science*, **2000**, *289*, 1730-1733.

25. Hone, J.; Llaguno, M. C.; Biercuk, M. J.; Johnson, A. T.; Batlogg, B.; Benes, Z.; Fischer, J. E. *Appl. Phys. A* **2002**, *74,* 339-343.

26. Chen, B.; Sun,Y.-P. – unpublished results

27. Dai, H. *Acc. Chem. Res*. **2002**, *35*, 1035

28. Zhang, W.; Zhu, Z.; Wang, F.; Wang, T.; Sun, L.; Wang, Z. *Nanotech.* **2004**, *15*, 936-939.

29. Cao, J. X.; Yan X. H.; Xiao, Y.; Ding, J. W. *Phys. Rev. B.* **2004**, *69*, 073407

30. Che, J.; Cagin, T.; Goddard, W. *Nanotech.* **2000**, *11*, 65-69.

31. Choi, S. U. S.; Zhang, Z. G.; Yu, W.; Lockwood, F. E.; Grulke, E. A. *Appl. Phys. Lett*., **2001**, *79*, 2252-2254.

32. Xie, H.; Lee, H.; Youn, W.; Choi, M. J. *Appl. Phys*., **2003**, *94*, 4967-4971.

33. Huxtable, S. T.; Cahill, D. G.; Shenogin, S.; Xue, L.P.; Ozisik, R.; Barone, P.; Usrey, M.; Strano, M. S.; Siddons, G.; Shim, M.; Keblinski, P., *Nat. Mater*. **2003**, *2*, 731-734.

34. Zhang, J.; Tanaka, M. and Matsumoto, T. *Comput. Methods Appl. Mech. Engrg.* **2004**, *193*, 5597-5609.

35. Nishimura, N.; Liu, Y. J. *Comput. Mech*. **2004**, *35*, 1-10.

36. Shenogin, S.; Xue, L.; Ozisik, R.; Keblinski, P. *J. Appl. Phys.* **2004**, *95*, 8136-8144.

37. Nan, C. W.; Liu, G.; Lin, Y. and Li, M. *Appl. Phys. Lett.* **2004**, *85*, 3549-3551

38. Kashiwagi, T.; Grulke, E.; Hilding, J.; Groth, K.; Harris, R.; Butler, K.; Shields, J.; Kharchenko, S.; Douglas J. *Polymer* **2004**, *45*, 4227-4239

39. Yang, Y.; Gupta, M. C.; Zalameda, J. N.; Winfree, W. P. *Micro& Nano Lett*., **2008**, *3*, 35-40

40. Wang, J.; Xie, H.; Xin, Z. *J. Appl. Phys.* **2008**, *104*, 113537

41. Kim, H.-S.; Chae, Y. S.; Park, B. H.; Yoon, J.-S.; Kang, M.; Jin, H.-J. *Current Applied Physics* **2008**, *8*, 803-806

42. Guthy, C.; Du, F.; Brand, S.; Winey, K. I.; Fischer, J. E. *Journal of Heat Transfer* **2007**, *129*, 1096-1099

43. Bonnet, P.; Sireude, D.; Garnier, B.; Chauvet, O. *Appl. Phys. Lett*. **2007**, *91*, 201910

44. Peters, J. E.; Papavassiliou, D. V.; Grady, B. P. *Macromolecules* **2008**, *41*, 7274-7277

45. Haggenmueller, R.; Guthy, C.; Lukes, J.R.; Fisher, J.E.; Winey, K.I. *Macromolecules* **2007**, *40*, 2417-2421

46. Abdullah, S.A.; Iqbal, A.; Frormann, L. *J. Appl. Polym. Sci.* **2008**, *110*, 196-202

47. Liu, C. H.; Huang, H.; Wu, Y.; Fan, S. S. *Appl. Phys. Lett.* **2004**, *84*, 4248-4250

48. Huang, H.; Liu, C.; Wu, Y.; Fan, S. *Adv. Mater*. **2005**, *17*, 1652-1656

49. Cai, D.; Song, M. *Carbon* **2008**, *46*, 2107-2112

50. Biercuk, M. J.; Llaguno, M. C.; Radosavljevic, M.; Hyun, J. K.; Johnson, A. T.; Fischer, J. E. *Appl. Phys. Lett.* **2002**, *80*, 2767-2769

51. Choi, E. S.; Brooks, J. S.; Eaton, D. L.; Al-Haik, M. S.; Hussaini, M. Y.; Garmestani, H.; Li, D.; Dahmen, K. *J. Appl. Phys.* **2003**, *94*, 6034-6039

52. Fischer, J. E.; Zhou, W.; Vavro, J.; Llaguno, M. C.; Guthy, C.; Haggenmueller, R.; Casavant, M. J.; Walters, D. E.; Smalley, R. E. *J. Appl. Phys.* **2003**, *93*, 2157-2163

53. Yu, A.; Itkis, M. E.; Bekyarova, E.; Haddon, R. C. *Appl. Phys. Lett.* **2006**, *89*, 133102

54. Du, F.; Guthy, C.; Kashiwagi, T.; Fischer, J. E.;.Winey, K. I. *J. Polym. Sci. B* **2006**, *44*, 1513-1519

55. Ivanov, I.; Puretzky, A.; Eres, G.; Wang, H.; Pan, Z.; Cui, H.; Jin, R.; Howe, J.; Geohegan, D. B. *Appl. Phys. Lett.* **2006**, *89*, 223110

56. Padgett, C. W.; Brenner, D. W. *Nano. Lett.* **2004**, *4*, 1051-1053

57. Shenogin, S.; Bodapati A.; Xue L.; Ozisik R.; Keblinski P. *Appl. Phys. Lett*. **2004**, *85*, 2229-2231

58. Clancy, T. C.; Gates, T. S. *Polymer* **2006**, *47*, 5990-5996

59. Gojny, F. G.; Wichmann, M. H. G.; Fiedler, B.; Kinloch, I. A.; Bauhofer, W.; Windle, A. H.; Schulte, K. *Polymer* **2006**, *47*, 2036-2045

60. Balandin, A. A.; Ghosh, S.; Bao, W.; Calizo, I.; Teweldebrhan, D.; Miao, F.; Lau, C. N. *Nano Lett.* **2008**, *8*, 902 - 907

61. Fukushima, H.; Drzal, L.T.; Rook, B. P.; Rich, M. J. *J. Therm. Anal. Cal.* **2006**, *85*, 235-238

62. Yu, A.; Ramesh, P.; Itkis, M. E.; Bekyarova, E.; Haddon, R.C. *J. Phys. Chem. C* **2007,** *111*, 7565-7569

63. Ghose, S.; Watson, K.A.; Delozier, D. M.; Working, D.C.; Connell, J.W., Smith, J.G.; Sun, Y.-P.; Lin, Y. *High Perform. Polym*. **2006**, *18,* 961-977

64. Debelak, B.; Lafdi, K. *Carbon* **2007**, *45*, 1727-1734

CHAPTER TWO

CARBON NANOSHEETS FOR HIGHLY THERMAL CONDUCTIVE POLYMERIC NANOCOMPOSITES

2.1 Introduction

Carbon materials are known for their thermal conductive properties.[1-6] Recently, carbon nanotubes (with an experimentally measured individual-nanotube thermal conductivity of 3,000 W/mK[5] and a value of up to 6,600 W/mK predicted theoretically[6]) have generated much excitement because of their potential use in polymeric nanocomposites with ultrahigh thermal conductivities.[7-11] So far, however, no such nanocomposites have been produced. Alternatively, there is increasing attention being paid to the use of exfoliated graphite in polymers to produce thermally conductive nanocomposites,[12-21] since the thermal conductivity of graphene was estimated to be as high as 5300 W/mK.[12,13] For example, Drzal and coworkers[15,16] reported that graphite could be intercalated via chemical oxidation, then rapidly exfoliated at high temperature; the exfoliated graphite could then be dispersed into polymeric matrices, including nylons and polyethylene, to produce composites with enhanced thermal conductivities. It was found that the thermal conductivity of the composites increased almost linearly with the graphite loading, with a value of up to 4.1 W/mK being recorded for a composite of nylon 6 with 20 vol% exfoliated graphite (compared to only 0.25 W/mK for the blank polymer).[15] Similarly, Haddon and coworkers processed natural graphite flakes into

"graphite nanoplatelets" (GNPs) by first treating them with a mixture of concentrated sulfuric acid and nitric acid for intercalation and then exfoliating via thermal shock upon rapid exposure of the intercalated graphite to various high temperatures in nitrogen.[19] The GNPs thus obtained were dispersed via a postprocessing treatment, in order to fabricate composites with epoxy. These GNP-epoxy composites were found to have thermal conductivities up to 6.44 W/mK at 25 vol% GNP loading, which is considerably higher than the value of the blank epoxy.[19]

Connell and coworkers[20] compared the thermal conductivities of extruded composite ribbons made of different nanoscale carbon fillers, including multiple-walled carbon nanotubes (MWNTs), vapor-grown nanofibers, and commercially available expanded graphite, in Ultem™ 1000 resin. The expanded graphite was found to be most effective, with the in-plane thermal conductivity reaching 6.7 W/mK in the ribbon sample containing 40 wt% graphite.

In this work, it will be reported that commercially available expanded graphite could be further exfoliated in a specifically designed process to produce nanometer-sized carbon structures (dubbed as "carbon nanosheets"). These carbon nanosheet-based materials were used as fillers in polymeric nanocomposites that exhibited ultrahigh thermal conductivities, setting, to the best of our knowledge, new records.

2.2 Experimental Section

Materials: The expanded graphite (surface enhanced flake graphite, grade 3805) sample was supplied by Asbury Carbons. The Bisphenol A epoxy-based polymer (EPONOL resin 53-BH-35, M_w = ca. 26,000) in a solvent mixture of methyl ethyl ketone and propylene glycol monomethyl ether was obtained from Hexion Specialty Chemicals. The polymer was recovered by precipitating in water and then completely removing the water. Poly(vinyl alcohol) (PVA, M_w = ca. 70,000-90,000) was purchased from Aldrich, and LaRC CP-2 polyimide (number-average molecular weight, M_n = ca. 17,000, obtained from the condensation of 4,4'-(hexafluoroisopropylidene)-diphthalic anhydride and 1,3-bis-(3-aminophenoxy)benzene) from SRS, Inc. These polymers were used as received. Sulfuric acid (93%), nitric acid (73%), and ethanol were obtained from ACROS, and dimethylformamide (DMF) from Mallinckrodt.

Carbon Nanosheets: The as-supplied expanded graphite sample was processed via a combination of alcohol and oxidative acid treatments. In a typical experiment, the sample (1 g) was added to an alcohol-water mixture (13:7 v/v, 400 mL), stirred at room temperature for 24 h, and then sonicated (VWR-250D, 120 W) for another 20 h. The sample was collected via filtration and then dried in a vacuum oven. A portion of this sample (500 mg) was added to a nitric acid-sulfuric acid mixture (1:3 v/v, 80 mL) that was precooled in an ice bath. Upon sonication for 2-3 days, the mixture was transferred into water (1 L). Then, the processed graphite was collected via filtration, washed

repeatedly with deionized water until a neutral pH was achieved, and dried in a vacuum oven.

Nanocomposite Films: An epoxy polymer sample was dissolved in hot DMF (about 5 mg/mL). Separately, the carbon-nanosheets sample (50 mg) was suspended in DMF (10 mL) via sonication for 1 h. The suspension was added dropwise to the hot DMF solution of the epoxy polymer (10 mL) under stirring. The mixture was concentrated, stirred vigorously for 12 h, and then cast into thin films (30-80 microns in thickness) on etched glass slides in a glovebox under nitrogen. The slides were immersed in water for 30 min to allow the nanocomposite thin films to be released, and the freestanding films were subsequently dried in a vacuum oven (80-100°C) before characterization.

Similarly, the polyimide and PVA polymers were dissolved in DMF and hot water, respectively. Suspensions of the carbon-nanosheets in DMF and water were prepared via homogenization (Omni International, THP115) for 30 min and then sonication for 30 min. The suspensions were added dropwise to the polyimide and PVA solutions, respectively, with stirring. The resulting mixtures were concentrated, stirred vigorously for 12 h, and then cast into thin films on glass slides in a glovebox under a nitrogen atmosphere. The freestanding films were dried in a vacuum oven (80-100°C) before measurements were taken.

Thin films of carbon nanosheets were only prepared by filtering the suspended carbon nanosheets and then drying in a vacuum ovent at 80-100°C.

Measurements: X-ray powder diffraction measurements were carried out using a Scintag XDS-2000 powder diffraction system. Raman spectra were measured using a

Jobin Yvon T64000 Raman spectrometer equipped with a Melles-Griot 35 mW He-Ne laser source providing 633 nm excitation, a triple monochromator, an Olympus BX-41 microscope, and a cooled Symphony detector. Atomic force microscopy (AFM) images were obtained in the acoustic AC mode using a Molecular Imaging PicoPlus system equipped with a multipurpose scanner for a maximum imaging area of 10 μm x 10 μm and a NanoWorld Pointprobe NCH sensor (125 μm in length). The height profile analysis was facilitated using the SPIP software distributed by Image Metrology. Transmission electron microscopy (TEM) was performed using a Hitachi HD-2000 S-TEM system and a Hitachi H-9500 TEM system; the selected area diffraction (SAD) measurements were performed on the latter. Carbon-coated or holey carbon-coated copper grids were used in the imaging experiments. For cross-sectional imaging, a film sample was first embedded into epoxy resin and then microtomed into slices of less than 100 nm thick using a Reichert-Jung Ultracut E Microtome with a 30° angle diamond knife at room temperature.

The in-plane thermal diffusivity in freestanding polymeric nanocomposite thin films was determined using an Ulvac LaserPIT thermal diffusivity/conductivity meter operated at room temperature in a vacuum of 0.01 Pa. The thin films measured were about 30 mm x 4 mm in size, with one surface (facing the laser in the instrument) coated with a thin layer of graphite. At least three frequencies were used in the measurement of each film sample, and the readings were averaged for the specific specimen. The cross-plane thermal diffusivities of the films were obtained using a Netzsch LFA 447 NanoFlash instrument (Xenon flash lamp, 304 V, and long pulse).[20,21]

The density and specific heat of the nanocomposite were estimated from those of the polymer and filler with the commonly used mixing rule.[27,28] Composite = $w_{polymer}$Polymer + w_{filler}Filler, where w denotes the respective weight fractions.

2.3 Results and Discussions

The processing required to produce the carbon nanosheets involved sequential alcohol and oxidative acid treatments. First, the as-supplied expanded-graphite sample was added to an alcohol-water mixture.[22] The resulting suspension was stirred at room temperature and then vigorously sonicated. The graphite sample recovered post-treatment was added to a nitric acid – sulfuric acid mixture that was precooled in an ice bath. Upon vigorous sonication, the processed graphite sample was recovered by rather straightforward procedures, including filtration, washing with water until the pH value was neutral, and drying in a vacuum oven.

The combination of alcohol and oxidative acid treatments yielded samples with a substantial presence of carbon nanosheets, according to characterization by microscopy and other techniques. A typical transmission electron microscopy (TEM) image of the processed sample is shown in Figure 2.1. The edges of the carbon nanosheets (which tend to scroll and fold,[23] as seen in the image) were used to estimate the thickness of the nanosheets, which was generally on the order of 2 - 8 nm. The electron diffraction patterns shown in Figure 2.1 correspond to two dominant periodicities of 2.13 and 1.23 Å, similar to those reported in the literature for thin crystalline graphene sheets.[23]

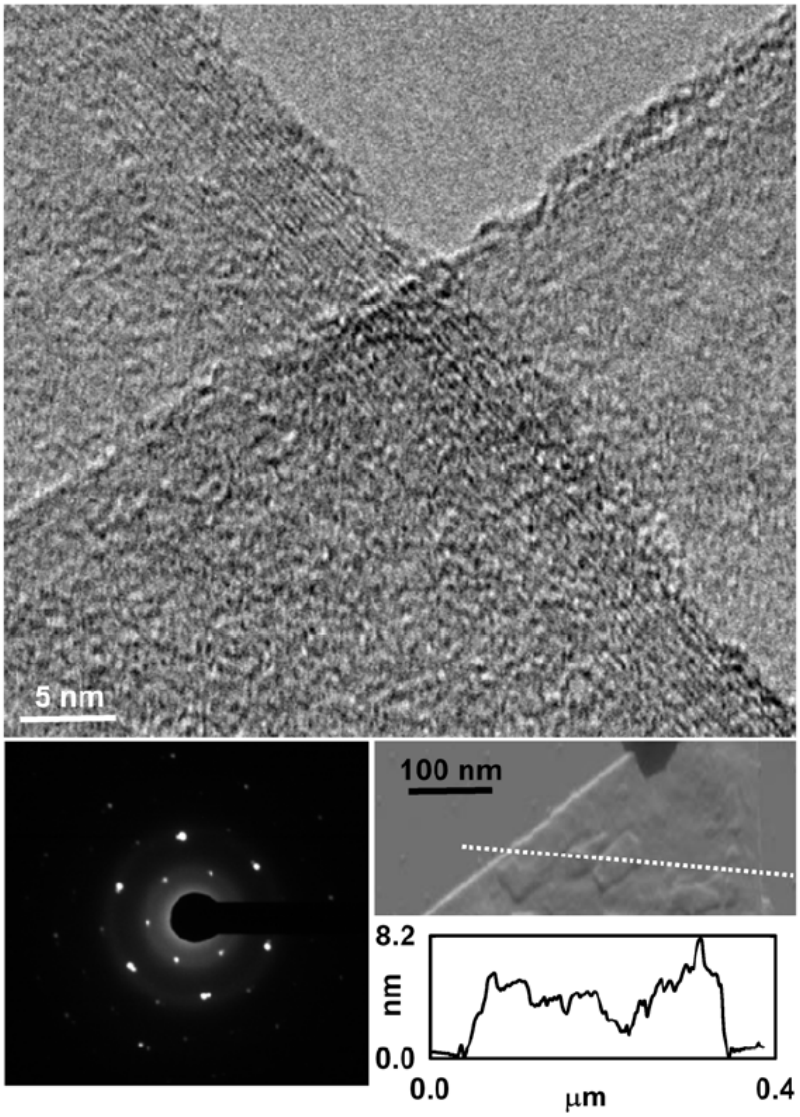

Figure 2.1 TEM image showing folded edges of two graphitic sheets (top) and their corresponding electron-diffraction patterns (bottom left). An AFM image (tapping-mode) of a sheet with a corresponding height profile (taken along the dashed line) is also shown (bottom right).

Also shown in Figure 2.1 is a typical atomic force microscopy (AFM) image of the carbon nanosheets obtained from the processed sample on a mica surface, where the height profile is consistent with the thickness of the nanosheets estimated in the TEM analysis (sheet dimension generally on the order of a micrometer).

With regards to bulk properties of the sample, powder X-ray diffraction results obtained before and after the alcohol and oxidative acid treatments showed a slight increase in the interlayer distance and, more meaningfully, a significant broadening in the diffraction peaks of the post-treatment sample. According to calculations based on the peak broadening using the Scherrer equation,[24] the average thickness of the graphite layer decreased from more than 20 nm in the pretreatment sample to 6-7 nm in the post-treatment sample, again in reasonable agreement with the TEM results.

The Raman spectroscopy results for the same samples were also consistent with a substantial presence of carbon nanosheets. The observed Raman G-band shifted to higher frequencies, indicative of a decrease in the number of graphene layers.[25] According to a demonstration by Eklund and coworkers, the decrease in the number of graphene layers (from 19 to one in their work) is correlated with the progressive shift of the frequency of the observed Raman G-band.[25]

To fabricate the polymeric nanocomposites, a weighted amount of the processed graphite sample (carbon nanosheets) was suspended in dimethylformamide (DMF) via sonication, and the suspension was added dropwise to a solution of epoxy (weight-average molecular weight, $M_W \sim 26{,}000$) in hot DMF with stirring. The resulting mixture was concentrated, vigorously stirred, and subsequently cast onto an etched glass slide.

The slide was purged with nitrogen gas and then immersed in water for 30 min to obtain a freestanding nanocomposite thin film (around 50 microns in thickness). After careful drying, the film was used in thermal diffusivity measurements.

The in-plane thermal diffusivity of a freestanding film was determined at room temperature using an instrument based on the laser-heating angstrom method.[26] At a carbon filler content of 33 vol% in the epoxy nanocomposite thin films (from repeated fabrication under the same conditions), the experimentally measured in-plane thermal diffusivity averaged 35 mm^2/s (values higher than 40 mm^2/s were recorded for some samples), which is several orders of magnitude higher than the value of the blank epoxy polymer film (0.12 mm^2/s). The thermal conductivity (λ) was calculated from thermal diffusivity (D) in terms of the equation:

$$\lambda = \rho C_P D, \qquad (1)$$

where ρ (density) and C_P (specific heat) for the nanocomposite were estimated from the respective values of the polymer and the filler using the commonly used mixing rule.[27,28] Again for the epoxy nanocomposites with 33 vol% carbon nanosheets, the λ values thus calculated (close to 80 W/mK on average, where ρ_c = 1.51 g/cm3, and C_{Pc} =1.45 J/gK) are much higher than those ever reported in the literature for composites of epoxy (or any other polymer) with exfoliated graphite fillers.[15-21] For example, the previously reported high in-plane thermal conductivity in composites of Ultem™ 1000 resin with expanded graphite was less than 7 W/mK at comparable graphite loadings.[20]

The carbon nanosheets were used with other polymeric matrices to fabricate nanocomposite thin films. The thermal diffusivities of these films varied somewhat from polymer to polymer, but remained high. For example, with polyimide (obtained from the condensation of 4,4'- (hexafluoroisopropylidene)diphthalic anhydride and 1,3-bis-(3-aminophenoxy)benzene, often referred to as LaRC CP-2) and poly(vinyl alcohol), the nanocomposite thin films exhibited in-plane thermal diffusivities on the order of 20 mm^2/s at carbon nanosheet loadings similar to those used in the epoxy nanocomposites discussed above. While less spectacular (compared with the average 35 mm^2/s in the epoxy nanocomposites), these thermal diffusivity values still set records for their respective polymeric nanocomposites.

As expected, the thermal diffusivities of the polymeric nanocomposites are strongly dependent on the carbon nanosheets content, with higher volume fractions consistently resulting in higher thermal diffusivities of the nanocomposites. This is demonstrated in Figure 2.2, which shows the dependence of the thermal diffusivity on volume fraction of nanosheets in the epoxy-carbon nanocomposite thin films.

The thermal-conductive properties of the polymeric nanocomposites produced with carbon nanosheets are highly anisotropic, with a large ratio between the in-plane and cross-plane thermal conductivities. For example, in thin films of the epoxy-polymer nanocomposite with a 33 vol% loading of carbon nanosheets, the experimentally measured cross-plane thermal diffusivities were generally about one-tenth to one-fifth of the average in-plane value discussed above. The highly anisotropic nature in the thermal conductivities of the nanocomposites is interesting but hardly surprising, likely a

reflection of the pseudo-2D structure of the carbon nanosheets and their associated 2D thermal conductive properties.[12,13,29,30] Thus, these polymeric composites of carbon nanosheets should be particularly useful in potential applications that require efficient directional thermal transport.

Results from powder X-ray diffraction measurements of the carbon nanosheets were generally unchanged after the dispersion of the nanosheets in the polymeric matrices. The dispersed carbon nanosheets were examined using cross-sectional TEM imaging. A thin film was microtomed in the direction perpendicular to the film surface, to yield slices less than 100 nm thick (used as specimen for high-resolution TEM imaging). Shown in Figure 2.3 are representative TEM images of the specimen at various resolutions, which essentially correspond to a direct view (from a cross-sectional orientation) of the nanoscale structure in the nanocomposite thin film that was microtomed. These images confirm that the graphitic fillers dispersed in the polymer matrix are indeed carbon sheets of nanoscale thickness (generally less than 10 nm).

The polymeric nanocomposites with carbon nanosheets appeared black in color, and remained elastic even at relatively high carbon loadings. As an example, the photographs in Figure 2.4 demonstrate the high degree of flexibility of the epoxy nanocomposite thin film with a 35 vol% carbon nanosheet loading. Polymeric nanocomposites with lower carbon nanosheet loadings were even more elastic and processable (they were melt-extruded into fiber-like structures and flexible tubing, for example). However, “films” of neat carbon nanosheets (without any polymer) were morphologically different, as expected. The preparation, appearance, and physical

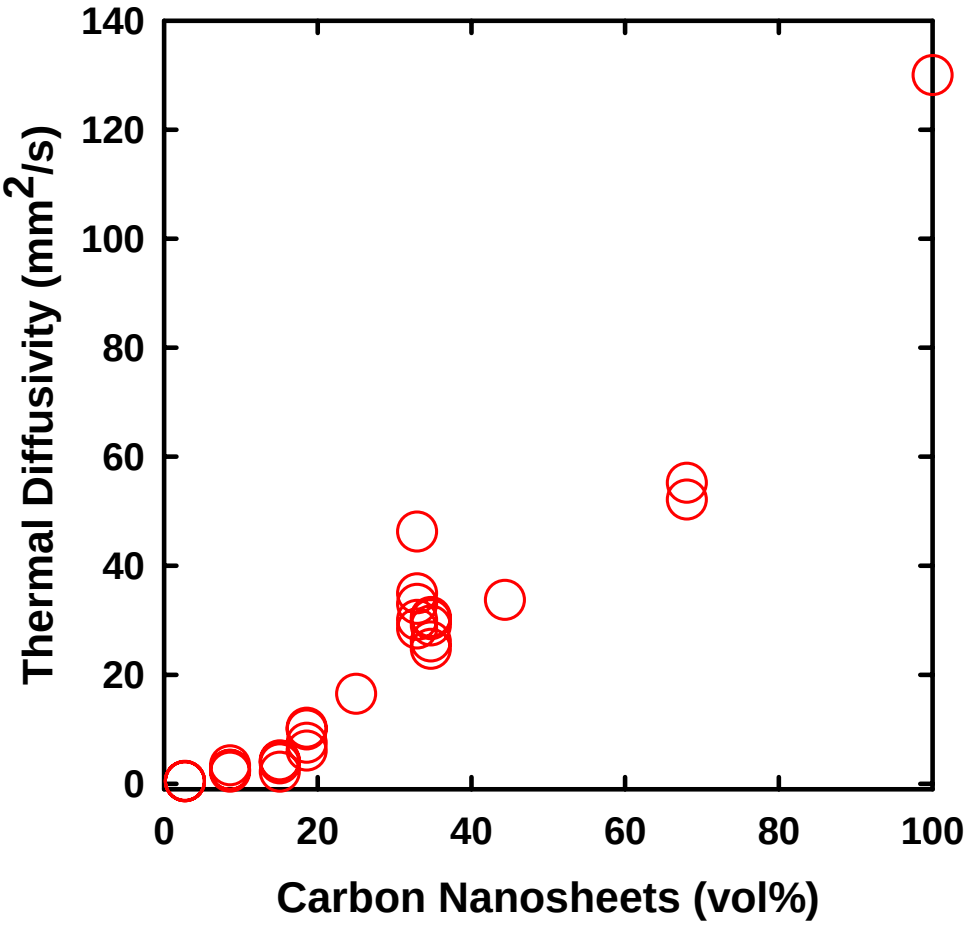

Figure 2.2 Dependence of the observed thermal diffusivity on the carbon-nanosheet loading in the epoxy-nanocomposite thin films

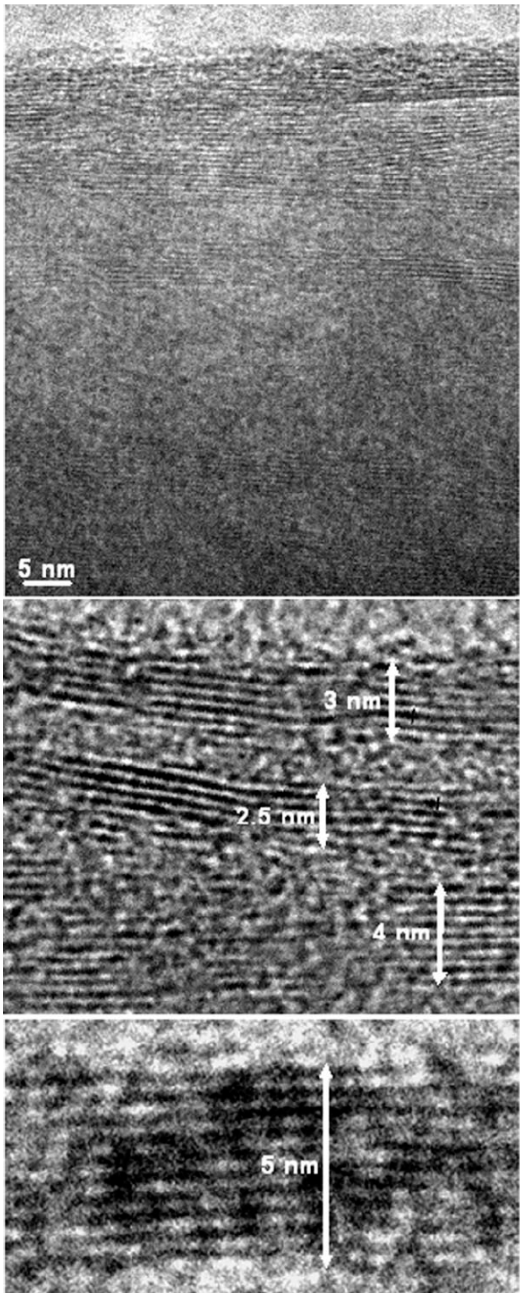

Figure 2.3 TEM images of various resolutions of slices of the microtomed (cross-sectional) epoxy-nanocomposite thin film

characteristics of these films were essentially the same as those of "bucky paper" made of single –walled carbon nanotubes,[31] but the thermal conductivities were significantly higher (Figure 2.2).[32]

The carbon nanosheets were apparently more effective fillers than carbon nanotubes (both single-walled, 5.5 W/mK and multiple-walled, 2 W/mK) for producing polymeric nanocomposites with high thermal conductivity. It has been acknowledged in the literature that the thermal conductivity of polymeric nanocomposites is mechanistically limited by the polymer-nanofiller interfacial thermal resistance.[33] Heat transport in polymeric nanocomposites is carried out by phonons of varying frequencies, with the phonons slowing down at the polymer-nanofiller interface as a result of material characteristics, such as the largely amorphous nature of the polymer. However, it is difficult to hypothesize any fundamental difference in the polymer-carbon interfaces between the carbon nanotubes and nanosheets (and thus possibly accounting for their significant difference in performance). Instead, it could be that the nanosheets as 2D nanofillers, reduce the overall number of polymer-nanofiller interfaces for heat transport in the resulting polymeric nanocomposites. Further investigation of the polymeric nanocomposites composed of carbon nanosheets is needed for better structural and mechanistic elucidations. Nevertheless, it is remarkable that the relatively inexpensive graphitic materials could be used with various polymers and with relatively simple processing to produce nanocomposites of record-setting anisotropic thermal conductivities, which may prove highly valuable in many technological applications.

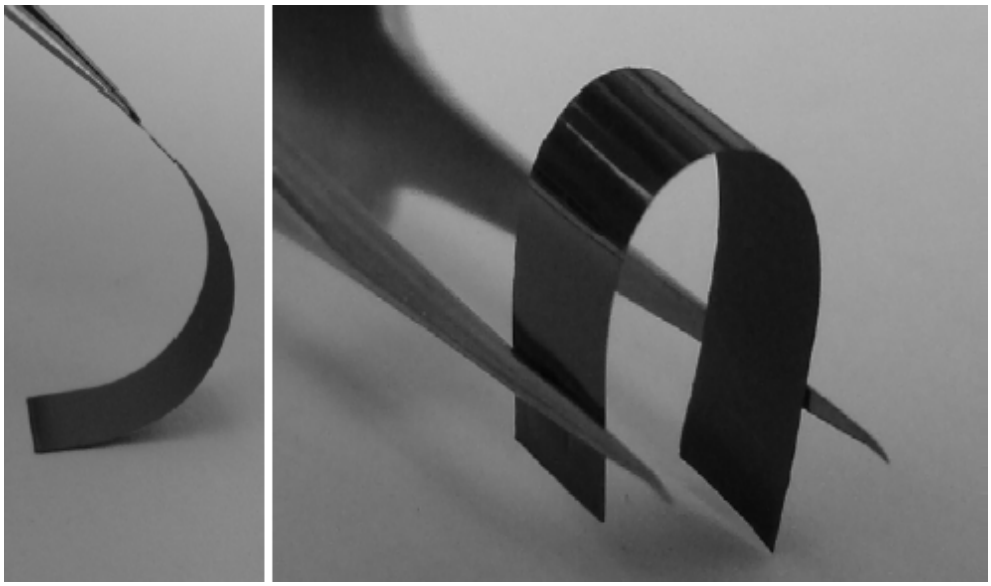

Figure 2.4 Photographs of an epoxy nanocomposite thin film (35 vol% carbon nanosheet loading) showing that the film is still flexible.

References

1. Pierson, H. O. *Handbook of carbon, graphite, diamond, and fullerens: properties, processing, and applications*, Noyes Publications, Park Ridge, NJ, **1993**.

2. Ruoff, R. S.; Lorents, D. C. *Carbon* **1995**, *33*, 925-930

3. Hone, J.; Llaguno, M. C.; Nemes, N. M.; Johnson, A. T.; Fischer, J. E.; Walters, D. A.; Casavant, M. J.; Schmidt, J.; Smalley, R. E. *Appl. Phys. Lett.* **2000**, *77*, 666–668

4. Choi, S. U. S.; Zhang, Z. G.; Yu, W.; Lockwood, F. E.; Grulke, E. A. *Appl. Phys. Lett*. **2001**, *79*, 2252-2254

5. Kim, P.; Shi, L.; Majumdar, A.; McEuen, P. L. *Phys. Rev. Lett*.**2001**, *87*, 215502

6. Berber, S.; Kwon, Y. K.; Tomanek, D. *Phys. Rev. Lett*.**2000**, *84*, 4613-4616

7. Biercuk, M. J.; Llaguno, M. C.; Radosavljevic, M.; Hyun, J. K.; Jonson, A. T.; Fischer, J. E. *Appl. Phys. Lett.* **2002**, *80*, 2767-2769

8. Choi, E. S.; Brooks, J. S.; Eaton, D. L.; Al-Haik, M. S.; Hussaini, M. Y.; Garmestani, H.; Li, D.; Dahmen, K. *J. Appl. Phys.* **2003**, *94*, 6034-6039

9. Nan, C. W.; Liu, G.; Lin, Y.; Li, M. *Appl. Phys. Lett.* **2004**, *85*, 3549-3551

10. Huang, H.; Liu, C.; Wu, Y.; Fan, S. *Adv. Mater.* **2005**, *17*, 1652-1656

11. Gojny, F. H.; Wichmann, M. H. G.; Fiedler, B.; Kinloch, I. A.; Bauhofer, W.; Windle, A. H.; Schulte, K. *Polymer* **2006**, *47*, 2036-2045

12. Balandin, A. A.; Ghosh, S.; Bao, W.; Calizo, I.; Teweldebrhan, D.; Miao, F.; Lau, C. N. *Nano Lett.* **2008**, *8*, 902-907

13. Ghosh, S.; Calizo, I.; Teweldebrhan, D.; Pokatilov, E. P.; Nika, D. L.; Balandin, A. A.; Bao, W.; Miao, F.; Lau, C. N. *Appl. Phys. Let.* **2008**, *92*, 151911

14. Geim, A. K.; Novoselov, K. S. *Nature Mater.* **2007**, *6*, 183-191

15. Fukushima, H.; Drzal, L. T.; Rook, B. P.; Rich, M. J. *J. Therm. Anal. Cal.* **2006,** *85*, 235-238

16. Kalaitzidou, K.; Fukushima, H.; Drzal, L. T. *Carbon* **2007,** *45*, 1446-1452

17. Hung, M.-T.; Choi, O.; Ju, Y. S.; Hahn, H. T. *Appl. Phys. Lett*. **2006**, *89*, 023117

18. Debelak, B.; Lafdi, K. *Carbon* **2007**, *45*, 1727-1734

19. Yu, A.; Ramesh, P.; Itkis, M. E.; Bekyarova, E.; Haddon, R. C. *J. Phys. Chem. C* **2007**, *111*, 7565-7569

20. Ghose, S.; Watson, K. A.; Delozier, D. M.; Working, D. C.; Connell, J. W.; Smith, J. G.; Sun Y.-P.; Lin, Y. *High Performance Polymers* **2006**, *18,* 961-977

21. Ghose, S.; Watson, K. A.; Working, D. C.; Connell, J. W.; Smith Jr, J. G.; Sun, Y.-P. *Composites Sci. Tech.* **2008,** *68*, 1843-1853

22. Chen, G.; Weng, W.; Wu, D.; Wu, C.; Lu, J.; Wang, P.; Chen, X. *Carbon* **2004,** *42*, 753-759

23. Meyer, J. C.; Geim, A. K.; Katsnelson, M. I.; Novoselov, K. S.; Booth T. J.; Roth, S. *Nature* **2007,** *446*, 60-64

24. Klug, H. P.; Alexander, L. E. *X-ray Diffraction Procedures*, John Wiley & Sons: New York, **1959**

25. Gupta, A.; Chen, G.; Joshi, P.; Tadigadapa, S.; Eklund, P. C. *Nano Lett*. **2006**, *6*, 2667-2673

26. Takahashi, F.; Fuji, K.; Hamada, Y.; Hatta, I. *Jpn. J. Appl. Phys.* **2000,** *39*, 6471-6473

27. Newnham, R. E., *Nonmechanical properties of composites: Concise Encyclopedia of Composite Materials,* (Ed. Kelly, A.), Pergamon Press, Oxford, **1994**.

28. Ishida, H.; Rimdusit, S. *J. Therm. Anal. Cal.* **1999,** *58*, 497-507

29. Saito, K.; Nakamura, J.; Natori, A. *Phys. Rev. B* **2007,** *76*, 115409

30. Peres, N. M. R.; Lopes dos Santos, J. M. B.; Stauber, T. *Phys. Rev. B* **2007,** *76*, 73412

31. Liu, J.; Rinzler, A. G.; Dai, H.; Hafner, J. H.; Bradley, R. K.; Boul, P. J.; Lu, A.; Iverson, T.; Shelimov, K.; Huffman, C. B.; Rodriguez-Macias, F.; Shon, Y.-S.; Lee, T. R.; Colbert, D. T.; Smalley, R. E. *Science* **1998**, *280*, 1253-

32. Itkis, M. E.; Borondics, F.; Yu, A.; Haddon, R. C. *Nano Lett* **2007**, *7,* 900-

33. Winey, K. I.; Kashiwagi, T.; Mu, M. *MRS Bull.* **2007,** *32*, 348-353

CHAPTER THREE

THERMAL CONDUCTIVE POLYMERIC/CARBON NANOCOMPOSITES – A MORE SYSTEMATIC INVESTIGATION

3.1 Introduction

The development of highly thermal conductive polymeric composite materials has become more important to many industries including computers and electronics, automotives, and aerospace. As presented in the previous chapter, exfoliated graphite based nanocomposites are promising candidates for the fabrication of thermal management materials. However, further increases of thermal conductivity in the polymeric nanocomposites are widely considered as major challenges, with significant opportunities in finding reliable and versatile methods to exfoliate graphite into single and/or few-layer graphene ("carbon nanosheets") without sacrificing other material properties.

Well-exfoliated graphite represents two-dimensional nanomaterials, different and often more advantageous than the unidirectional carbon nanotubes (CNTs) and vapor grown carbon nanofibers (VGCFs). Therefore, it is not surprising that currently there is extensive effort on developing practical methods to break natural graphite into single or few graphene layers.

The graphite intercalation and exfoliation experiments can be traced back to 1841, when Schauffauktl described for the first time an intercalated graphite sulfate.[1] Generally

speaking, the intercalation of 2D-infinitly layered graphite is achieved by penetration of a guest species between the carbon layers with subsequent expansion of the graphite along the c-axis. The known intercalating reagents vary from strong oxidants to powerful reductants and polymers[2]. The intercalation is sometimes assisted by thermal shock in order to further increase the exfoliation by vaporization of the intercalated guest. However, the graphite obtained by these methods is only partially exfoliated, with the graphene sheets often interlinked with each other.[3] According to a few studies on the exfoliation mechanism, all intercalation into graphite may involve adsorption of guest molecules, initially on the basal plane (00l), accompanied by electron transfer between the guest and graphite, and followed by opening the galleries closer to the basal plane which will further cause other galleries to open.[4-8]

There are three methods widely used so far to synthesize graphenes. Most physical studies of graphene are carried out on sheets obtained by the mechanical cleavage –"scotch-tape" technique,[9] wherein a single graphene sheet is removed at a time from highly ordered pyrolytic graphite. Although very ingenious, this method obviously cannot be used for large-scale applications or to study many of the chemical and materials properties of graphene. The second route to isolate graphene concentrates on the epitaxial growth of graphene films.[10-12] This is a promising method but requires expensive equipment and single crystals on which the graphene can be grown. A more general approach to obtain graphene is exfoliation of graphitic oxide.[13-15] Unfortunately, these materials are nearly amorphous, only dispersed in aqueous media (incompatible with most organic polymers), and the unique macroscopic properties of graphene are not

maintained due to destruction of the sp^2 network. In order to overcome these limitations, the graphite oxide is often chemically reduced[16-18] to restore the π-electron conjugation within the aromatic system. Although the materials obtain after reduction are showing improved properties, they are generally worse then those of individual graphene due to irreversible modifications to the graphite oxide during the exfoliation process.

Our understanding of the current challenges in the development of highly thermal conductive polymeric/graphene nanocomposites is such that: (1) a high degree of graphite exfoliation to produce the desired carbon nanosheets; (2) a complete dispersion and connectivity of the nanosheets in polymer matrices for proper interfacial bonding in the nanocomposites; and (3) a good alignment of the nanosheets in the polymer matrices are necessary. In this project we carried out a more systematic investigation on the graphite exfoliation by using treatments with acids and different solvents at both ambient and supercritical conditions. In addition we investigated the effect of exfoliation on the thermal conductivity of different polymeric carbon nanosheets composites.

3.2 Experimental Section

Materials: Expanded graphite (surface enhanced flake graphite, grade 3805, average particle size 10-15 μm) was supplied by Asbury Carbons. Bisphenol A epoxy resin (EPONOL resin 53-BH-35, MW ~ 26,000) in a solvent mixture (methyl ethyl ketone and propylene glycol monomethyl ether) was obtained from Hexion Specialty Chemicals. The resin was recovered by precipitating in water and then completely

removing the water. Poly(vinyl alcohol) (PVA, MW ~ 70,000-90,000; fully hydrolyzed) and boron tribromide were purchased from Aldrich, poly(ethylene-co-vinyl acetate) Elvax® 40w from DuPont, and LaRC CP-2 polyimide (Mn ~ 17,000, from the condensation of 4,4'-(hexafluoroisopropylidene)-diphthalic anhydride and 1,3-bis-(3-aminophenoxy)benzene) from SRS, Inc. Sulfuric acid (93%), nitric acid (73%), and ethanol (100%) were obtained from Acros Organics. Toluene, N,N-dimethylformamide (DMF), methylene chloride (CH_2Cl_2), and other solvents were purchased from Mallinckrodt. CH_2Cl_2 was dried with anhydrous calcium chloride and then distilled from calcium hydride.

Carbon Nanosheets from Exfoliation with Alcohol and/or Acids

CNS_{EtOH} - In a typical experiment, the as-supplied expanded graphite sample (1 g) was added to an alcohol-water mixture (13/7, v/v, 400 mL), stirred at room temperature for 24 h, and then sonicated (VWR-250D, 120 W) for another 20 h. The sample was collected via filtration and then dried in a vacuum oven.

CNS_{H+} - The as-supplied expanded graphite sample (500 mg) was added to a nitric acid-sulfuric acid mixture (1/3, v/v, 80 ml) pre-cooled in an ice bath. Upon sonication (VWR-250D, 120 W) for up to 48 h, the solution was transferred into water (1 L), filtered immediately, washed with water until neutral pH, and then dried in a vacuum oven.

$CNS_{EtOH/H+}$ -The above alcohol-treated sample (CNS_{EtOH}, 500 mg) was sonicated (VWR-250D, 120 W) in a nitric acid-sulfuric acid mixture (1/3, v/v, 80 mL) pre-cooled in an ice bath. Upon sonication for up to 72 h, the mixture was transferred into water (1 L),

recovered via filtration, followed by washing with water until neutral pH and then drying in a vacuum oven.

Exfoliation with Supercritical or Near-Critical Fluids

$CNS_{SC\text{-}EtOH}$ and $CNS_{SC\text{-}Tol}$ - In a typical experiment, the as-supplied expanded graphite sample (~50 mg) was sonicated (VWR-250D, 120 W) in ethanol for 1 h. The resulting suspension was transferred to a high-pressure reactor, which was filled with nitrogen gas and then closed. After heating at 350°C for 6 h, the reactor was cooled to room temperature to allow the recovery of the sample designated as $CNS_{SC\text{-}EtOH}$. The same experiment was carried out for toluene as the solvent, and heating at 250°C for 16 h yielded the sample designated as $CNS_{SC\text{-}Tol}$.

$CNS_{EtOH/SC\text{-}EtOH}$ - The above alcohol-treated sample (CNS_{EtOH}, ~50 mg) was sonicated in ethanol (10 mL) for 1 h before being transferred to the high-pressure reactor for heating at 350°C for up to 24 h.

$CNS_{H+/SC\text{-}EtOH}$ - The acid-treated sample (CNS_{H+} with sonication for 8 days in the acid treatment, ~50 mg) was suspended in ethanol (10 mL) via sonication for 1 h, and the suspension was transferred to the high-pressure reactor for heating at 350°C for 24 h.

$CNS_{(EtOH/H+)/SC\text{-}EtOH}$ and $CNS_{(EtOH/H+)/Mix(Tol\text{-}EtOH)}$ - The above-described $CNS_{(EtOH/H+)}$ sample (~50 mg) was suspended in ethanol (10 mL) via sonication (VWR-250D, 120 W) for 1 h, and the suspension was transferred to the high-pressure reactor for heating at 350°C for up to 48 h to yield $CNS_{(EtOH/H+)/SC\text{-}EtOH}$. The same treatment in a toluene-ethanol mixture (3/1, 2/1, 1/1, or 1/0 v/v, 10 mL) with heating at 350°C for 16 h yielded $CNS_{(EtOH/H+)/Mix(Tol\text{-}EtOH)}$.

$CNS_{(EtOH/H+)/SC-H2O}$ and $CNS_{(EtOH/H+)/SC-DMF}$ - The above described $CNS_{EtOH/H+}$ sample (~50 mg) was sonicated in water (10 mL) for 1 h, and the suspension was heated in the high-pressure reactor at 375°C for 24 h to yield $CNS_{(EtOH/H+)/SC-H2O}$. In the same procedure, the suspension of $CNS_{EtOH/H+}$ in DMF was heated at 340°C for 24 h to yield $CNS_{(EtOH/H+)/SC-DMF}$.

Exfoliation with Other Methods

$CNS_{(EtOH/H+)/RH-EtOH}$ - In this experiment the above $CNS_{EtOH/H+}$ (obtained by acid treatment for 6 and 48 hours, 100 mg) was rapidly heated to 1000°C for about 1 min in inert atmosphere (argon gas). The sample obtained after rapid heating was further treated in alcohol-water mixture (13/7, v/v, 40 ml) by stirring at room temperature (24 h) and then vigorous sonication (VWR-250D, 120W, 20 h). The sample was recovered by filtration and then dried in the vacuum oven, and it was designated as $CNS_{(EtOHlH+)/RH-EtOH}$.

$CNS_{(EtOH/H+)/Aq}$ - The above described $CNS_{EtOH/H+}$ sample (acid treated for 72 h, 150 mg) was stirred in dry CH_2Cl_2 (30 mL) at room temperature for 12 h and then sonicated (VWR-250D, 120 W) for 12 h. After the suspension was cooled to around -45°C, a solution of boron tribromide in dry CH_2Cl_2 (1 M, 25 mL) was added dropwise over 90 min. The resulting mixture was warmed back to room temperature and stirred for 4 days under inert atmosphere (nitrogen gas). The graphite mixture was then shaken with water (50 mL) to carefully hydrolyze excess reagent and boron complexes. The suspension was then centrifuged at 1,380g for 5-10 min to recover the precipitated sample, followed by washing with water and ether for several times.

Fabrication of Polymeric Nanocomposites

PVA-CNS - An aqueous suspension of the selected CNS sample (10 mg/mL) was prepared by homogenization (Omni International, THP115) for 30 min and then sonication (VWR- 250D, 120W) for 30 min. Separately, a PVA solution in hot water (20 mg/mL) was prepared. The CNS suspension was added dropwise to the PVA solution, and the mixture was stirred vigorously for 12 h, concentrated, and then cast into thin film on glass slide in glove-box under nitrogen atmosphere. The film was removed from the slide, and the freestanding film was subsequently dried in a vacuum oven (80-100°C) before measurements.

Elvax-CNS - Procedures similar to those described above were used to prepare the CNS suspentions in ethanol (10 mg/ml) and Elvax solution in toluene (25 mg/mL). The CNS suspension was then added dropwise to the polymer solution at 90°C with stirring to obtain a homogeneous and viscous mixture at room temperature. The blend was cast into thin film on a glass slide, followed by drying for 1-2 days with nitrogen protection.

Polyimide-CNS - A suspension of the selected CNS sample (150 mg) in DMF (10 mL) was prepared using the same procedure described above. The suspension thus obtained was added to a solution of CP-2 polyimide in DMF (350 mg, 2 mL) with vigorous stirring. Then, the homogeneous and viscous mixture was cast into thin film on a glass slide, and subsequently dried for 1-2 days under nitrogen protection.

Epoxy-CNS - The suspension of CNS in DMF (15 mg/mL) was added dropwise to a solution of epoxy resin in hot DMF. The mixture was vigorously stirred for 12 h at room temperature, and then cast into thin films on etched glass slide. Upon drying under

nitrogen overnight, the films were immersed in water for 30 min to obtain freestanding films, which were then dried in a vacuum oven before further characterization.

For polymeric nanocomposites with the CNS samples processed in supercritical fluids, the CNS suspension recovered from the high pressure reactor was directly added to the polymeric solution.

Measurements: X-ray powder diffraction measurements were carried out on a Scintag XDS-2000 powder diffraction system (Ni-filtered Cu Kα radiation, operated at 30 mA and 40 kV) in a step-scanning mode with a step size of 0.02° (2θ) and a data acquisition rate of 3 seconds per step. Raman spectra were measured on Jobin Yvon T64000 Raman spectrometer equipped with a Melles-Griot 35 mW He-Ne laser source providing 633 nm excitation, a triple monochromator, an Olympus BX-41 microscope, and a cooled Symphony detector. Transmission electron microscopy (TEM) was performed on a Hitachi HD-2000 S-TEM system and a Hitachi H-9500 TEM system operated at 300 kV. Carbon-coated or holey carbon-coated copper grids were used in the imaging experiments. For cross-sectional imaging, a film sample was first embedded into epoxy resin and then microtomed to slices of less than 100 nm in thickness by using a Reichert-Jung Ultracut E Microtome with a 30° angle diamond knife at room temperature or RMC Powertome X for cryosectioning.

The in-plane thermal diffusivity of freestanding polymeric nanocomposite thin films was determined on Ulvac LaserPIT thermal diffusivity/conductivity meter operated at room temperature and a vacuum of 0.01 Pa. A thin film (typically 30 mm x 4 mm in size) was coated on one surface (facing the laser in the instrument) with a thin layer of

graphite. Three or more frequencies were used in the measurement of each film sample, and the readings were then averaged for the specific specimen.

3.3 Results and Discussions

Exfoliation with Alcohol and/or Acid Treatments

The commercially available expanded graphite sample was further exfoliated in the treatment with alcohol only (CNS_{EtOH}), oxidative acids only (CNS_{H+}), or a combination of alcohol and acids sequentially ($CNS_{EtOH/H+}$). The resulting exfoliated samples were characterized and compared.

CNS_{EtOH} - In the treatment, the as-supplied expanded graphite sample was added to an alcohol-water mixture, and the resulting suspension was stirred at room temperature, followed by vigorous sonication. The treated sample was recovered via filtration and then dried for characterizations.

CNS_{H+} - The as-supplied expanded graphite sample was added to a nitric acid–sulfuric acid mixture (1/3, v/v) pre-cooled in an ice bath. Upon sonication for 24-48 h, a solution with green-brown hue was obtained, which was transferred to water, filtered, washed with water until neutral pH, and then dried in vacuum oven.

$CNS_{EtOH/H+}$ - The graphite sample obtained from the alcohol treatment (CNS_{EtOH}) was subsequently sonicated in nitric acid–sulfuric acid mixture (1/3, v/v) for different time periods up to 3 days. The suspended samples (exhibiting a green-brown color) were

recovered via filtration, followed by washing with water until neutral pH and then drying in vacuum oven.

Characterization, X-Ray The X-ray powder diffraction patterns of the graphite samples before and after the treatments were recorded. The diffraction patterns featured a peak around 26.5 degree due to (002) planes of ordered graphenes. The peaks in the treated samples were broader, and the average thickness of CNS was estimated by using Scherrer equation (1).

$$L_C\,(\text{rad}) = 0.89\lambda/\beta\cos\theta \qquad (1)$$

where L_C is the average crystallite size (thickness) along the stacking c-axis, λ is the wavelength of the X-ray source (1.5406 Å), β is the full-width-at-half-maximum of the diffraction peak, and θ is the diffraction angle.

The average thickness of the as-supplied expanded graphite samples was thus estimated to be on the order of 22 nm. The diffraction pattern of CNS_{EtOH} is compared with that of the as-supplied sample in Figure 3.1. According to the Scherrer equation, the average thickness of carbon nanosheets in CNS_{EtOH} was around 21 nm.

The X-ray diffraction profiles of the CNS_{H+} samples, prepared by variable amounts of sonication times, are compared in Figure 3.2. According to estimates based on the Scherrer equation, the average thickness of the nanosheets was around 10 nm in both samples (24-48 h sonication).

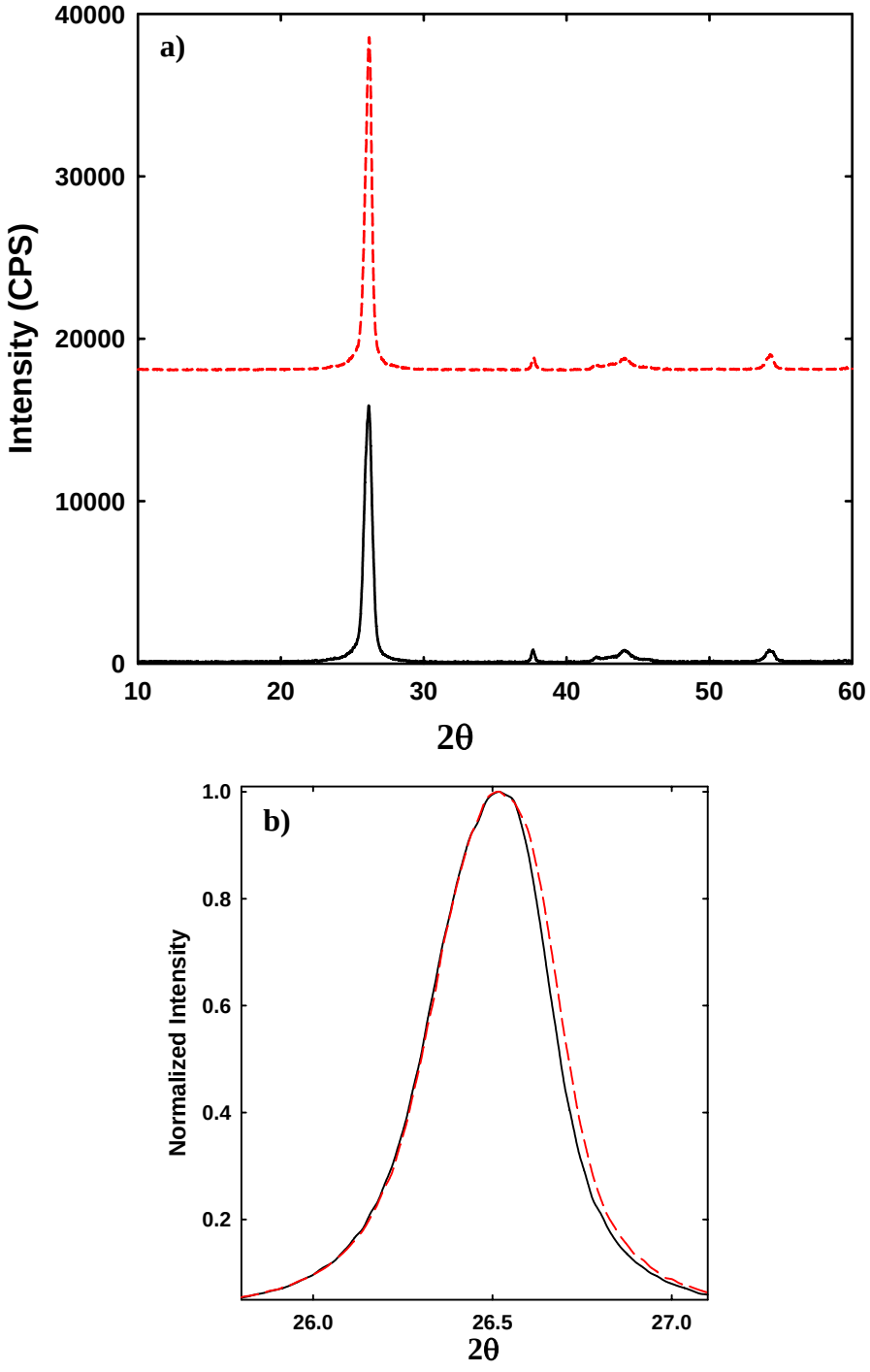

Figure 3.1 X-Ray powder diffraction patterns of (a) as-supplied expanded graphite (solid line) and CNS_{EtOH} (dash line), and (b) the corresponding (002) peaks (normalized intensity).

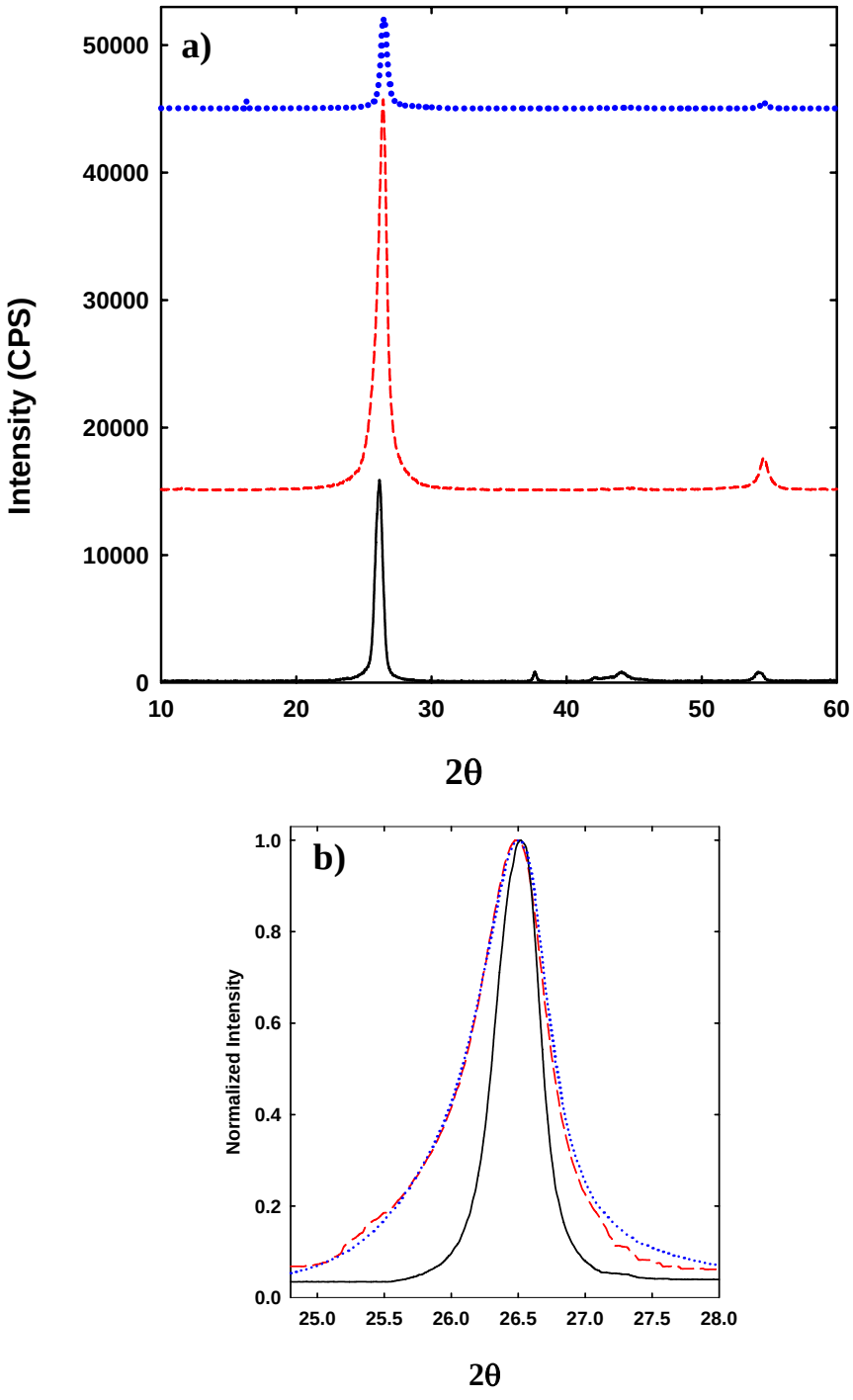

Figure 3.2 X-Ray powder diffraction patterns of (a) as-supplied expanded graphite (solid line), CNS_{H+} 24 h (dash line), CNS_{H+} 48 h (dotted line), and (b) the corresponding (002) peaks (normalized intensity)

Similarly, the (002) X-ray diffraction peak of $CNS_{EtOH/H+}$ became broader when the CNS_{EtOH} sample was sonicated in the acid mixture for 48-72 h (Figure 3.3), with the average thickness of the nanosheets decreasing to 6-7 nm according to the Scherrer equation estimation.

Characterization, Raman. The as-supplied expanded graphite sample and treated CNS samples (CNS_{EtOH} and $CNS_{EtOH/H+}$) were evaluated by Raman spectroscopy. The Raman spectra of the samples were generally similar, with the G-band at around 1,580 cm^{-1} and the 2D-band (due to the second order of zone-boundary phonons) at around 2,685 cm^{-1}. As shown in Figure 3.4(a), the position of G-band in $CNS_{EtOH/H+}$ is 3 cm^{-1} higher than the as-supplied expanded graphite. This upshift is partially due to the chemical doping and partially to the decrease in the number of layers based on the available research results on single and few graphene layers[19,20]. Among the different samples, there were also no significant differences in the shape and relative intensity of the 2D bands as shown in Figure 3.4(b), where, for clarity, were normalized against the G-band intensity. Since the optical penetration depth in the graphite is ~20 layers and the Raman spectra become hardly distinguishable from that of the graphite for specimens with more than 5 layers, we may conclude that the average number of layers in our samples is above 5.

Characterization, TEM. The specimens for TEM analyses were prepared by depositing the as-supplied graphite sample and $CNS_{EtOH/H+}$ on holly carbon-coated copper grids. A representative TEM image of the as-supplied graphite sample is shown in Figure 3.5, which reveals about 50 graphene layers, corresponding to a thickness of 22 nm.

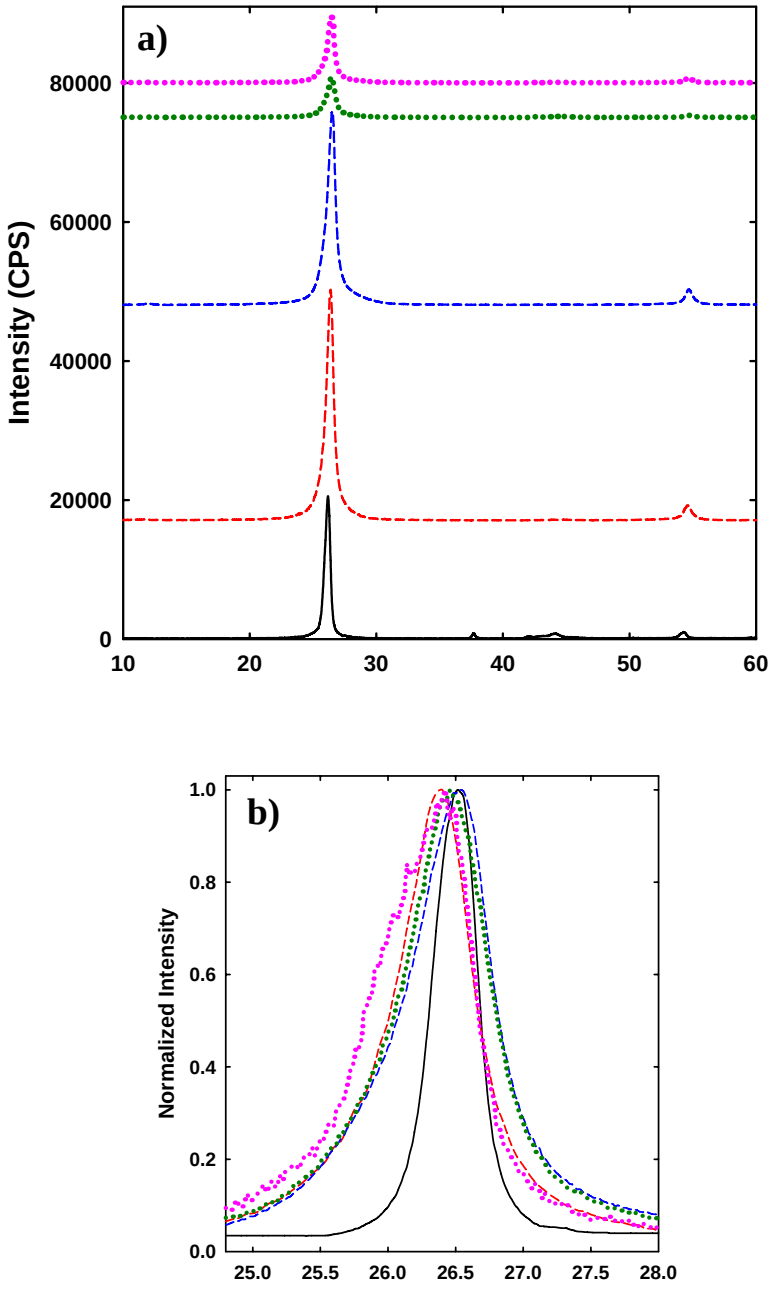

Figure 3.3 X-ray powder diffraction patterns of (a) as-supplied expanded graphite (solid line) and $CNS_{EtOH/H+}$ [stacked from the bottom to the top according to increasing the sonication time in acids 6, 24 h (dash line), 48, 72 h (dotted line)]; and (b) the corresponding (002) peaks (normalized intensity).

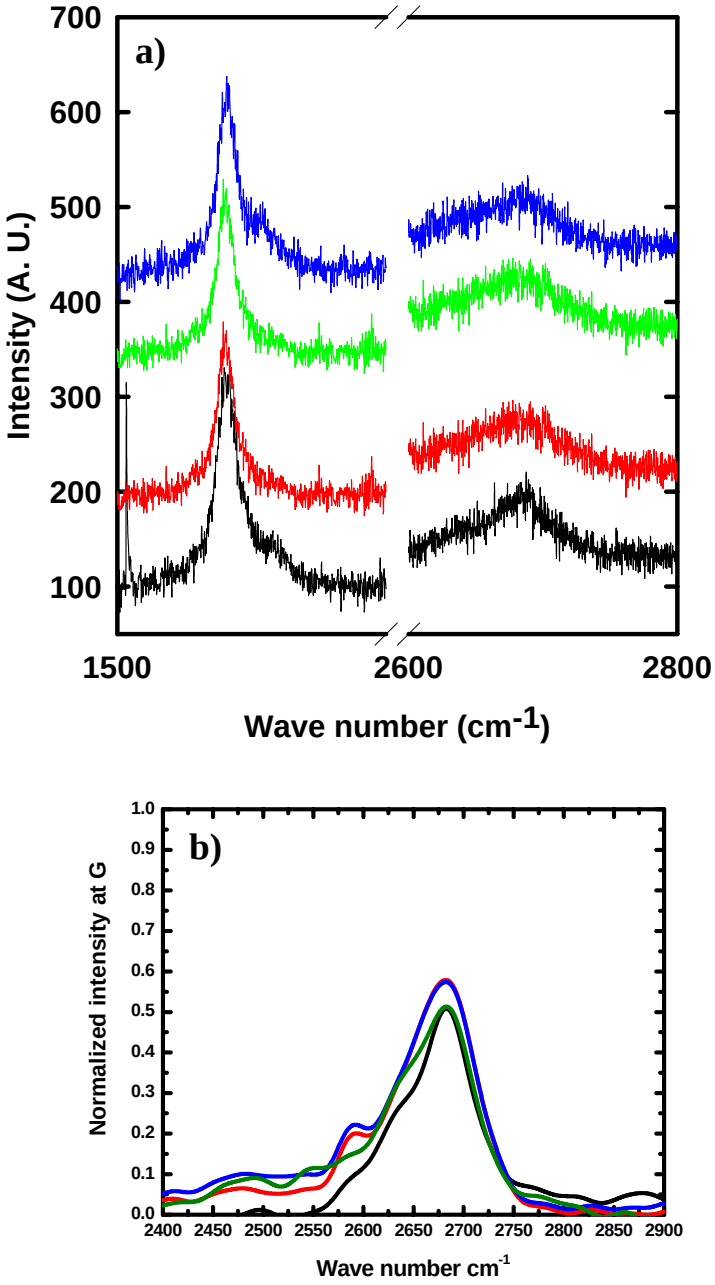

Figure 3.4 (a) Stacked Raman spectra of (from bottom to top) the as-supplied expanded graphite, CNS_{EtOH}, $CNS_{EtOH/H+}$ 48h, and $CNS_{EtOH/H+}$ 72 h; and (b) the corresponding normalized 2D bands.

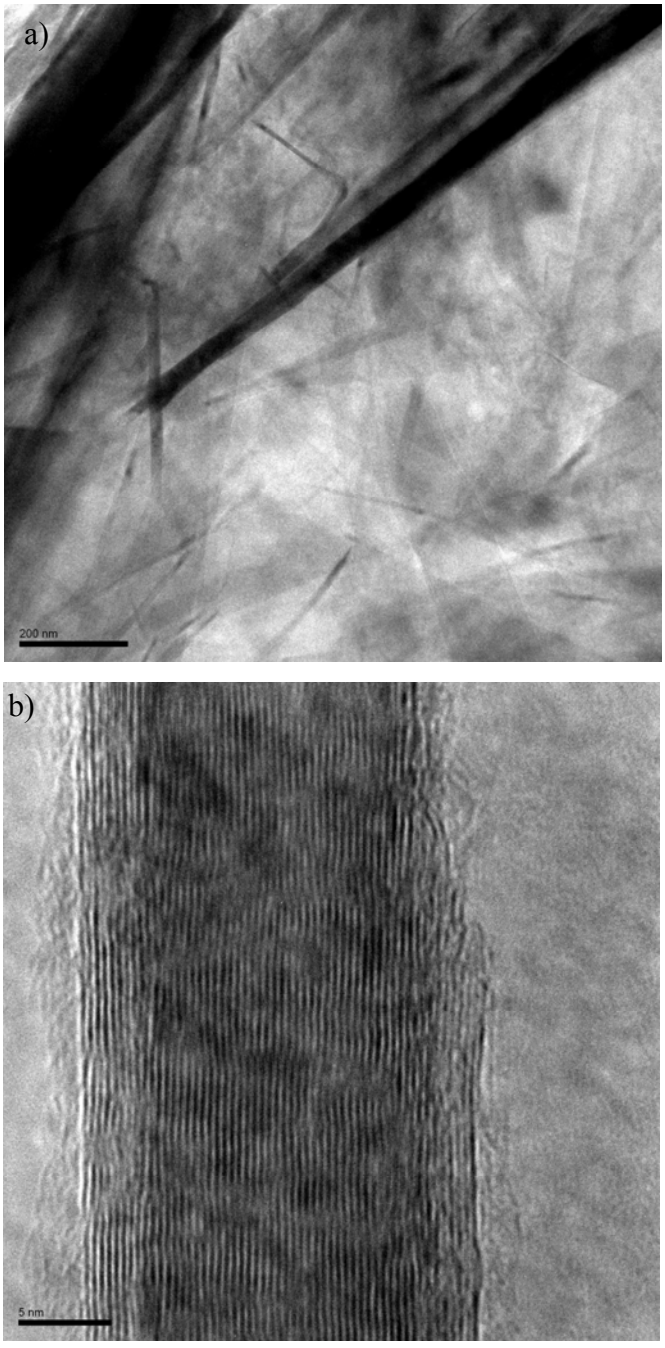

Figure 3.5 (a) TEM and (b) HR-TEM images of the as-supplied expanded graphite sample, with the latter showing ~ 50 graphene layers.

In comparison, the high resolution TEM image of the $CNS_{EtOH/H+}$ sample presented in Figure 3.6 shows a carbon nanosheet with about 10 graphene layers (4-5 nm thick). The general inspection of the sample in TEM suggested carbon nanoshees with thicknesses lower than 20 graphene layers.

Exfoliation with Supercritical or Near-Critical Fluids

As-supplied expanded graphite and treated CNS samples described above were used as starting materials for processing under supercritical or near-critical fluid conditions.

$CNS_{SC\text{-}EtOH}$ and $CNS_{SC\text{-}Tol}$ - An alcohol suspension of the as-supplied graphite sample was heated in a high-pressure reactor at 350°C (T_r (T/T_c) of 1.2 for the alcohol) for 6 h. Then, the treated sample was cooled to ambient temperature, and dried to yield the $CNS_{SC\text{-}EtOH}$ sample.

Similar processing conditions were applied to a toluene suspension of the same sample, but with the heating at 250°C (T_r of 0.88 for toluene) for 16 h, to yield the $CNS_{SC\text{-}Tol}$ sample.

$CNS_{EtOH/SC\text{-}EtOH}$ - The graphite sample obtained from the treatment with alcohol only (CNS_{EtOH}) as described in experimental section was suspended in alcohol and heated in a high-pressure reactor at 350 ºC for up to 24 h to yield $CNS_{EtOH/SC\text{-}EtOH}$.

$CNS_{H+/SC\text{-}EtOH}$ - An alcohol suspension of CNS_{H+} (sonicated for about 8 days in the original preparation) was transferred to the high-pressure reactor and heated to 350 ºC for 24 h.

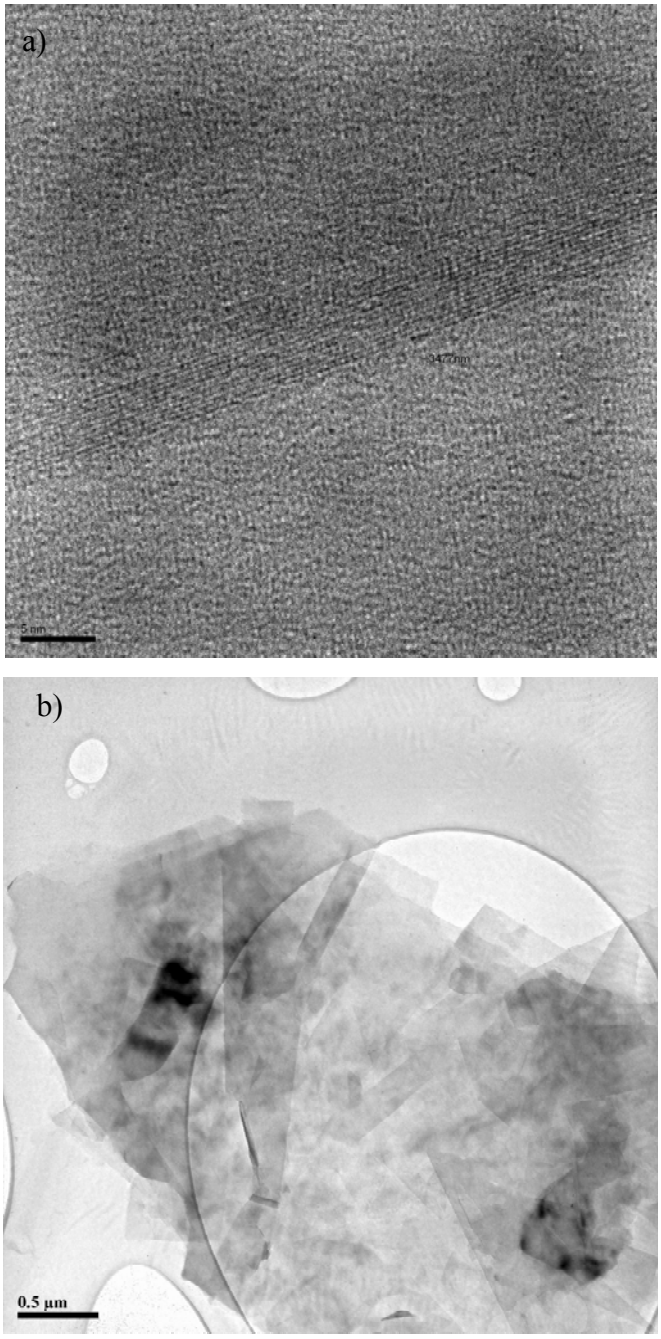

Figure 3.6 (a) HR-TEM image of a piece from the $CNS_{EtOH/H+}$ sample showing carbon nanosheet with ~10 graphene layers; and (b) TEM image of the same sample showing electron transparent, folded carbon nanosheets.

$CNS_{(EtOH/H+)/SC\text{-}EtOH}$ and $CNS_{(EtOH/H+)/Mix(Tol\text{-}EtOH)}$ - The $CNS_{EtOH/H+}$ sample (obtained by sonication for 48-72 h in the original acid treatment as described in the experimental section) was first sonicated in alcohol, and the resulting suspension was heated in the high-pressure reactor at 350 ºC for up to 48 h to yield $CNS_{(EtOH/H+)/SC\text{-}EtOH}$.

Similarly, the 48 h $CNS_{EtOH/H+}$ sample was suspended in a toluene-ethanol mixture (3/1, 2/1, 1/1, or 1/0, v/v) and heated in the high-pressure reactor to 350 ºC for 16 h to yield $CNS_{(EtOH/H+)/Mix(Tol\text{-}EtOH)}$.

$CNS_{(EtOH/H+)/SC\text{-}H2O}$ and $CNS_{(EtOH/H+)/SC\text{-}DMF}$ - The $CNS_{EtOH/H+}$ sample (obtained with sonication for 48-72 h in the original acid treatment as described in the experimental section) was suspended in water and heated in the high-pressure reactor at 375ºC (T_r of 1.0 for water) for 24 h to yield $CNS_{(EtOH/H+)/SC\text{-}H2O}$.

Similarly, the $CNS_{(EtOH/H+)/SC\text{-}DMF}$ was obtained with heating in DMF at 340ºC (T_r of 0.95 for DMF) for 24 h.

The samples processed under supercritical or near-critical fluid conditions exhibited significant increase in volume in comparison with those pre-treatment. In terms of visual inspection, the $CNS_{(EtOH/H+)/SC\text{-}H2O}$ and $CNS_{(EtOH/H+)/SC\text{-}DMF}$ samples appeared significantly better exfoliated, with larger increases in the sample volume post-treatment.

All of the samples were dispersed into polymeric matrices in the fabrication of polymeric/carbon nanocomposite thin films (see below) for thermal diffusivity (TD) measurements, which served as the means to evaluate the effectiveness of exfoliation and the performance of the carbon nanosheets in the corresponding samples. The samples

processed with supercritical alcohol and those with better TD performance were characterized by using several instrumental techniques.

Characterization, X-ray. Figure 3.7 compares the X-ray powder diffraction patterns of as-supplied expanded graphite and $CNS_{SC\text{-}EtOH}$ samples. The peak around 26.5 degree corresponding to (002) planes shows some broadness after supercritical treatment, with the average thickness decreasing from 22 nm in the as-supplied expanded graphite sample to around 14 nm after supercritical fluid treatment.

In a similar comparison, also shown in Figure 3.7, the same X-ray diffraction peak in the $CNS_{(EtOH/H+)/SC\text{-}EtOH}$ sample was broader than those in both as-supplied sample and $CNS_{SC\text{-}EtOH}$, with the average thickness of nanosheets estimated at around 10 nm in terms of Scherrer equation.

In addition to the slight decrease of the carbon nanosheets thickness, we have consistently observed a relatively large decrease in the intensity. Theoretically, graphite that has been "completely exfoliated" will show no diffraction peak of the (002) planes, thus this decrease in the intensity could be associated with the increase of the exfoliation degree.

Characterization, Raman. As shown in Figure 3.8, the Raman spectrum of $CNS_{(EtOH/H+)/SC\text{-}EtOH}$ also featured G-band and 2D-band, which were generally similar to those in the as-supplied sample and $CNS_{EtOH/H+}$.

Characterization, TEM. A representative TEM image of the $CNS_{(EtOH/H+)/SC\text{-}EtOH}$ sample is presented in Figure 3.9, where the carbon nanosheets appear folded and thin, in general, transparent to the electron beam.

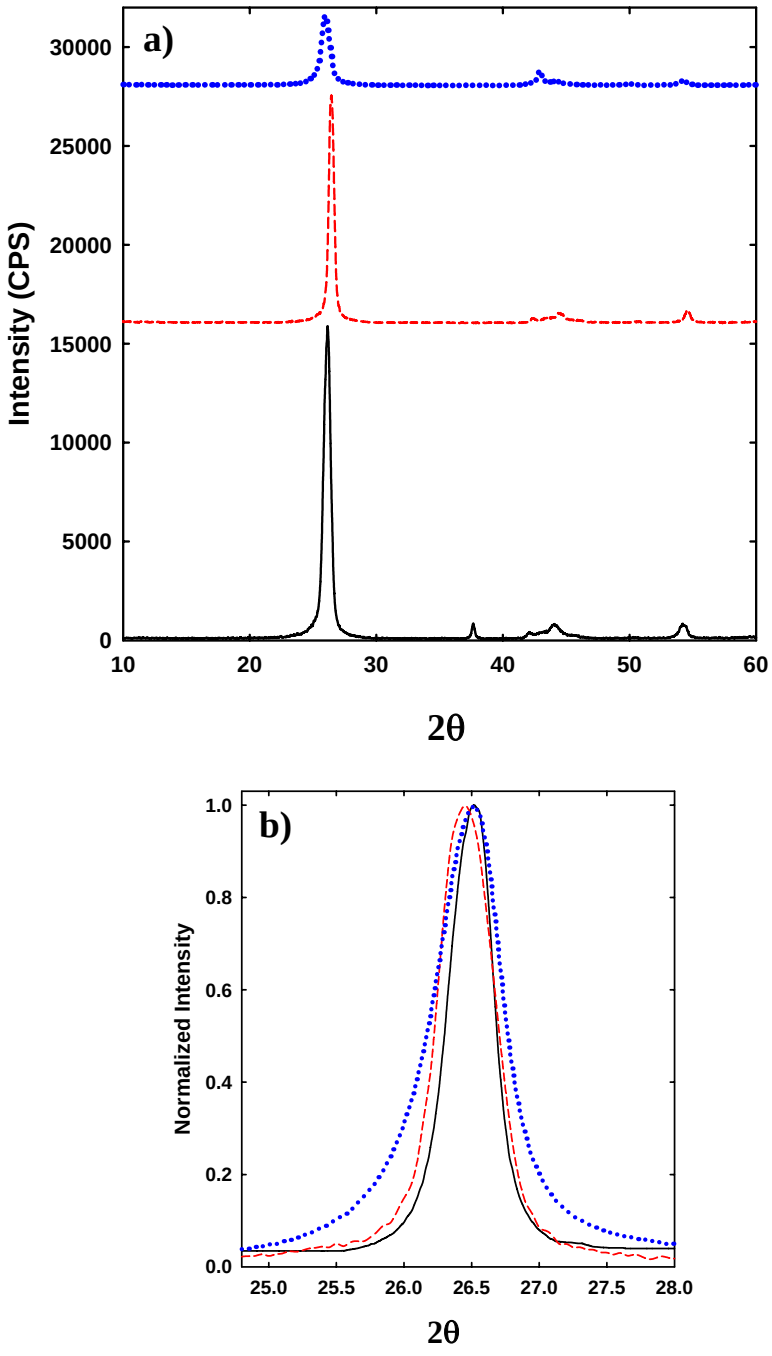

Figure 3.7 X-ray powder diffraction patterns of (a) as-supplied expanded graphite (solid line); $CNS_{SC\text{-}EtOH}$ (dash line); $CNS_{(EtOH/H+)/SC\text{-}EtOH}$ (dotted line); and (b) the corresponding (002) peaks (normalized intensity).

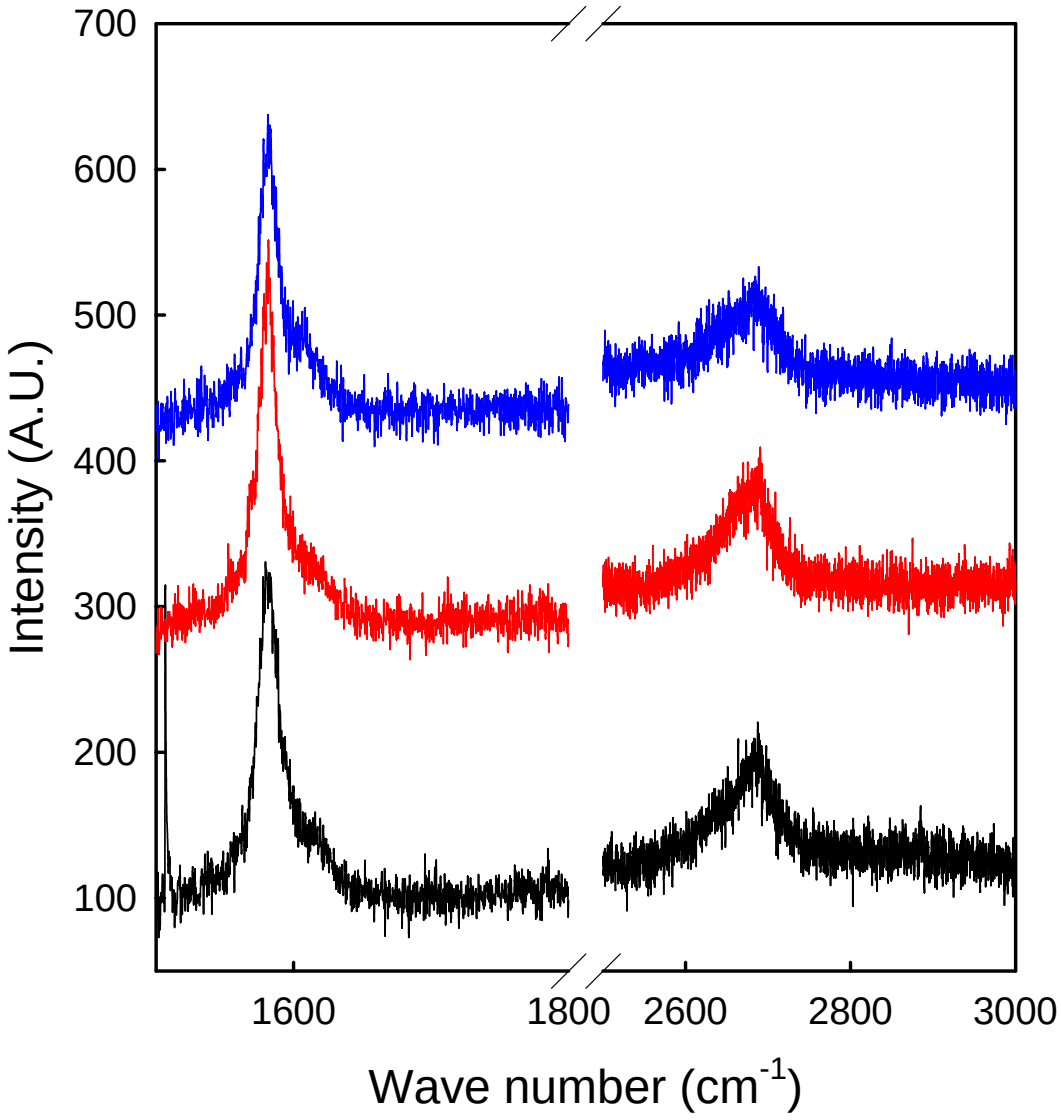

Figure 3.8 Raman spectra of the as-supplied expanded graphite (bottom); $CNS_{(EtOH/H+)/SC\text{-}EtOH}$ (middle); and $CNS_{EtOH/H+}$ (top).

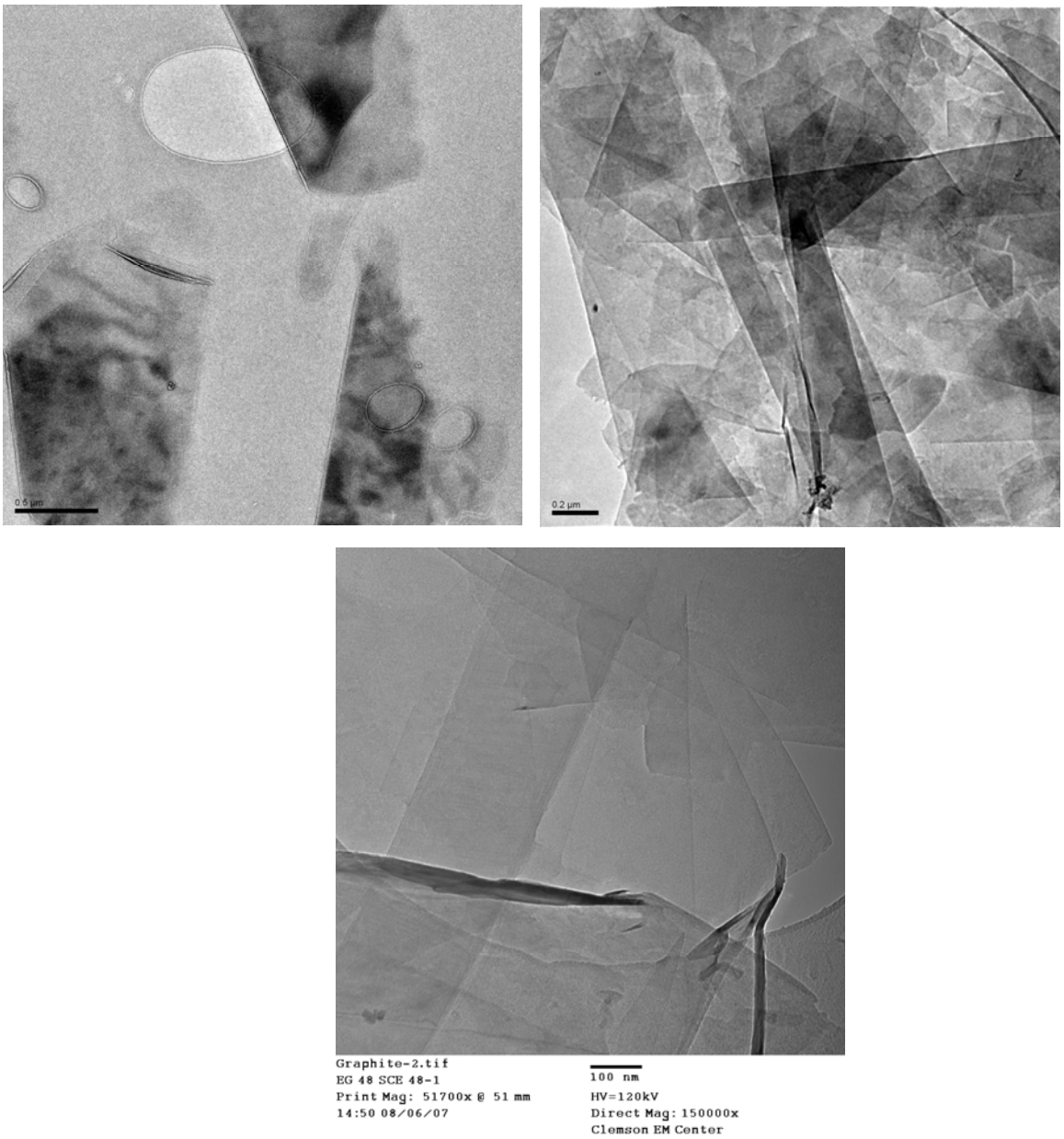

Figure 3.9 TEM images showing folded and electron transparent $CNS_{(EtOH/H+)/SC\text{-}EtOH}$ specimens.

Exfoliation with Other Methods

In these experiments the treated sample ($CNS_{EtOH/H+}$) was used to explore new exfoliation methods such as rapid heating followed by alcohol treatment and C-O cleavage with boron tribromide.

$CNS_{(EtOH/H+)/RH-EtOH}$ - The $CNS_{EtOH/H+}$ sample (obtained by sonication for 6 and 48 hours in the original acid treatment as described in the experimental section) was thermally exfoliated and then treated in alcohol-water mixture by stirring at room temperature and subsequent sonication to yield $CNS_{(EtOH/H+)/RH-EtOH}$.

$CNS_{(EtOH/H+)/Aq}$ - In this experiment a pre-dried sample of $CNS_{EtOH/H+}$ (obtained by sonication for 72 h in the original acid treatment as described in the experimental section) was homogenized and sonicated in dry CH_2Cl_2. To a cooled solution of relatively well dispersed graphite in CH_2Cl_2 was added dropwise a solution of BBr_3 in CH_2Cl_2 over 90 min. The solution was then allowed to react for 4 days at room temperature. At the end of the reaction time the graphite was carefully hydrolyzed with water to obtain the final product with a gum-spongy like appearance. During the hydrolysis process effervescence was observed as the HBr was released. The crud product, $CNS_{(EtOH/H+)/Aq}$, was recovered by centrifugation and intensively washing with water and ether. The sample thus obtained could readily be dispersed in water to form a relatively stable aqueous suspension but still gray in color (an indication on preservation of the graphite network).

The materials obtained at the end of these treatments were characterized using transmission electron microscopy (TEM) and X-ray diffraction (XRD), and their properties were evaluated in terms of thermal diffusivity.

Characterization, X-ray. The X-ray diffraction patterns of thermal exfoliation and boron tribromide treatment are presented in Figures 3.10 and 3.11, respectively. Using once again the Scherrer equation we were able to estimate the average thickness at about 20 and 8 nm for $CNS_{(EtOH/H+)/RH\text{-}EtOH}$ and $CNS_{(EtOH/H+)/Aq}$, respectively.

Characterization, TEM. The TEM image of $CNS_{(EtOH/H+)/Aq}$ in Figure 3.12 shows that the carbon nanosheets thus obtained are electron transparent with thickness ranging from 6 to 20 nm. As also shown in Figure 3.12, the CNS obtained by this method presents folds and scrolls at the edges, with large parts of the inner regions appearing featureless. Occasionally we would see surface contamination or adsorbates of unknown nature, such as those visible in Figure 3.12 (b).

In conclusion, the thermal exfoliation led to CNS with thickness much larger than that of $CNS_{EtOH/H+}$, while the treatment with boron tribromide yielded CNS with similar thickness to that of $CNS_{EtOH/H+}$.

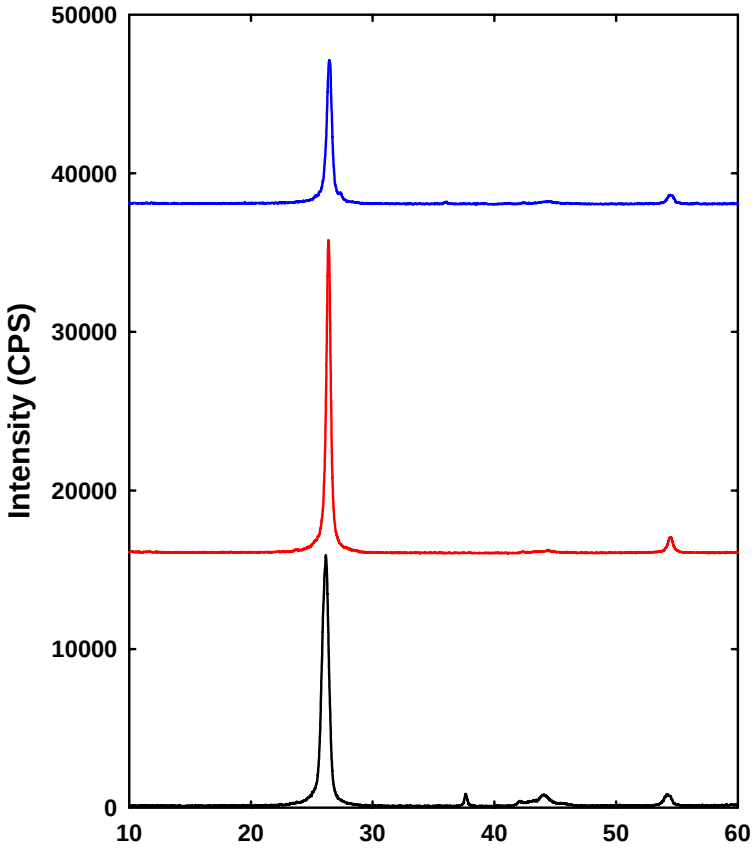

Figure 3.10 X-ray powder diffraction patterns of the as-supplied expanded graphite sample (bottom) and the $CNS_{(EtOH/H+)/RH-EtOH}$ processed sample from $CNS_{EtOH/H+}$ with 6 h (middle) and 48 h (top) acid treatment.

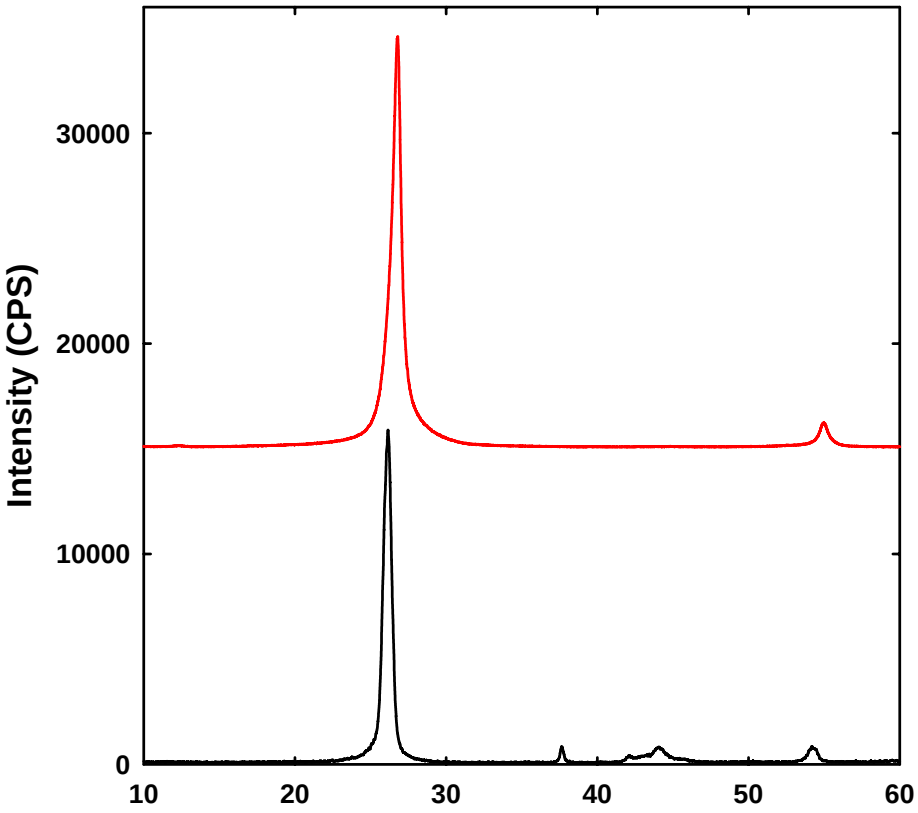

Figure 3.11 X-ray powder diffraction patterns of the as-supplied expanded graphite sample (bottom) and $CNS_{(EtOH/H+)/Aq}$ (top).

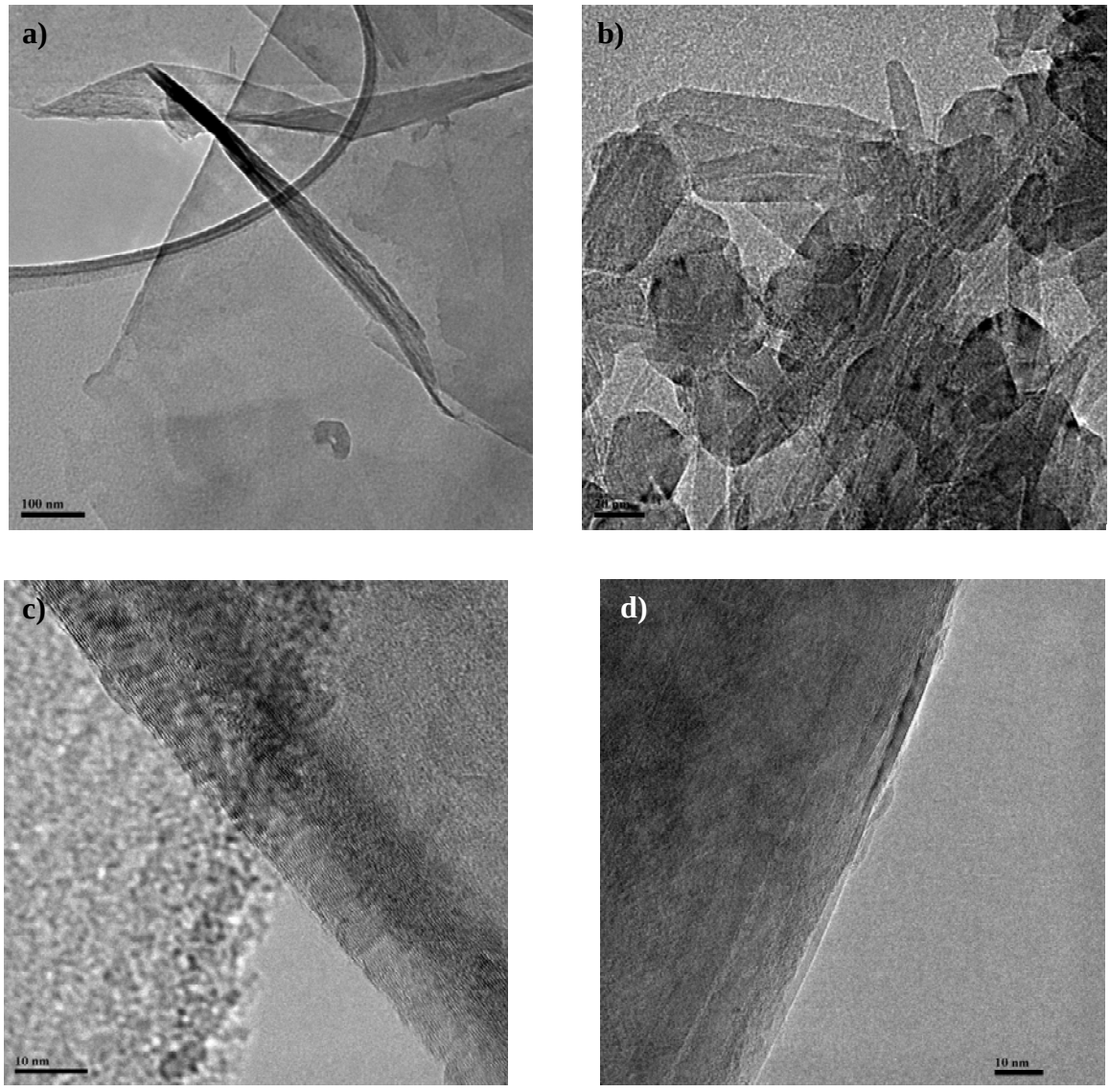

Figure 3.12 TEM (a,b) and HR-TEM (c,d) images of $CNS_{(EtOH/H+)/Aq}$.

Polymeric Nanocomposites

Polymeric composites of the as-supplied expanded graphite sample and processed CNS in PVA, Elvax (with 40 wt% acetate), polyimide (CP-2), and epoxy were prepared, and their thermal diffusivity at room temperature measured. The fabrication of these composites has been described in the experimental section. Briefly, a weighted amount of the carbon nanomaterial was suspended in water, ethanol or DMF (depending on the polymer in the nanocomposite) via combined homogenization and sonication. The colloidal suspensions thus obtained were added dropwise to a dilute solution of PVA in hot water, Elvax, in toluene, and polyimide or epoxy polymers in DMF. The resulting mixtures were vigorously stirred at room temperature for 12 h, concentrated, and subsequently cast on a glass slide. The slide was purged with nitrogen gas, and then the nanocomposite thin film (<100 microns in thickness) was peeled off to be freestanding. The slides with polyimide and epoxy resin nanocomposites were immersed in water for 30 minutes in order to release the freestanding film.

Upon careful drying, the films were used in thermal diffusivity measurements, and representative examples were characterized by X-Ray and TEM.

Thermal Diffusivity. The in-plane thermal diffusivity results of PVA-CNS composites with 20% and 30% CNS by weight are presented in Figure 3.13. Thermal diffusivity of these nanocomposites seems to depend on the method used to process the graphite, as well as on the sonication time in acids during the preparation of CNS. While thermal diffusivity values of the composites containing the as-supplied expanded graphite sample and alcohol treated CNS are almost the same, those of the composites containing

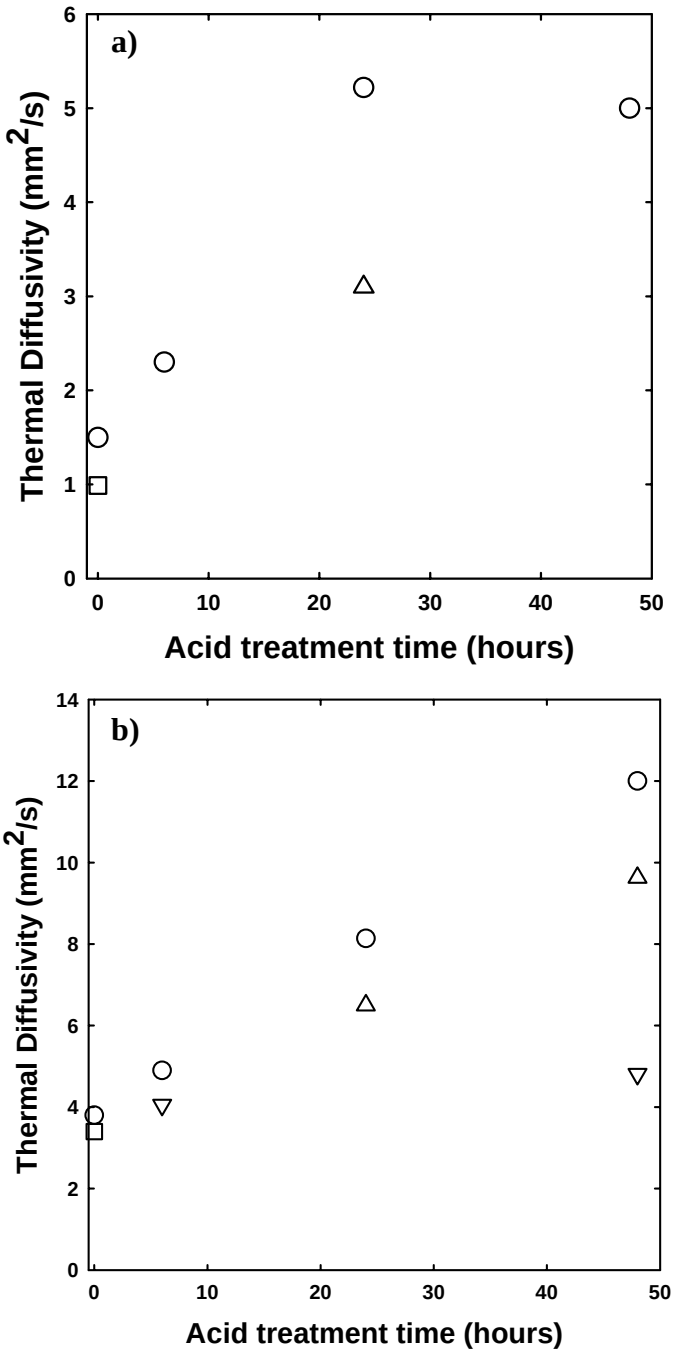

Figure 3.13 Thermal diffusivity results of PVA-CNS composites with (a) 20 wt% CNS and (b) 30 wt% CNS as a function of the acid treatment time in the processing of $CNS_{EtOH/H+}$ or CNS_{H+}.

□ : As-supplied expanded graphite; ○ : $CNS_{EtOH/H+}$; △ : CNS_{H+}; ▽ : $CNS_{(EtOH/H+)/RH-EtOH}$

$CNS_{EtOH/H+}$ increase monotonically with the increasing sonication time in the acid mixture from 6h to 48h. On the other hand, when the CNS from the acid treatment only (CNS_{H+}) was used to prepare the nanocoposites, thermal diffusivity was higher than that of the starting material but it was lower than the sample from the alcohol and then acid mixture treatment (with the same sonication time in acid mixture). As regarding the composites with CNS obtained after the thermal expansion and subsequent alcohol treatment, their performances in terms of thermal diffusivity were similar to those of the starting material.

Considering the thickness of the CNS evaluated by using Scherrer equation, all these results are suggesting that the thermal diffusivity of the nanocomposites depends upon the thickness of the carbon nanosheets. As shown in Figure 3.14 there is indeed an increase in thermal diffusivity with decreasing thickness of the carbon nanosheets.

Thermal diffusivity of PVA-nanocomposites containing CNS processed by super -critical ethanol at 350°C for 24 h is presented in Figure 3.15 which shows a similar trend to those from samples treated at ambient conditions. However, there is a significant decrease in the thermal diffusivity of the PVA nanocomposites containing $CNS_{(EtOH/H+)/SC-H2O}$. This low thermal diffusivity could be due to the oxidative effect of supercritical water, which could introduce defects in the graphene network and thus reduce the phonon mean free path. Further investigation of the treated sample by infrared spectroscopy and X-ray photoelectron spectroscopy could prove this hypothesis. Similar phenomenon could be observed when the CNS were sonicated for very long time in the acid mixture, thus relatively low thermal diffusivity of their nanocomposites as well.

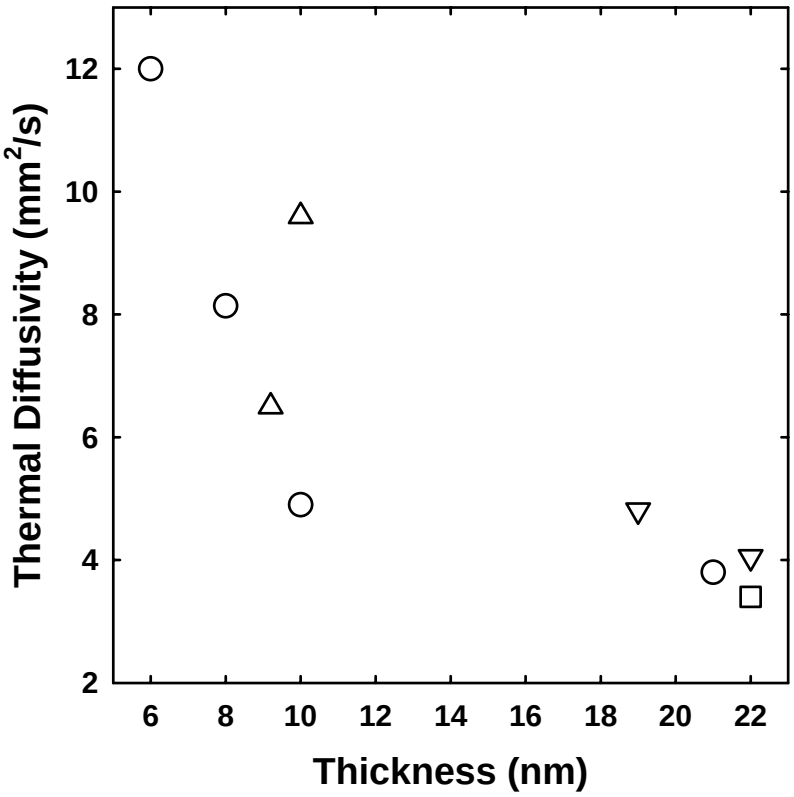

Figure 3.14 Thermal diffusivity results of PVA-CNS composites with 30 wt% CNS as a function of the CNS thickness determined by Scherrer equation.

□: As-supplied expended graphite; ○: $CNS_{EtOH/H+}$; △ : CNS_{H+}; ▽ : $CNS_{(EtOH/H+)/RH-EtOH}$

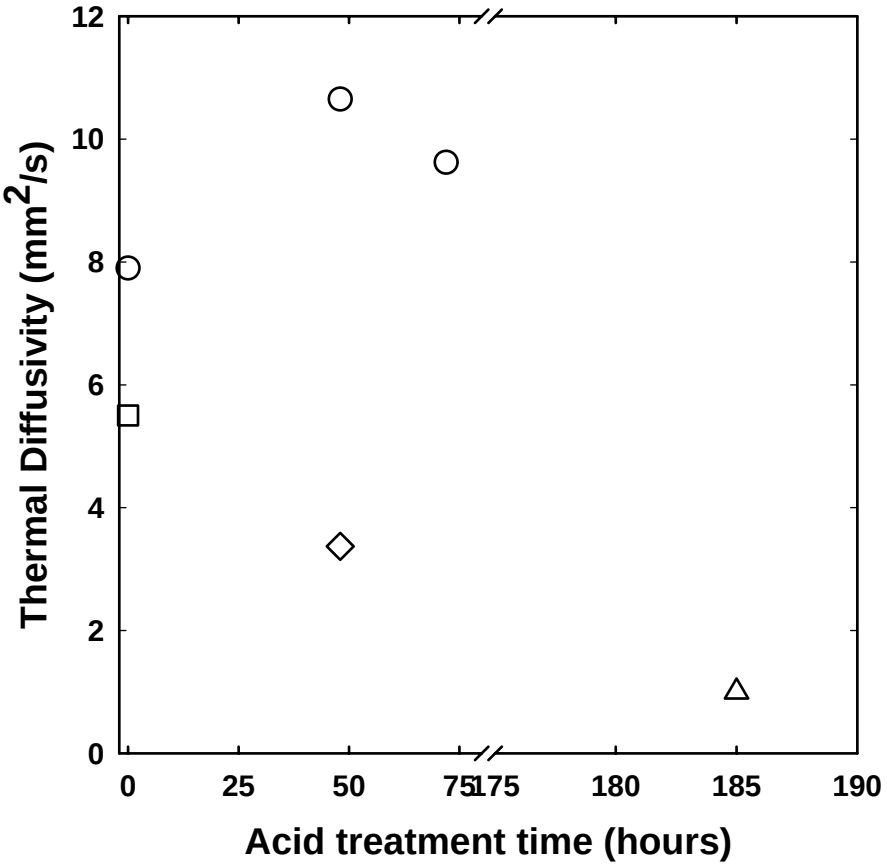

Figure 3.15 Thermal diffusivity results of PVA-CNS composites with 30 wt% CNS (from the supercritical fluid) as a function of the acid treatment time in the processing of $CNS_{EtOH/H+}$ or CNS_{H+}.

□ : $CNS_{SC\text{-}EtOH}$; ○ : $CNS_{(EtOH/H+)/SC\text{-}EtOH}$; △ : $CNS_{H+/SC\text{-}EtOH}$; ◇ : $CNS_{(EtOH/H+)/SC\text{-}H2O}$

The room temperature thermal diffusivity of the EVA-CNS (from the ambient and supercritical treatments) composites with 30 wt% filler loading is presented in Figure 3.16. Similar to the PVA-nanocomposites, the lowest value was for the as-supplied expanded graphite and the highest for the $CNS_{EtOH/H+}$ after 48 h acid treatment. As for the CNS treated in supercritical toluene at 250°C for 16 h, the thermal diffusivity of the EVA-nanocomposite was almost as low as the one from as-supplied expanded graphite. An even lower thermal diffusivity was obtained when the $CNS_{EtOH/H+}$ from the 48 h sonication in nitric acid-sulfuric acid mixture was treated in supercritical toluene at 350°C for 16 h. This poor performance could be due to the solvent polarity, so that toluene-ethanol mixtures were used. As illustrated in Figure 3.16, the thermal diffusivity of the EVA-nanocomposites increased with the increasing toluene to ethanol ratio, and reaching 6.4 mm^2/s at ratios of 2/1 and 3/1 v/v.

Similar thermal diffusivity results were obtained for the polyimide nanocomposites (Figure 3.17).

The thermal diffusivity results of the epoxy nanocomposites with CNS loading of 50 wt% are presented in Figure 3.18. The thermal diffusivity of these composites shows a relatively linear increase with increasing the sonication time of the CNS_{EtOH} in acid mixture, from 0 to 72 h. Similar to the previous polymeric matrices, thermal diffusivity of epoxy-CNS_{H+} was lower than that of epoxy-$CNS_{EtOH/H+}$ composites. Also shown in Figure 3.18 is the thermal diffusivity of epoxy-$CNS_{(EtOH/H+)/Aq}$ composite, which is lower than that of starting epoxy-$CNS_{EtOH/H+}$, with a slight increase when the DMF instead of water was used to disperse the $CNS_{(EtOH/H+)/Aq}$ into the polymer.

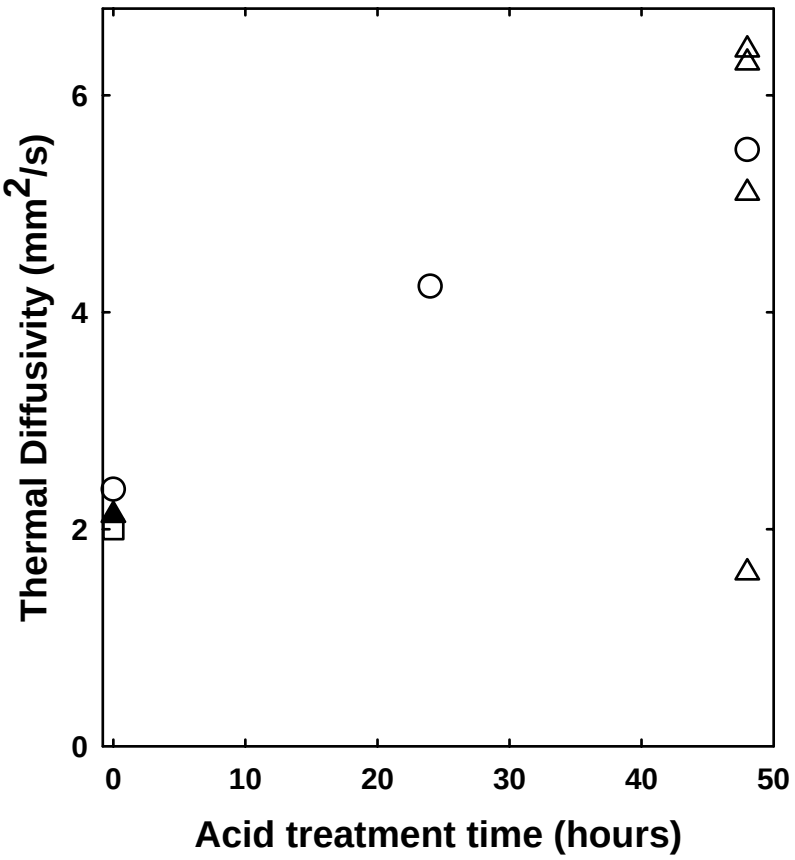

Figure 3.16. Thermal diffusivity results of EVA-CNS composites with 30 wt% CNS (from the processing at ambient and supercritical fluid) as a function of the acid treatment time in the processing of $CNS_{EtOH/H+}$.

□ :As-supplied expanded graphite; ○: $CNS_{EtOH/H+}$; ▲: CNS_{SC-Tol};
△ : $CNS_{(EtOH/H+)/Mix(Tol-EtOH)}$ (Tol-EtOH ratio from bottom to top 1/0,1/1, 2/1, and 3/1 v/v).

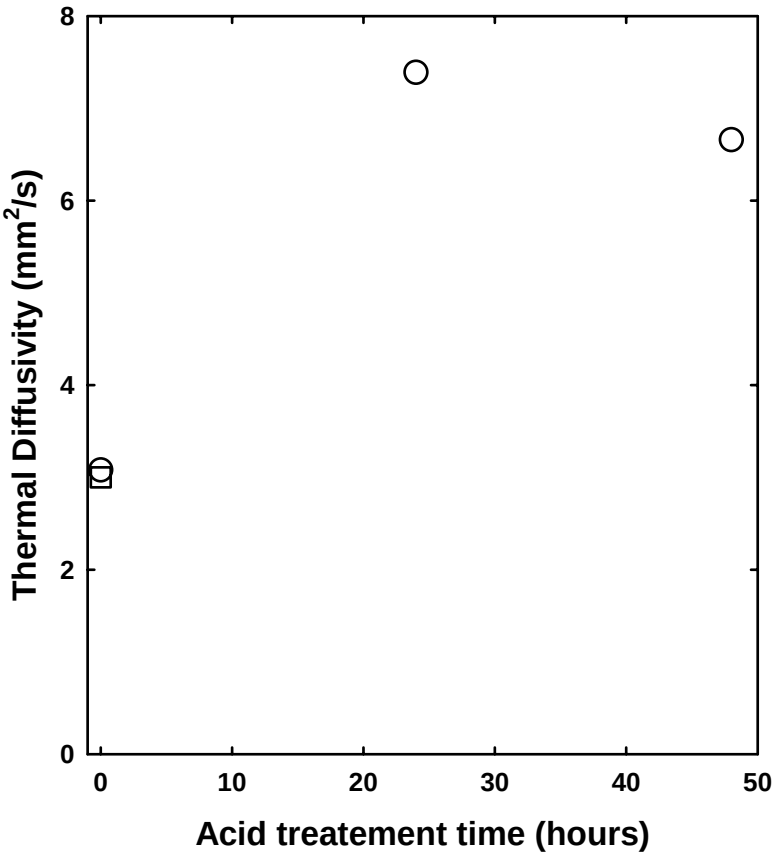

Figure 3.17 Thermal diffusivity results of polyimide-CNS composites with 30 wt% CNS as a function of the acid treatment time in the processing of $CNS_{EtOH/H+}$.

□ : As-supplied expanded graphite; ○ : $CNS_{EtOH/H+}$

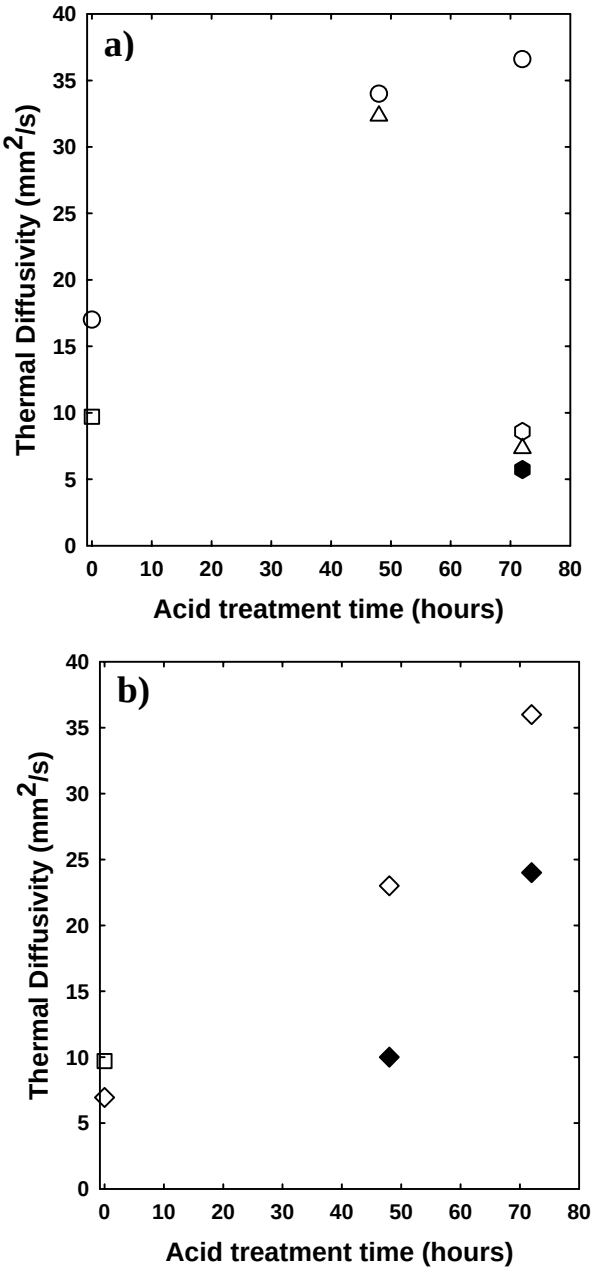

Figure 3.18 Thermal diffusivity results of epoxy-CNS composites with 50 wt% CNS as a function of the acid treatment time in the processing of $CNS_{EtOH/H+}$ or CNS_{H+}. (a) CNS processed at ambient conditions, and (b) CNS processed in supercritical fluid.

□ :As-supplied expended graphite; ○ : $CNS_{EtOH/H+}$; △ :CNS_{H+}; $CNS_{(EtOH/H+)/Aq}$ (⬢ water solvent) and (⬡ DMF solvent); ◇ :$CNS_{(EtOH/H+)/SC\text{-}EtOH}$; ◆ : $CNS_{(EtOH/H+)/SC\text{-}DMF}$

This could be the result of the C-O cleavage which probably produced shorter CNS. Even thought the thickness was similar to the starting material ($CNS_{EtOH/H+}$), the aspect ratio could be lower. Neither of the supercritical treatments led to higher performance in the thermal diffusivity of epoxy-nanocomposite. Between ethanol and DMF, it seems that ethanol was better.

Regardless of the polymeric matrix, there is a relatively low or at least marginal increase in the thermal diffusivity of polymeric composites containing $CNS_{EtOH/H+}$ treated in acid mixture for 72 h compare to those for 48 h. In order to understand if this phenomenon was due to the CNS, we prepared pellets of the carbon nanosheets from the exfoliation with alcohol and/or acid for their thermal diffusivity (Figure 3.19). As we can see, the highest thermal diffusivity was for the $CNS_{EtOH/H+}$ sonicated for 48 h in acid mixture. This result may suggest that the lateral size of the CNS became smaller after 48 h of sonication, thus increasing the connection points to result in an increase in the phonon scattering.

A histogram of polymer-$CNS_{EtOH/H+}$ and polymer-$CNS_{(EtOH/H+)/SC-EtOH}$ composites with 30 wt% CNS is given in Figure 3.20. The results show that the $CNS_{EtOH/H+}$ -epoxy composites are the best in terms of thermal diffusivity, while EVA nanocomposites are the worst. The differences illustrated in the histogram maybe related to the polymer morphology. The CNS may favor the crystallization of the crystalline epoxy and semicrystalline PVA polymers, which may form more rigid structures at the CNS-polymer interface to favor the phonon transport.

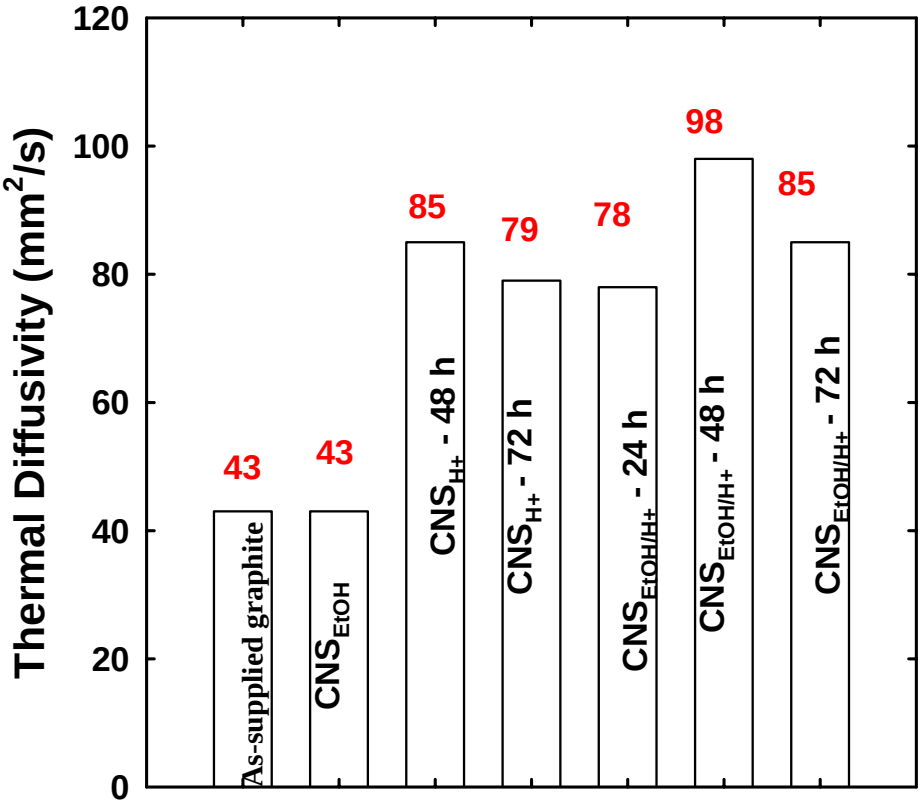

Figure 3.19 Thermal diffusivity results of as-supplied expanded graphite and processed CNS pellets without polymer.

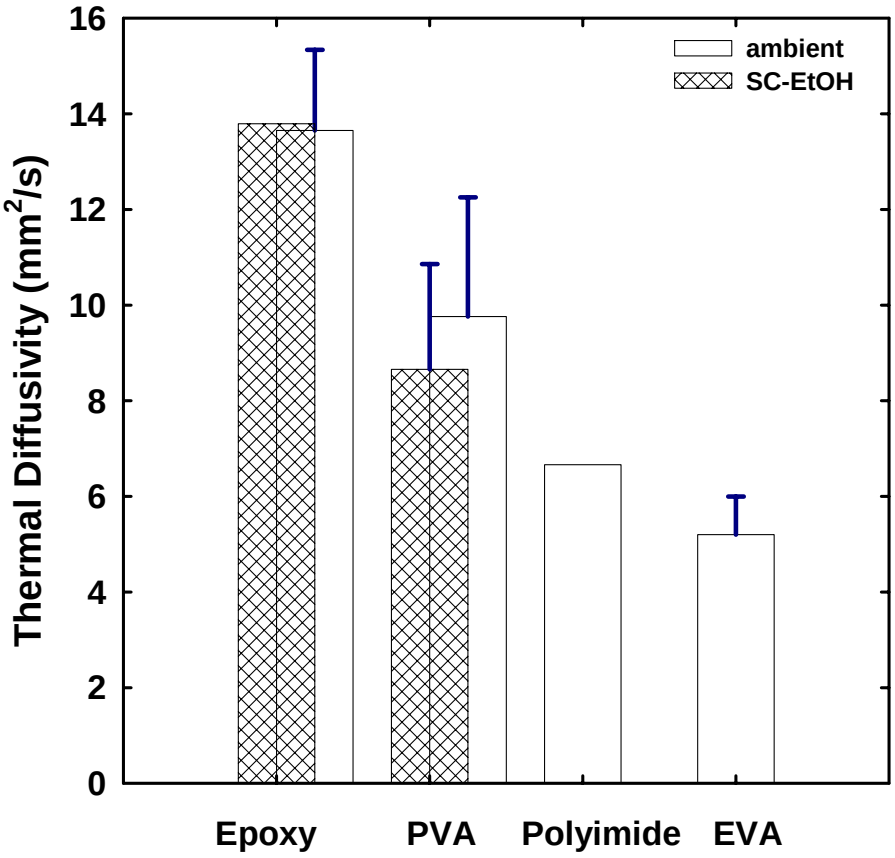

Figure 3.20 Thermal diffusivity results of $CNS_{EtOH/H+}$ and $CNS_{(EtOH/H+)/SC\text{-}EtOH}$ polymeric composites with 30 % CNS loading by weight.

As expected, the thermal diffusivities of the polymeric nanocomposites are strongly dependent on carbon nanosheets loadings. An increase in the fractions of the nanosheets consistently resulted in higher thermal diffusivities of the nanocomposites. This is demonstrated in Figure 3.21 for the epoxy-$CNS_{EtOH/H+,}$ polyimide-$CNS_{EtOH/H+,}$ PVA-$CNS_{EtOH/H+,}$ and PVA-$CNS_{(EtOH/H+)/SC-EtOH}$ thin films. It seems that the PVA nanocomposites are reaching a plateau at lower volume fractions, while polyimide and epoxy at much higher volume fractions.

The composites with 30 wt% $CNS_{EtOH/H+}$ in PVA, epoxy, polyimide and EVA were characterized by X-ray diffraction and TEM, and the results are compared in Figures 3.22 and 3.23, respectively.

Characterization, X-ray. The XRD results of the PVA, epoxy, EVA and polyimide nanocomposites are presented in Figure 3.22, which show the same reflection peaks at about 26.61, corresponding to (002) planes of the graphene layers. There is no evidence for a new crystal structure of the polymer, but the diffraction intensity decreased compare to the blank polymer, which may suggest that the crystallinity of each polymer was affected by the presence of CNS.

Characterization, TEM. Characteristic micrographs of these nanocomposites are presented in Figure 3.23. They are showing that PVA and epoxy form lamellar structure on top of the CNS, while EVA appears more like a leather structure. The size of one lamellar fibril from the TEM micrographs is around 5 and 12 nm for PVA and epoxy, respectively. Probably the more ordered lamellar structure is more favorable in the phonon transport than the leather one.

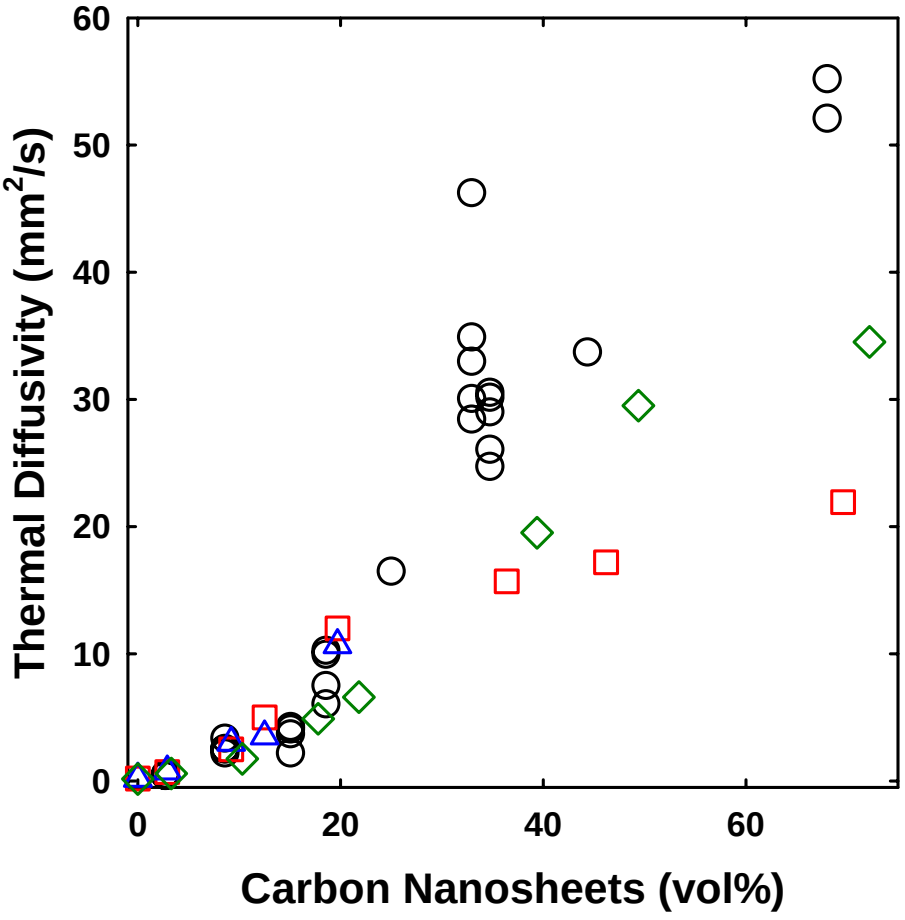

Figure 3.21 Thermal diffusivity dependence on the carbon nanosheets loading in polymer

○ : epoxy-$CNS_{EtOH/H+}$; □ : PVA- $CNS_{EtOH/H+}$; ◇ : Polyimide- $CNS_{EtOH/H+}$; △ : PVA-$CNS_{(EtOH/H+)/SC-EtOH}$.

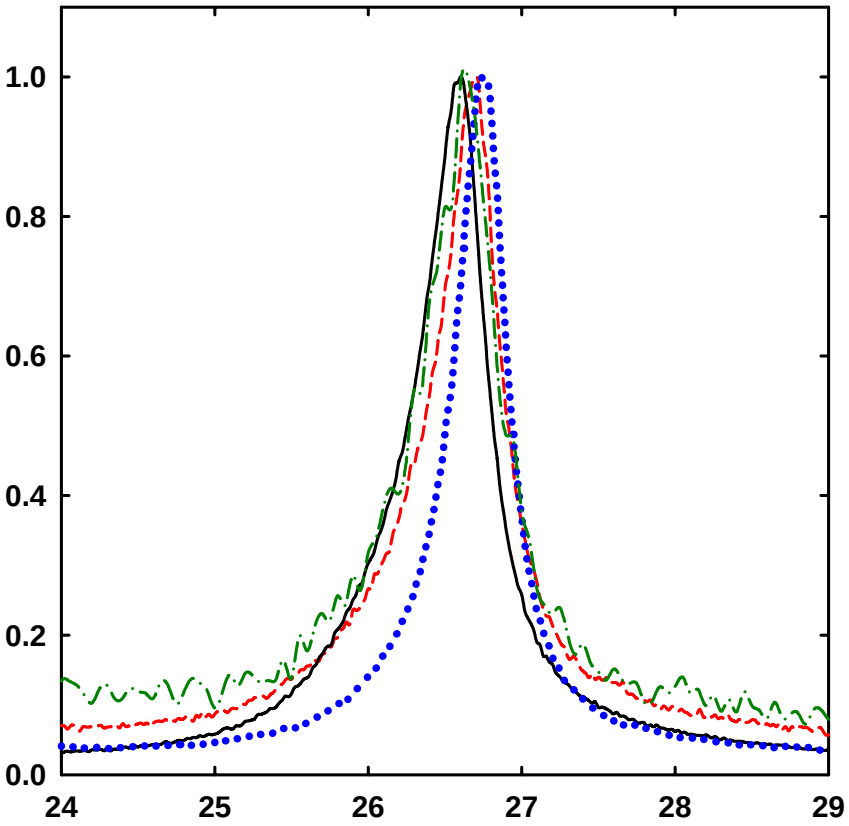

Figure 3.22 X-ray diffraction patterns of polyimide (solid line), PVA (dashed line), EVA (dash-dot line), and epoxy (dotted line) - $CNS_{EtOH/H+}$ composites with 30 wt% CNS loading.

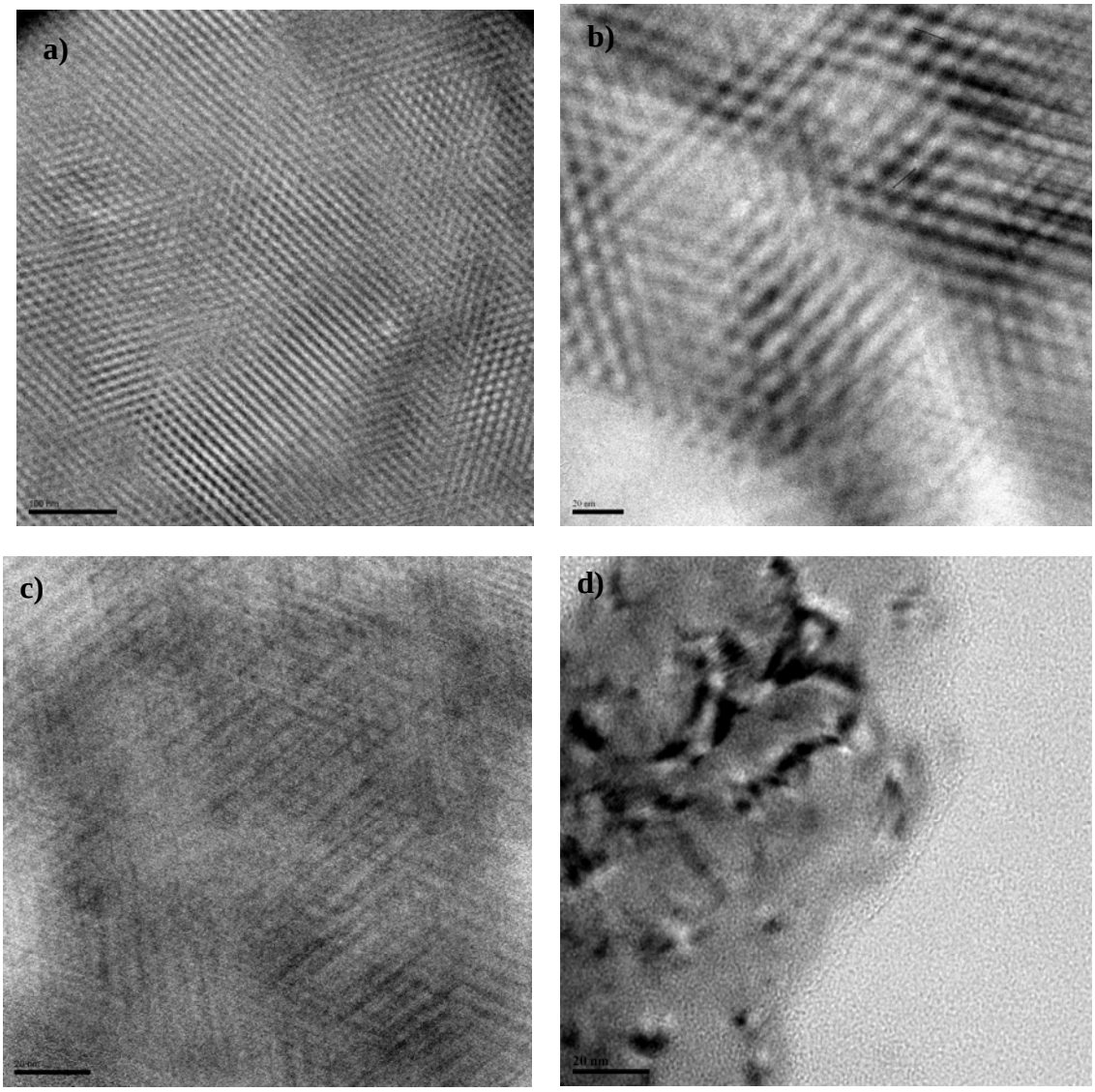

Figure 3.23 HR-TEM images of epoxy (a,b); PVA (c); and EVA (d) – $CNS_{EtOH/H+}$ composites.

Summary

In the studies presented in this chapter we used different methods in attempt to further exfoliate the commercially available expanded graphite. The effectiveness of these methods was evaluated by different characterization methods, as well as on the performance of thermal diffusivity in the resulting composites. Among all the exfoliation methods explored, the carbon nanosheets (CNS) produced by the alcohol and then nitric-acid sulfuric-acid sequentially are the lowest in thickness and the highest in thermal diffusivity.

While the CNS from the supercritical fluid treatments exhibited consistently lower thermal diffusivity and higher thicknesses than the starting $CNS_{EtOH/H+}$ (although visually they seem to be better exfoliated), the nanocomposites containing CNS processed by rapid heating and boron tribromide showed the lowest thermal diffusivities. There are few reasons that could be associated with these results: 1) Although the CNS were exfoliated in the supercritical fluid treatment, they tend to restack during the solvent removal for the characterization, thus showing a higher thickness. In order to overcome this limitation the rapid expansion of the supercritical fluid solution into a surfactant solution or polymeric matrix to prevent the restacking process could be used. 2) The lower thermal diffusivity of the composites could be a result of the decrease in their hydrophilicity after the supercritical fluid treatment. During the treatment at high temperature the oxygenated groups (carboxylic acid, hydroxyl or epoxy) could be destroyed so that the hydrophilic-hydrophilic interaction between polymer and CNS might be lowered in favor of the CNS aggregation, consequently reducing the thermal

diffusivity. 3) The boron tribromide probably not only exfoliates the expanded graphite but also forms CNS with lower size and higher defect concentration, which decrease the phonon mean free path in thermal transport.

In addition, it was observed that the epoxy and PVA nanocomposites showed higher thermal diffusivity than CP-2 and EVA nanocomposites at the same filler loading. The lower thermal diffusivity of the CP-2 nanocomposites was expected for the amorphous nature of the polymer, which should increase the interfacial phonon scattering and thus lower the thermal diffusivity. However, it was somewhat surprising that actually the semicrystalline EVA composites exhibited the lowest thermal diffusivity. Probably due to its branched structure (compared to PVA), the polymer could have a reduced tendency toward crystallization. Complementary investigation on the polymer crystal morphology next to the CNS surface as well as investigation of the crystallization kinetics may bring further understanding of these results.

In conclusion, CNS are very promising fillers in the development of light weight highly thermal conductive materials, once the few CNS layers could be effectively separated from the quite heterogeneous sample produced by the various methods investigated in this work.

References

1. Schauffautl, P. *J. Prakt. Chem*. **1841**, *21*, 155

2. Armaud, M.; Touzain, P. Proceedings of the Franco American Conference on Intercalation Compounds of Graphite"(F. L. Vogel and A. Herold, eds). Elsevier Sequoia, Lausanne, **1977**; reprinted from *Mater. Sci. Eng.* **1977**, *31*, 1-352, pp319-329

3. Weng, W.; Chen, G.H.; Wu, D.; Chen X.; Lu, J.; Wang, P. *J. Polym. Sci., Part B* **2004**, *42*, 2844–2856.

4. Hooley, J. G. Proceedings of the Franco American Conference on Intercalation Compounds of Graphite"(F. L. Vogel and A. Herold, eds). Elsevier Sequoia, Lausanne, **1977**; reprinted from *Mater. Sci. Eng*. **1977**, *31*, 1-352, pp 17-24

5. Hooley, J. G. in "Preparation and Crystal Growth of Materials with Layered Structures" (R. M. A. Lieth, ed.), pp 1-33, Reidel Publ., Dordrecht, Netherlands, **1977**

6. Young, D. A. *Carbon* **1977,** *15*, 373

7. Hibbs, J. D.; Young, D. A. *Chem. Phys. Lett*. **1978,** *53*, 361

8. Daumas, N.; Herold, A. *C.R. Hebd. Seances Acad. Sci., Ser. C*, **1969,** *268*, 373

9. Novoselov, K. S.; Geim, A. K.; Morozov, S. V.; Jiang, D.; Zhang, Y.; Dubons, S. V.; Grigorieva, I. V.; Firsov, A. A. *Science* **2004**, *306*, 666

10. Berger, C; Song, Z.; Li, X.; Wu, X.; Brown, N.; Naud, C.; Mayou, D.; Li, T.; Hass, J.; Marchenkov, A. N.; Conrad, E. H.; First, P. N.; Heer, W. A. *Science* **2006**, *312*, 1191-1196

11. Ohta, T.; Bostwick, A.; Seyller, T.; Horn, K.; Rotenberg, E. *Science* **2006**, *313*, 951-954

12. Coraux, J.; N'Diaye, A. T.; Busse, C.; Michely, T. *Nano Lett* **2008**, *8*, 565

13. Hummers, W. S.; Offerman, R. E. *J. Am. Chem. Soc.* **1958,** *80*, 1339

14. Li, D.; Muller, M. B.; Gilje, S.; Kaner, R. B.; Wallace, G. G. *Nature Nanotech*. **2008**, 3, 101-105

15. Dikin, D. A.; Stankovich, S.; Zimney, E. J.; Piner, R. D.; Dommett, G. H. B.; Evmenenko, G.; Nguyen, S. T.; Ruoff, R. S. *Nature* **2007**, *448*, 457-460

16. Stankovich, S.; Dikin, D. A.; Piner, R. D.; Kohlhaas, K. A.; Kleinhammes, A.; Jia, Y.; Wu, Y.; Nguyen, S. T.; Ruoff, R. S. *Carbon*, **2007**, *45*, 1558-1565

17. Stankovich, S.; Dikin, D. A.; Dommett, G. H. B.; Kohlhaas, K. M.; Zimney, E. J.; Stach, E. A.; Piner, R. D.; Nguyen, S. T.; Ruoff, R. S. *Nature*, **2006**, *442*, 282-286

18. Bourlinos, A. B.; Gournis,D.; Petridis, D.; Szabó,T. Szeri, A.; Dékány, I *Langmuir* **2003**, *19*, 6050-6055

CHAPTER FOUR

POLYMER FUNCTIONALIZATION AND SOLUBILIZATION OF CARBON NANOSHEETS

Single- and few-layer graphene materials, conceptually analogous to single-walled and multiple-walled carbon nanotubes (SWNTs and MWNTs, respectively), have attracted much recent attention for their interesting and/or unique properties.[1-7] For example, graphene is a zero-bandgap semiconductor with long-range ballistic transport and high carrier mobility.[4] It is one of the strongest materials, with Young's modulus in terapascals.[5] It is also highly thermal conductive, with estimated conductivity value as high as 5,300 W/mK.[6] A number of methods have been pursued for the production of graphene materials,[7-15] among which the chemical exfoliation of bulk graphite is particularly promising for larger quantities of few-layer graphene materials,[10-15] referred to here as "carbon nanosheets",[15] as fillers in polymeric nanocomposites.[15,16]

The carbon nanosheets are insoluble, and their dispersion in organic or aqueous medium is subject to aggregation and/or restacking (the reverse of exfoliation) effects. Therefore, chemical modification and functionalization of carbon nanosheets have been explored for their solublization and the subsequent fabrication of nanocomposite materials.[10-14,17,18] In the work reported here we used matrix polymer to functionalize and solubilize carbon nanosheets to allow solution-phase processing of polymer-carbon nanosheets composites containing no other foreign substances. While the poly(vinyl alcohol) results are presented, the same approach should be applicable to other polymers and targeted nanocomposite materials.

The carbon nanosheets were prepared by processing the expanded graphite sample acquired commercially (Asbury Carbons, grade 3805) with a combination of alcohol and oxidative acid treatments.[15] Briefly, the graphite sample was added to an alcohol-water mixture (13:7 v/v), stirred at room temperature for 24 h, and then sonicated (VWR-250D, 120 W) for 20 h. The sample recovered via filtration was added to a nitric acid-sulfuric acid mixture (1:3 v/v) pre-cooled in an ice bath. Upon sonication for 2-3 days, the mixture was transferred into water. The carbon nanosheets were obtained via filtration, washing and then drying. These nanosheets were generally less than 10 nm in thickness according to transmission electron microscopy (TEM) analyses of the cross-sectional slices obtained from microtoming (with the nanosheets dispersed in epoxy resin).[15] The effect of the alcohol treatment was probably primarily on the exfoliation, so was the treatment with the acid mixture coupled with prolonged sonication. The latter was probably more important to the chemical functionalization, for the oxidation to create carboxylic acid moieties at the edges and surface defect sites of the carbon nanosheets (Scheme 4.1). According to acid-base titration, the carboxylic acid population in the sample was 2 mole%, corresponding to about one per 50 carbons. This was somewhat more than the carboxylic acid population in similarly treated MWNTs[19] but less than that in SWNTs.[20]

The covalent functionalization of the carbon nanosheets with poly(vinyl alcohol) (PVA, MW ~ 70,000-90,000) was through the carbodiimide-activated esterification reaction between the carboxylic acid moieties on the nanosheets and hydroxyl groups on PVA (Scheme 1), similar to what was reported previously for the PVA functionalization

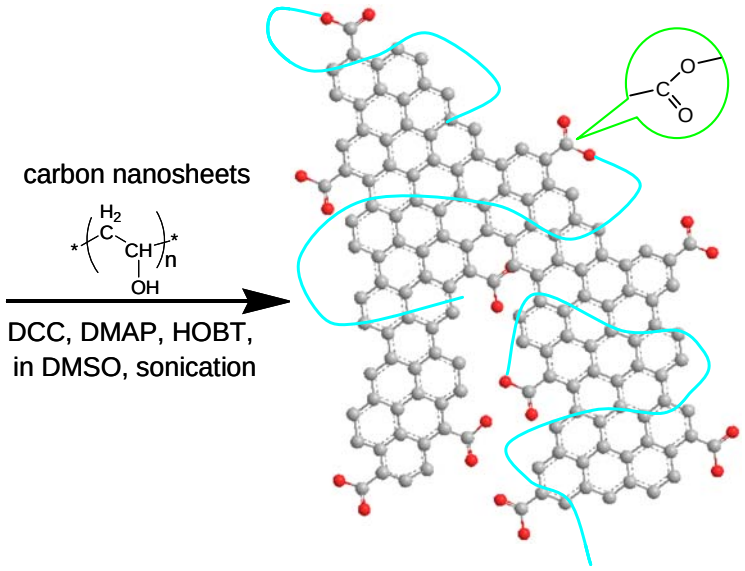

Scheme 4.1. The functionalization via esterification of the carboxylic acid moieties in oxidized carbon nanosheets by hydroxyl groups in PVA.

of carbon nanotubes.[21] In the reaction, a dispersion of carbon nanosheets in DMSO was prepared via sonication, and it was added to a solution of N,N'-dicyclohexylcarbodiimide (DCC), 4-(dimethylamino)-pyridine (DMAP), and N-hydroxybenzotriazole (HOBT) in DMSO. Upon sonication for 1 h, a separately prepared solution of PVA in DMSO was added, followed by sonication for 24 h. The reaction mixture was precipitated into acetone to recover the functionalized sample. For purification, the sample was dissolved in hot water, and then precipitated into acetone. The procedure was repeated three times, and the resulting sample was washed with acetone in Soxhlet extractor for 12 h to obtain the final PVA-funtionalized carbon nanosheets. According to thermogravimetric analysis (TGA), in which the polymer was selectively removed under nitrogen atmosphere, the functionalized sample contained about 15% by weight of carbon nanosheets.

The PVA-functionalized carbon nanosheets could be readily dispersed in DMSO or hot water to form what appeared as a stable solution (Figure 4.1), which enabled characterizations in terms of solution-phase techniques. The ^{1}H NMR spectrum of the PVA-functionalized carbon nanosheets in DMSO-d_6 solution was generally similar to that of PVA, except that the three hydroxyl proton signals found in the spectrum of PVA (4.2 ppm, 4.5 ppm, and 4.7 ppm for the isotactic, heterotactic, and syndiotactic triad)[22] were diminished in the spectrum of the functionalized sample. The solution-phase ^{13}C NMR spectra of the functionalized sample and PVA were also similar. The extra weak signals in the low-field region (around 140 ppm) in the spectrum of the functionalized sample could be due to carbons on the nanosheets,[13] though a more definite assignment

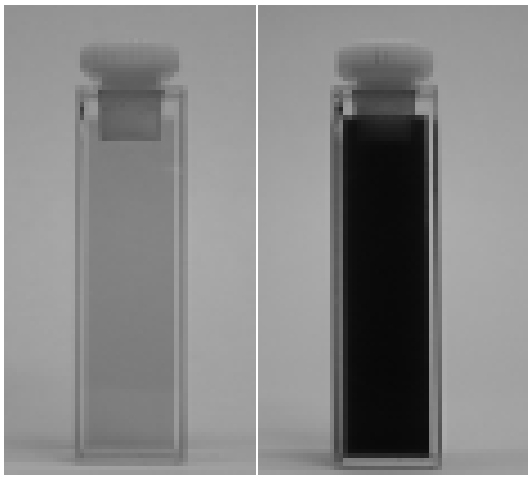

Figure 4.1. Aqueous solutions (left: dilute; right: concentrated) of the PVA-functionalized carbon nanosheets.

requires much more experimental effort on improving the signal quality (such as the use of ^{13}C-enriched sample).[23]

The presence of ester linkages in the PVA-functionalized carbon nanosheets was also hinted by the FT-IR spectrum of the sample, with a small peak at 1730 cm^{-1} characteristic of the C=O stretching mode.[24]

According to TEM imaging of the specimen prepared by microtoming the sample (Figure 4.2), the thickness of the functionalized carbon nanosheets was on the order of 5 nm or so (corresponding to around 6-7 graphene layers). The TEM results were generally similar to those of pre-functionalization nanosheets, suggesting that the functionalization reaction probably had no significant effects on the nanosheet structures.

The specimen for optical microscopy (Leica DMIRE2 confocal microscope with TCS SP2 SE scanning system) analyses was prepared by depositing a dilute solution of the functionalized carbon nanosheets onto a glass slide. The well-dispersed black objects found in the optical microscopy images did appear as sheets, especially in terms of the imaging in the reflective mode (Figure 4.3). The surface shape of the sheets was generally irregular, and the dimension quite diverse, though mostly less than 1.5 μm as measured by the longest edge-to-edge distance. It seems that the solubilization was selective toward those relatively smaller pieces of carbon nanosheets (larger pieces found in the residue).

The properties of PVA polymers in the functionalized sample were affected significantly by their interactions with the attached carbon nanosheets. According to differential scanning calorimetry (DSC) results, the glass transition temperature T_g

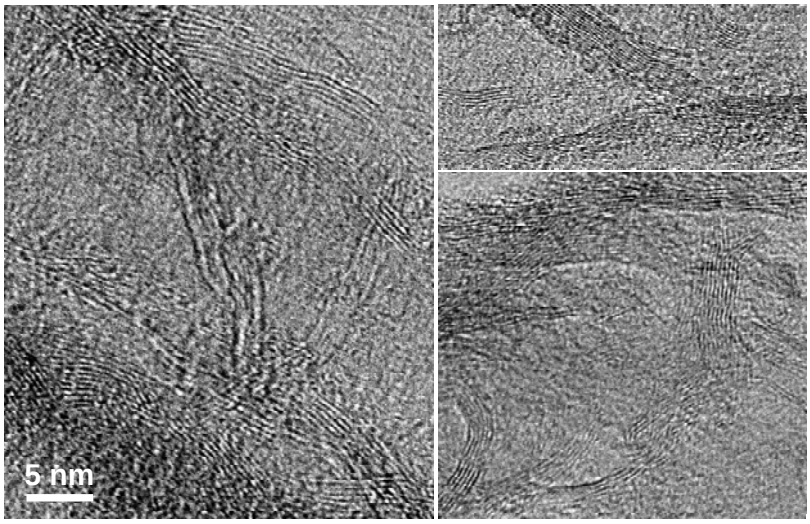

Figure 4.2. TEM images on the specimen of the functionalized sample from microtome.

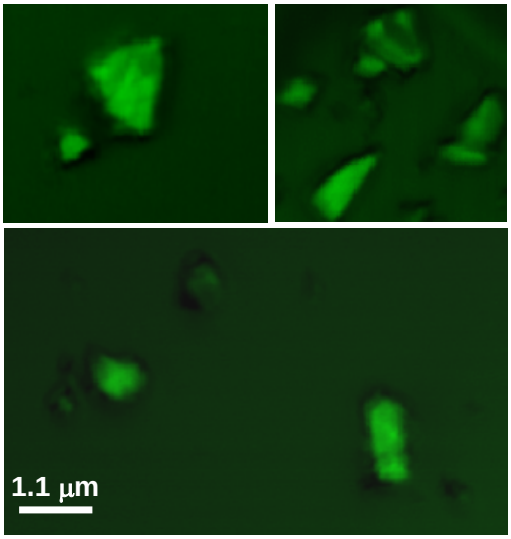

Figure 4.3. Confocal microscopy (reflection mode) images of the PVA-functionalized carbon nanosheets.

increased from 70°C in blank PVA polymer to about 90°C in the functionalized sample, suggesting that the interactions with the nanosheets reduced the polymer chain mobility substantially.

The Raman spectrum of the functionalized sample was generally similar to that of the pre-functionalization nanosheets, except for some luminescence background (Figure 4.4), as also observed in functionalized carbon nanotubes.

The aqueous solution of the PVA-functionalized carbon nanosheets was concentrated for the casting into an elastic thin film. The film was mechanically stretched to failure for an examination of the broken edges by using scanning electron microscopy (SEM). As shown in Figure 4.5, the SEM imaging results were consistent with the expected well-dispersed carbon nanosheets in the PVA polymer matrix.

In summary, the carbon nanosheets with thickness on the order of 5 nm could be functionalized with PVA polymer in the same esterification reaction as those for similar functionalizations of carbon nanotubes.[21,25] The PVA-functionalized carbon nanosheets were readily soluble in aqueous and polar organic solvents to form stable solution-like dispersions, which enabled solution-phase characterizations of the functionalized sample and also solution-phase processing for purposes such as the fabrication of PVA-carbon nanosheets composites without any dispersion agents or other foreign substances. The demonstrated functionalization-solubilization approach should be applicable to other polymers for their respective high-quality polymeric/carbon nanosheets composite materials.

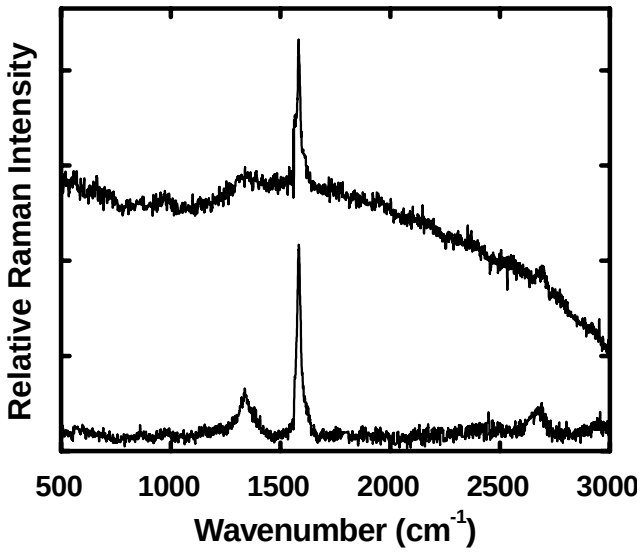

Figure 4.4. Raman spectra of carbon nanosheets before (bottom) and after PVA functionalization (top)

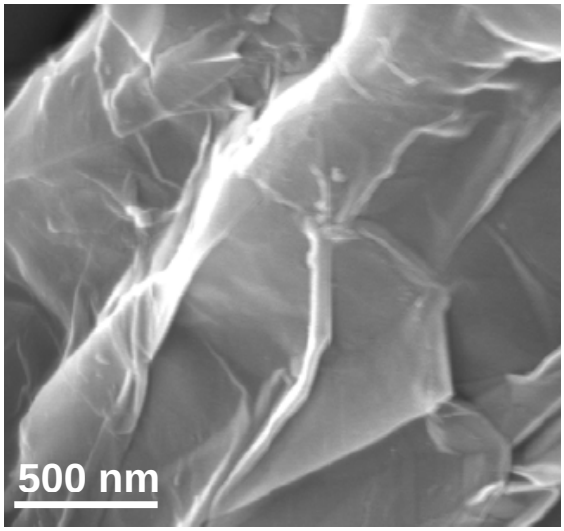

Figure 4.5. A representative SEM image on fracture surfaces of the PVA-carbon nanosheets composite film.

References

1. Geim, A. K.; Novoselov, K. S. *Nat. Mater*., **2007**, *6*, 183-191.
2. Wang, X. ; Zhi, L; Mullen, K. *Nano Lett*., **2008**, *8*, 323-327.
3. Wu, J.; Pisula, W.; Mullen, K. *Chem. Rev.*, **2007**, *107*, 718-747.
4. Du, X.; Skachko, I.; Barker, A.; Andrei, E. Y. *Nat. Nanotech.*, **2008**, *3*, 491-
5. Lee, C.; Wei, X.; Kysar, J. W.; Hone, J. *Science*, **2008**, *321*, 385-388.
6. Baladin, A. A.; Ghosh, S.; Bao, W.; Calizo, I.; Teweldebrhan, D.; Miao, F.; Lau, C. N. *Nano Lett*., **2008**, *8*, 902-907.
7. Novoselov, K. S.; Geim, A. K.; Morozov, S. V.; Jiang, D.; Zhang, Y.; Dubonos, S. V.; Grogorieva, I. V.; Forsov, A. A. *Science*, **2004**, *306*, 666-669.
8. Berger, C.; Song, Z.; Li, X.; Wu, X.; Brown, N.; Naud, C.; Mayou, D.; Li, T.; Hass, J.; Marchenkov, A. N.; Conrad, E. H.; First, P. N.; de Heer, W. A. *Science*, **2006**, *312*, 1191; and references therein.
9. Coraux, J.; N'Diaye, A. T.; Busse, C.; Michely, T. *Nano Lett*., **2008**, *8*, 565
10. Schniepp, H. C.; Li, J.-L.; McAllister, M. J.; Sai, H.; Herrera-Alonso, M.; Adamson, D. H.; Prud'homme, R.K.; Car, R.; Saville, D. A.; Aksay, I. A. *J. Phys. Chem. B*, **2006**, *110*, 8535-8539.
11. Gilje, S.; Han, S.; Wang, M.; Wang, K. L.; Kaner, R. B. *Nano Lett.*, **2007**, *7*, 3394

12. McAllister, M. J. ; Li, J.; Adamson, D. H.; Schniepp, H. C.; Abdala, A. A.; Liu, J.; Herrera-Alonso, M.; Milius, D. L.; Car, R.; Prud'homme, R. K.; Aksay, I. A. *Chem. Mater.*, **2007**, *19*, 4396-4404.
13. Si, Y.; Samulski, E. T. *Nano. Lett.*, **2008**, *8*, 1679-1682.
14. Li, D.; Muller, M. C.; Gilje, S.; Kaner, R. B.; Wallace, G. G. *Nat. Nanotech.*, **2008**, *3*, 101-105.
15. Veca, L. M.; Meziani, M. J.; Wang, W.; Wang, X.; Lu, F.; Zhang, P.; Lin, Y.; Fee, R.; Connell, J. W.; Sun, Y.-P. *Adv. Mater.*,**2009,** *21***,** DOI 10.1002/adma.200802317 ; and references therein.
16. Stankovich, S.; Dikin, D. A.; Dommett, G. H. B.; Kohlhass, K. M.; Zimney, E. J.; Stach, E. A.; Piner, R. D.; Nguyen, S. T.; Ruoff, R. S. *Nature*, **2006**, *442*, 282
17. Ramanathan, T. ; Abdala, A. A.; Stankovich, S.; Dikin, D. A.; Herrera-Alonso, M.; Piner, R. D.; Adamson, D. H.; Schniepp, H. C.; Chen, X.; Ruoff, R. S.; Nguyen, S. T.; Aksay, I. A.; Prud'Homme, R. K.; Brinson, L. C. *Nat. Nanotech.*, **2008**, *3*, 327-331.
18. Niyogi, S.; Bekyarova, E.; Itkis, M. E.; McWilliams, J. L.; Hamon, M. A.; Haddon, R.C. *J. Am. Chem. Soc*., **2006**, *128,* 7720 – 7721.
19. Yang, B. X.; Shi, J. H.; Pramoda, K. P.; Goh, S. H. *Nanotechnology*, **2007**, *18*, 125606.
20. Marshall, M. W.; Popa-Nita, S.; Shapter, J. G. *Carbon*, **2006**, *44*, 1137

21. Lin, Y.; Zhou, B.; Fernando, K. A. S.; Liu, P.; Allard, L. F.; Sun, Y.-P. *Macromolecules*, **2003**, *36*, 7199-7204.

22. Moritani, T.; Kuruma, I.; Shibatani, K.; Fujiwara, Y. *Macromolecules*, **1972**, *5*, 577-580.

23. Kitaygorodskiy, A.; Wang, W.; Xie, S. Y.; Lin, Y.; Fernando, K. A. S.; Wang, X.; Qu, L.; Chen, B.; Sun, Y. P. *J. Am. Chem. Soc.*, **2005**, *127*, 7517-7520; Cai, W.; Piner, R. D.; Stadermann, F. J.; Park, S.; Shaibat, M. A.; Ishii, Y.; Yang, D.; Velamakanni; An, S. J.; Stoller, M.; An, J.; Chen, D.; Ruoff, R. S. *Science*, **2008**, *321*, 1815-1817.

24. Chen, J.; Rao, A. M.; Lyuksyutov, S.; Itkis, M. E.; Hamon, M. A.; Hu, H.; Cohn, R. W.; Eklund, P. C.; Colbert, D. T.; Smalley, R. E.; Haddon, R. C. *J. Phys. Chem. B*, **2001**, *105*, 2525-2528.

25. Lin, Y.; Meziani, M. J.; Sun, Y.-P. *J. Mater. Chem.*, **2007**, *17*, 1-7.

Appendix

Selected Publications

1. Qu, L.; Veca, L. M.; Lin, Y.; Kitaygorodskiy, A.; Chen, B.; McCall, A. M.; Connell, J. W.; Sun, Y.-P. "Soluble Nylon – Functionalized Carbon Nanotubes from Anionic Ring-Opening Polymerization from Nanotube Surface." *Macromolecules* **2005**, *38*, 10328-10331.

2. Lin, Y.; Elkin, T.; Taylor, S.; Gu, L.; Chen, B.; Veca, L. M.; Zhou, B.; Yang, H.; Brown, J.; Joseph, R.; Jones, E.; Jiang, X.; Sun, Y.-P. "Preparation, Characterization, and Evaluation of Immuno Carbon Nanotubes." *Microchim Acta* **2006**, *152*, 249-254.

3. Zhou, B.; Lin, Y.; Veca, L. M.; Fernando, K. A. S.; Harruff, B. A.; Sun, Y.-P. "Luminescence Polarization Spectroscopy Study of Functionalized Carbon Nanotubes in a Polymeric Matrix." *J. Phys. Chem. B.* **2006**, *110*, 3001-3006.

4. Sun, Y.-P.; Zhou, B.; Lin, Y.; Wang, W.; Fernando, K. A. S.; Pathak, P.; Meziani, M. J.; Harruff, B. A.; Wang, X.; Wang, H.; Luo, P. G.; Yang, H.; Kose, M. E.; Chen, B.; Veca, L. M.; Xie, S.-Y. "Quantum-Sized Carbon Dots for Bright and Colorful Photoluminescence" *J. Am. Chem. Soc.* **2006**, *128*, 7756-7757.

5. Kose, M. E.; Harruff, B. A.; Lin, Y.; Veca, L. M.; Lu, F.; Sun, Y.-P. "Efficient Quenching of Photoluminescence from Functionalized Single-Walled Carbon Nanotubes by Nitroaromatic Molecules." *J. Phys. Chem. B.* **2006**, *110*, 14032-14034.

6. Zhou, B.; Lin, Y.; Hill, D. E.; Wang, W.; Veca, L. M.; Qu, L.; Pathak, P.; Meziani, M. J.; Diaz, J.; Connell, J. W.; Watson, K. A.; Allard, L. F.; Sun, Y.-P. "Polymeric nanocomposite films from functionalized vs suspended single-walled carbon nanotubes." *Polymer* **2006**, *47*, 5323-5329.

7. Cao, L.; Wang, X.; Meziani, M. J.; Lu, F.; Wang, H.; Luo, P. G.; Lin, Y.; Harruff, B. A.; Veca, L. M.; Murray, D.; Xie, S.-Y.; Sun, Y.-P. "Carbon Dots for Multiphoton Bioimaging." *J. Am. Chem. Soc.* **2007**, *129*, 11318-11319.

8. Fernando, K. A. S.; Lin, Y.; Wang, W.; Cao, L.; Meziani, M. J.; Wang, X.; Veca, L. M.; Zhang, P.; Quinn, R. A.; Allard, L. F.; Sun, Y.-P. "Diameter-Selective Fractionation of HiPco Single-Walled Carbon Nanotubes in Repeated Functionalization Reactions." *J. Phys. Chem. C* **2007**, *111*, 10254-10259.

9. Cheng, J.; Fernando, K. A. S.; Veca, L. M.; Sun, Y.-P.; Lamond, A. I.; Lam, Y. W.; Cheng, S. H. “Reversible Accumulation of PEGylated Single-Walled Carbon Nanotubes in the Mammalian Nucleus.” *ACS Nano* **2008**, *10*, 2085-2094.

10. Sun, Y.-P.; Wang, X.; Lu, F.; Cao, L.; Meziani, M. J.; Luo, P. G.; Gu, L.; Veca, L. M. “Doped Carbon Nanoparticles as a New Platform for Highly Photoluminescent Dots.” *J. Phys. Chem. C* **2008**, *112*, 18295-18298.

11. Wang, W.; Fernando, K. A. S.; Lin, Y.; Meziani, M. J.; Veca, L. M.; Cao, L.; Zhang, P.; Kimani, M. M.; Sun, Y.-P. “Metallic Single-Walled Carbon Nanotubes for Conductive Nanocomposites.” *J. Am. Chem. Soc.* **2008**, *130*, 1415-1419.

12. Gu, L.; Luo, P. G.; Wang, H.; Meziani, M. J.; Lin, Y.; Veca, L. M.; Cao, L.; Lu, F.; Wang, X.; Quinn, R. A.; Wang, W.; Zhang, P.; Lancher, S.; Sun, Y.-P. “Single-Walled Carbon Nanotube as a Unique Scaffold for the Multivalent Display of Sugers.” *Biomacromolecules* **2008**, *9*, 2408-2418.

13. Lu, F.; Gu, L.; Meziani, M. J.; Wang, X.; Luo, P. G.; Veca, L. M.; Cao, L.; Sun, Y.-P. “Advances in Bioapplications of Carbon Nanotubes.” *Adv. Mater*. **2009**, *21*, 139-152.

14. Cheng, J.; Chan, C. M.; Veca, L. M.; Poon, W. L.; Chan, P. K.; Qu, L.; Sun, Y.-P.; Cheng, S. H. “Acute and long-term effects after single loading of functionalized multi-walled carbon nanotubes into zebrafish (Danio rerio)” *Toxicol. Appl. Pharmacol*. **2009**, *235*, 216-225.

15. Komarneni, M.; Sand, A.; Goering, J.; Burghaus, U.; Lub, M.; Veca, L. M.; Sun, Y.-P. “Possible effect of carbon nanotube diameter on gas–surface interactions – The case of benzene, water, and n-pentane adsorption on SWCNTs at ultra-high vacuum conditions.” *Chem. Phys. Lett*. **2009**, *476*, 227-231.

16. Wang, W.; Lu, F.; Veca, L. M.; Meziani, M. J.; Wang, X.; Cao, L.; Gu, L.; Sun, Y.-P. “Carbon Nanotubes and Nanocomposites for Electrical and Thermal Applications.” In Encyclopedia of Inorganic Chemistry Eds. Lukehart, C. M. and Scott, R. A., John Wiley & Sons, Ltd **2008**, 169-189.

Soluble Nylon-Functionalized Carbon Nanotubes from Anionic Ring-Opening Polymerization from Nanotube Surface

Liangwei Qu,[†] L. Monica Veca,[†] Yi Lin,[†] Alex Kitaygorodskiy,[†] Bailin Chen,[†] Alecia M. McCall,[†] John W. Connell,[‡] and Ya-Ping Sun*,[†]

Department of Chemistry and Laboratory for Emerging Materials and Technology, Clemson University, Clemson, South Carolina 29634-0973, and Advanced Materials and Processing Branch, NASA Langley Research Center, Mail Stop 226, Hampton, Virginia 23681-2199

Received August 8, 2005
Revised Manuscript Received October 4, 2005

Introduction

The preparation of polymeric nanocomposites filled with single-walled carbon nanotubes (SWNTs) generally requires the nanotubes being homogeneously dispersed and compatible with the polymer matrix.[1−3] An effective approach for these requirements is to functionalize the nanotubes with polymers that are identical or structurally similar to the matrix polymers.[4] Among the widely pursued functionalization strategies is the "grafting-from" method, in which monomers or initiators are first attached to the nanotubes to serve as starting points for propagation.[5−9] The grafting-from strategy is generally similar to in situ polymerization,[10] but in a more controlled fashion. For example, the nanotube-bound radical initiators were used in the atom transfer radical polymerization to yield poly(methyl methacrylate)-, poly(*n*-butyl methacrylate)-, or poly(*tert*-butyl acrylate)-functionalized carbon nanotubes.[5]

Nylon is an important commodity polymer with a wide variety of applications, and naturally, there has been much interest in nanocomposites of nylon with carbon nanotubes.[11−16] For the investigation of these materials, the preparation of nylon-functionalized carbon nanotubes is highly relevant and beneficial. In a typical synthesis of nylon-6, ϵ-caprolactam is used as monomer in the efficient anhydrous polymerization with a base (anionic) as initiator.[17] In addition, the secondary amine in ϵ-caprolactam may be used to form an amide linkage with the defect-derived carboxylic acid moiety on the carbon nanotube surface. We report here that the covalent attachment of ϵ-caprolactam molecules to SWNTs could be the first step in a two-step grafting-from process of functionalizing the nanotubes with nylon-6. The second step was the anionic ring-opening polymerization of the nanotube-bound ϵ-caprolactam species with the same monomers in bulk (Scheme 1).[18]

Experimental Section

Materials. ϵ-Caprolactam was purchased from Aldrich. Thionyl chloride and sodium were obtained from Alfa Aesar. Deuterated solvents for NMR measurements were supplied by Cambridge Isotope Laboratories.

The sample of SWNTs (arc-discharge method) was supplied by Carbon Solutions, Inc. It was purified by using a combination of thermal oxidation and oxidative acid treatment. In a typical experiment, a nanotube sample (1 g) was thermally oxidized in air in a furnace at 300 °C for 30 min. After the thermal treatment, the remaining sample was added to an aqueous HNO_3 solution (2.6 M), and the mixture was refluxed for 24 h. Upon centrifuging at 1000*g* to discard the supernatant, the remaining solids were washed with deionized water until neutral pH and then dried under vacuum.

Scheme 1. Synthesis of Nylon-6-Functionalized Single-Walled Carbon Nanotubes (Nylon−SWNT)

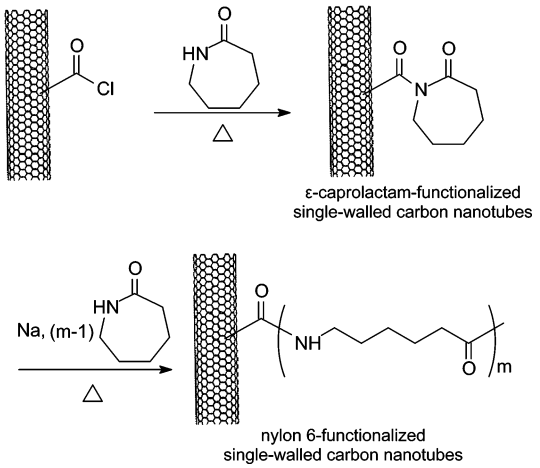

Measurements. NMR measurements were performed on a JEOL Eclipse +500 NMR spectrometer and a Bruker Avance 500 spectrometer that is equipped with a high-resolution magic-angle-spinning (HR-MAS) probe designed specifically for gel-phase NMR. Optical absorption spectra were recorded on a Shimadzu UV3100 spectrophotometer. Raman spectra were obtained on a Renishaw Raman spectrometer equipped with a 50 mW diode laser source for 785 nm excitation and a CCD detector. Thermogravimetric analysis (TGA) was carried out on a Mettler-Toledo TGA/SDTA851e system. Scanning electron microscopy (SEM) images were obtained on a Hitachi S4700 field-emission SEM system. Atomic force microscopy (AFM) analysis was conducted on a Molecular Imaging PicoPlus system equipped with a multipurpose scanner. The height profile analyses were assisted by using the SPIP software distributed by Image Metrology.

Caprolactam−SWNT. A purified SWNT sample (50 mg) was mixed with thionyl chloride (10 mL), and the mixture was stirred and refluxed (70 °C) for 24 h. Upon removal of excess thionyl chloride under vacuum, ϵ-caprolactam (5 g, 44 mmol) was added. The mixture was stirred at 110 °C for 24 h and then cooled to room temperature. Chloroform (20 mL) was added to the mixture, and the resulting suspension was filtered (0.22 μm PVDF membrane). The solid sample from the filtration was extracted with chloroform for 6 h in a Soxhlet extractor to remove any residual ϵ-caprolactam. Upon drying in a vacuum at room temperature, the ϵ-caprolactam-functionalized SWNTs (caprolactam−SWNT) were obtained as a dark-colored powdery sample.

Nylon−SWNT. A caprolactam−SWNT sample (50 mg) was mixed with ϵ-caprolactam (10 g, 88 mmol), and sodium (40 mg, 1.7 mmol) was added to the mixture as initiator for the polymerization reaction at 140 °C under nitrogen protection for 24 h (Scheme 1). The reaction mixture was dissolved in formic acid (10 mL), precipitated into water (50 mL), and filtered (0.22 μm PVDF membrane). The resulting solid sample was washed successively (25 mL each) with formic acid, water, and formic acid again to remove sodium salts and those polymers not attached to the nanotubes (until no such polymers found in the filtrate). The cleaned sample was dispersed in formic acid (10 mL), followed by centrifuging (3000*g*) to retain the dark-colored supernatant. The solvent formic acid

[†] Clemson University.
[‡] NASA Langley Research Center.

10.1021/ma051762n CCC: $30.25
Published on Web 11/04/2005

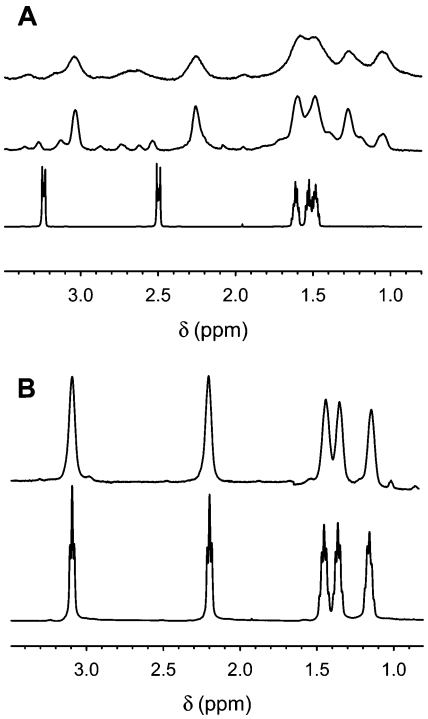

Figure 1. (A) ^{1}H NMR spectra of ϵ-caprolactam-functionalized single-walled carbon nanotubes (caprolactam−SWNT) dispersed in deuterated formic acid (top: measured in solution probe; middle: in high-resolution magic angle spinning probe) are compared with that of ϵ-caprolactam (bottom). (B) A comparison of ^{1}H NMR spectra of nylon-6-functionalized SWNTs (nylon−SWNT, top) and nylon-6 (bottom) in deuterated formic acid solutions.

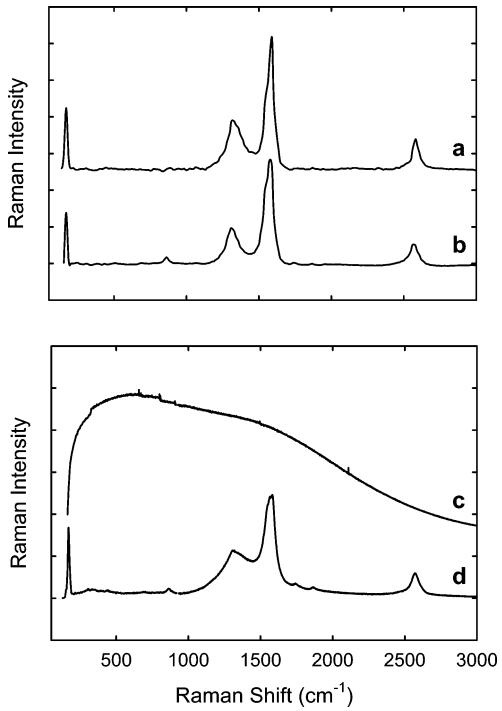

Figure 2. Raman spectra (785 nm excitation) of the purified single-walled carbon nanotube (SWNT) sample (a), caprolactam−SWNT (b), and nylon-6-functionalized SWNTs (nylon−SWNT) before (c) and after (d) thermal defunctionalization (800 °C, N_2).

was removed on a rotatory evaporator to yield nylon-6-functionalized SWNTs (nylon−SWNT) as black solids.

Results and Discussion

The functionalization of SWNTs with ϵ-caprolactam was the first step in the grafting-from process. The caprolactam−SWNT sample was generally insoluble in common organic solvents. Nevertheless, its dispersion in formic acid was used for ^{1}H NMR measurement, yielding rather broad resonances (Figure 1). The broadening was probably due in part to the heterogeneous nature of the dispersion, in addition to the high molecular weight and low mobility of carbon nanotubes. Better resolved proton signals were obtained from the same dispersion by using a high-resolution magic-angle-spinning (HR-MAS) probe designed specifically for gel-phase NMR (Figure 1). The resonances of the nanotube-attached ϵ-caprolactam were systematically shifted upfield from those of the starting ϵ-caprolactam, especially for the methylene protons near the expected amide linkage (3.24 and 2.50 ppm vs 3.03 and 2.25 ppm, Figure 1). In the literature,[20,21] similar upfield shifts have been attributed to effects associated with the large aromatic ring current in nanotubes, which are more pronounced when the protons are closer to the nanotube surface. The NMR results are consistent with the covalent attachment of ϵ-caprolactam molecules to SWNTs.

The FT-IR spectrum of the caprolactam−SWNT sample exhibited absorptions at 2930 and 2860 cm^{-1}, corresponding to the stretching modes of alkyl C−H in ϵ-caprolactam. As compared in Figure 2, the Raman spectrum (785 nm excitation) of the caprolactam−SWNT sample is similar to that of purified SWNTs, showing typical radial breathing mode (170 cm^{-1}), D-band (1310 cm^{-1}), tangential G-band (1580 cm^{-1}), and D*-band (2660 cm^{-1}) features. The absence of luminescence interference reflects the expected low functional group content in the caprolactam−SWNT sample, also consistent with the poor solubility of the sample. In thermogravimetric analysis (TGA) of the sample under inert atmosphere, the covalently attached ϵ-caprolactam on the nanotube surface could be selectively removed (or "thermal defunctionalization"),[1,4,6−8] which allowed an estimate of the ϵ-caprolactam content in the sample. The content was indeed low, ∼7% (w/w), as expected. It corresponds to on average one ϵ-caprolactam for every 125 nanotube carbons.

The second step in the grafting-from process was the sodium-initiated anionic ring-opening polymerization to obtain nylon-6-functionalized SWNTs. The final nylon−SWNT sample contained more than 70% of the starting SWNTs. The sample was soluble in some organic solvents, such as formic acid and *m*-cresol, resulting in dark-colored but optically transparent solutions.

The ^{1}H NMR spectrum of nylon−SWNT in deuterated formic acid is compared with that of commercially available nylon-6 (Acros, $M_n \sim 10\,000$) in Figure 1. The chemical shifts in the two spectra are generally similar, but the resonances of the nanotube-bound nylon moieties are obviously broader. Unlike in the dispersion of caprolactam−SWNT discussed above, the broadening here is probably due entirely to the nylon species being associated with the nanotubes (high molecular weight and low mobility) because the nylon−SWNT solution is homogeneous.

The nylon functionalities on the nanotube surface could also be selectively removed in TGA under an inert atmosphere (thermally defunctionalized), similarly allowing an estimate of the nanotube content. According to the amount of residue at 500 °C, the nylon−SWNT sample contained about 40% (w/w) of nanotubes.[22]

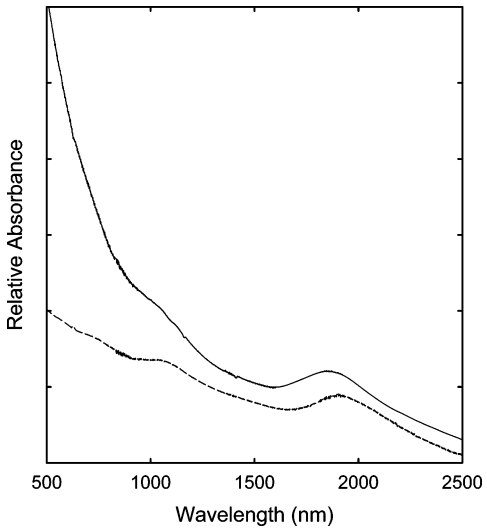

Figure 3. Absorption spectra of nylon-6-functionalized single-walled carbon nanotubes (nylon−SWNT, top) and the purified SWNT sample (bottom) on glass substrate.

The optical absorption spectrum of nylon−SWNT is shown in Figure 3. The broad S_{11} and S_{22} bands at 1870 and 1050 nm, respectively, are characteristic of the electronic transitions associated with the van Hove singularity pairs in semiconducting SWNTs.[23] The spectral similarity to that of purified SWNTs suggests that neither the polymerization reaction nor the presence of nylon functionalities on the nanotube surface changes in any substantial fashion the electronic transitions. Apparently, the nanotube electronic structures are largely preserved in the nylon-functionalized SWNTs, as also found in a number of other functionalizations that target the nanotube surface defect-derived carboxylic acids.[4,7]

The Raman characterization of nylon−SWNT was hindered by overwhelming luminescence interference, quite different from the same characterization of the precursor caprolactam−SWNT (Figure 2). As reported recently,[24] the substantial difference in the extent of luminescence interference in Raman measurements is an indication on how well the nanotubes are dispersed and functionalized. In the nylon−SWNT sample, soluble in selected solvents to form transparent solutions, the nanotubes were well-dispersed, and their surface defects were likely passivated as a result of the effective functionalization, thus corresponding to stronger nanotube defect-derived luminescence.[1,24] The thermal defunctionalization obviously "undispersed" the nanotubes, suppressing or completely eliminating the luminescence interference. As compared in Figure 2, the Raman spectrum of the thermally defunctionalized nylon−SWNT sample again exhibits features similar to those of purified SWNTs.

A direct SEM imaging of the nylon-functionalized SWNTs was somewhat difficult because of a significant amount of soft (nylon polymer) materials in the specimen (Figure 4). However, the removal of nylon via thermal defunctionalization obviously made the SEM analysis more straightforward, with the resulting image showing abundant SWNTs (Figure 4). AFM is applicable to the direct analysis of functionalized carbon nanotubes. For nylon−SWNT, the specimen for AFM analysis was prepared by spraying a dilute formic acid solution of the sample onto a mica substrate. During the spraying, the substrate was kept at 120 °C to facilitate rapid solvent evaporation in an effort to preserve the original nanotube dispersion in the solution. A representative AFM topographic image from the analysis of such a specimen is shown in Figure 5. There are apparently abundant nanotubes of different lengths (hundreds of nanometers), mostly well-dispersed to the individual nanotube level according to the height analysis (Figure 5). It seems that the AFM specimen was unusually well-prepared (with a significant population of well-dispersed individual SWNTs), which probably benefitted from the use of the highly polar solvent formic acid. The solvent effect might be that the nanotube surface is charged, as in the superacid dispersion[25] or electrolyte-assisted dispersion of carbon nanotubes,[26] thus resulting in more efficient exfoliation of the nanotube bundles (or preventing the functionalized SWNTs from aggregating).

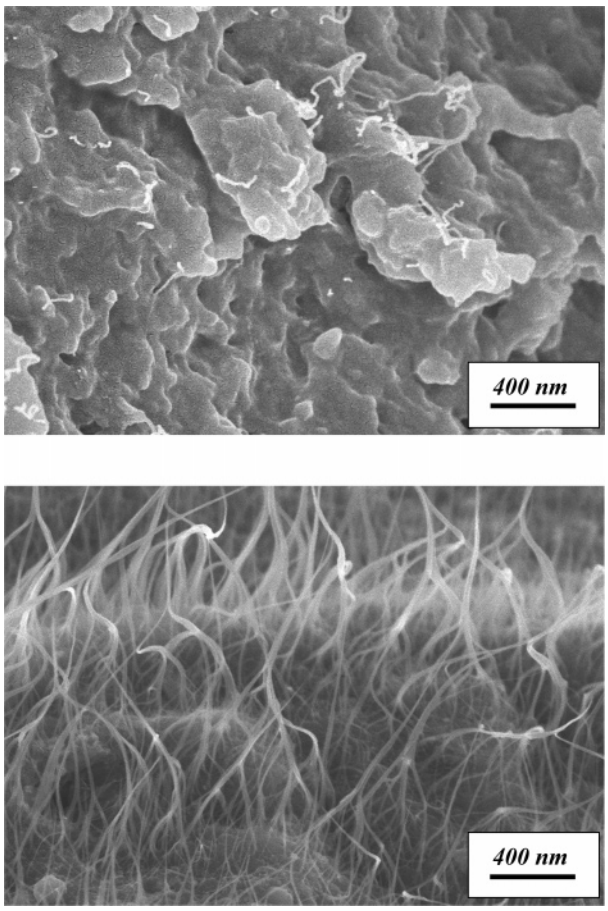

Figure 4. Scanning electron microscopy (SEM) images of the nylon-6-functionalized single-walled carbon nanotubes (nylon−SWNT) sample before (top) and after (bottom) thermal defunctionalization (800 °C, N_2).

In summary, the functionalization of SWNTs with nylon-6 was accomplished by using the grafting-from strategy in a two-step process, where the covalent attachment of ϵ-caprolactam molecules to nanotubes was followed by the anionic ring-opening polymerization of these bound ϵ-caprolactam species with the same monomers in bulk. The resulting sample was characterized systematically, and the results were supportive of the expected covalent functionalization of SWNTs by nylon-6. This is a relatively convenient but still reasonably controllable method to chemically modify carbon nanotubes with a commodity polymer of extremely wide uses. The solubility of the functionalized nanotube sample in some organic solvents may prove valuable to

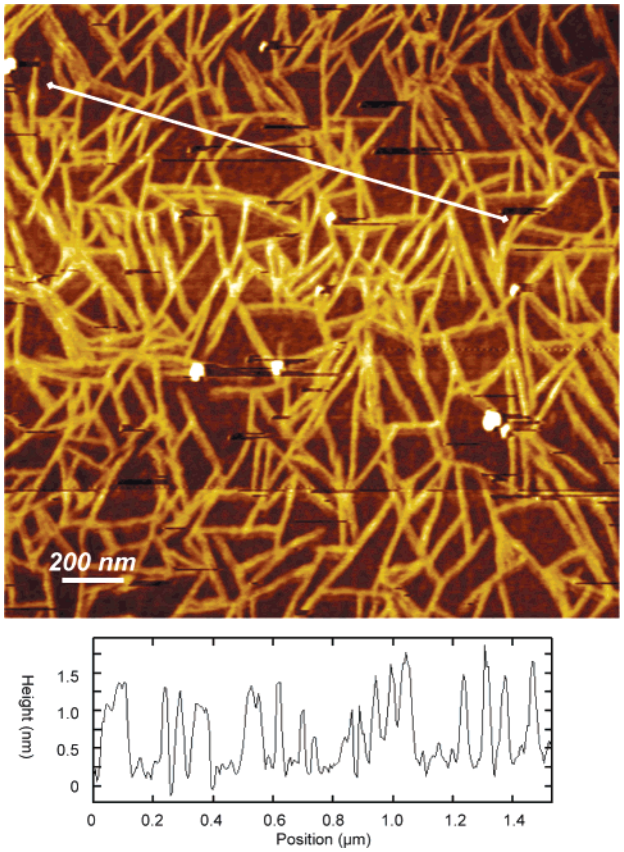

Figure 5. Atomic force microscopy (AFM) topography image (top) and height analysis (bottom) of a nylon-6-functionalized single-walled carbon nanotubes (nylon−SWNT) specimen (prepared by spraying the sample solution onto a heated mica substrate).

the homogeneous dispersion of SWNTs in nylon for high-quality nanocomposite materials.

Acknowledgment. We thank K. A. S. Fernando and B. Zhou for experimental assistance. Financial support from NASA and NSF is gratefully acknowledged. A.M. was a participant of the Summer Undergraduate Research Program sponsored jointly by NSF and Clemson University.

References and Notes

(1) Sun, Y.-P.; Fu, K.; Lin, Y.; Huang, W. *Acc. Chem. Res.* **2002**, *35*, 1096−1104.
(2) Grady, B. P.; Pompeo, F.; Shambaugh, R. L.; Resasco, D. E. *J. Phys. Chem. B* **2002**, *106*, 5852−5858.
(3) Mitchell, C. A.; Bahr, J. L.; Arepalli, S.; Tour, J. M.; Krishnamoorti, R. *Macromolecules* **2002**, *35*, 8825−8830.
(4) (a) Hill, D. E.; Lin, Y.; Rao, A. M.; Allard, L. F.; Sun, Y.-P. *Macromolecules* **2003**, *35*, 9466−9471. (b) Lin, Y.; Zhou, B.; Fernando, K. A. S.; Liu, P.; Allard, L. F.; Sun, Y.-P. *Macromolecules* **2003**, *36*, 7199−7204. (c) Qu, L.; Lin, Y.; Hill, D. E.; Zhou, B.; Wang, W.; Sun, X.; Kitaygorodskiy, A.; Suarez, M.; Connell, J. W.; Allard, L. F.; Sun, Y.-P. *Macromolecules* **2004**, *37*, 6055−6060.
(5) (a) Yao, Z.; Braidy, N.; Botton, G. A.; Adronov, A. *J. Am. Chem. Soc.* **2003**, *125*, 16015−16024. (b) Kong, H.; Gao, C.; Yan, D. *J. Am. Chem. Soc.* **2004**, *126*, 412−413. (c) Qin, S.; Qin, D.; Ford, W. T.; Resasco, D. E.; Herrera, J. E. *J. Am. Chem. Soc.* **2004**, *126*, 170−176. (d) Baskaran, D.; Mays, J. W.; Bratcher, M. S. *Angew. Chem., Int. Ed.* **2004**, *43*, 2138−2142.
(6) Liu, Y.; Adronov, A. *Macromolecules* **2004**, *37*, 4755−4760.
(7) (a) Kong, H.; Li, W.; Gao, C.; Yan, D.; Jin, Y.; Walton, D. R. M.; Kroto, H. W. *Macromolecules* **2004**, *37*, 6683−6686. (b) Xu, Y.; Gao, C.; Kong, H.; Yan, D.; Jin, Y. Z.; Watts, P. C. P. *Macromolecules* **2004**, *37*, 8846−8853. (c) Gao, C.; Jin, Y. Z.; Kong, H.; Whitby, R. L. D.; Acquah, S. F. A.; Chen, G. Y.; Qian, H.; Hartschuh, A.; Silva, S. R. P.; Henley, S.; Fearon, P.; Kroto, H. W.; Walton, D. R. M. *J. Phys. Chem. B* **2005**, *109*, 11925−11932.
(8) Qin, S.; Qin, D.; Ford, W. T.; Resasco, D. E.; Herrera, J. E. *Macromolecules* **2004**, *37*, 752−757.
(9) (a) Hong, C.-Y.; You, Y.-Z.; Wu, D.; Liu, Y.; Pan, C.-Y. *Macromolecules* **2005**, *38*, 2606−2611. (b) Hong, C.-Y.; You, Y.-Z.; Pan, C.-Y. *Chem. Mater.* **2005**, *17*, 2247−2254.
(10) Tang, B. Z.; Xu, H. *Macromolecules* **1999**, *32*, 2569−2576.
(11) Stevens, J. L.; Huang, A. Y.; Peng, H.; Chiang, I. W.; Khabashesku, V. N.; Margrave, J. L. *Nano Lett.* **2003**, *3*, 331−336.
(12) Xia, H.; Wang, Q.; Qiu, G. *Chem. Mater.* **2003**, *15*, 3879−3886.
(13) (a) Zhang, W. D.; Shen, L.; Phang, I. Y.; Liu, T. *Macromolecules* **2004**, *37*, 256−259. (b) Liu, T.; Phang, I. Y.; Shen, L.; Chow, S. Y.; Zhang, W.-D. *Macromolecules* **2004**, *37*, 7214−7222.
(14) Sandler, J. K. W.; Pegel, S.; Cadek, M.; Gojny, F.; van Es, M.; Lohmar, J.; Blau, W. J.; Schulte, K.; Windle, A. H.; Shaffer, M. S. P. *Polymer* **2004**, *45*, 2001−2015.
(15) Li, C. Y.; Li, L.; Cai, W.; Kodjie, S. L.; Tenneti, K. K. *Adv. Mater.* **2005**, *17*, 1198−1202.
(16) Endo, M.; Koyama, S.; Matsuda, Y.; Hayashi, T.; Kim, Y.-A. *Nano Lett.* **2005**, *5*, 101−105.
(17) Aharoni, S. M. *n-Nylons: Their Sythesis, Structure and Properties*; John Wiley & Sons: Chichester, 1997.
(18) During our investigation, Haddon and co-workers reported a scheme for preparing nanocomposites of nylon-6 with SWNTs, in which nitric acid-treated SWNTs were mixed with ϵ-caprolactam for in situ cationic ring-opening polymerization.[19]
(19) Gao, J.; Itkis, M. E.; Yu, A.; Bekyarova, E.; Zhao, B.; Haddon, R. C. *J. Am. Chem. Soc.* **2005**, *127*, 3847−3854.
(20) (a) Chen, J.; Liu, H.; Weimer, W. A.; Halls, M. D.; Waldeck, D. H.; Walker, G. C. *J. Am. Chem. Soc.* **2002**, *124*, 9034−9035. (b) Holzinger, M.; Abraham, J.; Whelan, P.; Graupner, R.; Ley, L.; Hennrich, F.; Kappes, M.; Hirsch, A. *J. Am. Chem. Soc.* **2003**, *125*, 8566−8580. (c) Ruther, M. G.; Frehill, F.; O'Brien, J. E.; Minett, A. I.; Blau, W. J.; Vos, J. G.; in het Panhuis, M. *J. Phys. Chem. B* **2004**, *108*, 9665−9668.
(21) According to the software ACD/HNMR Predictor for predicting NMR chemical shifts, amidation should result in downfield shifts of as much as 0.5−1 ppm for the adjacent caprolactam methylene protons. Therefore, the observed upfield shifts must be due to strong influence of the nanotube aromatic system, which overcomes the opposite effect from the amidation.
(22) Based on the population of ϵ-caprolactam in the caprolactam−SWNT sample, the composition in nylon−SWNT corresponds to about 20 repeating units in each nanotube-attached nylon-6 chain (molecular weight $\sim$ 2200).
(23) Niyogi, S.; Hamon, M. A.; Hu, H.; Zhao, B.; Bhowmik, P.; Sen, R.; Itkis, M. E.; Haddon, R. C. *Acc. Chem. Res.* **2002**, *35*, 1105−1113.
(24) Lin, Y.; Zhou, B.; Martin, R. B.; Henbest, K. B.; Harruff, B. A.; Riggs, J. E.; Guo, Z.-X.; Allard, L. F.; Sun, Y.-P. *J. Phys. Chem. B* **2005**, *109*, 14779−14782.
(25) Davis, V. A.; Ericson, L. M.; Parra-Vasquez, A. N. G.; Fan, H.; Wang, Y.; Prieto, V.; Longoria, J. A.; Ramesh, S.; Saini, R. K.; Kittrell, C.; Billups, W. E.; Adams, W. W.; Hauge, R. H.; Smalley, R. E.; Pasquali, M. *Macromolecules* **2004**, *37*, 154−160.
(26) Penicaud, A.; Poulin, P.; Derre, A.; Anglaret, E.; Petit, P. *J. Am. Chem. Soc.* **2005**, *127*, 8−9.

MA051762N

Microchim Acta 152, 249–254 (2006)
DOI 10.1007/s00604-005-0443-3

Microchimica Acta
Printed in Austria

Original Paper

Preparation, Characterization, and Evaluation of Immuno Carbon Nanotubes

Yi Lin[1], **Tara Elkin**[1], **Shelby Taylor**[1], **Lingrong Gu**[1], **Bailin Chen**[1], **Lucia Monica Veca**[1], **Bing Zhou**[1], **Hua Yang**[2], **Jessica Brown**[1], **Ronalda Joseph**[1], **Erin Jones**[2], **Xiuping Jiang**[2], and **Ya-Ping Sun**[1,*]

[1] Department of Chemistry and Laboratory for Emerging Materials and Technology, Clemson University, Clemson, SC 29634, USA
[2] Department of Food Science and Human Nutrition, Clemson University, Clemson, SC 29634, USA

Published online November 30, 2005

Abstract. Single-walled and multiple-walled carbon nanotubes were functionalized with bovine serum albumin protein to attain aqueous solubility and biocompatibility. These aqueous soluble carbon nanotube-protein conjugates were further conjugated with pathogen-specific antibody to form immuno carbon nanotubes. The experimental details on the conjugation and results from the characterization of the conjugates are presented. The potential of these immuno carbon nanotubes in the detection of pathogenic *Escherichia coli* O157:H7 was evaluated, and the evaluation results are discussed.

Key words: Carbon nanotubes; conjugation; *Escherichia coli* O157:H7; immunoassay; pathogen detection.

There has been much recent attention on potential biological applications of both single-walled (SWNT) and multiple-walled (MWNT) carbon nanotubes for their unique combination of properties, such as one-dimensional structure, high surface area, chemical inertness, excellent mechanical properties and rich electronic properties [1, 2]. For the targeted applications, there have been rationally designed chemical modifications to carbon nanotubes with biologically active species [3], including carbohydrates, amino acids, peptides, proteins, and nucleic acids. Practical uses of these bio-functionalized carbon nanotube samples *in vitro* or even *in vivo* have been explored, with examples such as drug and gene delivery [4–6] and specific recognition of bacteria [7, 8].

Aqueous soluble functionalized carbon nanotubes upon being coupled with antibodies may serve as excellent bioanalytical reagents in immunoassays. Their unique properties include the flexible and essentially linear structure with high aspect ratio and large surface area, and the availability of biofunctionalities in arrays. There might also be significant difference between SWNTs and MWNTs in bioanalyses, such that SWNTs are more flexible and thus relatively easier in the binding with the cell surface at multiple sites, while MWNTs are better dispersed in the functionalization and contain less impurity but more encapsulated ferromagnetic species for potentially magnetic separation purposes. We have previously reported some results on the conjugation of carbon nanotubes with proteins and antibodies for potential bioanalytical applications [7, 9, 10]. Here we provide a more detailed account for the preparation, characterization, and biological evaluation in the followup experiments toward the practical applications of the

* Author for correspondence. E-mail: syaping@clemson.edu

immuno carbon nanotubes in immunoassays in general and the rapid and sensitive pathogen detection in particular.

Experimental

Materials

Bovine serum albumin (BSA) protein (Fraction V, 98%), Micro-Lowry Total Protein Kit (Onishi & Barr modification), and Bicinchoninic Acid (BCA) Kit were purchased from Sigma-Aldrich, 1-ethyl-3-(3-dimethylaminopropyl) carbodiimide hydrochloride (EDAC, 98+%) and sodium azide (99%) from Alfa Aesar, the cellulose ester dialysis tubing from Spectrum Laboratories, affinity-purified goat anti-*E. coli* O157 antibody from Kirkegaard & Perry Laboratories, and the green fluorescence protein (plasmid vector pGFPuv, GFP) from ClonTech.

The SWNT and MWNT samples were either obtained commercially (Carbon Solutions, Inc. and Nanostructure & Amorphous Materials, Inc., respectively) or produced in the laboratory of Prof. A. M. Rao (Department of Physics and Astronomy, Clemson University) by using the arc-discharge (Ni/Y as catalyst) and CVD (xylene as precursor and ferrocene as catalyst) methods, respectively. Similar purification procedures were used for SWNTs and MWNTs. Typically, a nanotube sample (100 mg) was refluxed in diluted HNO_3 solution (2.6 M, 50 mL) for 5–24 h. The mixture was cooled to room temperature and then centrifuged at 3,000 *g*. The supernatant was discarded, and the remaining solid sample was washed repeatedly with deionized water until neutral and then dried in a vacuum oven to obtain the purified nanotube sample.

Measurements

Optical absorption spectra were recorded on a Shimadzu UV2101 or UV3100 spectrophotometer and a Thermo-Nicolet Nexus 670 FT-NIR spectrometer. Raman spectra were obtained on a Renishaw Raman spectrometer equipped with a 50 mW diode laser source for 780 nm excitation or a Jobin Yvon T64000 Raman spectrometer equipped with a 35 mW He–Ne laser source for 632.8 nm excitation. Thermogravimetric analysis (TGA) was performed on a Mettler-Toledo TGA/SDTA851e system. Scanning (SEM) and transmission (TEM) electron microscopy analyses were carried out on Hitachi S4700 FE-SEM and Hitachi HD-2000 Scanning-TEM systems, respectively. Atomic force microscopy (AFM) measurements were conducted in the acoustic AC mode on a Molecular Imaging Pico-Plus system.

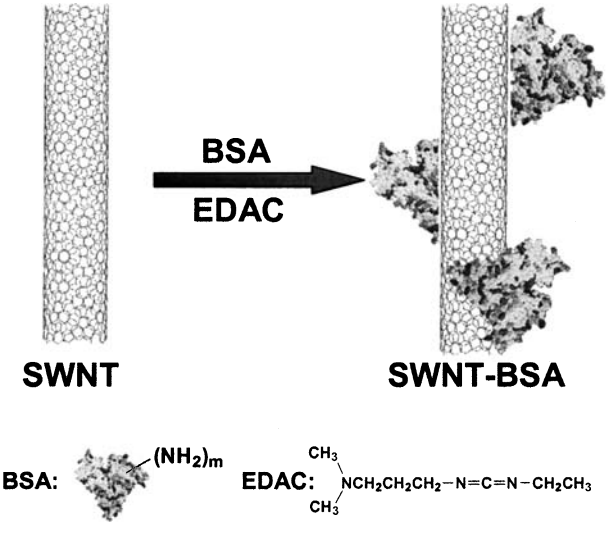

Scheme 1

Carbon Nanotube-BSA Conjugates

In a typical experiment to prepare the conjugate of SWNT with BSA (SWNT-BSA, Scheme 1), a purified SWNT sample (50 mg) was dispersed in a KH_2PO_4 buffer solution (20 mL, pH = 7.4) with EDAC (220 mg, 1.2 mmol), and the mixture was sonicated for 2 h. Then, BSA (500 mg) was added, and the mixture was stirred at room temperature for 24 h. The suspension from the reaction was centrifuged at 3,000 *g* to collect the supernatant for dialysis in a cellulose ester tubing (cutoff molecular weight 300,000) against deionized water for 3 days, in which any excess BSA and other byproducts and reagents were removed. The resulting aqueous solution was evaporated to yield SWNT-BSA as a dark-colored solid sample.

The preparation of MWNT-BSA was only slightly different. In a typical procedure, a purified MWNT sample (50 mg) was dispersed in a KH_2PO_4 buffer solution (20 mL, pH = 7.4) with EDAC (220 mg, 1.2 mmol). The mixture was sonicated for 2 h, followed by centrifuging at 3,000 *g* to discard the supernatant. The remaining solid sample containing EDAC-treated MWNTs was re-suspended in the same buffer solution (20 mL), and to which was added BSA (500 mg). The mixture was stirred at room temperature for 24 h, and the subsequent work-up procedure was the same as that for SWNT-BSA described above. The MWNT-BSA was also obtained as a dark-colored solid sample.

Immuno Carbon Nanotubes

In a typical conjugation experiment, a SWNT-BSA sample was suspended in phosphate buffer (PBS, 0.1 M, pH ~ 7.4). The suspension was mixed with a separately prepared PBS solution of goat anti-*E. coli* O157, and the mixture was subject to slow rotation at 40 rpm for 20–24 h at room temperature, followed by centrifuging at 14,000 *g* (Eppendorf Centrifuge 5417R) to remove any free antibody molecules. The sediment was washed several times by being suspended in PBS and then centrifugation to discard the supernatant. The final suspension contained the conjugate of SWNT-BSA with the *E. coli* O157 antibody (immuno-SWNTs).

The same procedure was applied to the preparation of immuno-MWNTs.

Bacterial Cell Culture and Bio-Evaluation of Immuno-Nanotubes

The *E. coli* O157:H7 strain C7927 was kindly provided by Prof. M. P. Doyle (University of Georgia). The cells were labeled with GFP by using a common procedure [11]. The GFP-labeled *E. coli* cells were grown in Tryptic soy broth supplemented with ampicillin (100 $\mu g\,mL^{-1}$) in a shaker incubator at 37 °C for 22 h. The as-cultured bacteria cells were washed several times with a sterile NaCl solution (0.8%), and then suspended and diluted in the same NaCl solution to an optical density of 0.7 at 630 nm (corresponding to bacteria concentration of $\sim 10^9$ CFU mL^{-1}). Serial dilutions were then performed to obtain different concentrations of pure *E. coli* cultures. In the enumeration of bacterial culture via colony formation, an aliquot (100 µL) of the culture was spread on a Tryptic soy agar (TSA) plate (supplemented with amphicillin) and incubated at 37 °C overnight. The enumeration was performed in duplicate.

In a typical experiment for the bio-evaluation, solutions of freshly-cultured *E. coli* cells and immuno carbon nanotubes were mixed. The mixture was subjected to slow rotation at 40 rpm for 1 h at room temperature, followed by centrifugation to remove unbound cells. The captured *E. coli* cells were re-suspended in PBS buffer for either colony enumeration or the fixation required for SEM imaging. The procedures for fixation and the preparation of SEM specimen have been reported elsewhere [8].

Results and Discussion

Carbon Nanotube-BSA Conjugates

Both SWNTs and MWNTs were functionalized with BSA via carbodiimide-activated amidation of the defect-derived carboxylic acid groups (generated during acid-treatment in the purification) on the carbon nanotube surface with the available pendant amino moieties (especially lysine residues) on BSA (Scheme 1) [9]. The SWNT-BSA and MWNT-BSA conjugates thus obtained were readily soluble in water, with solubilities over 5 mg mL^{-1} and 1 mg mL^{-1}, respectively, to result in dark-colored but still transparent and homogeneous solutions. The dark solution color must be due to well-dispersed carbon nanotubes because the protein is colorless. This was confirmed in the absorption spectral measurements. The spectrum of aqueous SWNT-BSA solution exhibits features at around 1,010 nm and 700 nm (Fig. 1), corresponding to the electronic transitions of the semiconducting (second van Hove singularity pair S_{22}) and metallic SWNTs, respectively [12, 13]. These absorption features suggest that the nanotube electronic structures are largely undisturbed in the conjugation with BSA, consistent with the expectation that the functionalization reaction targets primarily the surface defect sites of SWNTs [9, 10, 14]. Also as expected, the absorption spectrum of the MWNT-BSA conjugate is featureless, with the continuously decreasing absorption toward longer wavelengths, similar to those found in other functionalized MWNTs [14].

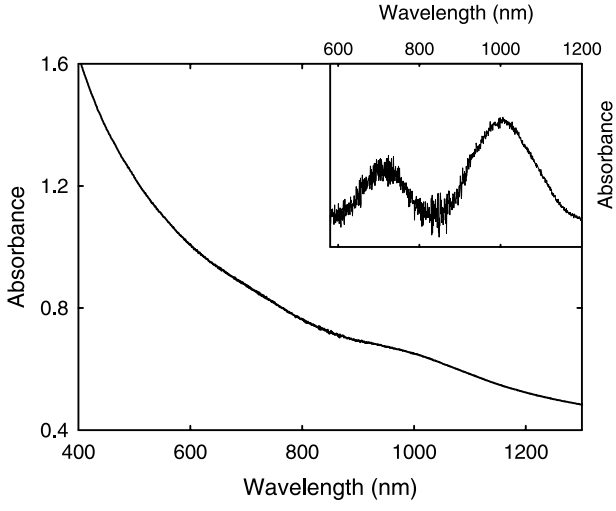

Fig. 1. The absorption spectrum of the SWNT-BSA conjugate in room-temperature D_2O solution. Shown in the inset is the same spectrum after the baseline subtraction

The Raman measurements of the SWNT-BSA and MWNT-BSA conjugates were subject to significant luminescence interference, as commonly observed in the same measurements of most other functionalized carbon nanotube samples [9, 14, 15]. In fact, the presence of strong luminescence has been considered as an indication that the carbon nanotubes are well-dispersed in these functionalized samples, because the luminescence is associated only with the well-dispersed nanotubes (inter-tube quenching minimized) in which the defects are well-passivated as a result of efficient functionalization [15]. However, since the luminescence is dependent on the nanotube dispersion and functionalization, it is diminished upon the removal of the functional groups either thermally or chemically [9, 14, 15]. In this work, the nanotube-bound BSA species in the conjugates could be decomposed and evaporated selectively in the thermogravimetric analysis (TGA) under inert atmosphere (a process often called thermal defunctionalization). The defunctionalized samples exhibited typical Raman features of, for example, G-band at 1,596 cm^{-1}, D-band at 1,330 cm^{-1} for MWNTs.

The TGA analysis in which the protein species could largely be removed from the nanotube surface (at 400 °C or less) was also used to estimate the nanotube contents in the conjugate samples [14, 16]. In this study, the SWNT-BSA and MWNT-BSA samples typically contained around 10–30% wt/wt of the nanotubes according to the TGA results. On the other hand, the aqueous solubility of the conjugate samples and the optical transparency of the resulting solutions also allowed the determination of protein contents by using classical analytical methods for proteins. The modified Lowry assay based on coloring the solution for quantitative spectrophotometry was employed [17]. In the analysis, a standard curve of optical density vs protein concentration was generated by using BSA solutions of known concentrations. However, because of the background of carbon nanotubes at the detection wavelength, the observed optical density values of the conjugate solutions that were treated with the Lowry reagents must be subtracted by those of the

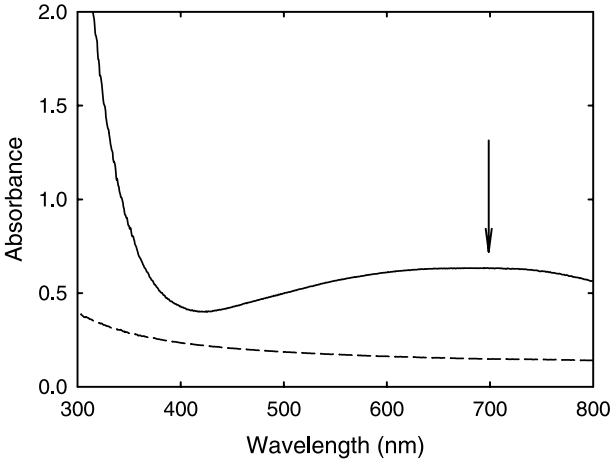

Fig. 2. Absorption spectra of the MWNT-BSA conjugate in aqueous solutions before (– – – –) and after (———) the treatment with Lowry reagents. The detection wavelength is marked by the arrow

same solutions without the treatment as blanks (Fig. 2). According to the modified Lowry assay, the total protein contents in SWNT-BSA and MWNT-BSA conjugates were 60–70% wt/wt, generally consistent with the estimates from TGA results.

The conjugate samples were also characterized by using microscopy techniques. As shown in Fig. 3, the

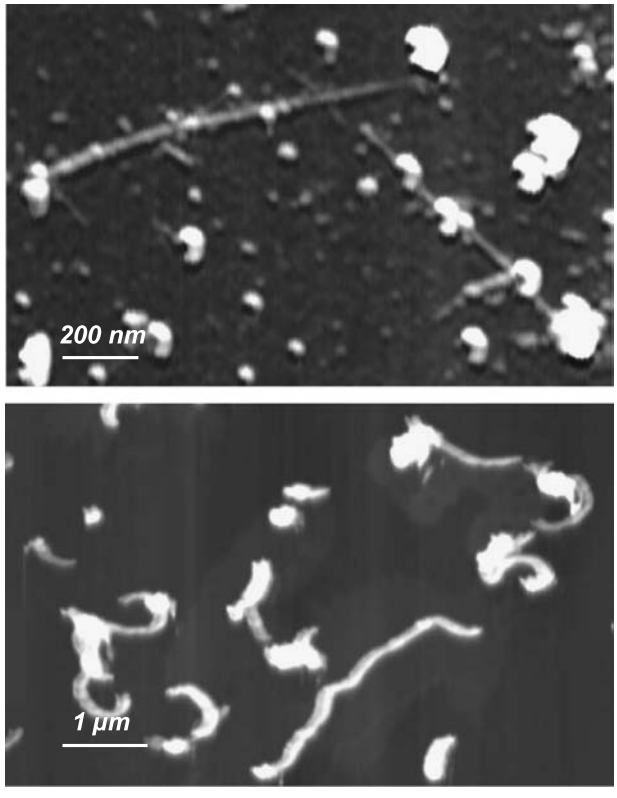

Fig. 3. Representative AFM images of SWNT-BSA (top) and MWNT-BSA (bottom) on mica substrates

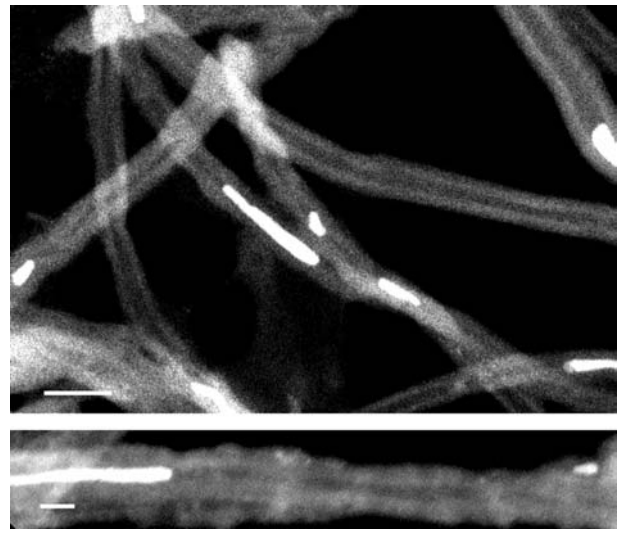

Fig. 4. TEM images (dark field) of the MWNT-BSA conjugate. The scale bars correspond to 50 nm (top) and 20 nm (bottom)

AFM images suggest that in both SWNT-BSA and MWNT-BSA there is a direct association of the proteins with the nanotubes [9], thus consistent with the expected conjugation. According to the TEM image (dark field, Fig. 4), the nanotubes in MWNT-BSA are well-dispersed. There are soft materials, likely BSA proteins, attached to the nanotube surface. In addition, the TEM images show encapsulated metal species (appearing bright) in the nanotube hollow interior, which are readily attributed to residues from the metal catalysts (iron-related compounds) used in the CVD production of MWNTs. These encapsulated species apparently survived the purification and chemical functionalization procedures. Similar catalyst residues were found in the functionalized SWNTs [18, 19], though the TEM imaging of well-dispersed SWNTs to examine the structural relationship between the nanotubes and the residual metal species was proven to be more difficult. Nevertheless, since these residues embedded in the functionalized nanotube samples are ferromagnetic, they may be explored in applications such as magnetic separations.

Immuno Carbon Nanotubes

As reported earlier [7], the nanotube-BSA conjugates could be further conjugated via simple adsorption with pathogen specific antibodies such as goat anti-*E. coli* O157 to yield immuno carbon nanotubes. In this work, an optimization in the amount of antibody adsorption was investigated in terms of the BCA (Bicinchoninic Acid) protein assay [20]. The assay

is sensitive in the low protein concentration regime in the determination of the maximum protein content when different amounts of the antibody were used. For example, in the preparation of immuno-MWNTs, different volumes (50–80 μL) of the antibody solution (10 μg mL^{-1}) were used in the mixing with a constant volume (800 μL) of the MWNT-BSA solution (10 μg mL^{-1}). Then, free antibody species were removed via centrifugation, and the resulting MWNT-BSA-antibody conjugate was subject to the BCA assay. In the assay, a higher observed optical density corresponds to the adsorption of more antibody species in the conjugation. The results shown in Fig. 5 suggest that the amount of antibody attachment reached the maximum when 70 μL of the antibody solution was used, or about 8.8 μL antibody solution per 100 μL of the MWNT-BSA solution (concentration: 10 μg mL^{-1}) [21]. In a similar set of experiments for immuno-SWNTs, the optimal ratio was found to be 80 μL of antibody solution per 100 μL of the SWNT-BSA solution (concentration: 8 μg mL^{-1}).

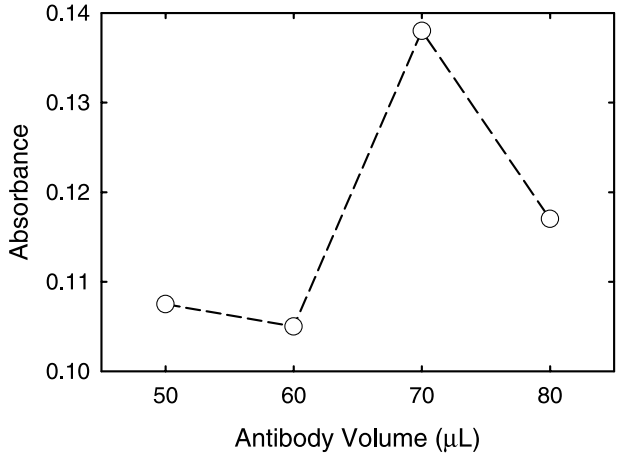

Fig. 5. The result from the BCA assay for the dependence on the amount of antibody in the preparation of immuno-MWNTs

The display of abundant antibody species on the surface of immuno carbon nanotubes facilitated the specific cell recognition. As reported earlier for the binding of the immuno-SWNTs with pathogenic *E. coli* O157:H7 cells [7], the immuno-MWNTs could serve the same purpose (Fig. 6). The binding was specific (antibody–antigen), because there was no meaningful attachment to the bacterial cells by the MWNT-BSA conjugate species without the antibody. However, the immuno-MWNTs appeared somewhat less efficient than the immuno-SWNTs in the targeting of the pathogenic cells, presumably due to the relatively larger sizes and less structural flexibility of MWNTs.

More quantitatively, the binding of immuno-SWNTs with the *E. coli* cells was evaluated by using colony enumeration. A serial dilutions of relatively low bacterial concentrations were used. As shown in Table 1, the immuno-SWNTs could apparently detect and capture the *E. coli* cells effectively. For example, at the initial cell count of 15 CFU per 100 μL, more than half of the cells were recovered by the immuno-SWNTs. The bacterial recovery could be as high as 80–90% with the use of a larger amount of immuno-SWNTs and/or a higher initial bacterial count (Table 1).

The presence of residual metal catalysts-derived species in the SWNT-BSA conjugate sample was

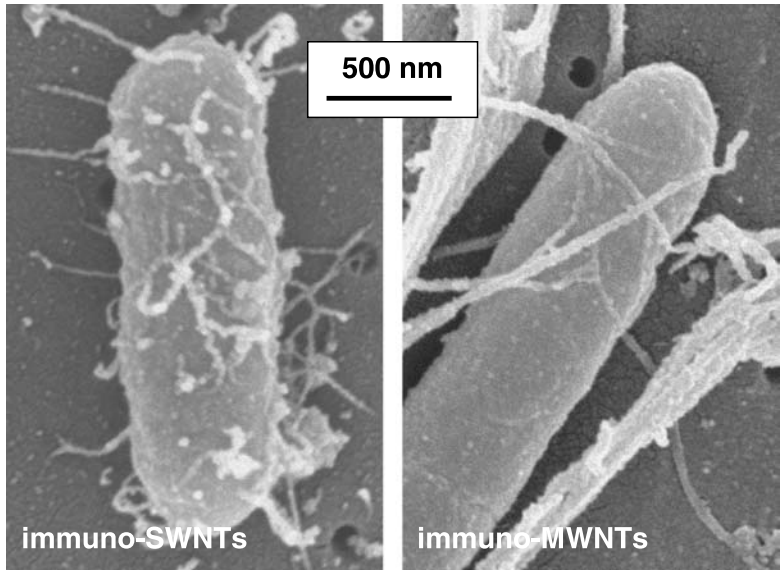

Fig. 6. SEM images for a comparison of *E. coli* cells captured by immuno-SWNTs (left) and immuno-MWNTs (right)

Table 1. Evaluation on Detection of *E. coli* O157:H7 by Immuno-SWNTs

Immuno-SWNTs ($8\,\mu g\,mL^{-1}$)	Initial cell count (CFU per 100 µL)	Detected (CFU per 100 µL)
100 µL	15	8
	87	60
	269	252
200 µL	19	16
	132	106

explored for the purpose of immunomagnetic separation. In the experiment, a solution of SWNT-BSA was placed in a magnetic separator (Dynal Biotech Model MPC-L) to isolate the magnetically active portion of the sample. Only a small fraction of the original sample was isolated within a few hours of the magnetic separation. The isolated SWNT-BSA sample was used in the conjugation with goat anti-*E. coli* O157 to yield magnetically responsive immuno-SWNTs. However, the subsequent experiment of using the immuno-SWNTs to capture *E. coli* cells for magnetic separation was not successful, with generally unsatisfactory recovery efficiency (few or no CFU detected over a long separation time). These results, though still preliminary, suggest that the magnetic residues in the immuno-SWNTs are probably insufficient for the purpose of immunomagnetic separation in the capturing and detection of pathogenic *E. coli*. A possible reason is that in SWNT samples the carbon cavities containing the magnetic residues are generally independent of the nanotubes, so that the magnetic separation step applied to the SWNT-BSA sample likely isolates mostly species associated with carbon impurities [18]. Therefore, the immuno-MWNTs with magnetic elements encapsulated in the nanotube structures may be more suitable for the intended application.

Conclusions

Carbon nanotube-BSA conjugates were synthesized via the classical carbodiimide-activated amidation reaction. The conjugates were characterized extensively by using optical spectroscopy, TGA, protein assay, and various microscopy methods. The results are consistent with the expected functionalization scheme targeting defect sites on the nanotube surface. The conjugates were further conjugated via direct adsorption with goat anti-*E. coli* O157 antibody species to form immuno carbon nanotubes. These are unique bioanalytical reagents for the targeting and detection of pathogenic *E. coli* cells. The microscopy and colony enumeration results suggest that the immuno carbon nanotubes are capable of sensitively capturing and effectively recovering the bacteria. Further investigation to couple with the immunomagnetic separation technique for rapid and ultrasensitive pathogen detection is in progress.

Acknowledgment. We thank Prof. M. P. Doyle for providing the *E. coli* strain and Prof. A. M. Rao for supplying the nanotube samples. Financial support from NSF is gratefully acknowledged. J. B., R. J., and E. J. were participants of the Summer Undergraduate Research Program sponsored jointly by NSF and Clemson University.

References

[1] Special issue on carbon nanotubes (2002) Acc Chem Res 35
[2] Theme: Advances in carbon nanotubes (2004) MRS Bull 29
[3] Lin Y, Taylor S, Li H, Fernando K A S, Qu L, Wang W, Gu L, Zhou B, Sun Y-P (2004) J Mater Chem 14: 527
[4] Pantarotto D, Singh R, McCarthy D, Erhardt M, Briand J-P, Prato M, Kostarelos K, Bianco A (2004) Angew Chem Int Ed 43: 5242
[5] Kam N W S, Jessop T C, Wender P A, Dai H (2004) J Am Chem Soc 126: 6850
[6] Lu Q, Moore J M, Huang G, Mount A S, Rao A M, Larcom L L, Ke P C (2004) Nano Lett 4: 2473
[7] Elkin T, Jiang X, Taylor S, Lin Y, Gu L, Yang H, Brown J, Collins S, Sun Y-P (2005) Chem Bio Chem 6: 640
[8] Gu L, Elkin T, Jiang X, Li H, Lin Y, Qu L, Tzeng T-R J, Joseph R, Sun Y-P (2005) Chem Commun 874
[9] Huang W, Taylor S, Fu K, Lin Y, Zhang D, Hanks T W, Rao A M, Sun Y-P (2002) Nano Lett 2: 311
[10] Lin Y, Allard L F, Sun Y-P (2004) J Phys Chem B108: 3760
[11] Jiang X, Morgan J, Doyle M P (2002) Appl Environ Microbiol 68: 2605
[12] Kataura H, Kumazawa Y, Maniwa Y, Umezu I, Suzuki S, Ohtsuka Y, Achiba Y (1999) Optical properties of single-walled carbon nanotubes. Synth Met 103: 2555
[13] The water absorption overshadowed the S_{11} band of the semiconducting SWNTs at around 1,800 nm
[14] Sun Y-P, Fu K, Lin Y, Huang W (2002) Acc Chem Res 35: 1096
[15] Lin Y, Zhou B, Martin R B, Henbest K B, Harruff B A, Riggs J E, Guo Z-X, Allard L F, Sun Y-P (2005) J Phys Chem B 109: 14779
[16] Lin Y, Rao A M, Sadanadan B, Kenik E A, Sun Y-P (2002) J Phys Chem B 106: 1294
[17] Ohnishi S T, Barr J K (1978) Anal Biochem 86: 193
[18] Kitaygorodskiy A, Wang W, Xie S-Y, Lin Y, Fernando K A S, Wang X, Qu L, Chen B, Sun Y-P (2005) J Am Chem Soc 127: 7517
[19] Haddon R C, Sippel J, Rinzler A G, Papadimitrakopoulos F (2004) MRS Bulletin 29: 252
[20] Smith P K, Krohn R I, Hermanson G T, Mallia F H, Gartner A K, Provenzano M D, Fujimoto E K, Goeke N M, Olson B J, Klenk D C (1985) Anal Biochem 150: 76
[21] The observed decrease of adsorption of antibody at higher concentration is probably due to the leaching effect as a result of over-coating

Luminescence Polarization Spectroscopy Study of Functionalized Carbon Nanotubes in a Polymeric Matrix

Bing Zhou, Yi Lin, L. Monica Veca, K. A. Shiral Fernando, Barbara A. Harruff, and Ya-Ping Sun*

Department of Chemistry and Laboratory for Emerging Materials and Technology, Clemson University, Clemson, South Carolina 29634-0973

Received: September 27, 2005; In Final Form: December 8, 2005

Single-walled carbon nanotubes (SWNTs) were well-functionalized for a study of their defect-derived luminescence properties. The soluble nanotube sample was homogeneously dispersed in poly(vinyl alcohol) (PVA) films via solution-phase mixing and then wet-casting. The PVA films embedded with the functionalized SWNTs were strongly luminescent according to spectroscopic and confocal microscopic results. The luminescence from the films was highly polarized, with the observed anisotropy value approaching the limit for collinear absorption and emission dipole moments. The films were mechanically stretched to align the embedded nanotubes, and results from luminescence measurements of the stretched films suggested that the excitation was strongly in favor of the direction along the nanotube axis. Mechanistic implications of the polarization spectroscopy results for the luminescent functionalized nanotubes in the polymeric matrix with and without the mechanic alignment are discussed.

Introduction

The electronic structures and transitions and related optical absorption and emission properties of carbon nanotubes have been attracting much attention.[1−4] For single-walled carbon nanotubes (SWNTs), the optical absorption is characterized by spectral features in the near-IR, corresponding to electronic transitions associated with the van Hove singularity pairs in the electronic density of states.[1,2] It has been reported that under well-controlled experimental conditions semiconducting SWNTs exhibit characteristic band-gap fluorescence.[4,5] These required conditions include the individual nanotube dispersion, often assisted by the use of surfactants to form micelles, and minimal nanotube surface doping effects and/or defects.[5−8] The band-gap fluorescence of semiconducting SWNTs is generally weak, with quantum yields estimated to be on the order of 0.001.[4,5,9]

Most carbon nanotubes have surface defects, especially with the fact that surface defects may be produced in the widely employed effective purification procedures (such as oxidative acid treatment).[10,11] These defects have been exploited as sites for covalent functionalization of carbon nanotubes for their dispersion and solubilization. It has been shown that the well-functionalized carbon nanotubes are strongly luminescent, with quantum yields higher than 10% under some conditions, and the observed emission spectra cover a broad visible wavelength region and extend well into the near-IR.[12−16] The strong luminescence often represents overwhelming interference in Raman measurements of functionalized carbon nanotubes, in particular when the functionalization is effective, and as a result the nanotubes are individually dispersed.[16,17] Mechanistically, the surface defects upon passivation in the functionalization may serve as excitation energy traps to be responsible for the strong luminescence.[12−16] In fact, the need for functionalization and the dependence of observed luminescence intensities on how well the nanotube surface defects are passivated via the functionalization have recently been demonstrated.[16] As in band-gap fluorescence,[4,5] the defect-derived luminescence is also sensitive to the intertube quenching in nanotube bundles, and thus the effective exfoliation to obtain individually dispersed nanotubes is required for the observation of high luminescence intensities.[16]

The luminescence from functionalized carbon nanotubes in solution is somewhat polarized,[13] suggesting the presence of correlation between the electronic transitions associated with absorption and emission. Since SWNTs with the one-dimensional structure are intrinsically anisotropic, their alignment in an anisotropic polymeric host provides an opportunity to study the anisotropic nature of their electronic structures and transitions. Of particular interest is the orientation of the electronic absorption that corresponds to the observed strong luminescence in functionalized nanotubes. In optical spectroscopic investigations, stretched poly(vinyl alcohol) (PVA) films are widely employed as anisotropic polymeric hosts for the alignment of linear molecular chromophores,[18] including carbon nanotubes.[19]

In the work reported here, we dispersed well-functionalized SWNTs into PVA films, which thus became strongly luminescent, with the observed anisotropy value approaching the limit for collinear absorption and emission dipole moments. The films were mechanically stretched to align the embedded nanotubes, and luminescence measurements were employed to evaluate the polarization of optical absorption with respect to the alignment. The results suggest that the strong luminescence is indeed associated with the excited states of functionalized carbon nanotubes and is polarized along the nanotube axis. There is also a valuable bonus from the reported investigation, namely, that luminescence polarization can be used as an effective and very sensitive tool in the evaluation of nanotube alignment in polymeric nanocomposites, especially those of high quality in which the carbon nanotubes are homogeneously dispersed.

Experimental Section

Materials. 1,6-Diphenyl-1,3,5-hexatriene (DPH), poly(propionylethylenimine) (PPEI, $M_W \approx 200\,000$ kDa), and poly(vinyl

10.1021/jp055501r CCC: $33.50
Published on Web 01/31/2006

alcohol) (PVA, $M_W \approx 70\,000-100\,000$ kDa, 98−99% hydrolyzed) were purchased from Aldrich. Arc-discharge SWNT samples were either purchased from Carbon Solutions Inc. or produced in the laboratory of Professor A. M. Rao (Department of Physics, Clemson University). The as-received samples were purified according to established procedures (the nitric acid treatment),[10,20] including the additional use of cross-flow filtration in some purification experiments.[11,21] No fundamental difference was found in the spectroscopic results with respect to the different sample sources and variations in the sample purification.

PPEI-EI−SWNT. Poly(propionylethylenimine-*co*-ethylenimine) (PPEI-EI) was prepared by partially hydrolyzing PPEI in an acid-catalyzed reaction. Details on the reaction and product characterization are already available in the literature.[22,23]

The functionalization of SWNTs with PPEI-EI was based on the acylation−amidation of the nanotube-bound carboxylic acid moieties, similar to what was reported earlier.[12,22] Briefly, a purified SWNT sample (20 mg) was refluxed with thionyl chloride (5 mL) for 24 h, followed by evaporation to remove the excess thionyl chloride. To the treated nanotube sample was added carefully dried PPEI-EI (200 mg), and the mixture was heated to ∼170 °C. After the reaction for 12 h under nitrogen protection, the mixture was cooled to room temperature. To the mixture was added chloroform, followed by brief sonication and then centrifugation (3000*g*) to retain the colored supernatant. The procedure of extraction with chloroform was repeated multiple times, and the soluble fractions were combined, concentrated, and precipitated into hexane. The PPEI-EI-functionalized SWNT (PPEI-EI−SWNT) sample was obtained as a dark-colored solid. The sample was characterized by a series of instrumental methods, as already reported in the literature.[20,24] According to the thermogravimetric analysis, the nanotube content in the PPEI-EI−SWNT sample used in this study was ∼10% (wt/wt).

PVA Films. A concentrated aqueous solution of PVA was prepared by dissolving PVA (2 g) in deionized water (10 mL) at 80 °C with vigorous stirring. Upon being cooled to ambient temperature, the solution was stirred slowly for up to 12 h for the removal of air bubbles. To the PVA solution was added dropwise an aqueous solution of PPEI-EI−SWNT (4 mg/mL, 5 mL) with constant stirring. The resulting mixture was stirred for another 4 h to obtain a viscous and colored solution without visible aggregates or air bubbles. The solution was poured onto a glass slide for film casting by using an adjustable film applicator (from Gardco). The supported film was placed in a dust-free environment at room temperature with continuous air flow for 24 h and then at 60 °C under vacuum for 48 h. The film (100−150 μm in thickness) could be peeled off the glass substrate to be free-standing. It was cut into 2 cm × 3 cm strips for mechanical stretching. In a typical stretching experiment, a film strip was mounted on a homemade manual stretching frame and heated to ∼110 °C (above the T_g of PVA ≈ 85 °C). A constant load was applied to both ends of the strip for stretching until the desired draw ratio (the length after stretching/the initial length), followed by cooling to room temperature.

Measurements. Optical absorption spectra were recorded on Shimadzu UV2101PC and UV3100 spectrophotometers and a Thermo-Nicolet Nexus 670 FT-NIR spectrometer. Luminescence emission spectra were measured on a Spex Fluorolog-2 emission spectrometer equipped with a 450 W xenon source, a Spex 340S dual-grating and dual-exit emission monochromator, and two detectors. The two gratings are blazed at 500 nm (1200 grooves/mm) and 1000 nm (600 grooves/mm). The room-temperature detector consists of a Hamamatsu R928P photomultiplier tube operated at 950 V, and the thermoelectrically cooled detector consists of a near-IR sensitive Hamamatsu R5108 photomultiplier tube operated at 1500 V. Unless specified otherwise, the reported spectra were corrected for nonlinear instrumental response by use of predetermined emission correction factors.

Two Melles-Griot dichroic sheet polarizers were used in a right-angle geometry in the luminescence emission measurements for the determination of luminescence anisotropy r[18]

$$P = (I_{HH}I_{VV} - I_{HV}I_{VH})/(I_{HH}I_{VV} + I_{HV}I_{VH}) \quad (1)$$

$$r = 2P/(3 - P) \quad (2)$$

where the indices V and H denote the vertical and horizontal positions of the polarizers, respectively, in the excitation and emission beam paths. The theoretical range of r is from −0.2 (absorption and emission transition dipoles perpendicular) to 0.4 (the two dipoles collinear).[18]

Confocal microscopy images were obtained on a Carl-Zeiss LSM510 laser scanning confocal fluorescence microscope equipped with an argon ion laser and a HeNe laser for excitation at multiple wavelengths. The oil immersion corrected objective lens allows magnifications up to 63 times (large numeric aperture number 1.3). The typical pinhole size for plane mode imaging was 150 μm.

Results

DPH-in-PVA Film. DPH was dispersed in a PVA film via solution mixing and then casting. The free-standing film was of high optical transparency, and the UV/vis absorption spectrum of DPH in the film was similar to that in the solution phase. At 370 nm excitation for the film, the observed fluorescence anisotropy r is 0.39, in excellent agreement with the literature results.[25,26]

The free-standing PVA film embedded with DPH was mechanically stretched to a draw ratio of 5. With a linear polarizer at the excitation slit in the emission spectrometer, the observed fluorescence spectra were strongly dependent on the relative orientation of the stretched film with respect to the polarization direction, exhibiting much higher intensities when the two were parallel. To take into consideration the nonlinear instrument response to the polarized light, the film before stretching was measured under the same experimental conditions to use the results as references. The average dichroic ratio (emission wavelengths 400−550 nm) with the correction for nonlinear instrument response was 13.6, again in excellent agreement with the results already in the literature.[18]

Functionalized SWNTs in PVA Film, No Stretching. Similar to the DPH-in-PVA film discussed above, the free-standing PVA films embedded with PPEI-EI−SWNT appeared homogeneous, with equally high optical quality (Figure 1). The optical absorption spectrum of the film with a relatively low PPEI-EI−SWNT loading is a featureless curve (Figure 2). However, at a higher nanotube loading in the film and/or with increased film thickness, the optical absorption spectra of PPEI-EI−SWNT in a PVA matrix exhibit the characteristic S_{11} and S_{22} bands in the near-IR, similar to those of purified SWNTs dispersed in a PVA film (Figure 2, inset).

Even at a low optical density, the PVA film embedded with PPEI-EI−SWNT is strongly luminescent, with the spectra generally similar to those in solution at the same excitation

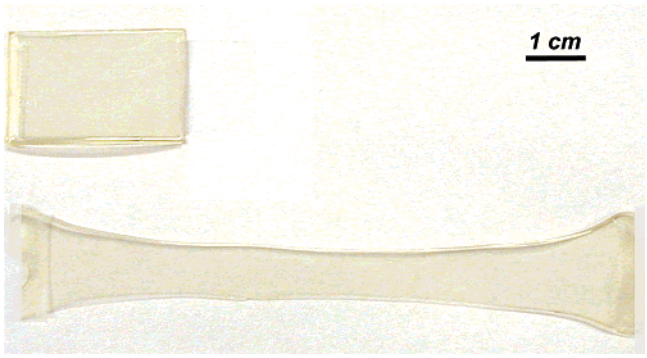

Figure 1. PVA films embedded with PPEI-EI−SWNT: as-prepared (top) and stretched to a draw ratio of 5 (bottom).

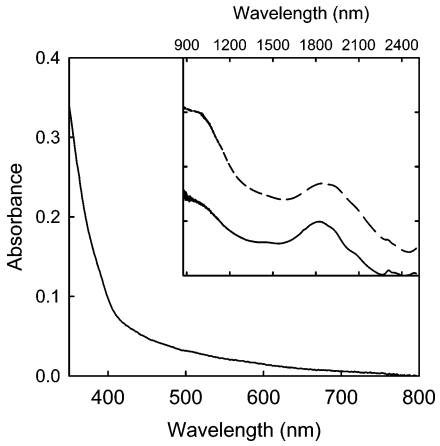

Figure 2. UV/vis absorption spectrum of PPEI-EI−SWNT in PVA film (the nanotube content on the order of 0.1 wt %/wt). Compared in the inset are the absorption spectra in near-IR for the same sample at a higher nanotube content (on the order of 2 wt %/wt, —) and purified SWNTs in PVA film (− − −).

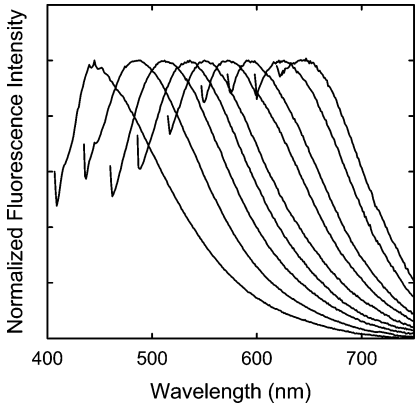

Figure 3. Luminescence emission spectra (normalized) of PPEI-EI−SWNT in PVA film with progressively longer excitation wavelengths of 400, 425, 450, 475, 500, 525, 550, 575, and 600 nm.

wavelengths. As shown in Figure 3, the observed emission spectra are dependent on the excitation in a similarly progressive fashion.[16]

The PVA film with PPEI-EI−SWNT was examined under a confocal microscope. Bright and homogeneous luminescence images (spatial resolution $\approx$ 0.5 μm) across the film were obtained. The confocal images at different depths beneath the film surface were examined to ensure their representation of the whole film matrix and to avoid any surface effects. Several available excitation wavelengths from 458 to 633 nm were used with respective long-pass emission filters on the confocal microscope, which all resulted in bright fluorescence images (Figure 4). The observed emission intensity expressed by the color intensity is generally uniform across the film, suggesting a good dispersion of the functionalized SWNTs in the PVA matrix and the absence of any microscopic phase separation.

Luminescence polarization measurement of PPEI-EI−SWNT in PVA film was carried out with two polarizers (one for excitation and the other for emission) in a right-angle geometry. The spectra were found to be strongly polarized. The anisotropy value (eq 2) for the excitation at 400 nm is 0.33, and it is generally independent of the emission wavelength (Figure 5). However, the polarization is somewhat dependent on the excitation wavelength (Table 1), larger at a longer excitation wavelength (0.39 for the excitation at 550 nm, Figure 5).

Functionalized SWNTs in PVA Film, Stretched. The PVA film embedded with PPEI-EI−SWNT was mechanically stretched to a draw ratio of up to 5, which was accompanied by a narrowing and thinning of the film (Figure 1). However, the nanotubes remained well-dispersed according to confocal microscopy images of the stretched films (Figure 6). These images also suggest that there is a preferential orientation of the functionalized nanotubes in the stretching direction. With the use of only one polarizer at the excitation slit, luminescence spectra of the stretched film corresponding to the polarizer being parallel and perpendicular to the stretching direction were measured. The nonlinear instrument responses in the two orientations were corrected by using a film of similar thickness but without the stretching (the same as the correction for the DPH-in-PVA film discussed above). The corrected luminescence emission intensities are obviously higher in the parallel direction than those in the perpendicular direction (Figure 7). The observed dichroic ratio is somewhat dependent on the excitation wavelength (Figure 7, inset).

The alignment of the functionalized SWNTs in the stretched PVA film was also evaluated in terms of the dependence of the observed dichroic ratio on the draw ratio. The excitation was at 500 nm, and the emission intensities obtained with the polarizer parallel and perpendicular to the stretching direction (after corrections in reference to the results of the unstretched film) were used to calculate the dichroic ratio. As shown in Figure 8 for the stretching with the film draw ratio from 1 to 7, the dichroic ratio initially increases rapidly with the increasing draw ratio and then reaches almost a plateau. Further stretching of the film to a draw ratio beyond 7 always resulted in the fracture of the film.

Discussion

The possibility of technical issues in experimental measurements of luminescence polarization was considered by using DPH as a calibration standard to evaluate the emission spectrometer, the measurement methods, and the sample preparation. DPH is a rodlike molecule, with the absorption and emission transition moments along the long molecular axis.[26] For DPH-in-PVA film at 370 nm excitation, the observed anisotropy value of 0.39 is in excellent agreement with what is known in the literature,[18,25] thus validating the experimental setup and methods.

Unlike in the determination of anisotropy in terms of eqs 1 and 2, corrections for the internal polarization of the spectrometer (such as different sensitivities of gratings and the detection toward light at different polarization angles) are required in the measurement of stretched film with only one polarizer at the excitation slit. Experimentally, unstretched films of similar optical densities to those of the stretched films were measured

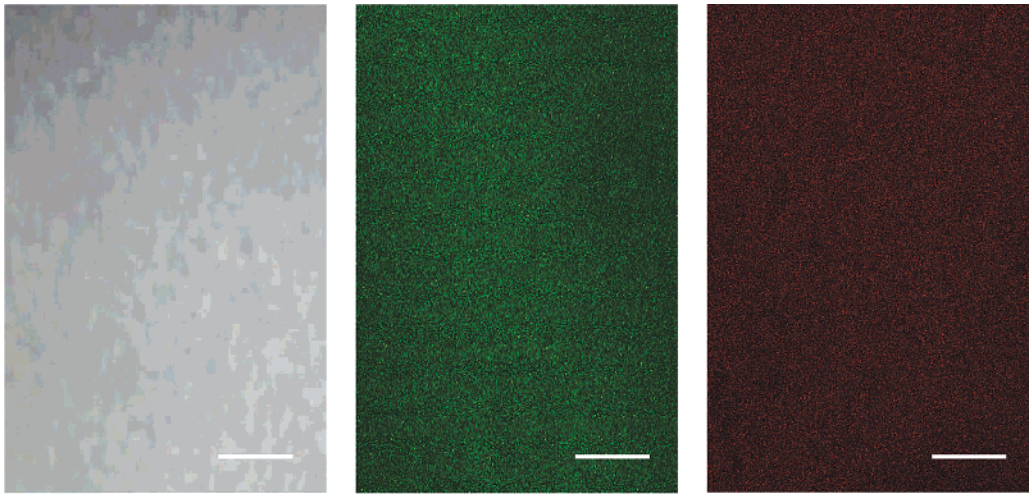

Figure 4. Optical (left) and confocal microscopy images (middle, 514 nm excitation, >530 nm detection; right, 633 nm excitation, >650 nm detection) of a PVA film embedded with PPEI-EI−SWNT (20 μm for all scale bars).

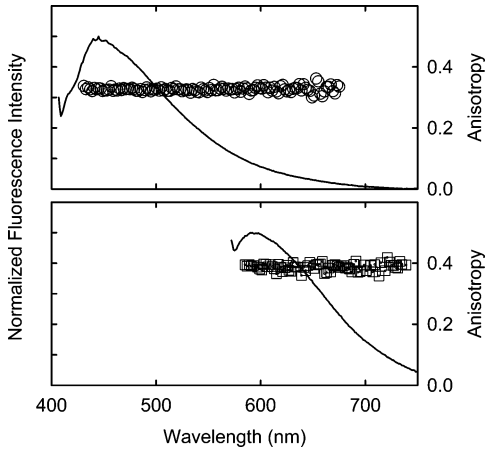

Figure 5. Luminescence emission spectra and corresponding anisotropy values of PPEI-EI−SWNT in PVA film with the excitation at 400 nm (top) and 550 nm (bottom).

TABLE 1: Luminescence Anisotropy (*r*) Values at Different Excitation Wavelengths

excitation wavelength (nm)	400	425	450	475	500	525	550	575	600
$r_{solution}$[a]	0.052	0.069	0.10	0.12	0.14	0.15	0.16	0.18	0.19
r_{film}	0.32	0.34	0.35	0.35	0.37	0.38	0.39	0.39	0.39

[a] From repeating the experiments reported in ref 13.

in the same instrument configuration to estimate the required corrections. It was found that the spectrometer used in this study is relatively uniform at different polarization angles, with the corrections generally less than 10%. For DPH in the stretched PVA film, the agreement between the dichroic ratio obtained in this study and the literature value is excellent.[18]

The exfoliation of bundled SWNTs was achieved via covalent functionalization with the aminopolymer PPEI-EI, where the nanotube surface defects were targeted for the formation of amide linkages.[12,17] In PPEI-EI−SWNT, the dispersion of the nanotubes and the passivation of surface defects are known to be especially effective, resulting in relatively strong visible luminescence. However, the covalent functionalization has little effect on the electronic transitions associated with the van Hove singularity pairs in semiconducting SWNTs,[16,21] with the S_{11} and S_{22} absorption features in the near-IR largely unchanged before and after the functionalization (Figure 2).

The selection of PPEI-EI−SWNT in this study was also due to their solubility in water; thus they are readily miscible with an aqueous solution of PVA to allow the fabrication of nanocomposite thin films via wet-casting.[21] The films were of high optical quality, exhibiting few scattering contributions in observed absorption and emission spectra. The microscopically homogeneous dispersion of nanotubes in the films was confirmed by the laser scanning confocal microscopy results for imaging at different depths of the film. The bright confocal images also allow a visual appreciation for the films being strongly luminescent (Figure 4).

The luminescence of the functionalized carbon nanotubes is obviously polarized in both solution and PVA thin film, namely, that the absorption and emission dipole moments are correlated despite the fact that the observed luminescence emission is likely associated with excited state energy trapping by well-passivated nanotube surface defects. This and the excitation wavelength dependence of luminescence properties seem to suggest that the excitation is at least partially localized in a distribution of electronic states in the functionalized carbon nanotubes. The anisotropy values in PVA thin films are clearly larger than those in solution (Table 1), which may be attributed to the restriction to any movement (and reorientation depolarization) of the nanotubes in the more rigid polymeric matrix. In particular, the excitation wavelength dependence of the anisotropy becomes less significant in the films (Table 1), with the limiting anisotropy value of 0.4 reached at longer excitation wavelengths. The results may be interpreted as such that there is probably somewhat more energy migration associated with excitation into higher energy states, but the depolarization effect is relatively insignificant. The absorption and emission dipole moments are close to being parallel for the functionalized carbon nanotubes dispersed in the polymeric matrix. However, the luminescence anisotropy results provide no information on the orientation of these parallel dipoles with respect to the nanotube structure. Experiments with the nanotubes aligned in stretched PVA films are required to address the issue.

The measurement of luminescence emissions from the stretched films is a more sensitive alternative to the direct determination of absorption polarization in reference to the film stretching direction. It has been established that the mechanical stretching of PVA film results in a significant alignment of the embedded SWNTs,[19] similar to the alignment of DPH in the same matrix discussed above. Thus, the observed dichroic ratio strongly in favor of the film stretching direction (Figure 7)

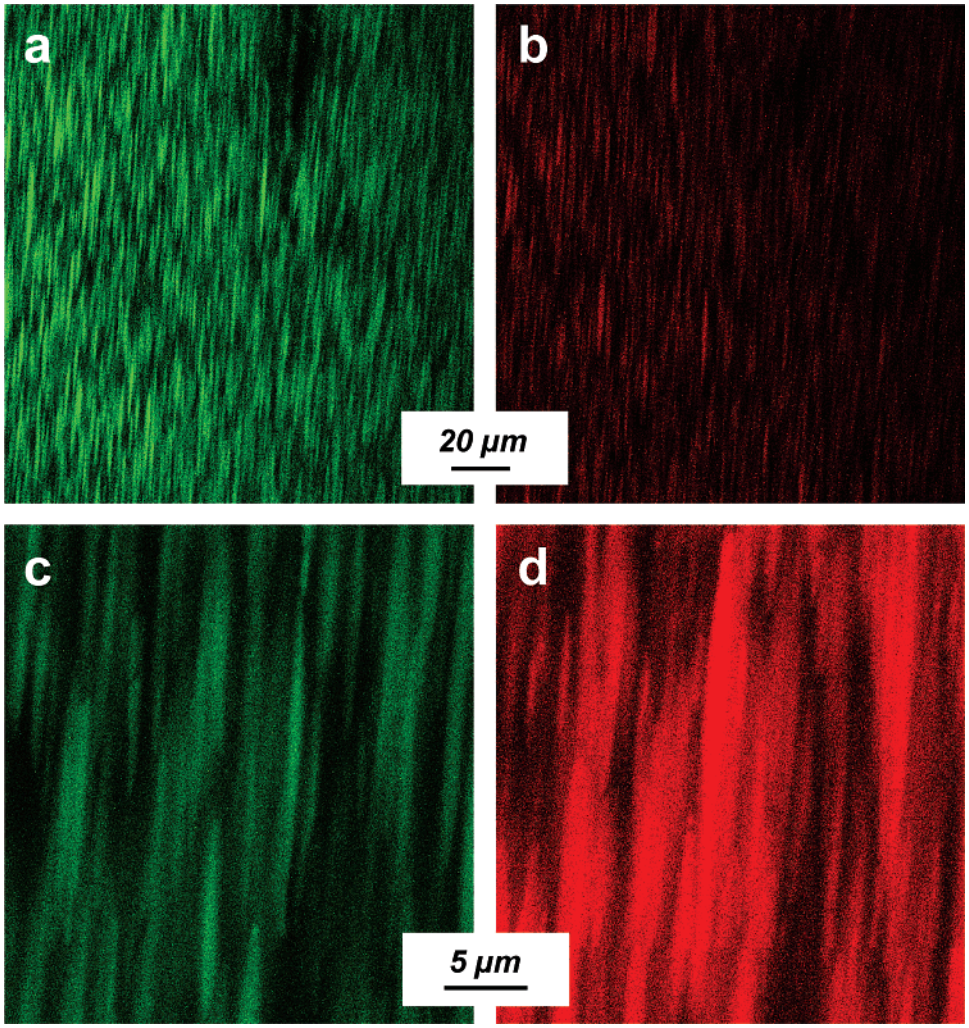

Figure 6. Confocal microscopy images of PPEI-EI−SWNT in PVA film after mechanical stretching to a draw ratio of about 5 (a and c, 514 nm excitation, >530 nm detection; b and d, 633 nm excitation, >650 nm detection).

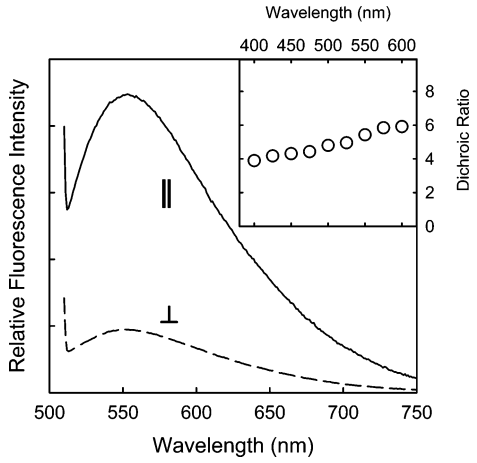

Figure 7. Luminescence emission spectra of PPEI-EI−SWNT in stretched PVA film (draw ratio ≈ 5) excited with polarized light parallel (||, —) and perpendicular (⊥, — — —) to the stretching direction. Shown in the inset is the excitation wavelength dependence of the observed dichroic ratio.

indicates that the electronic absorption responsible for the luminescence properties is along the nanotube long axis. When this is combined with the luminescence anisotropy results, an obvious conclusion is that both the absorption and emission dipole moments are coaxial with the functionalized carbon nanotubes.

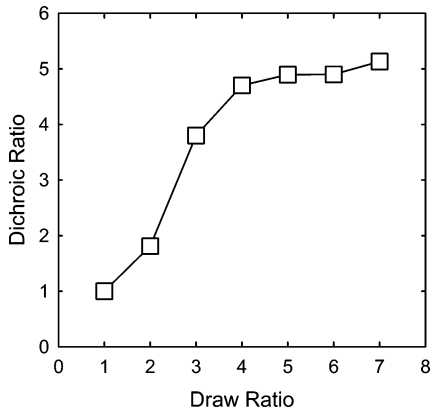

Figure 8. Observed dichroic ratio for PPEI-EI−SWNT in stretched PVA film as a function of the draw ratio (500 nm excitation).

Luminescence polarization spectroscopy apparently represents an effective tool in the evaluation of nanotube alignment in polymeric nanocomposites. For the functionalized SWNTs in the PVA film, the increasing dichroic ratio with the degree of stretching reflects the improvement in the nanotube alignment. The observed plateau in Figure 8 might be rationalized by the limitation or saturation in the use of stretched PVA film to create sufficient shear at large draw ratios. Separately, in the mechanical film stretching, the draw ratio for plain PVA films was generally limited to about 5 before the fracture of the films.[27]

For the PVA films embedded with PPEI-EI−SWNTs, however, a larger draw ratio up to 7 could be achieved. This might be explained as the effect of reinforcement associated with the homogeneously dispersed SWNTs, despite the relatively low nanotube content (on the order of 0.1 wt %).

According to the calculation by Ajiki et al.,[28] the optical absorption in the direction parallel to the nanotube axis is up to 20 times larger than the absorption in the perpendicular direction. The observed dichroic ratio is obviously significantly smaller than such a computational prediction. One might argue that the nanotube alignment in the stretched PVA film is still far from being optimal, thus the extremely high nanotube aspect ratio is not adequately reflected in the luminescence polarization results. However, the average persistence length in the structure of carbon nanotubes with respect to electronic absorption and emission should also be considered. This is particularly significant to the defect-derived luminescence emission, which by nature should correspond to limited persistence length. Therefore, it is probably desirable in further investigations to compare the dichroic ratios obtained from the luminescence emission experiments with those determined from direct polarized absorption measurements, though the latter might involve considerable technical difficulties. Also deserving attention in further investigations is the observed dependence of the dichroic ratio on the excitation wavelength (Figure 7), for which there are many mechanistic possibilities.

Summary and Conclusion

Carbon nanotubes were well-functionalized with PPEI-EI polymer to result in strong defect-derived luminescence. The functionalized nanotubes could be homogeneously dispersed into PVA polymer matrix to obtain equally luminescent films. The observed luminescence in the films was found to be strongly polarized to the limit for collinear absorption and emission dipole moments. The PVA films were mechanically stretched to align the embedded carbon nanotubes. The evaluation of the stretched films by polarized luminescence excitation suggested that the optical absorption responsible for the luminescence emissions was polarized along the nanotube axis. Thus, the reported results reaffirm the previous conclusion that the strong luminescence from well-functionalized and well-dispersed carbon nanotubes must be associated with the electronic excited states of the nanotubes and reveal the fact that the optical absorption and the defect-derived luminescence emission are not only strongly correlated but also both collinear with the nanotube axis. The luminescence and polarization properties of functionalized carbon nanotubes may find valuable applications, such as the probing of nanotube alignment in nanocomposites and other systems.

Acknowledgment. We thank R. B. Martin, W. Huang and K. Fu for experimental assistance and Professor. A. M. Rao for supplying a nanotube sample. Financial support from the National Science Foundation, NASA, and the Center for Advanced Engineering Fibers and Films (NSF-ERC at Clemson University) is gratefully acknowledged.

References and Notes

(1) Jorio, A.; Saito, R.; Hertel, T.; Weisman, R. B.; Dresselhaus, G.; Dresselhaus, M. S. *MRS Bull.* **2004**, *29*, 276−280.

(2) Kataura, H.; Kumasawa, Y.; Maniwa, Y.; Umezu, I.; Suzuki, S.; Ohtsuka, Y.; Achiba, Y. *Synth. Met.* **1999**, *103*, 2555−2558.

(3) Sun, Y.-P.; Riggs, J. E.; Henbest, K. B.; Martin, R. B. *J. Nonlinear Opt. Phys. Mater.* **2000**, *9*, 481−503.

(4) (a) O'Connell, M. J.; Bachilo, S. M.; Huffman, C. B.; Moore, V. C.; Strano, M. S.; Haroz, E. H.; Rialon, K. L.; Boul, P. J.; Noon, W. H.; Kittrell, C.; Ma, J.; Hauge, R. H.; Weisman, R. B.; Smalley, R. E. *Science* **2002**, *297*, 593−596. (b) Bachilo, S. M.; Strano, M. S.; Kittrell, C.; Hauge, R. H.; Smalley, R. E.; Weisman, R. B. *Science* **2002**, *298*, 2361−2366.

(5) (a) Lebedkin, S.; Hennrich, F.; Skipa, T.; Kappes, M. M. *J. Phys. Chem. B* **2003**, *107*, 1949−1956. (b) Lebedkin, S.; Arnold, K.; Hennrich, F.; Krupke, R.; Renker, B.; Kappes, M. M. *New J. Phys.* **2003**, *5*, 140.1−140.11.

(6) O'Connell, M. J.; Eibergen, E. E.; Doorn, S. K. *Nat. Mater.* **2005**, *4*, 412−418.

(7) Qin, S.; Qin, D.; Ford, W. T.; Herrera, J. E.; Resasco, D. E.; Bachilo, S. M.; Weisman, R. B. *Macromolecules* **2004**, *37*, 3965−3967.

(8) Lauret, J.-S.; Voisin, C.; Cassabois, G.; Roussignol, P.; Delalande, C.; Filoramo, A.; Capes, L.; Valentin, E.; Jost, O. *Physica E* **2004**, *21*, 1057−1060.

(9) Jones, M.; Engtrakul, C.; Metzger, W. K.; Ellingson, R. J.; Nozik, A. J.; Heben, M. J.; Rumbles, G. P. *Phys. Rev. B* **2005**, *71*, 115426.

(10) Haddon, R. C.; Sippel, J.; Rinzler, A. G.; Papadimitrakopoulos, F. *MRS Bull.* **2004**, *29*, 252−259.

(11) Liu, J.; Rinzler, A. G.; Dai, H.; Hafner, J. H.; Bradley, R. K.; Boul, P. J.; Lu, A.; Iverson, T.; Shelimov, K.; Huffman, C. B.; Rodriguez-Macias, F.; Shon, Y. S.; Lee, T. R.; Colbert, D. T.; Smalley, R. E. *Science* **1998**, *280*, 1253−1256.

(12) Riggs, J. E.; Guo, Z.; Carroll, D. L.; Sun, Y.-P. *J. Am. Chem. Soc.* **2000**, *122*, 5879−5880.

(13) Sun, Y.-P.; Zhou, B.; Henbest, K.; Fu, K.; Huang, W.; Lin, Y.; Taylor, S.; Carroll, D. L. *Chem. Phys. Lett.* **2002**, *351*, 349−353.

(14) Guldi, D. M.; Holzinger, M.; Hirsch, A.; Georgakilas, V.; Prato, M. *Chem. Commun.* **2002**, 1130−1131.

(15) Banerjee, S.; Wong, S. S. *J. Am. Chem. Soc.* **2002**, *124*, 8940−8948.

(16) Lin, Y.; Zhou, B.; Martin, R. B.; Henbest, K. B.; Harruff, B. A.; Riggs, J. E.; Guo, Z. X.; Allard, L. F.; Sun Y.-P. *J. Phys. Chem B* **2005**, *109*, 14779−14782.

(17) Sun, Y.-P.; Fu, K.; Huang, W.; Lin, Y. *Acc. Chem. Res.* **2002**, *35*, 1096−1104.

(18) (a) Lakowicz, R. J. *Principles of Fluorescence Spectroscopy*, 2nd ed.; Kluwer Academic/Plenum Publisher: New York, 1999. (b) Michl, J.; Bonacic-Koutechý, V. *Electronic Aspects of Organic Photochemistry*; John Wiley & Sons: New York, 1990.

(19) Rozhin, A. G.; Sakakibara, Y.; Kataura, H.; Matsuzaki, S.; Ishida, K.; Achiba, Y.; Tokumoto, M. *Chem. Phys. Lett.* **2005**, *405*, 288−293.

(20) Lin, Y.; Hill, D. E.; Bentley, J.; Allard, L. F.; Sun, Y.-P. *J. Phys. Chem. B* **2003**, *107*, 10453−10457.

(21) Lin, Y.; Zhou, B.; Fernando, K. A. S.; Liu, P.; Allard, L. F.; Sun, Y.-P. *Macromolecules* **2003**, *36*, 7199−7204.

(22) Lin, Y.; Rao, A. M.; Sadanadan, B.; Kenik, E. A.; Sun, Y.-P. *J. Phys. Chem. B* **2002**, *106*, 1294−1298.

(23) Sun, Y.-P.; Liu, B.; Moton, D. K. *Chem. Commun.* **1996**, 2699−2700.

(24) Fernando, K. A. S.; Lin, Y.; Sun, Y.-P. *Langmuir* **2004**, *20*, 4777−4778.

(25) Patra, D. *J. Appl. Spectrosc.* **2004**, *71*, 334−338.

(26) Valeur, B. *Molecular Fluorescence: Principles and Applications*; Wiley-VCH Verlag GmbH: Weinheim, Germany, 2001.

(27) Dirix, Y.; Tervoort, T. A.; Bastiaansen, C. *Marcomolecules* **1997**, *30*, 2175−2177.

(28) (a) Ajiki, H.; Ando, T. *Physica B* **1994**, *201*, 349−352. (b) Duesberg, G. S.; Loa, I.; Burghard, M.; Syassen, K.; Roth, S. *Phys. Rev. Lett.* **2000**, *85*, 5436−5439.

J|A|C|S
COMMUNICATIONS

Published on Web 05/23/2006

Quantum-Sized Carbon Dots for Bright and Colorful Photoluminescence

Ya-Ping Sun,* Bing Zhou, Yi Lin, Wei Wang, K. A. Shiral Fernando, Pankaj Pathak, Mohammed Jaouad Meziani, Barbara A. Harruff, Xin Wang, Haifang Wang, Pengju G. Luo,† Hua Yang,‡ Muhammet Erkan Kose, Bailin Chen, L. Monica Veca, and Su-Yuan Xie

Department of Chemistry and Laboratory for Emerging Materials and Technology, Clemson University, Clemson, South Carolina 29634-0973

Received February 16, 2006; Revised Manuscript Received April 17, 2006; E-mail: syaping@clemson.edu

Fluorescent semiconductor quantum dots have generated much excitement for a wide variety of promising applications, especially those in biology and medicine.[1] For both in vitro and in vivo uses, however, the known toxicity and potential environmental hazard associated with many of these materials may represent serious limitations.[1,2] Therefore, the search for benign nanomaterials of similar optical properties continues.[3,4] For quantum-sized silicon, the discovery of Brus and co-workers[4] on the strong luminescence in surface-oxidized nanocrystals has attracted extensive investigations of silicon nanoparticles and nanowires.[5−7] For example, silicon nanoparticles capped with water-soluble polymers, thus compatible with physiological media, have been studied for the luminescence labeling of cells.[7] Here we report a new finding on the quantum-sized carbon analogues,[8] namely, that nanoscale carbon particles ("carbon dots") upon simple surface passivation are also strongly photoluminescent in both solution and the solid state with spectral features and properties comparable to those of surface-oxidized silicon nanocrystals. These strongly emissive carbon dots may find applications similar to or beyond those of their widely pursued silicon counterparts.

The carbon dots were produced via laser ablation of a carbon target in the presence of water vapor with argon as carrier gas.[9] The carbon target was prepared by hot-pressing a mixture of graphite powder and cement, followed by stepwise baking, curing, and annealing in argon flow. A Q-switched Nd:YAG laser (1064 nm, 10 Hz) was used for the ablation, during which the carbon target was in a flow of argon gas carrying water vapor (through a water bubbler) at 900 °C and 75 kPa. The as-produced sample, according to electron microscopy analyses, was dominated by nanoscale carbon particles in aggregates of various sizes. There was no detectable photoluminescence from the sample and its aqueous suspension. The sample was treated in an aqueous nitric acid solution (up to 2.6 M) with refluxing for up to 12 h. The treated sample still exhibited no detectable photoluminescence. However, upon the surface passivation by attaching simple organic species to the acid-treated carbon particles (Scheme 1), bright luminescence emissions were observed (Figure 1).

Many organic molecules could serve as the purpose of surface passivation. For example, diamine-terminated oligomeric poly(ethylene glycol) $H_2NCH_2(CH_2CH_2O)_nCH_2CH_2CH_2NH_2$ (average $n \sim 35$, PEG_{1500N}) was used to react with the carbon nanoparticles (Scheme 1).[10] In a typical reaction, PEG_{1500N} (200 mg, 0.13 mmol) was mixed with an acid-treated particle sample, and the mixture was heated to 120 °C for 72 h. After the reaction, the mixture was cooled to room temperature and dispersed in water, followed by centrifuging (~1400*g*) for 30 min. The colored but homogeneous supernatant contained the carbon dots with PEG_{1500N} species attached to the surface (Scheme 1).[11] A small fraction of the supernatant was diluted for the preparation of microscopy specimens, deposited on a carbon-coated copper grid for scanning transmission electron microscopy (STEM) and on a mica surface for atomic force microscopy (AFM). The results suggest that these carbon dots are around 5 nm in diameter (Figure 2).

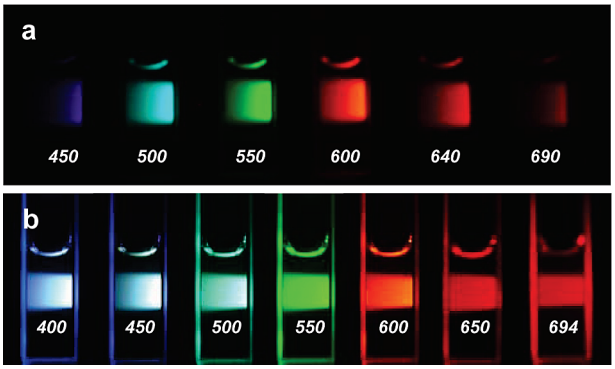

Figure 1. Aqueous solution of the PEG_{1500N}-attached carbon dots (a) excited at 400 nm and photographed through band-pass filters of different wavelengths as indicated, and (b) excited at the indicated wavelengths and photographed directly.

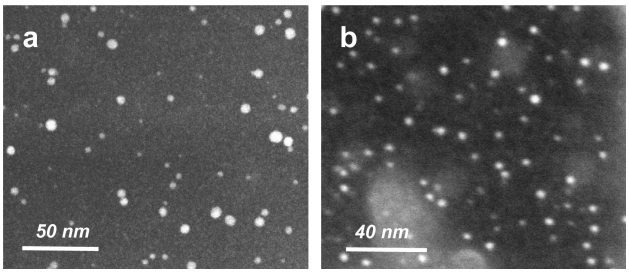

Figure 2. Representative STEM images of carbon dots surface-passivated with (a) PEG_{1500N} and (b) PPEI-EI.

Scheme 1

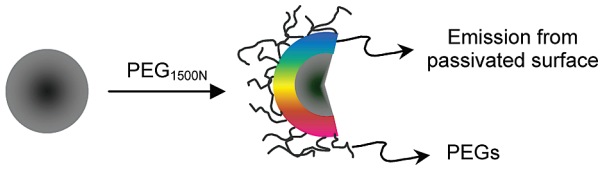

Other molecules or polymers, such as poly(propionylethyleneimine-*co*-ethyleneimine) (PPEI-EI), could also be used in largely the same reaction procedure for surface passivation to achieve similar results (Figure 2).

The passivated carbon dots with organic moieties attached to the surface are strongly photoluminescent both in the solution-like

† Also affiliated with Department of Biological Sciences (under the supervision of Dr. T.-R. J. Tzeng).
‡ Also affiliated with Department of Food Science and Human Nutrition (under the supervision of Dr. X. Jiang).

10.1021/ja062677d CCC: $33.50

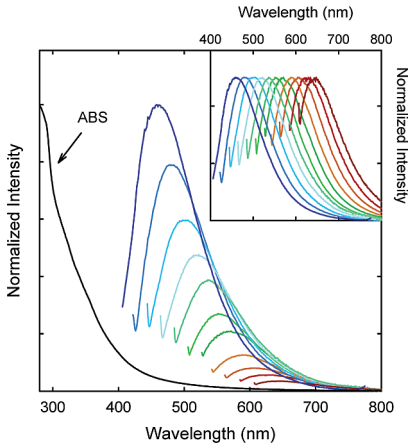

Figure 3. The absorption (ABS) and luminescence emission spectra (with progressively longer excitation wavelengths from 400 nm on the left in 20 nm increment) of PPEI-EI carbon dots in an aqueous solution. The emission spectral intensities are normalized to quantum yields (normalized to spectral peaks in the inset).

suspension and in the solid state, and the emissions cover the visible wavelength range and extend into the near-infrared (Figure 1). It should be pointed out that the organic and polymeric passivation agents (PEG_{1500N} and PPEI-EI) contain no visible or near-UV chromophores and therefore are obviously nonemissive at visible wavelengths. The observed bright and colorful luminescence emissions must be due to the surface-passivated carbon dots. As shown in Figure 3, the photoluminescence spectra of the carbon dots are generally broad and dependent on excitation wavelengths (Figure 1), which as in their silicon counterparts[4] may reflect not only effects from particles of different sizes in the sample but also a distribution of different emissive sites on each passivated carbon dot.

The brightness of the photoluminescence is reflected in the high emission quantum yields. At 400 nm excitation, the observed quantum yields were from about 4% to more than 10%, where the variation probably depended on the effectiveness of the reaction for surface passivation. For example, when a sample of PEG_{1500N}- or PPEI-EI-attached carbon dots was found to have the emission quantum yield at the lower end of the range, the sample could be reacted again with PEG_{1500N} or PPEI-EI under the same reaction conditions (thus improved surface passivation) to become more emissive with a higher quantum yield. Further effort is required to understand and better control the parameters dominating the particle surface passivation and resulting properties for carbon dots of brighter photoluminescence. Generally speaking, however, the presently observed luminescence emission yields of the carbon dots are comparable with those of traditionally prepared and passivated silicon nanocrystals.[4]

The photoluminescence of the carbon dots is stable with respect to photoirradiation, exhibiting no meaningful reduction in the observed intensities in the experiment of continuously repeating excitations for several hours. Unlike many other fluorescent nanoparticles,[12] there is no blinking in the luminescence emissions of the carbon dots according to laser scanning confocal microscopy analyses (commercially available gold nanocrystals as control under the same measurement conditions).

Mechanistically, the photoluminescence from carbon dots may be attributed to the presence of surface energy traps that become emissive upon stabilization as a result of the surface passivation. The requirement for surface passivation to become photoluminescent is apparently shared by the carbon dots and the silicon nanocrystals, for which a widely accepted mechanism for luminescence emission is the radiative recombination of excitons.[4] For the photoluminescent carbon dots reported here, however, there must be a quantum confinement of emissive energy traps to the particle surface, namely, that a large surface-to-volume ratio in a particle is necessary in order for the particle upon surface passivation to exhibit strong photoluminescence. There has already been experimental evidence supporting such a mechanistic argument. Larger carbon particles (30−50 nm in average diameter, for example) with the same surface passivation were found to be much less luminescent. Conversely, it might be expected that even higher photoluminescence quantum yields be achieved in smaller carbon dots with the same or similar surface morphology and passivation.

As in their silicon counterparts,[4,6] the carbon dots may, in principle, be separated or manipulated such that some of the inhomogeneity in photoluminescence is removed. On the other hand, the inhomogeneity may be exploited in the use of the surface-passivated carbon dots for optical labeling to allow the selection of different emission colors with different excitation wavelengths (in confocal microscopy, for example). The versatile surface functionalities as required for passivation will also be very useful for the carbon dots in bioimaging applications. The tethers, such as PEG_{1500N}, are not only aqueous compatible but also readily conjugated with antibodies or other bioactive molecules. Preliminary results on the optical imaging of biological species with the emissive carbon dots are provided in the Supporting Information.

Supporting Information Available: Additional characterization results, and preliminary results on the optical imaging of biological species. This material is available free of charge via the Internet at http://pubs.acs.org.

References

(1) Michalet, X.; Pinaud, F. F.; Bentolila, L. A.; Tsay, J. M.; Doose, S.; Li, J. J.; Sundaresan, G.; Wu, A. M.; Gambhir, S. S.; Weiss, S. *Science* **2005**, *307*, 538−544.

(2) (a) Derfus, A. M.; Chan, W. C. W.; Bhatia, S. N. *Nano Lett.* **2004**, *4*, 11−18. (b) Kirchner, C.; Liedl, T.; Kudera, S.; Pellegrino, T.; Javier, A. M.; Gaub, H. E.; Stolzle, S.; Fertig, N.; Parak, W. J. *Nano Lett.* **2005**, *5*, 331−338. (c) Lovric, J.; Cho, S. J.; Winnik, F. M.; Maysinger, D. *Chem. Biol.* **2005**, *12*, 1227−1234.

(3) (a) Bharali, D. J.; Lucey, D. W.; Jayakumar, H.; Pudavar, H. E.; Prasad, P. N. *J. Am. Chem. Soc.* **2005**, *127*, 11364−11371. (b) Seydack, M. *Biosens. Bioelectron.* **2005**, *20*, 2454−2469.

(4) Wilson, W. L.; Szajowski, P. F.; Brus, L. E. *Science* **1993**, *262*, 1242−1244.

(5) (a) Huisken, F.; Ledoux, G.; Guillos, O.; Reynaud, C. *Adv. Mater.* **2002**, *14*, 1861−1865. (b) Holmes, J. D.; Johnston, K. P.; Doty, C.; Korgel, B. A. *Science* **2000**, *287*, 1471−1473.

(6) (a) Belomoin, G.; Therrien, J.; Smith, A.; Rao, S.; Twesten, R.; Chaieb, S.; Nayfeh, M. H.; Wagner, L.; Mitas, L. *Appl. Phys. Lett.* **2002**, *80*, 841−843. (b) Hua, F.; Swihart, M. T.; Ruckenstein, E. *Langmuir* **2005**, *21*, 6054−6062.

(7) Li, Z. F.; Ruckenstein, E. *Nano Lett.* **2004**, *4*, 1463−1467.

(8) Other recent studies on luminescence from carbon materials: (a) Xu, X.; Ray, R.; Gu, Y.; Ploehn, H. J.; Gearheart, L.; Raker, K.; Scrivens, W. A. *J. Am. Chem. Soc.* **2004**, *126*, 12736−12737. (b) Yu, S.-J.; Kang, M.-W.; Chang, H.-C.; Chen, K.-M.; Yu, Y.-C. *J. Am. Chem. Soc.* **2005**, *127*, 17604−17605. (c) Bottini, M.; Balasubramanian, C.; Dawson, M. I.; Bergamaschi, A.; Belluci, S.; Mustelin, T. *J. Phys. Chem. B* **2006**, *110*, 831−836.

(9) Suda, Y.; Ono, T.; Akazawa, M.; Sakai, Y.; Tsujino, J.; Homma, N. *Thin Solid Films* **2002**, *415*, 15−20.

(10) Huang, W.; Fernando, S.; Allard, L. F.; Sun, Y.-P. *Nano Lett.* **2003**, *3*, 565−568.

(11) The linkages for the attachment might be similar to those found in the functionalization of carbon nanotubes at surface defect sites (see ref 10, for example).

(12) (a) Nirmal, M.; Dabbousi, B. O.; Bawendi, M. G.; Macklin, J. J.; Trautman, J. K.; Harris, T. D.; Brus, L. E. *Nature* **1996**, *383*, 802−804. (b) Krug, J. T.; Wang, G. D.; Emory, S. R.; Nie, S. *J. Am. Chem. Soc.* **1999**, *121*, 9208−9214. (c) English, D. S.; Pell, L. E.; Yu, Z.; Barbara, P. F.; Korgel, K. A. *Nano Lett.* **2002**, *2*, 681−685.

JA062677D

THE JOURNAL OF PHYSICAL CHEMISTRY B LETTERS

2006, *110,* 14032−14034
Published on Web 06/29/2006

Efficient Quenching of Photoluminescence from Functionalized Single-Walled Carbon Nanotubes by Nitroaromatic Molecules

Muhammet Erkan Kose,† Barbara A. Harruff,† Yi Lin, L. Monica Veca, Fushen Lu, and Ya-Ping Sun*

Department of Chemistry and Laboratory for Emerging Materials and Technology, Clemson University, Clemson, South Carolina 29634-0973

Received: May 26, 2006; In Final Form: June 19, 2006

The photoluminescence from functionalized single-walled carbon nanotubes was found to be highly sensitive to the presence of nitroaromatic compounds such as nitrobenzene, 4-nitrotoluene, and 2,4-dinitrotoluene. The strong luminescence quenching in solution was at the upper limit of diffusion-control and also showed significant static quenching contributions. Mechanistic implication of the results and potential applications are discussed.

There has been much recent interest in basic research toward potentially developing sensitive detection techniques for explosives including 2,4,6-trinitrotoluene (TNT), picric acid, and other nitroaromatic compounds.[1−12] Optical spectroscopic methods, especially those based on luminescence quenching, have emerged as more effective options due to their sensitivity, versatility, and rapid response time. Among widely investigated fluorophores for such a purpose are conjugated polymers such as substituted polyacetylenes,[9] pentiptycene polymers,[2] various PPVs,[11] and polysiloles.[10] For example, Sailor, Trogler, and coworkers reported the use of polysiloles and other metallole polymers for the detection of nitroaromatic molecules.[10] It was shown that the luminescence from metallole polymers was significantly quenched in the presence of trace amounts of nitroaromatic molecules and that the quenching was predominantly static because the luminescence lifetime was independent of the analyte concentration. The quenching of pyrene monomer and excimer emissions has also been used for probing the presence of nitro-compounds.[12] Recently, carbon nanotubes have been explored as new materials in sensors for explosives.[13] We found, which has also confirmed by others, that well-dispersed functionalized carbon nanotubes are strongly photoluminescent due to excited-state energy trapping by passivated surface defects.[14−19] Here we report that the nanotube luminescence emissions are sensitive to the presence of nitroaromatic compounds. The effective luminescence quenching presents new opportunities for the use of carbon nanotubes in the continuing development of novel optical sensors.

Single-walled carbon nanotubes (SWNTs, produced by the arc-discharge method) after purification according to established procedures[20] were functionalized with the aminopolymer poly(propionylethylenimine-*co*-ethylenimine) (PPEI-EI) in acylation-amidation reactions (Scheme 1).[14,21] The functionalized sample PPEI-EI−SWNT, soluble in both water and organic solvents such as methanol and chloroform, was characterized by using

SCHEME 1

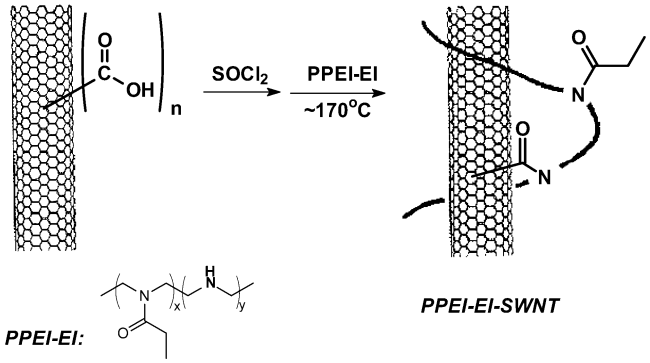

a series of instrumental techniques. For example, the PPEI-EI−SWNT sample was found to still exhibit the characteristic band-gap transition peaks at ∼1800 nm and ∼1000 nm in the optical absorption spectrum (Figure 1), consistent with the notion that the nanotube electronic structure is preserved in the functionalization targeting the nanotube surface defects. The functionalized SWNTs are also well-dispersed to the level of individual nanotubes (or very thin bundles), as confirmed by atomic force microscopy (AFM) imaging of the sample specimen on mica surface (Figure 1 inset). These results are in general agreement with those reported previsouly.[14,21] According to the thermogravimetric analysis (TGA) result, the nanotube content in the PPEI-EI−SWNT sample used in this study was ∼10% (wt/wt).

The acylation-amidation method is relatively more effective in the functionalization of SWNTs targeting carboxylic acid moieties that are associated with defects on the nanotube surface.[22] As a result, the PPEI-EI−SWNT sample was found to be strongly photoluminescent in both solution and the solid state. A luminescence spectrum of PPEI-EI−SWNT in benzonitrile solution is shown in Figure 2 (quantum yield ∼10%).[14] The spectrum and intensities are independent of the use of degassed or air saturated solutions, as expected from the relatively short luminescence lifetimes (see below). The lumi-

* Corresponding author. E-mail: syaping@clemson.edu
† These authors made equal contributions to the reported work.

10.1021/jp063251o CCC: $33.50

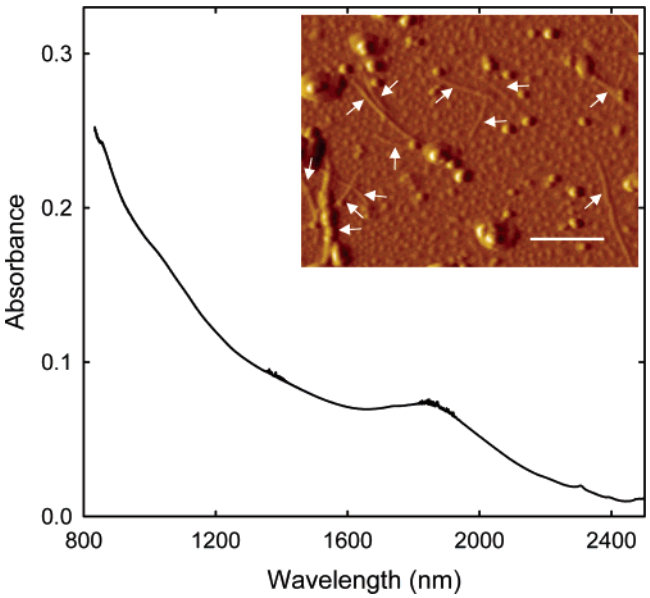

Figure 1. Near-IR absorption spectrum of a PPEI-EI−SWNT sample specimen in the solid state. Shown in the inset is a typical AFM amplitude image of the same sample (scale bar = 1 μm, some nanotubes marked by arrows).

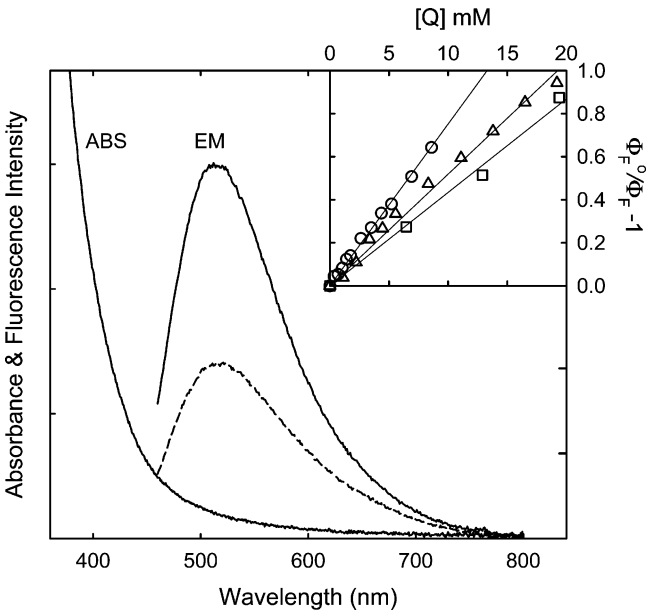

Figure 2. Absorption (ABS) and luminescence emission spectra (EM, 450 nm excitation) of PPEI-EI−SWNT in room-temperature benzonitrile solution in the absence (—) and presence of nitrobenzene (- - - -). Shown in the inset are Stern−Volmer plots for the quenching of luminescence intensities by nitrobenzene (□), 4-nitrotoluene (△), and 2,4-dinitrotoluene (○) in room-temperature methanol (450 nm excitation).

nescence emission is quenched by nitrobenzene, 4-nitrotoluene, or 2,4-dinitrotoluene (Figure 2), and the quenching is efficient. According to the Stern−Volmer plot for nitrobenzene, as an example, the quenching rate constant k_q of $\sim 2 \times 10^{10}$ M^{-1} s^{-1} (Table 1) suggests that the quenching is at the upper limit of diffusion control.

The luminescence quenching is somewhat dependent on the excitation wavelength, generally weaker at a longer excitation wavelength. For example, shown in Figure 3 are Stern−Volmer plots for the quenching with 4-nitrotoluene at four different excitation wavelengths. The slight excitation wavelength dependence should probably be expected considering the in-

TABLE 1: Results from the Quenching of Luminescence Quantum Yields[a]

		Stern−Volmer Constant (M^{-1}) at different excitation wavelengths (nm)				
quencher	solvent	400	425	450	475	500
nitrobenzene	methanol	67	56	42	31	23
	benzonitrile		29	22	17	12
	chloroform	26	3.6	3.6	3.3	1.6
4-nitrotoluene	methanol	109	65	49	38	30
	benzonitrile	34	14	11	7.7	6
2,4-dinitrotoluene	methanol	132	85	73	61	51

[a] The average luminescence lifetimes of PPEI-EI−SWNT in the absence of quencher are (407 nm excitation): 4.5 ns in benzonitrile, 5.3 ns in methanol, and 4.3 ns in chloroform.

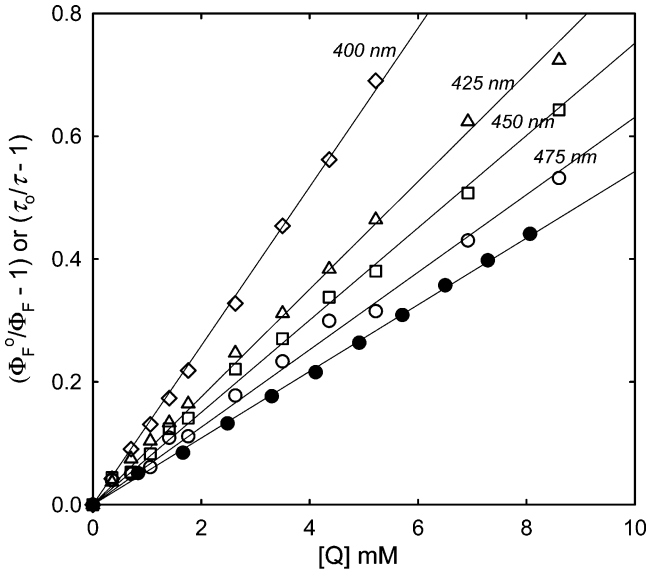

Figure 3. Stern−Volmer plots for the quenching of luminescence intensities by 2,4-dinitrotoluene at 400 nm (◊), 425 nm (△), 450 nm (□), and 475 nm (○) excitations. The same plot for the lifetime quenching under similar sample conditions (●, 407 nm excitation) is also shown for comparison.

homogeneous nature of the luminescence emissions (distributions of emissive species and/or sites).[14,18] The decrease in slope at a longer excitation wavelength in Figure 3 likely has more to do with the fact that the observed intrinsic luminescence quantum yield (in the absence of any quencher) decreases with increasing excitation wavelength.[14]

The luminescence quenching is also sensitive to the solvent environment. In a more polar solvent, methanol, the quenching is obviously more efficient than in benzonitrile (Table 1). The same dependence was found in less polar solvents. For example, there was only minor luminescence quenching of PPEI-EI−SWNT by nitrobenzene in chloroform, also with weaker excitation wavelength dependence for the quenching (Table 1).

Time-correlated single photon counting was used in the measurement of luminescence decays of PPEI-EI−SWNT in methanol with varying 2,4-dinitrotoluene concentrations (excitation at 407 nm). The decays are non-exponential (not mono-exponential), but can be fitted with a three-component equation. The average lifetimes calculated in terms of $\tau_{average} = \Sigma A_i \tau_i$, where A_i and τ_i are the preexponential factor (in percentage) and the lifetime of the component i, respectively, are used for the Stern−Volmer plot shown in Figure 3. The Stern−Volmer quenching constant as measured by the average luminescence lifetimes is 59 M^{-1}, considerably smaller than that from the quenching of luminescence quantum yields at a comparable

excitation wavelength (Table 1). Therefore, the quenching of photoluminescence from PPEI-EI−SWNT by 2,4-dinitrotoluene is diffusion-controlled but also has substantial contribution from static quenching (near-neighbor interactions).[23]

As reported in the literature,[2,9,13] electron transfer has been a common mechanism for the quenching of luminescence emissions by nitroaromatic compounds. The electron affinitive nature of the nitro moieties makes these molecules act as acceptors in the electron transfer processes. For photoexcited carbon nanotubes, however, their redox characteristics are still not well defined (or at least subject to debate). Most available studies have generally labeled carbon nanotubes as electron acceptors,[24] which may be due significantly to their structural relationships with fullerenes (well-known excellent electron acceptors). Nevertheless, the experimental results presented here seem consistent with a mechanism of electron transfer from the photoexcited functionalized carbon nanotubes to the nitroaromatic quenchers. Among the three nitro-compounds, 2,4-dinitrotoluene is more effective in the quenching, probably due to its lower reduction potential (−0.9 V vs NHE) than those of nitrobenzene and 4-nitrotoluene (−1.15 V and −1.19 V, respectively).[10] The generally much more efficient quenching in the more polar solvent methanol than in benzonitrile (especially the fact that the quenching is already at the upper limit of diffusion-control) may also be explained in terms of electron transfer as a dominating mechanism. These consistent explanations, however, are probably not sufficient for a conclusion that the excited states of carbon nanotubes can be quenched by nitroaromatic compounds through electron transfer interactions. There are other possibilities to be considered. For example, it might be that the passivated energy trapping sites associated with surface defects on the nanotubes (responsible for the photoluminescence) could serve as electron donors, namely that their redox characteristics may be different from the intrinsic photoexcited states of defect-free carbon nanotubes.[25] More investigations, especially those by employing transient spectroscopy techniques to detect charge transferred species, will be pursued for a more precise mechanistic elucidation.

In any case, the strong photoluminescence of functionalized carbon nanotubes may be exploited for detecting signatures of explosives.[27] The organic and aqueous solubilities of the functionalized carbon nanotubes along with their associated processibility make them viable candidates for optical sensors.

Acknowledgment. We thank R. B. Martin, W. Huang, and K. Fu for experimental assistance. Financial support from NSF, NASA, and the Center for Advanced Engineering Fibers and Films (NSF-ERC at Clemson University) is gratefully acknowledged.

References and Notes

(1) McQuade, D. T.; Pullen, A. E.; Swager, T. M. *Chem. Rev.* **2000**, *100*, 2537.

(2) Yang, J.-S.; Swager, T. M. *J. Am. Chem. Soc.* **1998**, *120*, 5321.

(3) Czarnick, A. W. *Nature* **1998**, *394*, 417.

(4) (a) Shriver-Lake, L. C.; Donner, B. L.; Ligler, F. S. *Environ. Sci. Technol.* **1997**, *31*, 837. (b) Lu, J.; Zhang, Z. *Anal. Chim. Acta* **1996**, *318*, 175.

(5) (a) Hakansson, K.; Coorey, R. V.; Zubarev, R. A.; Talrose V. L.; Hakansson, P. J. *J. Mass Spectrom.* **2000**, *35*, 337. (b) Luggar, R. D.; Farquharson, M. J.; Horrocks, J. A.; Lacey, R. J. *J. X-ray Spectrom.* **1998**, *27*, 87.

(6) Goldman, E. R.; Medintz, I. L.; Whitley, J. L.; Hayhurst, A.; Clapp, A. R.; Uyeda, H. T.; Deschamps, J. R.; Lassman, M. E.; Mattoussi, H. *J. Am. Chem. Soc.* **2005**, *127*, 6744.

(7) Sylvia, J. M.; Janni, J. A.; Klein, J. D.; Spencer, K. M. *Anal. Chem.* **2000**, *72*, 5834.

(8) Krausa, M.; Schorb, K. *J. Electroanal. Chem.* **1999**, *461*, 10.

(9) Liu, Y.; Mills, R. C.; Boncella, J. M.; Schanze, K. S. *Langmuir* **2001**, *17*, 7452.

(10) (a) Sohn, H.; Calhoun, R. M.; Sailor, M. J.; Trogler, W. C. *Angew. Chem., Int. Ed.* **2001**, *40*, 2104. (b) Sohn, H.; Sailor, M. J.; Magde, D.; Trogler, W. C. *J. Am. Chem. Soc.* **2003**, *125*, 3821.

(11) Chang, C.-P.; Chao, C.-Y.; Huang, J. H.; Li, A.-K.; Hsu, C.-S.; Lin, M.-S.; Hsieh, B. R.; Su, A.-C. *Synth. Met.* **2004**, *144*, 297.

(12) Focsaneanu, K. S.; Scaiano, J. C. *Photochem. Photobiol. Sci.* **2005**, *4*, 817.

(13) (a) Wang, J.; Hocevar, S. B.; Ogorevc, B. *Electrochem. Commun.* **2004**, *6*, 176. (b) Snow, E. E.; Perkins, F. K.; Houser, E. J.; Badescu, S. C.; Reinecke, T. L. *Science* **2005**, *307*, 1942.

(14) Riggs, J. E.; Guo, Z.; Carroll, D. L.; Sun, Y.-P. *J. Am. Chem. Soc.* **2000**, *122*, 5879.

(15) Sun, Y.-P.; Zhou, B.; Henbest, K.; Fu, K.; Huang, W.; Lin, Y.; Taylor, S.; Carroll, D. L. *Chem. Phys. Lett.* **2002**, *351*, 349.

(16) Guldi, D. M.; Holzinger, M.; Hirsch, A.; Georgakilas, V.; Prato, M. *Chem. Commun.* **2002**, 1130.

(17) Banerjee, S.; Wong, S. S. *J. Am. Chem. Soc.* **2002**, *124*, 8940.

(18) Lin, Y.; Zhou, B.; Martin, R. B.; Henbest, K. B.; Harruff, B. A.; Riggs, J. E.; Guo, Z. X.; Allard, L. F.; Sun Y.-P. *J. Phys. Chem. B* **2005**, *109*, 14779.

(19) Zhou, B.; Lin, Y.; Veca, L. M.; Fernando, K. A. S.; Harruff, B. A.; Sun, Y.-P. *J. Phys. Chem. B* **2006**, *110*, 3001.

(20) Qu, L.; Veca, L. M.; Lin, Y.; Kitaygorodskiy, A.; Chen, B.; McCall, A. M.; Connell, J. W.; Sun, Y.-P. *Macromolecules* **2005**, *38*, 10328.

(21) (a) Lin, Y.; Rao, A. M.; Sadanadan, B.; Kenik, E. A.; Sun, Y.-P. *J. Phys. Chem. B* **2002**, *106*, 1294−1298. (b) Lin, Y.; Hill, D. E.; Bentley, J.; Allard, L. F.; Sun, Y.-P. *J. Phys. Chem. B* **2003**, *107*, 10453.

(22) Sun, Y.-P.; Fu, K.; Huang, W.; Lin, Y. *Acc. Chem. Res.* **2002**, *35*, 1096−1104.

(23) Birks, J. B. *Organic Molecular Photophysics*; Birks, J. B., Ed.; Wiley: London, 1975; Vol. 2, p 529.

(24) Guldi, D. M.; Marcaccio, M.; Paolucci, D.; Paolucci, F.; Tagmatarchis, N.; Tasis, D.; Vazquez, E.; Prato, M. *Angew. Chem., Int. Ed.* **2003**, *42*, 4206.

(25) There were recent reports suggesting that carbon nanotubes may act as both electron donor and electron acceptor.[26] By monitoring the disappearance and reappearance of the S_{11} absorption bands, it was shown that SWNTs could be easily oxidized and reduced with various oxidants and reductants.

(26) (a) Zheng, M.; Diner, B. A. *J. Am. Chem. Soc.* **2004**, *126*, 15490. (b) O'Connell, M. J.; Eibergen, E. E.; Doorn, S. K. *Nat. Mater.* **2005**, *4*, 412.

(27) The quenching by the nitroaromatic compounds is relatively sensitive (less than 0.5 mM) with respect to the relatively short photoluminescence lifetimes of the functionalized SWNTs (which also offers the advantage of independence from the presence of air), and has a large dynamic range.

Available online at www.sciencedirect.com
SCIENCE DIRECT
ELSEVIER
Polymer 47 (2006) 5323–5329
polymer
www.elsevier.com/locate/polymer

Polymeric nanocomposite films from functionalized vs suspended single-walled carbon nanotubes

Bing Zhou [a], Yi Lin [a], Darron E. Hill [a], Wei Wang [a], L. Monica Veca [a], Liangwei Qu [a], Pankaj Pathak [a], Mohammed J. Meziani [a], Julian Diaz [a], John W. Connell [b], Kent A. Watson [c], Lawrence F. Allard [d], Ya-Ping Sun [a,*]

[a] *Department of Chemistry and Laboratory for Emerging Materials and Technology, Clemson University, Clemson, SC 29634-0973, USA*
[b] *NASA Langley Research Center, Advanced Materials and Processing Branch, Hampton, VA 23681-2199, USA*
[c] *National Institute of Aerospace, 100 Exploration Way, Hampton, VA 23666-6147, USA*
[d] *High Temperature Materials Laboratory, Oak Ridge National Laboratory, Oak Ridge, TN 37831-6062, USA*

Received 16 April 2006; received in revised form 17 May 2006; accepted 19 May 2006
Available online 12 June 2006

Abstract

The reported work was to demonstrate that the defect-derived photoluminescence in functionalized single-walled carbon nanotubes could be exploited in probing the dispersion of these nanotubes in polymeric nanocomposites because the luminescence emissions are sensitive to the degree of nanotube bundling and surface modification. The polyimide–SWNT nanocomposite thin films obtained from nanotubes with and without functionalization were compared. The spectroscopic results suggest that despite a similar visual appearance in the two kinds of films, the nanotube dispersion must be significantly better in the film with functionalized nanotubes, as reflected by the strong photoluminescence. In fact, the nanotubes embedded in polymer matrix that can be readily characterized by Raman spectroscopy are non-luminescent, while those that are difficult for Raman are strongly luminescent. Therefore, Raman and photoluminescence serve as complementary tools in the investigation of nanocomposites concerning the nanotube dispersion-related properties.

Keywords: Carbon nanotubes; Nanocomposites; Photoluminescence

1. Introduction

Polymeric nanocomposites with single-walled carbon nanotubes (SWNTs) as fillers have received much recent attention for their widely predicted superior electronic, thermal, and mechanical properties [1–3]. An important issue in the development of such nanocomposites is the dispersion of SWNTs, since as-produced SWNTs are severely bundled and entangled due largely to the strong inter-tube van der Waals interactions [1]. There is hardly any solubility of the nanotubes in common solvents, which substantially impairs their processibility. Thus, the direct incorporation of as-produced SWNTs into polymer matrices usually results in poor nanotube dispersion in the nanocomposites, with the actual performance significantly worse than expected [4]. In order to improve the dispersion, so as to maximize the transformation of the nanotube properties to the resulting nanocomposites, the functionalization of SWNTs has been identified as an effective approach [3–6]. For example, Lin et al. reported that poly(vinyl alcohol) (PVA) could be used to functionalize SWNTs for their exfoliation and solubilization and that the functionalized nanotube sample could be homogeneously dispersed into PVA matrix for high-quality nanocomposites without introducing any unwanted foreign materials [7].

In a different approach, selected polymers and common surfactant molecules have been used to aid the suspension of SWNTs in various solvents [8–10]. It has been shown that polyimide is particularly effective in stabilizing the nanotube suspension, and the resulting suspension can be used to fabricate polyimide–SWNT nanocomposites, which are also free from other agents [11]. The nanocomposites thus prepared are visually similar to those obtained from functionalized nanotube samples, despite their expected significant difference with respect to the dispersion of the embedded SWNTs.

* Corresponding author. Tel.: +1 864 656 5026; fax: +1 864 656 5007.
E-mail address: syaping@clemson.edu (Y.-P. Sun).

0032-3861/$ - see front matter © 2006 Elsevier Ltd. All rights reserved.
doi:10.1016/j.polymer.2006.05.055

Commonly employed nanoscale characterization techniques such as high-resolution electron microscopy may in principle be applied to an evaluation of the dispersion issue, though the preparation of specimens for the microscopy analyses can be challenging. For example, the microtome process to obtain ultra-thin slices of the nanocomposite often distorts the original distribution of embedded nanotubes in the polymer matrix [12]. As a result, optical spectroscopy methods including especially Raman are widely pursued for the characterization of polymer–SWNT nanocomposites in a convenient and rapid fashion [13–15]. However, Raman is not so useful in the investigation of nanocomposites obtained from homogeneously dispersed functionalized carbon nanotubes because of overwhelming interference of photoluminescence from these nanotubes [6,16].

In this work, we wanted to demonstrate that the photoluminescence in functionalized SWNTs could be exploited in probing the dispersion of these nanotubes in polymeric nanocomposites because the luminescence emissions are sensitive to the degree of nanotube bundling and surface modification. In fact, the nanotubes embedded in polymer matrix that can be readily characterized by Raman are non-luminescent, while those that are difficult for Raman are strongly photoluminescent. Therefore, Raman and photoluminescence may serve as complementary tools in the investigation of nanocomposites concerning the nanotube dispersion-related properties. The polyimide–SWNT nanocomposite films obtained from nanotubes with and without functionalization are compared. The films have also been analyzed by electron microscopy techniques to support the spectroscopic results.

2. Experimental section

2.1. Materials

4,4′-(Hexafluoroisopropylidene)diphthalic anhydride (99%) was purchased from Aldrich, 1,3-bis-(3-aminophenoxy)benzene (96%) from TCI, and 1-ethyl-3-(3-(dimethylamino)-propyl)carbodiimide hydrochloride (EDAC, 98+%) from Alfa Aesar. Dimethylformamide (DMF) and other solvents were obtained from Mallinckrodt and carefully distilled before use. The polyimide based on 4,4′-(hexafluoroisopropylidene)-diphthalic anhydride and 1,3-bis-(3-aminophenoxy)benzene (also known as LaRC CP-2™ or simply CP-2) was supplied by SRS, Inc. According to GPC analysis (linear polystyrene standards), the polymer molecular weight M_n was ~17,000 and polydispersity index ~3.

The sample of SWNTs (from the arc-discharge method) was purchased from Carbon Solutions, Inc. It was purified by using a combination of thermal oxidation and diluted nitric acid treatment, as already reported in the literature [17].

2.2. Measurements

UV/vis/near-IR absorption spectra were recorded on Shimadzu UV3100 spectrophotometer. Raman spectra were obtained on a Jobin Yvon T64000 spectrometer equipped with a Melles-Griot 35 mW He–Ne laser source for 632.8 nm excitation, a triple monochromator, a research grade Olympus BX-41 microscope, and a liquid-nitrogen-cooled Symphony detector. Luminescence emission spectra were measured on a Spex Fluorolog-2 emission spectrometer equipped with a 450 W xenon source, a Spex 340S dual-grating and dual-exit emission monochromator, and two detectors. The two gratings are blazed at 500 nm (1200 grooves/mm) and 1000 nm (600 grooves/mm). The room-temperature detector consists of a Hamamatsu R928P photomultiplier tube operated at 950 V, and the thermoelectrically cooled detector consists of a near-IR sensitive Hamamatsu R5108 photomultiplier tube operated at 1500 V. Unless specified otherwise, the reported spectra were corrected for non-linear instrumental response by use of predetermined emission correction factors. Scanning (SEM) and transmission (TEM) electron microscopy images were obtained on a Hitachi S4700 field-emission SEM system and a Hitachi HF-2000 TEM system, respectively. Composite film specimens for SEM imaging were subject to platinum sputtering for 60 s in order to suppress surface charging effect. The film thickness was measured by using a Nikon Digimicro Stand MS-11C with a MFC-101 digital display device.

2.3. PI-NH_2 and PI-NH_2–SWNT

Amine-terminated polyimide (PI-NH_2) was synthesized in conventional condensation polymerization of 1,3-bis(3-aminophenoxy)benzene and 4,4′-(hexafluoroisopropylidene)-diphthalic anhydride with a calculated excess of the former to ensure the amino group termination and the control of the polymer molecular weight to approximately 5000 [18]. The functionalization of SWNTs by PI-NH_2 was achieved in carbodiimide (EDAC)-activated amidation reaction of the terminal amino groups in PI-NH_2 with the defect-derived carboxylic acid groups on the nanotube surface, as reported previously [18] (Scheme 1).

2.4. Nanocomposite films

For film with suspended SWNTs, a purified SWNT sample (5 mg) was suspended in DMF (3 mL) and homogenized (PowerGen 125) for 1 h under flowing N_2. A DMF solution of the CP-2 polyimide (4 mL, 125 mg/mL) was added to the nanotube suspension under constant stirring, and the mixture was sonicated (VWR Aquasonic 150 HT) for 12 h. The resulting suspension was further stirred to slowly evaporate the solvent until the total volume reduced to approximately 2 mL. The viscous suspension thus obtained was cast onto a glass substrate with an adjustable film applicator (Gardco), and kept in flowing N_2 for 24 h. The film was further cured under the same atmosphere at 100 °C for 1 h, 150 °C for 1 h, 200 °C for 1 h, and finally dried in vacuum at 60 °C for 48 h.

For film with functionalized SWNTs, a DMF solution of PI-NH_2–SWNT (3 mL, 33 mg/mL) was added dropwise to a DMF solution of CP-2 (4 mL, 500 mg/mL) under constant stirring. The mixture was vigorously agitated until

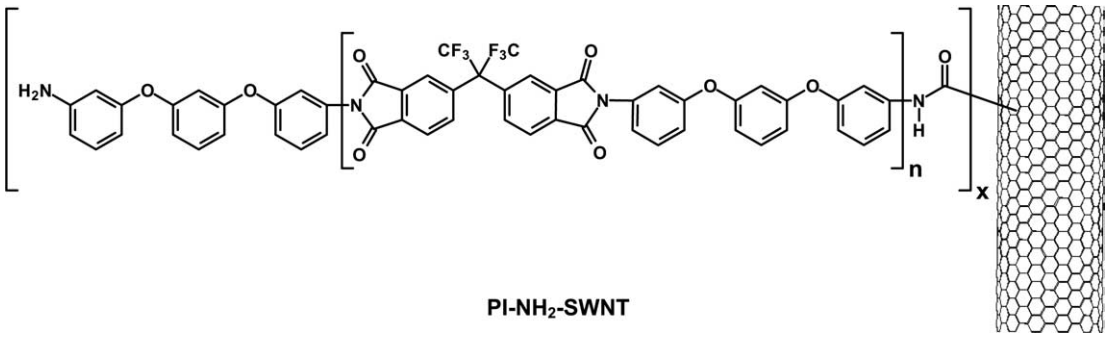

Scheme 1.

homogeneous, followed by essentially the same casting and drying procedures as described above.

3. Results and discussion

3.1. Purification and functionalization of SWNTs

The commercially available SWNT sample was purified by using an established procedure of first heat treatment (300 °C) in air and then refluxing in diluted nitric acid (2.6 M) to remove amorphous carbonaceous impurities and residual metal catalysts from the sample [17]. According to discussion in the literature concerning the effectiveness of the procedure [19,20], the purification should be adequate for the purpose of preparing polymeric nanocomposites used in this work.

The purified SWNT sample was used in the functionalization with PI-NH_2. The target of functionalization was the amidation of nanotube-bound carboxylic acid groups, which are known to be present in the oxidative acid-treated sample [6,21]. The functionalized nanotube sample PI-NH_2–SWNT was characterized by using various instrumental techniques to have the results calibrated with those reported previously [18]. For example, the ^{1}H NMR signals of the terminal aniline aromatic protons in PI-NH_2–SWNT were at 5.9–6.1 ppm, shifted upfield from those in the PI-NH_2 spectrum (6.0–6.4 ppm) due to effects of the large aromatic ring currents in the attached carbon nanotubes [18]. The PI-NH_2–SWNT sample was readily soluble in many organic solvents including THF and DMF to form dark-colored solutions. The solution-phase optical absorption spectrum of the sample in DMF exhibited features at $\sim$1800 cm^{-1} (despite the interference from solvent background) and $\sim$1000 cm^{-1}, corresponding to electronic transitions between the first (S_{11}) and second (S_{22}) van Hove singularity pairs in semiconducting SWNTs, respectively (Fig. 1(a)). The first electronic transition of metallic SWNTs (M_{11}) could also be detected at $\sim$700 cm^{-1} (Fig. 1(a)). The observation of these characteristic absorption features is consistent with the expectation that the functionalization of SWNTs targets the defect-derived carboxylic acid moieties on the nanotube surface. This mode of functionalization is known to preserve the electronic absorption properties of SWNTs [21].

It is known that SWNTs without functionalization may be dispersed into polar solvents with the aid of surfactants or polymers such as poly(phenylene vinylene) [22] and poly(vinyl pyrolidone) [8], due presumably to non-covalent interactions. The polyimide CP-2 is somewhat special in this regard [11], such that SWNTs are readily suspended in a DMF solution of CP-2, and the suspension appears homogeneous. The absorption spectrum of the suspended SWNTs is also shown in Fig. 1. However, while the suspension is stable and looks similar to the solution of the functionalized sample PI-NH_2–SWNT (similar absorption spectra as well, Fig. 1(a)), the molecular level structures and properties of the suspended and functionalized SWNTs must be different. A clear indication for such difference is in the results of nanotube photoluminescence, which is associated with passivated surface defects in exfoliated carbon nanotubes [6,16,23–25]. As compared in

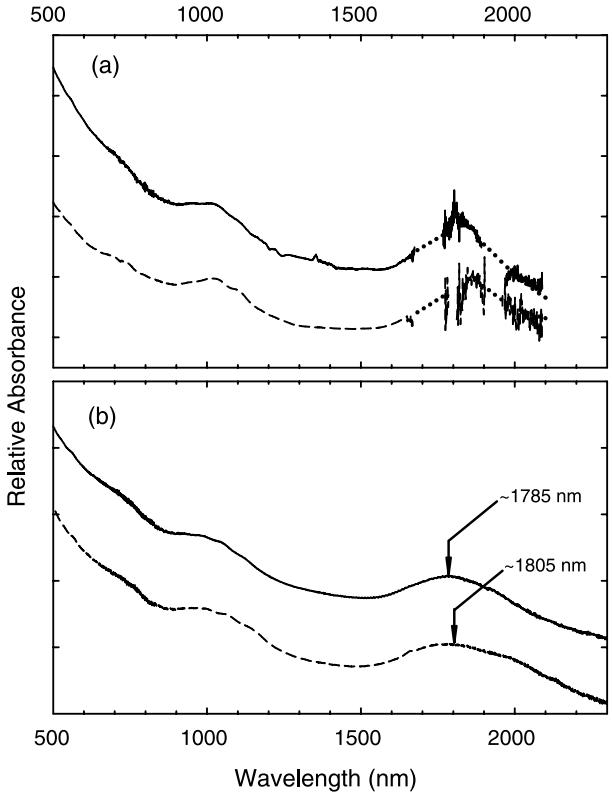

Fig. 1. (a) Optical absorption spectra of PI-NH_2–SWNT in DMF solution (—) and polyimide-assisted SWNT suspension in DMF (- - -). (b) Optical absorption spectra of nanocomposite films from the functionalized (—) and suspended (- - -) SWNTs.

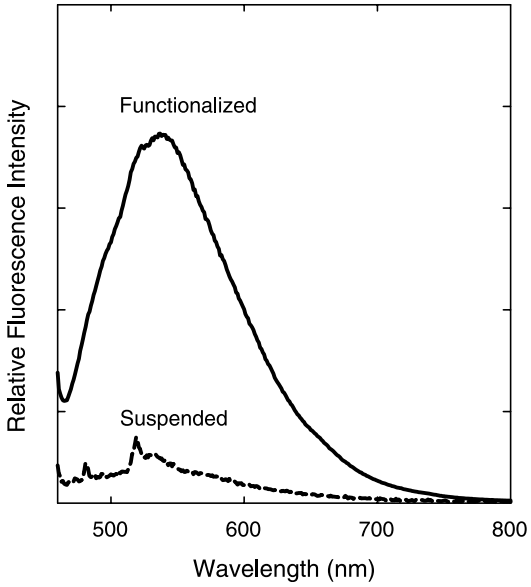

Fig. 2. Luminescence emission spectra (450 nm excitation) of PI-NH_2–SWNT in DMF solution (—) and polyimide-assisted SWNT suspension in DMF (- - -).

Fig. 2, the PI-NH_2–SWNT solution in DMF is strongly photoluminescent, whereas the apparently stable polyimide-assisted suspension of purified SWNTs in the same solvent with the same optical density at the excitation wavelength is hardly emissive. This is understandable because there is obviously a lack of passivation effect for surface defects in the suspended nanotubes, and the nanotubes in suspension are bundled (thus significant inter-tube quenching of photoexcited states) [16,23,26]. The difference in molecular level structures and properties between the functionalized and suspended SWNTs may represent a primary factor in the dispersion of the nanotubes in polymeric matrix.

3.2. Nanocomposite films

The solution of PI-NH_2–SWNT and the suspension of purified SWNTs, both in DMF, were used in the fabrication of polyimide (CP-2)–SWNT nanocomposite films via wet-casting. The fabrication procedures were largely similar between the two samples (except for the homogenization and sonication required for the suspended SWNTs), and the resulting films also appeared similar. Since the nanotube contents in the functionalized and suspended samples were known (from quantitative ^{1}H NMR signal integration [18] and the amount of added nanotubes, respectively), the nanotube contents in the resulting nanocomposite films were obtained by quantifying the amount of blank CP-2 polymer used in the preparation of the mixtures for wet-casting. The films from both the functionalized and suspended nanotube samples appeared similarly optically transparent when the nanotube loading was low or the films were ultra-thin.

The color of the films was dependent on the nanotube content and also the film thickness. The films with higher nanotube contents appeared black. For a better comparison, the two kinds of films obtained from the functionalized and suspended nanotube samples were controlled to the nanotube loading of 1% by weight and a similar thickness of about 80 μm. As shown in Fig. 1(b), optical absorption spectra of both films exhibit the characteristic S_{11} (around 1800 nm) and S_{22} (around 1000 nm) bands for semiconducting SWNTs and also the M_{11} absorption (around 700 nm) for metallic SWNTs, similar to those of the PI-NH_2–SWNT solution and suspended SWNTs in DMF (Fig. 1(a)). These spectral features confirm the expected preservation of electronic structures for the SWNTs embedded in the CP-2 polymer matrix.

In a closer examination of the absorption spectra, the S_{11} and S_{22} bands of the film with functionalized SWNTs are somewhat narrower in bandwidth than those of the film with suspended SWNTs, and the former are also slightly blue-shifted (Fig. 1(b)). These subtle changes in absorption spectral features are consistent with the improved dispersion of the functionalized SWNTs in the polymer matrix. As proposed in the literature [27], van der Waals interactions between nanotubes in a bundle help the overlap between electronic transition states and reduce the band gap of the nanotubes. Therefore, the exfoliation of bundled SWNTs brought about by functionalization gives rise to a better dispersion in the nanocomposite film resulting in narrower and blue-shifted band gap absorption bands.

The improved dispersion of the functionalized SWNTs in the nanocomposite film is reflected by the observation of strong photoluminescence in the visible (Fig. 3), as it is known that the nanotube defect-derived luminescence emission is sensitive to the exfoliation and surface passivation of the nanotubes [16]. Generally speaking, a better functionalization of SWNTs means more effective surface passivation of the defect sites and leads to more homogeneous dispersion (less bundling), which correspond to enhanced luminescence emissions with minimized inter-tube quenching [16]. For the film obtained from the suspended SWNTs, although the macroscopic appearance showed no dramatic difference from that of the film with functionalized SWNTs, the nanoscopic structure of the film must be different. The nanotube bundles in the original

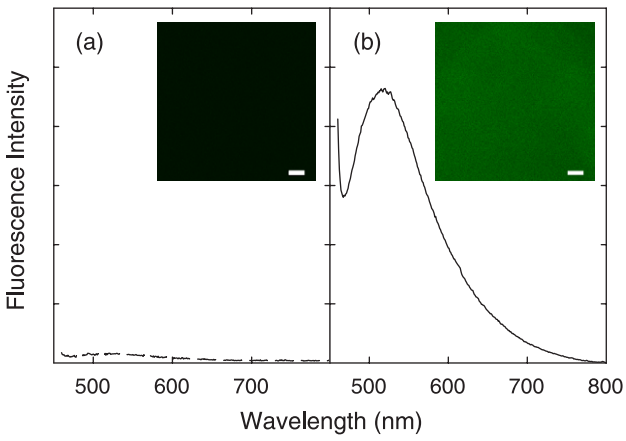

Fig. 3. Luminescence emission spectra (450 nm excitation) of the films from (a) suspended SWNTs and (b) PI-NH_2–SWNT. Shown in the insets are corresponding confocal microscopy images of the films (458 nm excitation, >469 nm detection; scale bars = 5 μm).

suspension were likely carried over into the nanocomposite film, and the bundled SWNTs embedded in the CP-2 polymer matrix were essentially non-luminescent (Fig. 3). Therefore, the measurement of defect-derived luminescence emissions serves as a convenient and non-destructive technique in the evaluation and analysis concerning the degree of nanotube dispersion in polymeric nanocomposites qualitatively or even quantitatively (by comparing different films or the use of standards).

The strong photoluminescence in functionalized nanotube samples is known to interfere with Raman analyses of these samples in an overwhelming fashion [6]. In fact, the better the nanotube functionalization and dispersion, the stronger the interference becomes. The Raman results on the two kinds of polyimide (CP-2)–SWNT nanocomposite films were as expected. For the film with functionalized SWNTs, the nanotube Raman signals could be detected only with the use of lower laser power at the expense of sensitivity, making the characteristic features of SWNTs poorly defined on top of a huge luminescence background in the observed Raman spectrum (Fig. 4). This is consistent with the film being strongly photoluminescent, as discussed above (Fig. 3). The film with suspended SWNTs, on the other hand, was non-luminescent, so that characteristic Raman features of the embedded SWNTs were clearly observed. With a subtraction of the luminescence background, the G-band and D*-band features for functionalized SWNTs in the film can be identified at 1593 and 2642 cm^{-1}, respectively, which are at slightly higher frequencies than those for the suspended SWNTs in film (1587 and 2631 cm^{-1}, respectively). Therefore, it might be argued that there is the commonly acknowledged enhancement in polymer–nanotube interactions [13–15] in the film with functionalized SWNTs. With probably similar effect, the radial breathing mode (RBM) feature at 179 cm^{-1} for the film with functionalized nanotubes is also at a slightly higher frequency than that of the film with suspended nanotubes (170 cm^{-1}).

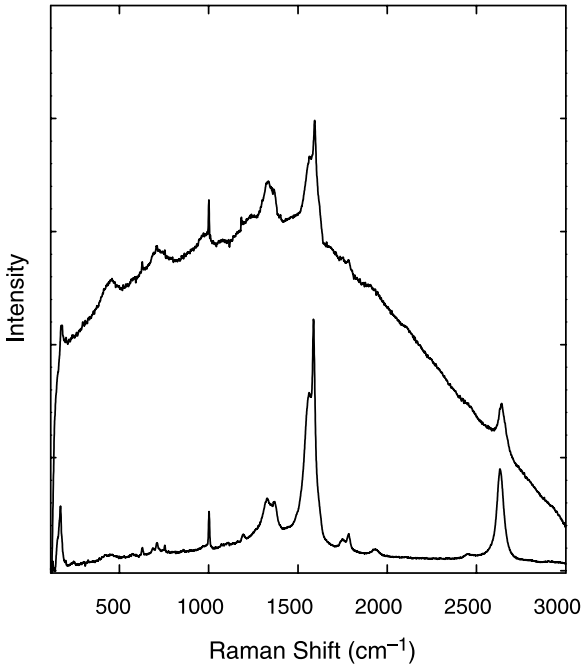

Fig. 4. Raman spectra (633 nm excitation) of the films with PI-NH_2–SWNT (top) and suspended SWNTs (bottom). Some small peaks in the spectra are due to imperfect correction for the polyimide signals.

In order to allow a more direct evaluation on the nanotube dispersion in the films, microtome technique was employed to obtain ultra-thin (about 100 nm) slices. An SEM image for a slice from the film with functionalized SWNTs is shown in Fig. 5, which seems consistent with a well-dispersion of the nanotubes in the film. The slice was also evaluated by using high-resolution TEM. The specimen was highly sensitive to the electron beam, which instantly created nanoscopic gaps in the film slice. There were mostly individual SWNTs bridging the gaps, as shown in Fig. 5. However, for the film with suspended SWNTs, the slices from microtome were of poor quality, inadequate for any conclusive SEM and TEM analyses.

Alternatively, the polyimide nanocomposite films with the functionalized and suspended SWNTs were both stretched to failure, and the fracture edges were examined by using SEM for the morphological characteristics (generally reflecting the

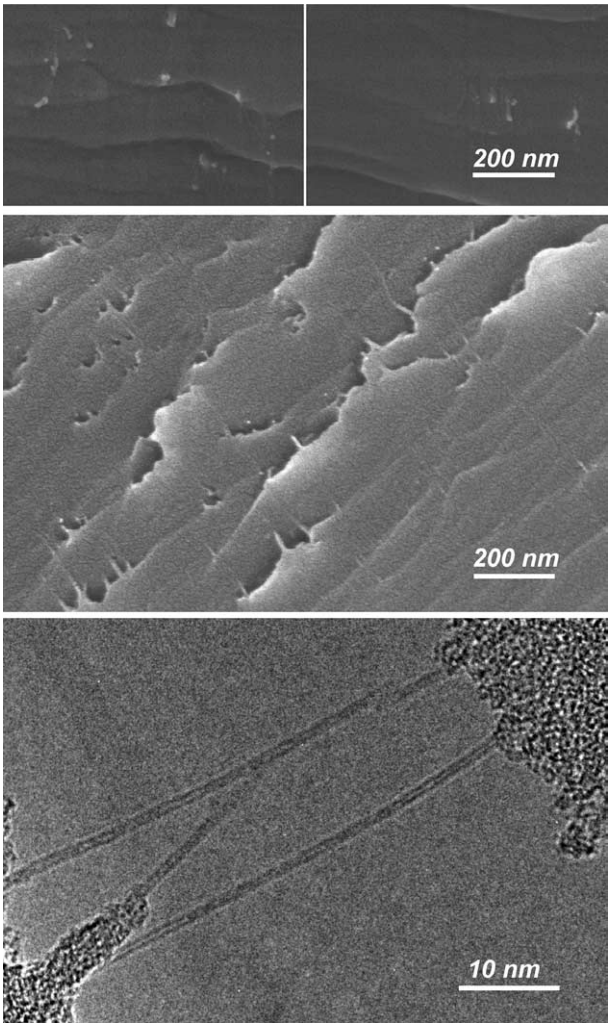

Fig. 5. Results from electron microscopy analyses of the films with suspended SWNTs (top: SEM images of a slice from microtome) and with PI-NH_2–SWNT (middle: SEM image of a slice from microtome; and bottom: TEM image of the specimen with a gap generated by the electron beam).

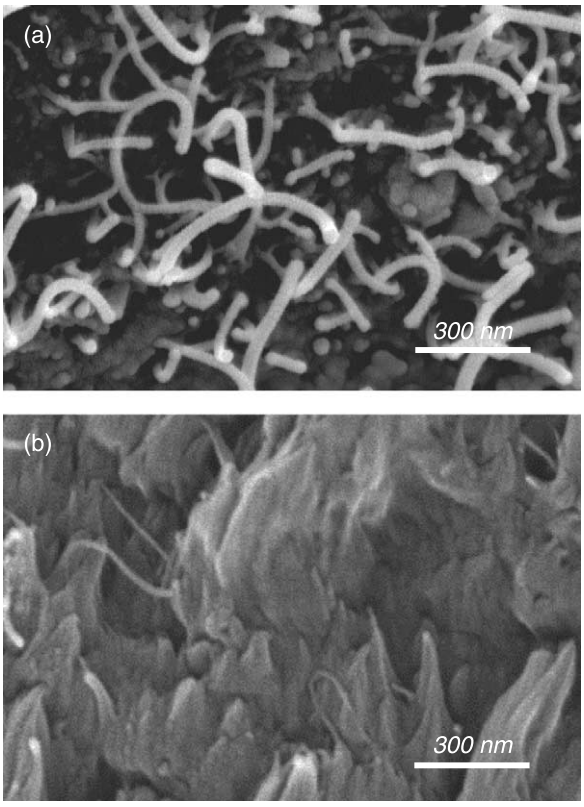

Fig. 6. SEM images on fracture edges of the films (stretched to failure) with (a) suspended SWNTs and (b) PI-NH_2–SWNT.

nanotube dispersion and load transfer efficiency in the films) [28,29]. As shown in Fig. 6, the fracture surface morphology is different between the two films. For the film from suspended SWNTs, there are plenty of exposed nanotube thick bundles on the fracture surface (the appearance of more nanotubes than what might be expected from the film composition probably due primarily to the nanotube bundles being pulled out of the polymer matrix in the stretching and also to inhomogeneous distributions of nanotubes in the film). This is obviously not the case at the fracture edge of the film from functionalized SWNTs. Despite the same overall nanotube loading, the homogeneous dispersion and better polymer wetting of functionalized SWNTs in the film are likely responsible for the apparently different fracture surface morphology (Fig. 6).

In summary, the polyimide–SWNT nanocomposite thin film prepared from polyimide-functionalized SWNTs was compared to that from purified SWNTs in polyimide-assisted suspension. At the same nanotube contents and film thicknesses, the visual appearance was hardly different between the two kinds of films. However, the nanotube dispersion must be significantly better in the film with functionalized SWNTs, as reflected by the strong photoluminescence in the luminescence emission spectroscopy and confocal microscopy results of the film. The results from other characterization techniques including optical absorption, Raman, and electron microscopy are consistent with the conclusion on the better dispersion of functionalized SWNTs in the film for improved compatibility with the matrix polymer and more efficient load transfer. Further studies to compare the two kinds of films for more specific material properties (such as mechanical [28], thermal, and electrical) and performance should be interesting.

Acknowledgements

We thank Dr Yang Liu, Dr. Haifang Wang, and Jennifer Roberts for experimental assistance. Financial support from NASA (through a cross-enterprise NRA), NSF, Center for Advanced Engineering Fibers and Films (NSF-ERC at Clemson University), and Office of Naval Research is gratefully acknowledged. D.E.H. was an awardee of the NASA Graduate Student Researcher Program (GSRP). J.D. was a participant of the Research Experience for Undergraduates (REU) program sponsored jointly by NSF and Clemson University. Research at Oak Ridge National Laboratory was sponsored by the Assistant Secretary for Energy Efficiency and Renewable Energy, Office of FreedomCAR and Vehicle Technologies, as part of the HTML User Program, managed by UT-Battelle LLC for DOE.

References

[1] Ajayan PM. Chem Rev 1999;99(7):1787–99.
[2] Baughman RH, Zakhidov AA, de Heer WA. Science 2002;297(5582):787–92.
[3] Tasis D, Tagmatarchis N, Bianco A, Prato M. Chem Rev 2006;106(3):1105–36.
[4] Mitchell CA, Bahr JL, Arepalli S, Tour JM, Krishnamoorti R. Macromolecules 2002;35(23):8825–30.
[5] Hill DE, Lin Y, Rao AM, Allard LF, Sun YP. Macromolecules 2002;35(25):9466–71.
[6] Sun YP, Fu K, Lin Y, Huang W. Acc Chem Res 2002;35(12):1096–104.
[7] Lin Y, Zhou B, Fernando KAS, Liu P, Allard LF, Sun YP. Macromolecules 2003;36(19):7199–204.
[8] O'Connell MJ, Boul P, Ericson LM, Huffman C, Wang YH, Haroz E, et al. Chem Phys Lett 2001;342(3-4):265–71.
[9] Moore VC, Strano MS, Haroz EH, Hauge RH, Smalley RE. Nano Lett 2003;3(10):1379–82.
[10] Lin Y, Taylor S, Li H, Fernando KAS, Qu L, Wang W, et al. J Mater Chem 2004;14(4):527–41.
[11] Delozier DM, Watson KA, Smith JG, Clancy TC, Connell JW. Macromolecules 2006;39(5):1731–9.
[12] Ajayan PM, Stephan O, Colliex C, Trauth D. Science 1994;265(5176):1212–4.
[13] Lourie O, Wagner HD. J Mater Res 1998;13(9):2418–22.
[14] Hadjiev VG, Iliev MN, Arepalli S, Nikolaev P, Files BS. Appl Phys Lett 2001;78(21):3193–5.
[15] Liu J, Liu T, Kumar S. Polymer 2005;46(10):3419–24.
[16] Lin Y, Zhou B, Martin RB, Henbest KB, Harruff BA, Riggs JE, et al. J Phys Chem B 2005;109(31):14779–82.
[17] Hill DE, Lin Y, Qu L, Kitaygorodskiy A, Connell JW, Allard LF, et al. Macromolecules 2005;38(18):7670–5.
[18] Qu L, Lin Y, Hill DE, Zhou B, Wang W, Sun X, et al. Macromolecules 2004;37(16):6055–60.
[19] Sen R, Rickard SM, Itkis ME, Haddon RC. Chem Mater 2003;15(22):4273–9.
[20] Haddon RC, Sippel J, Rinzler AG, Papadimitrakopoulos F. MRS Bull 2004;29(4):252–9.
[21] Niyogi S, Hamon MA, Hu H, Zhao B, Bhowmik P, Sen R, et al. Acc Chem Res 2002;35(12):1105–13.
[22] (a) Curran SA, Ajayan PM, Blau WJ, Carroll DL, Coleman JN, Dalton AB, et al. Adv Mater 1998;10(14):1091–3.

(b) Star A, Stoddart JF, Steuerman D, Diehl M, Boukai A, Wong EW, et al. Angew Chem Int Ed 2001;40(9):1721–5.
[23] Riggs JE, Guo Z, Caroll DL, Sun YP. J Am Chem Soc 2000;122(24): 5879–80.
[24] Sun YP, Zhou B, Henbest K, Fu K, Huang W, Lin Y, et al. Chem Phys Lett 2002;351(5-6):349–53.
[25] Zhou B, Lin Y, Veca LM, Ferando KAS, Harruff BA, Sun YP. J Phys Chem B 2006;110(7):2001–6.
[26] O'Connell MJ, Bachilo SM, Huffman CB, Moore VC, Strano MS, Haroz EH, et al. Science 2002;297(5581):593–6.
[27] Graff RA, Swanson JP, Barone PW, Baik S, Heller DA, Strano MS. Adv Mater 2005;17(8):980–4.
[28] Ajayan PM, Schadler LS, Giannaris C, Rubio A. Adv Mater 2000;12(10): 750–3.
[29] Paiva MC, Zhou B, Fernando KAS, Lin Y, Kennedy JM, Sun YP. Carbon 2004;42(14):2849–54.

J|A|C|S
COMMUNICATIONS

Published on Web 08/28/2007

Carbon Dots for Multiphoton Bioimaging

Li Cao, Xin Wang, Mohammed J. Meziani, Fushen Lu, Haifang Wang, Pengju G. Luo, Yi Lin, Barbara A. Harruff, L. Monica Veca, Davoy Murray, Su-Yuan Xie, and Ya-Ping Sun*

Department of Chemistry and Laboratory for Emerging Materials and Technology, Clemson University, Clemson, South Carolina 29634-0973

Received May 17, 2007; E-mail: syaping@clemson.edu

Two-photon fluorescence materials have attracted much recent attention for their many promising applications, especially in the growing field of biomedical imaging.[1−5] Among the best performing two-photon fluorescence materials are semiconductor quantum dots such as CdSe and related core−shell nanoparticles.[6−8] These quantum dots have been demonstrated in various optical imaging experiments in vitro and in vivo.[6,9,10] At the same time, however, heavy metals as the essential elements in available high-performance semiconductor quantum dots have prompted serious health and environmental concerns in the community and beyond. Therefore, the search for benign alternatives has become increasingly important and urgent. Recently, we found and reported[11] that nanosized pure carbon particles may be surface-passivated to exhibit bright photoluminescence in the visible. These photoluminescent carbon dots (C-Dots, Figure 1a) are of two distinctive features: one is that the underlying carbon particles are very small (sub-10 nm); and the other is that the particle surface is passivated by organic or other molecules via either covalent linkages or chemical adsorption.[11] Mechanistically, the carbon-based photoluminescence has been attributed to passivated defects on the carbon particle surface acting as excitation energy traps.[11,12] Here we report that the C-Dots also exhibit strong luminescence with two-photon excitation in the near-infrared. The estimated two-photon absorption cross-sections of the C-Dots are comparable to those of available high-performance semiconductor quantum dots. In addition, the two-photon luminescence microscopy imaging of the C-Dots internalized in human cancer cells is demonstrated.

The C-Dots were prepared as previously reported.[11] Poly(propionylethylenimine-*co*-ethylenimine) (PPEI-EI, with EI fraction ∼20%) was used as the surface passivation agent. The C-Dots thus prepared were readily soluble in water to yield a colored aqueous solution. Shown in Figure 1b is a representative AFM image of the C-Dots on mica surface, from which feature sizes of generally less than 5 nm are identified.

The specimen for optical microscopy was prepared by first dropping a small aliquot of the aqueous solution on cover glass and then evaporating the water. A Leica confocal fluorescence microscope equipped with an argon ion laser and a femtosecond pulsed Ti:sapphire laser was used. The C-Dots were found to be strongly emissive in the visible with either the argon ion laser excitation (458 nm) or the femtosecond pulsed laser for two-photon excitation in the near-infrared (800 nm). As compared in Figure 2, the one- and two-photon luminescence images for the same scanning area match well. The C-Dots were photostable under the two-photon imaging conditions (upon repeated 800 nm excitations equivalent to generating the image in Figure 2b for at least 3000 times, no meaningful changes in emission intensities).

The same microscope setup was used to measure the two-photon spectra. For the same specimen (C-Dots deposited on cover glass), the observed spectra vary slightly from spot to spot, reflecting the inhomogeneous nature of the sample. A representative two-photon luminescence spectrum of average C-Dots is shown in Figure 3

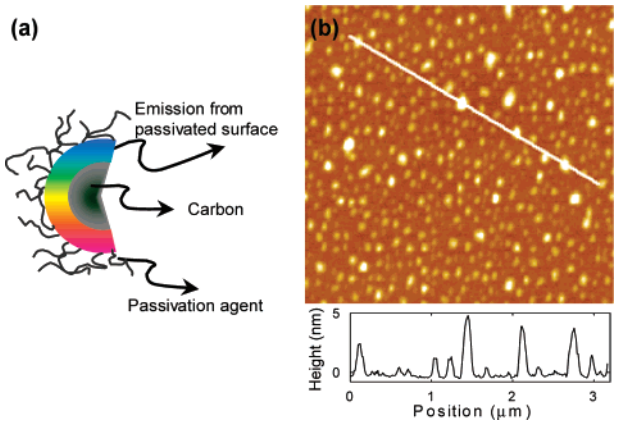

Figure 1. (a) The C-Dot structure; (b) AFM topography image of C-Dots on mica substrate, with the height profile along the line in the image.

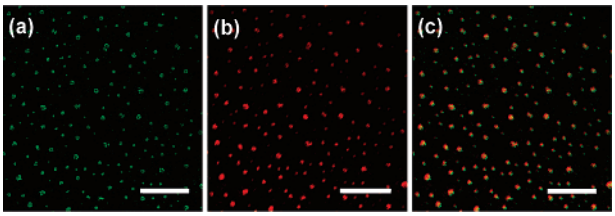

Figure 2. Luminescence images (all scale bars 20 μm) of the C-Dots with (a) argon ion laser excitation at 458 nm and (b) femtosecond pulsed laser excitation at 800 nm; (c) is an overlay of (a) and (b).

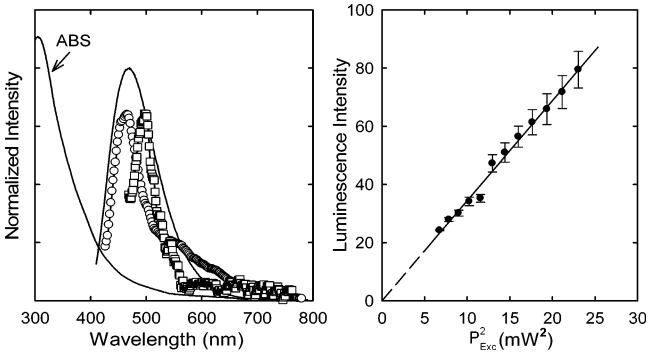

Figure 3. (Left) The one-photon (□, 458 nm excitation) and two-photon (○, 800 nm excitation) luminescence spectra of the C-Dots on glass substrate (prepared with infinite dilution, and optical spot diameter ∼500 nm, covering multiple dots immobilized on the substrate) are compared with solution-phase absorption (ABS) and luminescence (solid line, 400 nm excitation) spectra. (Right) The quadratic relationship of the observed two-photon luminescent intensity of the C-Dots on glass substrate with the excitation laser power at 800 nm (P_{Exc}, as measured at the focal plane).

(left). Its bandwidth is comparable with that in the one-photon spectrum of the C-Dots on surface (458 nm excitation), but significantly narrower than that of the solution-phase spectrum (400

10.1021/ja073527l CCC: $37.00

nm excitation, Figure 3 (left)). These results again suggest inhomogeneity in the sample. The immobilization of the dots on surface might have allowed the measurement of small fractions in which the emissive species or sites are more homogeneous, with the narrower luminescence bands for both one- and two-photon excitations.

The two-photon in nature for the luminescence with the pulsed infrared laser excitation was confirmed by the dependence of observed luminescence intensities on the excitation laser power. The luminescence signals were collected with an external detector on the confocal microscope, and the laser powers for excitation were determined by using a precision power meter in the focal plane (thus free from effects of reflection and transmission losses associated with all optical components in the system). As also shown in Figure 3 (right), the quadratic relationship between the excitation laser power and the luminescence intensity is obvious, thus confirming that the excitation with two near-infrared photons was indeed responsible for the observed visible luminescence of C-Dots.

The two-photon absorption cross-section $\sigma_2(\lambda)$ of C-Dots was estimated by determining the two-photon luminescence intensities of the specimen and a reference under the same experimental conditions: $\sigma(\lambda) = \sigma_{2,\mathrm{ref}}(\lambda)$ $(\langle F(t)\rangle/\langle F_{\mathrm{ref}}(t)\rangle)/(\Phi/\Phi_{\mathrm{ref}})$, where $\langle F(t)\rangle$'s represent averaged luminescence photon fluxes (or experimentally observed emission intensities), Φ's are luminescence quantum yields, and the subscript ref denotes values for the reference compound. By using rhodamine B as the reference,[13] the two-photon absorption cross-sections of C-Dots at different excitation wavelengths were calculated from the experimental results. At 800 nm, the average σ_2 value for the C-Dots was 39 000 $\pm$ 5000 GM (Goeppert-Mayer unit, with 1 GM $= 10^{-50}$ cm^4 s/photon). It makes the C-Dots comparable in high-performance to other two-photon luminescent nanomaterials.[6,8,14,15] For example, the two-photon absorption cross-section for CdSe quantum dots at 800 nm varies in the range of 780−10 300 GM, depending on the particle sizes.[8] For CdSe/ZnS core−shell quantum dots (fluorescence at 605 nm), the two-photon absorption cross-section was estimated to be on the order of 50 000 GM.[6]

In an exploratory experiment to demonstrate the potential of C-Dots for cell imaging with two-photon luminescence microscopy, human breast cancer MCF-7 cells were cultured in terms of the established protocol.[16] Upon incubation with the C-Dots in an aqueous buffer at 37 °C, the MCF-7 cells became brightly illuminated when imaged on the fluorescence microscope with excitation by 800 nm laser pulses. As shown in Figure 4, the C-Dots were able to label both the cell membrane and the cytoplasm of MCF-7 cells without reaching the nucleus in a significant fashion. The translocation of the C-Dots from outside the cell membrane into the cytoplasm is temperature dependent, with no meaningful C-Dots internalization observed at 4 °C. While endocytosis is likely, an understanding of the internalization mechanism still requires more investigations. In addition, a better accumulation of C-Dots in the cell (even in the nucleus) may be achieved by C-Dots coupled with membrane translocation peptides such as TAT (a human immunodeficiency virus-derived protein), which facilitates the translocation of the tissue by overcoming the cellular membrane barrier and enhances the intracellular labeling efficiency.[17,18] This is being pursued along with a comparison between one- and two-photon luminescence imaging of cells labeled with C-Dots.

In summary, C-Dots are strongly two-photon active, with the pulsed laser excitation in the near-infrared to result in bright luminescence in the visible. The estimated two-photon absorption cross-sections of the C-Dots are comparable to those of the best-performing semiconductor quantum dots or core−shell nanoparticles already reported in the literature. Available results from exploratory experiments of luminescence imaging in vitro suggest that the C-Dots are internalized into the human breast cancer cells likely through endocytosis, demonstrating the potential of the C-Dots in cell imaging with two-photon luminescence microscopy.

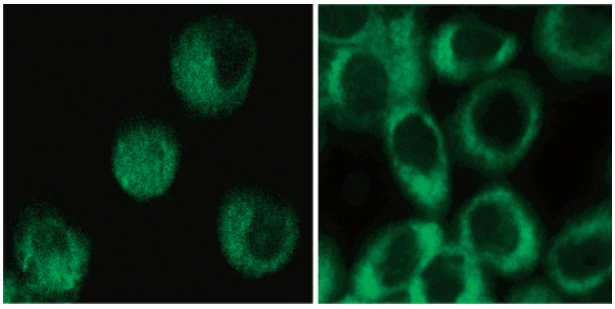

Figure 4. Representative two-photon luminescence image (800 nm excitation) of human breast cancer MCF-7 cells with internalized C-Dots. More details on the cell experiment: MCF-7 cells (approximately 5×10^5) were seeded in each well of a four-chambered Lab-Tek coverglass system (Nalge Nunc) and cultured at 37 °C. All cells were incubated until approximately 80% confluence was reached. Separately, an aqueous solution of the C-Dots (0.9 mg/mL) was passed through a 0.2 μm sterile filter membrane (Supor Acrodisc, Gelman Science). The filtered solution (20−40 μL) was mixed with the culture medium (300 μL) and then added to three wells of the glass slide chamber (the fourth well used as a control) in which the MCF-7 cells were grown. After incubation for 2 h, the MCF-7 cells were washed three times with PBS (500 μL each time) and kept in PBS for the optical imaging.

Acknowledgment. Financial support from the DoD Breast Cancer Research Program, NIH, and NSF is gratefully acknowledged. D.M. was an undergraduate participant jointly sponsored by NSF (DMR-0243734) and Clemson University.

Supporting Information Available: Complete ref 11 and histograms of luminescence intensities in the images. This material is available free of charge via the Internet at http://pubs.acs.org.

References

(1) Xu, C.; Zipfel, W.; Shear, J. B.; Williams, R. M.; Webb, W. W. *Proc. Natl. Acad. Sci. U.S.A.* **1996**, *93*, 10763−10768.
(2) Cahalan, M. D.; Parker, I.; Wei, S. H.; Miller, M. J. *Nat. Rev. Immun.* **2002**, *2*, 872−880.
(3) Zipfel, W. R.; Williams, R. M.; Webb, W. W. *Nat. Biotechnol.* **2003**, *21*, 1369−1377.
(4) Helmchen, F.; Denk, W. *Nat. Methods* **2005**, *2*, 932−940.
(5) Wang, B.; Halbhuber, G. K. J. *Ann. Anat.* **2006**, *188*, 395−409.
(6) Larson, D. R.; Zipfel, W. R.; Williams, R. M.; Clark, S. W.; Bruchez, M. P.; Wise, F. W.; Webb, W. W. *Science* **2003**, *300*, 1434−1436.
(7) Chen, W.; Joly, A. G.; McCready, D. E. *J. Chem. Phys.* **2005**, *122*, 224708 (1−7).
(8) Pu, S. C.; Yang, M. J.; Hsu, C. C.; Lai, C. W.; Hsieh, C. C.; Lin, S. H.; Cheng, Y. M.; Chou, P. T. *Small* **2006**, *2*, 1308−1313.
(9) Gao, X.; Cui, Y.; Levenson, R. M.; Chung, L. W. K.; Nie, S. *Nat. Biotechnol.* **2004**, *22*, 969−976.
(10) Grecco, H. E.; Lidke, K. A.; Heintzmann, R.; Lidke, D. S.; Spagnuolo, C.; Martinez, O. E.; Jares-Erijman, E. A.; Jovin, T. M. *Micro. Res. Technol.* **2004**, *65*, 169−179.
(11) Sun, Y.-P.; et al. *J. Am. Chem. Soc.* **2006**, *128*, 7756−7757.
(12) Zhou, J.; Booker, C.; Li, R.; Zhou, X.; Sham, T. K.; Sun, X.; Ding, Z. *J. Am. Chem. Soc.* **2007**, *129*, 744−745.
(13) Xu, C.; Webb, W. W. *J. Opt. Soc. Am. B* **1996**, *13*, 481−491.
(14) Wang, H.; Huff, T. B.; Zweifel, D. A.; He, W.; Low, P. S.; Wei, A.; Cheng, J.-X. *Proc. Natl. Acad. Sci. U.S.A.* **2005**, *102*, 15752−15756.
(15) Padilha, L. A.; Fu, J.; Hagan, D. J.; Van Stryland, E. W.; Cesar, C. L.; Barbosa, L. C.; Cruz, C. H. B.; Buso, D.; Martucci, A. *Phys. Rev. B* **2007**, *75*, 075325 (1−8).
(16) Lu, Q.; Moore, J. M.; Huang, G.; Mount, A. S.; Larcom, L.; Ke, P. C. *Nano Lett.* **2004**, *4*, 2473−2477.
(17) Santra, S.; Yang, H.; Stanley, J. T.; Holloway, P. H.; Moudgil, B. M.; Walter, G.; Mericle, R. A. *Chem. Common*. **2005**, *25*, 3144−3146.
(18) Stroh, M.; Zimmer, J. P.; Duda, D. G.; Levchenko, T. S.; Cohen, K. S.; Brown, E. B.; Scadden, D. T.; Torchilin, V. P.; Bawendi, M. G.; Fukumura, D.; Jain, R. K. *Nat. Med.* **2005**, *11*, 678−682.

JA073527L

Diameter-Selective Fractionation of HiPco Single-Walled Carbon Nanotubes in Repeated Functionalization Reactions

K. A. Shiral Fernando,[†] Yi Lin,[†] Wei Wang,[†] Li Cao,[†] Mohammed J. Meziani,[†] Xin Wang,[†] Monica L. Veca,[†] Puyu Zhang,[†] Robert A. Quinn,[†] Lawrence F. Allard,[‡] and Ya-Ping Sun*[,†]

Department of Chemistry and Laboratory for Emerging Materials and Technology, Clemson University, Clemson, South Carolina 29634-0973, and High Temperature Materials Laboratory, Oak Ridge National Laboratory, Oak Ridge, Tennessee, 37831-6062

Received: March 24, 2007; In Final Form: May 13, 2007

The functionalization reaction of the diamine-terminated oligomeric poly(ethylene glycol) with a purified HiPco single-walled carbon nanotube sample was repeated multiple times to yield the corresponding number of soluble fractions and the final insoluble residue. According to results from the characterization with various instrumental techniques, these soluble fractions and the final residue all have different nanotube diameter distributions from that found in the starting sample. A general conclusion is that the functionalization and solubilization are selective toward smaller diameter nanotubes, regardless of their being semiconducting or metallic. Mechanistic implications, especially with respect to the post-production separation in terms of the nanotube metallicity, are discussed.

Introduction

A single-walled carbon nanotube (SWNT) is characterized by a pair of chiral indices (n, m), which determine the tube diameter d in terms of the relationship as follows.[1]

$$d = [3(n^2 + nm + m^2)]^{1/2} a_{C-C}/\pi \quad (1)$$

where a_{C-C} is the nearest neighbor carbon−carbon distance. The indices also define the metallicity of the nanotube: a semiconducting SWNT with mod [(n-m), 3] ≠ 0 and a metallic SWNT with mod [(n-m), 3] = 0.[1] Various production methods for SWNTs generally yield mixtures of different chiralities. In fact, it is well known that the SWNTs from the high-pressure CO disproportionation (HiPco) process are of a particularly broad distribution in tube diameters (∼0.7−1.3 nm).[2,3]

There have been significant efforts on post-production separation of SWNTs aimed toward their ultimate "purification" in terms of chiralities, with especially heavy emphasis on harvesting semiconducting- or metallic-enriched SWNTs.[4−6] Interestingly, with only a few exceptions,[7−9] the reported post-production separation experiments have been centered on HiPco-SWNTs.[10−16] The separation effort exploits potentially selective interactions of functional molecules with semiconducting or metallic SWNTs. For example, Tour, Smalley, and co-workers reported that some highly reactive species such as diazonium salts were preferentially added to the sidewalls of metallic HiPco-SWNTs.[10] Similar preferential additions of nitronium ions and fluorine gas were reported recently by others.[13,15] Papadimitrakopoulos and co-workers initiated the approach of using long-chain molecules bearing amino moieties to remove some semiconducting HiPco-SWNTs from the purified mixture,[7,16] where the basis of separation was apparently the selectivity of the functionalization agent octadecylamine (ODA) toward semiconducting nanotubes for their solubilization. Maeda et al.[14] reported recently that an opposite selectivity could be achieved with the use of smaller amine molecules such as octylamine and propylamine, namely that metallic instead of semiconducting nanotubes were enriched in the supernatant. On the other hand, the reactivity and interactions of a nanotube with other species are known to be dependent on the tube diameter (or the graphene curvature corresponding to pyramidalization and π-orbital misalignment).[17,18] In fact, there is an inverse relationship between the nanotube reactivity and diameter, with the smaller SWNTs being more reactive. Therefore, a significant issue in the post-production separation of SWNTs is the likely interplay between the selectivity toward the tube diameter and the selectivity toward the semiconducting or metallic characteristics. According to reports on the reactivity-based post-production separation, the nitronium ion attack prefers smaller diameter metallic SWNTs,[13] while the ozonation reaction is selective toward smaller diameter SWNTs regardless of metallicity.[19] Also, the selective interactions of ODA molecules with semiconducting SWNTs were found to be more pronounced with the nanotubes of smaller diameters.[16]

We reported previously an investigation on repeated functionalization reactions to sequentially extract soluble fractions from arc-discharge-produced SWNTs.[20] Despite the intrinsically narrow diameter distribution in the starting nanotube sample, the fractionation results with the use of diamine-terminated oligomeric poly(ethylene glycol) (PEG_{1500N}) as functionalization agent suggest a clear preference of the functionalization reaction toward smaller diameter SWNTs. In the work presented here, the same approach and similar experimental conditions were applied to the repeated functionalization reactions with HiPco-SWNTs, in which the diameter-selective fractionation in the solubilization became more evident. The results from the characterization of the fractionated samples are described, and their implication to the effort on using similar functionalization reactions for post-production separation of semiconducting and metallic SWNTs is discussed.

[†] Clemson University.
[‡] Oak Ridge National Laboratory.

10.1021/jp0723463 CCC: $37.00
Published on Web 06/22/2007

Experimental Section

Materials. Diamine-terminated oligomeric poly(ethylene glycol) ($H_2NCH_2CH_2CH_2(OCH_2CH_2)_nCH_2NH_2$ with $n \sim 35$, or PEG_{1500N}) and sodium dodecyl sulfate (SDS) were purchased from Aldrich, and deuterated chloroform and D_2O were purchased from Cambridge Isotope Laboratories. Dialysis tubing (cellulose membrane) with a molecular weight cutoff of ~12,000 was obtained from Sigma-Aldrich.

The HiPco-SWNT sample was supplied by Carbon Nanotechnologies, Inc. and was purified by using a procedure adapted from what is available in the literature.[21] In the purification, the as-supplied nanotube sample (500 mg) was treated with intermittent microwave (800 W) for 20 cycles of 60 s on and 300 s off, followed by refluxing in diluted nitric acid solution (2.6 M, 250 mL) for 12 h. Upon centrifugation (1380*g*) to discard the supernatant, the solid was repeatedly washed with deionized water until neutral pH was obtained, and then the sample was dried under vacuum to yield the purified HiPco-SWNT sample (~250 mg).

Measurements. Several centrifuge machines were used for low- (Fisher Scientific, Centrific Model 228) and high-speed centrifugation (Beckman-Coulter Optima L90K ultracentrifuge with a type 90 Ti fixed-angle rotor). UV/vis/near-IR absorption spectra were recorded on a Shimadzu UV3600 spectrophotometer. Raman spectra were obtained on a Renishaw Raman spectrometer equipped with a 50 mW diode laser source for 785 nm excitation, and a Jobin-Yvon T64000 spectrometer equipped with a triple monochromator, a research-grade Olympus BX-41 microscope, a liquid-nitrogen-cooled symphony detector, and two excitation sources (Melles-Griot 35 mW He:Ne laser for 632 nm and Spectra-Physics 40 mW argon-ion laser for 514 nm excitations). Thermogravimetric analysis (TGA) experiments were performed on a Mettler-Toledo TGA/SDTA851e system. Transmission electron microscopy (TEM) digital images were obtained on Hitachi HF-2000 TEM and Hitachi HD-2000 STEM/TEM systems.

Functionalization Reactions.[20,22] In a typical experiment, a mixture of purified HiPco-SWNTs (225 mg) and PEG_{1500N} (3.8 g) was heated to 120 °C and stirred under nitrogen protection for 4 days. After the reaction, the mixture was cooled to room temperature and then extracted repeatedly with water for the soluble fraction. Each extraction involved the addition of deionized water (15 mL) and then centrifuging at 1380*g* to collect the colored supernatant. Typically five repeats were necessary until the supernatant became colorless. The combined soluble fraction was cleaned via dialysis (membrane molecular weight cutoff of ~12,000) against fresh deionized water for 3 days, and then evaporated to remove water. The insoluble residue after the repeated extractions was dried under vacuum for the next round of functionalization reaction.

In each subsequent functionalization reaction, the same PEG_{1500N}/nanotube weight ratio of 17/1 was used, and so were the reaction conditions. The reaction mixture was extracted in the same procedure to separate the soluble fraction from the insoluble residue.

All soluble fractions from the repeated functionalization reactions and the final insoluble residue were dried for their various characterization experiments.

Results and Discussion

The functionalization of HiPco-SWNTs with PEG_{1500N} was under thermal reaction conditions.[20,22,23] Mechanistically, there is presumably the formation of a zwitterionic bond between the amino group in PEG_{1500N} and the nanotube-bound carboxylic acid (due to the oxidation of carbon nanotube defect),[22,23] though noncovalent direct adsorption of PEG_{1500N} species on the nanotube graphitic surface may also play a significant role in the solubilization of the nanotube.[7] Nevertheless, the functionalization of HiPco-SWNTs with PEG_{1500N} for the nanotube solubilization was relatively robust. The solid-state samples for the soluble fractions from the repeated functionalization reactions could readily be dissolved in water or various polar organic solvents. These aqueous or organic solutions were stable over an extended period of time (at least several months), again demonstrating the robustness of the functionalization and solubilization.

TABLE 1: Nanotube Contents in the Soluble Fractions and the Final Residue

fraction	nanotube content[a] (mg)
1	71 (30%)[b]
2	65 (28%)
3	17 (7.2%)
4	11 (4.7%)
5	5 (2.1%)
final residue	66 (28%)

[a] Determined by TGA in inert (nitrogen) atmosphere. [b] Shown in parentheses are weight percents against the total amount including all fractions and the final residue.

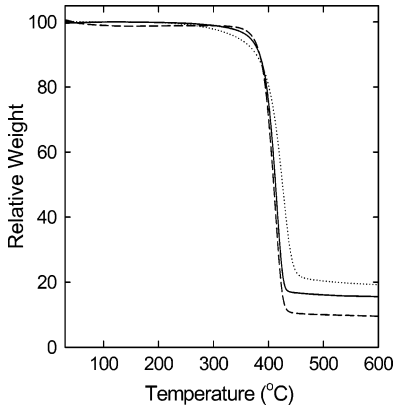

Figure 1. TGA traces (N_2, 10 °C/min) of the first (—) and second (- - -) soluble fractions and the final residue (...).

Fractionation. A total of five soluble fractions were collected from the five repeats of functionalization reactions. The amount of nanotubes solubilized in each functionalization reaction varied, with the first and second reactions solubilizing 32% and 28% of the starting HiPco-SWNTs, respectively (Table 1). By the fifth reaction, the amount of nanotubes solubilized decreased to 2% of the starting HiPco-SWNTs (Table 1), suggesting no need for further repeats.

The nanotube contents in the soluble fractions and the final residue (listed in Table 1) were determined by using TGA. Shown in Figure 1 are typical TGA traces for the samples. At a heating rate of 10 °C/min in nitrogen atmosphere, the PEG_{1500N} functional groups could be removed completely at about 450 °C,[20,22] while the defunctionalized HiPco-SWNTs remained stable. Quantitatively, the amount of recovered nanotubes from the five soluble fractions and the final residue totaled 235 mg (about 71% in the soluble fractions and 29% in the final residue), in reasonable agreement with the amount of starting HiPco-SWNTs (225 mg). As detailed in Table 1, the nanotube contents in the soluble fractions decreased significantly in subsequent functionalization reactions after the first two repeats, indicating the inhomogeneous nature of the starting purified HiPco-SWNT sample with respect to functionalization and solubilization.

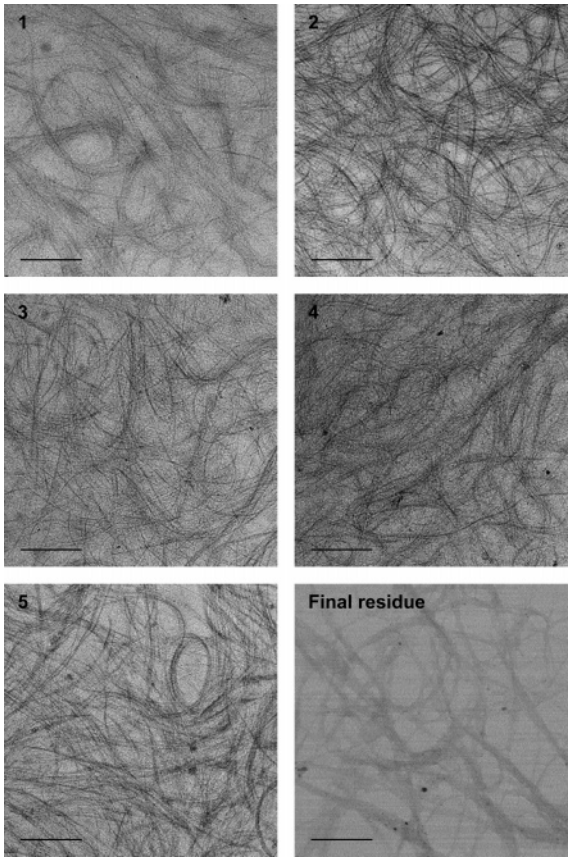

Figure 2. TEM images of the five soluble fractions and the final residue (all scale bars are 200 nm).

The different fractions share some similar material properties. For example, TEM techniques were used to characterize the soluble fractions and the final residue. In the specimen preparation, a drop of diluted aqueous solution of the soluble fraction (or aqueous suspension for the final residue) was placed onto a carbon or holey carbon-coated copper grid, followed by solvent evaporation. The TEM images of the soluble fractions show no meaningful differences, as compared in Figure 2. For the final residue, the TEM image suggests that the nanotubes are in larger bundles than those in the soluble fractions, as one might expect.

The soluble fractions were also evaluated by using ^{1}H NMR. At a relatively dilute concentration of 10 mg/mL in $CDCl_3$, the observed spectra of the fractions appear similar, each with a broad signal centered at ~3.6 ppm (Supporting Information). This is readily assigned to the ethylene protons in the PEG_{1500N} functional groups. The broadness of the peak is consistent with the functional groups being attached to SWNTs, which are species with large molecular weights and low mobilities.[24]

Diameter Selectivity. The optical spectroscopy results of the soluble fractions and the final residue suggest significant diameter preference in the repeated functionalization reactions, resulting in different diameter distributions of HiPco-SWNTs in the various fractions.

The solution-phase optical absorption spectra of the soluble fractions (except for the fifth fraction due to limited sample quantity) were measured in D_2O to avoid spectral interference in the near-IR region. The solutions were prepared by directly dissolving the solid samples into D_2O. Similarly, the starting purified HiPco-SWNT sample and the final residue were suspended in D_2O with the assistance of SDS (0.5 mg/mL), which is a surfactant widely used in the literature for optical

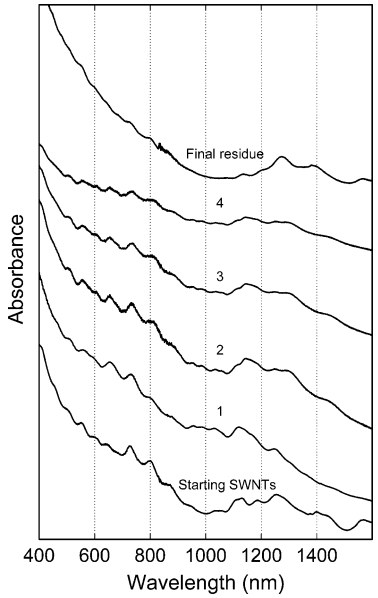

Figure 3. UV/vis/near-IR absorption spectra of the starting purified HiPco-SWNT sample and the final residue suspended in water (both with the assistance of SDS), and the soluble factions in D_2O solutions.

spectroscopy of SWNTs.[25] These solutions and suspensions in D_2O (all with 2 mg/mL nanotube-equivalent concentrations) were centrifuged at 137 000*g* for 2 h before the optical spectral measurements. As shown in Figure 3, the spectrum of the starting purified sample is resolved with spectral features typical of HiPco-SWNTs after similar purification treatment.[26] The peak features at 900−1600 nm and 550−900 nm are commonly assigned to groups of electronic transitions corresponding to the first and second pairs of van Hove singularities in the density of states (DOS) for various semiconducting SWNTs (denoted as S_{11} and S_{22}), respectively, and those at 400−650 nm corresponding to first transitions of various metallic SWNTs (denoted as M_{11}).[3,10,12,27] The absorption spectra of the solubilized samples remain similarly resolved with S_{11}, S_{22}, and M_{11} peak features in their respective spectral ranges (Figure 3), suggesting that the nanotube electronic structures are retained in the functionalization with PEG_{1500N}. This is consistent with previously reported results on the PEG_{1500N} functionalization of SWNTs from other production methods.[20,22]

A closer examination of the absorption spectra reveals significant and systematic changes in the detailed spectral peak features from fraction to fraction, reflecting the underlying variations in diameter distributions of the HiPco-SWNTs. For the S_{11} bands, more features of the first soluble fraction are at shorter wavelengths (roughly below 1200 nm) in comparison with those of the starting purified sample. In the later soluble fractions, however, more significant spectral features are in the longer wavelength region (especially above 1200 nm). The changes in S_{22} bands are in a similar trend, with those of the first soluble fraction featured more in the 650−750 nm region, while those of later fractions are more in the 750−900 nm region (Figure 3). It is known that electronic transition energies of SWNTs are inversely related to the nanotube diameters. Thus, the absorption results suggest that the smaller diameter semiconducting SWNTs were preferentially solubilized in the earlier fractions.

The diameter-selective fractionation in the repeated functionalization reactions is more evident in the results of resonance Raman spectroscopy. The Raman measurements were performed at multiple excitation wavelengths of 785 nm (1.58 eV), 632 nm (1.96 eV), and 514 nm (2.41 eV). In order to avoid the

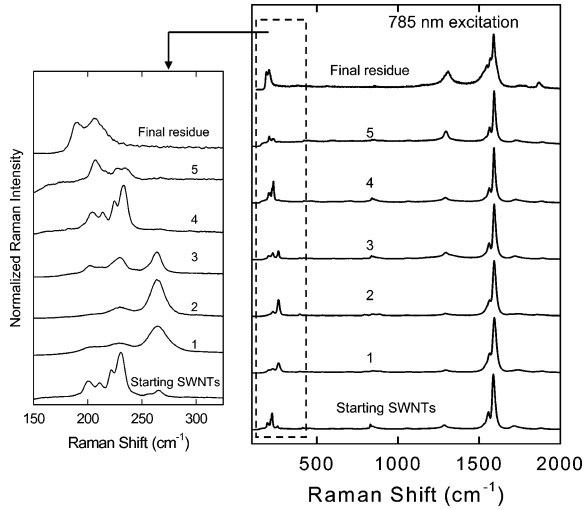

Figure 4. Raman spectra (with the enlarged RBM region at left, 785 nm excitation) of the starting purified HiPco-SWNT sample, the soluble fractions after thermal defunctionalization, and the final residue.

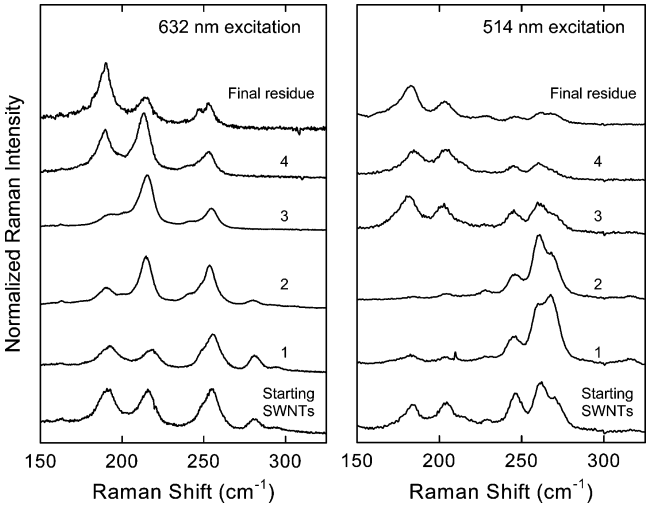

Figure 5. Raman spectra (the RBM region only) with 632 and 514 nm excitations are compared for the starting purified HiPco-SWNT sample, the soluble fractions after thermal defunctionalization, and the final residue.

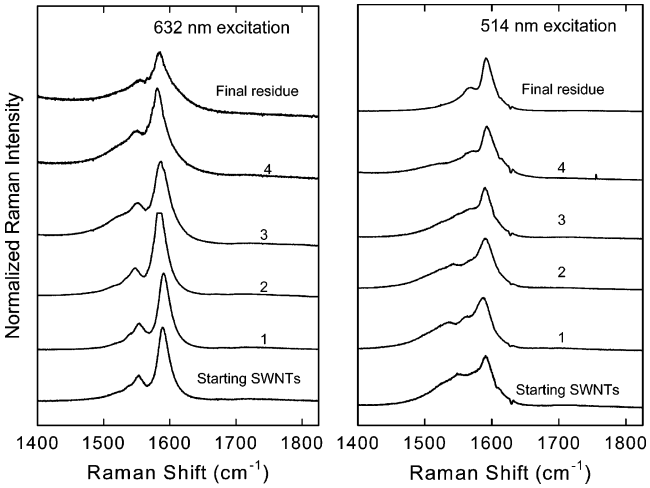

Figure 6. Raman G-bands with 632 and 514 nm excitations are compared for the starting purified HiPco-SWNT sample, the soluble fractions after thermal defunctionalization, and the final residue.

known luminescence interference with functionalized nanotube samples,[24] the soluble fractions and the final residue were thermally defunctionalized (heated to 600 °C and kept for 2 h in inert atmosphere) before the Raman characterization.

For the starting purified sample, the Raman spectrum at 785 nm excitation exhibits typical features of the G-band at 1592 cm^{-1}, D-band at 1330 cm^{-1}, and radial breathing modes (RBMs) in the 100−300 cm^{-1} region (Figure 4), in agreement with those reported previously.[10−16] Here the 785 nm excitation is in resonance with mostly semiconducting HiPco-SWNTs of various diameters but with few of their metallic counterparts.[12] Also shown in Figure 4 are Raman spectra of the soluble fractions and the final residue with the same 785 nm excitation. The G-band features are similar among all these samples, with the bands being relatively narrow and symmetrical. However, there are systematic changes in the RBM region, with the spectra of the earlier fractions enriched with higher frequency features (corresponding to smaller diameter semiconducting SWNTs) and with those of the later fractions and the final residue with lower frequency features (corresponding to larger diameter semiconducting SWNTs). For example, the spectrum of the first soluble fraction shows the 264 cm^{-1} peak higher in intensity than peaks in the 188−216 cm^{-1} and 217−242 cm^{-1} regions, but the spectrum of the fifth soluble fraction exhibits a nearly opposite peak intensity pattern (those of the other fractions are apparently intermediate between the two) (Figure 4). In the spectrum of the final residue, only peaks at 189 and 206 cm^{-1} could be observed. It is known that the RBM peak frequency (ω_{RBM}, cm^{-1}) is inversely related to the corresponding SWNT diameter (d, nm) in terms of the equation $\omega_{RBM} = 223.5/d + 12.5$ (see also Supporting Information).[27] Thus, the initial functionalization reaction in multiple repeats was obviously selective toward the smaller diameter nanotubes among the population of semiconducting HiPco-SWNTs.

The Raman spectra were also measured with 632 and 514 nm excitations (coupled with the use of a triple monochromator) for a closer examination of the low-frequency region, despite the fact that different HiPco-SWNTs (from those with 785 nm excitation) are in resonance with these excitation wavelengths. The RBM features in the spectra exhibit systematic changes in a trend similar to that found with the 785 nm excitation. Generally the earlier fractions are with more intense higher-frequency RBM features, and the later fractions and the final residue are with more intense lower-frequency RBM features (Figure 5). For the 632 nm excitation, smaller diameter semiconducting and larger diameter metallic HiPco-SWNTs are in resonance. The Raman RBMs again suggest that the smaller diameter semiconducting nanotubes are preferentially solubilized in the initial functionalization reactions. The Raman results obtained with 514 nm excitation also suggest similarly preferential solubilization of smaller diameter nanotubes, except that the resonance of 514 nm is with smaller diameter metallic (short M_{11} wavelengths) and larger diameter semiconducting (long S_{33} wavelengths) HiPco-SWNTs (see also Supporting Information).[7,12−16]

For both 632 and 514 nm excitations, the corresponding G-band features in the Raman spectra of the different fractions also exhibit systemic changes in opposite patterns. As compared in Figure 6, the G-bands for 632 nm excitation of subsequent soluble fractions and then the final residue are progressively broader and increasingly unsymmetrical. However, an opposite trend is associated with the 514 nm excitation, where the G-bands of the earlier soluble fractions are unsymmetrical and those of the later soluble fractions and the final residue are narrower and more symmetrical (Figure 6). It is known that the broadened and unsymmetrical appearance of the G-band (or the BWF line-shape)[28] serves as a signature for the significant presence of metallic SWNTs in the sample.[4−16] Thus, the Raman

G-band results with 632 and 514 nm excitations are consistent with the enrichment of larger diameter HiPco-SWNTs (indicating semiconducting and metallic ones, respectively) in the later soluble fractions and the final residue.

Overall the optical absorption spectra and resonance Raman results with three different excitation wavelengths apparently suggest that the functionalization reaction of PEG_{1500N} with the purified HiPco-SWNT sample is selective toward those nanotubes of smaller diameters, regardless of their being semiconducting or metallic. This may have significant implications to the effort on the post-production separation of semiconducting and metallic SWNTs.[4−16]

Mechanistic and Other Implications. A characteristic feature of as-supplied or purified HiPco-SWNTs is the broad distribution of nanotubes of different diameters. Therefore, it is hardly surprising that the diameter selectivity becomes an issue in various functionalization reactions. For the thermal reaction conditions used in this study, the preference of PEG_{1500N} molecules toward smaller diameter HiPco-SWNTs is probably associated with their direct adsorption onto the nanotube surface. The role of such noncovalent but specific interactions in the solubilization of carbon nanotubes has been suggested for other long-chain functionalization agents with primary amine moieties.[7,16] As for the selectivity toward smaller diameter HiPco-SWNTs, the specific interactions responsible for the direct adsorption may be mechanistically similar to those found in the addition of highly reactive species to the nanotube sidewalls.[10,13,15]

The diameter selectivity in functionalization reactions (including the adsorption) could potentially alter the population balance between semiconducting and metallic nanotubes if the two nanotube types were of different diameter distributions, which could thus result in the observation of enrichment in one over the other in various reaction mixtures or fractions. Hypothetically, should the starting sample be populated with more smaller diameter semiconducting nanotubes than their metallic counterparts, the preferential solubilization of the former would obviously leave more metallic nanotubes in the insoluble residue, and vice versa. Therefore, it might be possible, at least in principle, that the interplay between diameter and metallicity fractionations in the functionalization and solubilization of HiPco-SWNTs with long-chain amino compounds like PEG_{1500N} and ODA could be driven primarily by the diameter selectivity. This is an interesting topic that deserves further investigations.

In summary, the repeated functionalization reactions of PEG_{1500N} molecules with purified HiPco-SWNTs resulted in multiple soluble factions and the final insoluble residue. These fractions have different nanotube diameter distributions from that found in the starting purified HiPco-SWNT sample. A general conclusion is that the first nanotubes solubilized are smaller diameter ones, regardless of their being semiconducting or metallic. The results reported here and those already in the literature suggest that because of the intrinsically broad diameter distribution in HiPco-SWNTs, diameter selectivity plays an important role in the reactions or specific interactions designed or exploited for the post-production separation of the nanotubes into semiconducting and metallic enriched fractions. Further experimental investigations on the existing and other amine-bearing functionalization or dispersion agents are required for a better understanding of the various selectivities.

Acknowledgment. Financial support from NSF, NASA, South Carolina Space Grant Consortium, and the Center for Advanced Engineering Fibers and Films (CAEFF, an NSF-ERC at Clemson University) is gratefully acknowledged. R.A.Q. was an undergraduate participant jointly sponsored by CAEFF and NSF-REU (DMR-0243734). Research at Oak Ridge National Laboratory was sponsored by the Assistant Secretary for Energy Efficiency and Renewable Energy, Office of FreedomCAR and Vehicle Technologies, as part of the HTML User Program, managed by UT-Battelle LLC for DOE (DE-AC05-00OR22725).

Supporting Information Available: ^{1}H NMR spectra of the soluble fractions and a table showing calculated nanotube diameters from Raman RBM peaks. This material is available free of charge via the Internet at http://pubs.acs.org.

References and Notes

(1) Dresselhaus, M. S.; Dresselhaus, G.; Eklund, P. C. *Science of Fullerenes and Carbon Nanotubes*; Academic Press: San Diego, 1996.

(2) Bronikowski, M. J.; Willis, P. A.; Colbert, D. T.; Smith, K. A.; Smalley, R. E. *J. Vac. Sci. Technol. A* **2001**, *19*, 1800.

(3) Hamon, M. A.; Itkis, M. E.; Niyogi, S.; Alvaraez, T.; Kuper, C.; Menon, M.; Haddon, R. C. *J. Am. Chem. Soc.* **2001**, *123*, 11292.

(4) Lin, Y; Fernando, K. A. S.; Wang, W.; Sun, Y.-P. In *Carbon Nanotechnology: Recent developments in Chemistry, Physics, Material Science and Device Applications*; Dai, L., Ed.; Elsevier: Netherlands, **2006**; p 255.

(5) Krupke, R.; Hennrich, F. *Adv. Eng. Mater*. **2005**, *7*, 111.

(6) Banerjee, S.; Benny, T. H.; Wong, S. S. *J. Nanosci. Nanotechnol*. **2005**, *5*, 841.

(7) Chattopadhyay, D.; Galeska, I.; Papadimitrakopoulos, F. *J. Am. Chem. Soc*. **2003**, *125*, 3370.

(8) Chen, Z.; Du, X.; Du, M.-H.; Rancken, C. D.; Peng, H.-P.; Rinzler, A. G. *Nano Lett.* **2003**, *3*, 1245.

(9) Li, H.; Zhou, B.; Lin, Y.; Gu, L.; Wang, W.; Fernando, K. A. S.; Kumar, S.; Allard, L. F.; Sun, Y. -P. *J. Am. Chem. Soc*. **2004**, *126*, 1014.

(10) Strano, M. S.; Dyke, C. A.; Usrey, M. L.; Barone, P. W.; Allen, M. J.; Shan, H.; Kittrell, C.; Hauge, R. H.; Tour, J. M.; Smalley, R. E. *Science* **2003**, *301*, 1519.

(11) Krupke, R.; Hennirich, F.; Lohneysen, H. V.; Kappes, M. M. *Science* **2003**, *301*, 144.

(12) (a) Zheng, M.; Jagota, A.; Semke, E. D.; Diner, B. A.; McLean, R. S.; Lustig, S. R.; Richardson, R. E.; Tassi, N. G. *Nat. Mater.* **2003**, *2*, 338. (b) Zheng, M.; Jagota, A.; Strano, M. S.; Santos, A. P.; Barone, P.; Chou, S. G.; Diner, B. A.; Dresselhaus, M. S.; Mclean, R. S.; Onoa, G. B.; Samsonidze, G. G.; Semke, E. D.; Usrey, M.; Walls, D. J. *Science* **2003**, *302*, 1545.

(13) An, K. H.; Park, J. S; Yang, C. M.; Jeong, S. Y.; Lim, S. C.; Kang, S.; Lee, Y. H. *J. Am. Chem. Soc*. **2005**, *127*, 5196.

(14) (a) Maeda, Y.; Kimura, S.-I.; Kanda, M.; Hirashima, Y.; Hasegawa, T.; Wakahara, T.; Lian, Y.; Nakahodo, T.; Tsuchiya, T.; Akasaka, T.; Lu, J.; Zang, X.; Tokumoto, H.; Saito, R. *J. Am. Chem. Soc*. **2005**, *127*, 10287. (b) Maeda, Y.; Kanda, M.; Hashimoto, M.; Tadashi, H.; Kimura, S.-I.; Lian, Y.; Wakahara, T.; Akasaka, T.; Kazaoui, S.; Minami, N.; Okazaki, T.; Hayamizu, Y.; Hata, K.; Lu, J.; Nagase, S. *J. Am. Chem. Soc.* **2006**, *128*, 12239.

(15) Yang, C. M.; An, H. K.; Park, J. S.; Park, Lim, S. C.; Cho, S.−H.; Lee, Y. S.; Park, W.; Lee, Y. H. *Phys. Rev. B*. **2006**, *73*, 75419.

(16) (a) Samsonidze, G. G.; Chou, S. G.; Santos, A. P.; Brar, V. W.; Dresselhaus, G.; Dresselhaus, M. S.; Selbst, A.; Swan, A. K.; Unlu, M. S.; Goldberg, B. B.; Chattopadhyay, D.; Kim, S. N.; Papadimitrakopoulos, F. *Appl. Phys. Lett*. **2004**, *85*, 100. (b) Brar, V. W.; Samsonidze, G. G.; Santos, A. P.; Chou, S. G.; Chattopadhyay, D.; Kim, S. N.; Papadimitrakopoulos, F.; Zheng, M.; Jagota, A.; Onoa, G. B.; Swan, A. K.;Ünlü, M. S.; Goldberg, B. B.; Dresselhaus, G.; Dresselhaus, M. S. *J. Nanosci. Nanotechnol.* **2005**, *5*, 209.

(17) Niyogi, S.; Hamon, M. A.; Hu, H.; Zhao, B.; Bhowmik, P.; Sen, R.; Itkis, M. E.; Haddon, R. C. *Acc. Chem. Res.* **2002**, *35*, 1105.

(18) Hirsch, A.; Vostrowsky, O. *Top. Curr. Chem*. **2005**, *245*, 193.

(19) Banerjee, S.; Wong, S. S. *Nano Lett.* **2004**, *4*, 1445.

(20) Huang, W.; Fernando, S.; Lin, Y.; Zhou, B.; Allard, L. F.; Sun, Y.-P. *Langmuir* **2003**, *19*, 7084.

(21) Martinez, M. T.; Callejas, M. A.; Benito, A. M.; Maser, W. K.; Cochet, M.; Andres, J. M.; Schreiber, J.; Chauvet, O.; Fierro, J. L. G. *Chem. Comm*. **2002**, 1000.

(22) Huang, W.; Fernando, S.; Allard, L. F.; Sun, Y.-P. *Nano. Lett.* **2003**, *3*, 565.

(23) Chen, J.; Rao, A. M.; Lyuksyutov, S.; Itkis, M. E.; Hamon, M. A.; Hu, H.; Cohn, R. W.; Eklund, P. C.; Colbert, D. T.; Smalley, R. E.; Haddon, R. C. *J. Phys. Chem. B* **2001**, *105*, 2525.

(24) Sun, Y.-P.; Fu, K.; Lin, Y.; Huang, W. *Acc. Chem. Res.* **2002**, *35*, 1096.

(25) O'Connell, M. J.; Bachilo, S. M.; Huffman, C. B.; Moore, V. C.; Strano, M. S.; Haroz, E. H.; Rialon, K. L.; Boul, P. J.; Noon, W. H.; Kittrell, C.; Ma, J.; Hauge, R. H.; Weisman, R. B.; Smalley, R. E. *Science* **2002**, *297*, 593.

(26) See, for example: Bahr, J. L.; Yang, J.; Kosynkin, D. V.; Bronikowski, M. J.; Smalley, R. E.; Tour, J. M. *J. Am. Chem. Soc*. **2001**, *123*, 6536.

(27) (a) Bachilo, S. M.; Strano, M. S.; Kittrell, C.; Hauge, R. H.; Smalley, R. E.; Weisman, B. *Science* **2002**, *298*, 2361. (b) Weisman, R. B.; Bachilo, S. M. *Nano Lett.* **2003**, *3*, 1235.

(28) Brown, S. D. M.; Jorio, A.; Corio, P.; Dresselhaus, M. S.; Dresselhaus, G.; Saito, R.; Kneipp, K. *Phys. Rev. B* **2001**, *63*, 155414.

Reversible Accumulation of PEGylated Single-Walled Carbon Nanotubes in the Mammalian Nucleus

Jinping Cheng,[†] K. A. Shiral Fernando,[‡] L. Monica Veca,[‡] Ya-Ping Sun,[‡] Angus I. Lamond,[§] Yun Wah Lam,[†,*] and Shuk Han Cheng[†,*]

[†]Department of Biology and Chemistry, City University of Hong Kong, Hong Kong, [‡]Department of Chemistry and Laboratory for Emerging Materials and Technology, Clemson University, Clemson, South Carolina 29634-0973, and [§]Wellcome Trust Centre for Gene Regulation and Expression, College of Life Sciences, University of Dundee, Dundee DD1 5EH, Scotland, U.K.

ARTICLE

ABSTRACT Carbon nanotubes (CNTs) have been shown to cross cell membranes and can mediate the internalization of macromolecules. These characteristics have constituted CNTs as an exciting new tool for drug delivery and biological sensing. While CNTs exhibit great potential in biomedical and pharmaceutical applications, neither the cell penetration mechanism of CNTs nor the intracellular fate of the internalized CNTs are fully understood. In this study, time-lapse fluorescence microscopy was used to investigate the intracellular distribution of FITC labeled PEGylated single-walled CNTs (FITC-PEG-SWCNTs) in living cells and shown that PEGylated SWCNTs entered the nucleus of several mammalian cell lines in an energy-dependent process. The presence of FITC-PEG-SWCNTs in the cell nucleus did not cause discernible changes in the nuclear organization and had no effect on the growth kinetics and cell cycle distribution for up to 5 days. Remarkably, upon removal of the FITC-PEG-SWCNTs from the culture medium, the internalized FITC-PEG-SWCNTs rapidly moved out of the nucleus and were released from the cells. Thus, the intracellular PEGylated SWCNTs were highly dynamic and the cell penetration of PEGylated SWCNTs appeared as bidirectional. These observations suggest SWCNTs may be used as an ideal nanovector in biomedical and pharmaceutical applications.

KEYWORDS: carbon nanotubes · nucleus · live-cell imaging · fluorescence recovery after photobleaching · cell penetration · cellular efflux

The distinctive optical, magnetic and conducting properties of nanoparticles, made from a variety of materials, have made these nanoscale substances attractive candidates in the development of new tools for molecular imaging, biosensing, and other areas of biomedical research. Carbon nanotubes (CNTs) are among the most promising nanoparticles for such applications because CNTs, unlike other types of nanomaterials, have better biocompatibility[1,2] and do not require the conjugation of antibodies or cell penetrating peptides for cell internalization.[3−5] In addition, CNTs can easily be functionalized and linked to fluorescent beacons, nucleic acids, or other small molecules.[6] These properties make CNTs an ideal candidate for a "smart" nanoparticle-based system for drug delivery and *in vivo* bioimaging. The use of CNTs in the targeted delivery of biomolecules into biological systems carries enormous medical and commercial potentials and a detailed understanding of the cell penetration mechanism and intracellular dynamics of CNTs is paramount for the development of these nanomaterials as drug delivery vehicles.[7]

Although several previous reports have demonstrated that CNTs are able to translocate across cell membrane,[4,8] the cell penetration mechanism and the intracellular dynamic fate of the internalized CNTs are not well understood. There are several possible mechanisms that have been proposed for cell penetration of CNTs. Some studies suggested that CNTs cause localized damage on the cell membrane through which cargos enter the cells.[9] Spearing has been shown to enhance this "hole-punching" process and improve the efficiency of delivery into mammalian cells.[10] On the other hand, Kam *et al.* proposed that cells take up the CNTs through an energy-requiring mechanism, such as endocytosis.[11] There is presently no consensus regarding the mechanism for the entry.

After cell penetration, the intracellular fate of the internalized CNTs appears to vary. Nuclear accumulation was observed although most related studies have reported that water soluble CNTs modified with functional groups resided in the cytoplasm upon incubation.[4,8,12,13] One study has reported that intense G-band signal was observed in the nuclear region in exposed HeLa cells using the confocal Raman imaging analysis; however, the nuclear accumulation of CNTs was not inferred because of the lack of conclusive evidence of CNT-like structures in the nucleus through ultrasections analysis under transmission electron

Ⓦ This paper contains enhanced objects available on the Internet at http://pubs.acs.org/journals/ancac3.

*Address correspondence to yunwlam@cityu.edu.hk, bhcheng@cityu.edu.hk

Received for review July 22, 2008 and accepted September 15, 2008.

Published online September 30, 2008.
10.1021/nn800461u CCC: $40.75

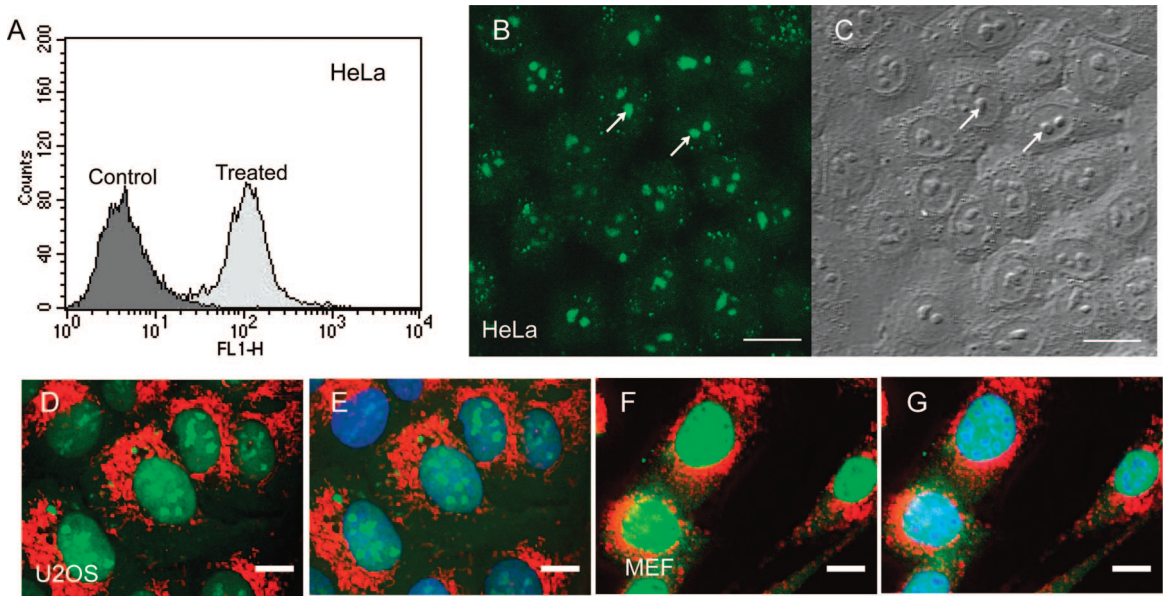

Figure 1. The cell penetration of FITC-PEG-SWCNTs and its nuclear accumulation in mammalian cells. (A) FACS analysis of HeLa cells treated with FITC-PEG-SWCNTs for 48 h showed that the treated cells took up the FITC-PEG-SWCNTs uniformly. (B) Live cell imaging showed that FITC-PEG-SWCNTs accumulated in the nucleus, mainly in the nucleolus (arrows), of HeLa cells. (C) DIC image of panel B. (D−G) U2OS cells (D, E) and MEF (F, G) were incubated with FITC-PEG-SWCNTs and then organellar markers. Signals from PEGylated SWCNTs (green) did not coincide with mitochondria (red, D−G)) but with nuclei (blue, E, G). Note that the distributions of FITC-PEG-SWCNTs between the nucleolus and the nucleoplasm are different in these three cell lines. Scale bars: (B, C) 20 μm; (D−G) 10 μm.

microscopy.[14] The nuclear accumulation of CNTs has been demonstrated by Bianco and co-workers;[8] furthermore, they reported that peptide functionalized multiwalled CNTs could cross the nuclear membrane and be successfully used for plasmid DNA delivery.[3] Previous reports focused mainly on the uptake of the CNTs and little work has been done with respect to the behaviours of CNTs after their penetration into cells. For example, intracellular transferrin-conjugated nanogold particles are known to be released from cells through exocytosis,[15] but it is not clear whether a similar process also occurs for CNTs. A better understanding of the intracellular properties of CNTs is therefore essential for the development of this nanomaterial as a drug delivery vector. In this study, nuclear accumulation of single walled CNTs conjugated with polyethylene glycol (PEG) and labeled with fluorescent dye FITC (FITC-PEG-SWCNTs) were demonstrated in several mammalian cell lines. The intracellular organization and cell division properties of the CNT-treated cells were then studied. The cellular uptake and release of FITC-PEG-SWCNTs were observed using time-lapse fluorescence microscopy. The cellular uptake of FITC-PEG-SWCNTs was compared with Texas-Red labeled Dextran as the endocytosis marker. Fluorescence after photobleaching (FRAP) was used to measure the intranuclear mobility of FITC-PEG-SWCNTs after the uptake. This work extends the current understanding of the interactions between CNTs and biological systems, such as the dynamic fate, intracellular behavior, and the uptake and release mechanism.

RESULTS AND DISCUSSION

Cell Penetration and Nuclear Accumulation of FITC-PEG-SWCNTs. FITC-PEG-SWCNTs were prepared by conjugating FITC to highly purified SWCNTs *via* PEG_{1500N} linkers (detailed information on the preparation and characterization of FITC-PEG-SWCNTs can be found in Supporting Information, supplementary Figures 1−3). We investigated the cell penetrating property of PEG-SWCNTs by incubating human cervical carcinoma cells HeLa with FITC-PEG-SWCNTs for 48 h. After extensive washing, the treated cells were analyzed by flow cytometry. As shown in Figure 1A, FITC fluorescence was detected in virtually all treated cells, suggesting that a substantial amount of FITC-PEG-SWCNTs had become associated with HeLa cells. Free FITC did not associate with HeLa cells (data not shown). The cellular association of FITC-PEG-SWCNTs was time and dose dependent (supplementary Figure 4), with cellular green fluorescence detectable as soon as after 1 h of incubation.

The detection of cellular FITC by flow cytometry suggested that PEGylated SWCNTs could either enter the cells or adhere to the cell surface. The intracellular distribution of FITC-PEG-SWCNTs in a number of mammalian cell lines was revealed by live cell fluorescence microscopy. Figure 1 panels B and C show HeLa cells incubated with FITC-PEG-SWCNTs. The green fluorescence signal was predominately in the cell nucleus with a weaker cytoplasmic staining in some cells. In most cells, FITC-PEG-SWCNTs were observed to be enriched in a few intranuclear structures. Bright-field DIC images indicated that these intranuclear structures were nucleoli (Figure 1B,C, arrows). To further characterize the sub-

cellular distribution of FITC-PEG-SWCNTs, CNT-treated cells were counterstained by a mixture of cell permeable dyes Hoechst 33342 and MitoTracker to label the nucleus and mitochrondria, respectively. The dyes were used at concentrations that did not cause detectable cell toxicity and did not interfere with normal mitosis for at least 24 h.[16,17] FITC-PEG-SWCNT was observed to coincide with Hoechst 33342 (Figure 1E,G), indicating the internalized SWCNT was predominately nuclear. This confirms that the green fluorescence detected by flow cytometry represented intracellular SWCNTs and supports previous observations that modified SWCNTs can effectively cross cell membranes.

The detection of FITC-PEG-SWCNTs in cell nucleus was observed in six mammalian cell lines (Figure 1 and supplementary Figure 5), of different histological origins, transformation status and p53 expression levels (supplementary Table 1). All of the tested cells have normal mitochondrial morphology and function, as indicated by MitoTracker staining (red in Figure 1D−G and supplementary Figure 5). The nuclear accumulation of FITC-conjugated CNTs was also observed for MWCNTs while using PEG_{1500N} as the functionalization group (data not shown), suggesting that the nuclear accumulation of PEGylated CNT is a general property of this nanomaterial. While the nuclear targeting mechanism of CNTs is not known, it is possible that the internalized PEGylated SWCNTs are retained in the nucleus through binding with specific nuclear proteins or nucleic acids. Future investigations will include the study of the effect of the molecular weight and surface coverage of PEG on the cellular uptake, intracellular distribution, and dynamic fate of CNT.

The nucleolar accumulation of FITC-PEG-SWCNTs appeared to change through time (see later) and was variable in different mammalian cell lines (Figure 1). The green fluorescence from the conjugated PEG-SWCNTs was predominately detectable in the nucleolus of HeLa cells (Figure 1B), U2OS cells (Figure 1D), and HT1080 cells (supplementary Figure 5A). However, the nucleolar accumulation of FITC-PEG-SWCNTs was not apparent in MEF (Figure 1F), C33A and HEK293 cells (supplementary Figure 5C,D).

To the best of the researchers' knowledge, PEGylated CNTs are one of the few nanomaterials that accumulate in mammalian cell nuclei without the need of cell-penetrating and nuclear-localizing tags. Several types of nanoparticles can also enter cells without any conjugation, but these nanomaterials are trapped in the endosome.[18,19] Many studies reported a predominately cytoplasmic localization of CNTs [8,12,13] instead of a nuclear accumulation. The intracellular location of different kinds of CNTs has not been systematically studied and the cause of this discrepancy is not clear.

The Cell Penetration Mechanism. To characterize the cell penetration process, FITC-PEG-SWCNTs-treated cells were exposed to a mixture of three dyes: cell permeable dyes DRAQ5[20] and MitoTracker, as well as an impermeable dye DAPI. FITC-PEG-SWCNTs-treated cells (from an incubation of 24 h) were effectively stained by both DRAQ5 and Mitotracker, but could still exclude DAPI (Figure 2A), suggesting that the internalization of FITC-PEG-SWCNTs is not a result of nonspecific membrane damages that lead to a general influx of external molecules. This result indicated that whatever the mechanism used by FITC-PEG-SWCNTs to enter cells, the plasma membrane was still intact enough to exclude a dye of 350 Daltons.

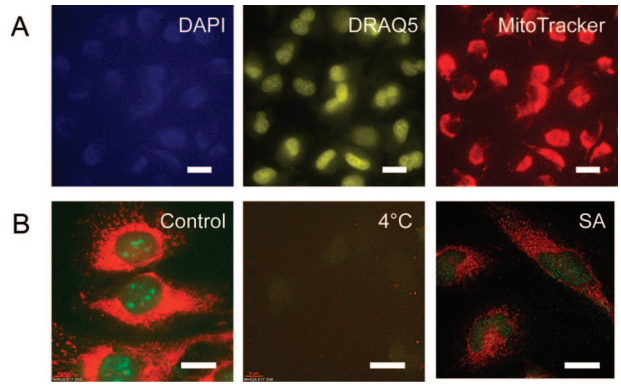

Figure 2. (A) HeLa cells excluded impermeable dye DAPI while they internalized cell permeable dyes (DRAQ5 and MitoTracker). Cells with intracellular FITC-PEG-SWCNTs (incubated for 24 h) had normal nuclear and mitochondrial morphology (DRAQ5 and MitoTracker, respectively). (B) While HeLa cells can uptake FITC-PEG-SWCNTs after coincubation for 2−3 h at 37 °C (control), they cannot take up FITC-PEG-SWCNTs efficiently at 4 °C and during energy depletion (4 °C and SA); SA = sodium azide. Scale bars: (A) 10 μm; (B) 20 μm.

To further investigate the possible mechanism for the cell penetration of PEGylated SWCNT, we studied the effect of energy depletion on its cellular uptake. Cellular internalization of FITC-PEG-SWCNTs was abolished at 4 °C and in sodium azide-treated cells (Figure 2B), indicating that the cellular uptake of PEGylated SWCNTs is an active transporting process requiring energy supply. Previous studies have suggested that mammalian cells could take up CNTs through endocytosis.[13] Here, the cellular uptake of PEGylated SWCNTs was compared with the endocytosis marker Dextran. As shown in Figure 3, after 3 h of coincubation, FITC-PEG-SWCNTs (green) located in the nucleus (Figure 3A) (verified by DRAQ5 staining, Figure 3D) while Texas-Red labeled Dextran (red) stayed in the endosomes in the cytoplasm (Figure 3B) in HeLa cells. The distinct intracellular locations of FITC-PEG-SWCNTs and Dextran indicated either SWCNTs were retained in the endosomes for much shorter time than Dextran, or that CNTs and Dextran entered the cells by different mechanisms. This experiment also suggested that the cellular uptake of CNTs did not affect the endosome function as the cells with PEG-SWCNTS could internalize Texas-Red labeled Dextran as efficiently as cells that had not been treated with CNTs (Figure 4B,C, and supplementary Figure 6).

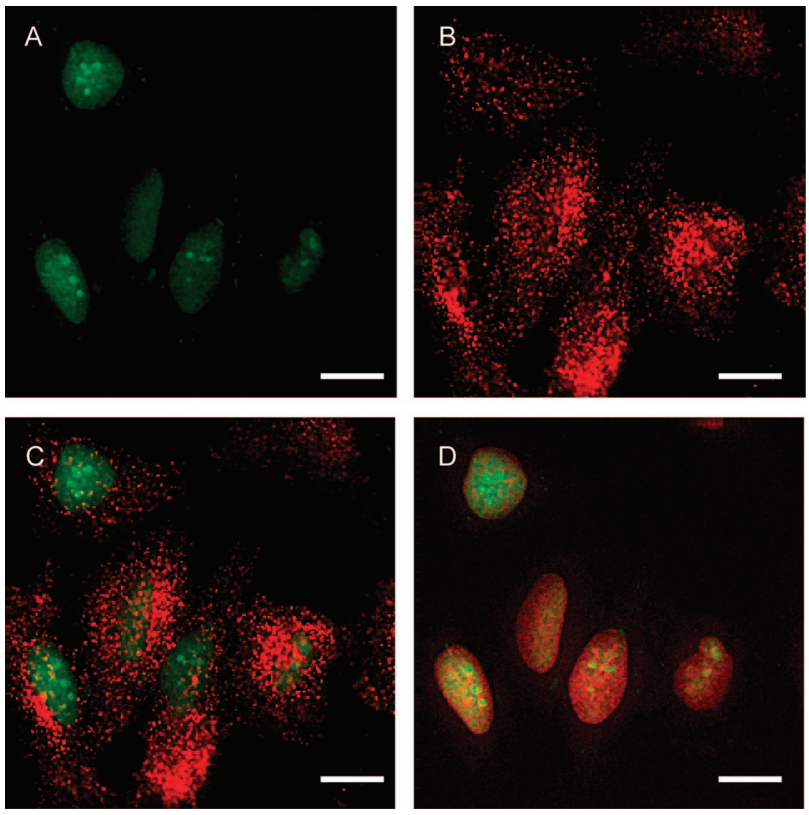

Figure 3. After incubation for 3 h, FITC-PEG-SWCNTs accumulated in the nucleus in HeLa cells (A, C, and D), but Texas-Red labeled Dextran resided in the endosomes of cytoplasm in HeLa cells (B). The green fluorescence signal from intracellular resided FITC-PEG-SWCNTs did not overlap with the red fluorescent signal from intracellular Dextran (C). But the green fluorescence signal from intracellular FITC-PEG-SWCNTs overlapped well with the signal from DNA staining using DRAQ5 (pseudocolored as red in this panel), and the overlapped part generated a yellow color in the nucleus (D). Scale bars: 10 μm.

Effect on Nuclear Organization and Cell Division. The effect of FITC-PEG-SWCNT treatment on cell proliferation was studied. Cell cycle study showed that the cellular uptake of FITC-PEG-SWCNTs did not alter the distribution of cell cycle stages after HeLa cells were exposed to PEG-SWCNTs for 48 h (Figure 4A,B). Flow cytometry analysis also did not show an obvious increase of apoptotic or multinucleated cells (Figure 4A,B and other data not shown). HeLa cells treated with PEGylated SWCNT were monitored by bright-field microscopy for 5 days (Figure 4C), and the statistical data showed that the cell number increased normally as compared to the untreated control (Figure 4D).

Time-lapse imaging showed FITC-PEG-SWCNT-treated cells went through mitosis with no observable abnormality. Figure 5 presents a time-lapse sequence that shows mitosis of mouse embryonic fibroblasts containing FITC-PEG-SWCNTs. Before mitosis, SWCNTs were enriched in the nucleus. Upon nuclear envelope breakdown at the onset of mitosis, SWCNTs became diffused throughout the entire cell during mitosis (Figure 5, arrows). At the end of the anaphase, the FITC signal accumulated in the nuclei of the daughter cells again. We did not observe any enrichment of SWCNTs on mitotic chromosomes. This suggests that SWCNTs do not exclusively bind to chromatin, but may be tethered to proteins or RNAs that are reimported into the nucleus after mitosis. It will be important in the future to identify the cellular macromolecules that interact with CNTs. To the best of the researchers' knowledge, this is the first direct visual evidence that proves CNT-treated cells can go through mitosis, hence further demonstrating that the intracellular presence of SWCNTs does not lead to activation of any major mitotic checkpoints.

Indirect immunofluorescence using antibodies specific for proteins located in nucleoli, Cajal bodies, nuclear pore complexes, splicing speckles and microtubules indicated that none of these structures were observably affected by FITC-PEG-SWCNT accumulation (Figure 6). The perinucleolar location of coilin and rounding up of splicing speckles occurred as a result of transcription inhibition.[21,22] It is inferred that transcription in the CNT-treated cells remains active because these characteristic changes in nuclear organization associated with transcription inhibition was not observed. Taken together, we did not detect any change in the intracellular structure and any discernible toxicity to cultured cells, at least within the time scale (up to 5 days) used in this study. It has been reported that exposure to SWCNTs could inhibit mitosis in human lymphocyte cultures.[23] Our data here showed, at least in cultured mammalian cells, that the presence of PEGylated SWCNTs did not appear to affect the distribution of cell cycle stages, the proliferation rate, and the nuclear structure of cells.

The Release of SWCNTs from the Cells after Internalization. The intracellular dynamics of the internalized PEGylated SWCNTs was examined by live-cell time-lapse microscopy. After incubated with FITC-PEG-SWCNTs for 24 h, HeLa cells were rinsed with fresh medium and observed with the live-cell fluorescence microscopy. The green fluorescence was predominately detectable in the nucleolus, as judged by DIC morphology (Figure 7). Time-lapse microscopy of the FITC-PEG-SWCNT-treated cells showed that the FITC fluorescence was released from the nucleolus and became diffusely distributed in the nucleus within approximately an hour after the removal of SWCNT from the medium (Figure 7). The rapid loss of nucleolar accumulation suggests that the intranuclear distribution of SWCNTs is highly dynamic and responsive to the extracellular SWCNT concentration. This phenomenon also explains the apparent difference in nucleolar SWCNT signals in HeLa cells observed in different experiments (*e.g.*, compare Figure

1B with Figure 8; the latter was imaged more than 1 h after the FITC-PEG-SWCNT treated cells were washed).

The dynamic behavior of the internalized SWCNTs after wash-out was further investigated by time-lapse microscopy. HeLa cells, treated with FITC-PEG-SWCNTs for 24 h, were washed with PBS and then stained with Mitotracker and Hoechst 33342 for 20 min in fresh cell culture medium. Figure 8A and video 1, video 2, and video 3, show that the intracellular level of FITC fluorescence (green) decreased after the removal of the FITC-PEG-SWCNTs from the medium, but the signals from DNA dye Hoechst 33342 (blue) appeared stable. The decrease of the FITC signals was not likely a result of photobleaching, because the nucleolar fluorescence, which was the strongest signal in most cells, disappeared before the fluorescence in the nucleoplasm (Figure 7 and data not shown). Importantly, during the 7 h time course, there was an increase of extracellular FITC fluorescence (Figure 8A and video 1), suggesting an extracellular accumulation of FITC-PEG-SWCNTs. By measuring the FITC signals in the same intracellular and extracellular volume through time, the decrease of the intracellular level of FITC fluorescence was shown to correspond closely with the increase in the extracellular FITC level, whereas the extracellular intensities of Hoechst 33342 and Mitotracker signals remained unchanged (Figure 8B). It is therefore inferred that the decrease of intracellular FITC-PEG-SWCNTs fluorescence was caused by the release of SWCNTs from the cells. This unexpected result implies that the translocation of SWCNTs through the plasma membrane and nuclear envelope can be bidirectional. SWCNTs are not likely to form stable, irreversible complexes with endogenous cellular structures, but can move in and out of the cell in accordance to the external SWCNT concentration. This remarkable property renders SWCNTs as an ideal vehicle for drug delivery because SWCNTs can penetrate cell membranes without causing any toxic effects, at least during the short-term (Figure 4). SWCNTs can also be removed from cells simply through washing (Figure 8), thus eliminating or reducing the potential dangers of long-term health issues caused by the cellular accumulation of SWCNTs.

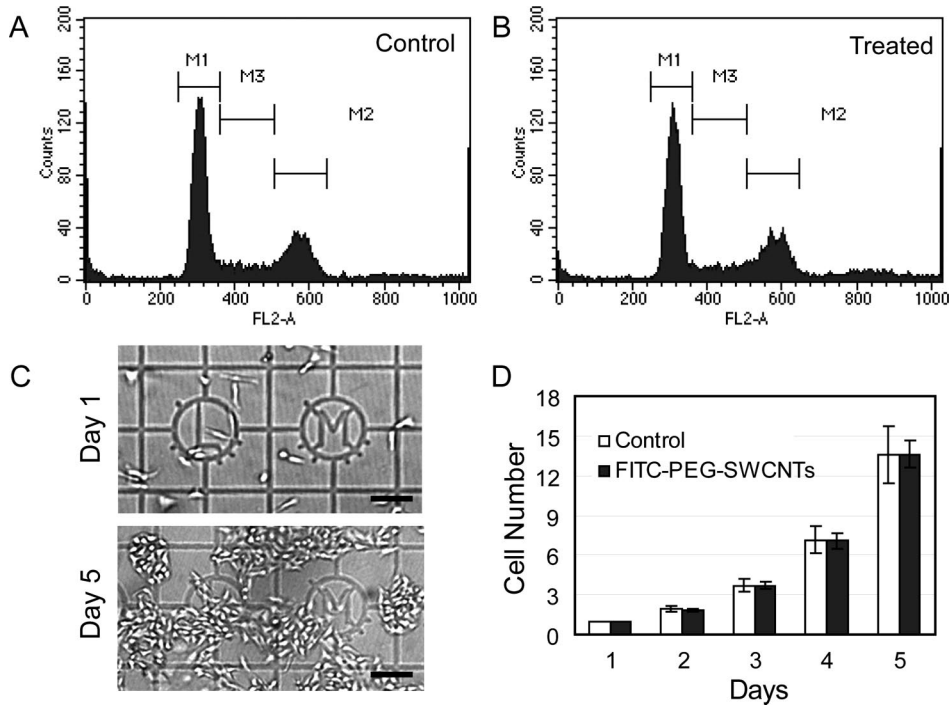

Figure 4. Flow cytometry cell cycle analysis of the propidium iodide-stained untreated HeLa cells (A) and cells incubated with FITC-PEG-SWCNTs for 48 h (B) showed that the treated cells had similar cell cycle distribution compared to the control. The proliferation analysis showed that proliferation rates of HeLa cells that were exposed to FITC-PEG-SWCNTs for up to 5 days are similar to the untreated cells (D). The cell number was measured by counting the number of cells per square (shown in panel C) every 24 h. The graph of panel C showed an example of the proliferation assay that was imaged, in the same region of the coverslip that HeLa cells were cultured for 1 day (day 1) and 5 days (day 5) after treatment with FITC-PEG-SWCNTs. Note the absence of dead cells.

FRAP Analysis for Intracellular SWCNTs. To confirm that this intracellular distribution of FITC fluorescence

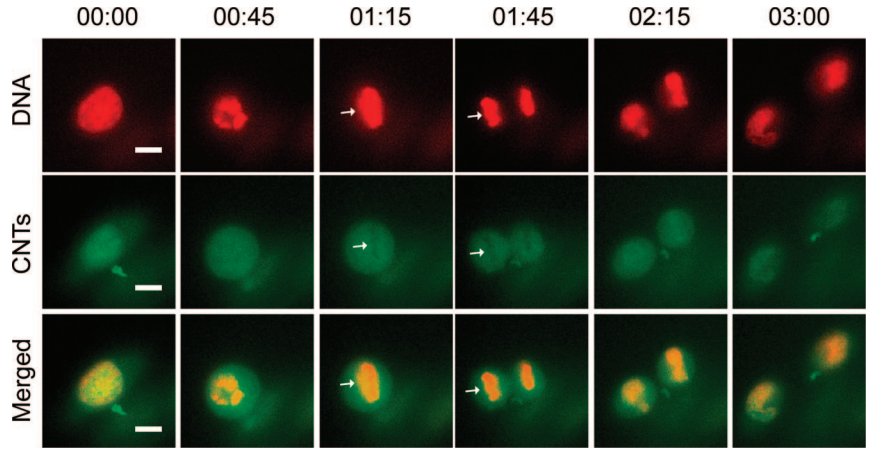

Figure 5. The intracellular localization of FITC-PEG-SWCNTs did not affect cell division. Time-lapse sequence showing the mitosis of mouse embryonic fibroblasts treated with FITC-PEG-SWCNTs for 24 h (middle panels). The mitotic chromosomes were labeled with DRAQ5 (pseudocolored as red, upper panels). Note that CNTs were excluded from mitotic chromosomes (white arrows). Scale bars correspond to 10 μm.

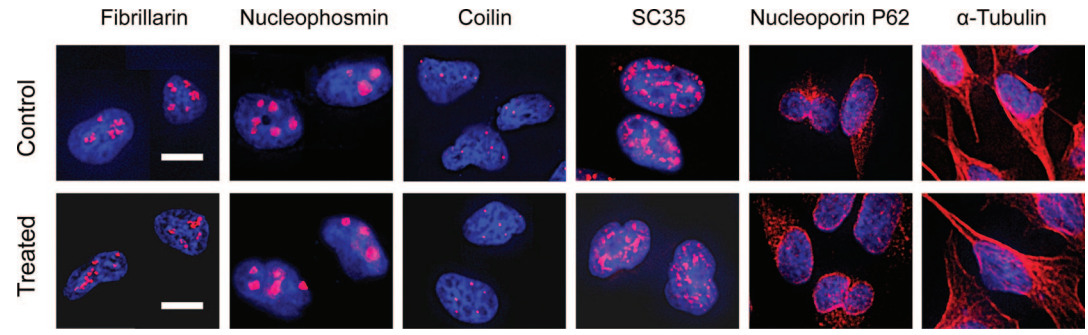

Figure 6. Internalization of FITC-PEG-SWCNTs for 48 h caused no detectable changes in the morphology of the nucleolus (Fibrillarin, nucleophosmin), Cajal bodies (Coilin), splicing speckles (SC35), the nuclear envelope (Nuclearporin p62), and microtubules (α-Tubulin). Scale bars correspond to 10 μm.

faithfully reported the localization of SWCNTs and was not due to free FITC generated by the breakdown of the internalized SWCNTs, FRAP analysis was performed on the FITC-PEG-SWCNT-treated cells. HeLa cells were treated with FITC-PEG-SWCNTs for 48 h and washed, and the FITC fluorescence in a small nuclear region was then photobleached (Figure 9A, upper panels). The subsequent recovery in fluorescence in the photobleached region measures the intranuclear mobility of the fluorescent molecules, which in turn depends on the size of the macromolecular complex that contain this fluorescent label.[24] Figure 9B (red curve) shows the FRAP measurement of nuclear FITC-PEG-SWCNT signals. The recovery half-time was more than 1 min, which is comparable to many typical protein complexes in the human nucleus,[25] and is considerably slower than free, unbound molecules, such as GFP.[26,27] Next, we delivered FITC-PEG-SWCNTs directly into HeLa cells by bead loading, a technique commonly used for introducing macromolecules into cells through reversible damages to plasma membrane caused by glass beads.[28] Like the PEGylated SWCNTs that entered cells physiologically, the bead-loaded SWCNTs also localized in the cell nucleus, with enrichment in the nucleolus (Figure 9A, middle panels), whereas bead-loaded FITC distributed evenly throughout the cells (Figure 9A, lower panels). This suggests that FITC-PEG-SWCNTs can be targeted to the nucleus regardless of the cell penetration methods.

FRAP analyses were performed on cells immediately after being bead-loaded with FITC-PEG-SWCNTs. As shown in Figure 9B (green curve), the kinetics of fluorescence recovery of the bead-loaded FITC-PEG-SWCNTs was virtually indistinguishable from that of FITC-PEG-SWCNTs physiologically internalized by cells. This indicates that an exposure of FITC-PEG-SWCNTs to the intracellular environment for 48 h did not affect their mobility. In contrast, FRAP measurement of free FITC introduced into HeLa cells by bead loading[28] (Figure 9A, lower panels, and Figure 9B, blue curve) showed a much poorer bleaching efficiency and a much faster recovery than FITC-PEG-SWCNT. This is consistent with the extremely fast mobility of the small FITC molecules, a phenomenon well-documented for other small, freely diffusing fluorophores such as unconjugated GFP.[29−31] Taken together, observations by FRAP analysis showed further evidence that the intracellular FITC signals were from the intact PEG-SWCNTs and intracellular SWCNTs were dynamic.

CONCLUSIONS AND PERSPECTIVES

The potential widespread use of CNTs has led to a strong public concern about the impact of these new nanomaterials on human health and the environment. Information concerning the potential biological effects that are related to CNTs is still insufficient. Our study suggested that well-purified SWCNTs, functionalized with PEG_{1500N}, resided in the intracellular nucleus and were nontoxic to cultured mammalian cells upon exposure. Previous cytotoxicity study of CNTs gave rise to much controversy. Contaminants associated with CNTs have been shown to induce in-

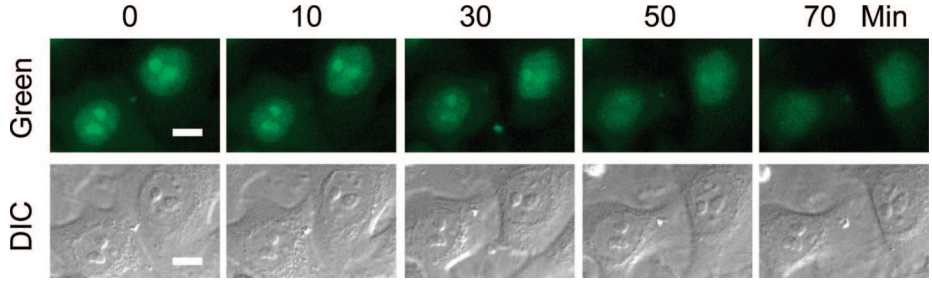

Figure 7. Intracellular distribution and dynamics of FITC-PEG-SWCNTs in HeLa cells. Time-lapse sequence showing the change of the intracellular distribution of FITC-PEG-SWCNTs (incubated for 24 h) in HeLa cells after the removal of the SWCNTs in the culture medium. The numbers on top indicate the time after the removal of SWCNTs from the medium (in minutes). Scale bars: 10 μm.

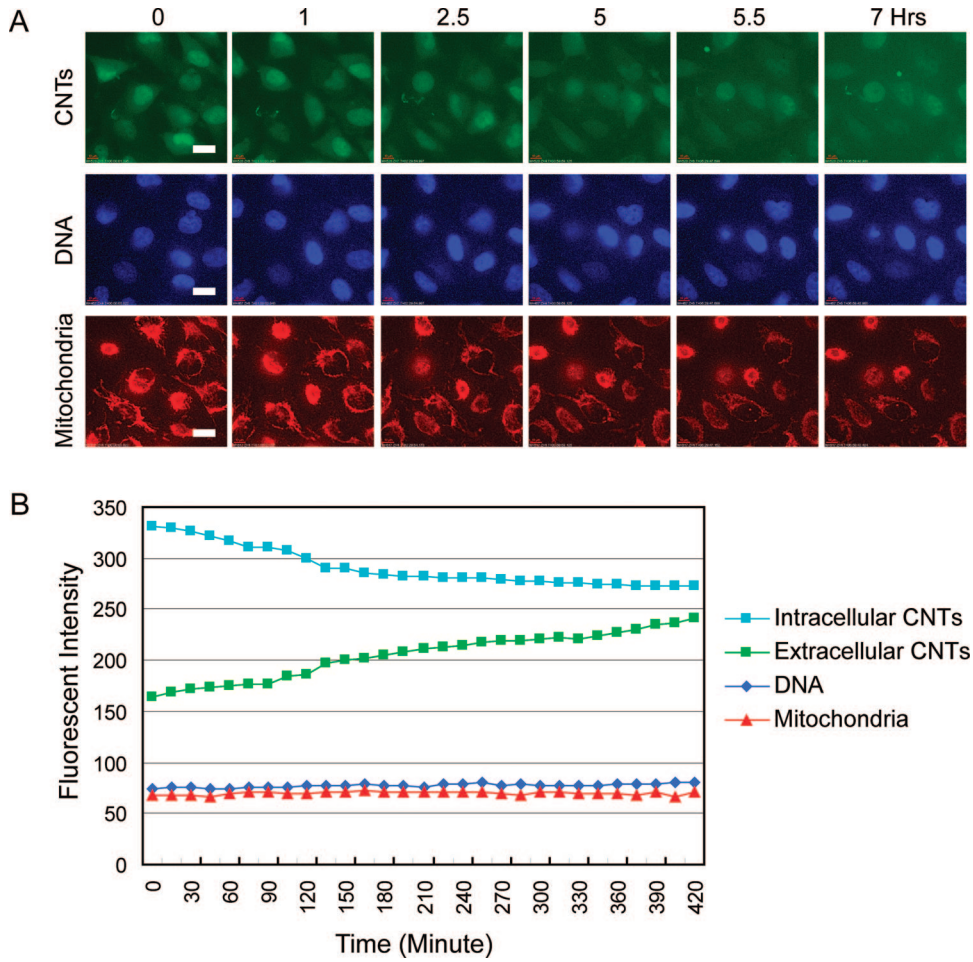

Figure 8. Release of the intracellular FITC-PEG-SWCNTs after the cell internalization. (A) HeLa cells were incubated with FITC-PEG-SWCNTs (green) for 24 h and stained with Hoechst 33342 (blue) and MitoTracker (red) before time-lapse imaging for 7 h in fresh medium. (B) Quantitative analysis of the fluorescence signals in panel A. One region in the extracellular space was selected and the intensities of signals from FITC-PEG-SWCNTs (green data points), MitoTracker (red data points), and Hoechst 33342 (blue data points) were measured. An area of the same size was selected in the intranuclear space and the intensity of the FITC-PEG-SWCNTs (cyan data points) was measured. Scale bars correspond to 20 μm.

Ⓦ Video 1 shows the direct observation of the release of FITC-PEG-SWCNTs from the SWCNT-treated cells.

Ⓦ Video 2 shows the stable distribution of DNA.

Ⓦ Video 3 shows mitochondria markers in the same SWCNT-treated cells.

tracellular oxygen species,[32] whereas highly purified CNTs are less toxic[33] or even nontoxic.[1] The conflicting information sometimes was due to the technical problems when common cytotoxicity assays were applied for CNTs.[34] For example, MTT assay was commonly used to study cell proliferation, but it will generate a fake cytotoxic effect since SWCNTs appear to interact with tetrazolium salts such as MTT.[34] Here we studied the cell proliferation by direct cell number counting using live-cell imaging with the aid of the marked coverslips. This proliferation study through imaging analysis avoided potential nonspecific chemical interactions and is more direct.

In this study, FITC was used to label the PEGylated SWCNTs in living cultured mammalian cells, and time-lapse live-cell microscopy was used to characterize the behavior of SWCNTs after cell entry. It was assumed that FITC, being a biological inactive dye, did not affect the intracellular behaviours of SWCNTs. Future studies will be done using the intrinsic optical properties of SWCNTs to study the intracelluar fate and cell uptake. Here, we have shown that FITC-PEG-SWCNTs accumulated in the nucleus, mainly in the nucleolus in some cell lines, the site of ribosomal biogenesis,[35,36] and were highly dynamic inside the cells. It has been shown that through live-cell time-lapse imaging and immunofluorescence, the architecture of the nucleus for cells treated with PEG-SWCNTs were not detectably affected. Since the organization of the cell nucleus is functionally linked to the regulation of gene expression and is known to be deformed in cells with abnormal metabolism,[37,38] it is inferred that the normal

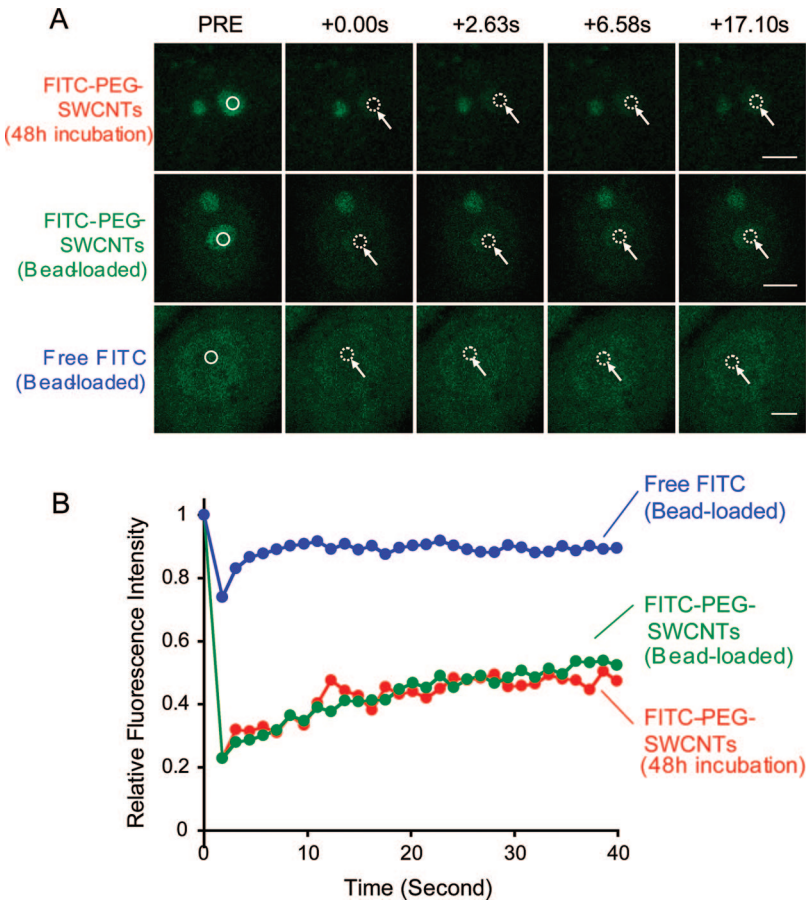

Figure 9. FRAP analysis of the intracellular FITC-PEG-SWCNTs. (A) Small regions (dotted circles) in the nuclei of live HeLa cells containing FITC-PEG-SWCNTs internalized after an incubation of 48 h (upper panels), FITC-PEG-SWCNTs internalized as a result of bead loading (middle panels) and bead-loaded free FITC (lower panels) were photobleached. The fluorescence intensities in the circled regions were monitored by time-lapse imaging over at least 40 s. Numbers on top indicate the time after photobleaching (in seconds). Scale bars: 5 μm. (B) Recovery of fluorescence intensities in the bleached areas (relative to the prebleached levels) over time: blue data points, free FITC; green data points, bead-loaded FITC-PEG-SWCNTs; red data points, FITC-PEG-SWCNTs internalized by incubation for 48 h.

nuclear structure of SWCNT-treated cells is further evidence that the intracellular accumulation of SWCNTs does not harbor any serious toxicity.

The behavior of FITC-PEG-SWCNTs, as revealed by FRAP, is similar to most nuclear proteins studied[25,39] and is consistent with the view that the mammalian nucleus has a highly crowded microenvironment in which macromolecules form transient, but specific interactions with each other.[40] The FRAP analysis that has been reported is the first study of its kind on CNT and can be used as the basis for further characterizations of the intracellular behavior in nanoparticles. SWCNTs can also be used for investigating the intranuclear environment, such as molecular crowding, using optical and other biophysical methodologies.[41]

This study has examined the intracellular and dynamic fate of internalized FITC-PEG-SWCNTs in mammalian cells. Remarkably, the intranuclear distribution of SWCNTs depended on the extracellular concentration of SWCNTs. When PEGylated SWCNTs were removed from the culture medium, the nucleolar SWCNTs rapidly moved to the rest of the nucleus and were eventually released from the cells. This concentration-dependent cellular accumulation of chemicals has been described for some nuclear dyes,[42] but has never been directly observed for nanoparticles. This remarkable property suggests a possible controllable clearance of SWCNTs after the completion of delivery. The controllable entrance and release of SWCNTs by setting intracellular and extracellular conditions provide strong support that SWCNTs may be an ideal tool to be used as nanovectors in biomedical and pharmaceutical applications.

METHODS AND EXPERIMENTS

Preparation and Characterization of PEGylated SWCNTs. SWCNTs were purchased from Carbon Solutions, Inc. The CNT purification, functionalization, and characterization for SWCNTs have been reported elsewhere.[6,43] For purification, SWCNTs were first burned in the furnace at 300 °C in air for 30 min to remove the amorphous carbon and then were further purified by refluxing in an aqueous HNO_3 solution (2.6 M, 48 h), washing repeatedly with water for 3 days, and drying. The samples after purification were validated with thermogravimetric analysis, electron microscopy, and Raman characterization. Nanotube-bound carboxylic acids were then used to attach aminopolymers polyethylene glycol (PEG) to the nanotubes *via* amide linkages.[44] The PEG-SWCNTs were luminescent and the visible/near-IR absorption spectra of the as-purified SWCNTs and PEGylated SWCNTs were also studied. The PEG-SWCNTs were then labeled with fluorescent dye fluorescein isothocyanate (FITC) to facilitate biological imaging. Detailed information on the preparation and characterization of SWCNT samples can be found in Supporting Information.

Cell Culture, Incubation of Living Cells in Nanotube Solutions and Microscopy. Human adenocarcinoma cells (HeLa, ATCC No: CCL2), human cervical cancer cell (C33A, ATCC No: HTB31), human embryonic kidney cells (HEK293, ATCC No: CRL1573), human sarcoma cells (HT1080, ATCC No: CC1121), human bone osteosarcoma cells (U2OS, ATCC No: HTB96), and mouse embryonic fibroblast (MEF, ATCC No: SCRC1008.2) were purchased from American-type Culture Collection (ATCC, VA, USA) and cultured in Dulbecco's modified Eagle's medium (Invitrogen, UK) with 10% fetal bovine serum (Invitrogen, UK). For live-cell imaging experiments, cells grown in chambered coverglasses (Lab-Tek 155411, NUNC) were mounted on a wide-field fluorescence microscope (DeltaVision Spectris; Applied Precision, UK) that was fitted with an environmental chamber (Solent Scientific) to maintain temperature at 37 °C and a Cool Snap charge-coupled device camera (Roper Scientific). Some additional images (*e.g.*, Figure 1B,C) were taken on a Leica TCS SP5 confocal microscope.

The FITC-PEG-SWCNTs were diluted in culture medium to 55 μg/mL (CNT's equivalent concentration) and incubated for durations that are indicated in the study figures. After the incubation with PEGylated SWCNTs, the cells in some experiments were stained for 20 min with Hoechst 33342 (0.25 μg/ml, Sigma) or DRAQ5 (5 μM, cell-permeant far-red fluorescence DNA probe, Biostatus) or DAPI (0.25 μg/ml, Sigma), and MitoTracker (25 nM, Molecular Probes). After the staining, the staining solution was removed and the cells were washed with cell culture medium for 5 min, three times.

Before imaging, growth medium was replaced with a custom-made phenol red-free, CO_2 independent medium (Invitrogen, UK). In all experiments, an Olympus 40× oil immersion lens (NA 1.35) was used. DIC imaging was implemented with the appropriate prism insert (Olympus). For time-lapse live-cell imaging, ten optical sections (1.2 μm each) were collected at regular intervals of 5 min with an exposure time of 35 ms. All images were recorded using a binning of 2 × 2 on the CH350 charge-coupled device camera, yielding an effective pixel size of 0.102 μm × 0.102 μm.

The microscopy images were viewed as three-dimensional sum projections (Figure 4C), single optical sections (Figures 5, 6, 7, and 8) or maximum intensity projections (Figures 1D−G, 2 and 3 and supplementary Figure 5). Data analysis was performed using the SoftWoRx image processing program (Applied Precision, UK), with additional analysis (Figure 9 and supplementary Figure 4) performed using MetaMorph (Universal Imaging).

FRAP Photokinetic Experiments. The FRAP experiments were performed on a Leica TCS SP5 confocal microscope. To briefly summarize, small regions in the cells were photobleached using a 488 nm laser (100% laser power for 0.3 s) and time-lapse sequences of single optical sections were collected by bidirectional scanning using 10% of laser power for about 40 s at the interval of about one image per second. The FRAP data were measured by the built-in Leica software LAS LF and plotted using Excel. Bead loading of FITC-PEG-SWCNTs and FITC was completed as described.[28] Cells were analyzed by FRAP within 30 min after bead loading.

ATP Depletion Experiments. The ATP depletion was conducted with 10 mM sodium azide (Sigma, s-8032). The cells were incubated with the ATP depletion drug and FITC-PEG-SWCNTs for 2−3 h simultaneously. After the coincubation, the cells were washed and incubated with the same ATP depletion CO_2 independent culture medium (Invitrogen) before the live cell staining and imaging. The mitochondria were stained as the marker of the ATP supply with MitoTracker (25 nM, Molecular Probes). The uptake of the PEG-SWCNTs was visualized with green fluorescent signal.

The incubation of HeLa cells with FITC-PEG-SWCNTs was carried out in the cold room with a temperature of 4 °C with CO_2 independent culture medium (Invitrogen). The control group of the cells was cultured in a 37 °C incubator with CO_2-independent culture medium (Invitrogen). The Texas-Red labeled Dextran (Invitrogen) was used as the positive control of the endocytosis uptake and was coincubated with the cells together with PEG-SWCNTs after 3 h of incubation; live-cell imaging was recorded as above.

Antibodies, Fixation, Immunofluorescence, and Imaging. All fixation, permeabilization, and immunostaining were performed at room temperature. Cells grown on glass coverslips were washed in phosphate buffered saline (PBS) and fixed for 10 min with freshly made 4% paraformaldehyde in PBS. Permeabilization was performed with 0.5% Triton X-100 in PBS for 10 min. Cells were subsequently washed three times in PBS and then blocked with 10% goat serum in PBS for 20 min before incubated with primary antibody for 1 h. Three washes with PBS were carried out before incubation with affinity-purified Texas red-conjugated goat antimouse secondary antibody (Jackson ImmunoResearch Laboratories) for 45 min. Finally, cells were stained with DAPI (0.3 μg/ml; Sigma). After a final set of washes, cells were mounted in Vectashield media (Vector Laboratories).

The following antibodies were used in the study. Fibrillarin was detected by mouse monoclonal antibody 72B9 (1:25, a generous gift from Professor E.M. Tan, Scripps Institute). Nucleoporin was detected by mouse monoclonal antibody 414 (1:100, Convance). Splicing factor SC35 was detected by mouse monoclonal antibody anti-SC35 (1:100, Sigma S4045). Coilin was detected by monoclonal antibody 5P10 (1:25). Nucleophosmin was detected by mouse monoclonal antibody anti-B23 (1:100, Sigma B0566); microtubules were detected by mouse anti-α-tubulin DM1A monoclonal antibody (1:100, Sigma T6199).

Immunostained specimens were examined by using a 40× NA 1.3 Plan-Apochromat objective. Three-dimensional images were recorded on a Zeiss DeltaVision Restoration microscope (Applied Precision, UK) that was equipped with a three-dimensional motorized stage and a Photometrics CH350 camera containing a 1401E charge-coupled device (Eastman Kodak Co., UK). For each sample, 10 optical sections separated by 0.2 μm were recorded. Exposures were chosen so that images yielded gray scale units between 200 and 2000, remaining well above the camera dark current, but below the 4096-U maximum.

Cell Proliferation Assay and Flow Cytometry. The cells were seeded one day earlier on a grid coverslip (Eppendorf Cellocate Square size 175 μm) in a 60 mm dish (Merck no. 402/0322/12). The cells were incubated with PEG-SWCNTs continuously for 4 days. The same areas on the coverslip, recognized by grid coordination, were imaged using a 10× lens (Zeiss Planneofluar, NA 0.30 every 24 h during the 4 day period. The cell number in the imaged area was counted. This method allows repeated measurements of the same cell populations over time and is therefore more accurate than comparing averages of different cell populations.

Cells were analyzed by using a flow cytometry (FACS, Becton Dickinson) after incubation in various nanotube solutions. The cells were fixed with cold 70% ethanol and then stained with 50 μg/ml propidium iodide (P3566, Invitrogen) supplemented with 50 μg/ml RNase A (Roche). Dual detection of red fluorescence was carried out with the fixed cells for the cell cycle analysis and green fluorescence with the live cells for the uptake analysis. The data that is presented in this study represents the mean red and green fluorescence obtained with a population of 10000 cells.

Acknowledgment. The work described in this paper was substantially supported by a grant from the Research Grants Council of the Hong Kong SAR (Project No. CityU 160108). The Clemson group was supported by the U.S. National Science Foundation. A. I. Lamond is a Wellcome Trust principal investigator. L. Qu is thanked for experimental assistance and the Cheng, Sun, and Lamond groups for fruitful discussions and comments.

Supporting Information Available: Supplementary figures and tables; detailed preparation and characterization of PEGylated SWCNTs; purification and functionalization procedures; TGA and AFM details. This material is available free of charge *via* the Internet at http://pubs.acs.org.

REFERENCES AND NOTES

1. Zanello, L. P.; Zhao, B.; Hu, H.; Haddon, R. C. Bone Cell Proliferation on Carbon Nanotubes. *Nano Lett.* **2006**, *6*, 562–567.
2. Dumortier, H.; Lacotte, S.; Pastorin, G.; Marega, R.; Wu, W.; Bonifazi, D.; Briand, J. P.; Prato, M.; Muller, S.; Bianco, A. Functionalized Carbon Nanotubes are Non-Cytotoxic and Preserve the Functionality of Primary Immune Cells. *Nano Lett.* **2006**, *6*, 1522–1528.
3. Pantarotto, D.; Singh, R.; McCarthy, D.; Erhardt, M.; Briand, J. P.; Prato, M.; Kostarelos, K.; Bianco, A. Functionalized Carbon Nanotubes for Plasmid DNA Gene Delivery. *Angew. Chem., Int. Ed.* **2004**, *43*, 5242–5246.
4. Shi Kam, N. W.; Jessop, T. C.; Wender, P. A.; Dai, H. Nanotube Molecular Transporters: Internalization of Carbon Nanotube-Protein Conjugates Into Mammalian Cells. *J. Am. Chem. Soc.* **2004**, *126*, 6850–6851.
5. Wu, W.; Wieckowski, S.; Pastorin, G.; Benincasa, M.; Klumpp, C.; Briand, J. P.; Gennaro, R.; Prato, M.; Bianco, A. Targeted Delivery of Amphotericin B to Cells by Using Functionalized Carbon Nanotubes. *Angew. Chem., Int. Ed.* **2005**, *44*, 6358–6362.

6. Sun, Y. P.; Fu, K. F.; Lin, Y.; Huang, W. J. Functionalized Carbon Nanotubes: Properties and Applications. *Acc. Chem. Res.* **2002**, *35*, 1096–1104.
7. Lin, Y.; Taylor, S.; Li, H. P.; Fernando, K. A. S.; Qu, L. W.; Wang, W.; Gu, L. R.; Zhou, B.; Sun, Y. P. Advances Toward Bioapplications of Carbon Nanotubes. *J. Mater. Chem.* **2004**, *14*, 527–541.
8. Pantarotto, D.; Briand, J. P.; Prato, M.; Bianco, A. Translocation of Bioactive Peptides Across Cell Membranes by Carbon Nanotubes. *Chem. Commun.* **2004**, 16–17.
9. Rojas-Chapana, J.; Troszczynska, J.; Firkowska, I.; Morsczeck, C.; Giersig, M. Multi-Walled Carbon Nanotubes for Plasmid Delivery into *Escherichia coli* Cells. *Lab Chip* **2005**, *5*, 536–539.
10. Cai, D.; Mataraza, J. M.; Qin, Z. H.; Huang, Z.; Huang, J.; Chiles, T. C.; Carnahan, D.; Kempa, K.; Ren, Z. Highly Efficient Molecular Delivery into Mammalian Cells Using Carbon Nanotube Spearing. *Nat Methods* **2005**, *2*, 449–454.
11. Kam, N. W.; Liu, Z.; Dai, H. Carbon Nanotubes as Intracellular Transporters for Proteins and DNA: An Investigation of the Uptake Mechanism and Pathway. *Angew. Chem., Int. Ed.* **2006**, *45*, 577–581.
12. Monteiro-Riviere, N. A.; Nemanich, R. J.; Inman, A. O.; Wang, Y. Y.; Riviere, J. E. Multi-Walled Carbon Nanotube Interactions with Human Epidermal Keratinocytes. *Toxicol. Lett.* **2005**, *155*, 377–384.
13. Kam, N. W.; Dai, H. Carbon Nanotubes as Intracellular Protein Transporters: Generality and Biological Functionality. *J. Am. Chem. Soc.* **2005**, *127*, 6021–6026.
14. Yehia, H. N.; Draper, R. K.; Mikoryak, C.; Walker, E. K.; Bajaj, P.; Musselman, I. H.; Daigrepont, M. C.; Dieckmann, G. R.; Pantano, P. Single-Walled Carbon Nanotube Interactions with HeLa Cells. *J. Nanobiotechnol.* **2007**, *5*, 1–17.
15. Chithrani, B. D.; Chan, W. C. Elucidating the Mechanism of Cellular Uptake and Removal of Protein-Coated Gold Nanoparticles of Different Sizes and Shapes. *Nano Lett.* **2007**, *7*, 1542–1550.
16. Trinkle-Mulcahy, L.; ersen, J.; Lam, Y. W.; Moorhead, G.; Mann, M.; Lamond, A. I. Repo-Man Recruits PP1 Gamma to Chromatin and is Essential for Cell Viability. *J. Cell Biol.* **2006**, *172*, 679–692.
17. Kimura, H.; Cook, P. R. Kinetics of Core Histones in Living Human Cells: Little Exchange of H3 and H4 and Some Rapid Exchange of H2B. *J. Cell Biol.* **2001**, *153*, 1341–1353.
18. Duan, H.; Nie, S. Cell-Penetrating Quantum Dots Based on Multivalent and Endosome-Disrupting Surface Coatings. *J. Am. Chem. Soc.* **2007**, *129*, 3333–3338.
19. Gemeinhart, R. A.; Luo, D.; Saltzman, W. M. Cellular Fate of a Modular DNA Delivery System Mediated by Silica Nanoparticles. *Biotechnol. Prog.* **2005**, *21*, 532–537.
20. Martin, R. M.; Leonhardt, H.; Cardoso, M. C. DNA Labeling in Living Cells. *Cytometry A* **2005**, *67*, 45–52.
21. Carmo-Fonseca, M.; Pepperkok, R.; Carvalho, M. T.; Lamond, A. I. Transcription-Dependent Colocalization of the U1, U2, U4/U6, and U5 snRNPs in Coiled Bodies. *J. Cell Biol.* **1992**, *117*, 1–14.
22. Haaf, T.; Ward, D. C. Inhibition of RNA Polymerase II Transcription Causes Chromatin Decondensation, Loss of Nucleolar Structure, and Dispersion of Chromosomal Domains. *Exp. Cell Res.* **1996**, *224*, 163–173.
23. Szendi, K.; Varga, C. Lack of Genotoxicity of Carbon Nanotubes in a Pilot Study. *Anticancer Res.* **2008**, *28*, 349–352.
24. Houtsmuller, A. B.; Vermeulen, W. Macromolecular Dynamics in Living Cell Nuclei Revealed by Fluorescence Redistribution After Photobleaching. *Histochem. Cell Biol.* **2001**, *115*, 13–21.
25. Dundr, M.; Hoffmann-Rohrer, U.; Hu, Q.; Grummt, I.; Rothblum, L. I.; Phair, R. D.; Misteli, T. A Kinetic Framework for a Mammalian RNA Polymerase *in vivo*. *Science* **2002**, *298*, 1623–1626.
26. Griffis, E. R.; Altan, N.; Lippincott-Schwartz, J.; Powers, M. A. Nup98 is a Mobile Nucleoporin with Transcription-Dependent Dynamics. *Mol. Biol. Cell* **2002**, *13*, 1282–1297.
27. Swaminathan, R.; Hoang, C. P.; Verkman, A. S. Photobleaching Recovery and Anisotropy Decay of Green Fluorescent Protein GFP-S65T in Solution and Cells: Cytoplasmic Viscosity Probed by Green Fluorescent Protein Translational and Rotational Diffusion. *Biophys. J.* **1997**, *72*, 1900–1907.
28. McNeil, P. L.; Warder, E. Glass Beads Load Macromolecules into Living Cells. *J. Cell Sci.* **1987**, *88*, 669–678.
29. Sprague, B. L.; McNally, J. G. FRAP Analysis of Binding: Proper and Fitting. *Trends Cell Biol.* **2005**, *15*, 84–91.
30. Ali, G. S.; Reddy, A. S. ATP Phosphorylation and Transcription Regulate the Mobility of Plant Splicing Factors. *J. Cell Sci.* **2006**, *119*, 3527–3538.
31. Christensen, M. O.; Barthelmes, H. U.; Feineis, S.; Knudsen, B. R.; Andersen, A. H.; Boege, F.; Mielke, C. Changes in Mobility Account for Camptothecin-Induced Subnuclear Relocation of Topoisomerase I. *J. Biol. Chem.* **2002**, *277*, 15661–15665.
32. Pulskamp, K.; Diabate, S.; Krug, H. F. Carbon Nanotubes Show no Sign of Acute Toxicity but Induce Intracellular Reactive Oxygen Species in Dependence on Contaminants. *Toxicol. Lett.* **2007**, *168*, 58–74.
33. Nimmagadda, A.; Thurston, K.; Nollert, M. U.; McFetridge, P. S. F. Chemical Modification of SWNT Alters *in vitro* Cell-SWNT Interactions. *J. Biomed. Mater. Res., Part A* **2006**, *76A*, 614–625.
34. Worle-Knirsch, J. M.; Pulskamp, K.; Krug, H. F. Oops They Did it Again! Carbon Nanotubes Hoax Scientists in Viability Assays. *Nano Lett.* **2006**, *6*, 1261–1268.
35. Boisvert, F. M.; van, K. S.; Navascues, J.; Lamond, A. I. The Multifunctional Nucleolus. *Nat. Rev. Mol. Cell Biol.* **2007**, *8*, 574–585.
36. Lam, Y. W.; Trinkle-Mulcahy, L.; Lamond, A. I. The Nucleolus. *J. Cell Sci.* **2005**, *118*, 1335–1337.
37. Jackson, D. A.; Pombo, A.; Iborra, F. The Balance Sheet for Transcription: an Analysis of Nuclear RNA Metabolism in Mammalian Cells. *FASEB J.* **2000**, *14*, 242–254.
38. Leonhardt, H.; Rahn, H. P.; Cardoso, M. C. Functional Links Between Nuclear Structure, Gene Expression, DNA Replication, and Methylation. *Crit Rev. Eukaryot. Gene Expr.* **1999**, *9*, 345–351.
39. Chen, D.; Huang, S. Nucleolar Components Involved in Ribosome Biogenesis Cycle Between the Nucleolus and Nucleoplasm in Interphase Cells. *J. Cell Biol.* **2001**, *153*, 169–176.
40. Misteli, T. The Concept of Self-Organization in Cellular Architecture. *J. Cell Biol.* **2001**, *155*, 181–185.
41. Richter, K.; Nessling, M.; Lichter, P. Experimental Evidence for the Influence of Molecular Crowding on Nuclear Architecture. *J. Cell Sci.* **2007**, *120*, 1673–1680.
42. Frias, J. C.; Bobba, G.; Cann, M. J.; Hutchison, C. J.; Parker, D. Luminescent Nonacoordinate Cationic Lanthanide Complexes as Potential Cellular Imaging and Reactive Probes. *Org. Biomol. Chem.* **2003**, *1*, 905–907.
43. Huang, W. J.; Fernando, S.; Allard, L. F.; Sun, Y. P. Solubilization of Single-Walled Carbon Nanotubes with Diamine-Terminated Oligomeric Poly(ethylene glycol) in Different Functionalization Reactions. *Nano Lett.* **2003**, *3*, 565–568.
44. Huang, W. J.; Taylor, S.; Fu, K. F.; Lin, Y.; Zhang, D. H.; Hanks, T. W.; Rao, A. M.; Sun, Y. P. Attaching Proteins to Carbon Nanotubes *via* Diimide-Activated Amidation. *Nano Lett.* **2002**, *2*, 311–314.

THE JOURNAL OF PHYSICAL CHEMISTRY C LETTERS

18295

2008, *112,* 18295–18298
Published on Web 10/31/2008

Doped Carbon Nanoparticles as a New Platform for Highly Photoluminescent Dots

Ya-Ping Sun,* Xin Wang, Fushen Lu, Li Cao, Mohammed J. Meziani, Pengju G. Luo, Lingrong Gu, and L. Monica Veca

Department of Chemistry and Laboratory for Emerging Materials and Technology, Clemson University, Clemson, South Carolina 29634-0973

Received: August 27, 2008; Revised Manuscript Received: October 18, 2008

There have been rapid advances in the development and applications of semiconductor quantum dots (QDs) represented by CdSe/ZnS. However, a serious limitation of these QDs is the necessary use of toxic heavy metals. It is reported here that small carbon nanoparticles doped with inorganic salts serve as a highly promising new platform for brightly photoluminescent dots. The photoluminescent carbon dots with the carbon core doped with ZnO (C_{ZnO}-Dots) or ZnS (C_{ZnS}-Dots) in aqueous solutions are competitive to the commercially available CdSe/ZnS QDs in luminescence brightness.

Introduction

There have been rapid advances in the development and applications of semiconductor quantum dots (QDs), especially for the more fluorescent core−shell dots based on CdSe nanocrystals with a wide-bandgap semiconductor shell.[1−3] Despite their demonstrated performance and widely discussed potentials, however, a major limitation is their necessary use of heavy metals such as cadmium.[3a,4] In the continuing search for benign (nontoxic) alternatives,[4−10] Sun and co-workers found and reported that nanosized pure carbon particles may be surface-passivated by organic molecules (dubbed "carbon dots") to exhibit bright photoluminescence in the visible with either one- or two-photon excitation.[8,9] Carbon dots compare favorably with the semiconductor QDs in many properties (carbon being a nontoxic element, no-blinking, etc.),[8,9] but their brightness (emission quantum yields up to 15−20%) is still lower than that of the best-performing CdSe/ZnS core−shell dots. In this work, we found that carbon nanoparticles may be doped with inorganic salts such as ZnO or ZnS before their surface passivation by organic molecules to achieve much higher photoluminescence quantum yields. These new dots with a doped carbon core (Figure 1) are performance-wise competitive to the commercially available CdSe/ZnS dots, especially in aqueous solutions (where shortcomings of the CdSe/ZnS dots are known in the literature[3b,11]). The results suggest that small salt-doped carbon nanoparticles represent a new platform for quantum dotlike optical nanomaterials.

Results and Discussion

Experimentally, carbon nanoparticles from laser ablation were processed in terms of the nitric acid treatment, dialysis, and then centrifugation to retain the supernatant, in which the suspended nanoparticles were generally less than 10 nm in size according to electron microscopy analyses. The doping of the carbon nanoparticles with ZnO or ZnS was achieved in an aqueous suspension of the nanoparticles with $Zn(CH_3COO)_2$ through hydrolysis with NaOH or precipitation with Na_2S, respectively. For the former, the sample was thermally annealed to convert $Zn(OH)_2$ to ZnO. No thermal annealing step was necessary for ZnS-doped carbon nanoparticles.

A sample (200 mg) containing either ZnO- or ZnS-doped carbon nanoparticles was dispersed in an aqueous solution of sodium dodecyl sulfate (1 wt %, 120 mL) via sonication for 30 min. Upon filtration, the filter cake was washed repeatedly with water, dried, and then mixed thoroughly with the diamine-polyethylene glycol $H_2NCH_2(CH_2CH_2O)_{35}CH_2CH_2CH_2NH_2$ (PEG_{1500N}, 1.9 g). The mixture was heated to 110 °C and stirred for 72 h under nitrogen protection. It was then cooled to room temperature and dispersed in water, followed by centrifuging at 25 000*g* to retain the supernatant. The reaction conditions were the same as those used previously in the functionalization of carbon nanotubes,[12] where the PEG_{1500N} amino groups and the carboxylic acid moieties on the oxidized carbon surface (still naked areas on ZnO- or ZnS-doped carbon nanoparticles) form zwitterion pairs.[12,13] Additionally, there may also be strong PEG_{1500N} adsorption on the particle surface, as also observed in the functionalized carbon nanotubes.

The carbon dots with ZnO- or ZnS-doped carbon cores ("C_{ZnO}-Dots" or "C_{ZnS}-Dots", respectively) were characterized by using microscopy techniques. Shown in Figure 2 are the TEM images of C_{ZnS}-Dots, which suggest typical dot sizes around 4−5 nm. At a higher imaging resolution, the doping of a carbon particle with ZnS could be visualized (Figure 2 and also Figure 1). The results from energy dispersive X-ray (EDX) analyses of C_{ZnS}-Dots on a silicon grid confirmed the presence of C, Zn, and S. Also shown in Figure 2 are AFM images of C_{ZnO}-Dots on a mica substrate.

Thermogravimetric analysis (TGA) measurements of the C_{ZnO}-Dots and C_{ZnS}-Dots samples were performed at 10 °C/min, first to 600 °C in nitrogen to remove the surface functional groups and then to 800 °C in air to oxidize the carbon core into carbon dioxide (purged out of the system). According to the TGA results, the core C:ZnO and C:ZnS ratios in C_{ZnO}-Dots and C_{ZnS}-Dots were approximately 3:1 and 2:1, respectively,

* Corresponding author. E-mail: syaping@clemson.edu.

10.1021/jp8076485 CCC: $40.75

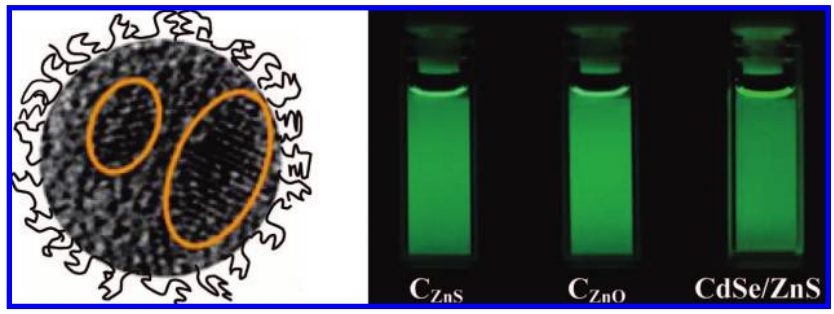

Figure 1. Left: cartoon illustration on carbon dots with a doped carbon core (from an experimental HR-TEM image with ZnS lattice fringes circled). Right: aqueous solutions of C_{ZnS}-Dots and C_{ZnO}-Dots (450 nm excitation for both) compared with a commercial toluene solution of CdSe/ZnS dots (matching optical density at excitation), all photographed through a 475 nm cutoff filter.

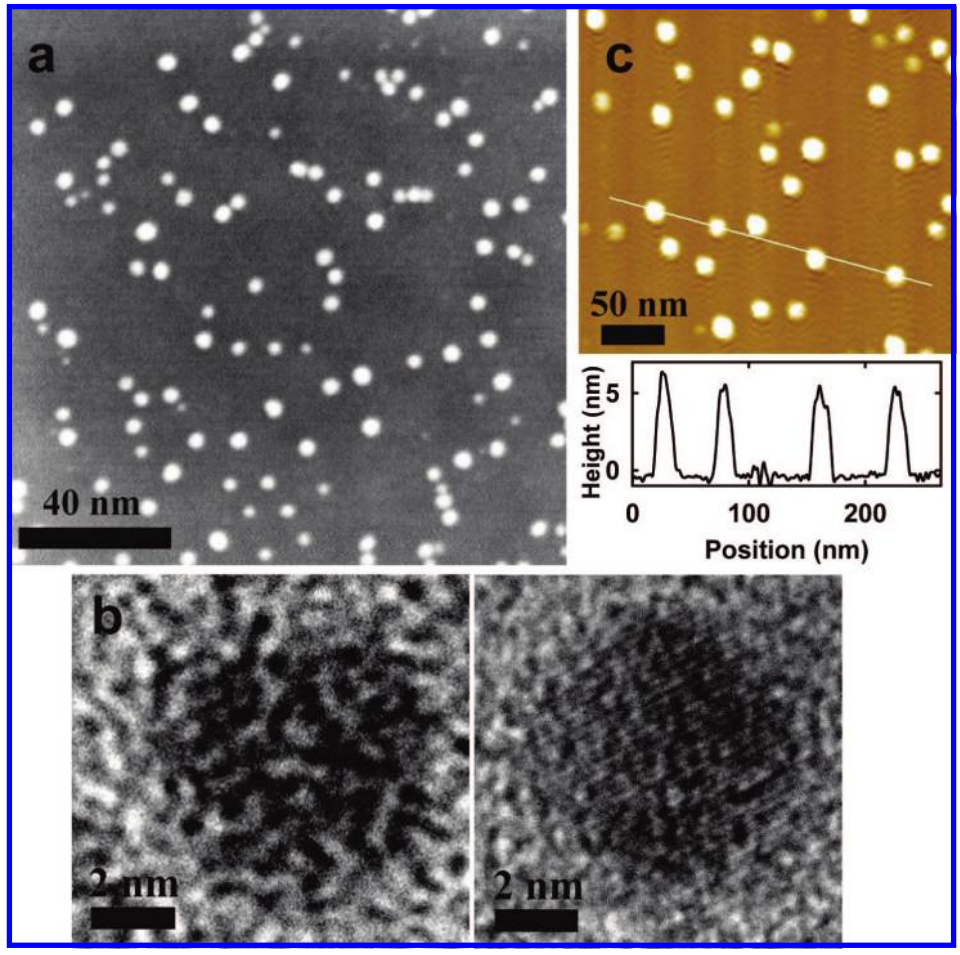

Figure 2. (a) TEM (Z-contrast) images of C_{ZnS}-Dots. (b) High-resolution TEM images of individual carbon dots without doping (left) and with ZnS-doping (right, showing lattice fringes). (c) AFM topography images of C_{ZnO}-Dots on a mica substrate (and the height profile along the line).

in terms of weight (corresponding to 20:1 and 13:1, respectively, in molar ratios).

The absorption and luminescence emission spectra of C_{ZnO}-Dots and C_{ZnS}-Dots are rather similar (Figure 3). For both samples, the absorption spectra feature a shoulder in the blue region, where the absorptivities are on the order of 100 [(mole of core carbon atoms)/L]$^{-1}$cm^{-1}. The excitation into the absorption shoulder results in strong bluish green luminescence emissions (Figure 3 and also Figure 1). The observed emission quantum yields (440 nm excitation, quinine sulfate as the fluorescence standard) for C_{ZnS}-Dots in aqueous solution are consistently higher than 50% (varying somewhat from batch to batch, up to 15%, in about a dozen of repeated sample preparations). This is competitive to the performance of commercially available organic-based CdSe/ZnS core−shell dots (NN-LABS, LLC, Figure 1).

The currently available C_{ZnO}-Dots in aqueous solution are slightly less luminescent than C_{ZnS}-Dots, with observed quantum yields around 45% (also varying somewhat from batch to batch, up to 15%, in repeated sample preparations).

Mechanistically, the photoluminescence in carbon dots has been attributed to passivated defects on the carbon particle surface acting as excitation energy traps, for which the covalently attached organic molecules serve as the passivation agents.[8,9] While the role of ZnO or ZnS doping in the substantial enhancement of photoluminescence performance is not clear (no precedent to follow), we propose that the dopant may provide secondary yet more effective surface passivation in

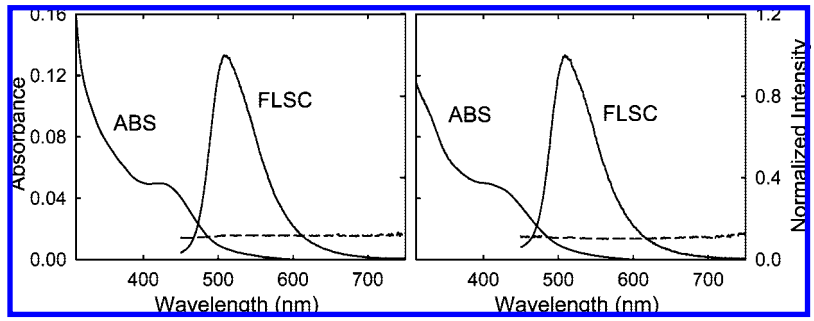

Figure 3. Absorption (ABS) and luminescence emission (FLSC, 440 nm excitation, normalized against the peak intensity) spectra of C_{ZnS}-Dots (left) and C_{ZnO}-Dots (right) in aqueous solutions. As also shown for comparison, the carbon nanoparticles doped with ZnS or ZnO but without PEGs were not emissive (dashed lines, ×10 and offset by 0.1 for easier viewing).

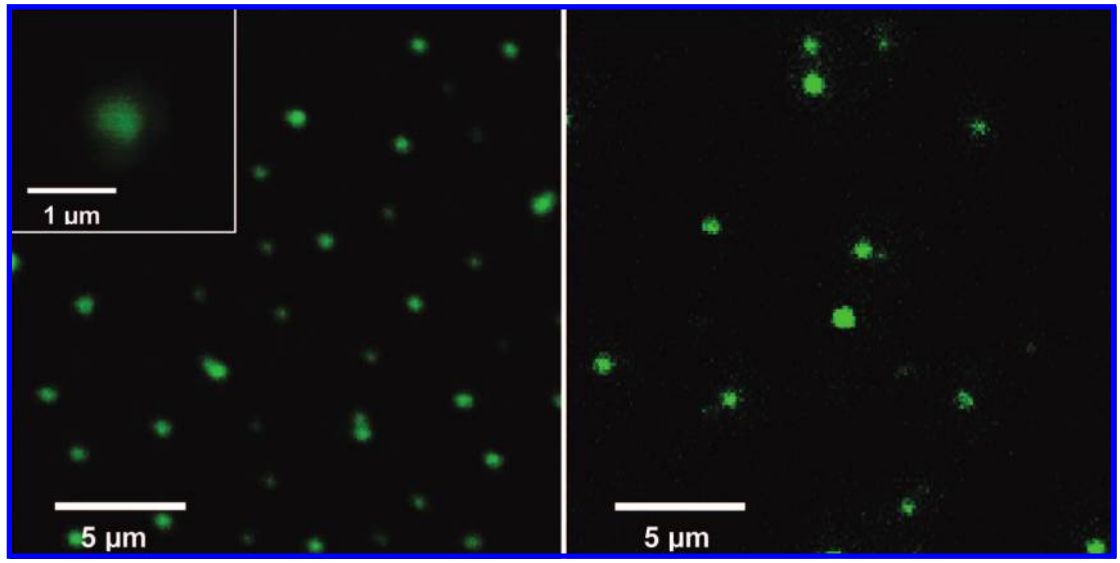

Figure 4. One- (left, 458 nm excitation) and two-photon (right, 800 nm excitation) luminescence images of the C_{ZnS}-Dots and that for the specimen from an infinitely diluted solution (left inset).

combination with the organic passivation agents. Results from repeated control experiments suggested that the functionalization of ZnO- or ZnS-doped carbon nanoparticles by the organic (PEG_{1500N}) molecules is necessary for the observed very strong photoluminescence, as compared in Figure 3.

The C_{ZnO}-Dots and C_{ZnS}-Dots are both strongly luminescent under multiphoton excitation conditions, a property that they share with the original carbon dots.[9] The two-photon excitation at 800 nm with a femtosecond pulsed laser (Spectra Physics Tsunami Ti-Sapphire) resulted in bright luminescence emissions in the visible region, which were generally similar to those observed with one-photon excitation at 458 nm (argon ion laser). For example, shown in Figure 4 are luminescence images of C_{ZnS}-Dots obtained on a confocal microscope (Leica DMIRE2 with TCS SP2 SE scanning system) with one- and two-photon excitations. Even with infinite dilution of the solution used in the preparation of the specimen, the resulting luminescence emissions from presumably individual dots could still be readily detected (Figure 4). These results suggest great potentials of these dots in one- and two-photon luminescence imaging applications.

In summary, small carbon nanoparticles doped with inorganic salts apparently serve as a highly promising new platform in the development of quantum dotlike optical nanomaterials for imaging and other applications. The C_{ZnO}-Dots and C_{ZnS}-Dots in aqueous solutions are competitive to the commercially available organic-based CdSe/ZnS QDs in luminescence brightness. Beyond the blue−green regions, carbon dots with doped carbon cores for other colors are being pursued.

Experimental Section

Materials. Zinc acetate dihydrate and sodium sulfide were purchased from Alfa, sodium hydroxide from Aldrich, and the poly(ethylene glycol) diamine (~35 repeating units for a molecular weight of 1500) from Fluka. *N,N*-Dimethylformamide and sodium dodecyl sulfate were supplied by Acros and VWR, respectively. Millipore Durapore membrane filters (0.22 μm, GV membrane) were obtained from Fisher Scientific, dialysis membrane tubing from Spectrum Laboratories, and carbon- and silicon-coated copper grids from Electron Microscopy Sciences. Water was deionized and purified by being passed through a Labconco WaterPros water purification system.

For the ZnS doping, the laser ablation-produced carbon nanoparticle sample[8,9] (1 g) was refluxed in an aqueous nitric acid solution (2.6 M) for 12 h, neutralized via dialysis (membrane molecular weight cutoff ~ 1000) against a large volume of fresh water, and then centrifuged at 1000*g* for 5 min. The supernatant was retained and evaporated to remove water. The recovered carbon nanoparticles (600 mg) were dispersed in DMF (200 mL) with the aid of ultrasonication (VWR model 250D) for 30 min. To the suspension was added zinc acetate dihydrate (680 mg, 3.1 mmol) under vigorous stirring, followed by slow dropwise addition of an aqueous Na_2S solution (0.62 M, 5 mL) at room temperature. The mixture was centrifuged at

3000*g*, and the precipitate was retained and repeatedly washed with distilled water to obtain the ZnS-doped carbon nanoparticles (881 mg).

In the doping with ZnO, the same initial treatments of carbon nanoparticles were applied to obtain their dispersion in DMF (600 mg/200 mL). To the dispersion was added zinc acetate dihydrate (680 mg, 3.1 mmol) under vigorous stirring, followed by slow dropwise addition of an aqueous NaOH solution (1.25 M, 5 mL) at room temperature. The mixture was centrifuged at 3000*g* to discard the supernatant. The precipitate was repeatedly washed with water, evaporated to remove water, and then dried at 60 °C in a vacuum oven. The sample was annealed at 200 °C for 2 h to obtain the ZnO-doped carbon nanoparticles (830 mg).

Measurements. Baxter Megafuge (model 2630) and Beckman-Coulter ultracentrifuge (Optima L90K with a type 90 Ti fixed-angle rotor) were used for low- and high-speed centrifugations, respectively. Thermogravimetric analysis (TGA) was performed on a TA Instruments Q500 TGA (up to 800 °C with air or nitrogen gas).

Transmission electron microscopy (TEM) imaging was carried out on a Hitachi HD-2000 S-TEM system and a Hitachi H-9500 TEM system. The same S-TEM system was used for the in situ energy dispersive X-ray spectroscopy (EDX) analysis. Atomic force microscopy (AFM) images were obtained in the acoustic AC mode on a Molecular Imaging PicoPlus system equipped with a multipurpose scanner and a NanoWorld Pointprobe NCH sensor. The height profile analysis was assisted by using the SPIP software distributed by Image Metrology.

UV/vis absorption spectra were recorded on a Shimadzu UV2101-PC spectrophotometer. Photoluminescence spectra were measured on a Spex Fluorolog-2 emission spectrometer equipped with a 450 W xenon source and a detector consisting of a Hamamatsu R928P photomultiplier tube operated at 950 V. A Leica laser scanning confocal fluorescence microscope (DMIRE2, with Leica TCS SP2 SE scanning system) was used for optical imaging and spectral measurements. The microscope was equipped with an argon ion laser (JDS Uniphase) and a femtosecond pulsed (∼100 fs at 80 MHz) Ti:Sapphire laser (Spectra-Physics Tsunami with a 5 W Millennia pump). An oil immersion objective lens (Leica X63/1.40) was used in both one- and two-photon imaging experiments. For the two-photon measurements, an external nondescanned detector (NDD) was used for higher signals.

Acknowledgment. Financial support from the NIH, the American Chemical Society Petroleum Research Fund, and the DoD Breast Cancer Research Program is gratefully acknowledged. The instrumentations used in this work were acquired with funding from the NSF.

Supporting Information Available: Figure S1. This material is available free of charge via the Internet at http://pubs.acs.org.

References and Notes

(1) (a) Colvin, V. L.; Schlamp, M. C.; Alivisatos, A. P. *Nature* **1994**, *370*, 354–357. (b) Alivisatos, A. P. *Science* **1996**, *271*, 933–937.

(2) (a) Hines, M. A.; Guyot-Sionnest, P. *J. Phys. Chem.* **1996**, *100*, 468–471. (b) Peng, X. G.; Schlamp, M. C.; Kadavanich, A. V.; Alivisatos, A. P. *J. Am. Chem. Soc.* **1997**, *119*, 7019–7029. (c) Alivisatos, A. P. *Nat. Biotechnol.* **2004**, *22*, 47–52.

(3) (a) Michalet, X.; Pinaud, F. F.; Bentolila, L. A.; Tsay, J. M.; Doose, S.; Li, J. J.; Sundaresan, G.; Wu, A. M.; Gambhir, S. S.; Weiss, S. *Science* **2005**, *307*, 538–544. (b) Medintz, I. L.; Uyeda, H. T.; Goldman, E. R.; Mattoussi, H. *Nat. Mater.* **2005**, *4*, 435–446.

(4) (a) Derfus, A. M.; Chan, W. C. W.; Bhatia, S. N. *Nano Lett.* **2004**, *4*, 11–18. (b) Gao, X. H.; Cui, Y. Y.; Levenson, R. M.; Chung, L. W. K.; Nie, S. M. *Nat. Biotechnol.* **2004**, *22*, 969–976. (c) Kirchner, C.; Liedl, T.; Kudera, S.; Pellegrino, T.; Javier, A. M.; Gaub, H. E.; Stolzle, S.; Fertig, N.; Parak, W. J. *Nano Lett.* **2005**, *5*, 331–338. (d) Lovric, J.; Cho, S. J.; Winnik, F. M.; Maysinger, D. *Chem. Biol.* **2005**, *12*, 1227–1234. (e) It should be noted that toxicity is a complicated topic, and the reference here is only for the widely acknowledged fact that cadmium is a toxic heavy metal, irrespective of the extensive effort on minimizing or eliminating the effect in vivo. Carbon as an element is not intrinsically toxic.

(5) (a) Wilson, W. L.; Szajowski, P. F.; Brus, L. E. *Science* **1993**, *262*, 1242–1244. (b) Li, Z. F.; Ruckenstein, E. *Nano Lett.* **2004**, *4*, 1463–1467.

(6) Bharali, D. J.; Lucey, D. W.; Jayakumar, H.; Pudavar, H. E.; Prasad, P. N. *J. Am. Chem. Soc.* **2005**, *127*, 11364–11371.

(7) Yu, S.-J.; Kang, M.-W.; Chang, H.-C.; Chen, K.-M.; Yu, Y.-C. *J. Am. Chem. Soc.* **2005**, *127*, 17604–17605.

(8) Sun, Y.-P.; Zhou, B.; Lin, Y.; Wang, W. J.; Fernando, K. A. S.; Pathak, P.; Meziani, M. J.; Harruff, B. A.; Wang, X.; Wang, H.; Luo, P. J. G.; Yang, H.; Kose, M. E.; Chen, B.; Veca, L. M.; Xie, S. Y. *J. Am. Chem. Soc.* **2006**, *128*, 7756–7757.

(9) Cao, L.; Wang, X.; Meziani, M. J.; Lu, F. S.; Wang, H. F.; Luo, P. J. G; Lin, Y.; Harruff, B. A.; Veca, L. M.; Murray, D.; Xie, S.-Y.; Sun, Y.-P. *J. Am. Chem. Soc.* **2007**, *129*, 11318–11319.

(10) (a) Zhou, J. G.; Booker, C.; Li, R. Y.; Zhou, X. T.; Sham, T. K.; Sun, X. L.; Ding, Z. F. *J. Am. Chem. Soc.* **2007**, *129*, 744–745. (b) Liu, H. P.; Ye, T.; Mao, C. D. *Angew. Chem., Int. Ed.* **2007**, *46*, 6473–6475. (c) Bourlinos, A. B.; Stassinopoulos, A.; Anglos, D.; Zboril, R.; Karakassides, M.; Giannelis, E. P. *Small* **2008**, *4*, 455–458. (d) Bourlinos, A. B.; Stassinopoulos, A.; Anglos, D.; Zboril, R.; Georgakilas, V.; Giannelis, E. P. *Chem. Mater.* **2008**, *20*, 4539–4541.

(11) Bakalova, R.; Zhelev, Z.; Aoki, I.; Kanno, I. *Nat. Photo.* **2007**, *1*, 487–489.

(12) Huang, W. J.; Fernando, K. A. S.; Allard, L. F.; Sun, Y.-P. *Nano Lett.* **2003**, *3*, 565–568.

(13) Chen, J.; Rao, A. M.; Lyuksyutov, S.; Itkis, M. E.; Hamon, M. A.; Hu, H.; Cohn, R. W.; Eklund, P. C.; Colbert, D. T.; Smalley, R. E.; Haddon, R. C. *J. Phys. Chem. B* **2001**, *105*, 2525–2528.

JP8076485

J|A|C|S
ARTICLES
Published on Web 01/04/2008

Metallic Single-Walled Carbon Nanotubes for Conductive Nanocomposites

Wei Wang, K. A. Shiral Fernando, Yi Lin, Mohammed J. Meziani, L. Monica Veca, Li Cao, Puyu Zhang, Martin M. Kimani, and Ya-Ping Sun*

Department of Chemistry and Laboratory for Emerging Materials and Technology, Clemson University, Clemson, South Carolina 29634-0973

Received September 8, 2007; E-mail: syaping@clemson.edu

Abstract: This article reports an unambiguous demonstration that bulk-separated metallic single-walled carbon nanotubes offer superior performance (consistently and substantially better than the as-produced nanotube sample) in conductive composites with poly(3-hexylthiophene) and also in transparent conductive coatings based on PEDOT:PSS. The results serve as a validation on the widely held view that the carbon nanotubes are competitive in various technologies currently dominated by conductive inorganic materials (such as indium tin oxide).

Introduction

Since the discovery of single-walled carbon nanotubes (SWNTs), there has been much excitement about their superior and in many cases unique properties,[1,2] including their being ballistic conductors.[3] In reality, the high electrical conductivity is associated only with metallic SWNTs, but all of the available production methods for SWNTs yield mixtures of metallic and semiconducting nanotubes. Moreover, metallic SWNTs generally represent the minority fraction in the mixtures (statistically 1:2 for metallic/semiconducting).[1,2] Thus, post-production separation of metallic and semiconducting SWNTs has been pursued by a number of research groups,[4−6] with various strategies based on physical and chemical means.[7−12] We reported earlier a separation method that is uniquely suited for SWNTs produced from the arc-discharge and laser ablation techniques.[11] The separation is based on the observation that semiconducting SWNTs are selectively solubilized via noncovalent interactions with planar aromatic molecules, such as derivatized free-base porphyrin (Scheme 1) or pyrene with long alkyl chains (to facilitate the solubilization of the noncovalently attached nanotubes in common organic solvents).[11] Thus, the metallic and semiconducting fractions are obtained from the residue and supernatant, respectively, in the solubilization-based separation process. While there has been much discussion on great potentials and promises of bulk-separated metallic or semiconducting SWNTs,[4−6] experimental demonstration of such has been scarce.[13−15] Here, we report the use of the bulk-separated metallic fraction from arc-discharge SWNTs in conductive polymeric nanocomposites to demonstrate unambiguously the superior performance of metallic SWNTs.

Results and Discussion

The nanotube sample produced from the arc-discharge method was purified by using oxidative acid treatment in procedures that are well-established in the literature.[16,17] The separation

(1) Ajayan, P. M. *Chem. Rev.* **1999**, *99*, 1787−1799.
(2) Dresselhaus, M. S.; Dresselhaus, G.; Eklund, P. C. *Science of Fullerenes and Carbon Nanotubes;* Academic Press: San Diego, CA, 1996.
(3) White, C. T.; Todorov, T. N. *Nature* **1998**, *393*, 240−242.
(4) Lin, Y.; Fernando, K. A. S.; Wang, W.; Sun, Y.-P. In *Carbon Nanotechnology: Recent Developments in Chemistry, Physics, Materials Science and Device Applications;* Dai, L., Ed., Elsevier: Amsterdam, 2006, pp 255−295.
(5) Krupke, R.; Hennrich, F. *Adv. Eng. Mater.* **2005**, *7*, 111−116.
(6) Banerjee, S.; Benny, T. H.; Wong, S. S. *J. Nanosci. Nanotechnol.* **2005**, *5*, 841−855.
(7) Krupke, R.; Hennrich, F.; von Lohneysen, H.; Kappes, M. M. *Science* **2003**, *301*, 344−347.
(8) (a) Zheng, M.; Jagota, A.; Semke, E. D.; Diner, B. A.; Mclean, R. S.; Lustig, S. R.; Richardson, R. E.; Tassi, N. G. *Nat. Mater.* **2003**, *2*, 338−342. (b) Zheng, M.; Jagota, A.; Strano, M. S.; Santos, A. P.; Barone, P.; Chou, S. G.; Diner, B. A.; Dresselhaus, M. S.; Mclean, R. S.; Onoa, G. B.; Samsonidze, G. G.; Semke, E. D.; Usrey, M.; Walls, D. J. *Science* **2003**, *302*, 1545−1548.
(9) (a) Strano, M. S.; Dyke, C. A.; Usrey, M. L.; Barone, P. W.; Allen, M. J.; Shan, H.; Kittrell, C.; Hauge, R. H.; Tour, J. M.; Smalley, R. E. *Science* **2003**, *301*, 1519−1522. (b) Seo, K.; Kim, C.; Choi, Y. S.; Park, K. A.; Lee, Y. H.; Kim, B. *J. Am. Chem. Soc.* **2003**, *125*, 13946−13947. (c) Zhang, G. Y.; Qi, P. F.; Wang, X. R.; Lu, Y. R.; Li, X. L.; Tu, R.; Bangsaruntip, S.; Mann, D.; Zhang, L.; Dai, H. J. *Science* **2006**, *314*, 974−977.
(10) Chattopadhyay, D.; Galeska, I.; Papadimitrakopoulos, F. *J. Am. Chem. Soc.* **2003**, *125*, 3370−3375.
(11) Li, H.; Zhou, B.; Lin, Y.; Gu, L.; Wang, W.; Fernando, K. A. S.; Kumar, S.; Allard, L. F.; Sun, Y.-P. *J. Am. Chem. Soc.* **2004**, *126*, 1014−1015.
(12) (a) Maeda, Y.; Kimura, S.-I.; Kanda, M.; Hirashima, Y.; Hasegawa, T.; Wakahara, T.; Lian, Y.; Nakahodo, T.; Tsuchiya, T.; Akasaka, T.; Lu, J.; Zang, X.; Tokumoto, H.; Saito, R. *J. Am. Chem. Soc.* **2005**, *127*, 10287−10290. (b) Maeda, Y.; Kanda, M.; Hashimoto, M.; Tadashi, H.; Kimura, S.-I.; Lian, Y.; Wakahara, T.; Akasaka, T.; Kazaoui, S.; Minami, N.; Okazaki, T.; Hayamizu, Y.; Hata, K.; Lu, J.; Nagase, S. *J. Am. Chem. Soc.* **2006**, *128*, 12239−12242.
(13) Arnold, M. S.; Green, A. A.; Huvat, J. F.; Stupp, S. I.; Hersam, M. C. *Nat. Nanotechnol.* **2006**, *1*, 60−65. In addition, there were reports on selectively etching away metallic SWNTs to leave the semiconducting ones for field-effect transistor devices.[9c,14,15]
(14) (a) Balasubramanian, K.; Sordan, R.; Burghard, M.; Kern, K. A. *Nano Lett.* **2004**, *4*, 827−830. (b) An, L.; Fu, Q.; Lu, C. G.; Liu, J. *J. Am. Chem. Soc.* **2004**, *126*, 10520−10521.
(15) (a) So, H. M.; Kim, B. K.; Park, D. W.; Kim, B. S.; Kim, J. J.; Kong, K. J.; Chang, H. J.; Lee, J. O. *J. Am. Chem. Soc.* **2007**, *129*, 4866−4867. (b) Zheng, G.; Li, Q. Q.; Jiang, K. L.; Zhang, X. B.; Chen, J.; Ren, Z.; Fan, S. S. *Nano Lett.* **2007**, *7*, 1622−1625.
(16) (a) Hu, H.; Zhao, B.; Itkis, M. E.; Haddon, R. C. *J. Phys. Chem. B* **2003**, *107*, 13838−13842. (b) Itkis, M. E.; Perea, D. E.; Niyogi, S.; Rickard, S. M.; Hamon, M. A.; Hu, H.; Zhao, B.; Haddon, R. C. *Nano Lett.* **2003**, *3*, 309−314.

Scheme 1

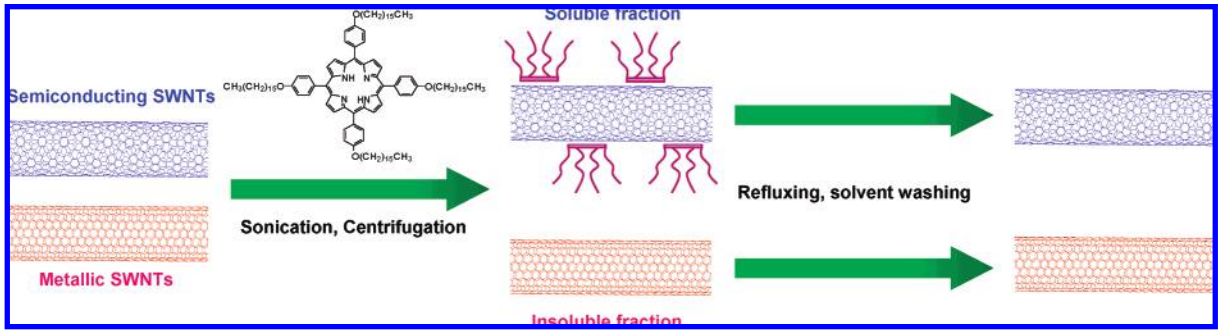

Scheme 2. Molecular Structure of DomP

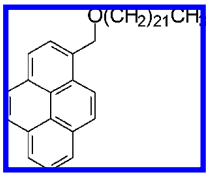

experiment for the purified SWNTs was carried out under conditions similar to those reported previously,[11] except for the use of 1-docosyloxymethyl pyrene (DomP, Scheme 2) as the planar aromatic agent.[18] The separated metallic fraction was recovered by thoroughly removing any residual separation agent. Results from electronic microscopy analyses revealed no significant difference in the separated metallic fraction from the preseparation purified SWNTs (Figure 1).

The resonance Raman spectrum (632-nm excitation) of the separated metallic fraction exhibits a Breit−Wigner−Fano (BWF) feature in the G-band region much more pronounced than that of the preseparation purified sample (Figure 2),[19] suggesting substantial enrichment of metallic SWNTs in the separated fraction. More quantitatively, the optical absorption spectral features (Figure 2) due to the electronic transitions between the van Hove singularity pairs of semiconducting SWNTs were carefully measured, which allowed an estimate of the content of metallic SWNTs in the separated fraction:[4] about 2.5 times that in the preseparation purified sample or about 82% if the content in the latter is at the statistical limit of 1/3.

The separated metallic fraction was dispersed in regioregular poly(3-hexylthiophene) (P3HT) for P3HT/SWNT nanocomposite films of improved electrical conductivity. In the film fabrication experiment, nanotubes were added to a solution of P3HT in chlorobenzene, and the resulting mixture in dark green color appeared homogeneous and stable (without precipitation).[20] For the comparison between the separated metallic fraction and the preseparation purified SWNTs, two mixtures of P3HT with 10% (wt/wt) respective nanotube samples were cast into a pair of thin films in a glovebox (under nitrogen to prevent any oxidation or chemical doping). The absorption spectral features of the nanocomposite films in the visible exhibited no meaningful difference from those of the blank P3HT film, suggesting no ground-state complex formation between the polymers and SWNTs. The results from scanning electron microscopy (SEM) analyses were also similar between the films, both with no nanotubes visible on the film surface. However, when the films were stretched to failure, SWNTs at the torn edges could be observed in the SEM imaging of both films.

As compared in Figure 3 for the two films of the same 10% (wt/wt) nanotube content, the one with the separated metallic fraction is obviously more conductive than the other with preseparation purified SWNTs. The electrical conductivity calculated from the current−voltage ($I-V$) curves of the

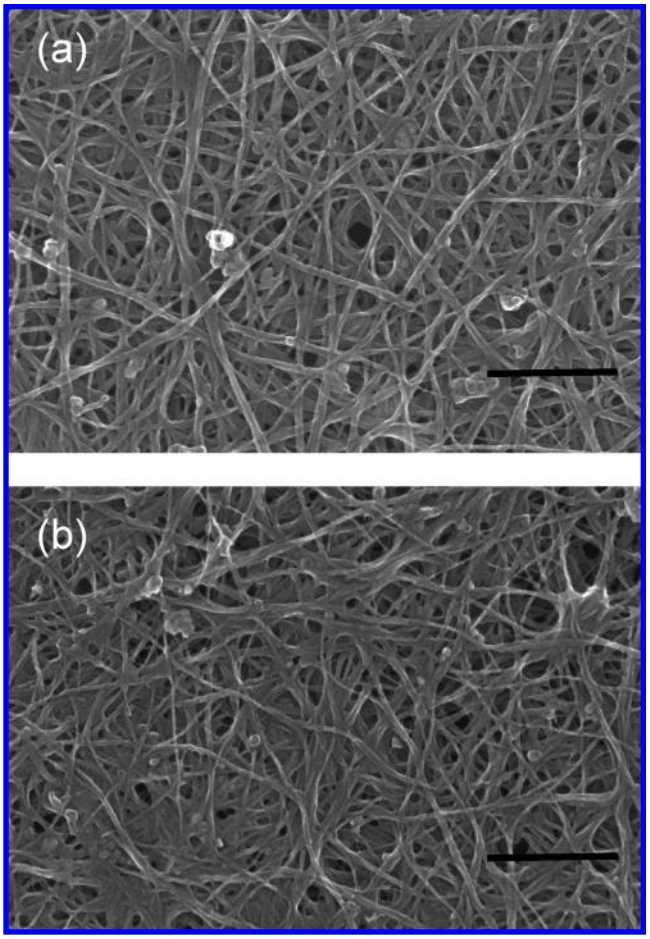

Figure 1. SEM images of (a) the preseparation sample and (b) separated metallic SWNTs (scale bar = 300 nm).

(17) Qu, L. W.; Lin, Y.; Hill, D. E.; Zhou, B.; Wang, W.; Sun, X.; Kitaygorodskiy, A.; Suarez, M.; Connell, J. W.; Allard, L. F.; Sun, Y.-P. *Macromolecules* **2004**, *37*, 6055−6060.
(18) Fernando, K. A. S.; Lin, Y.; Wang, W.; Kumar, S.; Zhou, B.; Xie, S.-Y.; Cureton, L. T.; Sun, Y.-P. *J. Am. Chem. Soc.* **2004**, *126*, 10234−10235.
(19) Pimenta, M. A.; Marucci, A.; Empedocles, S. A.; Bawendi, M. G.; Hanlon, E. B.; Rao, A. M.; Eklund, P. C.; Smalley, R. E.; Dresselhaus, G.; Dresselhaus, M. S. *Phys. Rev. B* **1998**, *58*, R16016−R16019.
(20) Ikeda, A.; Nobusawa, K.; Hamano, T.; Kikuchi, J. *Org. Lett.* **2006**, *8*, 5489−5492.

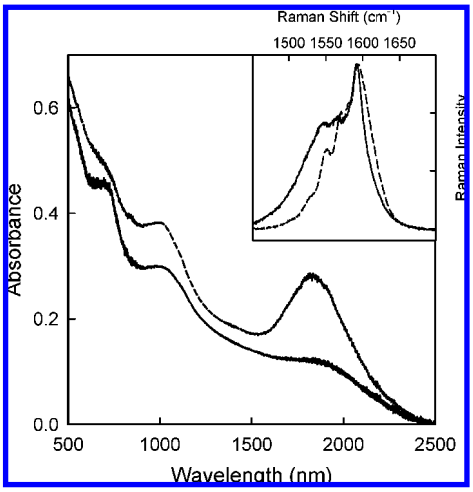

Figure 2. Optical absorption spectra of the preseparation sample (– – –) and separated metallic SWNTs (—), and their corresponding Raman G-bands (632-nm excitation) in the inset.

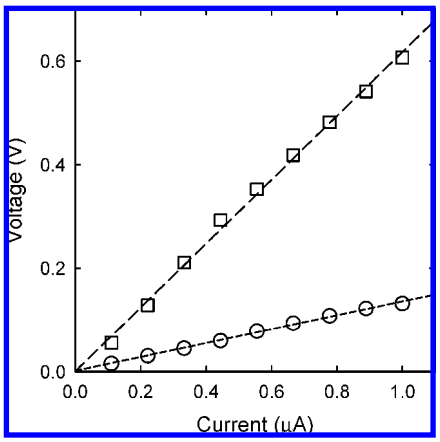

Figure 3. *I*−*V* curves for the P3HT/SWNT composite films (10 wt % nanotubes for both) with preseparation purified SWNTs (□) and separated metallic SWNTs (○). Dashed lines represent the best fits from linear regression.

composite films is 10^{-2} S/cm for the former and 2.3×10^{-3} S/cm for the latter, compared with the conductivity of 10^{-6} to 10^{-7} S/cm for blank P3HT films.[21]

P3HT/SWNT composite films with various loadings (up to 20% by weight) of separated metallic fraction and preseparation purified nanotube sample were fabricated and evaluated for their electrical conductivity results. The comparison in Figure 4a shows clearly that the films with the enriched metallic SWNTs are consistently more conductive than those with the preseparation mixture at the same nanotube sample loadings. In fact, the increase in conductivity is more than an order of magnitude with the use of separated metallic fraction at 20% (wt/wt) nanotube sample loading in the films (Figure 4a). It seems that the film conductivity is dictated by available conductive channels, namely the amount of metallic SWNTs. Thus, the actual contents of metallic SWNTs in the nanocomposite films are calculated from the known compositions in both the separated metallic fraction and the preseparation purified nanotube sample. As shown in Figure 4b, the relationship between the actual contents of metallic SWNTs in the films

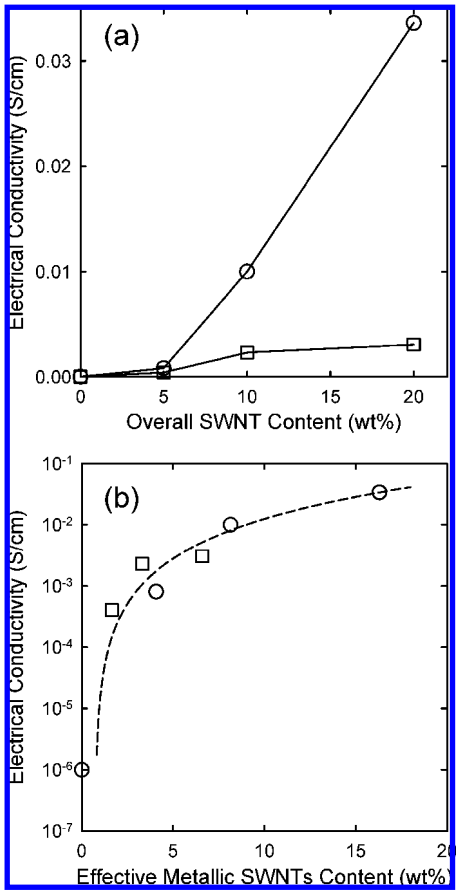

Figure 4. Electrical conductivity results of P3HT/SWNT composite films depending on (a) different amounts of preseparation (□) and separated metallic (○) nanotube samples, and (b) their corresponding effective metallic SWNT contents in the films (dashed line: the best fit in terms of the percolation theory equation).

and the film electrical conductivity values follows the percolation theory:[22,23]

$$\delta = |x - x_c|^{\alpha} \qquad (1)$$

where δ is the electrical conductivity, x the content of metallic SWNTs, x_c the percolation threshold where the transition takes place, and α the critical exponent for the conductivity (an index for system dimensionality, theoretically 1.3 and 1.94 for ideal 2D and 3D systems, respectively).[22] The best fit in Figure 4b corresponds to x_c of 0.74% (wt/wt) and α of 1.92. It makes sense that these films behave like 3D systems because the film thickness (about 1 μm) is considerably greater than the average diameters of the dispersed SWNTs or their bundles.[24]

P3HT is highly colored, so that the films with and without embedded nanotubes are of poor optical transparency in the visible region. To prepare optically transparent conductive thin films, poly(3,4-ethylene dioxythiophene):poly(styrene sulfonate) (PEDOT:PSS) was used as matrix. The films were made ultrathin, essentially thin coatings on glass substrate (Figure 5 inset), to facilitate the optical transparency. The film (coating) thickness was controlled in terms of the optical transmittance at 550 nm.

(21) Chen, T.; Wu, X.; Rieke, R. D. *J. Am. Chem. Soc.* **1995**, *117*, 233−244.
(22) Kymakis, E.; Alexandou, I.; Amaratunga, G. A. J. *Synth. Met.* **2002**, *127*, 59−62.
(23) Aarab, H.; Baitoul, M.; Wery, J.; Almairac, R.; Lefrant, S.; Faulques, E.; Duvail, J. L.; Hamedoun, M. *Synth. Met.* **2005**, *155*, 63−67.
(24) Bekyarova, E.; Itkis, M. E.; Cabrera, N.; Zhao, B.; Yu, A.; Gao, J.; Haddon, R. C. *J. Am. Chem. Soc.* **2004**, *127*, 5990−5995.

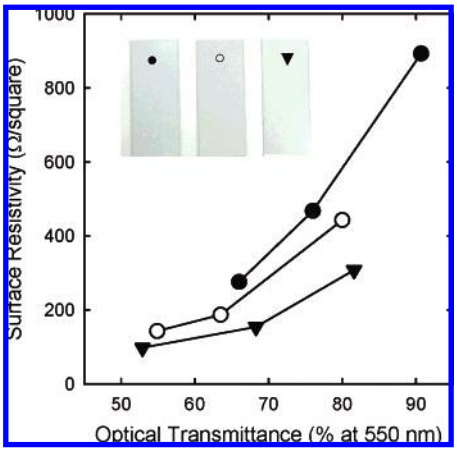

Figure 5. Surface resistivity results of PEDOT:PSS/SWNT films on glass substrate with the same 10 wt % nanotube content (○: preseparation purified sample and ▼: separated metallic SWNTs; and for comparison, ●: blank PEDOT:PSS without nanotubes) but different film thickness and optical transmittance at 550 nm. Shown in the inset are representative films photographed with tiger paw print as background.

The same approach of solution-phase dispersion and then wet-casting was applied to the fabrication of PEDOT:PSS/SWNT nanocomposite coatings on glass substrate. As well-established, PEDOT:PSS was processed as an aqueous dispersion.[25] For solvent compatibility, DMSO was used to disperse nanotubes. The suspension of the nanotubes in DMSO was mixed with the aqueous PEDOT:PSS solution, and the mixture was used for fabricating the transparent conductive coating via spraying. Two PEDOT:PSS/SWNT mixtures with one containing 10% (wt/wt) of the separated metallic fraction and the other 10% (wt/wt) of the preseparation purified nanotube sample were prepared and so was an aqueous solution of neat PEDOT:PSS (also containing the same amount of DMSO) as reference. Depending on the amount of solution or mixture sprayed, the coating thickness varies, as reflected by the variation in optical transmittance at 550 nm. These coatings were measured carefully for their surface resistivity values. The results compared in Figure 5 demonstrate clearly the enhanced electrical conductivity with the separated metallic SWNTs in the transparent conductive films.

In the development for alternatives to the currently dominating indium tin oxide (ITO) technology,[26] PEDOT:PSS transparent conductive films have been demonstrated for some successful uses in organic optoelectronic devices.[27,28] For example, the organic photovoltaic cell with PEDOT:PSS electrode was found to be only 15% less in efficiency when compared to the same cell with a classic ITO electrode.[28] A strategy already discussed in the literature on further improving the performance of transparent PEDOT:PSS electrode is the incorporation of SWNTs.[29−31] The results presented above suggest that the use of bulk-separated metallic SWNTs might offer the necessary conductivity enhancement without sacrificing the optical transparency to make the resulting PEDOT:PSS/SWNT composite films competitive to ITO coatings for transparent electrodes and other applications.

We deliberately used conductive polymers in this study to have different nanotube samples (the preseparation purified nanotubes and the separated metallic and semiconducting fractions) similarly dispersed to allow their comparative performance evaluation on a morphologically equivalent basis. For transparent conductive thin films composed solely of SWNTs, their properties and performance are quite sensitive to the selection of fabrication techniques and many other experimental parameters (including especially the morphological characteristics of the nanotube samples). It remains a significant technical challenge to take full advantage of the separated metallic SWNTs for transparent conductive films of performance much beyond the state of the art.

In summary, semiconducting SWNTs could be extracted from the purified nanotube sample through their preferential interactions with planar aromatic species, yielding substantially enriched metallic SWNTs. When dispersed in conductive polymer thin films, the metallic SWNTs enhance the electrical conductivity of the resulting nanocomposites significantly more than the starting purified nanotube sample. The results not only validate the post-production separation approach, but also demonstrate unambiguously the great potentials of metallic SWNTs in conductive nanocomposites and other relevant applications.

Experimental Section

Materials. Regioregular P3HT (M_w = 50 000, polydispersity index = 1.3−1.6) was purchased from Rieke Metal, Inc., and PEDOT:PSS (Baytron PH500, ~1 wt % solid content) was purchased from H. C. Stark. Solvents THF, DMSO, and DMF were obtained from Mallinckrodt and distilled before use, and chlorobenzene was from Acros.

DomP was synthesized and characterized according to the procedures and methods reported previously.[18]

The SWNT sample from the arc-discharge production method was supplied by Carbon Solutions, Inc. The as-received sample was purified by a combination of thermal oxidation and oxidative acid treatments as reported previously.[17] Briefly, the sample (1 g) was heated in a furnace to 300 °C in air for 30 min and then refluxed in diluted nitric acid (2.6 M, 500 mL) for 24 h. The solid was collected via centrifugation, washed repeatedly with deionized water until neutral pH, and then dried in vacuum oven to obtain the purified sample (330 mg).

Measurements. Optical absorption spectra were recorded on Shimadzu UV3100 and UV3600 spectrophotometers. Raman spectra were measured on a Renishaw Raman spectrometer (50 mW diode laser for 785-nm excitation) and Jobin Yvon T64000 Raman spectrometer (Melles-Griot 35 mW He−Ne laser for 632.8-nm excitation). The latter was also equipped with triple monochromator and Olympus BX-41 microscope. SEM images were obtained on a Hitachi S4700 field emission system.

I−*V* relationships for the nanocomposite thin films were determined by using the traditional four-probe method with Keithley 2400 multimeter controlled by Lab Tracer 2.0 software (Keithley Instruments, Inc.) and a probe station (multiheight probe, Jandel). Electrical conductivity values were calculated according to $\sigma = [(\pi/\ln 2)*(I/V)]/t$, where t is the specimen thickness. Surface resistivity values were calculated according to $R_s = (\ln 2/\pi)*(V/I)$.

Separation. In a typical experiment, a purified SWNT sample (150 mg) was added to a solution of DomP in dry THF (10 mg/mL, 30

(25) Groenendaal, L.; Jonas, F.; Freitag, D.; Pielartzik, H.; Reynolds, J. R. *Adv. Mater.* **2000**, *12*, 481−494.
(26) Gruner, G. *J. Mater. Chem.* **2006**, *16*, 3533−3539.
(27) Kim, W.; Palilis, L. C.; Makinen, A. J.; Kim, H.; Uchida, M.; Kafai, Z. H. *Mater. Res. Soc. Symp. Proc.* **2004**, *814*, 343−353.
(28) Kushto, G. P.; Kim, W.; Kafai, Z. H. *Appl. Phys. Lett.* **2005**, *86*, 093502.
(29) Carroll, D. L.; Czerw, R.; Webster, S. *Synth. Met.* **2005**, *155*, 694−697.
(30) Moon, J. S.; Park, J. H.; Lee, T. Y.; Kim, Y. W.; Yoo, J. B.; Park, C. Y.; Kim, J. M.; Jin, K. W. *Diamond Relat. Mater.* **2005**, *14*, 1882−1887.
(31) Kymakis, E.; Klapsis, G.; Koudoumas, E.; Stratakis, E.; Kornilios, N.; Vidakis, N.; Franghiadakis, Y. *Eur. Phys. J.: Appl. Phys.* **2007**, *36*, 257−259.

mL). The mixture was homogenized (Fisher Scientific Power Gen 125) for 1 h and then sonicated (VWR model 250D) for 24 h. The mixture was centrifuged at 1380*g* for 1−2 min to remove the supernatant. The residue containing enriched metallic SWNTs was refluxed in THF for 24 h and then washed repeatedly with THF until the solution from the washing exhibited no pyrene absorption.

Nanocomposite Films. In typical fabrication of P3HT/SWNT films, the purified or separated metallic SWNT sample (2.5 mg) was suspended in chlorobenzene (5 mL) and homogenized for 10 min. It was mixed with a solution of P3HT (47.5 mg) in chlorobenzene, and the mixture was homogenized for 20 min and then sonicated for 24 h. The drop-casting of the P3HT/SWNT composite thin films on clean glass slides was performed in a glovebox under nitrogen atmosphere. The films were dried in vacuum before conductivity measurements.

For PEDOT:PSS/SWNT films, the selected SWNT sample (5 mg) was suspended in DMSO (45 mL) with homogenization for 10 min and then sonication for 1 h. The suspension was mixed with aqueous PEDOT:PSS solution (5 mL). The mixture was sonicated for 1 h, followed by centrifuging at 2256*g* for 10 min to remove any solid residues. The supernatant was used for spray-coating onto glass substrates that were maintained at 150 °C. The resulting films were dried in vacuum before optical transmittance and surface resistivity measurements.

Acknowledgment. We thank Dr. Zakya Kafafi of Naval Research Laboratory for valuable suggestions. Financial support from the NSF, NASA, Center for Advanced Engineering Fibers and Films (NSF-ERC at Clemson University), and South Carolina Space Grant Consortium is gratefully acknowledged. M.M.K. was a participant of the summer undergraduate research program jointly sponsored by the NSF (DMR-0243734) and Clemson University.

JA0768035

Single-Walled Carbon Nanotube as a Unique Scaffold for the Multivalent Display of Sugars

Lingrong Gu, Pengju G. Luo, Haifang Wang,† Mohammed J. Meziani, Yi Lin, L. Monica Veca, Li Cao, Fushen Lu, Xin Wang, Robert A. Quinn, Wei Wang, Puyu Zhang, Sebastian Lacher, and Ya-Ping Sun*

Department of Chemistry and Laboratory for Emerging Materials and Technology, Clemson University, Clemson, South Carolina 29634-0973

Received April 13, 2008; Revised Manuscript Received July 17, 2008

Single-walled carbon nanotube (SWNT) is a pseudo-one-dimensional nanostructure capable of carrying/displaying a large number of bioactive molecules and species in aqueous solution. In this work, a series of dendritic β-D-galactopyranosides and α-D-mannopyranosides with a terminal amino group were synthesized and used for the functionalization of SWNTs, which targeted the defect-derived carboxylic acid moieties on the nanotube surface. The higher-order sugar dendrons were more effective in the solubilization of SWNTs, with the corresponding functionalized nanotube samples of improved aqueous solubility characteristics. Through the functionalization, the nanotube apparently serves as a unique scaffold for displaying multiple copies of the sugar molecules in pairs or quartets. Results on the synthesis and characterization of these sugar-functionalized SWNTs and their biological evaluations in binding assays with pathogenic *Escherichia coli* and with *Bacillus subtilis* (a nonvirulent simulant for *Bacillus anthracis* or anthrax) spores are presented and discussed.

Introduction

Multivalent carbohydrate ligands are known to be considerably more potent than their monovalent counterparts in biological ligand−receptor interactions.[1,2] Therefore, there has been growing recent interest in various multivalent ligands and their associated configurations for a wide range of applications,[3] including the development of high-affinity inhibitors and drugs.[2] Among more extensively studied scaffolds for the display of multivalent carbohydrate ligands are dendrimers,[4] linear and polydispersed polymers,[5] metal nanoparticles,[6] polymeric nanospheres,[7,8] and so on. For example, Stoddart and co-workers synthesized a highly branched carbohydrate dendrimer containing 3−36 peripheral α-D-mannose copies and evaluated their binding affinity to Con A lectin.[9] Disney et al. reported the use of a carbohydrate-conjugated fluorescent polymer, poly(*p*-phenylene ethynylene), to detect pathogenic *Escherichia coli*.[10] For the binding with *E. coli*, Wu and co-workers attached α-D-mannose moieties to gold nanoparticles to target selectively the type 1 pili of the ORN178 strain.[6a] Qu, et al. developed sugar-coated polystyrene nanobeads for the binding and agglutination of *E. coli* cells.[7]

Single-walled carbon nanotubes (SWNTs) have attracted much recent attention for potential biological applications,[11−18] including their functionalization with various bioactive species such as carbohydrates,[12] DNAs,[13] proteins,[14] and peptides.[15] The unique pseudo-one-dimensional structure of a SWNT has been exploited to serve as a linear and semiflexible nanoscale carrier for displaying multiple copies of biomolecules in specific interactions with cells. A representative example is due to Elkin et al.,[16] who used the bovine serum albumin-functionalized SWNTs in conjugation with *E. coli*-specific antibody to capture the pathogen in physiological solution. In another example, Gu et al. solubilized SWNTs via covalent functionalization with the derivatized 2-aminoethyl-β-D-galactopyranoside (Scheme 1) in likely the amidation of nanotube-bound carboxylic acids.[17] These β-D-galactose-functionalized nanotubes (Gal-SWNT), each displaying multiple copies of the sugar, were found to have adhesion to pathogenic *E. coli* O157:H7 to result in significant cell agglutination.[17] Recently, Wang et al. found that monosaccharides (β-D-galactoses or α-D-mannoses)-functionalized SWNTs bind to and aggregate effectively *Bacillus anthracis* (Sterne) spores in the presence of a divalent cation (such as Ca^{2+}) and that the binding is unique to the nanotube-displayed carbohydrates.[18]

In the functionalization of nanotubes with tethered β-D-galactoses and α-D-mannoses, the carboxylic acid moieties on the nanotubes, which are resulted from the oxidation of the surface defects, have been targeted.[19] With limited defect sites on the nanotube surface, a higher population of multivalent ligands could be attained by using sugar dendrons (Scheme 1) in the nanotube functionalization. The resulting larger number of displayed ligands per nanotube also corresponds to significantly improved aqueous solubility of the functionalized nanotube samples,[20] which not only enhances biocompatibility but also enables more quantitative characterization for a better understanding of the structural details on the nanotubes displaying multivalent carbohydrate ligands. Here we report the synthesis and characterization of dendritic β-D-galactopyranosides and α-D-mannopyranosides for the functionalization of SWNTs (Scheme 1). As the functionality varies from mono- or bis- to tetra-, the population of the sugar moieties in the functionalized nanotube sample increases, as are improved solubility and related properties. Results from the biological evaluation of these sugar-functionalized SWNTs in binding assays with pathogenic *E. coli* and with *Bacillus subtilis* (a nonvirulent simulant for *Bacillus anthracis* or anthrax) spores are presented and discussed.

* To whom correspondence should be addressed. E-mail: syaping@clemson.edu.

† On leave from College of Chemistry and Molecular Engineering, Peking University, Beijing, China.

10.1021/bm800395e CCC: $40.75
Published on Web 08/20/2008

Scheme 1. Carbon Nanotubes Functionalized with Gal-, Man-, or their Dendrons

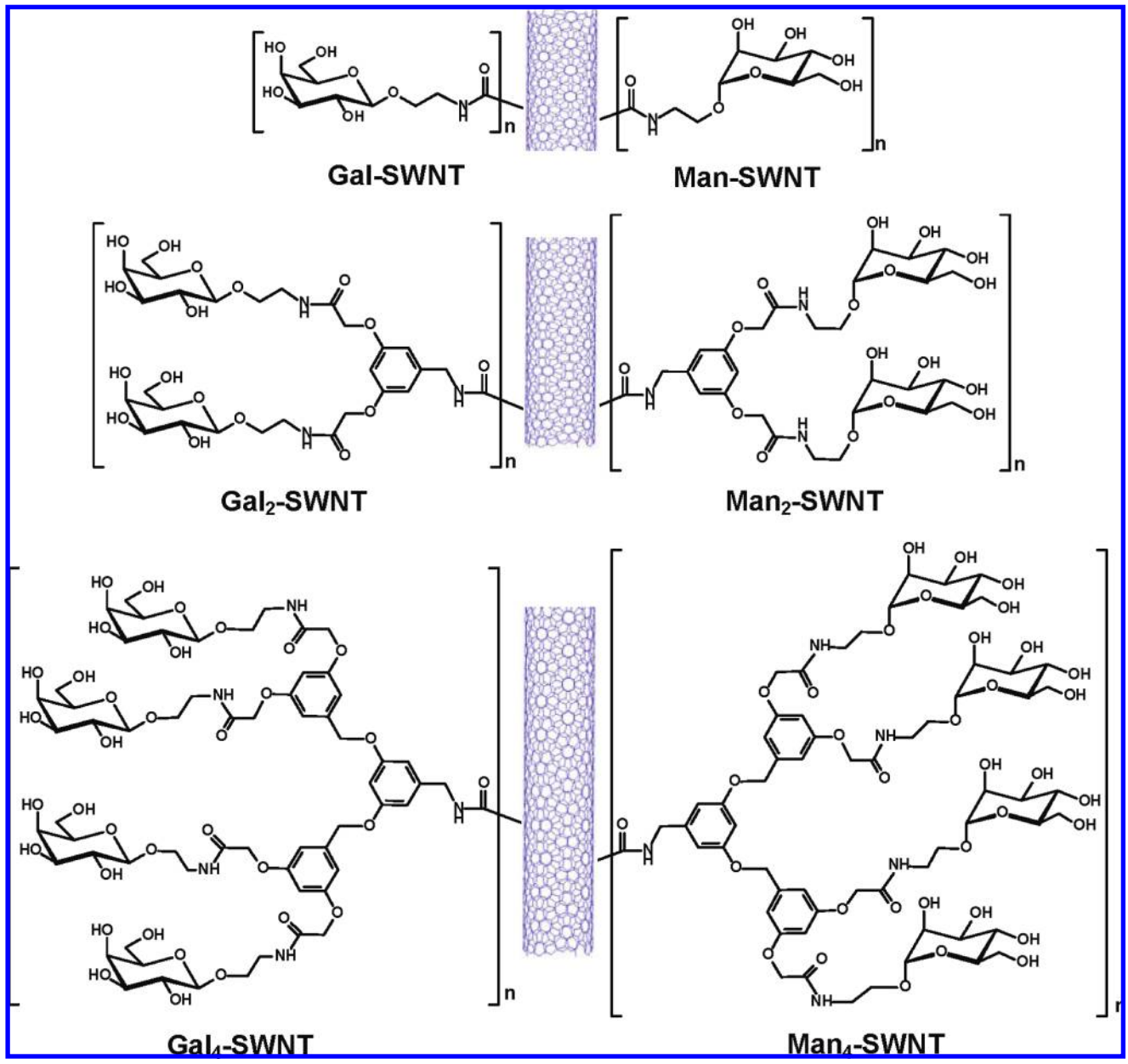

Experimental Section

Materials. *t*-Butyl bromoacetate, *N*-hydroxy-succinimide, triphenylphosphine, trifluoroacetic acid (TFA), palladium (10 wt % on activated carbon), and Amberlite IR-120 (plus) ion-exchange resin were purchased from Sigma-Aldrich. 3,5-Dihydroxybenzyl alcohol, 18-crown-6, *N*,*N*′-dicyclohexyl-carbodiimide, β-D-galactose-pentaacetate, α-D-mannose, and anthrone were obtained from Acros. *N*-Bromosuccinimide was supplied by ACOCADO Research Chemicals, Ltd. Solvent grade THF was dried and distilled over molecular sieves and then distilled over sodium before use. Other solvents were either spectrophotometry/HPLC grade or purified via simple distillation. Deuterated NMR solvents were obtained from Cambridge Isotope Laboratories.

The SWNT sample from the arc-discharge production was supplied by Carbon Solutions, Inc. It was purified by using a combination of thermal oxidation and oxidative acid treatment. In a typical experiment, a nanotube sample (1 g) was thermally oxidized in air in a furnace at 300 °C for 30 min. After the thermal treatment, the remaining sample was added to an aqueous HNO_3 solution (2.6 M), and the mixture was refluxed for 48 h. Upon centrifuging at 1380 *g* (Fisher Scientific Centric 228 Centrifuge), the supernatant was discarded and the remaining solids were washed with deionized water until neutral pH and then dried under vacuum. Acid−base titration was used to estimate the population of carboxylic acid groups in the purified sample. Briefly, a portion of the sample was stirred in aqueous $NaHCO_3$ solution (0.05 M, 50 mL) for 3 days. Then, the nanotubes were removed via vigorous centrifuging, and the remaining solution was diluted 1-to-5. One aliquot (50 mL) was mixed with aqueous HCl solution (0.05 M, 10 mL), and the mixture was boiled for 30 min to remove CO_2 completely, followed by the titration of the excess HCl with aqueous NaOH (0.05 M).

Measurements. NMR measurements were carried out on a JEOL Eclipse +500 NMR spectrometer and a Bruker Advance 500 NMR spectrometer equipped with a high-resolution magic-angle-spinning (HR-MAS) probe designed specifically for gel-phase NMR. Matrix-assisted laser desorption ionization-time-of-flight (MALDI-TOF) MS was performed on a Bruker AutoFlex system, and 2,5-dihydroxybenzoic acid was used as the sample matrix. Thermogravimetric analysis (TGA) results were obtained on a TA Instruments Q500 TGA, with a scanning rate of 10 °C/min for measurements in nitrogen or air. Optical absorption spectra were recorded on a Shimadzu UV3600 UV/vis/NIR

Scheme 2. Syntheses of Various Sugar Dendrons

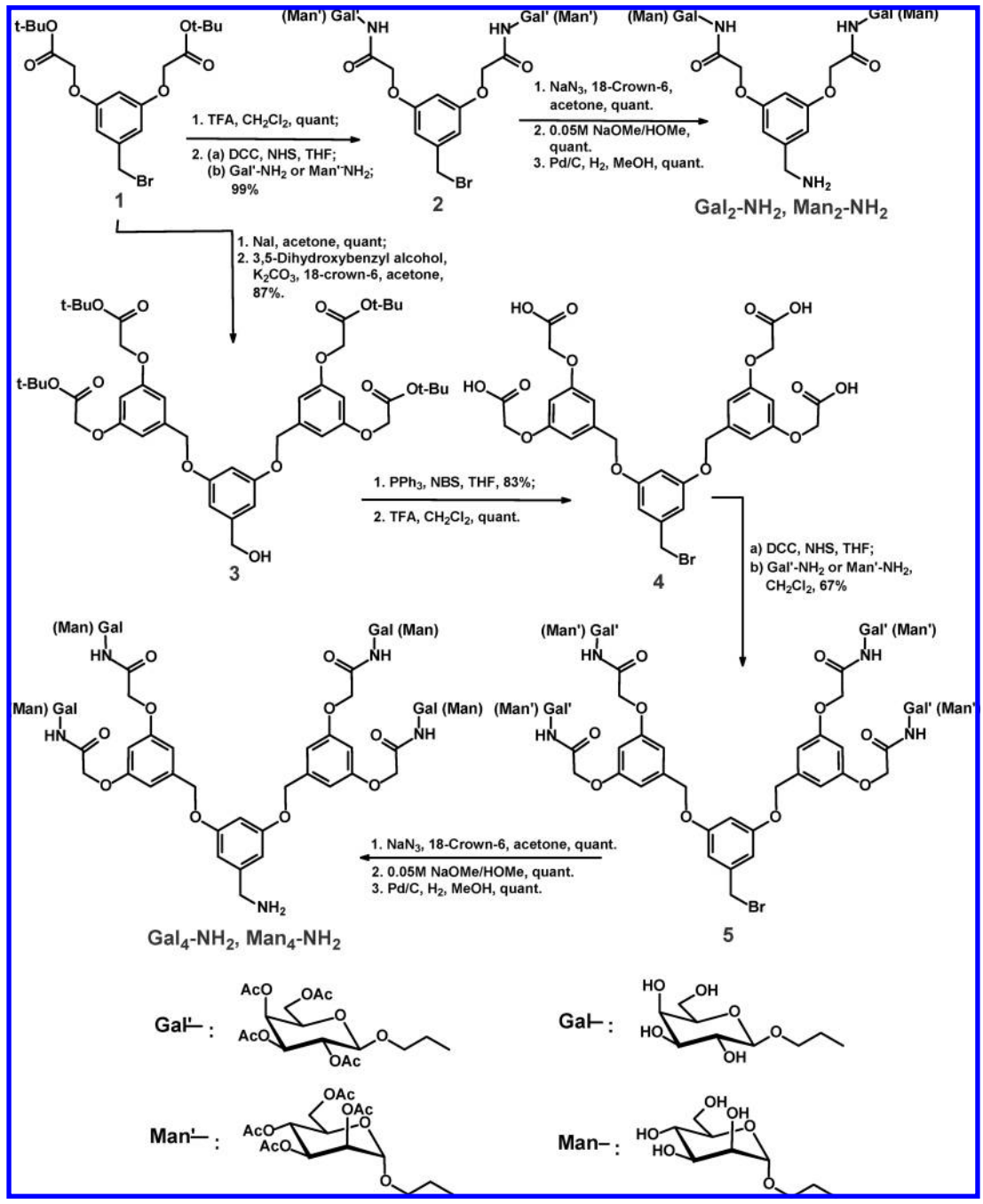

spectrophotometer. Raman spectra were measured on a Johin Yvon T64000 Raman spectrometer equipped with a Melles-Griot 35 mW He:Ne laser source for 633 nm excitation, a triple monochromator, a research grade Olympus BX-41 microscopy and a liquid nitrogen-cooled symphony detector. Optical microscopy measurements were performed on a Zeiss Axiovert 135 fluorescence microscope. Scanning electron microscopy (SEM) images were obtained on a Hitachi S4800 field-emission SEM system and a Hitachi HD-2000 TEM/STEM system.

Sugar Dendrons. The sugar monomers (Gal- and Man-) were prepared using procedures already available in the literature (Supporting Information).[22] For the sugar dendrons, the compound **1** (Scheme 2) was synthesized from *t*-butyl bromoacetate (through iodide substitution) and 3,5-dihydroxybenzyl alcohol also according to procedures already reported in the literature (Supporting Information).[23]

Compound 2. A solution of **1** (1.51 g, 3.5 mmol) in dry CH_2Cl_2 (10 mL) was prepared, and at 0 °C, trifluoroacetic acid (4 mL) was added. The mixture was warmed back to room temperature and stirred for 12 h. The precipitate was collected via filtration and then dried in a vacuum oven to yield the hydrolyzed product **1′** as a white solid (1.1

Table 1. Results on Man-, Man_2-, and Man_4- in Functionalization/Solubilization of SWNTs

molar ratio of sugar−NH_2 to nanotube−COOH	starting SWNTs solubilized[a] (%)		
	Man-	Man_2-	Man_4-
1:1	7.5		
2:1	13		
4:1	20		
5:1	24		
6:1	23		
20:1	24		
100:1	22	35	50

[a] Some might argue that nanotubes are dispersed, not solubilized. However, in the literature, the kind of functionalization used in this work is generally referred to as solubilization.

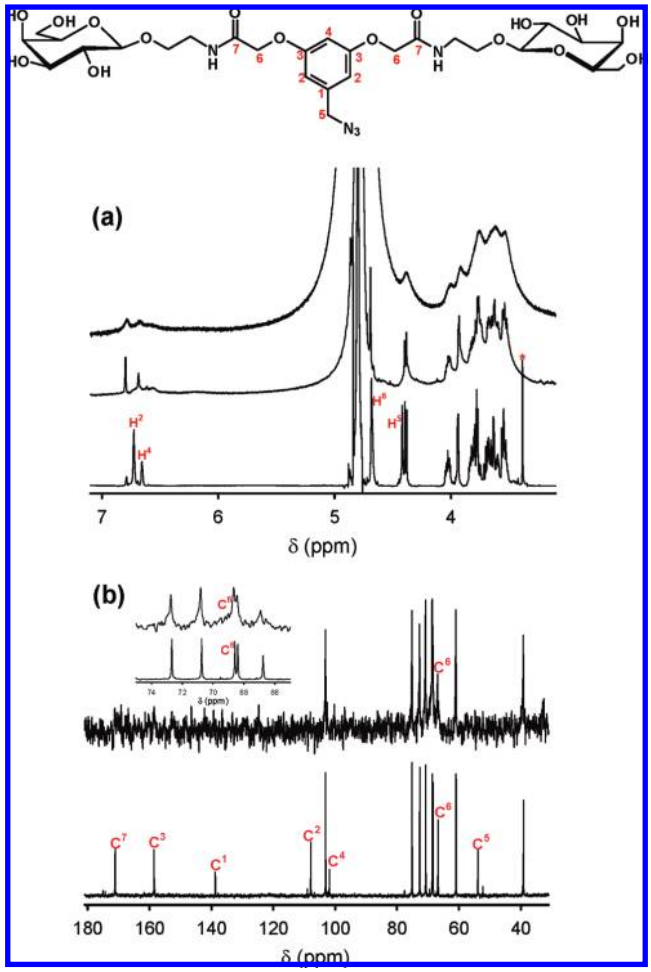

Figure 1. Comparisons for (a) the ^{1}H NMR spectra of Gal_2-SWNT (top, solution phase; middle, gel phase) and Gal_2-N_3 (bottom); and (b) the ^{13}C NMR spectra of Gal_2-SWNT (top, with inset) and Gal_2-N_3 (bottom), all in D_2O. The peak marked with * was due to residual methanol in the sample.

g, quantitative). ^{1}H NMR (500 MHz, CD_3OD) δ 6.66 (d, 2H), 6.51 (t, 1H), 4.67 (s, 4H), 4.51 (s, 2H) ppm; ^{13}C NMR (125.7 MHz, CD_3OD) δ 170.96, 159.22, 140.54, 108.13, 101.56, 64.62, 32.26 ppm.

At 0 °C, a solution of *N*,*N*′-dicyclohexyl-carbodimide (990.3 mg, 4.8 mmol) in dry THF (20 mL) was added dropwise over 30 min to another THF solution (30 mL) of **1′** (638.7 mg, 2 mmol) and *N*-hydroxy-succinimide (552.4 mg, 4.8 mmol). The mixture was warmed back to room temperature and stirred in the dark for 12 h. The precipitated urea was removed via filtration, and the remaining solution was slowly dropped into a CH_2Cl_2 solution (20 mL) of freshly prepared Gal′-NH_2 (2.0 g, 4.8 mmol).[20] After stirring for 12 h and then solvent removal, the reaction mixture was separated on a silica gel column (first hexane−ethyl acetate at 10/90 v/v, and then methanol−ethyl acetate at 5/95 v/v) to yield **2**(Gal′) as a white solid (2.13 g, 99%). ^{1}H NMR (500 MHz, $CDCl_3$) δ 6.96 (t, 2H, NH), 6.71 (d, 2H), 6.64 (t, 1H), 5.41 (dd, 2H), 5.23 (dd, 2H), 5.03 (dd, 2H), 4.52 (s, 4H), 4.51(d, 2H), 4.45 (s, 2H), 4.19−4.14 (m, 4H), 4.0−3.92 (m, 4H), 3.74−3.67 (m, 4H), 3.55−3.48 (m, 2H), 2.18 (s, 6H), 2.07 (s, 6H), 2.04 (s, 6H), 2.02 (s, 6H) ppm; ^{13}C NMR (125.7 MHz, $CDCl_3$) δ 170.36, 170.17, 170.10, 169.46, 167.68, 158.59, 140.84, 109.09, 102.38, 101.30, 70.86, 70.75, 68.79, 68.49, 67.51, 66.96, 61.25, 38.82, 32.65, 20.70, 20.65 (2C), 20.57 ppm. MALDI-TOF MS (M+Na+): 1089.37 (theoretically 1087.24).

The same procedure was applied to the synthesis of **2**(Man′) (2.13 g, 99%). ^{1}H NMR (500 MHz, $CDCl_3$): δ 7.08 (t, 2H, NH), 7.01 (d, 2H), 6.59 (t, 1H), 5.37 (dd, 2H), 5.31−5.27 (m, 4H), 4.87 (d, 2H), 4.55 (s, 4H), 4.46 (s, 2H), 4.28−4.25 (dd, 2H), 4.15−4.12 (m, 2H), 4.00−3.97 (m, 2H), 3.88−3.85 (m, 2H), 3.71−3.64 (m, 2H), 3.63−3.57

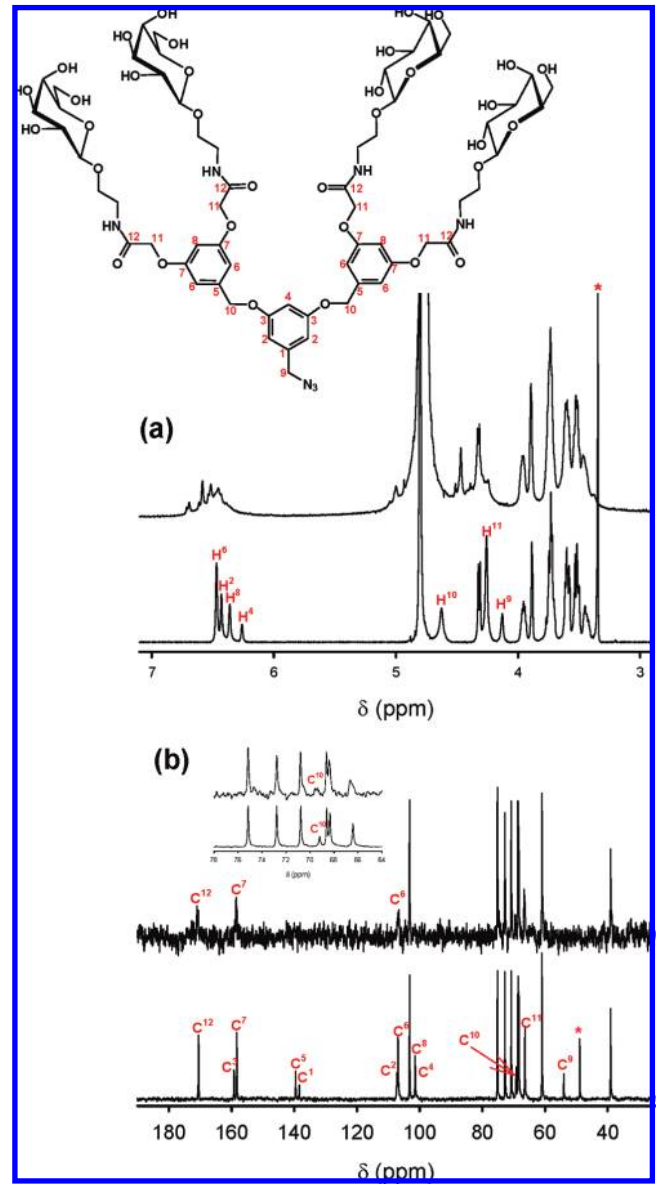

Figure 2. Comparisons for (a) the ^{1}H NMR spectra of Gal_4-SWNT (top) and Gal_4-N_3 (bottom); and (b) the ^{13}C NMR spectra of Gal_4-SWNT (top, with inset) and Gal_4-N_3 (bottom), all in D_2O. The peaks marked with * were due to residual methanol in the sample.

(m, 4H), 2.18 (s, 6H), 2.12 (s, 6H), 2.05 (s, 6H), 2.00 (s, 6H) ppm; ^{13}C NMR (125.7 MHz, $CDCl_3$): δ 170.63, 170.09, 170.06, 169.68, 167.83, 158.43, 140.75, 108.99, 102.09, 97.58, 69.36, 68.96, 68.92, 67.25, 66.82, 66.05, 62.52, 38.38, 32.66, 20.85, 20.70 (2C), 20.61 ppm. MALDI-TOF MS (M + Na^+): 1088.54 (theoretically 1087.24).

Gal_2-N_3 and Man_2-N_3. The azide substitution and deprotection reactions of **2** were similar to those reported previously,[20] yielding quantitatively Gal_2-N_3 [^{1}H NMR (500 MHz, CD_3OD) δ 6.65−6.63 (m, 3H), 4.50 (s, 4H), 4.29 (s, 2H), 4.19 (d, 2H), 3.95−3.86 (m, 2H), 3.80−3.78 (dd, 2H), 3.72−3.62 (m, 6H), 3.57−3.38 (m, 10H) ppm; ^{13}C NMR (125.7 MHz, CD_3OD) δ 169.58, 159.17, 138.59, 107.72, 103.86, 101.72, 75.38, 73.49, 71.15, 68.89, 68.14, 66.99, 61.14, 53.94, 39.00 ppm. MALDI-TOF MS (M + Na^+): 714.83 (theoretically, 714.24)] and Man_2-N_3 [^{1}H NMR (500 MHz, CD_3OD) δ 6.66−6.65 (m, 3H), 4.74 (d, 2H), 4.54 (s, 4H), 4.33 (s, 2H), 3.81−3.74 (m, 6H), 3.69−3.64 (m, 4H), 3.61−3.51 (m, 8H), 3.48−3.43 (m, 2H) ppm; ^{13}C NMR (125.7 MHz, CD_3OD) δ 169.70, 159.18, 138.71, 107.72, 101.65, 101.33, 73.51, 71.23, 70.73, 67.26, 67.01, 65.73, 61.58, 54.02, 38.62 ppm. MALDI-TOF MS (M^+): 690.77 (theoretically, 691.25)]. These compounds were relatively stable, and they were freshly reduced to Gal_2-NH_2 and Man_2-NH_2 before the nanotube functionalization reaction.

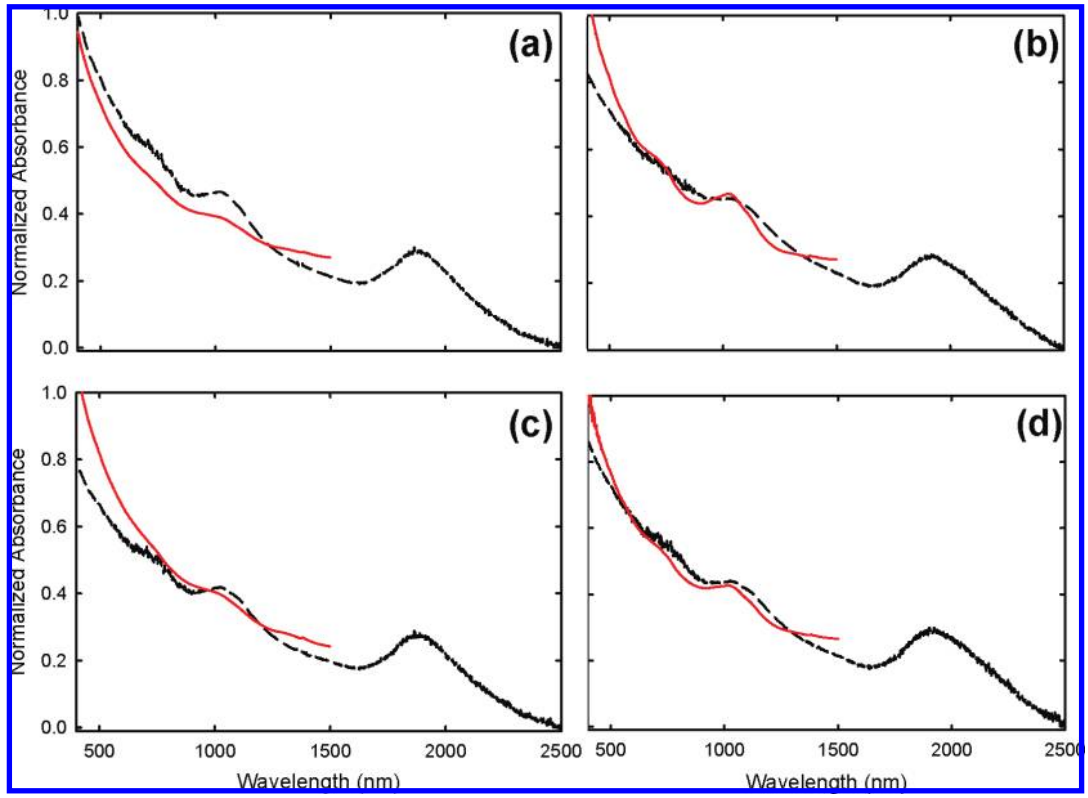

Figure 3. Optical absorption spectra of (a) Gal_2-SWNT; (b) Gal_4-SWNT; (c) Man_2-SWNT; and (d) Man_4-SWNT in D_2O solution (solid line) and in the solid-state on glass substrate (dashed line). For the spectral comparison between solution-phase and solid-state, the spectra in each corresponding pair were normalized by multiplying factors to the spectra to make their absorbance values the same at a selected wavelength (1000 nm for Man_2-SWNT as an example).

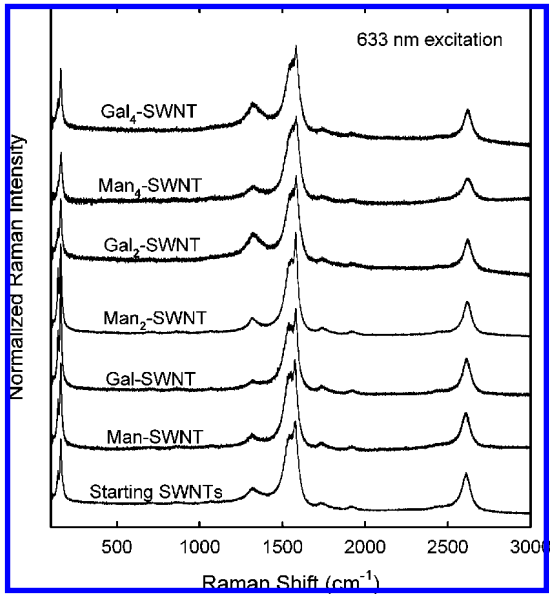

Figure 4. Raman spectra (633 nm excitation) of the functionalized SWNTs and the starting purified nanotube sample are compared.

Compound 3. There were two steps (Scheme 2), with the first step being the conversion of the bromide in **1** to iodide (**1″**). Compound **1** (3.018 g, 7 mmol) and sodium iodide (10 g, 67 mmol) were refluxed in acetone (50 mL) for 12 h. The reaction mixture was allowed to cool, and then the solvent was evaporated completely. The residue was partitioned between water and chloroform. The organic layer was collected and dried with anhydrous $MgSO_4$, followed by the removal of solvent to yield **1″** (3.56 g, quantitative). ^{1}H NMR (500 MHz, $CDCl_3$) δ 6.53 (d, 2H), 6.37 (t, 1H), 4.48 (s, 4H), 4.35 (s, 2H), 1.50 (s, 18H)

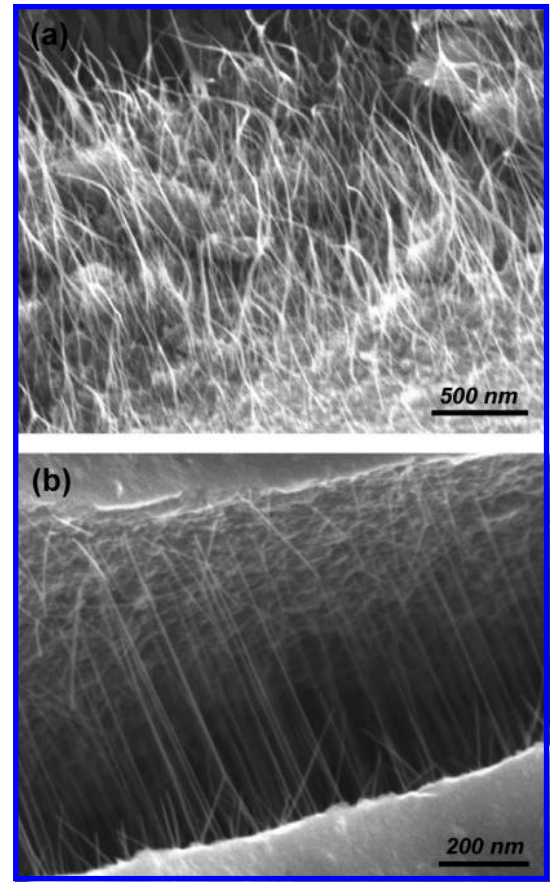

Figure 5. SEM images of a Gal_2-SWNT specimen (ultrathin film): (a) at the edge of the specimen and (b) in the fractured portion of the specimen.

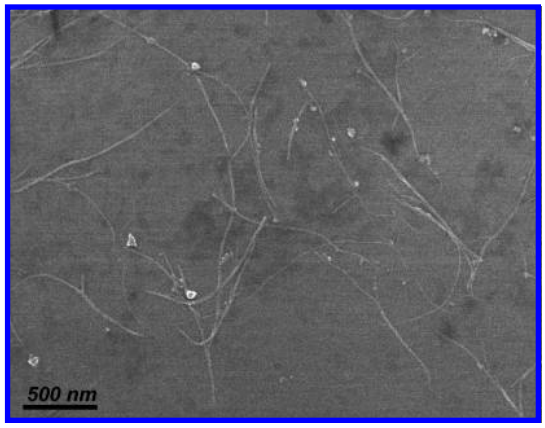

Figure 6. SEM image of the Gal_4-SWNT specimen (on carbon-coated cupper grid) prepared from a very dilute sample solution.

ppm; ^{13}C NMR (125.7 MHz, $CDCl_3$) δ 167.74, 159.17, 141.42, 108.16, 101.75, 82.64, 65.80, 28.16, 5.14 ppm.

In the second step, a solution of 3,5-dihydroxybenzyl alcohol (490 mg, 3.5 mmol), K_2CO_3 (2 g, 14 mmol), and 18-crown-6 (172 mg, 0.7 mmol) in acetone (30 mL) was prepared, and to the solution was added **1″** (3.56 g, 7 mmol). After refluxing for 36 h and then solvent removal, the reaction mixture was partitioned between water and ethyl acetate. The aqueous portion was repeatedly extracted with ethyl acetate. The combined ethyl acetate solution was dried with anhydrous $MgSO_4$, followed by silica gel column (hexane−ethyl acetate at 1:1.5) separation to obtain **3** (2.55 g, 87% yield). ^{1}H NMR (500 MHz, $CDCl_3$) δ 6.56 (d, 4H), 6.55 (d, 2H), 6.45 (t, 1H), 6.40 (t, 2H), 4.93 (s, 4H), 4.60 (s, 2H), 4.47 (s, 8H), 1.46 (s, 36H) ppm; ^{13}C NMR (125.7 MHz, $CDCl_3$) δ 167.87, 159.95, 159.24, 143.88, 139.60, 106.48, 105.72, 101.40, 101.23, 82.49, 69.71, 65.76, 65.03, 28.09 ppm. MALDI-TOF MS ($M + Na^+$): 863.29 (theoretically, 863.38).

Compound 4. The first step was to convert the benzyl alcohol in **3** to benzyl bromide (**3′**). Compound **3** (3.075 g, 3.675 mmol) was added to a THF (20 mL) solution of triphenyl phosphine (1.44 g, 5.5 mmol). After stirring for 7 min, *N*-bromosuccinimide (979 mg, 5.5 mmol) was added and the mixture was stirred for 5 min more. Water was added to quench the reaction. The crude product was extracted with chloroform three times. The organic fraction was dried with anhydrous $MgSO_4$, condensed, and purified by silica gel chromatography with hexane−ethyl acetate (3/1 v/v) as eluent. Compound **3′** was obtained as a white solid (2.76 g, 83% yield). ^{1}H NMR (500 MHz, $CDCl_3$) δ 6.59 (d, 2H), 6.58 (d, 4H), 6.47 (t, 1H), 6.44 (t, 2H), 4.93 (s, 4H), 4.49 (s, 8H), 4.39 (s, 2H), 1.48 (s, 36H) ppm; ^{13}C NMR (125.7 MHz, $CDCl_3$) δ 167.72, 159.89, 159.27, 139.84, 139.27, 108.25, 106.47, 102.16, 101.50, 82.36, 69.81, 65.79, 33.44, 28.04 ppm. MALDI-TOF MS ($M + Na^+$): 927.31 (theoretically, 925.30).

A solution of **3′** (2.4 g, 2.6 mmol) in CH_2Cl_2 (20 mL) was prepared, and at 0 °C, trifluoroacetic acid (4 mL) was added. The mixture was warmed back to room temperature and stirred for 12 h. The precipitate was collected by vacuum filtration and then dried in a vacuum oven to yield **4** as a white solid (1.78 g, quantitative). ^{1}H NMR (500 MHz, CD_3OD) δ 6.68 (d, 2H), 6.67 (t, 4H), 6.56 (t, 1H), 6.51 (t, 2H), 5.02 (s, 4H), 4.66 (s, 8H), 4.49 (s, 2H) ppm; ^{13}C NMR (125.7 MHz, CD_3OD) δ 171.07, 159.98, 159.33, 140.35, 139.87, 108.29, 106.21, 101.81, 101.03, 69.42, 64.65, 32.59 ppm. MALDI-TOF MS ($M + Na^+$): 703.19 (theoretically, 701.05).

5(Gal′) and 5(Man′). A total of two THF solutions (10 mL each) were prepared, with one for **4** (340 mg, 0.5 mmol) and *N*-hydroxysuccinimide (345 mg, 3 mmol) and the other for *N*,*N*′-dicyclohexylcarbodiimide (619 mg, 3 mmol). At 0 °C, the second solution was added to the first dropwise over 30 min. The reaction mixture was gradually warmed to room temperature and stirred in the dark for 12 h. The insoluble urea was removed by filtration, and the filtrate was slowly dropped into a CH_2Cl_2 solution (20 mL) of freshly prepared Gal′-NH_2 (1.0 g, 2.4 mmol).[20] After stirring for 12 h and then solvent removal, the reaction mixture was separated on silica gel column (first hexane−ethyl acetate at 1:9 and then methanol−ethyl acetate at 1:9) to afford **5**(Gal′) as white solids (728 mg, 67% yield). ^{1}H NMR (500 MHz, $CDCl_3$) δ 6.94 (t, 4H, NH), 6.66 (d, 4H), 6.59 (d, 2H), 6.58 (d, 2H), 6.48 (t, 1H), 5.31 (d, 4H), 5.13 (dd, 4H), 4.98−4.92 (m, 8H), 4.44 (s, 8H), 4.42 (d, 4H), 4.36(s, 2H), 4.10−4.02 (m, 8H), 3.90−3.82 (m, 8H), 3.68−3.56 (m, 8H), 3.46−3.40 (m, 4H), 2.07 (s, 12H), 1.97 (s, 12H), 1.94 (s, 12H), 1.92 (s, 12H) ppm; ^{13}C NMR (125.7 MHz, $CDCl_3$) δ 170.44, 170.26, 170.18, 169.55, 167.89, 158.79, 158.71, 140.13, 140.02, 108.31, 107.03, 102.20, 102.16, 101.29, 70.83, 70.77, 69.59, 68.78, 68.55, 67.47, 67.00, 61.31, 38.85, 33.40, 20.75, 20.72, 20.70, 20.65 ppm. MALDI-TOF MS ($M + Na^+$): 2195.56 (theoretically, 2193.60).

The same procedure was applied to the synthesis of **5**(Man′) (1.37 g, 63% yield). ^{1}H NMR (500 MHz, $CDCl_3$) δ 7.06 (t, 4H, NH), 6.68 (d, 4H), 6.60 (d, 2H), 6.56 (t, 2H), 6.50 (t, 1H), 5.32−5.29 (tt, 4H), 5.24−5.18 (m, 8H), 4.97 (s, 4H), 4.81 (s, 4H), 4.50 (s, 8H), 4.38(s, 2H), 4.23−4.19 (m, 4H), 4.09−4.03 (tt, 4H), 3.95−3.92 (m, 4H), 3.82−3.78 (m, 4H), 3.66−3.49 (m, 12H), 2.11 (s, 12H), 2.06 (s, 12H), 1.96 (s, 12H), 1.94 (s, 12H) ppm; ^{13}C NMR (125.7 MHz, $CDCl_3$) δ 170.73,, 170.15 (2C), 169.77, 168.00, 159.85, 158.60, 140.09, 139.95, 108.30, 107.05, 102.20, 101.96, 97.65, 69.60, 69.42, 69.03, 68.92, 67.31, 66.91, 66.10, 62.56, 38.47, 33.48, 20.94, 20.79, 20.76, 20.66 ppm. MALDI-TOF MS ($M + Na^+$): 2194.28 (theoretically, 2193.60).

Gal_4-N_3 and Man_4-N_3. The first step was to convert the bromide in **5** to azide (Gal′$_4$-N_3 and Man′$_4$-N_3). For Gal′$_4$-N_3, a solution of **5**(Gal′) (728 mg, 0.34 mmol) in acetone (20 mL) was prepared, and to the solution was added sodium azide (0.22 g, 3.4 mmol) and 18-crown-6 (54 mg, 0.2 mmol). The mixture was refluxed for 12 h and then cooled to room temperature. The solvent was evaporated, and the residue was partitioned between water and ethyl acetate. The aqueous layer was extracted with ethyl acetate twice. All of the ethyl acetate fractions were combined and dried with anhydrous $MgSO_4$. The solvent was evaporated, and the residue was dried in a vacuum oven to yield Gal′$_4$-N_3 as a white solid (715 mg, quantitative). ^{1}H NMR (500 MHz, $CDCl_3$) δ 6.98 (t, 4H, NH), 6.65 (s, 4H), 6.59 (s, 2H), 6.52 (s, 1H), 6.50 (s, 2H), 5.32 (d, 4H), 5.13 (dd, 4H), 4.96 (s, 4H), 4.93 (d, 4H), 4.44 (s, 8H), 4.42 (d, 4H), 4.22 (s, 2H), 4.07 (d, 8H), 3.90−3.83 (m, 8H), 3.68−3.56 (m, 8H), 3.45−3.40 (m, 4H), 2.07 (s, 12H), 1.96 (s, 12H), 1.94 (s, 12H), 1.91 (s, 12H) ppm; ^{13}C NMR (125.7 MHz, $CDCl_3$) δ 170.47, 170.29, 170.19, 169.61, 167.97, 159.96, 158.70, 140.03, 137.98, 107.33, 106.97, 102.13, 101.89, 101.25, 70.81, 70.77, 69.57, 68.79, 68.53, 67.43, 67.01, 61.32, 54.69, 38.86, 20.75, 20.72, 20.70, 20.65 ppm. MALDI-TOF MS ($M + Na^+$): 2157.43 (theoretically, 2156.69). The same procedure was applied to the synthesis of Man′$_4$-N_3 (1.02 g, quantitative). ^{1}H NMR (500 MHz, $CDCl_3$) δ 7.01 (t, 4H, NH), 6.64 (d, 4H), 6.53 (t, 2H), 6.51 (t, 1H), 6.49 (d, 2H), 5.29−5.26 (dd, 4H), 5.22−5.17 (m, 8H), 4.95 (s, 4H), 4.78 (d, 4H), 4.46 (s, 8H), 4.20−4.17 (m, 6H), 4.03(dd, 4H), 3.93−3.89 (m, 4H), 3.79−3.74 (m, 4H), 3.63−3.57 (m, 4H), 3.57−3.46 (m, 8H), 2.08 (s, 12H), 2.02 (s, 12H), 1.93 (s, 12H), 1.91 (s, 12H) ppm; ^{13}C NMR (125.7 MHz, $CDCl_3$) δ 170.74, 170.16 (2C), 169.76, 168.00, 160.05, 158.51, 139.99, 137.95, 107.35, 107.00, 101.95, 101.89, 97.66, 69.59, 69.42, 69.03, 68.91, 67.30, 66.90, 66.10, 62.54, 54.77, 38.47, 20.95, 20.79, 20.75, 20.66 ppm. MALDI-TOF MS (M^+): 2134.08 (theoretically, 2133.69).

For Gal_4-N_3, a solution of Gal′$_4$-N_3 (715 mg, 0.334 mmol) in CH_3ONa/CH_3OH (0.05 M, 30 mL) was prepared. After the solution was stirred for 12 h, Amberlite IR-120(plux) ion-exchange resin was added to adjust the pH to 7.0. The resin was removed via filtration, and the solution was dried with anhydrous $MgSO_4$, followed by solvent evaporation to yield Gal_4-N_3 as a white solid (490 mg, quantitative). ^{1}H NMR (500 MHz, D_2O) δ 6.47 (s, 4H), 6.43 (s, 2H), 6.36 (s, 2H), 6.26 (s, 1H), 4.63 (s, 4H), 4.32 (d, 4H), 4.26 (s, 8H), 4.13 (s, 2H), 3.97−3.94 (m, 4H), 3.88 (d, 4H), 3.77−3.70 (m, 12H), 3.62−3.57 (m, 8H), 3.54−3.50 (m, 8H), 3.47−3.41 (m, 4H) ppm; ^{13}C NMR (125.7 MHz, D_2O) δ 170.53, 159.21, 158.31, 139.53, 138.37, 107.24, 106.85,

Table 2. Compositions in the Functionalized Nanotube Samples and Related Parameters

	sugar content[a] (%)	SWNT content[a] (%)	avg No. of nanotube carbon per sugar unit[b]	aqueous solubility (SWNT-equivalent, mg/mL)	starting SWNTs solubilized (%)
Gal-SWNT	45	43	14	0.83	11
Man-SWNT	47	42	13	0.84	22
Gal_2-SWNT	44	19	6	1.7	20
Man_2-SWNT	45	18	6	1.6	35
Gal_4-SWNT	37	23	9	3.1	27
Man_4-SWNT	35	29	11	4.3	50

[a] The remaining (100% − sugar content − SWNT content) is the content of linkers/tethers. [b] The degree of functionalization exceeding that for the estimated COOH population might be due to preferable solubilization of those nanotubes with more than average COOH contents and also some noncovalent but strong adsorption of the amines.

103.18, 101.40 (2C), 75.15, 72.77, 70.76, 69.19, 68.59, 68.33, 66.41, 60.95, 54.02, 39.07 ppm. MALDI-TOF MS ($M + Na^+$): 1484.50 (theoretically 1484.52). The same procedure was applied to the quantitative conversion of Man'_4-N_3 to Man_4-N_3. ^{1}H NMR (500 MHz, D_2O) δ 6.41 (s, 4H), 6.37 (s, 2H), 6.34 (s, 2H), 6.23 (s, 1H), 4.75 (s, 4H), 4.61 (s, 4H), 4.24 (s, 8H), 4.05 (s, 2H), 3.81 (m, 4H), 3.76 (d, 4H), 3.70−3.65 (m, 12H), 3.62−3.57 (m, 4H), 3.54−3.50 (m, 8H), 3.47−3.42 (m, 4H), 3.36−3.32 (m, 4H) ppm; ^{13}C NMR (125.7 MHz, D_2O) δ 169.42, 159.23, 158.34, 139.63, 138.36, 107.43, 106.79, 101.57, 101.30, 99.67, 72.88, 70.64, 70.10, 69.20, 66.69, 66.50, 65.70, 60.93, 54.02, 38.61 ppm. MALDI-TOF MS (M^+): 1461.38 (theoretically, 1461.53).

Nanotube Functionalization. Before the functionalization reaction, Gal_4-N_3 and Man_4-N_3 were reduced to Gal_4-NH_2 and Man_4-NH_2 by the classical palladium-catalyzed hydrogenation. At 0 °C, to a solution of Gal_4-N_3 or Man_4-N_3 (800 mg, 0.55 mmol) in methanol−H_2O (10 mL) was added Pd/C (10 wt % palladium on activated carbon, 70 mg). The reaction mixture was gradually warmed to room temperature and stirred with the purging of hydrogen gas for 4 h. The Pd/C was removed by filtration, and the filtrate was evaporated to obtain Gal_4-NH_2 or Man_4-NH_2.

In the functionalization of SWNTs with Gal_4-NH_2, a purified nanotube sample (20 mg) was mixed with 1-ethyl-3-(3-dimethylaminoprop-yl) carbodiimide (EDAC, 112 mg, 60 mmol) in aqueous KH_2PO_4 buffer (45 mL, pH = 7.4). Upon sonication for 2 h, the freshly prepared Gal_4-NH_2 (0.55 mmol) was added. After sonication for another 36 h, the reaction mixture was loaded into a membrane tubing (cutoff molecular weight ~ 12000) for dialysis against deionized water for 3 days. The suspension from the dialysis was centrifuged at 3000 *g* for 30 min to obtain a dark but optically transparent solution of Gal_4-SWNT. ^{1}H NMR (500 MHz, D_2O) 6.72 (broad), 6.61 (s, broad), 6.55 (broad), 6.50−6.40 (broad), 4.50 (s, broad), 4.35 (d, broad), 3.98 (s, broad), 3.93 (s, broad), 3.76 (s, broad), 3.64 (broad), 3.54 (broad), 3.50 (broad) ppm; ^{13}C NMR (125.7 MHz, D_2O) δ 170.99, 158.48, 106.61, 103.17, 75.14, 72.74, 70.77, 69.58, 68.60, 68.36, 66.60, 60.94, 39.06 ppm. Similarly, for Man_4-SWNT, ^{1}H NMR (500 MHz, D_2O) 6.5−6.2 (broad), 4.35−4.10 (broad), 3.91 (s, broad), 3.85 (d, broad), 3.77 (d, broad), 3.67 (t, broad), 3.55−3.40 (broad), 3.43 (broad) ppm; ^{13}C NMR (125.7 MHz, D_2O) δ 170.41, 159.19, 158.28, 139.46, 106.98, 101.21, 99.66, 72.87, 70.61, 70.10, 69.18, 66.70, 66.44, 65.66, 60.93, 38.58 ppm.

Sugar Test. The spectrophotometric method with the anthrone reagent was used to determine sugar contents.[21] In a typical experiment, a solution of sugar-functionalized SWNTs (50 μL) was mixed with deionized water (50 μL), HCl (37%, 1 mL), formic acid (0.1 mL), and anthrone reagent (8 mL, 0.2 mg/mL in 80% H_2SO_4). The solution mixture was kept in a boiling water bath for 12 min and then rapidly cooled in an ice bath for 30 min. The UV/vis absorption of the mixture was measured and corrected for the solution absorption preheating (before the coloring process). Separately, the standard sugar (β-D-galactose or α-D-mannose) solutions of known concentration (1.0 mg/mL) were prepared. Various aliquots of the standard solutions (0, 25, 50, 75, and 100 μL) were tested by using the same procedure above to establish standard curves, from which the sugar content in the functionalized nanotube sample was obtained.

Assay for *E. coli*. The green fluorescent protein (GFP)-expressing *E. coli* O157:H7/pWM1007 was transformed through electroporation.[24] The frozen *E. coli* samples were recovered and cultured on tryptic soy agar (TSA) plates supplemented with kanamycin (50 μg/mL). After overnight growth at 37 °C, the bacteria were harvested and washed with phosphate buffer solution (PBS) via the centrifuging-suspending cycle three times. Finally, the *E. coli* cells were suspended in PBS to an optical density of 0.6 at 600 nm (~10^8 cells/mL).

In cell adhesion and precipitation experiment, a suspension (25 μL) of *E. coli* O157:H7/pWM1007 cells was 2-fold serially diluted and incubated with a solution (10 μL) of either Gal-SWNT (0.14 mg/mL) or Gal_2-SWNT (0.13 mg/mL) for 3 h at room temperature with gentle inversions of the tubes at 15 min intervals. The precipitates at the tube bottom were collected and wet-mounted onto a glass slide for microscopy analyses.

For the colony-forming unit (CFU) reduction assay, the same procedure described above was used, and at the end of incubation the mixture was centrifuged with a low force (300 *g*) for 30 s. The supernatant was collected and 10-fold serially diluted. At each dilution, 100 μL was plated out (in triplicate) onto TSA agar plates by using spread plate technique. The plates were incubated overnight at 37 °C. CFU was counted, and the percentage of CFU reduction was calculated and compared to that of the control without the sugar-functionalized SWNTs.

Assay for *B. subtilis* Spores. *B. subtilis* spores (strain ATCC33234) were supplied by American type Culture Collection (Manassas, VA), and the spore suspension was prepared by following established procedures. In a typical binding experiment, an aqueous suspension of *B. subtilis* spores (40 μL, 2.6×10^8 CFU/mL) was mixed with a solution of α-D-mannose-functionalized SWNTs (40 μL, 0.2 mg/mL α-D-mannose equivalent concentration) or with distilled water (40 μL) as control, followed by the addition of aqueous $CaCl_2$ (20 μL, 100 mM). The mixtures (sample and control) were rotated for 12 h. A small aliquot (10 μL) of the sample (or control) was dropped onto a glass slide (covered with cover glass slide) for optical microscopy analyses.

Results and Discussion

The sugar dendrons Gal_2-NH_2, Man_2-NH_2, Gal_4-NH_2, and Man_4-NH_2 were prepared by using trisubstituted benzenes (3,5-dihydroxybenzyl alcohol and **1**) as building blocks in classical etherification and carbodiimide-activated amidation reactions (Scheme 2), with generally high product yields. The synthetic strategy was such that the dendritic framework was constructed first before being coupled with the amine-tethered monosaccharide. A significant advantage of the strategy was that sugar molecules were involved only in the end steps, thus difficulties associated with the sugar deprotection and stereohindrance were avoided.

The same carbodiimide-activated amidation was used in the functionalization of SWNTs with the dendrons, with the tethered

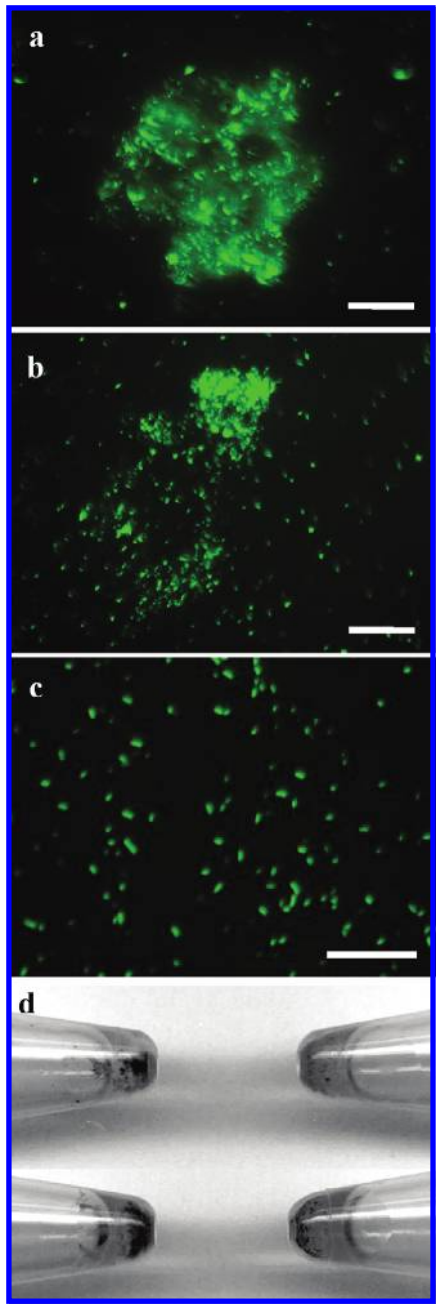

Figure 7. Fluorescence microscopy images (10 μm for all scale bars) on the agglutination of *E. coli* O157:H7 (GFP-expressing) cells by (a) Gal_2-SWNT, (b) Gal-SWNT, and (c) the control (cells only). (d) A visual comparison on the amount of precipitates (in centrifuge tubes) associated with the agglutination of *E. coli* O157:H7 cells (top, 5×10^7 cells/mL; bottom, 10^8 cells/mL) by Gal_2-SWNT (left) and Gal-SWNT (right).

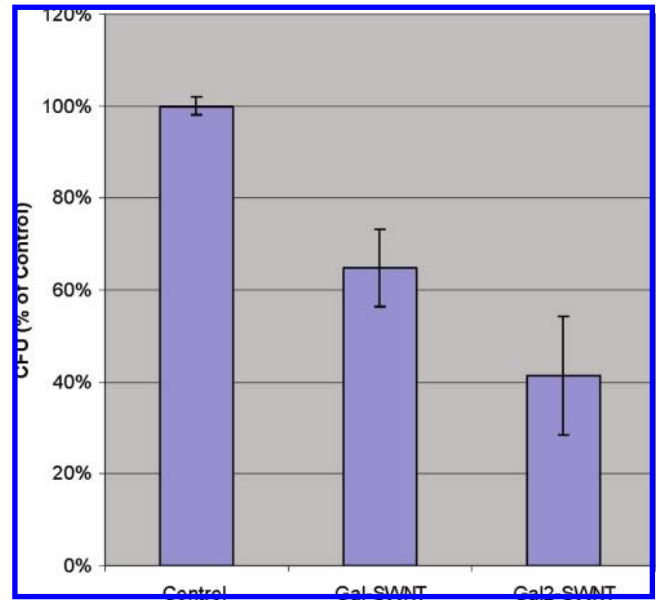

Figure 8. Results from the CFU reduction assay for *E. coli* O157:H7 in the presence of Gal_2-SWNT, Gal-SWNT, and PBS only as control.

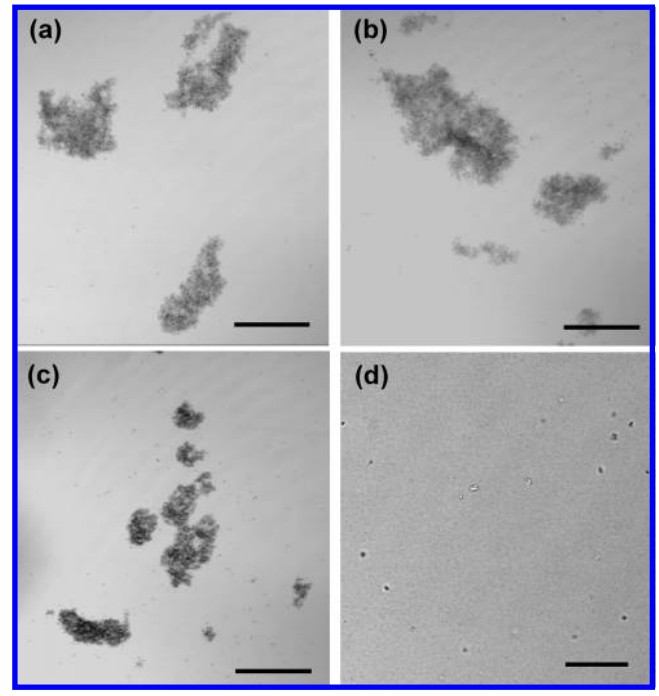

Figure 9. Optical microscopy images on the aggregation of *B. subtilis* spores by (a) Man-SWNT, (b) Man_2-SWNT, and (c) Man_4-SWNT in the presence of calcium cation (all scale bars = 75 μm). (d) The control with *B. subtilis* spores alone (scale bar = 20 μm).

amino groups coupling with the surface defects-derived carboxylic acids on the nanotubes.[19,25] The functionalization reaction was heterogeneous in nature, so that as typical an excess amount of the functionalization agent was used. For the functionalization with 2′-aminoethyl-α-D-mannopyranoside (Man-), the molar ratio of Man- to the nanotube-bound carboxylic acids (estimated at 5% mole fraction of the nanotube carbons based on titration results) was varied. The results in Table 1 show that the amount of SWNTs solubilized in the functionalization reached a plateau at the Man-to-acid molar ratio of 5 or so. Thus, at the molar ratio of 100, the amount of solubilized nanotubes should represent the limit for the functionalization agent under the otherwise defined experimental parameters and conditions. As shown in Table 1, the percentage of the starting purified SWNTs solubilized in the functionalization reaction increased from about 25% for Man- to 35% for Man_2- and to 50% for Man_4-. The higher-order sugar dendrons were obviously more effective in the functionalization and solubilization of SWNTs.

The sugar dendron-functionalized carbon nanotube samples, Gal_2-SWNT, Man_2-SWNT, Gal_4-SWNT, and Man_4-SWNT, are all readily soluble in water (see note in Table 1), allowing their being investigated with solution-phase techniques. The first was the characterization of the samples by NMR, both in solution and in the gel phase.[26] For example, the ^{1}H NMR spectra of

Gal_2-SWNT and Gal_2-N_3 in solutions are compared in Figure 1a. The signals of the nanotube sample are obviously significantly broader than those of the corresponding free dendron, which may be attributed to the high molecular weight and low mobility of carbon nanotubes.[26a] For the gel-phase NMR measurement of the same Gal_2-SWNT sample in a high resolution-magic angle spinning (HR-MAS) probe specifically for the gel-phase, the ^{1}H spectrum is better resolved, with the signal patterns in the sugar region comparable with those of the free dendron (Figure 1a). The aromatic proton signals for Gal_2-SWNT are slightly shifted downfield, 6.82 ppm and 6.70 ppm for the nanotube-bound dendron from 6.72 ppm and 6.66 ppm for the free dendron, respectively, which might be due to the formation of amide linkages affecting the aromatic ring in the close vicinity. The same effects could be responsible for the absence of the benzyl proton signal in the spectrum of Gal_2-SWNT because the proton is right next to the nanotube. This proton has a chemical shift of 4.36 ppm in the spectrum of Gal_2-N_3. It is known in the literature that the effect of large aromatic ring currents in carbon nanotubes on the local magnetic environment of protons in close proximity causes their resonance to either shift into the region where it is difficult to be identified or to become too broad to be detected.[26,27]

Similar ^{1}H NMR results, including effects on the signal broadening and shifting, were found for other dendron-functionalized SWNTs. Shown in Figure 2a is a similar comparison between the ^{1}H NMR spectra of Gal_4-SWNT and Gal_4-N_3 in solutions, and the comparison between Man_4-SWNT and Man_4-N_3 is largely the same.

^{13}C NMR spectra of the dendron-functionalized SWNTs, especially Gal_4-SWNT and Man_4-SWNT, were readily obtained in solution, unlike those of Gal-SWNT and Man-SWNT whose relatively poor solubility (thus low solution concentrations) made their ^{13}C NMR measurements rather difficult.[17] For the comparisons between Gal_2-SWNT and Gal_2-N_3 (Figure 1b) and between Gal_4-SWNT and Gal_4-N_3 (Figure 2b), there are signal broadening effects from free dendrons to those attached to SWNTs, though relatively less so from Gal_4-N_3 to Gal_4-SWNT as one would expect. There are Gal carbon resonances in both Gal_2-SWNT (Figure 1b) and Gal_4-SWNT (Figure 2b) spectra, and the latter also exhibits some of the tether carbon signals due to the higher solution concentration and perhaps also to these carbons being farther away from the nanotubes (less affected by their large ring currents[26a,27]).

The optical absorption spectra of the functionalized SWNTs were measured both in solution (only down to 1500 nm because of the overwhelming interference from D_2O beyond that) and in the solid state (samples deposited on the surface of glass slides). The S_{11} (~1880 nm) and S_{22} (~1050 nm) bands due to van Hove singularity transitions in semiconducting SWNTs[28] and the weak M_{11} transition (~740 nm) in metallic SWNTs were all present in the spectra of dendron-functionalized nanotube samples (Figure 3), suggesting the electronic properties of the nanotubes were largely preserved in the functionalization targeting defects-derived carboxylic acid moieties on the nanotube surface, as also observed in many other such functionalization schemes.[17,26] The solution spectra of Gal_4-SWNT and Man_4-SWNT were somewhat better resolved than their solid-state counterparts (Figure 3). For Gal_2-SWNT and Man_2-SWNT, the generally weaker absorption bands in the solution spectra were probably a simple result of their lower solubility (thus lower solution concentrations).

The sugar dendron-functionalized SWNTs were characterized by Raman with 633 nm excitation. Interestingly, unlike in other well-functionalized nanotube samples,[26,29] no substantial luminescence interference was observed. Thus, resonance Raman spectra could be measured for all of the dendron-SWNT samples without their being thermally or chemically defunctionalized first. As compared in Figure 4, the Raman spectra of the different dendron-SWNT samples are largely similar among themselves and also similar to that of the starting purified nanotube sample, exhibiting the typical radial breathing mode peaks around 140 and 160 cm^{-1}, D-band around 1300 cm^{-1}, tangential G-band around 1580 cm^{-1}, and D*-band around 2600 cm^{-1}.

Scanning electron microscopy (SEM) technique was used to examine the morphology of sugar dendron-functionalized nanotube samples. Shown in Figure 5 are SEM images for the Gal_2-SWNT sample, for which the specimen was prepared by drop-casting an ultrathin film from the sample solution. Abundant nanotubes were observed, with their being randomly oriented at the edge of the specimen (Figure 5a) but more ordered in the fractured portion of the same specimen (Figure 5b). For Gal_4-SWNT, a very dilute aqueous solution was used to prepare the SEM specimen (depositing a few drops and then evaporating the water). The image shows generally dispersed nanotubes (Figure 6).

The thermal defunctionalization behavior of the dendron-SWNT samples was very different from those of many other functionalized carbon nanotubes.[19,30] The functional groups (sugar dendrons) could not be removed from the nanotubes in thermogravimetric analysis (TGA) scans (under inert atmosphere to 800 °C) and, instead, they were carbonized under the thermal defunctionalization conditions. For TGA in air, the carbon nanotubes were burned at temperatures similar to those for the sugars. Therefore, the usually effective TGA estimate of nanotube contents in the functionalized samples was not applicable, and the compositions in dendron-SWNT samples were determined in terms of sugar analyses.

The sugar contents in the dendron-SWNT samples were quantified by spectrophotometry with the anthrone reagent.[21] Results thus obtained for the sample compositions are shown in Table 2. There are no meaningful differences in sample compositions between Gal- and Man-, Gal_2- and Man_2-, or Gal_4- and Man_4- as functional moieties, despite the fact that the Gal-based functionalization agents are consistently less effective (a lower percentage of starting purified SWNTs solubilized) than their Man-based counterparts in the nanotube solubilization (Table 2). The poorer solubilization performance of the Gal-based agents is probably due at least in part to the significantly lower (by a factor of 3 to 4) aqueous solubility of β-D-galactose than that of α-D-mannose.[31]

The known sample compositions also allow the calculation for the average number of nanotube carbons per sugar unit in the samples (Table 2). From Gal- (or Man-) to Gal_2- (or Man_2-), the number decreases significantly, namely, that more sugars are displayed on the same amount of SWNTs. For Gal_4-SWNT and Man_4-SWNT, even though there is no advantage in the number of sugars displayed (because of the relatively larger amount of tethering moieties for the display), the improved aqueous solubility and the specific configuration of β-D-galactoses or α-D-mannoses displayed in quartet may offer properties that are not available to other configurations.

It has been reported that Gal-SWNT binds to *E. coli* O157:H7 to result in significant cell agglutination.[17] The same assay was used to evaluate the binding of Gal_2-SWNT with the same *E. coli* strain. As shown in Figure 7, there was obviously significant aggregation of the cells in the presence of Gal_2-SWNT. The amount of aggregates (precipitates at the bottom

of the centrifuge tube) was larger for a higher starting *E. coli* concentration of 10^8 cells/mL than that of 5×10^7 cells/mL (Figure 7). Between Gal_2-SWNT and Gal-SWNT under similar experimental conditions, the amount of recovered aggregates was clearly larger in the former than in the latter (Figure 7). This was reflected more quantitatively in results from the CFU reduction assay. As compared in Figure 8, Gal_2-SWNT was obviously more effective in the agglutination of *E. coli* O157:H7 cells to result in a more significant CFU reduction. Mechanistically, the binding responsible for the cell agglutination is attributed to specific ligand−receptor interactions of the nanotube-displayed β-D-galactoses with *E. coli* surface galactose-binding-protein.[17] The more favorable binding by Gal_2-SWNT seems to suggest that the paired β-D-galactoses could be more effective in the specific interactions. However, the multivalent binding of carbohydrates with cell surface receptors is a complicated phenomenon.[1,2,32] A more definitive conclusion requires more systematic investigations with these and other assays.

The complexity with desired quantitative evaluations of the sugar-functionalized SWNTs in binding assays is also reflected in the results on *B. subtilis* spores. *B. subtilis* is a commonly used nonvirulent simulant for *Bacillus anthracis* (anthrax),[33] with surface expressed with various carbohydrates.[33] As reported previously for *B. anthracis* (Sterne) spores,[18] Man-SWNT also bound to *B. subtilis* spores for their significant aggregation in the presence of calcium cation (Figure 9). Similarly, Man_2-SWNT and Man_4-SWNT were both capable of binding and aggregating *B. subtilis* spores in the same assay, as also illustrated in Figure 9. However, a more quantitative comparison of the different α-D-mannose-functionalized SWNTs samples was hindered by other issues beyond simply the different displays of α-D-mannoses in Man_2-SWNT and Man_4-SWNT. For example, it was found that for Man_2-SWNT samples of somewhat different Man/nanotube ratios (from slight variations in reaction conditions in the synthesis) their bindings with the spores (and the associated degrees of aggregation) were obviously different. Such effects were more pronounced in the binding assay of Man_4-SWNT with *B. subtilis* spores in the presence of calcium cation. Especially for Man_4-SWNT samples of slightly higher Man/nanotube ratios, the binding assay resulted in well-dispersed aggregates of an irregular rod-like shape (20−50 μm in length and 5−10 μm in diameter according to optical microscopy analyses). We speculate that some of these complications might be due to the divalent cation-mediated interactions between the paired α-D-mannoses in Man_2-SWNT and Man_4-SWNT, which could be competing with the binding with cell surface receptors. Further investigations are required for a better understanding of the results.

Summary and Conclusion

A series of dendritic β-D-galactopyranosides and α-D-mannopyranosides with a terminal amino group were synthesized and used for the functionalization of SWNTs targeting the defect-derived carboxylic acid moieties on the nanotube surface. The functionalized nanotube samples were characterized by using established NMR, optical spectroscopy, and microscopy techniques. The results suggest that the higher-order sugar dendrons are more effective in the solubilization of SWNTs, with the corresponding functionalized nanotube samples of improved aqueous solubility characteristics, and that the nanotube is indeed a unique pseudo-one-dimensional scaffold for displaying multiple copies of the sugar molecules in pairs or quartets. These multivalent carbohydrate configurations may potentially offer interesting chemical and biochemical properties and functions, despite some of the complications that are yet to be understood (as reflected in the results of the binding assay with *B. subtilis* spores).

Acknowledgment. Financial support from NSF, NASA, South Carolina Space Grant Consortium, and the Center for Advanced Engineering Fibers and Films (CAEFF, an NSF-ERC at Clemson University) is gratefully acknowledged. R.A.Q. and S.L. were undergraduate research participants jointly sponsored by CAEFF and NSF-REU (DMR-0243734).

Supporting Information Available. Synthesis of Gal-N_3, Man-N_3, and compound **1**. This information is available free of charge via the Internet at http://pubs.acs.org.

References and Notes

(1) Mammen, M.; Choi, S. K.; Whitesides, G. M. *Angew. Chem., Int. Ed.* **1998**, *37*, 2755–2794.
(2) Choi, S. K. *Synthetic Multivalent Molecules: Concepts and Biomedical Applications*; John Wiley & Sons, Inc.: Hoboken, NY, 2004.
(3) Gestwicki, J. E.; Cairo, C. W.; Strong, L. E.; Oetjen, K. A.; Kiessling, L. L. *J. Am. Chem. Soc.* **2002**, *124*, 14922–14933.
(4) (a) Jayaraman, N.; Nepogodiev, S. A.; Stoddart, J. F. *Chem.—Eur. J.* **1997**, *3*, 1193–1199. (b) Lundquist, J. J.; Toone, E. J. *Chem. Rev.* **2002**, *102*, 555–578. (c) Cloninger, M. J. *Curr. Opin. Chem. Biol.* **2002**, *6*, 742–748.
(5) Kiessling, L. L.; Gestwicki, J. E.; Strong, L. E. *Curr. Opin. Chem. Biol.* **2000**, *4*, 696–703.
(6) (a) Lin, C.; Yeh, Y.; Yang, C.; Chen, C.; Chen, G.; Chen, C.; Wu, Y. *J. Am. Chem. Soc.* **2002**, *124*, 3508–3509. (b) Hernaiz, M. J.; de la Fuente, J. M.; Barrientos, A. G.; Penades, S. *Angew. Chem., Int. Ed.* **2002**, *41*, 1554–1557.
(7) (a) Qu, L.; Luo, P. G.; Taylor, S.; Lin, Y.; Huang, W.; Anyadike, N.; Tzeng, T.-R. J.; Stutzenberger, F.; Latour, R. A.; Sun, Y.-P. *J. Nanosci. Nanotechnol.* **2005**, *5*, 319–322. (b) Qu, L.; Gu, L.; Li, H.; Taylor, S.; Elkin, T.; Luo, P. G.; Tzeng, T.-R. J.; Jiang, X.; Latour, R. A.; Stutzenberger, F.; Williams, A.; Sun, Y.-P. *J. Biomed. Nanotechnol.* **2005**, *1*, 61–67.
(8) Molugu, S.; Qu, L.; Lin, Y.; Sun, Y.-P.; Tzeng, T.-R. J.; Stutzenberger, F.; Latour, R. A. *J. Biomed. Nanotechnol.* **2006**, *2*, 1–10.
(9) Ashton, P. R.; Hounsell, E. F.; Jayaraman, N.; Nilsen, T. M.; Spencer, N.; Stoddart, J. F.; Young, M. *J. Org. Chem.* **1998**, *63*, 3429–3437.
(10) Disney, M. D.; Zheng, J.; Swager, T. M.; Seeberger, P. H. *J. Am. Chem. Soc.* **2004**, *126*, 13343–13346.
(11) (a) Lin, Y.; Taylor, S.; Li, H.; Fernando, K. A. S.; Qu, L.; Wang, W.; Gu, L.; Zhou, B.; Sun, Y.-P. *J. Mater. Chem.* **2004**, *14*, 527–541. (b) Lin, Y.; Li, H.; Gu, L.; Luo, P. G.; Veca, L. M.; Wang, H.; Sun, Y.-P. *Bioapplications of Carbon Nanotubes in Chemistry of Carbon Nanotubes*; Basiuk, V. A., Basiuk, E. V., Eds.; American Scientific Publishers: Valencia, CA, 2008, in press.
(12) (a) Pompeo, F.; Resasco, D. E. *Nano Lett.* **2002**, *2*, 369–373. (b) Matsuura, K.; Hayashi, K.; Kimizuka, N. *Chem. Lett.* **2003**, *32*, 212–213. (c) Hasegawa, T.; Fujisawa, T.; Numata, M.; Umeda, M.; Matsumoto, T.; Kimura, T.; Okumura, S.; Sakurai, K.; Shinkai, S. *Chem. Commun.* **2004**, *19*, 2150–2151.
(13) (a) Lu, Q.; Moore, J. M.; Huang, G.; Mount, A. S.; Rao, A. M.; Larcom, L. L.; Ke, P. C. *Nano Lett.* **2004**, *4*, 2473–2477. (b) Kam, N. W. S.; O'Connell, M.; Wisdom, J. A.; Dai, H. J. *Proc. Natl. Acad. Sci. U.S.A.* **2005**, *112*, 11600–11605. (c) Pantarotto, D.; Singh, R.; McCarthy, D.; Erhardt, M.; Briand, J.-P.; Prato, M.; Kostarelos, K.; Bianco, A. *Angew. Chem., Int. Ed.* **2004**, *43*, 5242–5246.
(14) (a) Huang, W.; Taylor, S.; Fu, K.; Lin, Y.; Zhang, D. H.; Hanks, T. W.; Rao, A. M.; Sun, Y.-P. *Nano Lett.* **2002**, *2*, 311–314. (b) Kam, N. W. S.; Dai, H. J. *J. Am. Chem. Soc.* **2005**, *127*, 6021–6026.
(15) (a) Pantarotto, D.; Partidos, C. D.; Graff, R.; Hoebeke, J.; Briand, J. P.; Prato, M.; Bianco, A. *J. Am. Chem. Soc.* **2003**, *125*, 6160–6164. (b) Pantarotto, D.; Partidos, C. D.; Hoebeke, J.; Brown, F.; Kramer, E.; Briand, J. P.; Muller, S.; Prato, M.; Bianco, A. *Chem. Biol.* **2003**, *10*, 961–966.
(16) Elkin, T.; Jiang, X.; Taylor, S.; Lin, Y.; Gu, L.; Yang, H.; Brown, J.; Collins, S.; Sun, Y.-P. *ChemBioChem* **2005**, *6*, 640–643.
(17) Gu, L.; Elkin, T.; Jiang, X.; Li, H.; Lin, Y.; Qu, L.; Tzeng, T.-R. J.; Joseph, R.; Sun, Y.-P. *Chem. Commun.* **2005**, *7*, 874–876.

(18) Wang, H.; Gu, L.; Lin, Y.; Lu, F.; Meziani, M. J.; Luo, P. J.; Wang, W.; Cao, L.; Sun, Y.-P. *J. Am. Chem. Soc.* **2006**, *128*, 13364–13365.

(19) (a) Huang, W.; Lin, Y.; Taylor, S.; Gaillard, J.; Rao, A. M.; Sun, Y.-P. *Nano Lett.* **2002**, *2*, 231–234. (b) Sun, Y.-P.; Fu, K.; Lin, Y.; Huang, W. *Acc. Chem. Res.* **2002**, *35*, 1096–1104.

(20) Gu, L.; Lin, Y.; Qu, L.; Sun, Y.-P. *Biomacromolecules* **2006**, *7*, 400–402.

(21) Jermyn, M. A. *Anal. Biochem.* **1975**, *68*, 332–335.

(22) Chernyak, A. Y.; Sharma, G. V. M.; Kononov, L. O.; Krishna, P. R.; Levinsky, A. B.; Kochetkov, N. K.; Rao, A. V. R. *Carbohydr. Res.* **1992**, *223*, 303–309.

(23) Vutukuri, D. R.; Basu, S.; Thayumanavan, S. *J. Am. Chem. Soc.* **2004**, *126*, 15636–15637.

(24) Luo, P. G. Carbohydrate-Biofunctionalized Nanomaterials as Anti-adhesion and Detection Agents for Bacterial Pathogens, Ph.D. Dissertation, Clemson University, Clemson, S.C., 2006, pp 79−105.

(25) It has also been suggested recently that as a result of the oxidative acid treatment carbonaceous fragments with COOH groups are created and adsorbed onto the SWNTs, see. (a) Salzmann, C. G.; Llewellyn, S. A.; Tobias, G.; Ward, M. A. H.; Huh, Y.; Green, M. L. H. *Adv. Mater.* **2007**, *19*, 883–887. (b) Yu, H.; Jin, Y.; Peng, F.; Wang, H.; Yang, J. *J. Phys. Chem. C* **2008**, *112*, 6758–6763.

(26) (a) Qu, L.; Lin, Y.; Hill, D. E.; Zhou, B.; Wang, W.; Sun, X.; Kitaygorodskiy, A.; Suarez, M.; Connell, J. W.; Allard, L. F.; Sun, Y. P. *Macromolecules* **2004**, *37*, 6055–6060. (b) Qu, L.; Veca, L. M.; Lin, Y.; Kitaygorodskiy, A.; Chen, B.; McCall, A. M.; Connell, J. W.; Sun, Y.-P. *Macromolecules* **2005**, *38*, 10328–10331.

(27) (a) Chen, J.; Liu, H.; Weimer, W. A.; Halls, M. D.; Waldeck, D. H.; Walker, G. C. *J. Am. Chem. Soc.* **2002**, *124*, 9034–9035. (b) Holzinger, M.; Abraha, J.; Whelan, P.; Graupner, R.; Ley, L.; Hennrich, F.; Kappes, M.; Hirsch, A. *J. Am. Chem. Soc.* **2003**, *125*, 8566–8580.

(28) Zhou, B.; Lin, Y.; Li, H.; Huang, W.; Connell, J. W.; Allard, L. F.; Sun, Y.-P. *J. Phys. Chem. B* **2003**, *107*, 13588–13592.

(29) Hill, D.; Lin, Y.; Qu, L.; Kitaygorodskiy, A.; Connell, J. W.; Allard, L. F.; Sun, Y.-P. *Macromolecules* **2005**, *38*, 7670–7675.

(30) Lin, Y.; Taylor, S.; Li, H.; Fernando, K. A. S.; Qu, L.; Wang, W.; Gu, L.; Zhou, B.; Sun, Y.-P. *J. Mater. Chem.* **2004**, *14*, 527–541.

(31) According to the MSDS data sheets (www.fishersci.com).

(32) Krishnamurthy, V. M.; Estroff, L. A.; Whitesides,G. M. In *Fragment-based Approaches in Drug Discovery*; Jahnke, W., Erlanson, D. A., Eds.; Wiley-VCH Verlag GmbH & Co. KGaA: New York, 2006.

(33) Fox, A.; Stewart, G. C.; Waller, L. N.; Fox, K. F.; Harley, W. M.; Price, R. L. *J. Microbiol. Methods* **2003**, *54*, 143–152.

BM800395E

Advances in Bioapplications of Carbon Nanotubes

By *Fushen Lu, Lingrong Gu, Mohammed J. Meziani, Xin Wang, Pengju G. Luo, Lucia Monica Veca, Li Cao,* and *Ya-Ping Sun**

This progress report provides an overview on recent advances in bioapplications of carbon nanotubes including the chemical modification of carbon nanotubes, targeting specifically their covalent and noncovalent conjugations with a variety of biological and bioactive species (proteins and peptides, DNAs/RNAs, and carbohydrates). Furthermore, the significant recent development and progress in the use of carbon nanotubes for biosensors, drug and other delivery systems, bioimaging, etc. and in the understanding of in vivo biodistribution and toxicity of carbon nanotubes are reported.

1. Introduction

Carbon nanotubes are pseudo-one-dimensional carbon allotropes of high aspect ratio, high surface area, and excellent material properties such as ultimate electrical and thermal conductivities and mechanical strength.[1–3] While these all-carbon hollow graphitic nanomaterials may conceptually be viewed as ''rolled-up'' structures of one or more layers of graphene sheets for single-walled (SWNT) or multiple-walled (MWNT) carbon nanotubes, respectively, their formation is generally spontaneous in various production methods. There have been major advances in the availability of carbon nanotubes, both in quality and quantity, which has in turn stimulated the worldwide pursuit of carbon nanotubes for technological applications.[3,4] Nevertheless, carbon nanotubes (especially SWNTs) are still relatively expensive, so that their uses in higher-value but lower-quantity technologies are probably better justified in the near term. As one of such technological areas of enormous potential, bioapplications of carbon nanotubes have attracted much attention, with significant recent progress generating much excitement in the research community.

The unique properties of carbon nanotubes offer a wide range of opportunities and application potential in biology and medicine. For example, the rich electronic properties of carbon nanotubes have been explored for the development of highly sensitive and specific nanoscale biosensors.[5,6] Promising results have been produced on the use of carbon nanotubes in various electroanalytical nanotube devices,[7] and as electromechanical actuators for artificial muscles.[8] The optical absorption of carbon nanotubes in the near-infrared has been used for the laser heating cancer therapy.[9] In recent years, the rapid development toward maturation of methodologies for the chemical modification and functionalization of carbon nanotubes has helped to address many biocompatibility-related issues, opening up an even wider range of bioapplication opportunities in areas such as drug delivery,[10] bioconjugation and specific recognition, including interestingly the use of sugar-functionalized carbon nanotubes to bind and aggregate anthrax spores.[11] The biological fate and consequences of carbon nanotubes in vitro and in vivo have also been investigated for an understanding of the important issues on environmental impact and toxicity.[12]

In an earlier report,[13] we highlighted then the available methodologies for the aqueous dispersion and solubilization of carbon nanotubes and discussed some representative results on modifications of carbon nanotubes with various biological and bioactive species. Along the same line, here we report the recent advances in the chemical modification of carbon nanotubes targeting specifically their bioapplications, review various approaches and developments toward the use of carbon nanotubes in biology and medicine, and provide some perspectives on further investigations and emerging opportunities.

2. Functionalization of Carbon Nanotubes

There has been significant recent progress in the development and implementation of various covalent and noncovalent functionalization methods for chemical modification and solubilization of carbon nanotubes.[14,15] The maturation that has been achieved in the functionalization and especially the aqueous solubilization of carbon nanotubes is particularly beneficial to the biocompatibilization of the nanotubes toward bioapplications. Among now widely used covalent functionalization approaches are addition reactions derived from those traditionally for graphite surfaces or established for fullerenes (Scheme 1A), and coupling reactions targeting oxidized defect sites on the carbon nanotube surface, commonly the surface defect-derived carboxylic acid moieties to react with amines and alcohols for amide and ester linkages, respectively (Scheme 1B).

[*] Prof. Y.-P. Sun, Dr. F. Lu, Dr. L. Gu, Dr. M. J. Meziani, X. Wang Dr. P. G. Luo, L. M. Veca, Dr. L. Cao
Department of Chemistry and Laboratory for Emerging Materials and Technology
Hunter Hall, Clemson University Clemson, South Carolina 29634-0973 (USA)
E-mail: syaping@clemson.edu

DOI: 10.1002/adma.200801491

For some functional groups such as amines, the covalent amidation functionalization is likely accompanied by significant noncovalent interactions or the adsorption of the functional groups on the nanotube surface, thus substantially improving some properties of the functionalized nanotube samples (such as excellent aqueous solubility for a hydrophilic functionalization agent[16]).

Noncovalent functionalization approaches are equally important to the biocompatibilization and bioapplications of carbon nanotubes.[15] Among commonly used schemes are hydrophobic or π–π interactions. Because it is noncovalent, the functionalization does not disrupt the conjugated electronic structure in nanotubes, though the strong interactions may still significantly affect the electronic transitions in the nanotubes (often considered as surface doping effects).[17] The functionalization procedures are generally straightforward, and a variety of functionalization agents including surfactants, polymers, polynuclear aromatic compounds, and biomolecules have been used for the noncovalent dispersion of carbon nanotubes. For example, dispersions of mostly individual SWNTs have been obtained by using sodium dodecyl sulphate (SDS) under ultrasonication- ultracentrifugation conditions[18] for nearly complete optical assignments of SWNTs[19] and for further chemical manipulation of individual nanotubes.[20] Like SDS, many other anionic, cationic, and non-ionic surfactants are also capable of dispersing individual SWNTs. However, the amount of nanotubes dispersed by SDS or other surfactants is generally small (on the order of 5% or less).[21] The use of polymers instead of surfactants has not improved the dispersion efficiency in any substantial fashion.[21]

Chemical modification and functionalization of carbon nanotubes for their dispersion and solubilization have evolved

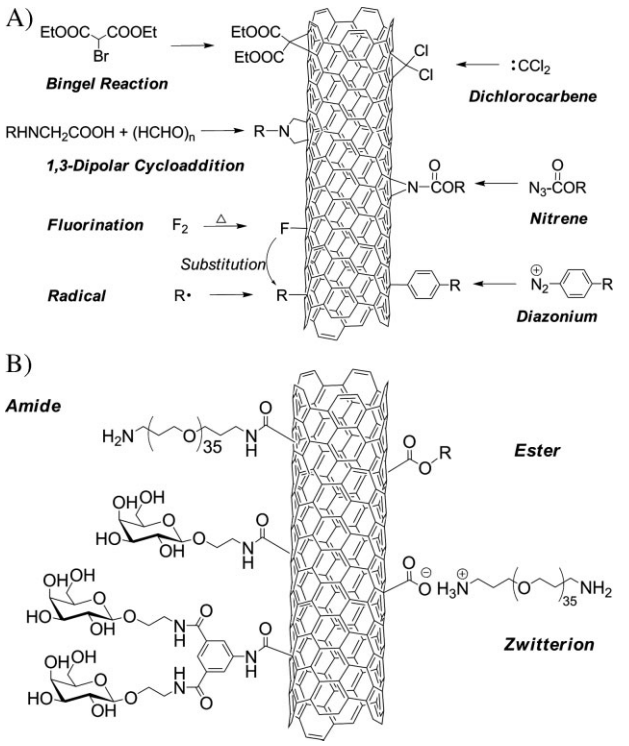

Scheme 1. A) Covalent addition reactions on the sidewall of carbon nanotubes. B) Reactions targeting carboxylic acids (derived from nanotube surface defects).

Fushen Lu received his Ph.D. in organic chemistry in 2005 from the Institute of Chemistry, Chinese Academy of Sciences, Beijing, China, under the supervision of Prof. Yuliang Li and Prof. Liangbing Gan. He is currently a senior research associate with Prof. Ya-Ping Sun in the Department of Chemistry at Clemson University. His research is on the development of nanostructures and nanomaterials for optical, electronic, and biomedical applications.

Lingrong Gu received her B.S. in chemistry in 1998 and M.S. in polymer chemistry & physics in 2001, both from Zhejiang University in Hangzhou, China. Since 2002, she has been a graduate student pursuing a Ph.D. in chemistry under the supervision of Prof. Ya-Ping Sun at Clemson University. Her research is on the functionalized carbon nanotubes for biological applications.

Ya-Ping Sun earned his Ph.D. in 1989 at the Florida State University. After a postdoctoral fellowship at the University of Texas, he joined the Clemson faculty as an assistant professor in 1992 and was promoted to associate professor in 1996 and full professor in 1999. Since 2003, he has been the endowed Frank Henry Leslie Chair Professor of Natural & Physical Sciences. Dr. Sun's research focus is on the development of nanomaterials and other novel materials for various technological applications, especially those in biology and medicine.

into a rather broad research field. Highlighted below are more specifically some recent advances in the modification and functionalization of carbon nanotubes with biological or biocompatible molecules or systems.

2.1. Proteins and Peptides

Proteins could be conjugated with carbon nanotubes via either spontaneous adsorption onto the nanotube surface or the immobilization more controllably in functionalization reactions. For example, Nepal and Geckeler demonstrated that common proteins such as lysozyme, histone, hemoglobin, myoglobin, ovalbumin, bovine serum albumin, trypsin, and glucose oxidase were good dispersing agents for SWNTs and that the ability to disperse by these proteins depended on various factors including the primary structure and pH.[22] Proteins with more basic residues (histone and lysozyme) were more effective in the dispersion of SWNTs. For pH effect in the functionalization of SWNTs with hemoglobin, either a low (acidic) or high (basic) pH was required for enhanced solubilization.[22]

In a study by Poenitzsch et al. on the dispersion of SWNTs with amphiphilic helical peptides,[23] the effectiveness of the peptides was found to be dependent on the electron density of the aromatic residue on the hydrophobic face. There has also been evidence on the selectivity of proteins towards metallic SWNTs, which was proposed to be potentially useful in the separation of as-produced nanotube samples (generally mixtures of metallic and semiconducting SWNTs).[22]

Sun and coworkers functionalized SWNTs covalently with bovine serum albumin (BSA) or horse spleen ferritin in classical carbodiimide-activated amidation reactions.[24,25] The resulting BSA-functionalized SWNTs were coated with goat anti-*Escherichia coli* O157 to form immuno-SWNTs under physiologically compatible conditions.[26] These immuno-SWNTs were able to recognize pathogenic *E. coli* O157:H7 cells through specific antibody-antigen interactions (conjugates without the antibody as negative control), as confirmed by imaging results from scanning electron microscopy (SEM) (Fig. 1).[26] The bacterial recovery determined by colony enumeration was up to 80–90% when a relatively larger amount of immuno-SWNTs and/or a relatively higher initial bacterial count were used.[27]

Similarly, Kane and coworkers functionalized MWNTs covalently through an oligomeric ethylene glycol linker with a specific peptide sequence which binds to the heptameric receptor-binding subunit of anthrax toxin.[28] The nanotube-peptide conjugate selectively destroyed the anthrax toxin due to the nanotube-mediated generation of reactive oxygen species following near-IR irradiation.[28]

The immuno-nanotube approach was expanded with the introduction of magnetic components, namely the preparation of immunomagnetic carbon nanotubes. Sun and coworkers isolated BSA-functionalized magnetic MWNTs (those encapsulated with iron and/or iron oxides) via magnetic separation, and then coated them with anti-*E. coli* O157. The resulting immunomagnetic MWNTs were used for the immunomagnetic separation of pathogenic *E. coli* O157:H7 in pure and mixed (with *Salmonella typhimurium*) cultures.[29] The immunomagnetic separation was

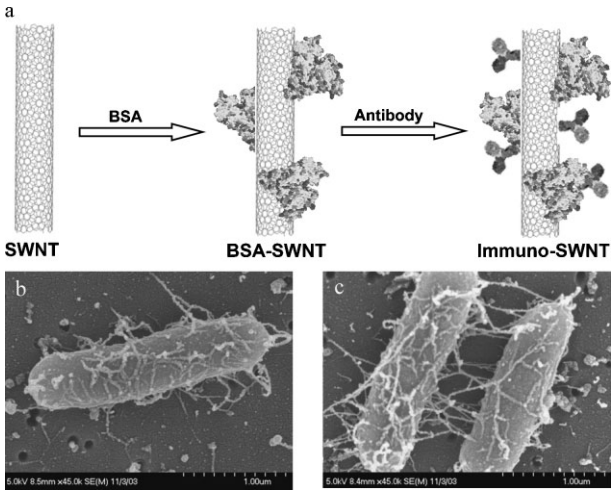

Figure 1. a) Scheme on the formation of immuno-SWNT. b,c) SEM images of immuno-SWNT binding to *E. coli* cells. Reproduced with permission from [26].

quite efficient, with the bacteria in aqueous buffer being captured by the immunomagnetic MWNTs and precipitated in a commercial magnetic separator within 5 min. The colony enumeration revealed that the sensitivity for such capture of bacteria was approximately 40 bacterial counts per 0.1 mL aqueous buffer. The capture was also highly selective, with no bound background bacteria even at a relatively high interfering concentration (selective toward *E. coli* O157:H7 at 800 colony forming units (CFU)/0.1 mL with background flora of *S. typhimurium* DT104 cells at ~3 000 CFU/0.1 mL).[29]

2.2. DNAs/RNAs

Similar to proteins, DNAs and RNAs could be attached to carbon nanotubes noncovalently by adsorption[30–32] and covalently in carbodiimide-activated coupling reactions either directly[33,34] or through a bifunctional linker.[35] For example, Hamers and coworkers used the bifunctional linker approach to functionalize sidewalls of carbon nanotubes in several steps, starting by the reaction of a 4-nitrobenzenediazonium salt, then the electrochemical reduction of $-NO_2$ to $-NH_2$ for reaction with a heterobifunctional cross-linker to introduce a maleimide group, followed by coupling with 5′-thiol-modified single strand DNA (ssDNA).[35] The nanotube-bound ssDNAs were able to recognize their appropriate complementary sequence with a high degree of selectivity.

The specific interaction between DNA sequences grafted on the carbon nanotube surface was used in the assembling of nanotubes into architectures necessary for electrical circuits and molecular sensing applications. In an exploration on DNA-directed multicomponent self-assembly of carbon nanotubes and gold nanoparticles,[31–33] ssDNA was first grafted onto the nanotube surface via direct wrapping or carbodiimide-activated coupling to form ssDNA-SWNT conjugates and then hybridized

with complimentary DNA sequences grafted (via the specific thiol-gold interaction) on gold nanoparticles. The DNA-directed assembly was found to be reversible: formation at low temperature and dissociation at high temperature.[31] The assembly approach has also been used in probing the surface defect sites of carbon nanotubes. In a recent study,[36] amine-terminated ssDNA sequences were covalently attached to the broken tips and sidewall defects of SWNTs (via the amidation of defect-derived carboxylic acids), followed by their binding with gold nanoparticles that were modified with complementary DNA sequences, where the gold nanoparticles served as readily detectable probes.

The functionalization (or wrapping) of carbon nanotubes with DNA not only imparts aqueous solubility but also allows a more precise control of the interfacial properties. For example, Dai and coworkers adsorbed poly-T DNA noncovalently (via π-stacking of the base-pairs) onto SWNT sidewalls to enable ultrathin dielectrics for nanotube electronics.[37] As reported, the DNA functionalization made it possible to fabricate SWNT field effect transistors (FETs) free of gate-leakage for potentially ultimate performance. The same group also grafted short interfering RNA (siRNA) onto the carbon nanotube surface, where the thiol-modified siRNA cargo molecules were linked to aqueous solubilized SWNTs (functionalized with an amine-terminated surfactant) through cleavable disulfide bonds.[38] According to results from in vitro delivery experiments, these siRNA-SWNT conjugates could effectively silence (50–60% knockdown) both CD4 receptor and CXCR4 co-receptor which are required for HIV to entry into human T cells and infection.

The nanotube-bound DNAs have been shown to largely retain their biological activities. Luciferase DNA containing T7 promoter sequence were adsorbed onto SWNT "buckypaper", and ~36% of the bound DNA remained functional as compared to the native (solution-based) DNA in RNA polymerase-catalyzed transcription/translation reaction.[39] The interaction between DNA and carbon nanotubes is also generally stable. In fact, the stability has recently allowed the separation of the dispersed nanotubes into well-defined subpopulations.[30,40,41] The ssDNA-wrapped SWNTs were separated into multiple fractions, each with a different length distribution, and the fractions were examined for their cellular toxicity with different cell lines.[40] According to the competitive cell uptake assays, SWNTs above a length threshold (~200 nm) were excluded from the cells, whereas those below the threshold were able to access the cell interior, significantly decreasing the metabolic activity, namely that shorter SWNTs could be more toxic to cells than longer ones.[40]

The mechanism on the DNA wrapping of carbon nanotubes is not fully understood, though a number of driving forces have been discussed,[30,42] such as van der Waals and hydrophobic (π–π stacking) interactions, the entropy loss due to the confinement of the DNA backbone, and electronic interactions between DNA and carbon nanotubes. There have also been studies of DNA-nanotube conjugates and the associated conformational change of DNA on the nanotube surface by a combination of molecular dynamic stimulation, circular dichroism, and optical spectroscopy.[43–45] It was found that the double-stranded DNA noncovalently wrapping SWNTs underwent conformational transition from right-handed B form to the left-handed Z form upon the addition of divalent cations such as Hg^{2+}, corresponding to a detectable red shift in the band-gap emission of SWNTs (Fig. 2).[45] Thus, these DNA-wrapped nanotubes were used to detect ions in whole blood, tissue, and within living mammalian cells.[45]

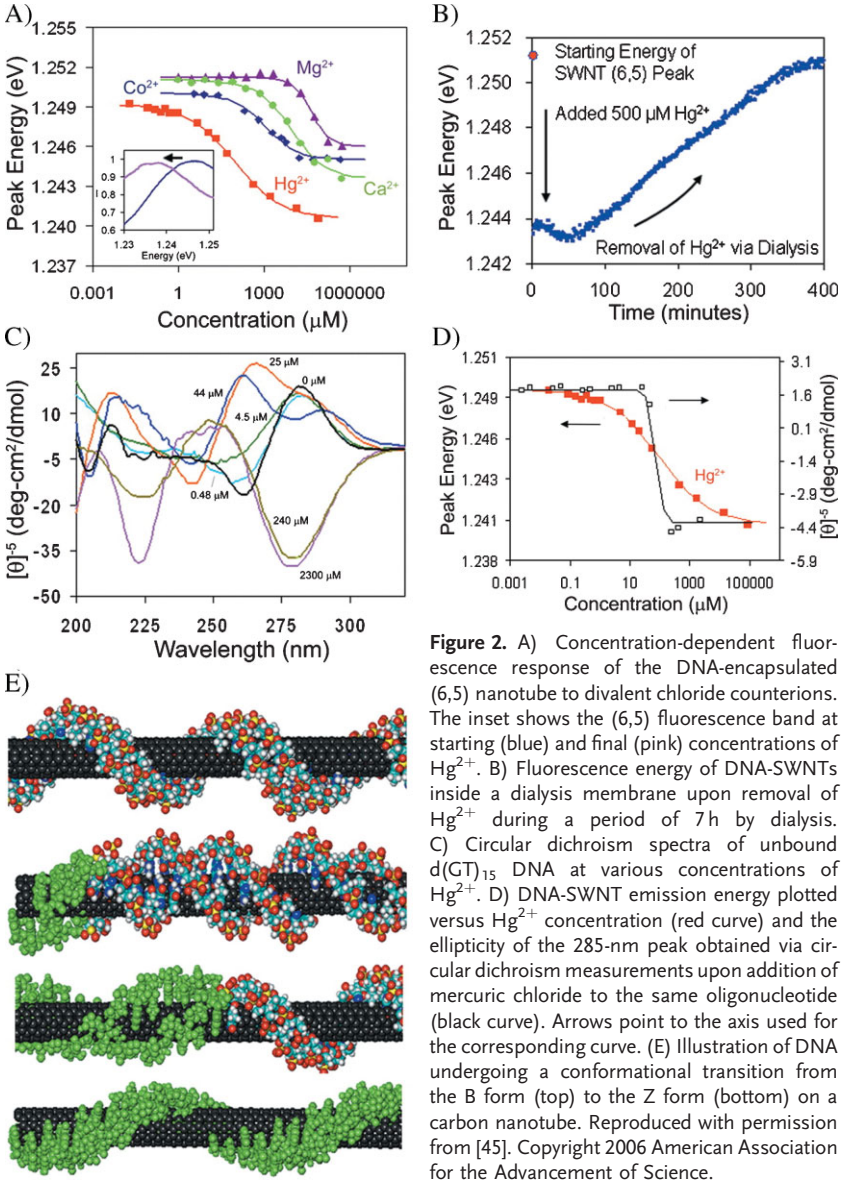

Figure 2. A) Concentration-dependent fluorescence response of the DNA-encapsulated (6,5) nanotube to divalent chloride counterions. The inset shows the (6,5) fluorescence band at starting (blue) and final (pink) concentrations of Hg^{2+}. B) Fluorescence energy of DNA-SWNTs inside a dialysis membrane upon removal of Hg^{2+} during a period of 7 h by dialysis. C) Circular dichroism spectra of unbound $d(GT)_{15}$ DNA at various concentrations of Hg^{2+}. D) DNA-SWNT emission energy plotted versus Hg^{2+} concentration (red curve) and the ellipticity of the 285-nm peak obtained via circular dichroism measurements upon addition of mercuric chloride to the same oligonucleotide (black curve). Arrows point to the axis used for the corresponding curve. (E) Illustration of DNA undergoing a conformational transition from the B form (top) to the Z form (bottom) on a carbon nanotube. Reproduced with permission from [45]. Copyright 2006 American Association for the Advancement of Science.

Generally DNA-nanotube conjugates are widely pursued for their interesting and promising prospects in a number of areas, including especially nanoscale devices, biosensors, electronic sequencing, and therapeutic delivery, taking advantage of the unique pseudo-one-dimensional cylindrical structure of carbon nanotubes and the sequence-specific pairing interaction and conformational flexibility of DNA.

2.3. Carbohydrates

Another advantageous use of the unique pseudo-one-dimensional structure of carbon nanotubes has been in the multivalent display of carbohydrate ligands for various biological functions and interactions.[11,46–52] Carbohydrates are highly hydrophilic biomolecules and used extensively in the functionalization of carbon nanotubes through either covalent bonding[11,48,49] or noncovalent wrapping.[46,47,50–52] The nanotube-displayed carbohydrates not only impart significant aqueous solubility and biocompatibility, but also offer the kind of bioactivities that are apparently not available with other displaying platforms such as polymeric nanoparticles. For example, Sun and coworkers recently demonstrated that the monosaccharide (galactose or mannose)-functionalized SWNTs could effectively bind and aggregate anthrax (*Bacillus anthracis*) spores in the presence of a divalent cation like Ca^{2+} (Fig. 3), with the reduction in CFU reaching 97.7% as a result of the aggregation.[11] Interestingly, however, the polymeric nanoparticles (polystyrene beads of ~120 nm in diameter) functionalized with the same sugars exhibited no similar binding and aggregation of the spores under the same experimental conditions, suggesting the uniqueness of SWNT as a linear and semi-flexible scaffold for multivalent displaying of the monosaccharides. The Ca^{2+}-mediated binding and aggregation of *B. anthracis* spores were found to be reversible, a complete de-aggregation of the spores when free Ca^{2+} was removed by adding the chelating agent ethylene diamine tetraacetic acid (EDTA). Therefore, mechanistically the binding was probably a result of divalent cation-mediated carbohydrate-carbohydrate interactions between the SWNT-displayed multivalent monosaccharides and the sugar moieties on the spore surface.[11]

The binding of galactose-functionalized SWNTs (Gal-SWNT) with pathogenic *E. coli* O157:H7 cells required no divalent cation mediation, resulting in significant cell agglutination.[48] The same behavior was not found with mannose- or BSA-functionalized SWNTs, namely that the binding and agglutination were specific to the nanotube-displayed galactose ligands. This could be due to the presence of galactose-binding proteins on the *E. coli* cell surface. It is well-established in the literature that the multivalency is required for any effective carbohydrate-carbohydrate or carbohydrate-protein interactions.[53] Interestingly, however, when galactose molecules were displayed in pairs in the sugar dendron-functionalized carbon nanotubes (thus, in principle, enhanced carbohydrate multivalency), their binding with the pathogenic *E. coli* for cell agglutination was improved only marginally.[49,54]

The sugar functionalization and solubilization of carbon nanotubes could also be achieved via noncovalent wrapping

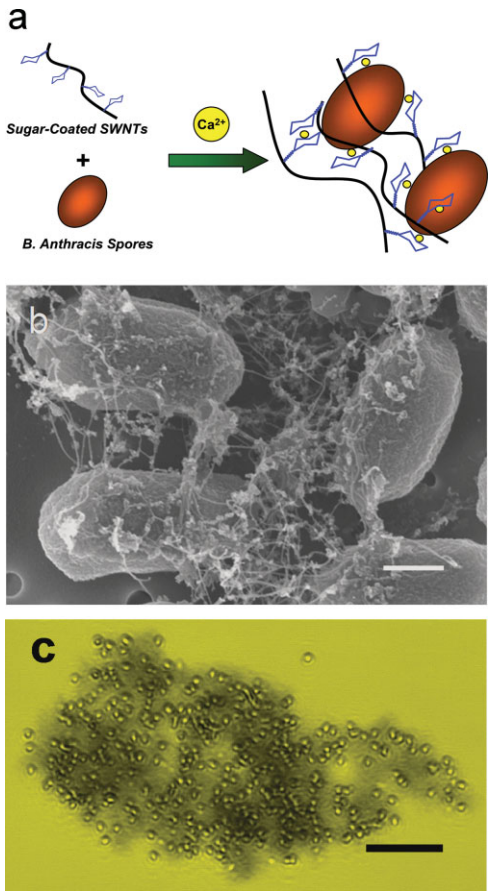

Figure 3. a) Scheme on the Ca^{2+}-mediated aggregation of anthrax spores with sugar-functionalized SWNTs. b) SEM (scale bar = 500 nm) and c) optical microscopy (scale bar = 20 μm) images of a typical aggregate. Reproduced with permission from [11]. Copyright 2006 American Chemical Society.

with polysaccharides.[47,50–52] For example, Liu et al. used alginic acid (AA), a natural polysaccharide constituted with repeated β-D-mannuronic acid (M) and α-L-guluronic acid (G) segments, to solubilize MWNTs by sonication.[51] Results from transmission electron microscopy (TEM) and NMR analyses of the AA-MWNT complex suggested that the nanotubes were partially wrapped by AA in a configuration possibly with the M segments lying down and the G segments standing up on the nanotube surface. The addition of divalent or trivalent metal cations, such as Zn^{2+}, Ni^{2+}, Co^{2+}, Pb^{2+}, La^{3+}, and Eu^{3+}, resulted in precipitation of the AA-MWNT complex. The precipitates could be re-dispersed in water by chelating the metal cations with EDTA.

Shinkai and coworkers also reported noncovalent functionalization of SWNTs with polysaccharides schizophyllan and curdlan (an analogue of schizophyllan containing the main chain but missing the side chain).[47,50,52] Schizophyllan has a natural triple-helix structure, which can be dissociated into single chain in DMSO and can also be re-constituted by simply replacing DMSO with water. The hollow helical column in schizophyllan is considered hydrophobic, similar to that in cyclodextrin, capable of entrapping/hosting as-grown or shortened SWNTs. This was

accomplished by mixing and sonicating schizophyllan with nanotubes in DMSO, and then exchanging with water. The results from microscopy analyses of these polysaccharide-SWNT host-guest complexes are quite interesting (Fig. 4).[50]

3. Bioapplications

There has been much recent effort on demonstrating the feasibility and potentials for uses of carbon nanotubes in a variety of biological and biomedical systems and devices. Significant progress has been made to overcome some of the fundamental and technical barriers toward bioapplications of carbon nanotubes, especially on issues concerning their aqueous solubility and their conjugation with or integration into bioactive molecules and/or biological species. Highlighted below are some interesting recent studies and achievements in representative areas of the broader field concerning bioapplications of carbon nanotubes.

3.1. Biosensors

Carbon nanotubes, especially SWNTs, are size-wise comparable with many biomacromolecules (e.g., DNA on the order of 1 nm in size). The ultimate electrical properties and their sensitivity to changes in the surrounding environment have made carbon nanotubes ideal components in biosensors, such as electrodes for signal transmission and detectors for sensing chemical and biological materials. Both electrochemical sensors and those based on field effect transistor (FET) have been developed and/or fabricated in different configurations and mechanisms. A number of recent review articles on the subject, especially on electrochemical sensors, have been published.[6,55,56]

Semiconducting SWNTs are widely considered as the most promising nanoscale molecular sensors for their extremely high sensitivity and fast response time. In general, the FET is constructed by a substrate (gate), two microelectrodes (source and drain), and a SWNT (or SWNT network) bridging the electrodes. A SWNT FET is usually fabricated by casting a dispersion of bulk SWNTs or by directly growing the nanotubes via a chemical vapor deposition (CVD) method on a substrate either before or after the electrodes are patterned.[57] The functions of the transistors are associated with their diffusive electron transport properties. The current flow in SWNT FET is extremely sensitive to the substance adsorption or other related events, on which the sensing is based. For example, upon the binding of biological macromolecules to the nanotube in the device, a change in the charge state perturbs the current flow in the nanotube, thus producing detectable signals for the sensing. A wide variety of applications for such a device have been explored, including especially the detection of proteins, antibody-antigen interactions, glucose, DNA and DNA hybridization, and single nucleotide polymorphism. The detection limit for the sensing of proteins or protein-protein interactions has generally been in the range of 100 pM to 100 nM.[58] In a recent study, however, Byon and Choi modified the geometry of the SWNT FET device to improve the sensitivity to 1 pM for both nonspecific and specific protein bindings.[59] The substantially higher sensitivity (a factor of 10 000) was accredited mainly to the larger thin and wide Schottky contact area, which was achieved by evaporating electrode metals using a shadow mask on a tilted angle sample stage. This work may accelerate the progress toward the realization of nanoscale and label-free electronic biosensor systems.

Antibodies are often used as specific targeting agents in FET devices for highly selective biosensing.[58–60] Alternatively, synthetic oligonuleotides (i.e., aptamers) have demonstrated advantages (stability, small size, etc.) in the specific detection of amino acids,

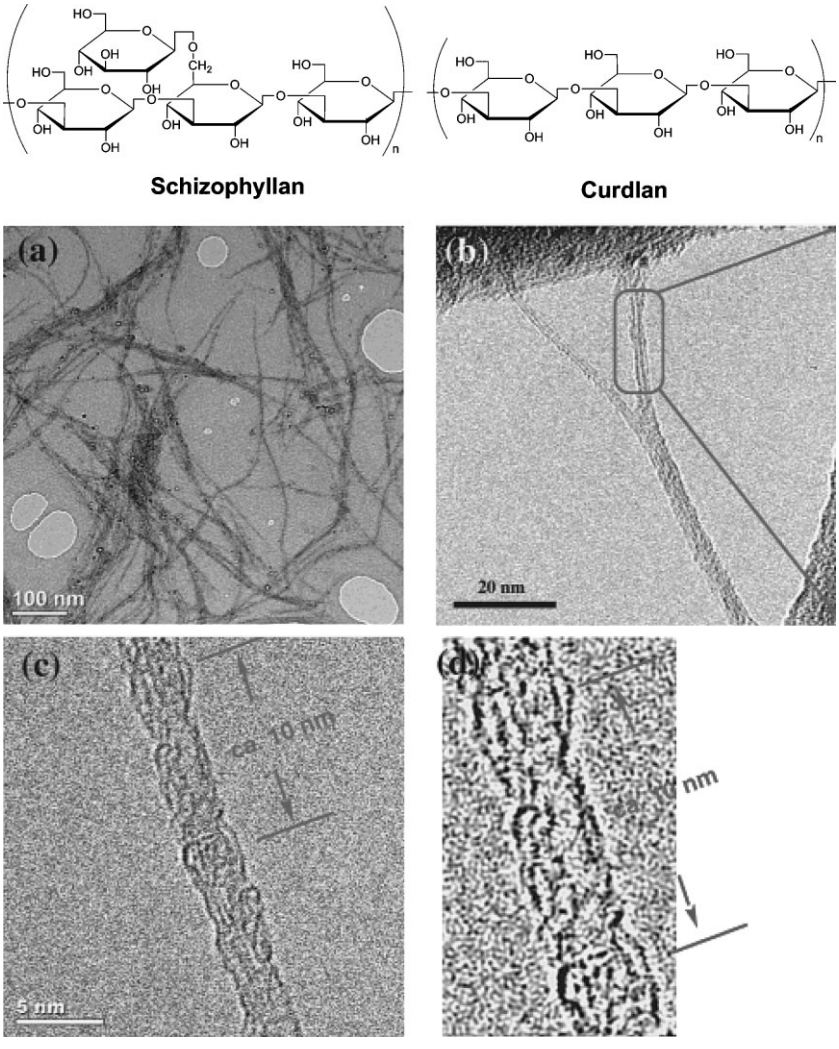

Figure 4. (top) The chemical structures of schizophyllan and curdlan. a) TEM image of as-grown-SWNT/s-SPG composite, and b) and c) its magnified picture. d) The original image of (c) was Fourier filtered to enhance the contrast of the composite. Reproduced with permission from [50]. Copyright 2005 American Chemical Society.

drugs, and proteins. In the FET sensors, aptamer-modified carbon nanotubes were used for the detection of immunoglobulin E (IgE).[61] The modification was the immobilization of 5′-amino-modified aptamer onto the nanotube surface with the aid of the linker molecule 1-pyrenebutanoic acid succinimidyl ester. There was a sharp decrease in the source-drain current in the presence of the targeted IgE, and the net current change increased with the IgE concentration. The detection limit for IgE was 250 pM. In a comparison between devices based on the aptamer-modified and monoclonal antibody-modified carbon nanotubes, the former exhibited a better performance in the detection of IgE under similar experimental conditions.[61]

Star et al. fabricated carbon nanotube FETs as selective detectors for DNA immobilization and hybridization.[62] The device with immobilized synthetic oligonucleotide specifically recognized the target DNA sequences, including H63D single-nucleotide polymorphism discrimination in *HFE* gene (responsible for hereditary hemochromatosis).[62] Upon the addition of divalent cation Mg^{2+} there was a significant increase in the extent and overall efficiency of DNA hybridization on nanotubes, increasing the sensitivity by three orders of magnitude to push the detection limit down to 1 pM.[62] Gui et al. employed the same FET configuration in the fabrication of a device with two different metal contacts (Au and Cr) for electrical detection of DNA hybridization.[63]

The sensing mechanism for nanotube-based FETs has been debated, though it is generally acknowledged that unlike silicon nanowire devices, SWNT devices are operated in terms of the Schottky barrier modulation effect[58,64] as well as the chemical gating effect.[65,66] The former dominates when the isoelectric point of the targeted protein is close to the medium pH.[58] According to a recent report, experimentally the effect of protein adsorption on the relationship (*I–V* curve) between source-drain current and the liquid gate potential could be used as a tool to identify the sensing mechanism in the SWNT transistor.[67] It was found that the sensing was indeed due to a combination of Schottky barrier and electrostatic gating effects. While earlier reports suggested that the sensitive region was limited to the nanoscale contacts,[58,59] these new results seemed to indicate that strong electrostatic gating could also occur along the bulk of the SWNT channel. The new finding was consistent with another recent study of DNA immobilization on back-gated SWNT network.[65]

There is still much room for further development in carbon nanotube FETs for biosensing, especially with respect to localizing nanoscale contacts of SWNTs with bio-surfaces and improving the fabrication of devices with complex arrays of semiconducting SWNTs. As discussed earlier, semiconducting SWNTs are used in FETs.[56,68] With rare exceptions,[69] however, as-produced SWNTs are mixtures of semiconducting and metallic nanotubes (in a ratio close to the statistical limit of 2-to-1).[70] Therefore, selective removal of metallic SWNT for purer semiconducting ones, such as improving the post-fabrication electrical breaking down technique[71] or taking advantage of the recent advances in post-production separation of semiconducting SWNTs from the as-produced mixtures,[70,72,73] may prove highly beneficial. Finally, much remains to be explored on directly connecting living cells to these nanoelectronic devices for probing and understanding electronic responses in living systems.

3.2. Bio-Delivery

As an alternative to the extensively investigated drug delivery systems for improved pharmacological profiles and therapeutic properties, such as liposomes, polymers, dendrimers, and a variety of nanomaterials, carbon nanotubes have been pursued for their potentially high loading capacity and the ability to penetrate into cells without the need for any external transporter system. There has been significant recent progress in the demonstration on using carbon nanotubes as effective carriers for shuttling and delivering various peptides, proteins, nucleic acids, and small molecular drugs into living cells.[10]

Pastorin et al. employed a ''double functionalization'' strategy to attach both fluorescein isothiocyanate (FITC, a fluorescent probe) and methotrexate (MTX, an anticancer drug) onto the sidewall of MWNTs via the 1,3-cycloaddition reaction of azomethine ylides.[74] Synthetically, the nanotubes were first co-functionalized with two orthogonally protected amino groups, followed by selective de-protection and then derivatization with FITC and MTX. According to in vitro experiments with Jurkat cells, the nanotube-bound drugs were rapidly internalized into the cells to accumulate in the cell cytoplasm.[74] The same group reported that pluronic copolymer-dispersed MWNTs could form supramolecular complexes with doxorubicin (DOX, a popular anticancer drug) via π stacking of the DOX aromatic hydroxyl-anthraquinonic rings on the nanotube surface.[75] The fluorescence intensity of the nanotube-bound DOX was suppressed due to the known quenching effect. According to the toxicological assay with MCF-7 human breast cancer cells, there was a significant enhancement in cytotoxic activity with the DOX-nanotube complexes (the copolymer-DOX and free DOX as controls, and no cytotoxicity with the pluronic copolymer-dispersed MWNTs), and the enhancement was attributed to a more effective delivery of DOX with the aid of MWNTs.[75]

Dai and coworkers complexed SWNTs with a large amount of DOX, where the complexation was noncovalent attachment again via π-stacking.[76] Two aqueous soluble SWNT samples were used, phospholipid (PL)-SWNT from dispersion with the surfactant PL-PEG (~120 PEG units) and PEG-SWNT from the covalent functionalization of oxidized SWNTs with the PEG (220 units). The DOX attachment to and release from the nanotubes were found to be dependent on pH and the diameter of SWNTs, generally lower pH and smaller diameter in favor of DOX dissociation from the nanotubes. According to the in vitro toxicity experiments, the DOX-loaded PL-SWNT induced significant U87 cancer cell death and cell apoptosis (PL-SWNT without DOX as negative control), similar to free DOX, though the IC_{50} (half-maximum inhibitory concentration) value for the nanotube-bound DOX (~8 μM) was higher than that of free DOX (~2 μM).[76] For specifically targeting U87 cancer cells, a cyclic arginine-glycine-aspartic acid (RGD) peptide (recognizing integrin $\alpha_v\beta_3$ receptors up-regulated in solid tumors) was conjugated to the terminal groups in PL-SWNT. The effectiveness of the targeted delivery of the nanotube-bound DOX was reflected in the lower IC_{50} value (~3 μM) for the RGD positive U87 cancer cells, with MCF-7 cells (short of corresponding receptors) as negative control showing no improvement in the IC_{50} value (Fig. 5).

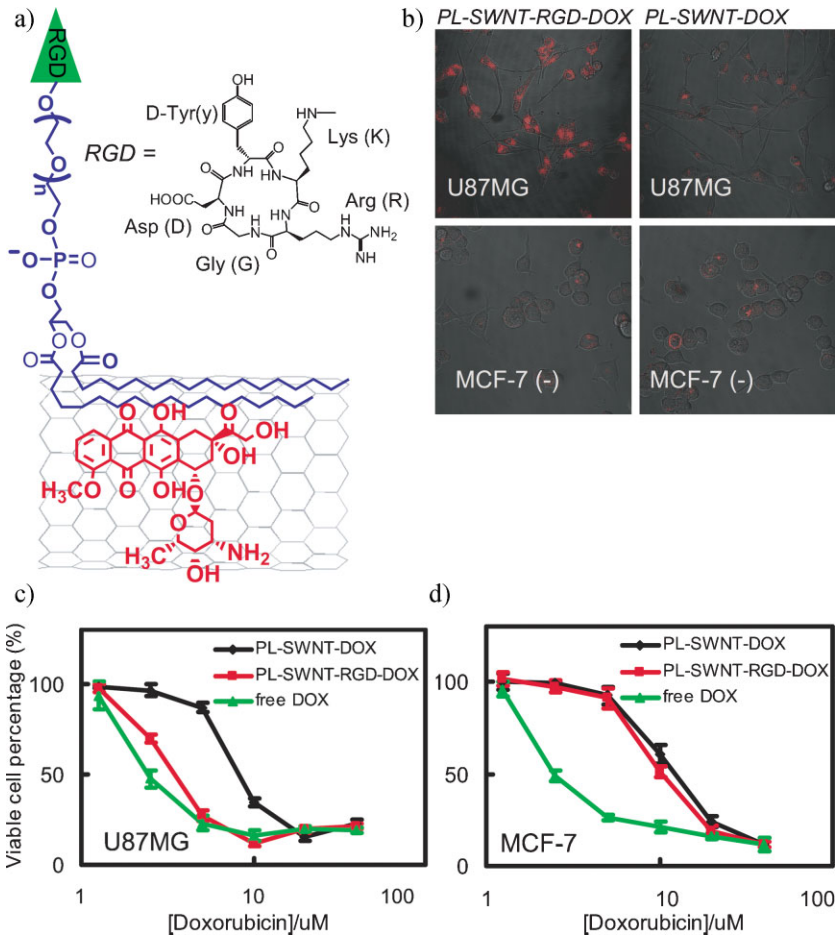

Figure 5. RGD peptide selectively enhances doxorubicin delivery by SWNTs and toxicity to integrin $\alpha_v\beta_3$-positive cells. a) Schematic structure of PL-SWNT-RGD-DOX, i.e., SWNT functionalized with RGD at the termini of PEG and loaded with doxorubicin on the sidewall by π-stacking. b) Confocal fluorescence images of integrin $\alpha_v\beta_3$-U87MG cells (top) and negative MCF-7 cells (bottom) treated with either PL-SWNT-DOX (right) or PL-SWNT-RGD-DOX (left). The concentration of DOX was 2 μM in all experiments. The U87MG cells incubated with PL-SWNT-RGD-DOX showed stronger DOX fluorescence in the cells than in the other three cases. c) and d) Concentration dependent survival curves of U87MG cells (c) and MCF-7 cells (d) treated by various samples, as indicated. The viable cell percentage was measured by the MTS assay. PL-SWNT-DOX had a lower toxic effect than free DOX on both types of cells, while PL-SWNT-RGD-DOX exhibited increased toxicity to U87MG cells but not to MCF-7 cells. Reproduced with permission from [76]. Copyright 2007 American Chemical Society.

Similarly, Feazell et al. used the soluble functionalized SWNTs to deliver multiple cisplatin prodrug centers for their internalization.[77] The platinum(IV) complex, *c,c,t*-[Pt(NH$_3$)$_2$Cl$_2$(OEt)(O$_2$CCH$_2$CH$_2$CO$_2$H)], was tethered to nanotubes through PL-PEG linkages. The platinum(IV) complex by itself was nearly nontoxic to NTera-2 cancer cells, but its conjugate with SWNT exhibited a dramatic enhancement in cytotoxicity, along with a significant increase (six times) in the cellular platinum concentration. These results were consistent with an effective delivery of platinum(IV) with SWNTs.[77]

Beyond small molecular drugs, other bioactive species such as RNAs were also successfully delivered into cells with the use of nanotubes.[38,78] For example, Zhang et al. conjugated siRNA with SWNTs and specifically targeted murine telomerase reverse transcriptase (mTERT) expression to form the mTERT-siRNA: SWNT+ complex.[78] These specifically biofunctionalized SWNTs successfully entered three cultured murine tumor cell lines, silenced the expression of the targeted gene, inhibited cell proliferation and promoted cell senescence in vitro, and also suppressed tumor in vivo. The functionalized SWNTs ready for the specific conjugation might represent a new class of molecular transporters for applications in gene therapeutics. Similarly, by being grafted onto carbon nanotubes, siRNA was also delivered into human T cells and primary cells, exhibiting superior silencing effects over conventional liposome-based nonviral agents.[38]

For eventual in vivo applications of the widely pursued carbon nanotube delivery systems, a critical challenge is to be able to keep the nanotubes in the bloodstream long enough for their intended functions.[79] In a recent study by Wang, Sun, and coworkers,[80] the functionalization of SWNTs with oligomeric poly(ethylene glycol) ("PEGylation") was found to be remarkably effective in achieving prolonged blood circulatinon (half-time on the order of 20 hours for the PEGylated nanotubes). Experimentally, skeleton ^{13}C-enriched SWNTs were functionalized with the oligomeric PEGs by targeting the nanotube surface defects in well-established reactions. The plasma pharmacokinetic study was performed by injecting male KM mice intravenously with a solution of the PEGylated SWNTs, and by quantifying the nanotube concentrations in the blood post-exposure at different time intervals in terms of the ^{13}C isotopic abundance determination (isotope ratio mass spectrometry). At one day post-exposure, for example, about 30% injected dose (% ID) remained in blood circulation, compared to only 0.2% ID for pristine SWNTs at the same time post-exposure.[81] In a similar study by Dai and coworkers,[82] a comparable blood circulation time was obtained for SWNTs noncovalently functionalized with branched PEGs. There were also preliminary results[80] suggesting that the tumor uptake of the PEGylated SWNTs benefited from their prolonged blood circulation. For the EMF6 model (breast cancer in BABL/c mice) and the Lewis model (lung cancer in C57BL mice), the tumor uptakes of intravenously administered PEGylated SWNTs were 8% ID/g and 9% ID/g, respectively,[80] considerably higher than those for SWNTs without covalent PEGylation (in the absence of any specific targeting moieties).[83]

Mechanistically, the pathway of the carbon nanotube-enabled or associated delivery is still being debated, despite the experimental demonstrations on the efficiency of such delivery. One issue is on the entry mechanism that regulates the cellular

internalization of SWNTs and their carried cargos. Dai and coworkers proposed an endocytosis uptake mechanism on the basis of the observed temperature dependence in cellular uptake of carbon nanotubes,[84–86] whereas the group of Kostarelos, Bianco, and Prato suggested an energy-independent non-endocytic mechanism involving insertion and diffusion of nanotubes through the lipid bilayer of the cell membrane.[87,88] Experimentally, Dai and coworkers functionalized shortened SWNTs (50–200 nm in length) with DNAs and proteins noncovalently to study their uptake by HeLa (adherent) and HL60 (nonadherent) cells.[86] According to their results, these short SWNTs transported the bioactive cargos into living cells in an energy-dependent fashion. They suggested that the endocytosis pathway for these well-dispersed, short SWNTs with bioconjugation was through clathrin-coated pits rather than caveolae or lipid rafts.[86] The same group also studied larger aggregates of DNA-functionalized SWNTs (200 nm–2 μm long and up to 15 nm in diameter) for their uptake by HeLa cells. The results were similar to those of the shortened SWNTs, consistent with endocytosis. However, the mechanistic elucidation on the cellular uptake of these relatively large nanotube aggregates could be less certain due to complications such as their low solubility.

The group of Kostarelos, Bianco, and Prato[87,88] disagreed by suggesting that the large biomolecules solubilizing carbon nanotubes could alter the nanotube interactions with cells and affect the intracellular transport kinetics. In experiments designed to support their suggestion and to examine key steps in the cellular uptake process, Kostarelos et al. functionalized both SWNTs and MWNTs with a wide range of molecules and bioactive species, including ammonium, small molecule fluorescent probes, anticancer drugs, and antibiotics.[88] All of these functionalized nanotubes were found to be taken up by a wide variety of cells and intracellularly trafficked through different cellular barriers to the perinuclear region, even under endocytosis-inhibiting conditions. The molecular simulation results also seemed consistent with the hypothesis that carbon nanotubes act as ''nano-needles'' to pierce or penetrate the plasma membrane.[89]

It appears that some of the disagreements or seemingly contradicting results on the cellular uptake mechanism might be due to different characteristics associated with the specific nanotube constructs and/or different experimental procedures.[88] More specifically, the non-endocytic internalization was found largely for small molecules covalently attached carbon nanotubes, while translocation via endocytosis was for larger biopolymers or aqueous soluble macromolecules conjugated SWNTs.[88] Nevertheless, mechanistic debate is healthy and stimulating, and an improved mechanistic understanding is critical to further development of carbon nanotube transporters for delivery applications in vitro and in vivo.

There has also been a kind of delivery that is independent of any cellular uptake mechanism.[90] Chen et al. developed a nanotube-based delivery configuration dubbed ''nano-injector'', which went through the cell membrane via physical insertion.[90] For the delivery of fluorescent quantum dots (QDs), biotinylated (via a disulfide linker) pyrene was synthesized for attachment (possibly π stacking) to MWNT as an atomic force microscopy (AFM) tip. The biotin moieties on the tip were readily conjugated with steptavidin-coated QDs (5–50 per nanotube). The nano-injection by the MWNT could deliver the QDs into a specific cell, which could then be released via the cleavage of the disulfide linker.[90] A major advantage was suggested for this approach that the delivery-release processes could be repeated many times without cell damage.[90]

3.3. Bioimaging

Potential cellular and sub-cellular imaging applications of carbon nanotubes (SWNTs in particular) have attracted much attention.[91–98] These applications would take advantage of the unique physical and chemical properties of carbon nanotubes and also their exceptional capability in penetrating cell membranes. The majority of the bioimaging studies with carbon nanotubes have been in two categories: the direct optical imaging relying on the intrinsic fluorescence (including the band-gap emission of semiconducting SWNTs in the near-IR[18] and the visible emission due to passivated surface defects in functionalized SWNTs and MWNTs[99]), and the indirect imaging based on nanotube-attached fluorescent or radioactive agents.

The band-gap fluorescence in individual semiconducting SWNTs was discovered by the group led by Weisman and Smalley.[18] In as-produced SWNTs, typically about two-thirds are semiconducting. When these nanotubes were individualized in the exfoliation involving no chemical modification or damage to the nanotubes, fluorescence emission could be observed in the near-IR spectral region. For semiconducting SWNTs of a nanometer in diameter and several hundred nanometers in length, the emission covers the spectral region of 900–1 600 nm. Since most natural biomolecules are relatively transparent and nonemissive in this region, the sharp nanotube fluorescence spectra may be detected even in a more complex biological environment. The band-gap fluorescence emission is apparently sensitive to surface defects on the nanotubes, quenched in oxidized or functionalized SWNTs. However, as first reported by Sun and coworkers,[99] both SWNTs and MWNTs with surface defects exhibit relatively strong photoluminescence upon chemical functionalization at the defect sites, and the emission is brighter with better functionalization.[100] The defect-derived photoluminescence is excitation wavelength dependent in the visible and extending into the near-IR. Therefore, the well-functionalized carbon nanotubes are also amenable to optical bioimaging applications.

Dai and coworkers used semiconducting SWNTs as near-IR fluorescent tags for selective probing of cell surface receptors and cell imaging.[98] The nanotubes were dispersed noncovalently with the amine-terminated surfactant PL-PEG-NH_2, and the resulting nanotube-bound residual amine groups were conjugated with thiolated Rituxan (an antibody recognizing the CD20 cell surface receptor) and Herceptin (recognizing the HER2/neu receptor on certain breast cancer cells). In solution, emissions of these antibody-conjugated SWNTs were in the 1 000–1 600 nm spectral region (at 785 nm excitation), namely that the known near-IR fluorescence of semiconducting SWNTs was preserved after the antibody conjugation. The fluorescence quantum yield was relatively low, but sufficient for the imaging experiments.

According to near-IR fluorescence imaging in vitro, there was specific binding of the antibody-conjugated SWNTs to the host cells.[98] The fluorescence intensity results suggested high specificity for the different antibodies (55:1 and 20:1 for host cells:non-host cells).

Cherukuri et al. used near-IR fluorescence to study the uptake of pluronic surfactant-dispersed pristine SWNTs into macrophage-like cells.[91] Macrophage samples that were incubated in growth media containing the dispersed SWNTs exhibited characteristic nanotube fluorescence spectra. The fluorescence intensities increased smoothly with incubation time and external nanotube concentration. The near-IR fluorescence microscopy at wavelengths beyond 1 100 nm yielded high contrast images showing the localization of nanotubes in numerous intracellular vesicles. It appeared that the cellular uptake of SWNTs was through phagocytosis.[91] The population growth in macrophage cultures was unaffected by exposure to nanotubes at $\sim 4\,\mu g\ mL^{-1}$ concentration. Leeuw et al. also used near-IR fluorescence microscopy to image SWNTs in organisms and biological tissues of nanotube-fed *Drosophila* larvae.[94] The estimate was that only a very small fraction (~10 ppb) of the ingested nanotubes became incorporated into organs of the larvae. These studies demonstrated that near-IR fluorescent SWNTs could be used as effective probes for potential diagnostic applications.[94]

The much brighter visible (extending to the near-IR) photoluminescence in functionalized carbon nanotubes has also found applications in bioimaging. Lacerda et al. used SWNTs that were covalently linked with NH_3^+-terminated aliphatic appendages (SWNT-NH_3^+, emission peak at 485 nm with 395 nm excitation) in confocal laser scanning microscopy to visualize the interaction of SWNT-NH_3^+ with human caucasian lung carcinoma A549 cells (Fig. 6).[92] There was the intracellular and perinuclear localization of SWNT-NH_3^+, but no cell plasma membrane damage at a dose up to $500\,\mu g\ mL^{-1}$ and 24 h post-incubation. This was the first report on the visible florescence imaging of SWNTs in cells without the need for large fluorescent labels attached to biopolymers or macromolecules. The imaging methodology thus developed may serve as a widely applicable tool for elucidating the intracellular transport mechanism of carbon nanotubes.

For indirect optical imaging, carbon nanotubes essentially serve as carriers for the fluorescent molecular labels. In the study by Dai and coworkers,[95] as-produced SWNTs were sonicated in an aqueous solution of fluorescein-poly(ethylene glycol) (Fluor-PEG, 114 PEG units) and purified via centrifugation to obtain Fluor-PEG-functionalized SWNTs. Compared to those of free fluorscein, the absorption peak of the nanotube-attached Fluor-PEG in phosphate buffer solution (pH 7.4) was red-shifted by several nanometers, and the fluorescence was quenched by about two-thirds. According to the bio-evaluation results, these functionalized SWNTs served as both intracellular transporter and fluorescent marker, with their uptake by mammalian cells (BT474 breast cancer cells) and also their enabling the detection of fluorescence inside the cells.[95]

In addition to fluorescence-based imaging, radioisotope tracing and the use of special microscopy techniques have also been effective in the study of carbon nanotubes in vitro and in vivo.[93,96] For example, Porter, et al. visualized individual SWNTs in cells through a new technique called low-loss energy-filtered transmission electron microscopy in combination with electron energy loss spectrum imaging.[96] The technique made it possible to directly determine the distribution of SWNTs in both stained and unstained cells. It also enabled the tracking of cellular actions of the nanotubes, such as their entering the cytoplasm, localizing

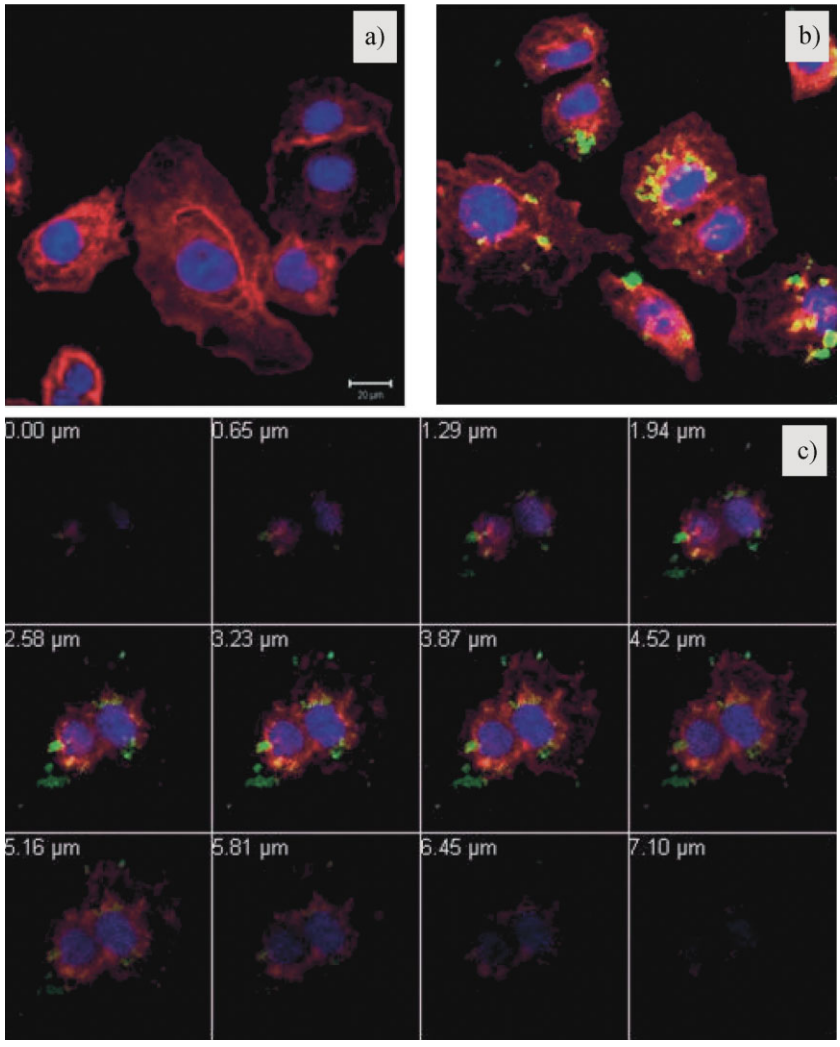

Figure 6. Multiple stain confocal images of A549 cells a) incubated for 2 h (37 °C, 5% CO_2) in the absence of SWNT-NH_3^+ (control) and b) in the presence of 20 μg of SWNT-NH_3^+ (scale bar = 20 μm). c) Z-stack imaging data obtained from the preparation where A549 cells were incubated with 20 μg of SWNT-NH_3^+. Cellular membranes were stained in red with WGA-TRITC and nuclei were counterstained in blue with TO-PRO 3. Reproduced with permission from [92].

within the cell nucleus, and causing cell mortality in a dose dependent manner.[96]

3.4. In vivo Biodistribution and Toxicity

The widespread interests and rapid advances in the use of carbon nanotubes for new materials and technologies have promoted growing biosafety concerns and the recognition that a fundamental understanding of the pharmacological and toxicological properties of carbon nanotubes is necessary or even urgent. As a result, there have been increasing activities in the respective areas.[12,101]

Biocompatibility and bioavailability of carbon nanotubes in vivo are important to many of the currently pursued bioapplications. A number of studies have been commissioned with aims toward systematic and quantitative in vivo analyses of carbon nanotubes on issues such as distribution, metabolism, degradation, clearance, and bioaccumulation. For pristine carbon nanotubes (not chemically modified or functionalized) in biological systems, there have been more experimental challenges due to a general lack of quantitative detection methods. Yang, et al.[81] developed an approach to use skeleton ^{13}C-enriched pristine SWNTs for quantification with isotope ratio mass spectrometry. The biodistribution of the SWNTs (^{13}C-enriched) in mice was determined at different time intervals post-exposure.[81] As shown in Figure 7, the SWNTs were apparently cleared from blood stream quickly and distributed throughout most organs within 24 h. The primary accumulations were in lungs, liver, and spleen, and the nanotubes were retained in these organs at relatively high accumulation levels over 28 days. Most noticeable and interesting was the possible accumulation (1–3% ID) in the brain (for the SWNTs to cross the blood brain barrier). While the accumulation level of SWNTs in liver was relatively constant, there was a gradual decrease of accumulation in lungs from 15% ID to 9.4% ID in the monitoring period, for which secretion by the alveolar macrophage as mucus through mucociliary transport and translocation through the lymph nodes were considered as possible clearance pathways. The pristine nanotubes could hardly be detected in urine and feces in terms of either ^{13}C isotope ratio mass spectroscopy measurements or TEM analyses, obviously different from their modified or functionalized counterparts (reported to be cleared from the animal mostly through the renal excretion route[93,102]).

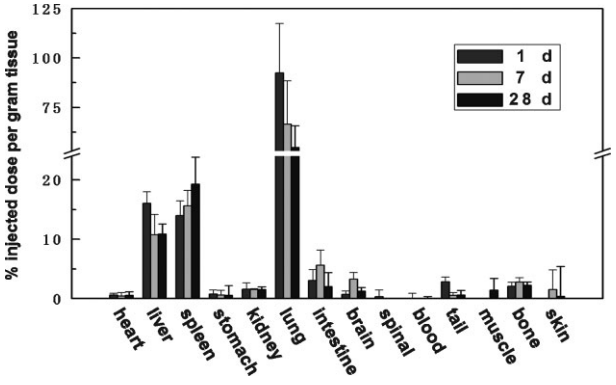

Figure 7. The biodistribution of pristine SWNTs (skeleton ^{13}C-enriched) in mice at different time points post-exposure. Data are presented as the mean ± SD ($n = 3$). Reproduced with permission from [81]. Copyright 2007 American Chemical Society.

For functionalized carbon nanotubes, radiotracing has become a generally adoptable method for visualizing their biological behavior in animals, with ^{111}In,[93] ^{125}I,[103] ^{64}Cu,[83] ^{99m}Tc[104] and ^{14}C.[105] as radiolabels. In the study by Singh et al.,[93] sidewall functionalized SWNTs including the radioactive ^{111}In label were intravenously administrated into mice. The nanotubes were rapidly cleared from systemic blood circulation (half life ~3 h) through the renal excretion route, without being retained in any of reticuloendothelial system (RES) organs.[93] For comparison, the same group prepared three MWNT samples, including purified MWNTs with serum protein coating and the diethylentriaminepentaacetic dianhydride (DTPA)-functionalized MWNTs with and without the radioactive ^{111}In label, for the administration into mice intravenously.[97] The purified MWNTs were accumulated in liver and lungs, but no similar accumulation for the DTPA-functionalized MWNTs. In another study by Chen, Dai, and coworkers,[83] SWNTs from the HiPco production technique were wrapped in the surfactant PL-PEG with the radioactive ^{64}Cu label for the investigation on biodistribution and tumor targeting ability in mice by using in vivo positron emission tomography (PET), *ex vivo* biodistribution analysis, and Raman spectroscopy. It was found that the SWNTs wrapped with PL-PEG were surprisingly stable in vivo and exhibited relatively long blood circulation times and low RES uptake. These nanotubes upon linking to an RGD peptide could also efficiently target integrin-positive tumor in mice.[83]

As demonstrated in the studies highlighted above and others, radiolabeling of the organic molecules on nanotube surface can be readily achieved. However, the labeled nanotube conjugates may suffer from decreasing or even losing activity over time due to decay or dissociation (from the nanotubes) of the label. Thus, direct detection and quantification of carbon nanotubes in vivo and/or *ex vivo* based on the intrinsic physical and chemical properties of the nanotubes could be more advantageous in some studies to monitor the biological behavior of carbon nanotubes over both short and long terms. For example, Liu, et al. used intrinsic Raman signature to probe the blood circulation and long-term fate of SWNTs noncovalently functionalized with several linear and branched PL-PEGs in mice.[82] The coating with PEGs was very effective to achieve long blood circulation and low RES uptake, with the near-complete clearance from main organs via biliary and renal pathways occurring in about 2 months[82] (probably due to improved hydrophilicity and resistance to protein nonspecific binding). Cherukuri et al. used near-IR fluorescence of individualized SWNTs to determine the blood elimination kinetics and biodistribution of the nanotubes in rabbits (Fig. 8).[106] It was found that the nanotube concentration in the blood serum decreased exponentially with a half life of one hour, and significant nanotube concentration was detected only in the liver at 24 h after intravenous administration.

Yang et al. again applied isotope ratio mass spectrometry, coupled with the covalent functionalization of skeleton ^{13}C-enriched SWNTs with the diamine-terminated PEGs (PEGylation), to the determination of in vivo biodistribution.[80] These PEGylated SWNTs intravenously administrated into mice were distributed throughout most organs within one hour and

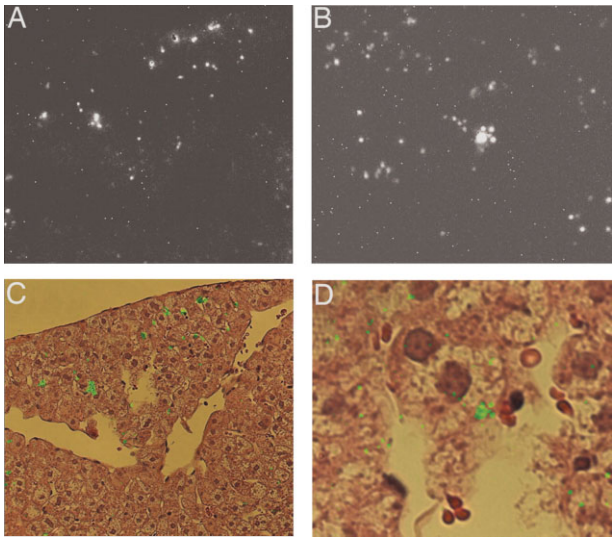

Figure 8. Micrographs at two magnifications of liver tissue from rabbits killed 24 h after i.v. administration of suspended SWNTs. A) and B) Near-IR SWNT fluorescence images with field widths of 390 μm (A) and 83 μm (B). Scattered isolated bright pixels are artifacts from defective sensor elements in the near-IR camera; all larger features represent emission from SWNTs. In C) and D), the SWNT fluorescence from A and B is shown overlaid as false-color green onto visible bright-field images from adjacent 3-μm-thick specimen slices that had been stained with hematoxylin and eosin. Reproduced with permission from [106]. Copyright 2006 National Academy of Sciences, USA.

significantly accumulated in liver and spleen, similar to pristine SWNTs.[81] At day 7 post exposure, ~25% ID and ~3% ID of the PEGylated SWNTs remained in liver and spleen, respectively. However, their uptake by RES was significantly reduced (28% ID) in comparison with that of the corresponding pristine SWNTs (37% ID).[81] According to this and other studies, there are obvious differences between pristine and functionalized SWNTs in their biodistributions and time dependencies post-exposure, suggesting that the surface functionality and morphological and dispersion characteristics of carbon nanotubes do have significant biological consequences.

It has made into headlines that carbon nanotubes might potentially be toxic.[107] Carbon nanotubes may enter the body via many routes, such as intravenous, dermal, subcutaneous, inhalational, intraperitoneal, or oral.[108] Preliminary in vivo toxicity studies on respiratory and skin exposure to pristine carbon nanotubes did show some harmful effects,[12,109,110] so that there should be precautions to limit the exposure. However, the toxicity of carbon nanotubes seems to depend on many factors, including dosage, physical form, and chemical attachment.[12,101]

In an in vitro study, Cui et al. explored the biocompatibility of as-produced SWNTs with the human HEK293 kidney cells, and they found that the nanotubes could inhibit cell proliferation and at the same time decrease the cell's ability to adhere in a dose and time-dependent manner.[111] In another recent study aimed at issues concerning the lack of aqueous solubility and the contamination of residual metal catalysts in carbon nanotubes, Isobe et al. used water-soluble and metal-free carbon nanohorn aggregate (covalently bonded class of self-aggregated nanotubes) to examine cytotoxicity on 3T3 and HeLa cell lines.[112] The results suggested very low cytotoxicity, even lower than that of quartz microparticles, though there were still doubts on the reliability of the results because of some experimental problems.[112] The structural differences between nanohorns and nanotubes should also be noted.

Chemically modified or functionalized carbon nanotubes and thus aqueous soluble have generally exhibited no apparent or less cytotoxicity to all living cell lines that have been investigated.[113,114] For example, Dumortier et al. found that carbon nanotubes functionalized in 1,3-dipolar cycloaddition reaction or treated with oxidation and then amidation could be taken up rapidly by B and T lymphocytes as well as macrophages without affecting the overall cell viability.[113] It was also found that the highly water-soluble modified carbon nanotubes did not affect the functional activity of different types of immunoregulatory cells.[113]

In the in vivo experiments on pristine and the PEGylated SWNTs in mice, Yang et al.[80,81] did not find any of the animals exhibiting any signs of acute toxicity response during the experimental period, even at a high exposure of 80 mg pristine or 24 mg PEGylated SWNTs (nanotube equivalent, both skeleton ^{13}C-enriched) per kilogram body weight, consistent with other reports. In a recent toxicity study by Schipper et al., the covalently and noncovalently functionalized SWNTs were injected into a small number of mice, and results suggested no evidence of toxicity over 4 months.[115]

In fact, overall the available in vivo biodistribution studies have generally reported no acute toxicity or negative health effects of the carbon nanotubes on the animals involved in the experiments. However, further investigations are necessary and are probably in progress in many laboratories on the potential toxicity and related issues.

4. Summary

The research on the modification and functionalization of carbon nanotubes has become an increasingly mature topic. As a result, many biocompatible and/or bioactive carbon nanotubes and related systems have been developed and synthesized for widespread investigations on their potential bioapplications. Since our last report,[13] there has obviously been a dramatic proliferation of activities in this field. The positive trend and also the expansion into other areas that are not covered in this report are expected to continue in a rapid pace. In further studies, however, more efforts should be and will likely be devoted to demonstrate that carbon nanotubes not only "can be used" but also "are uniquely suited" for various applications in biology and medicine.

Acknowledgements

Financial support from NSF, NASA, NIH, South Carolina Space Grant Consortium, and the Center for Advanced Engineering Fibers and Films (NSF-ERC at Clemson University) is gratefully acknowledged.

Received: May 31, 2008
Published online: December 2, 2008

[1] *Carbon Nanotubes: Synthesis, Structure, Properties and Applications*, (Eds: M. Dresselhaus, G. Dresselhaus, P. Avouris), Springer, Berlin, Germany **2001**.

[2] Special Issue on Carbon Nanotubes, *Acc. Chem. Res.* **2002**, *35*(12), 997
[3] P. M. Ajayan, *Chem. Rev.* **1999**, *99*, 1787.
[4] R. E. Smalley Memorial Issue, *J. Phys. Chem. C* **2007**, *111*(48), 17671.
[5] J. Wang, *Electroanalysis* **2005**, *17*, 7.
[6] Y. Yun, Z. Dong, V. Shanov, W. R. Heineman, H. B. Halsall, A. Bhattacharya, L. Conforti, R. K. Narayan, W. S. Ball, M. J. Schulz, *Nano Today* **2007**, *2*, 30.
[7] G. A. Rivas, M. D. Rubianes, M. C. Rodríguez, N. F. Ferreyra, G. L. Luque, M. L. Pedano, S. A. Miscoria, C. Parrado, *Talanta* **2007**, *74*, 291.
[8] a) R. H. Baughman, C. Cui, A. A. Zakhidov, Z. Iqbal, J. N. Barisci, G. M. Spinks, G. G. Wallace, A. Mazzoldi, D. De Rossi, A. G. Rinzler, O. Jaschinski, S. Roth, M. Kertesz, *Science* **1999**, *284*, 1340. b) A. M. Fennimore, T. D. Yuzvinsky, W.-Q. Han, M. S. Fuhrer, J. Cumings, A. Zettl, *Nature* **2003**, *424*, 408.
[9] N. W. S. Kam, M. O'Connell, J. A. Wisdom, H. Dai, *Proc. Natl. Acad. Sci. USA* **2005**, *102*, 11600.
[10] a) N. W. S. Kam, H. Dai, *Phys. Status Solidi B* **2006**, *243*, 3561. b) L. Lacerda, S. Raffa, M. Prato, A. Bianco, K. Kostarelos, *Nano Today* **2007**, *2*, 38. c) M. Prato, K. Kostarelos, A. Bianco, *Acc. Chem. Res.* **2008**, *41*, 60.
[11] H. Wang, L. Gu, Y. Lin, F. Lu, M. J. Meziani, P. G. Luo, W. Wang, L. Cao, Y.-P. Sun, *J. Am. Chem. Soc.* **2006**, *128*, 13364.
[12] a) C. W. Lam, J. T. James, R. McCluskey, S. Arepalli, R. L. Hunter, *Crit. Rev. Toxicol.* **2006**, *36*, 189. b) J. Kolosnjaj, H. Szwarc, F. Moussa, in *Bio-Applications of Nanoparticles*, (Ed: W. C. W. Chan), Springer book series: Adv. Exp. Med. Biol., New York, U.S.A. **2007**, *620*, p. 181.
[13] Y Lin,, S. Taylor, H. Li, K. A. S. Fernando, L. Qu, W. Wang, L. Gu, B. Zhou, Y.-P. Sun, *J. Mater. Chem.* **2004**, *14*, 527.
[14] a) S. Banerjee, T. Hemraj-Benny, S. S. Wong, *Adv. Mater.* **2005**, *17*, 17. b) K. Balasubramanian, M. Burghard, *Small* **2005**, *1*, 180.
[15] D. Tasis, N. Tagmatarchis, A. Bianco, M. Prato, *Chem. Rev.* **2006**, *106*, 1105.
[16] W. Huang, S. Fernando, L. F. Allard, Y.-P. Sun, *Nano Lett.* **2003**, *3*, 565.
[17] K. A. S. Fernando, Y. Lin, W. Wang, S. Kumar, B. Zhou, S. Y. Xie, L. T. Cureton, Y.-P. Sun, *J. Am. Chem. Soc.* **2004**, *126*, 10234.
[18] M. J. O'Connell, S. M. Bachilo, C. B. Huffman, V. C. Moore, M. S. Strano, E. H. Haroz, K. L. Rialon, P. J. Boul, W. H. Noon, C. Kittrell, J. Ma, R. H. Hauge, R. B. Weisman, R. E. Smalley, *Science* **2002**, *297*, 593.
[19] S. M. Bachilo, M. S. Strano, C. Kittrell, R. H. Hauge, R. E. Smalley, R. B. Weisman, *Science* **2002**, *298*, 2361.
[20] C. A. Dyke, J. M. Tour, *Nano Lett.* **2003**, *3*, 1215.
[21] V. C. Moore, M. S. Strano, E. H. Haroz, R. H. Hauge, R. E. Smalley, *Nano Lett.* **2003**, *3*, 1379.
[22] D. Nepal, K. E. Geckeler, *Small* **2007**, *3*, 1259.
[23] a) V. Z. Poenitzsch, D. C. Winters, H. Xie, G. R. Dieckmann, A. B. Dalton, I. H. Musselman, *J. Am. Chem. Soc.* **2007**, *129*, 14724. b) G. R. Dieckmann, A. B. Dalton, P. A. Johnson, J. Razal, J. Chen, G. M. Giordano, E. Munoz, I. H. Musselman, R. H. Baughman, R. K. Draper, *J. Am. Chem. Soc.* **2003**, *125*, 1770.
[24] a) W. Huang, S. Taylor, K. Fu, Y. Lin, D. Zhang, T. W. Hanks, A. M. Rao, Y.-P. Sun, *Nano Lett.* **2002**, *2*, 311. b) K. Fu, W. Huang, Y. Lin, D. Zhang, T. W. Hanks, A. M. Rao, Y.-P. Sun, *J. Nanosci. Nanotechnol.* **2002**, *2*, 457.
[25] Y. Lin, L. F. Allard, Y.-P. Sun, *J. Phys. Chem. B* **2004**, *108*, 3760.
[26] T. Elkin, X. Jiang, S. Taylor, Y. Lin, L. Gu, H. Yang, J. Brown, S. Collins, Y.-P. Sun, *ChemBioChem* **2005**, *6*, 640.
[27] Y. Lin, T. Elkin, S. Taylor, L. Gu, B. Chen, L. M. Veca, B. Zhou, H. Yang, J. Brown, R. Joseph, E. Jones, X. Jiang, Y.-P. Sun, *Microchim. Acta* **2006**, *152*, 249.
[28] A. Joshi, S. Punyani, S. S. Bale, H. Yang, T. Borca-Tasciuc, R. S. Kane, *Nat. Nanotechnol.* **2008**, *3*, 41.
[29] Y. Lin, X. Jiang, T. Elkin, K. A. S. Fernando, L. Gu, S. Taylor, H. Yang, E. Jones, W. Wang, Y.-P. Sun, *J. Nanosci. Nanotechnol.* **2006**, *6*, 868.
[30] M. Zheng, A. Jagota, M. S. Strano, A. P. Santos, P. Barone, S. G. Chou, B. A. Diner, M. S. Dresselhaus, R. S. Mclean, G. B. Onoa, G. G. Samsonidze, E. D. Semke, M. Usrey, D. J. Walls, *Science* **2003**, *302*, 1545.
[31] Y. Chen, H. Liu, T. Ye, J. Kim, C. Mao, *J. Am. Chem. Soc.* **2007**, *129*, 8696.
[32] X. Han, Y. Li, Z. Deng, *Adv. Mater.* **2007**, *19*, 1518.
[33] S. Li, P. He, J. Dong, Z. Guo, L. Dai, *J. Am. Chem. Soc.* **2005**, *127*, 14.
[34] X. Wang, F. Liu, G. T. S. Andavan, X. Jing, K. Singh, V. R. Yazdanpanah, N. Bruque, R. R. Pandey, R. Lake, M. Ozkan, K. L. Wang, C. S. Ozkan, *Small* **2006**, *2*, 1356.
[35] C.-S. Lee, S. E. Baker, M. S. Marcus, W. Yang, M. A. Eriksson, R. J. Hamers, *Nano Lett.* **2004**, *4*, 1713.
[36] W. Yang, M. J. Moghaddam, S. Taylor, B. Bojarski, L. Wieczorek, J. Herrmann, M. J. McCall, *Chem. Phys. Lett.* **2007**, *443*, 169.
[37] Y. Lu, S. Bangsaruntip, X. Wang, L. Zhang, Y. Nishi, H. Dai, *J. Am. Chem. Soc.* **2006**, *128*, 3518.
[38] Z. Liu, M. Winters, M. Holodniy, H. Dai, *Angew. Chem. Int. Ed.* **2007**, *46*, 2023.
[39] K. Rege, G. Viswanathan, G. Zhu, A. Vijayaraghavan, P. M. Ajayan, J. S. Dordick, *Small* **2006**, *2*, 718.
[40] M. L. Becker, J. A. Fagan, N. D. Gallant, B. J. Bauer, V. Bajpai, E. K. Hobbie, S. H. Lacerda, K. B. Migler, J. P. Jakupciak, *Adv. Mater.* **2007**, *19*, 939.
[41] L. Zhang, S. Zaric, X. Tu, X. Wang, W. Zhao, H. Dai, *J. Am. Chem. Soc.* **2008**, *130*, 2686.
[42] S. Manohar, T. Tang, A. Jagota, *J. Phys. Chem. C* **2007**, *111*, 17835.
[43] a) X. Zhao, J. K. Johnson, *J. Am. Chem. Soc.* **2007**, *129*, 10438. b) R. R. Johnson, A. T. C. Johnson, M. L. Klein, *Nano Lett.* **2008**, *8*, 69.
[44] a) M. E. Hughes, E. Brandin, J. A. Golovchenko, *Nano Lett.* **2007**, *7*, 1191. b) S. Meng, W. L. Wang, P. Maragakis, E. Kaxiras, *Nano Lett.* **2007**, *7*, 2312.
[45] D. A. Heller, E. S. Jeng, T.-K. Yeung, B. M. Martinez, A. E. Moll, J. B. Gastala, M. S. Strano, *Science* **2006**, *311*, 508.
[46] X. Chen, G. S. Lee, A. Zettl, C. R. Bertozzi, *Angew. Chem. Int. Ed.* **2004**, *43*, 6112.
[47] T. Hasegawa, T. Fujisawa, M. Numata, M. Umeda, T. Matsumoto, T. Kimura, S. Okumura, K. Sakurai, S. Shinkai, *Chem. Commun.* **2004**, 2150.
[48] L. Gu, T. Elkin, X. Jiang, H. Li, Y. Lin, L. Qu, T.-R. J. Tzeng, R. Joseph, Y.-P. Sun, *Chem. Commun.* **2005**, 874.
[49] L. Gu, Y. Lin, L. Qu, Y.-P. Sun, *Biomacromolecules* **2006**, *7*, 400.
[50] M. Numata, M. Asai, K. Kaneko, A.-H. Bae, T. Hasegawa, K. Sakurai, S. Shinkai, *J. Am. Chem. Soc.* **2005**, *127*, 5875.
[51] Y. Liu, P. Liang, H. Y. Zhang, D. S. Guo, *Small* **2006**, *2*, 874.
[52] M. Numata, K. Sugikawa, K. Kaneko, S. Shinkai, *Chem. Eur. J.* **2008**, *14*, 2398.
[53] M. Mammen, S.-K. Choi, G. M. Whitesides, *Angew. Chem. Int. Ed.* **1998**, *37*, 2754.
[54] L. Gu, Ph. D. Thesis, Clemson University **2008**.
[55] a) E. Katz, I. Willner, *ChemPhysChem* **2004**, *5*, 1084; b) K. Balasubramanian, M. Burghard, *Anal. Bioanal. Chem.* **2006**, *385*, 452; c) B. L. Allen, P. D. Kichambare, A. Star, *Adv. Mater.* **2007**, *19*, 1439; d) S. N. Kim, J. F. Rusling, F. Papadimitrakopoulos, *Adv. Mater.* **2007**, *19*, 3214.
[56] P. Avouris, Z. Chen, V. Perebeinos, *Nat. Nanotechnol.* **2007**, *2*, 605.
[57] P. Stokes, S. I. Khondaker, *Nanotechnology* **2008**, *19*, 175202.
[58] R. J. Chen, H. C. Choi, S. Bangsaruntip, E. Yenilmez, X. Tang, Q. Wang, Y.-L. Chang, H. Dai, *J. Am. Chem. Soc.* **2004**, *126*, 1563.
[59] H. R. Byon, H. C. Choi, *J. Am. Chem. Soc.* **2006**, *128*, 2188.
[60] C. Li, M. Curreli, H. Lin, B. Lei, F. N. Ishikawa, R. Datar, R. J. Cote, M. E. Thompson, C. Zhou, *J. Am. Chem. Soc.* **2005**, *127*, 12484.
[61] K. Maehashi, T. Katsura, K. Kerman, Y. Takamura, K. Matsumoto, E. Tamiya, *Anal. Chem.* **2007**, *79*, 782.
[62] A. Star, E. Tu, J. Niemann, J.-C. P. Gabriel, C. S. Joiner, C. Valcke, *Proc. Natl. Acad. Sci. USA* **2006**, *103*, 921.
[63] E. L. Gui, L.-J. Li, K. Zhang, Y. Xu, X. Dong, X. Ho, P. S. Lee, J. Kasim, Z. X. Shen, J. A. Rogers, S. G. Mhaisalkar, *J. Am. Chem. Soc.* **2007**, *129*, 14427.

[64] S. Heinze, J. Tersoff, R. Martel, V. Derycke, J. Appenzeller, P. Avouris, *Phys. Rev. Lett.* **2002**, *89*, 106801.
[65] A. Star, J.-C. P. Gabriel, K. Bradley, G. Gruner, *Nano Lett.* **2003**, *3*, 459.
[66] K. Bradley, M. Briman, A. Star, G. Gruner, *Nano Lett.* **2004**, *4*, 253.
[67] I. Heller, A. M. Janssens, J. Mannik, E. D. Minot, S. G. Lemay, C. Dekker, *Nano Lett.* **2008**, *8*, 591.
[68] a) J. Kong, N. R. Franklin, C. Zhou, M. G. Chapline, S. Peng, K. Cho, H. Dai, *Science* **2000**, *287*, 622. b) P. G. Collins, K. Bradley, M. Ishigami, A. Zettl, *Science* **2000**, *287*, 1801.
[69] a) Y. Li, D. Mann, M. Rolandi, W. Kim, A. Ural, S. Hung, A. Javey, J. Cao, D. W. Wang, E. Yenilmez, Q. Wang, J. F. Gibbons, Y. Nishi, H. Dai, *Nano Lett.* **2004**, *4*, 317. b) S. M. Bachilo, L. Balzano, J. E. Herrera, F. Pompeo, D. E. Resasco, R. B. Weisman, *J. Am. Chem. Soc.* **2003**, *125*, 11186.
[70] Y. Lin, K. A. S. Fernando, W. Wang, Y.-P. Sun, in *Carbon Nanotechnology*, (Ed: L. Dai), Elsevier, The Netherlands **2006**, p. 255.
[71] P. G. Collins, M. S. Arnold, P. Avouris, *Science* **2001**, *292*, 706.
[72] D. Chattopadhyay, I. Galeska, F. Papadimitrakopoulos, *J. Am. Chem. Soc.* **2003**, *125*, 3370.
[73] H. Li, B. Zhou, Y. Lin, L. Gu, W. Wang, K. A. S. Fernando, S. Kumar, L. F. Allard, Y.-P. Sun, *J. Am. Chem. Soc.* **2004**, *126*, 1014.
[74] G. Pastorin, W. Wu, S. Wieckowski, J. P. Briand, K. Kostarelos, M. Prato, A. Bianco, *Chem. Commun.* **2006**, 1182.
[75] H. Ali-Boucetta, K. T. Al-Jamal, D. McCarthy, M. Prato, A. Bianco, K. Kostarelos, *Chem. Commun.* **2008**, 459.
[76] Z. Liu, X. Sun, N. Nakayama-Ratchford, H. Dai, *ACS Nano* **2007**, *1*, 50.
[77] R. P. Feazell, N. Nakayama-Ratchford, H. Dai, S. J. Lippard, *J. Am. Chem. Soc.* **2007**, *129*, 8438.
[78] Z. Zhang, X. Yang, Y. Zhang, B. Zeng, S. Wang, T. Zhu, R. B. S. Roden, Y. Chen, R. Yang, *Clin. Cancer Res.* **2006**, *12*, 4933.
[79] V. P. Torchilin, *Adv. Drug Delivery Rev.* **2006**, *58*, 1532.
[80] S.-T. Sheng, K. A. S. Fernando, J.-H. Liu, J. Wang, H.-F. Sun, Y. Liu, M. Chen, Y. Huang, X. Wang, H. Wang, Y.-P. Sun, *Small* **2008**, *4*, 940.
[81] S.-T. Yang, W. Guo, Y. Lin, X. Deng, H. Wang, H. Sun, Y. Liu, X. Wang, W. Wang, M. Chen, Y. Huang, Y.-P. Sun, *J. Phys. Chem. C* **2007**, *111*, 17761.
[82] Z. Liu, C. Davis, W. Cai, L. He, X. Chen, H. Dai, *Proc. Natl. Acad. Sci. USA* **2008**, *105*, 1410.
[83] Z. Liu, W. Cai, L. He, N. Nakayama, K. Chen, X. Sun, X. Chen, H. Dai, *Nat. Nanotechnol.* **2007**, *2*, 47.
[84] N. W. S. Kam, T. C. Jessop, P. A. Wender, H. Dai, *J. Am. Chem. Soc.* **2004**, *126*, 6850.
[85] N. W. S. Kam, H. Dai, *J. Am. Chem. Soc.* **2005**, *127*, 6021.
[86] N. W. S. Kam, Z. Liu, H. Dai, *Angew. Chem. Int. Ed.* **2006**, *45*, 577.
[87] D. Pantarotto, J. Briand, M. Prato, A. Bianco, *Chem. Commun.* **2004**, 16.
[88] K. Kostarelos, L. Lacerda, G. Pastorin, W. Wu, S. Wieckowski, J. Luangsivilay, S. Godefroy, D. Pantarotto, J.-P. Briand, S. Muller, M. Prato, A. Bianco, *Nat. Nanotechnol.* **2007**, *2*, 108.
[89] C. F. Lopez, S. O. Nielsen, P. B. Moore, M. L. Klein, *Proc. Natl. Acad. Sci. USA* **2004**, *101*, 4431.
[90] X. Chen, A. Kis, A. Zettl, C. R. Bertozzi, *Proc. Natl. Acad. Sci. USA* **2007**, *104*, 8218.
[91] P. Cherukuri, S. M. Bachilo, S. H. Litovsky, R. B. Weisman, *J. Am. Chem. Soc.* **2004**, *126*, 15638.
[92] L. Lacerda, G. Pastorin, D. Gathercole, J. Buddle, M. Prato, A. Bianco, K. Kostarelos, *Adv. Mater.* **2007**, *19*, 1480.
[93] R. Singh, D. Pantarotto, L. Lacerda, G. Pastorin, C. Klumpp, M. Prato, A. Bianco, K. Kostarelos, *Proc. Natl. Acad. Sci. USA* **2006**, *103*, 3357.
[94] T. K. Leeuw, R. M. Reith, R. A. Simonette, M. E. Harden, P. Cherukuri, D. A. Tsyboulski, K. M. Beckingham, R. B. Weisman, *Nano Lett.* **2007**, *7*, 2650.
[95] N. Nakayama-Ratchford, S. Bangsaruntip, X. Sun, K. Welsher, H. Dai, *J. Am. Chem. Soc.* **2007**, *129*, 2448.
[96] A. E. Porter, M. Gass, K. Muller, J. N. Skepper, P. A. Midgley, M. Welland, *Nat. Nanotechnol.* **2007**, *2*, 713.
[97] L. Lacerda, A. Soundararajan, R. Singh, G. Pastorin, K. T. Al-Jamal, J. Turton, P. Frederik, M. A. Herrero, S. Li, A. Bao, D. Emfietzoglou, S. Mather, W. T. Phillips, M. Prato, A. Bianco, B. Goins, K. Kostarelos, *Adv. Mater.* **2008**, *20*, 225.
[98] K. Welsher, Z. Liu, D. Daranciang, H. Dai, *Nano Lett.* **2008**, *8*, 586.
[99] J. E. Riggs, Z. Guo, D. L. Carroll, Y.-P. Sun, *J. Am. Chem. Soc.* **2000**, *122*, 5879.
[100] Y. Lin, B. Zhou, R. B. Martin, K. B. Henbest, B. A. Harruff, J. E. Riggs, Z. Guo, L. F. Allard, Y.-P. Sun, *J. Phys. Chem. B* **2005**, *109*, 14779.
[101] L. Lacerda, A. Bianco, M. Prato, K. Kostarelos, *Adv. Drug Delivery Rev.* **2006**, *58*, 1460.
[102] H. Wang, J. Wang, X. Deng, H. Sun, Z. Shi, Z. Gu, Y. Liu, Y. Zhao, *J. Nanosci. Nanotechnol.* **2004**, *4*, 1019.
[103] X. Deng, S. Yang, H. Nie, H. Wang, Y. Liu, *Nanotechnology* **2008**, *19*, 075101.
[104] J. Guo, X. Zhang, Q. Li, W. Li, *Nucl. Med. Biol.* **2007**, *34*, 579.
[105] X. Deng, G. Jia, H. Wang, H. Sun, X. Wang, S. Yang, T. Wang, Y. Liu, *Carbon* **2007**, *45*, 1419.
[106] P. Cherukuri, C. J. Gannon, T. K. Leeuw, H. K. Schmidt, R. E. Smalley, S. A. Curley, R. B. Weisman, *Proc. Natl. Acad. Sci. USA* **2006**, *103*, 18882.
[107] C. A. Poland, R. G. Duffin, I. Kinloch, A. Maylnard, W. A. H. Wallace, A. Seaton, V. Stone, S. Brown, W. Macnee, K. Donaldson, *Nat. Nanotechnol.* **2008**, *3*, 423.
[108] H. C. Fischer, W. C. W. Chan, *Curr. Opin. Biotechnol.* **2007**, *18*, 565.
[109] J. Muller, F. Huaux, D. Lison, *Carbon* **2006**, *44*, 1048.
[110] N. A. Monteiro-Riviere, A. O. Inman, *Carbon* **2006**, *44*, 1070.
[111] D. Cui, F. Tian, C. S. Ozkan, M. Wang, H. Gao, *Toxicol. Lett.* **2005**, *155*, 73.
[112] H. Isobe, T. Tanaka, R. Maeda, E. Noiri, N. Solin, M. Yudasaka, S. Iijima, E. Nakamura, *Angew. Chem. Int. Ed.* **2006**, *45*, 6676.
[113] H. Dumortier, S. Lacotte, G. Pastorin, R. Marega, W. Wu, D. Bonifazi, J.-P. Briand, M. Prato, S. Muller, A. Bianco, *Nano Lett.* **2006**, *6*, 1522.
[114] C. M. Sayes, F. Liang, J. L. Hudson, J. Mendez, W. Guo, J. M. Beach, V. C. Moore, C. D. Doyle, J. L. West, W. E. Billups, K. D. Ausman, V. L. Colvin, *Toxicol. Lett.* **2006**, *161*, 135.
[115] M. L. Schipper, N. Nakayama-Ratchford, C. R. Davis, N. W. S. Kam, P. Chu, Z. Liu, X. Sun, H. Dai, S. S. Gambhir, *Nat. Nanotechnol.* **2008**, *3*, 216.

Toxicology and Applied Pharmacology 235 (2009) 216–225

Contents lists available at ScienceDirect

Toxicology and Applied Pharmacology

journal homepage: www.elsevier.com/locate/ytaap

Acute and long-term effects after single loading of functionalized multi-walled carbon nanotubes into zebrafish (*Danio rerio*)

Jinping Cheng [a], Chung Man Chan [a], L. Monica Veca [d], Wing Lin Poon [b], Po Kwok Chan [c], Liangwei Qu [d], Ya-Ping Sun [d,*], Shuk Han Cheng [a,*]

[a] Department of Biology and Chemistry, City University of Hong Kong, Hong Kong
[b] Department of Biochemistry (Science), Chinese University of Hong Kong, Hong Kong
[c] Department of Knowledge Transfer Office, City University of Hong Kong, Hong Kong
[d] Department of Chemistry and Laboratory for Emerging Materials and Technology, Clemson University, Clemson, South Carolina 29634-0973, USA

ARTICLE INFO

Article history:
Received 18 September 2008
Revised 18 November 2008
Accepted 4 December 2008
Available online 16 December 2008

Keywords:
Multi-walled carbon nanotubes
Zebrafish
In vivo biodistribution
Long-term effects
Survival
Reproduction potential

ABSTRACT

Carbon nanotubes (CNTs) are widely explored for biomedical applications, but there is very limited information regarding their *in vivo* biodistribution and biocompatibility. Here, we report the *in vivo* biodistribution and long-term effects of functionalized multi-walled carbon nanotubes (MWCNTs) in developing zebrafish. The fluorescent-labeled MWCNTs were introduced into zebrafish embryos at 1-cell stage and at 72 h post fertilization through microinjection. After single injection, both acute and long-term interactions between zebrafish and functionalized MWCNTs were studied. The injected FITC-BSA-MWCNTs (at 1-cell stage) were allocated to all blastoderm cells of the embryos through proliferation, and were distinctively excluded from the yolk cell. When introduced into the circulation system, FITC-BSA-MWCNTs moved easily in the compartments and finally were cleaned out by the body at 96 h after the loading. At early stages, the treated zebrafish embryos generated immune response by accumulating circulating white blood cells at the trunk region. Under transmission electron microscope, many lysosome-like vesicles were observed in the blastoderm cells of the treated embryos. The zebrafish loaded with MWCNTs had normal primordial germ cells at early stage and produced second generation later on. However, the larvae of the second generation had obviously lower survival rates as compared to the untreated groups, suggesting a negative effect on the reproduction potential. These results suggest that extensive purification and functionalization processes can help improve the biocompatibility of CNTs. This study also indicates that purified CNTs may have long-term toxicity effects when they were delivered into the body.

Introduction

Emerging development in nanotechnology shows potential applications such as electronic devices, biological and chemical sensors, and biomaterials. It is expected that half of all drug discovery and delivery technology will be based on nanotechnology by 2015 (Wei, 2005; Emerich and Thanos, 2005). Carbon nanotubes (CNTs) are one of the most widely explored nanomaterials in various fields with their distinctive properties (Klumpp et al., 2006). It is predicted that the global market for CNTs will grow to between $1 billion to $2 billion by 2014 (Thayer, 2007). With the increasing industrial demands and production capacity, a better understanding of how to safely develop and use these engineered nanomaterials is widely concerned.

Previous study showed that contaminants associated with raw CNTs can induce hatching delay in zebrafish embryos (Cheng et al., 2007). Raw CNTs can be purified to remove those associated contaminants, such as metal catalysts (Sun et al., 2002). The purified CNTs can be further chemically modified (Sun et al., 2002), and the chemical modification (functionalization) can help improve the solubility[1] by conjugation with various molecules (Hirsch, 2002; Sun et al., 2002). CNTs have been conjugated with lots of drug molecules (e.g. anticancer, antiviral or antibacterial agents) (Bianco et al., 2005a,b). Previous studies demonstrated that chemically modified CNTs can cross cell membranes and deliver attached cargos

* Corresponding authors. Y.-P. Sun is to be contacted at Department of Chemistry and Laboratory for Emerging Materials and Technology, Clemson University, Clemson, South Carolina 29634-0973, USA. Fax: +864 656 5007. S.H. Cheng, Department of Biology and Chemistry, City University of Hong Kong, Hong Kong. Fax: +852 2788 7406.
E-mail addresses: syaping@clemson.edu (Y.-P. Sun), bhcheng@cityu.edu.hk (S.H. Cheng).

[1] Here the term "solubility" is loosely defined, as it has been commonly used in the literature. One might imagine that the functionalized nanotubes are individually dispersed in the solvent.

0041-008X/$ – see front matter © 2008 Elsevier Inc. All rights reserved.
doi:10.1016/j.taap.2008.12.006

into cells. The *in vivo* biomedical and pharmaceutical explorations of functionalized CNTs have increased dramatically in recent years (Bianco et al., 2005a,b; Klumpp et al., 2006; Liu et al., 2007). The chemically modified CNTs have been studied for targeted delivery with specific biomarkers (Kam and Dai, 2005), diagnostic agents (McDevitt et al., 2007; Wu et al., 2005) as well as therapeutic molecules (Bianco, 2004; Kam et al., 2005; Jia et al., 2003). Modified CNTs have also been investigated as implant materials for medical treatment for bones (Zanello et al., 2006), as well as scaffolds for other tissue engineering purposes (Mattson et al., 2000; Abarrategi et al., 2008).

Before these modified CNTs can be used in the clinic, it is crucial to find out where they go and end up once they are introduced into the body. Furthermore, because of the large number of *in vivo* diagnostics and therapy applications coming from modified CNTs, there may be great potential for the loading of modified CNTs in the biological systems and for the discharge of modified CNTs into the environment. One cannot exclude the possibility that modified CNTs may be found in the organisms once they were released into the environment. However, the information regarding the *in vivo* toxicology study of the modified CNTs in the biological systems is still limited (Nel et al., 2006). One study demonstrated that well dispersed hydroxylated CNTs injected into the mice moved easily in the compartments and tissues and finally accumulated in liver and kidney (Wang et al., 2004) and these modified CNTs have been successfully used for efficient liver tumor targeting (Liu et al., 2007). With the increasing *in vivo* applications of functionalized CNTs, it is important to gain an understanding of their potential *in vivo* biocompatibility and safety in biological systems (Fischer and Chan, 2007). In addition, interactions of these artificial nanomaterials with the human body are very important factors in determining clinical use. Because the nanomaterials incorporated delivery system may be ultimately introduced into the organisms, the information about their *in vivo* biological behavior and consequences becomes very important (Deng et al., 2007). Considering the long-term effect of the *in vivo* applications, chronic impact studies of functionalized nanomaterials such as a full life span analysis are most biologically relevant to determine their biocompatibility and safety (Curtis et al., 2006). To date, however, this kind of information is still very limited.

The purpose of this study was to characterize the *in vivo* biodistribution and long-term effects of functionalized CNTs in developing zebrafish from a whole life span analysis. Fluorescently labeled CNTs modified with functional molecules were used for better and easy tracking in this study. Zebrafish as a small fish species has attracted much interest as remarkable animal models for organogenesis and human disease (Garrity et al., 2002) because they are transparent and grow fast. As well, their organs and tissues are functionally equivalent to those of mammals (Wittbrodt et al., 2002). Using the transparent zebrafish, the *in vivo* biodistribution, biocompatibility and safety of functionalized CNTs in developing zebrafish was investigated. Zebrafish embryos were exposed to BSA-MWCNTs and PPEI-EI-MWCNTs using two different exposure methods including microinjection at 1-cell stage and microinjection into the cardiovascular system at 72 h post fertilization (hpf). This study contributes to *in vivo* biocompatibility and safety study of modified nanomaterials.

Materials and methods

Preparation and characterization of BSA-MWCNTs. Multi-walled CNTs (MWCNTs) were supplied by Nanostructured & Amorphous Materials. The as-supplied MWCNT sample was dispersed in aqueous HNO_3 (2.6 M) and refluxed for 48 h. These purification steps were designed to remove carbonaceous impurities and metal catalysts. The resulting suspension was centrifuged (~1400 *g*), and the sediment was collected and repeatedly washed with deionized water until neutral pH. Upon the removal of water, the sample was dried in vacuum to yield the purified MWCNT sample. The purity of the sample was validated by using thermogravimetric analysis (TGA) on a Mettler Toledo TGA/SDTA851e system with a typical heating rate of 10 °C/min.

The bovine serum albumin (BSA) functionalized MWCNTs (BSA-MWCNTs) were prepared through the amidation reactions (Huang et al., 2002). In a typical experiment, a purified MWCNT sample (35 mg) was homogenized in MES (2-(*N*-morpholino)ethanesulfonic acid) buffer solution (0.1 M, pH=5.6, 20 mL) for 30 min. 1-ethyl-3-(3-dimethylaminopropyl) carbodiimide (EDAC, 200 mg) and *N*-hydroxysuccinimide (NHS, 250 mg) were added to the solution. The mixture was sonicated for 2 h, followed by centrifugation at 6000 rpm for 4 min to keep the sediments. The solid sample was washed with MES buffer solution (0.1 M) 3 times, and then dispersed in PBS buffer solution (pH=7.4, 20 mL) for reaction with BSA (350 mg). After sonication for 2 h and then stirring at room temperature for 48 h, the resulting mixture was transferred to a cellulose ester dialysis membrane tubing (cutoff molecular weight 100,000) for dialysis against fresh water. After 3 days of dialysis, the mixture was centrifuged at 3000 rpm for 10 min to retain the dark-colored supernatant. Upon the evaporation of water, the BSA-MWCNTs sample was obtained. The unused amine groups in BSA (bound to MWCNTs) were targeted for the labeling with the fluorescent dye FITC (fluorescein isothiocyanate). In the experiment, a freshly prepared solution of FITC in DMSO (1 mg/mL) was mixed with an aqueous solution of BSA-MWCNTs (pH=9). The reaction was carried out in the dark at 4 °C for 12 h. The reaction mixture was dialyzed against fresh deionized water for 3 days to obtain the FITC-labeled BSA-MWCNTs sample (FITC-BSA-MWCNTs). The commercially supplied FITC-BSA (Sigma-Aldrich) was used as a control.

Electron microscopy imaging was conducted on a Hitachi HD-2000 scanning transmission electron microscope (S-TEM) operated at 200 kV. Atomic force microscopy (AFM) images were obtained in the acoustic AC mode on a Molecular Imaging PicoPlus system equipped with a multipurpose scanner for a maximum imaging area of 10 μm×10 μm and a NanoWorld Pointprobe NCH sensor (125 μm in length). The length and height profile analyses were assisted by using the SPIP software distributed by Image Metrology.

The detailed preparation of PPEI-EI-MWCNTs can be found in the supporting information.

Zebrafish maintenance and experimental set-up. Mature zebrafish were purchased from a local commercial source (Chong Hing Aquarium, Hong Kong, China). The zebrafish colony was maintained as described previously (Cheng et al., 2000). Embryos were obtained by photo-induced spawning over green plants and were cultured at 28.5 °C in filtered tap water. The developmental age of the embryos was measured according to the number of hpf and staged according to the method described by Kimmel et al. (1995).

After the light was turned on for photo-induced spawning, embryos were collected within 15 min after fertilization and selected under a dissecting microscope for microinjection at 1-cell stage experiments. Otherwise, embryos were examined at 4 hpf under a dissecting microscope and only embryos that developed normally and reached the blastula stage were selected for cardiovascular loading.

Loading of FITC-BSA-MWCNTs into zebrafish embryos at 1-cell stage by microinjection. The FITC-BSA-MWCNTs were loaded into zebrafish embryos by microinjection at 1-cell stage. Zebrafish embryos were collected into the microinjection plate filled with incubation medium. The FITC-BSA-MWCNTs were then injected into the embryonic cell or yolk of the embryos with a nitrogen-driven micro-injector (Narishige) within 45 min after fertilization. After microinjection, the embryos were incubated at 28.5 °C for further development.

Here is the detailed information for microinjection. Fine-glass microinjection capillary tubes without filament (WPI #TW-100) were pulled and were separated into two microinjection pipettes with Narishige micropipette puller (PC-10). The pipettes were then sharpened with Narishige microforge (MF-900) before use. The microinjection pipette was connected to the micro-injector (Narishige M300 Microinjector) for injection. Microinjection plates were made from 90 mm (diameter)×15 mm (high) Petri dishes. A mold with grooves and bulges was placed to touch the surface of warm molten 1% agarose to produce grooves for trapping eggs for easier injection. The microinjection pipette was calibrated every time before microinjection. About 2 ng of the prepared FITC-BSA-MWCNTs (CNTs equivalent weight) was loaded into the embryo. About 0.54 ng of FITC-BSA (BSA equivalent weight) was loaded into the embryos as a BSA control in some experiments. The dose of FITC-BSA was adjusted according to the BSA amount carried into the cells when the FITC-BSA-MWCNTs were injected.

Biodistribution in the larvae after loading of FITC-BSA-MWCNTs into blood system. The method of microangiography was used to introduce FITC-BSA-MWCNTs into the circulation system of zebrafish embryos. The procedures of microangiography are adopted (Weinstein et al., 1995; Isogai et al., 2003) with some modification. At 4 hpf, embryos were examined under a dissecting microscope and only embryos that developed normally and reached the blastula stage were selected for subsequent experiments. Selected zebrafish embryos at 72 hpf were mounted laterally in 0.3% agarose covered with embryo culture medium. FITC-BSA-MWCNTs were injected into the sinus venous. After injection, FITC-BSA-MWCNTs would circulate throughout the whole vascular network, lighting up each blood vessel with active blood flow from the heart. The embryos loaded with FITC-BSA-MWCNTs in the blood systems were examined after 30 min, 24 h, 48 h and 96 h after microinjection on the Zeiss LSM410 system (LSM 410, Zeiss, Germany) and the confocal images were then further processed for following analysis.

In vivo biodistribution and scoring of phenotypes. The *in vivo* biodistribution of FITC-BSA-MWCNTs loaded at 1-cell stage in developing zebrafish embryos were studied both under a fluorescent and a confocal microscopy. The embryos loaded with FITC-BSA-MWCNTs were scored and imaged under a light microscopy (Nikon Eclipse TE200, Nikon, Japan) at different developmental stages (1–2 cell stage, 50% epiboly, 12 hpf and 24 hpf) before mass pigment formation. To study the intracellular distribution of FITC-BSA-MWCNTs in the embryonic cells, the embryos loaded with FITC-BSA-MWCNTs, and FITC-BSA as a control, were examined under Zeiss LSM410 confocal microscopy (LSM 410, Zeiss, Germany).

Response of embryonic cells after the loading of FITC-BSA-MWCNTs at 1-cell stage. The response of embryonic cells loaded with FITC-BSA-MWCNTs and FITC-BSA were studied under TEM. Zebrafish embryos loaded with FITC-BSA-MWCNTs were collected at 1 hpf and 4 hpf separately. The embryos were fixed in fixation buffer (2% PFA, 2.5% Glutaraldehyde, 0.1 M cacodylate buffer, pH 7.2, 4% sucrose, 1% tannic acid) overnight at 4 °C. The fixed embryos were washed with washing buffer (0.1 M cacodylate buffer (pH 7.2)) for 10 min three times at 4 °C. Then, the embryos were post-fixed with 1% OsO_4 in 0.1 M cacodylate buffer (pH 7.2) at RT for 2 h. The post-fixed embryos were transferred from the washing buffer into the water and then dehydrated gradually with ethanol. The dehydrated embryos were gradually transferred to acetone and then pure resin (Spurr's). The embryos were embedded in pure resin for 4 h at RT, and then the resin was polymerized at 70 °C for 2 days before sectioning. The embryos were sectioned (70 nm) using ultracut UCT (Leica) and placed on copper grids and double stained with 5% uranyl acetate solution and Reynolds' lead citrate solution. The tissue was examined and photographed with a TEM (Philips Tecnai 12 BioTWIN) operating at 80 kV.

Expression pattern of biomarkers in the loaded embryos. Four markers, *MMP9* as the innate immune response marker, *vasa* as a germ line marker, *Zash* as the subset of neurons marker and *MyoD* as the myotomes marker, were analyzed at 24 hpf in embryos loaded with FITC-BSA-MWCNTs using whole mount *in situ* hybridization according to the method described by Westerfield (1995). Antisense RNA for *MMP9*, *vasa, Zash and MyoD* was synthesized by linearizing the plasmids and transcribing with T7 or SP6 polymerase and Digoxigenin-11-UTP (Boehringer, Indianapolis, IN, USA). Zebrafish embryos were loaded with FITC-BSA-MWCNTs at 1-cell stage by microinjection, and were collected and fixed at 24 hpf. Collected embryos were fixed in 4% PFA (Sigma-Aldrich) in PBS at 4 °C overnight, dehydrated in a methanol (MeOH) series and stored in absolute MeOH at −20 °C to increase permeability. Embryos were then digested with Proteinase K (Sigma-Aldrich) and re-fixed before incubation with the antisense probes at 65 °C overnight. Probes were removed with high-stringency washes at 65 °C. Embryos were then incubated with preabsorbed goat serum (Sigma-Aldrich) for 4 h at room temperature. After washing, 5-bromo-4-chloroindolyl phosphate was added as the substrate and nitro blue tetrazolium was added as the coupler (DAKO, Glostrup, Denmark). The FITC-BSA-MWCNTs loaded embryos and untreated control embryos were examined using an inverted microscope (Nikon Eclipse TE200, Nikon, Japan), images of FITC-BSA-MWCNT-treated and untreated control embryos were captured with a cooled color digital camera (TK-C1381, JVC, Japan), and then data was collected and stored using a digital camera attached to a computer.

Staining of cytoskeleton structure and nucleus of the treated embryos. The staining of the microfilament structures and the nucleus of the zebrafish embryos were performed as described in Cheng et al. (2004). For early stage embryos, glass Petri dish was used for removing the chorion and 1% agarose coated Petri dish was used for staining. At sphere epiboly (4 hpf), 50% epiboly, and 75% epiboly, embryos were fixed with 4% PFA in PBS overnight at 4 °C, after which they were washed thoroughly with PBS. All subsequent washing steps were performed for 5 min and were carried out with gentle shaking. To label F-actin and nucleus, embryos were incubated with 0.08 μg/ml Rhodamine–phalloidin (Invitrogen, Carlsbad, CA) and Sytox-green (Invitrogen, Carlsbad, CA), at RT for 1 h in the dark, after which they were washed extensively with PBTD (PBS with 0.1% Tween-20 and 1% DMSO) containing 1% BSA (PBTD/BSA). Images were collected with water immersion Achroplan×20/0.5NA and ×40/0.75NA objectives on the Nikon C1 Confocal Microscopy system (Nikon C1, Nikon, Japan). The FITC and Rhodamine fluorescence was visualized by using 488-nm excitation/520-nm emission and 568-nm excitation/585-nm emission, respectively.

Life cycle effects of FITC-BSA-MWCNTs on the loaded embryos. The survival rates of the zebrafish loaded with FITC-BSA-MWCNTs from 1-cell stage and their offspring were studied. The survival rates of the first generation of zebrafish were recorded at day 14, day 28 and day 56 after the loading of FITC-BSA-MWCNTs and the survival rates of their second generation were recorded at day 14 after birth. The counting was carried out by capturing images by a digital camera without disturbing the zebrafish. Each experiment was conducted on 50 zebrafish embryos loaded with 2 ng of FITC-BSA-MWCNTs at 1-cell stage through injection. All data are presented as the mean±standard deviation (SD) from three separate experiments. Significant differences between mean values were determined using two-way analysis of variance (ANOVA) and Tukey's post hoc test. The two main factors for analysis of variance were treatment and time. The level of statistical significance in all cases was $p<0.05$ at the same studied

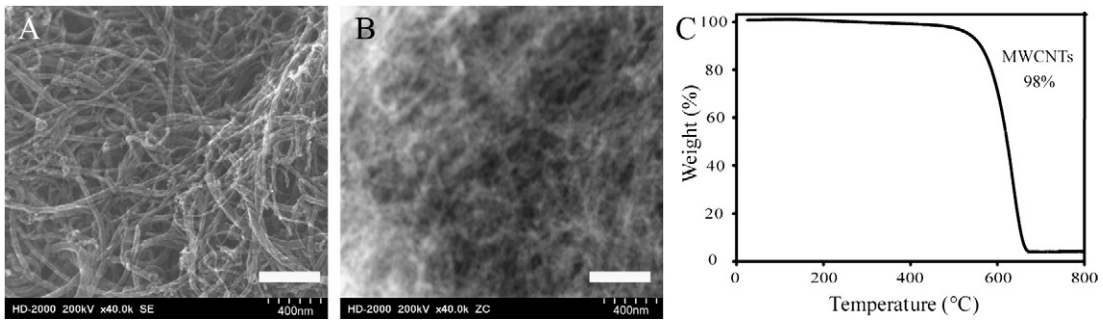

Fig. 1. STEM characterization and TGA analysis of purified MWCNTs. Representative STEM bright-field image (A) showed that purified MWCNTs were quite clear and without obvious amorphous carbon. Corresponding STEM Z-contrast image (B) demonstrated that no metal particles were found by contrast difference in the purified MWCNTs sample. TGA data (C) showed that MWCNTs after purification comprised of 98% of total sample weight. Scale bar: 400 nm.

time point. Percentage data were log-transformed before analysis. The ANOVA was performed using SigmaStat 3.0 software (SPSS, Chicago, IL, USA).

Results

Characterization of prepared BSA-MWCNT sample

MWCNTs, after purification, were studied by TGA and characterized by scanning TEM (S-TEM, Fig. 1) as well as by common SEM and TEM (Supplementary Fig. 1). The S-TEM bright-field image (Fig. 1A) provided the general morphology information on the MWCNTs sample. The Z-contrast mode in S-TEM was used for direct observation of metal particles (residual catalysts from the nanotube production) in the MWCNTs sample because of the large contrast difference between carbon and metals. The Z-contrast image (Fig. 1B) suggested that the purified MWCNTs sample was largely free from metal particles. This was consistent with the TGA result (Fig. 1C).

The carboxylic acid moieties on the surface of purified MWCNTs (derived from the oxidation of surface defect sites) were targeted by BSA (containing amine groups) in the amidation reaction for the covalent conjugation. AFM studies confirmed the successful attachment of BSA to MWCNTs and the well dispersion of BSA-MWCNTs (Fig. 2A). According to statistical analyses of the AFM images (Fig. 2), the average length of BSA-MWCNTs was about 0.8±0.5 μm, and median length 0.7 μm (Fig. 2B), and the average diameter was about 19.9±8.25 nm, and median diameter 17.5 nm (Fig. 2C).

In vivo biodistribution of FITC-BSA-MWCNTs in developing zebrafish embryos

For the embryos injected with FITC-BSA-MWCNTs (~2 ng per embryo, CNTs equivalent weight) at 1-cell stage, no mortality or developmental defects was observed during all the observed developmental period. At 1–2 cells stage (Fig. 3A), green fluorescence from FITC-BSA-MWCNTs was detected in the blastoderm cells as indicated by the white arrows. The green fluorescent signal associated with FITC-BSA-MWCNTs was then allocated evenly to all of the blastoderm cells through cell division. At 50% epiboly stage, FITC-BSA-MWCNTs signal was concentrated in all blastoderm cells (white arrows in Fig. 3B) and was excluded from the yolk cell. The blastoderm cell preference of FITC-BSA-MWCNTs was also observed in the following

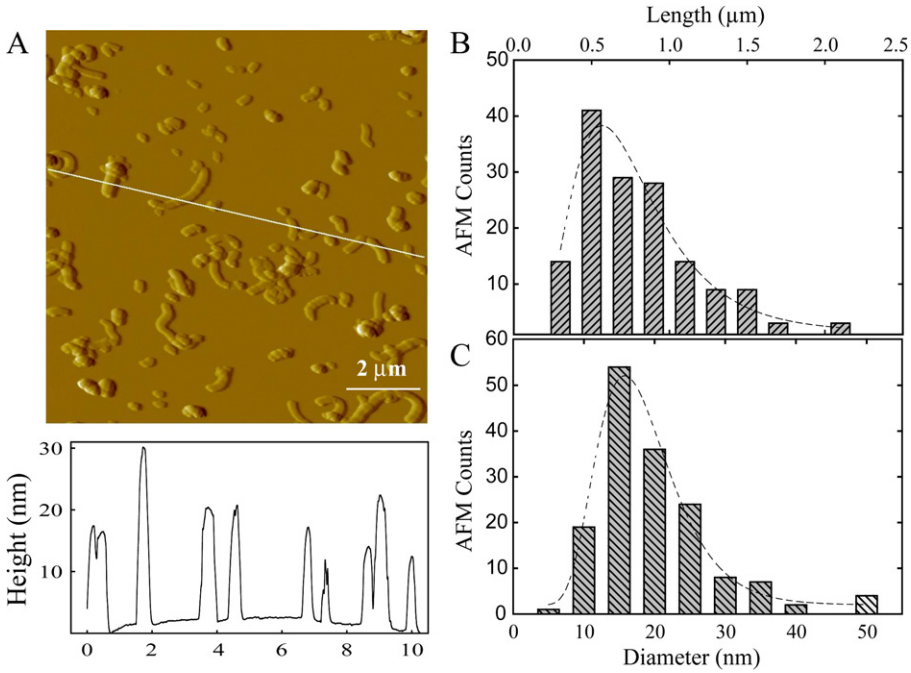

Fig. 2. AFM characterization and size information of BSA-MWCNTs. The BSA-MWCNTs sample was well dispersed and BSA protein was uniformly coated on the surface of MWCNTs as shown by AFM image (A). The length (Mean±SD) of the studied BSA-MWCNTs was 0.8±0.5 μm (B), and the diameter (Mean±SD) of BSA-MWCNTs was 19.9±8.25 nm (C). The scale information is indicated on the AFM image (A).

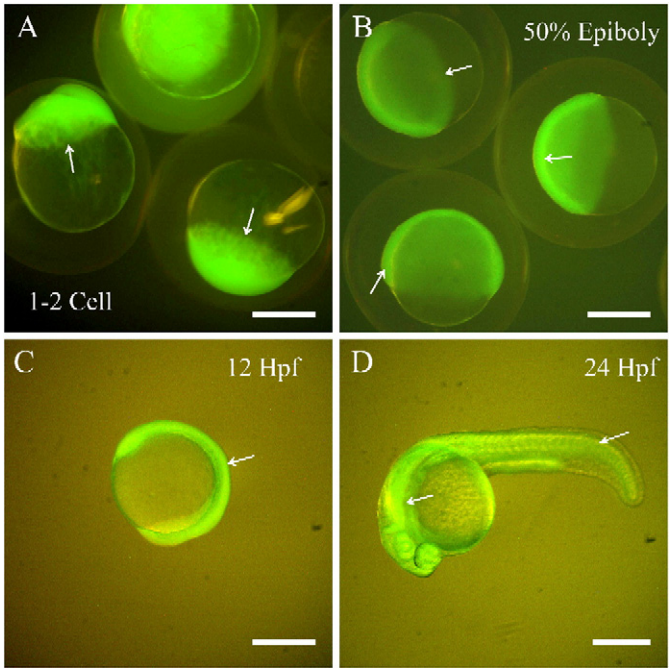

Fig. 3. *In vivo* biodistribution of FITC-BSA-MWCNTs in developing zebrafish embryos at different developmental stages. Zebrafish embryos were loaded with 2 ng of FITC-BSA-MWCNTs (CNTs equivalent weight) at 1-cell stage through microinjection. According to the green fluorescence signal from FITC-BSA-MWCNTs, the loaded FITC-BSA-MWCNTs were distributed in the blastoderm cells but not the yolk cells at all observed developmental stages, including 1–2 cells stage (A), 50% epiboly (B), 12 hpf (C) and 24 hpf (D). Scale bar: 250 μm.

developmental stages, such as at 12 hpf (Fig. 3C) and at 24 hpf (Fig. 3D). When the tissues and organs were already formed, FITC-BSA-MWCNTs could still locate in those blastoderm cells all along the body and kept excluded from the yolk cell (Fig. 3D). The distribution profile of FITC-BSA-MWCNTs was identified again by confocal microscope (Supplementary Fig. 2), and the results demonstrated the same blastoderm cells concentrated distribution.

When FITC-BSA-MWCNTs were injected into the yolk cell of the embryos at 1-cell stage, they showed similar blastoderm cell concentrated distribution although the fluorescent signal was a little bit weaker at first and became intensive later (data not shown). There were frequent exchanges between the blastoderm cells and the yolk cell during early developmental stages of zebrafish embryos. The cytoplasmic stream of the yolk could help FITC-BSA-MWCNTs move to the blastoderm cells although it took longer time for the FITC-BSA-MWCNTs to move to the blastoderm cells in this case as compared to the direct blastoderm cell injection delivery.

Based on the above observations, FITC-BSA-MWCNTs showed higher affinity to the blastoderm cells than the yolk cell. The yolk was known to be composed mainly of lipid to afford energy supply for the embryos at early stages. This result suggested that FITC-BSA-MWCNTs have lower affinity to lipid as compared to the protein enriched intracellular environment.

Intracellular biodistribution of FITC-BSA-MWCNTs in the embryonic blastoderm cells

FITC-BSA-MWCNTs and FITC-BSA were delivered into the embryos at 1-cell stage and both of them accumulated in the blastoderm cells but not in the yolk cell, although there were frequent exchanges between the blastoderm cells and the yolk cell during that period (data not shown, similar as Fig. 3). However, there was a difference in their intracellular distribution (Fig. 4) in the blastoderm cells at 3 hpf. It was noticed that FITC-BSA-MWCNTs remained in both cytoplasm and nucleus of the blastoderm cells (white arrows in Fig. 4A), while FITC-BSA was excluded from the nucleus and stayed only in the cytoplasm of the blastoderm cells (red arrows in Fig. 4B). The cytoplasm and nucleus biodistribution of FITC-BSA-MWCNTs made the green fluorescent signal homogenous in the blastoderm cells (Fig. 4A).

The data suggested that FITC-BSA-MWCNTs can enter the nucleus of blastoderm cells while FITC-BSA cannot. It also suggested that MWCNTs have special property in nuclear membrane penetration. However, there was intensive cell division and the cell proliferation rate was very fast (15 min) at early stage. This nuclear accumulation of FITC-BSA-MWCNTs in blastoderm cells might be a special distribution profile during cell division. Thus, the nuclear accumulation of FITC-BSA-MWCNTs in zebrafish blastoderm cells requires further investigation.

Biodistribution and clearance of FITC-BSA-MWCNTs in zebrafish larvae when loaded into cardiovascular systems

The biodistribution and clearance of FITC-BSA-MWCNTs in zebrafish larvae were studied by introducing FITC-BSA-MWCNTs into the cardiovascular system at 72 hpf through intravascular loading. As shown in Fig. 5, FITC-BSA-MWCNTs first distributed all along the blood circulation system and then moved to the muscles and other tissues easily. It was found that FITC-BSA-MWCNTs went into the floor plate, the brain ventricle, and notochord in the larvae 30 min after the loading (Fig. 5A). The loaded FITC-BSA-MWCNTs finally accumulated

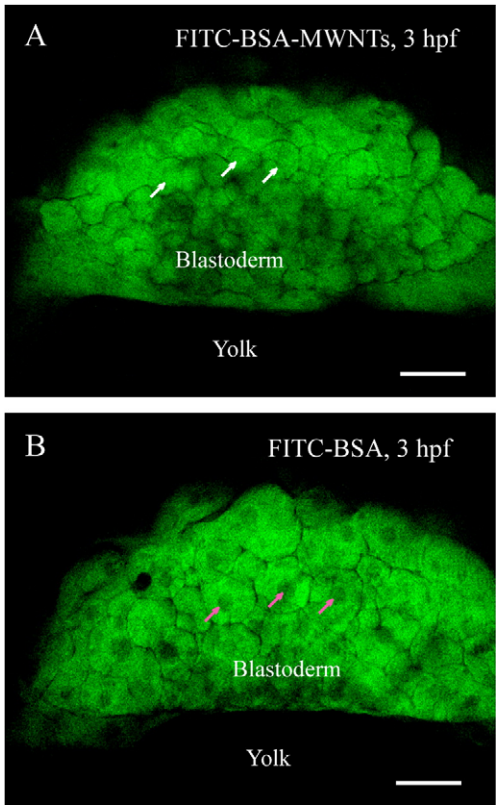

Fig. 4. Representative live images showing intracellular distribution of FITC-BSA-MWCNTs (A) and FITC-BSA (B) in zebrafish embryos at 3 hpf. Both FITC-BSA-MWCNTs and FITC-BSA were delivered into zebrafish embryos at 1-cell stage with 2 ng dosage (CNTs equivalent weight) through microinjection. Both FITC-BSA-MWCNTs and FITC-BSA accumulated in blastoderm cells but not the yolk cells. The loaded FITC-BSA-MWCNTs translocated into the nucleus (white arrows in A) of the blastoderm cells while most FITC-BSA was kept in the cytoplasm of the blastoderm cells (red arrows in B) in the observed time point. Scale bars: 50 μm.

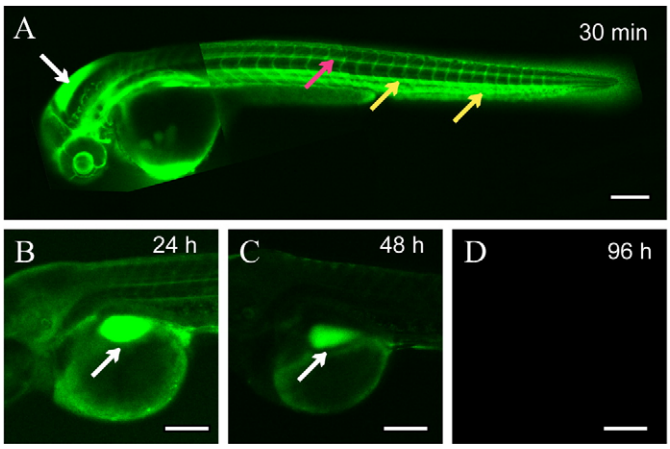

Fig. 5. *In vivo* biodistribution of FITC-BSA-MWCNTs in zebrafish larvae through intravascular loading at 72 hpf. The intravascular loaded FITC-BSA-MWCNTs reached the floor plate (red arrow in A), 4th ventricle (white arrow in A) and blood vessels (yellow arrow in A) within 30 min. Most of the loaded FITC-BSA-MWCNTs gradually accumulated in one swim bladder structured region of the larvae at 24 h (white arrow in B) and 48 h (white arrow in C) after the delivery. The intravascular loaded FITC-BSA-MWCNTs were gradually excreted out from the embryos, and there was no detectable signal at around 96 h after the delivery (D). Scale bar: 200 μm.

at one specific region, a swim bladder structured organ, after 24 h (Fig. 5B) and 48 h (Fig. 5C) of delivery. Examination of frozen sections confirmed that the FITC-BSA-MWCNTs were adsorbed by the tissues and accumulated in different organs (Supplementary Fig. 3). The injected FITC-BSA-MWCNTs had a relatively long circulation time as compared to normal dyes or other nanomaterials, which took less than 24 h (Cheng et al., 2001).

Zebrafish larvae exhibited highly concentrated FITC-BSA-MWCNTs in the swim-bladder structured organ, but no detectable fluorescent signal of FITC-BSA-MWCNTs was observed from other organs after 48 h. Fluorescent intensity from FITC-BSA-MWCNTs in the swim-bladder structured organ was concentrated from other tissues, which suggested that the swim bladder structured organ has a priority to accumulate FITC-BSA-MWCNTs particles. Since the swim bladder is known as a detoxifying organ, the results indicated that the zebrafish larvae managed to clean out the injected carbon nanoparticles effectively. These FITC-BSA-MWCNTs were gradually excreted out from zebrafish larvae, and there was no detectable signal at around 96 h after delivery (Fig. 5D).

Cellular response of embryonic cells after loaded with FITC-BSA-MWCNTs

The cellular response of the embryonic cells of zebrafish embryos after the loading of FITC-BSA-MWCNTs was investigated under TEM. The embryos were fixed and ultra-sectioned and then the samples were investigated under the TEM to observe the cellular response. Many lysosome-like vesicles came up within 15 min after FITC-BSA (Fig. 6B) and FITC-BSA-MWCNTs (Fig. 6C) were delivered into the embryos at 1-cell stage (white arrows in Figs. 6B and C), while untreated control embryos did not have such vesicles (Fig. 6A). These vacuole structures still existed at 4 hpf, more than 3 h after the loading

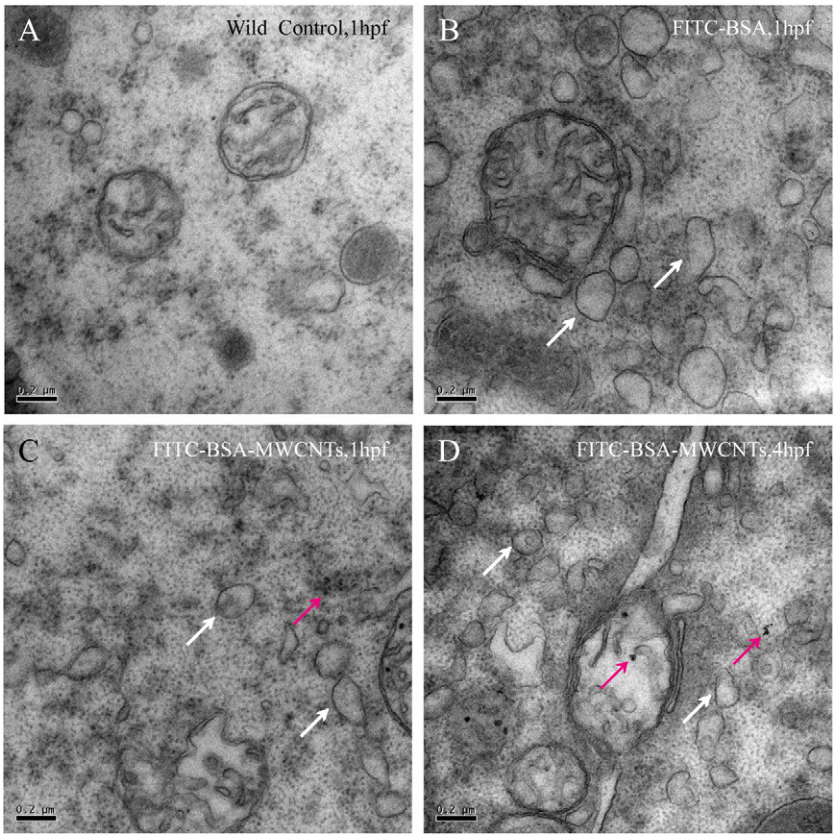

Fig. 6. Cellular responses of the embryonic blastoderm cells to the loading of MWCNTs. Many lysosome-like vesicles formed within 15 min after FITC-BSA (B) and FITC-BSA-MWCNTs (C) were delivered into the embryos at 1-cell stage (see white arrows in B and C), while untreated control embryos did not have such vesicles (A). These lysosome-like vesicles existed at 4 hpf which is more than 3 h after the loading of FITC-BSA-MWCNTs (D). The loaded FITC-BSA-MWCNTs were randomly distributed in the blastoderm cells (see red arrows in C and D). Scale bar: 200 nm.

of FITC-BSA-MWCNTs. The continuous presence of vacuole structures suggested that the blastoderm cells were trying to remove those carbon nanoparticles after the invasive loading. The blastoderm cells had similar cellular response to FITC-BSA-MWCNTs as compared to FITC-BSA (Figs. 6B and C), indicating that the forming of the lysosome-like vesicles is a general phenomenon. These vesicles may be lysosomes since lysosomes are digestive organelles. One study on the translocation of fullerenic nanoparticles has also found that many lysosome-like vesicles were formed after the fullerenic nanoparticles were internalized by the mammalian cells (Li et al., 2008).

It was noticed that FITC-BSA-MWCNTs, present as small aggregates, were randomly located in the blastoderm cells without specific preference to the intracellular organelles (red arrows in Figs. 6C and D).

Immune response after the delivery and the primordial germ cells

The phenotype scoring analysis showed no obvious deformation or malformation in the treated zebrafish embryos to adult stages as compared to the wild type controls. The morphological images of the treated embryos at 4 hpf and 6 hpf showed that the injected embryos developed normally (Supplementary Fig. 4).

The immune responses of the embryos loaded with MWCNTs were studied using *MMP9* as the marker. Members of the Matrix Metalloproteinases (*MMPs*) family are important for the remodeling of the extracellular matrix in a number of biological processes including a variety of immune responses (Yoong et al., 2007). One member of the family, *MMP9*, also known as gelatinase B, is highly expressed in specific myeloid cell populations in which they play a role in the innate immune response (Yoong et al., 2007).

To determine the spatial expression pattern of *MMP9* with and without the loading of MWCNTs, whole mount *in situ* hybridization was performed and the results are shown in Fig. 7. The embryos, loaded with 2 ng of MWCNTs at 1-cell stage, showed a change in *MMP9* expression level and pattern (red arrowhead in Fig. 7B), as compared to the control embryos (dark arrowhead in Fig. 7A). It is known that *MMP9* expression from 24 hpf was presented in a population of circulating white blood cells, which migrates to the site of trauma (Yoong et al., 2007). The circulating white blood cells marked by *MMP9* expression (visualized by the blue color) were localized in the head region near the eye (data not shown), and along the trunk of the embryos at 24 hpf (Fig. 7A). When the embryos were loaded with MWCNTs, the signal for *MMP9* increased noticeably in the trunk region, while the distribution of the circulating blood cells was concentrated in certain regions (Fig. 7B). The *MMP9* was previously found to be significantly up-regulated in the zebrafish larvae in response to exposure of low levels of cadmium chloride and methyl mercury chloride (Yang et al., 2007). Our results suggested that zebrafish embryos may generate innate immune response at later developmental stages when being injected with MWCNTs at 1-cell stage.

The effects on the reproduction system by loading MWCNTs into embryos at 1-cell stage were evaluated using *vasa* as a germ line marker since early life stages are generally most sensitive to toxic effects. The gene expression profiles of *vasa* in embryos loaded with MWCNTs and untreated control embryos were studied. The primordial germ cells marked by *vasa* (red arrow in Fig. 7D) in the treated embryos were not affected as compared to the control (dark arrow in Fig. 7C). The results indicated that embryos loaded with MWCNTs from 1-cell stage maintained a proper reproductive systems and the production of germ cells was not affected.

Using the myogenic regulatory factor, *MyoD*, as a marker, the myotomes were found to be well organized, with arrowhead-shaped alignment both in MWCNT-exposed and control embryos (Supplementary Figs. 5A & B). The subset of neurons in the peripheral cuticular and central nervous systems in the treated zebrafish embryos were well developed (Supplementary Figs. 5C & D) as determined using zebrafish achaete-scute homolog (*zash*), as the marker. All of the molecular and cellular experimental results provided further evidence that the exposed embryos developed normally.

Influence on cytoskeleton structure and nucleus distribution

The cytoskeleton staining results showed that the microfilament structure of the treated embryos was quite intact and was not disturbed by the loaded MWCNTs as compared with the control (Supplementary Fig. 6). After mass cell proliferation, the embryos loaded with MWCNTs proceeded cell migration successfully and formed the nucleus of yolk syncytial layer at 4 hpf and 5.3 hpf (white dots marked area in Figs. 8D and E), which is similar as the control (white dots marked area in Figs. 8A and B). As the F-actin marks the cell boundary, the cell morphology and size information could be derived from F-actin staining. The F-actin staining combined with nucleus staining results revealed that the embryos loaded with MWCNTs had associated and well organized cells (Fig. 8D and E) as untreated control embryos (Figs. 8A and B). The nucleus of the enveloping and deep layer cells of the treated embryos were well organized as the untreated control (yellow arrowhead in Fig. 8). No apoptosis was observed in the studied embryos. The treated embryos had the continuous punctuate band of actin at the leading edge of the enveloping layer (yellow arrow in Fig. 8C) at 75% epiboly as the control (yellow arrow in Fig. 8F).

The cytoskeleton structure is important for maintaining cell morphology and complex function of the cell components. When MWCNTs went into the blastoderm cells of the embryos, the cells had to distinguish MWCNTs from their own cytoskeleton structure because MWCNTs shared similar fibers structure and size as that of the microfilaments and microtubules in the blastoderm cells. As the embryos loaded with MWCNTs proceeded to normal development for more than 3 days, the embryos seemed to have their own way to recognize the microfilament structures from MWCNTs.

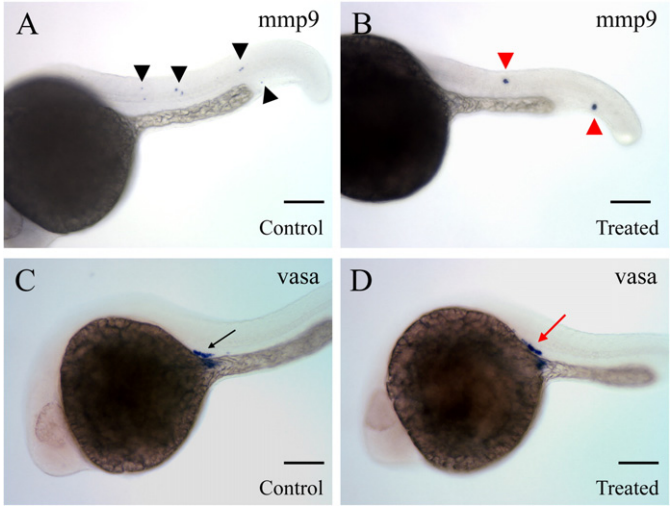

Fig. 7. Whole mount *in situ* hybridization with *MMP9* (A, B) and *Vasa* (C, D) labeled probes at 24 hpf on wild type and MWCNTs loaded embryos. The circulating white blood cells showed expression of *MMP9* (blue color) along the trunk. The expression profile of *MMP9* in the embryos loaded with FITC-BSA-MWCNTs (B) was changed and up-regulated through accumulation of white blood cells (red arrowheads in B) as compared to the control (dark arrowheads in A). The gene expression pattern of *vasa* was not obviously affected in the embryos loaded with FITC-BSA-MWCNTs (red arrow in D) compared to the control (dark arrow in C). The arrowheads and arrows indicate the position of cells expressing *MMP9* and *Vasa* respectively. Scale bar: 150 μm.

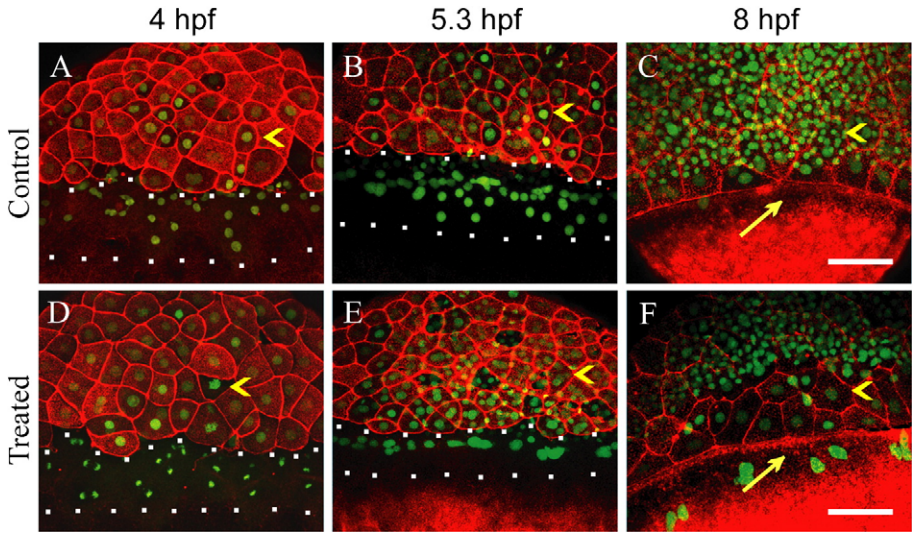

Fig. 8. Effects of BSA-MWCNTs on the cytoskeleton structure of the treated embryos. Representative F-actin and nucleus staining images of embryos loaded with 2 ng (CNTs equivalent weight) of FITC-BSA-MWCNTs (D, E, F) and wild type control (A–C) at 4, 5.3 and 8 hpf (n=8). Red signal indicated the F-actin by Rhodamine-phalloidin staining and green signal is the Sytox-green staining results of the nucleus. White dots surrounded area indicates the yolk syncytial layer. Yellow arrowheads point to specific cells with one nucleus inside the cell boundary marked by F-actin. Yellow arrows point to the continuous punctuate band of actin at the leading edge of the enveloping layer. Each image is a projected stack of confocal optical sections. Scale bar: 50 μm.

Life cycle effects on the survival rates and the reproduction of next generation

A life-cycle test with zebrafish was carried out with the loading of FITC-BSA-MWCNTs as well as PPEI-EI-MWCNTs at 1-cell stage under normal fish culture conditions. The survival rates of the first generation of the zebrafish loaded with FITC-BSA-MWCNTs and PPEI-EI-MWCNTs at different developmental stages were compared with the wild type control. Similar survival rates were observed in both treated and untreated groups, as shown in Fig. 9A and Supplementary Fig. 7A respectively. Larval development was not delayed, and after reaching maturity, these MWCNT-treated fishes performed spawning and produced next generation normally. Effects on spawning were not influenced by the loading of MWCNTs, which was coincided with the above primordial germ cell expression study.

A significant reduction of survival rates of the second generation, as illustrated in Fig. 9B and Supplementary Fig. 7B respectively, was found in the fish loaded with FITC-BSA-MWCNTs and PPEI-EI-MWCNTs at day 14. The embryos loaded with MWCNTs from the beginning of development possessed normal survival rates and produced next generation properly but the second generation showed decreased survival rates. Although the underlying mechanism is unknown, these findings indicate that the further reproduction potential of fish populations might be disturbed by a long-term loading with MWCNTs from fertilization until sexual maturity.

Discussion

Safe manufacturing and application of nanomaterials is an emerging issue with the bloom of nanotechnology (Medina et al., 2007). Understanding the interaction of CNTs with the biological system is essential for the realization of their safe applications. Well functionalized MWCNTs were used to investigate the *in vivo* distribution of modified carbon nanoparticles in zebrafish. The findings gathered in this study help to determine the interaction, behavior and potential toxicity of coated nanomaterials in the developing biological organisms. When MWCNTs were delivered into zebrafish through microinjection into the cells, they mainly concentrated in the blastoderm cells but not in the yolk cell. Previous study reported that fluorescent polystyrene nanoparticles accumulated in the oil droplets of medaka embryos (Kashiwada, 2006) by direct exposure. In this study, fluorescent dye FITC labeled MWCNTs were excluded from the yolk cell in zebrafish embryos. A study of the

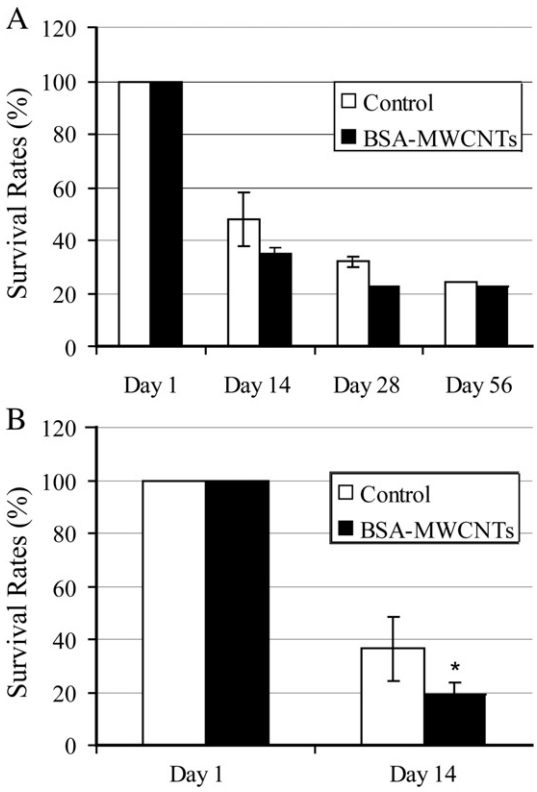

Fig. 9. Survival rates (mean±SD) of zebrafish *(Danio rerio)* loaded with BSA-MWCNTs (A) and larval survival rates (mean±SD) of their second generations (B). The survival rates of zebrafish loaded with BSA-MWCNTs from 1-cell stage and control at day 14, day 28 and day 56 were shown in dark and blank, respectively. The zebrafish loaded with BSA-MWCNTs had similar survival rates as compared to the control at all studied developmental stages (A). The offspring of the zebrafish loaded with BSA-MWCNTs at 1-cell stage had significant lower survival rates as compared to that of control (B) (p<0.05). The survival rates indicate the survival percentage of each case (n=50) from three experiments (n=150).

distribution of water-miscible C_{60} fullerene in rats (Yamago et al., 1995) found that 91.7% of intravenously administered water-miscible fullerene was distributed to the liver. However, in this study, the intravascular loaded MWCNTs mainly accumulated in the swim bladder structured organ but not in the liver. This distribution difference may be caused by the specific nanoparticles. The exposure route may also play a role in the bioaccumulation process considering the different administrative methods used. Multiple physicochemical and environmental factors should also be considered (Hardman, 2006). The distribution profile difference suggests that nanoparticles may generate different biological effects in the biological systems, and one kind of nanoparticles may also show different impacts if administrated differently.

This study investigated the biocompatibility of MWCNTs in an aquatic organism, zebrafish, through both acute and whole life span analysis. There was no lethal effect upon exposure and no developmental defects were observed in the treated zebrafish. The embryos loaded with MWCNTs from 1-cell stage preceded to cell proliferation properly and survived well in the whole life span. It might be the strong maternal control effect at the early development stage, which guaranteed correct cell proliferation even with minor interruptions, such as loading with the invaded MWCNTs. Another study also reported that well purified and functionalized CNTs did not exert genetic toxicity in mammalian cells in terms of cell cycle distribution and cell division upon 5 days continuous exposure (Cheng et al., 2008).

When it comes to the cell migration movements, which are dependent on the zygotic control, the embryos initiated the epiboly with its own zygotic controlled genetic information. It was noticed that the cell movement was not disturbed by the loaded fiber structured CNTs. The MWCNT-treated embryos exerted immune response and the circulating white blood cells relocated in the body, and those interrupted blastoderm cells tried to produce many vesicles to remove the invaded foreigners. These responses suggest that the treated embryos are trying to clean up the loaded MWCNTs. After being loaded into the circulation system, the MWCNTs penetrated the blood-brain barrier and reached the brain ventricle, gradually accumulated into swim bladder region and finally were cleaned up by the body. There is a cleaning up mechanism in response to the intravascular loading in zebrafish larvae. The removal comparison between these two administration methods suggests that the intravascular loading is more useful when considering MWCNTs as the drug carrier since the intravascular loading strategy can remove the nanomaterials after their delivery functions in the body.

Early life stages are generally most sensitive to toxicant exposure. The 1-cell stage injection should be more sensitive as compared to circulation system injection at 72 h post fertilization. For example, zebrafish embryos get tolerant to some treatments post 3 days of embryonic development, such as morpholino. Considering that the 1-cell stage injection is more sensitive to toxicant exposure while circulation system injection might be more potentially used in clinic purposes, both 1-cell stage injection and circulation system injection were used. However, most of the toxicology study end points in this study were taken from 1-cell stage injection.

The development and reproduction of fish are highly complex processes and a number of studies have demonstrated that these processes, including growth, sexual differentiation, and maturation of gametes and spawning, can be adversely affected by metals and organic pollutants at sublethal concentrations (Van den et al., 2003). Development and reproduction is an important issue when considering the long term effect of releasing nanomaterials into the environment or incorporating the nanomaterials into the organisms. Several molecular markers for primordial germ cells have been identified for zebrafish. One of these is *vasa*, which is expressed at all developmental stages of the developing germ line, except mature sperm (Raz, 2003). The transcripts of *vasa* serve as a marker for the developing germ line in the zebrafish (Yoon et al., 1997; Krovel and Olsen, 2002). Toxicant exposures may affect critical events in the development of the reproductive system, ranging from early primordial germ cells determination to gonad differentiation, gametogenesis, external genitalia, or signaling events regulating sexual behavior (Pryor et al., 2000). The zebrafish loaded with MWCNTs formed primordial germ cells at early stage and produced second generation. However, their offspring had significant lower survival rates at larvae stage as compared to the untreated groups. The results showed a negative impact on the reproduction potential in the long term for the loaded zebrafish.

It has been reported that survival rates of zebrafish (Danio rerio) are different in different origins (Diekmann and Nagel, 2005). The survival rates of zebrafish from one species can also vary much depending on the diet and method of food delivery. Survival rates were reported in the range of ~15–80% through 28 days post fertilization (Goolish et al., 1999). In this study, all of the control and treated zebrafish were raised up with the same diet and food delivery method. The survival rates comparison between the control and treatment groups can help determine the effect of loading with MWCNTs on the zebrafish survival along their life span. In this study we did not observe obvious difference in terms of biodistribution and survival rates among two surface molecules, PPEI-EI and BSA. The similar *in vivo* biodistribution pattern and survival rates after the exposure to MWCNTs modified with different surface molecules may suggest that MWCNTs played an important role in the *in vivo* biodistribution pattern in zebrafish.

The biocompatibility of nanomaterials is an important factor for their potential *in vivo* applications. Experimental data showed modification of nanoparticles can also change their *in vitro* behavior (Nimmagadda et al., 2006). These modifications may result in unanticipated effects both on the material's properties as well as the organisms exposed to the nanomaterial. Another related study also illustrated that the cytotoxic response of cells in culture is dependant on the degree of functionalization of the CNTs (Sayes et al., 2006). Raw MWCNTs has been found to induce inflammatory and fibrotic responses in the lungs of treated rats (Muller et al., 2005). The present study showed that well purified and modified MWCNTs did not exert serious toxic impacts in the loaded zebrafish, at least in their own life span. This study suggests that intensive purification and functionalization processes can help improve the biocompatibility of CNTs in the biological systems. The studied MWCNTs were composed of 98% of the sample. The remaining 2% residues effect was minimized by the further functionalization process. The chemical modification process added BSA protein on the surface of MWCNTs and this surface modification can help decrease their potential toxicity and increase their biocompatibility when loaded into the biological systems.

With the typically small amount of modified nanoparticles being produced in each batch, it is essential to gather knowledge about how each step of chemical production and modification would generate harmful side products. This present study explored the application of zebrafish as a test system for *in vivo* nanotoxicology. The zebrafish system only takes up a small amount of test nanomaterials and provides easy tracking on biodistribution and subsequent biological responses within the transparent embryos. Zebrafish embryos offer an inexpensive and ethically acceptable vertebrate model that will not only be useful in the toxicological assessment of the tens of thousands of compounds to be tested, but can also help to evaluate the developmental toxicity of novel compounds at an early stage of drug development. The zebrafish test system can be further applied for the *in vivo* evaluation of the emerging nanomaterials as well as other emerging compounds.

Conflict of interest statement

The authors declare that there are no conflicts of interest.

Acknowledgments

The work described in this paper was substantially supported by a grant from the Research Grants Council of the Hong Kong SAR (Project No. CityU 160108) to S. H. Cheng. The Clemson group was supported by the U.S. National Science Foundation. K. A. S. Fernando and F.S. Lu are thanked for experimental assistance. C. N. Cheng is thanked for the help of microfilament staining. C. W. Cheng is thanked for the help of cryo-section. The MMP9 plasmid is a kind gift from Prof. U. Strähle′ s lab at Institute of Toxicology and Genetics in Forschungszentrum Karlsruhe, Germany. Michelle Hui is thanked for her critical reading of our paper.

Appendix A. Supplementary data

Supplementary data associated with this article can be found, in the online version, at doi:10.1016/j.taap.2008.12.006.

References

Abarrategi, A., Gutierrez, M.C., Moreno-Vicente, C., Hortiguela, M.J., Ramos, V., Lopez-Lacomba, J.L., Ferrer, M.L., del, M.F., 2008. Multiwall carbon nanotube scaffolds for tissue engineering purposes. Biomaterials 29, 94–102.

Bianco, A., 2004. Carbon nanotubes for the delivery of therapeutic molecules. Expert Opin. Drug Deliv. 1, 57–65.

Bianco, A., Kostarelos, K., Partidos, C.D., Prato, M., 2005a. Biomedical applications of functionalised carbon nanotubes. Chem. Commun. (Cambridge, U. K.) 5, 571–577.

Bianco, A., Kostarelos, K., Prato, M., 2005b. Applications of carbon nanotubes in drug delivery. Curr. Opin. Chem. Biol. 9, 674–679.

Cheng, S.H., Wai, A.W.K., So, C.H., Wu, R.S.S., 2000. Cellular and molecular basis of cadmium-induced deformities in zebrafish embryos. Environ. Toxicol. Chem. 19, 3024–3031.

Cheng, S.H., Chan, P.K., Wu, R.S., 2001. The use of microangiography in detecting aberrant vasculature in zebrafish embryos exposed to cadmium. Aquat. Toxicol. 52, 61–71.

Cheng, J.C., Miller, A.L., Webb, S.E., 2004. Organization and function of microfilaments during late epiboly in zebrafish embryos. Dev. Dyn. 231, 313–323.

Cheng, J., Flahaut, E., Cheng, S.H., 2007. Effect of carbon nanotubes on developing zebrafish (*Danio rerio*) embryos. Environ. Toxicol. Chem. 26, 708–716.

Cheng, J., Fernando, K.A.S., Veca, L.M., Sun, Y.P., Lamond, A.I., Lam, Y.W., Cheng, S.H., 2008. Reversible accumulation of PEGylated single-walled carbon nanotubes in the mammalian nucleus. ACS Nano 2 (10), 2085–2094.

Curtis, J., Greenberg, M., Kester, J., Phillips, S., Krieger, G., 2006. Nanotechnology and nanotoxicology: a primer for clinicians. Toxicol. Rev. 25, 245–260.

Deng, X., Jia, G., Wang, H., Sun, H., Wang, X., Yang, S., Wang, T., Liu, Y., 2007. Translocation and fate of multi-walled carbon nanotubes in vivo. Carbon 45, 1419–1424.

Diekmann, M., Nagel, R., 2005. Different survival rates in zebrafish (*Danio rerio*) from different origins. J. Appl. Ichthyol. 21 (5), 451–454.

Emerich, D.F., Thanos, C.G., 2005. Nanomedicine. Curr. Nanosci. 1, 177–188.

Fischer, H.C., Chan, W.C., 2007. Nanotoxicity: the growing need for in vivo study. Curr. Opin. Biotechnol. 18, 565–571.

Garrity, D.M., Childs, S., Fishman, M.C., 2002. The heartstrings mutation in zebrafish causes heart/fin Tbx5 deficiency syndrome. Development 129, 4635–4645.

Goolish, E.M., Okutake, K., Lesure, S., 1999. Growth and Survivorship of larval zebrafish *Danio rerio* on processed diets. N. Am. J. Aquac. 61, 189–198.

Hardman, R., 2006. A toxicologic review of quantum dots: toxicity depends on physicochemical and environmental factors. Environ. Health Perspect. 114, 165–172.

Hirsch, A., 2002. Functionalization of single-walled carbon nanotubes. Angew. Chem. Int. Ed. Engl. 41, 1853–1859.

Huang, W.J., Taylor, S., Fu, K.F., Lin, Y., Zhang, D.H., Hanks, T.W., Rao, A.M., Sun, Y.P., 2002. Attaching proteins to carbon nanotubes via diimide-activated amidation. Nano Lett. 2, 311–314.

Isogai, S., Lawson, N.D., Torrealday, S., Horiguchi, M., Weinstein, B.M., 2003. Angiogenic network formation in the developing vertebrate trunk. Development 130, 5281–5290.

Jia, L., Wong, H., Wang, Y., Garza, M., Weitman, S.D., 2003. Carbendazim: disposition, cellular permeability, metabolite identification, and pharmacokinetic comparison with its nanoparticle. J. Pharm. Sci. 92, 161–172.

Kam, N.W., Dai, H., 2005. Carbon nanotubes as intracellular protein transporters: generality and biological functionality. J. Am. Chem. Soc. 127, 6021–6026.

Kam, N.W., Liu, Z., Dai, H., 2005. Functionalization of carbon nanotubes via cleavable disulfide bonds for efficient intracellular delivery of siRNA and potent gene silencing. J. Am. Chem. Soc. 127, 12492–12493.

Kashiwada, S., 2006. Distribution of nanoparticles in the see-through medaka (*Oryzias latipes*). Environ. Health Perspect. 114, 1697–1702.

Kimmel, C.B., Ballard, W.W., Kimmel, S.R., Ullmann, B., Schilling, T.F., 1995. Stages of embryonic-development of the zebrafish. Dev. Dyn. 203, 253–310.

Klumpp, C., Kostarelos, K., Prato, M., Bianco, A., 2006. Functionalized carbon nanotubes as emerging nanovectors for the delivery of therapeutics. Biochim. Biophys. Acta 1758, 404–412.

Krovel, A.V., Olsen, L.C., 2002. Expression of a vas::EGFP transgene in primordial germ cells of the zebrafish. Mech. Dev. 116, 141–150.

Li, W., Chen, C., Ye, C., Wei, T., Zhao, Y., Lao, F., Chen, Z., Meng, H., Gao, Y., Yuan, H., Xing, G., Zhao, F., Chai, Z., Zhang, X., Yang, F., Han, D., Tang, X., Zhang, Y., 2008. The translocation of fullerenic nanoparticles into lysosome via the pathway of clathrin-mediated endocytosis. Nanotechnology 19, 145102.

Liu, Z., Cai, W., He, L., Nakayama, N., Chen, K., Sun, X., Chen, X., Dai, H., 2007. In vivo biodistribution and highly efficient tumour targeting of carbon nanotubes in mice. Nat. Nano 2, 47–52.

Mattson, M.P., Haddon, R.C., Rao, A.M., 2000. Molecular functionalization of carbon nanotubes and use as substrates for neuronal growth. J. Mol. Neurosci. 14, 175–182.

McDevitt, M.R., Chattopadhyay, D., Kappel, B.J., Jaggi, J.S., Schiffman, S.R., Antczak, C., Njardarson, J.T., Brentjens, R., Scheinberg, D.A., 2007. Tumor targeting with antibody-functionalized, radiolabeled carbon nanotubes. J. Nucl. Med. 48, 1180–1189.

Medina, C., Santos-Martinez, M.J., Radomski, A., Corrigan, O.I., Radomski, M.W., 2007. Nanoparticles: pharmacological and toxicological significance. Br. J. Pharmacol. 150, 552–558.

Muller, J., Huaux, F., Moreau, N., Misson, P., Heilier, J.F., Delos, M., Arras, M., Fonseca, A., Nagy, J.B., Lison, D., 2005. Respiratory toxicity of multi-wall carbon nanotubes. Toxicol. Appl. Pharmacol. 207, 221–231.

Nel, A., Xia, T., Madler, L., Li, N., 2006. Toxic potential of materials at the nanolevel. Science 311, 622–627.

Nimmagadda, A., Thurston, K., Nollert, M.U., McFetridge, P.S., 2006. Chemical modification of SWNT alters in vitro cell-SWNT interactions. J. Biomed. Mater. Res. A. 76, 614–625.

Pryor, J.L., Hughes, C., Foster, W., Hales, B.F., Robaire, B., 2000. Critical windows of exposure for children's health: the reproductive system in animals and humans. Environ. Health Perspect. 108 Suppl 3, 491–503.

Raz, E., 2003. Primordial germ-cell development: the zebrafish perspective. Nat. Rev. Genet. 4, 690–700.

Sayes, C.M., Liang, F., Hudson, J.L., Mendez, J., Guo, W., Beach, J.M., Moore, V.C., Doyle, C.D., West, J.L., Billups, W.E., Ausman, K.D., Colvin, V.L., 2006. Functionalization density dependence of single-walled carbon nanotubes cytotoxicity in vitro. Toxicol. Lett. 161, 135–142.

Sun, Y.P., Fu, K.F., Lin, Y., Huang, W.J., 2002. Functionalized carbon nanotubes: properties and applications. Acc. Chem. Res. 35, 1096–1104.

Thayer, A.M., 2007. Carbon nanotubes by the metric ton. Chem. Eng. News 85, 29–35.

Van den, B.K., Verheyen, R., Witters, H., 2003. Effects of 17alpha-ethynylestradiol in a partial life-cycle test with zebrafish (*Danio rerio*): effects on growth, gonads and female reproductive success. Sci. Total Environ. 309, 127–137.

Wang, H., Wang, J., Deng, X., Sun, H., Shi, Z., Gu, Z., Liu, Y., Zhao, Y., 2004. Biodistribution of carbon single-wall carbon nanotubes in mice. J. Nanosci. Nanotechnol. 4, 1019–1024.

Wei, C.M., 2005. Nanomedicine — foreword. Dm Disease-A-Month 51, 322–324.

Weinstein, B.M., Stemple, D.L., Driever, W., Fishman, M.C., 1995. Gridlock, a localized heritable vascular patterning defect in the zebrafish. Nat. Med. 1, 1143–1147.

Westerfield, M., 1995. The Zebrafish Book. A Guide for the Laboratory Use of Zebrafish (Danio rerio), 3rd Edition. University of Oregon Press, Oregon.

Wittbrodt, J., Shima, A., Schartl, M., 2002. Medaka—a model organism from the Far East. Nat. Rev. Genet. 3, 53–64.

Wu, W., Wieckowski, S., Pastorin, G., Benincasa, M., Klumpp, C., Briand, J.P., Gennaro, R., Prato, M., Bianco, A., 2005. Targeted delivery of amphotericin B to cells by using functionalized carbon nanotubes. Angew. Chem. Int. Ed. Engl. 44, 6358–6362.

Yamago, S., Tokuyama, H., Nakamura, E., Kikuchi, K., Kananishi, S., Sueki, K., Nakahara, H., Enomoto, S., Ambe, F., 1995. In vivo biological behavior of a water-miscible fullerene: 14C labeling, absorption, distribution, excretion and acute toxicity. Chem. Biol. 2, 385–389.

Yang, L., Kemadjou, J.R., Zinsmeister, C., Bauer, M., Legradi, J., Muller, F., Pankratz, M., Jakel, J., Strahle, U., 2007. Transcriptional profiling reveals barcode-like toxicogenomic responses in the zebrafish embryo. Genome Biol. 8, R227.

Yoon, C., Kawakami, K., Hopkins, N., 1997. Zebrafish vasa homologue RNA is localized to the cleavage planes of 2- and 4-cell-stage embryos and is expressed in the primordial germ cells. Development 124, 3157–3165.

Yoong, S., O'Connell, B., Soanes, A., Crowhurst, M.O., Lieschke, G.J., Ward, A.C., 2007. Characterization of the zebrafish matrix *metalloproteinase 9* gene and its developmental expression pattern. Gene Expr. Patterns 7, 39–46.

Zanello, L.P., Zhao, B., Hu, H., Haddon, R.C., 2006. Bone cell proliferation on carbon nanotubes. Nano Lett. 6, 562–567.

Carbon Nanotubes and Nanocomposites for Electrical and Thermal Applications

Wei Wang, Fushen Lu, Lucia Monica Veca, Mohammed J. Meziani, Xin Wang, Li Cao, Lingrong Gu and Ya-Ping Sun

Clemson University, Clemson, SC, USA

1 INTRODUCTION

Carbon nanotubes are newly discovered carbon allotropes, with unique cylindrical hollow structures of extremely large aspect ratios.[1,2] One may conceptually visualize their structures by taking single or multiple graphene sheets and rolling them up into seamless tubes.[3] Depending on the number of the graphene layers, carbon nanotubes are further categorized into single-walled carbon nanotubes (SWNT), double-walled carbon nanotubes (DWNT), and multiple-walled carbon nanotubes (MWNT). The distance between the coaxial graphene layers in MWNTs is about 0.34 nm, which is close to that in graphite. For SWNTs, the rolling up of a graphene sheet needs to match carbon atoms on the edges, which can be described by a chiral vector, $\boldsymbol{C}_h$,[3,4]

$$\boldsymbol{C}_h = n\boldsymbol{a}_1 + m\boldsymbol{a}_2 \quad (1)$$

where $\boldsymbol{a}_1$ and $\boldsymbol{a}_2$ are unit vectors along the hexagonal lattice, and n and m are numbers of the steps along the vectors. In fact, (n, m) is commonly referred to as the *chiral index* for a specific SWNT. When $n = m$, the nanotube is an ''armchair'', while $n = 0$ or $m = 0$, the nanotube is a ''zigzag''. All other SWNTs are called *chiral* nanotubes (Scheme 1).[5] It is now well established that a SWNT is either metallic (including semimetallic) or semiconducting, depending on its chirality.[6] For an armchair SWNT ($n = m$), the conductance and valence bands in the electronic density of states (DOS) overlap, so that the nanotube is metallic. If $n - m = 3q$ and $q \neq 0$ (where q is an integer), the corresponding SWNTs are semimetallic, with a small band gap of several millielectronvolts. For $n - m \neq 3q$, the nanotubes are semiconductors with a significant band gap near the Fermi level. Statistically (without any bias toward either type in the production), the ratio between metallic and semiconducting SWNTs should be 1 : 2. For MWNTs, the coaxial layers may be of different chiralities with negligible interlayer electronic coupling, and, as a result, MWNTs generally exhibit metallic characteristics.

There are now many ways to produce carbon nanotubes, including electric arc-discharge, laser ablation, and various chemical vapor deposition (CVD) techniques such as the CoMoCat process and the HiPco process. The production generally involves vaporizing carbon targets or decomposing carbon stocks, and sequentially rearranging carbon atoms into tubular structures with the assistance of catalysts.[7–10] The as-produced carbon nanotubes are typically several hundred nanometers to several microns in length. The average diameter and diameter distribution of SWNTs are dependent on their production methods, while diameters of MWNTs generally vary in the range 10–100 nm. For example, SWNTs produced from arc-discharge and laser-ablation methods are relatively more uniform in diameter (typically 1.2–1.4 nm), while those

Nanomaterials: Inorganic and Bioinorganic Perspectives. Edited by Charles M. Lukehart and Robert A. Scott.
 ISBN 978-0470-51644-7

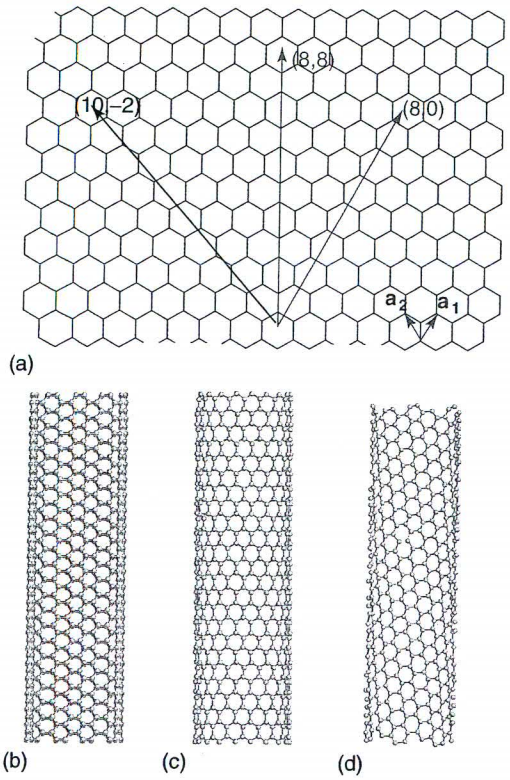

Scheme 1 (a) The two chiral vectors a_1 and a_2 on a graphene sheet; (b) an armchair SWNT (8,8); (c) a zigzag SWNT (8,0); and (d) a chiral SWNT (10,−2). (From Ref. 5)

from the HiPco method have broad diameter distributions (0.7–1.3 nm). As pseudo-one-dimensional nanostructures of very high surface areas, carbon nanotubes, SWNTs, in particular, are generally severely bundled due to the strong van der Waals force (on the order of 0.5 eV nm^{-1}).[11] Most electron microscopy images of pristine or purified SWNTs are typically those of nanotube bundles (Figure 1).

Carbon nanotubes are often described as the ultimate nanofibers because of their superior mechanical properties.[12] However, their electrical and thermal properties are just as unique and impressive.[13] According to estimates from theoretical calculations, metallic SWNTs should have exceptionally high electrical conductivity of up to 10^6 S cm^{-1},[14,15] higher than that of copper metal at room temperature. Experimental measurements on single or bundled SWNT yielded somewhat lower value, on the order of 10^4 S cm^{-1}.[8,16] Carbon nanotubes are also excellent thermal conductors. Theoretical calculation predicted that an isolated (10,10) SWNT should have a very high thermal conductivity of 6600 W m^{-1} K^{-1} at room temperature.[17] Experimentally, though not as high as predicted, the thermal conductivity of an individual MWNT was found to be about 3000 W m^{-1} K^{-1}.[18,19] These superior properties of carbon nanotubes, combined with their high aspect ratio and uniquely high mechanical performance, make them ideal fillers in polymeric nanocomposite materials for electrical and thermal applications.

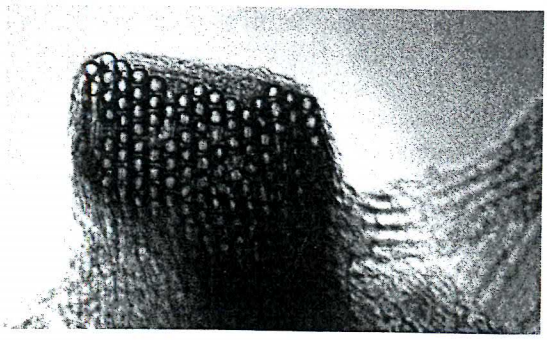

Figure 1 TEM image showing bundled SWNTs. (Reprinted with permission from Thess *et al.*[8] © 1996. Reprinted with permission from AAAS)

2 POLYMERIC/CARBON NANOTUBES COMPOSITES

Ever since the discovery of carbon nanotubes, there has been much interest in their uses in polymeric carbon nanotubes composites.[20–25] However, despite their widely acknowledged and discussed superior properties and performance potentials, carbon nanotubes are not readily dispersed into polymeric matrices for the desired nanocomposite materials. In fact, the homogeneous dispersion of carbon nanotubes, especially SWNTs, has been a major challenge in the development of polymeric carbon nanotube composites. The nanotubes are severely bundled or aggregated, and are essentially insoluble in any solvent systems, hindering any solution-phase processing. Among early examples, polymeric carbon nanotube composites were fabricated via simple mixing, either in solution or in the melt state, with the aid of high shear forces such as sonication. However, the preparation based on simple polymer-nanotube blends typically results in composites of relatively poor dispersion of the nanotubes, which compromises the predicted or expected performance.[25] Other mixing methods, such as dry powder mixing,[26] latex mixing,[27] and coagulation[28] have been adopted in an effort to improve the nanotube dispersion, though each method has its own limitation. The results are generally far from satisfactory.

Improved polymeric carbon nanotube composites were prepared by using in situ polymerization, namely, polymerization of monomers in the presence of carbon nanotubes.[29] In fact, most of the epoxy-nanotube composites, which represent the earliest examples for using carbon nanotubes in polymeric nanocomposites, were fabricated by using this method.[30] Experimentally, carbon nanotubes were firstly dispersed in low molecular weight precursors, followed

by adding hardening agents to cure the polymer to have the dispersed nanotubes ''locked'' inside the polymer matrix.

2.1 Functionalization of Carbon Nanotubes

There have been extensive investigations on the chemical modification and functionalization of carbon nanotubes to make them more processible (*see* ***Carbon Nanotubes, Single-Walled: Functionalization by Intercalation***).[31–35] Of particular interest are those that result in the solubilization of the carbon nanotubes, thus enabling conventional wet processing and fabrication of the relevant polymeric nanocomposites. The functionalization could be noncovalent or covalent in nature. In the noncovalent functionalization, the functional molecules are anchored onto the nanotube surface via van der Waals forces for the solubilization of the functionalized nanotubes in organic solvents or aqueous media. Several classes of functional molecules based on different kinds of noncovalent interactions have been examined, including hydrophobic (e.g., sodium dodecyl sulfate (SDS)[36,37] and poly(vinyl pyrolidone) PVP[38]) and $\pi-\pi$ interactions (e.g., pyrenes[39] and poly(arylene ethynylene)s[40]). Some polymers such as poly(phenylene vinylene) derivatives [41,42] or biological species such as DNA[43] have also been used to functionalize carbon nanotubes, presumably by conformational matching. For covalent functionalization, there are primarily two different routes. One is the addition reaction to the nanotube graphitic sidewall, involving generally highly reactive species such as fluorine (*see* ***Carbon Nanotubes: Fluorinated Derivatives***),[44] aryl diazonium compounds,[11] nitrenes,[45] azomethine ylides,[46] etc. A more versatile alternative is the targeting of the defect-derived carboxylic acid groups on the nanotube surface,[31–35,47,48] which are often associated with the oxidative conditions used in the nanotube purification procedures. These carboxylic acid groups, typically accounting for a few percent of the nanotube carbons, may be functionalized with molecules or polymers bearing amino or hydroxyl moieties in classical reactions such as amidation and esterification.

The functionalized carbon nanotubes could be dispersed homogeneously into a polymer matrix via solution-phase processing, where the matrix polymer and functionalized nanotubes are both soluble in a common solvent. For example, Grady *et al.*[49] prepared polypropylene–SWNT composites by mixing solutions of polypropylene and octadecylamine (ODA)-functionalized SWNTs. However, there is a potentially significant problem with such use of functionalized carbon nanotubes because, generally speaking, the quantity of functional groups required for the solubility of carbon nanotubes is substantial. These small-molecule functional groups are often unwanted, potentially acting as ''impurities'' in the intended polymeric nanocomposites to negatively affect their properties and performance.

One strategy to improve the compatibility is to use polymer-functionalized carbon nanotubes for polymeric nanocomposites. Among several approaches used to attach polymers to carbon nanotubes is the ''grafting-to'' method, where the polymer is attached to the nanotube surface via covalent bonding. For example, Wu *et al.* generated polymeric anions on a poly(*N*-vinyl carbazole) (PVK) and polybutadiene backbone by reacting the polymers with organometallic reagents such as sodium hydride or butyl lithium, and then attached the polymeric anions to SWNTs in classical nucleophilic reactions.[50] Also popular has been the ''grafting-from'' method, where the chemically modified nanotube is used as the initiator for polymerization. For example, Viswanathan *et al.* used excess *sec*-butyl lithium to generate carbanions on the nanotube surface, so that both free *sec*-butyl lithium and the nanotube-bound carbanions could initiate polymerization reactions upon the addition of styrene monomers to achieve improved compatibility of the nanotubes with the polystyrene (PS) matrix.[51] Recently, several research groups reported further modification to the grafting-from method.[52–54] As shown in Scheme 2, the nanotube-bound initiators were prepared for grafting various polymers onto the nanotube surface via atomic transfer radical polymerization (ATRP). Kong *et al.*[52] and Qin *et al.*[53] functionalized MWNTs and SWNTs, respectively, with hydroxyl-containing ATRP initiators via esterification reactions at nanotube surface defect sites. These nanotube-bound initiators were then used for the polymerization of different monomers, including styrene,[52] methyl methacrylate,[53] and butyl methacrylate.[54] Most of these polymer-functionalized carbon nanotubes, in which the polymer structures were more controllable, were found to be soluble in common organic solvents.

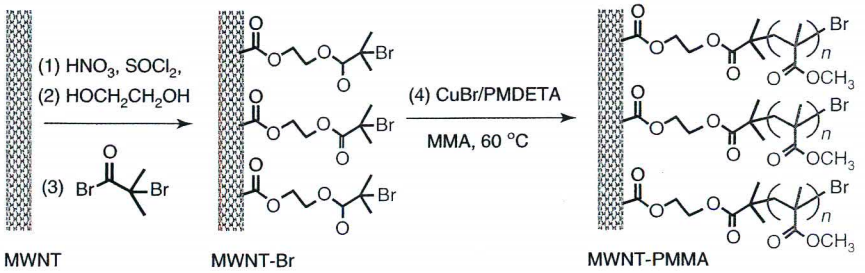

Scheme 2 Polymerization on nanotube surface via ATRP. (From Ref. 52)

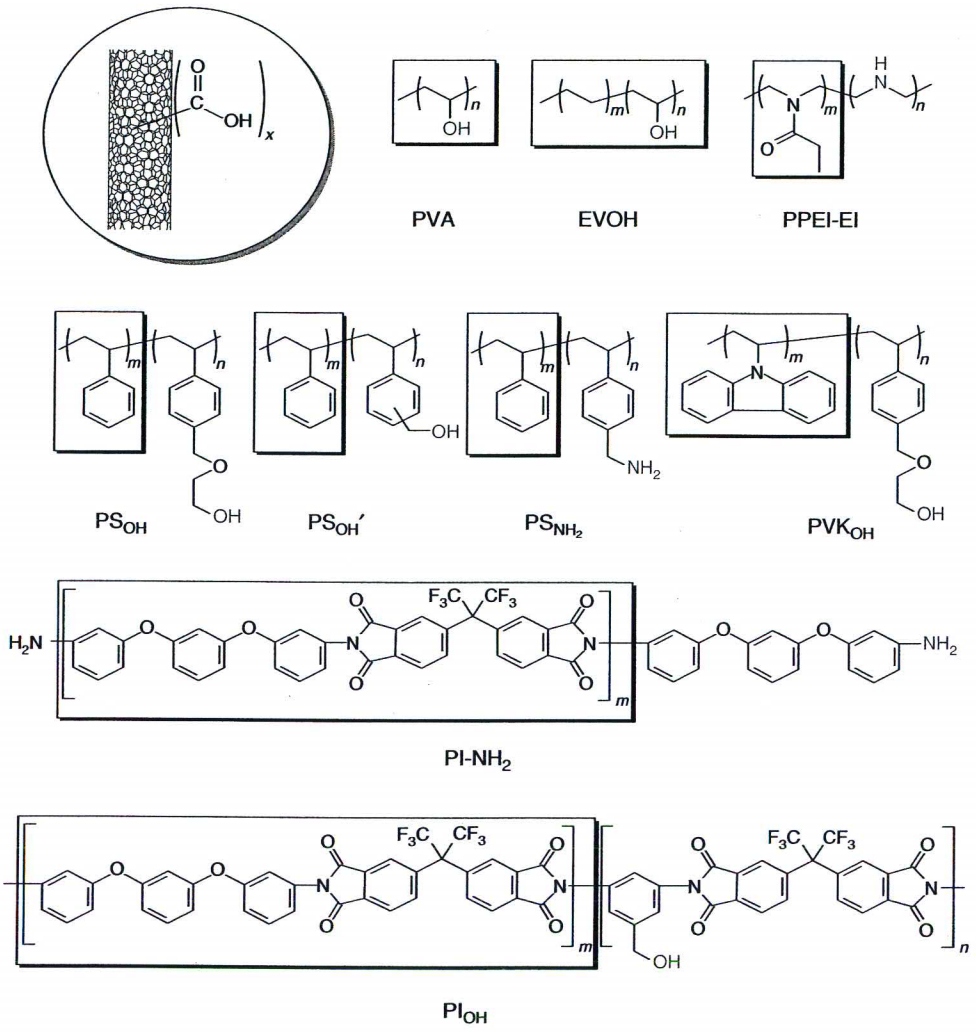

Scheme 3 Representative polymers for the functionalization and solubilization of carbon nanotubes (with the matrix polymer structural motifs and groups for functionalization reactions highlighted). (From Ref. 55)

2.2 Matrix Polymers as Functionalization Agents for Enhanced Compatibility

The selection of right functionalization agents is obviously important to the properties of the functionalized carbon nanotubes and ultimately to the performance of the resulting polymeric carbon nanotube composites. In order not to introduce foreign materials (essentially impurities) into the targeted nanocomposites, the best strategy is to select and use functionalization agents that are structurally identical or maximally similar to the matrix polymers.[55] It not only helps the homogeneous dispersion of the functionalized carbon nanotubes but also prevents any possibilities of microscopic phase separation in the resulting nanocomposites. By targeting the defect-derived carboxylic acid groups on the nanotube surface, Sun and coworkers prepared functionalized carbon nanotubes of a variety of monomeric and polymeric functional groups (Scheme 3).[55–63] The emphasis on covalent functionalization at the defect sites has been due to the fact that nanotube electronic structures are largely preserved postfunctionalization.[55] These functionalized carbon nanotubes are mostly soluble in common solvent systems, allowing convenient wet processing in the fabrication of desired polymeric nanocomposites.

A good example of such strategy was the functionalization of carbon nanotubes with poly(vinyl alcohol) (PVA).[58] The pendant hydroxyl groups in the polymer were used for the esterification of the nanotube defect-derived carboxylic acids, thus providing direct matrix–filler bonding. Because the carboxylic acids were associated with only a small fraction of the nanotube carbons, the electronic structures of the nanotubes were preserved both in the functionalized sample and in the final composite films, as reflected in their respective optical absorption spectra (Figure 2). The electronic transitions corresponding to the van Hove singularity pairs in the DOS of semiconducting (S_{11}, ~1800 nm and S_{22},

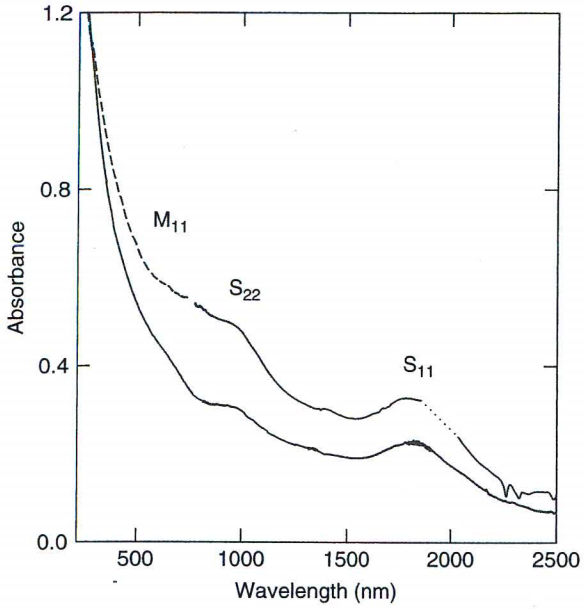

Figure 2 Optical absorption spectra of PVA-functionalized SWNTs (red curve) and a free-standing PVA-SWNT nanocomposite thin film fabricated from the same sample (blue curve). (Reprinted with permission from Lin *et al.*[58] © 2003 American Chemical Society)

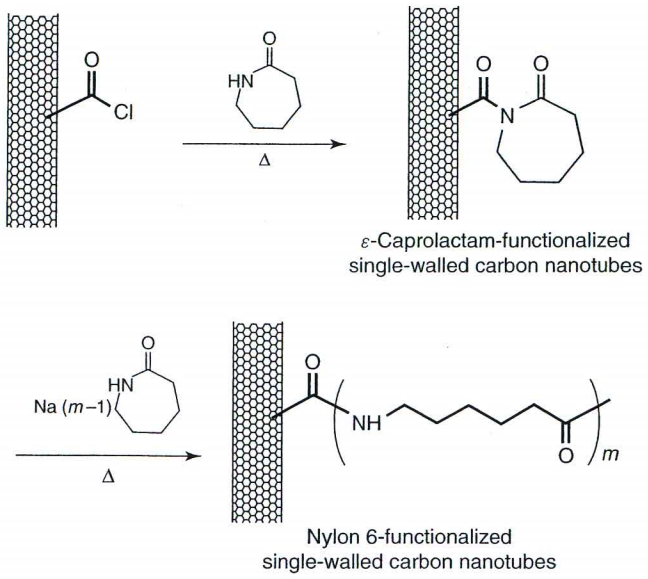

Scheme 4 Reaction scheme for the preparation of nylon-6-functionalized SWNTs. (From Ref. 62)

~1000 nm) and metallic (M_{11}, ~700 nm) SWNTs remained largely unchanged. The significant solubility of PVA-functionalized carbon nanotube in hot water allowed easy fabrication of impurity-free PVA–carbon nanocomposite films at different nanotube loadings. A low loading of the functionalized sample (1 wt%) dispersed in the PVA polymer matrix hardly changed the crystallinity, but the Young's modulus and yield stress increased by about 25 and 40%, respectively, from those of the PVA polymer, indicating efficient load transfer as a result of the excellent interfacial bonding. The favorable matrix–filler interactions also allowed the effective alignment of the carbon nanotubes in PVA thin films via mechanical stretching.[64]

Other polymers containing PVA moieties, such as poly(ethylene-*co*-vinyl alcohol) (EVOH, Scheme 3),[63] were covalently attached onto SWNTs via the same esterification reaction. The common solubility of EVOH-functionalized SWNTs and neat EVOH in a polar solvent like dimethyl sulfoxide (DMSO) made it possible to conveniently fabricate EVOH/SWNT nanocomposite films of variable nanotube contents via wet casting. This represents another example of homogeneously dispersing carbon nanotubes into polymeric matrices without introducing any other dispersion materials.

A combination of this strategy on nanotube dispersion and solubilization by using matrix polymers with the grafting-from method was applied in the preparation of nylon/carbon nanotube composites without any unwanted foreign materials.[62,65] For the functionalization of SWNTs with nylon-6, the precursor ε-caprolactam for nylon-6 was first attached to the nanotubes via amide linkages.[62] The grafting was from the anionic ring-opening polymerization (AROP) of the nanotube-bound ε-caprolactam into the bulk that contained the same monomer (Scheme 4). The functionalized samples were found to share solubility with nylon-6 polymer in formic acid, which thus allowed intimate mixing of the nanotubes and nylon-6 in various proportions for processing in solution or melt.

In the same strategy, polymers with amino or hydroxyl end groups have also been used for the functionalization of carbon nanotubes without introducing potential impurities into the final nanocomposites. More specifically, an amine-terminated polyimide (PI-NH_2, Scheme 3) synthesized from the condensation of 4,4′-(hexafluoroisopropylidene) diphthalic anhydride with 1,3-bis(3-aminophenoxy)benzene was covalently grafted to carbon nanotubes via the amidation of the surface defect-derived carboxylic acids.[59] The PI-NH_2 was designed to be structurally identical to the matrix PI on which the targeted nanocomposites was based. The shared solubility of the PI-NH_2-functionalized carbon nanotubes with the matrix PI in a polar solvent like dimethylformamide (DMF) and their intimate miscibility in solution allowed the relatively convenient wet casting of the desired high-quality (optically transparent and homogeneous) nanocomposite thin films (Figure 3).[59]

Other than directly preparing polymers that contain amine or hydroxyl groups for the nanotube functionalization, these functional groups could also be introduced into some polymers under consideration, without fundamentally altering their structures. For example, the commercially available poly(propionylethylenimine) (PPEI) could be partially hydrolyzed to introduce a controlled

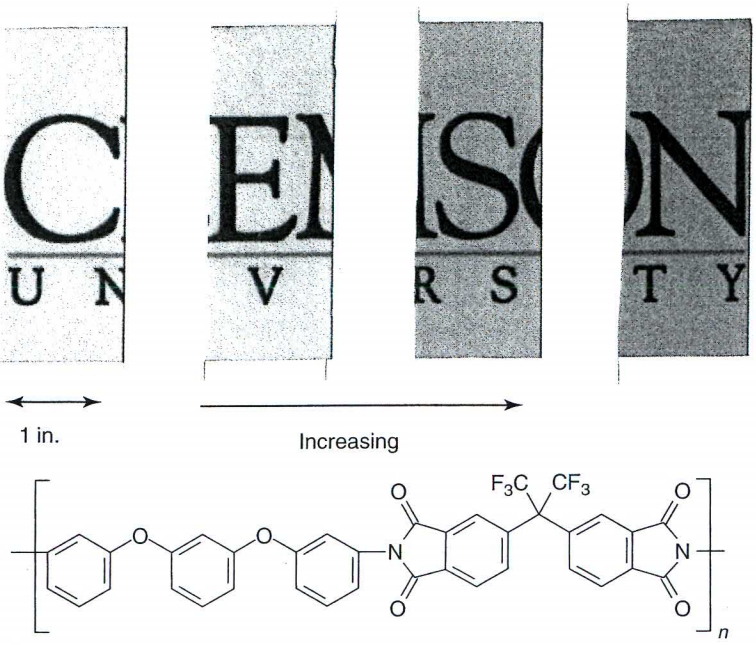

Figure 3 Pictures of four nanocomposite films of polyimide (the polymer structure shown) with different contents of SWNTs on a piece of paper printed with the logo of Clemson University (for a demonstration of the optical transparency). (Reprinted with permission from Qu *et al.*[59] © 2004 American Chemical Society)

fraction of secondary amine moieties. The resulting copolymer poly(propionylethylenimine-*co*-ethylenimine) (PPEI-EI) (Scheme 3) has been very effective in the functionalization of carbon nanotubes under various sets of reaction conditions, to obtain functionalized samples of excellent solubility characteristics in common organic solvents and water.[66–69] For example, the PPEI-EI-functionalized carbon nanotubes were intimately miscible and fully compatible with the parent PPEI and other polymers such as PVA for nanocomposites.[70] In fact, fluorescent PPEI-EI-functionalized SWNTs were homogeneously embedded in PVA film and visualized in confocal microscopy imaging without obvious deviation. Upon mechanical stretching, while the nanotubes remained well dispersed, their preferential alignment along the stretching direction was well illustrated in the confocal images.[70]

Most copolymers used in this strategy have been specifically prepared from comonomers in polymerization reactions. For the desired compatibility, a copolymer could be designed such that the major corepeating units are the same as those in the matrix polymer, with minor corepeating units containing amino or hydroxyl moieties for linkages with the nanotube defect-derived carboxylic acid groups. For the important commercial polymer, PS, as an example, PS random copolymers with derivatized styrene units (in Scheme 3, ~7% for PS_{OH}, ~11% for PS_{OH}', and ~20% for PS_{NH_2}) were synthesized from radical copolymerization of styrene and corresponding styrene derivatives.[56,57] The units with pendant hydroxyl groups were introduced for the purpose of nanotube functionalization, and the results confirmed the effectiveness of the approach. The functionalized carbon nanotube samples exhibited similar solubility characteristics to those of PS homopolymers, which allowed wet processing of PS–carbon nanotube composite blends and films. The successful fabrication of optically high-quality nanocomposite thin film reflects the excellent compatibility of functionalized carbon nanotubes with PS.[56]

In the strategy to functionalize carbon nanotubes with copolymers that are structurally similar to the matrix polymers, the minor comonomers could be slightly different in molecular structure from the major corepeating units. Their fractions in the copolymers are generally kept small enough to minimize potentially negative effects on the compatibility of the copolymers with the corresponding matrix polymers. One example was the incorporation of 3,5-diaminobenzyl alcohol as a comonomer in the condensation for PI.[61] The resulting PI copolymer (Scheme 3, PI_{OH}, with one pendant hydroxyl group per seven repeating units) was similarly effective in the functionalization and solubilization of carbon nanotubes (in comparison with the amino-terminated PI-NH_2 discussed above) for high-quality PI-carbon nanocomposite films.

2.3 Benefits and Issues

The functionalization and solubilization of carbon nanotubes offer significant benefits in the preparation

of high-quality polymeric carbon nanotube composites. Among two somewhat related major benefits are improvements in the exfoliation of carbon nanotubes (especially SWNTs) into individual tubes or thin bundles, and in the processibility, both of which enable the homogeneous dispersion of carbon nanotubes in the selected polymer matrix for optimal performance. For nanocomposites in specific applications, such as thin films of sufficient electrical conductivity to mitigate static charges,[71,72] the use of functionalized carbon nanotubes allows a significant reduction in the nanotube loading, and thus minimizes any potential negative effects on other properties of the polymeric nanocomposites (high optical quality and transmittance, for example).

The characterization of polymeric nanocomposites with well-dispersed carbon nanotubes posts additional challenges beyond those for pristine or functionalized nanotube samples. Scanning and transmission electron microscopy techniques are useful, though special sample preparation procedures such as microtomy are often required.[59,62,64] Even for microtomed slices, while the imaging of functionalized MWNTs embedded in polymer matrices is still relatively straightforward, the same for SWNTs can be very difficult, requiring special effort such as the use of holy-carbon grids, and so on.[73] Complementary to electron microscopy, optical spectroscopic techniques have been effective in the characterization of carbon nanotubes. For SWNTs functionalized at surface defect sites, their near-IR electronic transitions are largely preserved either in the functionalized samples or after being dispersed into the polymeric matrices. Therefore, optical absorption spectroscopy serves as a convenient tool in the characterization of SWNTs in polymeric nanocomposites. At a more quantitative level, the functionalized SWNTs exhibit absorption bands that are blue-shifted and narrower in width as an effect of debundling.[73] The same effect is believed to move the G-band toward a higher frequency in the Raman spectrum of SWNTs.[73–76] Particularly interesting and useful is the fact that carbon nanotubes upon the functionalization at surface defect sites exhibit strong visible and near-IR luminescence.[66,77] Mechanistically, the photoluminescence is attributed to excited-state energy trapping sites associated with passivated nanotube surface defects. The effective exfoliation of carbon nanotubes for being dispersed primarily as individual nanotubes (thus with minimal intertube quenching effect) is a necessary prerequisite to observe such luminescence. Therefore, the defect-derived luminescence may be used as a tool to probe the dispersion of functionalized carbon nanotube in polymeric matrices.[70,73,77,78] In a recent demonstration,[73] the nanocomposites with functionalized carbon nanotubes (PI-NH_2-SWNT) exhibited strong luminescence, whereas those with purified SWNTs at the same nanotube loading were essentially nonemissive in the visible and near-IR regions (Figure 4).

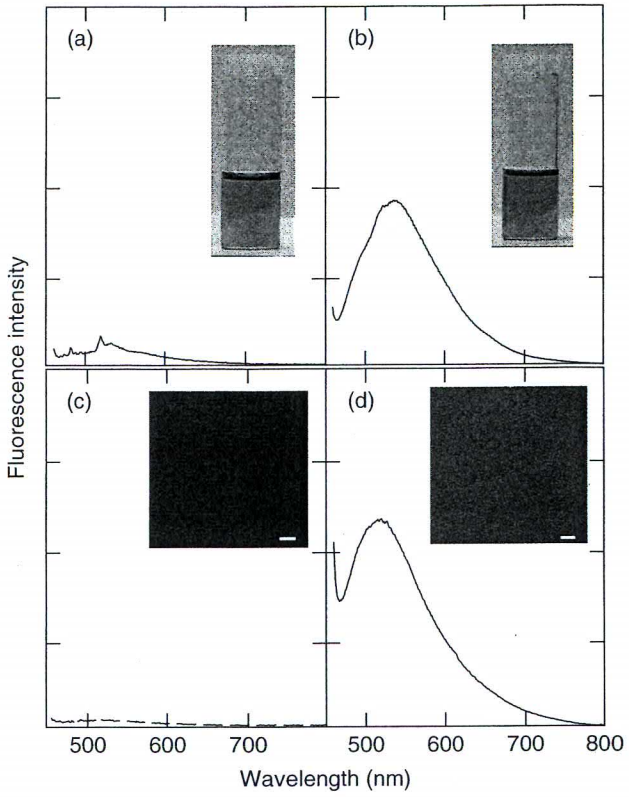

Figure 4 Photoluminescence spectra (450-nm excitation) from (a) SWNTs dispersed with the aid of polyimide in DMF, (b) the polyimide-functionalized SWNTs (PI-NH_2-SWNT) in DMF solution with similar nanotube content to that in (a), (c) a film from the suspension of SWNTs, and (d) a film from the PI-NH_2-SWNT solution. The insets are photographs (in (a) and (b)), and confocal images (in (c) and (d), 458-nm excitation, 469-nm detection; scale bars = 5 mm). (From Lin *et al.*[55] Reproduced by permission of The Royal Society of Chemistry)

3 ELECTRICAL PROPERTIES AND APPLICATIONS

Carbon nanotubes are dispersed into polymeric matrices for desired electrical properties of the resulting nanocomposites.[24,79,80] A variety of potential applications for these nanocomposites, ranging from static charge dissipation[81] to electromagnetic interference (EMI) shielding,[82–84] have been explored and investigated. For the latter, polymeric nanocomposites dispersed with conductive carbon nanotubes are more advantageous than conventional metal-based EMI shielding materials in several aspects, such as corrosion resistance, light weight, flexibility, and low costs, with comparable performance.[84] The nanocomposite with 15 wt% SWNTs loading was found to have EMI shielding efficiency of about 50 dB at 10 MHz and 15–20 dB in the range 0.5–1.5 GHz.

3.1 Electrical Conductive Polymeric/Carbon Nanotube Composites

For superior electrical properties, the dispersion of carbon nanotubes in polymeric nanocomposites is an important parameter.[79,80] As discussed earlier, since pristine carbon nanotubes are bundled and insoluble, their exfoliation and solubilization via chemical modification and functionalization are often required. Generally enhanced performance with the use of noncovalently or covalently functionalized carbon nanotubes has been demonstrated.[85–90] For example, Ramasubramaniam *et al.* used poly(phenylene ethylene) (PPE) to wrap SWNTs.[85] These PPE-functionalized (noncovalently) SWNTs were soluble in many organic solvents, enabling solution-phase processing for the fabrication of PS/SWNT (with PPE wrapping) nanocomposites (Figure 5a). The resulting PS nanocomposites exhibited low percolation threshold with much improved electrical conductivity, 6.89 S cm^{-1} at 7 wt% nanotube loading, higher by 5 orders of magnitude than that of a similar PS/SWNT nanocomposite prepared from in situ polymerization.[85] Various potential applications of these polymeric nanocomposites were proposed and discussed (Figure 5b).

Noncovalent functionalization has its advantages in preserving the electrical properties of carbon nanotubes with minimal damage to the nanotube surface. However, the use of dispersion agents that are different from matrix polymers may potentially affect negatively other nanocomposite properties, such as mechanical strength and long-term stability. Covalent functionalization of carbon nanotubes at the surface defect sites also largely preserves the electrical properties of carbon nanotubes,[31,55] thus representing another popular approach in the development of polymeric nanocomposites for potential electrical applications.[60,86,87] For example, Li *et al.* functionalized MWNTs with alkyl alcohols of various alkyl chain lengths (Scheme 5) to demonstrate that the increased solubility of functionalized MWNTs could improve nanotube dispersion in the polymer matrix, and therefore result in higher electrical conductivity in the corresponding nanocomposites.[86] Interestingly, at the same nanotube loading, the conductivity of polysulfone nanocomposite with hexadecyl alcohol-functionalized MWNTs was higher by almost 4 orders of magnitude than that of the nanocomposite with butyl alcohol-functionalized MWNTs. Again, the use of functionalization agents significantly differing from matrix polymers could result in various degrees of phase separation in the nanocomposites. The incompatibility of alkyl alcohols with polysulfone matrix could be responsible for the conductivity inhomogeneity in the nanocomposites.[86] A more elegant strategy is to design and prepare functionalized carbon nanotubes, in which the functional agents are structurally identical or largely similar to the selected matrix polymer for intimate mixing and compatibility,[55] as demonstrated by Wang *et al.* specifically on polymeric carbon nanotube composites for desired electrical properties.[60]

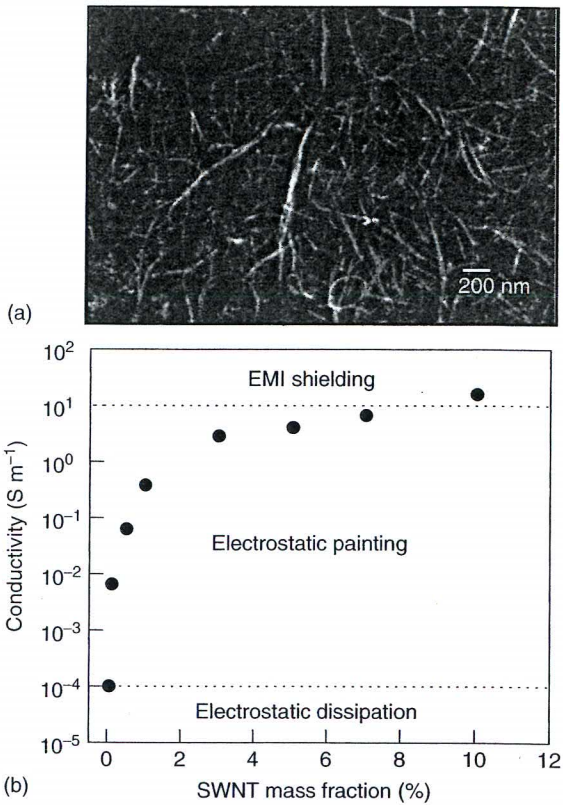

Figure 5 (a) SEM images of the polystyrene/PPE-functionalized SWNTs (5 wt%) composite film. (b) The room-temperature electrical conductivity of polystyrene/PPE-functionalized SWNT composites vs. nanotube concentration in the composites and their potential applications. (Reprinted with permission from Ramasubramaniam and Chen[85] *Appl. Phys. Lett.*, **83**, 2928–2930. © 2003, American Institute of Physics)

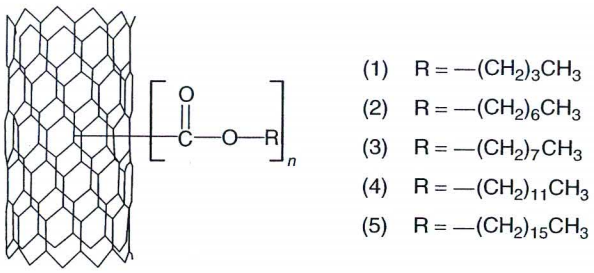

Scheme 5 MWNTs functionalized with alcohols of various alkyl chain lengths. (From Ref. 86)

In the work by Wang *et al.*,[60] a PVK copolymer with minor units containing pendant hydroxyl groups (PVK_{OH}, Scheme 3) was synthesized for the covalent functionalization of SWNTs. The PVK copolymer-functionalized SWNTs were readily soluble in common organic solvents, with the solution miscible with that of PVK polymer. The excellent compatibility of the functionalized nanotubes

with the PVK matrix enabled the fabrication of high-quality nanocomposite thin films for studies of optical properties. These nanocomposite films were found to be significantly photoconductive (enhanced charge dissipation under photoillumination).[60]

Similarly, a polythiophene copolymer, poly[3-(2-hydroxyethyl)-2,5-thienylene] (PHET), was synthesized for the functionalization of MWNTs (Scheme 6).[87] The resulting polythiophene nanocomposite with 50 wt% PHET-functionalized MWNTs was found to be 28 times more conductive than the nanocomposite of the same nanotube loading but prepared from simple ultrasonic mixing of PHET with unfunctionalized MWNTs, demonstrating the importance of nanotube homogeneous dispersion and compatibility with the matrix polymer for the electrical conductivity of corresponding nanocomposites.

In the use of polymer-functionalized carbon nanotubes for polymeric nanocomposites of enhanced electrical conductivity, a potentially significant issue is the possibility for the polymeric functional groups to form an insulating layer on the nanotube surface, which could decrease the electrical conductivity of the nanotube. For example, Bekyarova *et al.* reported that the chemical functionalization of SWNTs with ODA and poly(*m*-aminobenzensulfonic acid) (PABS) resulted in a reduction in the electrical conductivity of nanotube by 2–3 orders of magnitude, with an associated increase in the percolation threshold by a factor of 5.[88]

There are many potential applications of polymeric nanocomposites from the homogeneous dispersion of carbon nanotubes. While the electrical conductivities of resulting nanocomposites are generally not high (especially at relatively low nanotube loadings), they are sufficient for dissipating static charges in the corresponding polymer matrices that are otherwise insulating. A classical case was the successful use of SWNTs to impart electrical conductivity in PI and related polymeric materials suitable for space applications, such as solar sails and ultrathin membranes for light-weight space structures.[72,89–92] In the work by Smith *et al.*[92] amide acid polymers with alkoxysilane groups were employed as end caps to functionalize SWNTs in hydrolysis reaction. The functionalized SWNTs were mixed with the selected matrix polymers in solution at different concentration ratios for the casting of optically transparent thin films. The percolation threshold was estimated to be 0.03–0.04 wt% SWNTs in the nanocomposite films (Figure 6a). At the nanotube loadings only slightly above the percolation threshold (such as 0.05 wt%), the electrical conductivity in the nanocomposite films was sufficient for effective dissipation of static charges, while other film properties, including excellent optical transparency and flexibility, were preserved.[92] In a follow-up study by the same group,[72] a crumple test was performed to show how the robustness and stability in electrical conductivity of the polymeric nanocomposites benefited from the improved mechanical properties with the embedding of SWNTs. As illustrated in Figure 6(b), the observed surface resistivity of the nanocomposite films remained largely unchanged despite their being subjected to the harsh mechanical manipulation.[72]

3.2 Separated Metallic SWNTs for Enhanced Performance

In the development of polymeric carbon nanotube composites, SWNTs are often considered to be more superior for desirable properties of the nanocomposites such as high optical quality and transparency, lower carbon loading, mechanical properties, etc.[20–25] For electrical properties and applications, metallic and semiconducting SWNTs are produced as mixtures by all of the available production methods, but only the metallic ones are highly conductive. More disappointing is the fact that metallic SWNTs generally represent the minority fraction in the mixtures. Therefore, postproduction separation of metallic SWNTs from their mixtures with semiconducting SWNTs has been pursued by a number of research groups,[4,93–95] with various strategies that exploit the generally subtle physical and chemical differences between metallic and semiconducting SWNTs.[96–119] A few relatively more effective postproduction separation methods are highlighted below.

Both dielectrophoresis[96,97] and DNA wrapping[43,98,99] exploit the relatively higher polarizability of metallic SWNTs

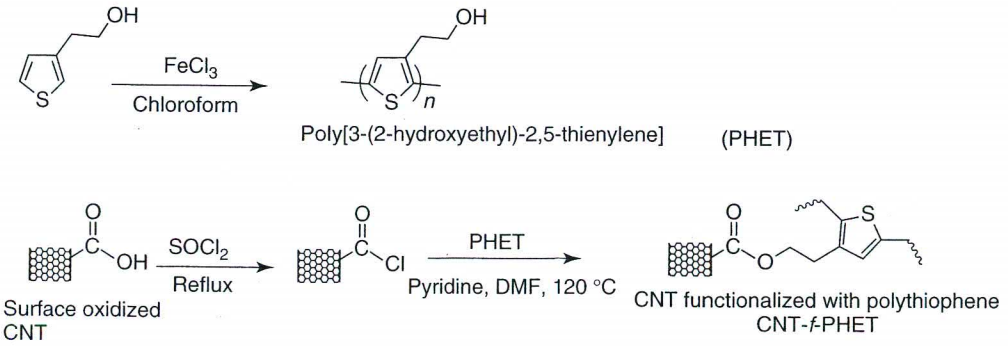

Scheme 6 The functionalization of SWNTs with a derivatized polythiophene. (From Ref. 87)

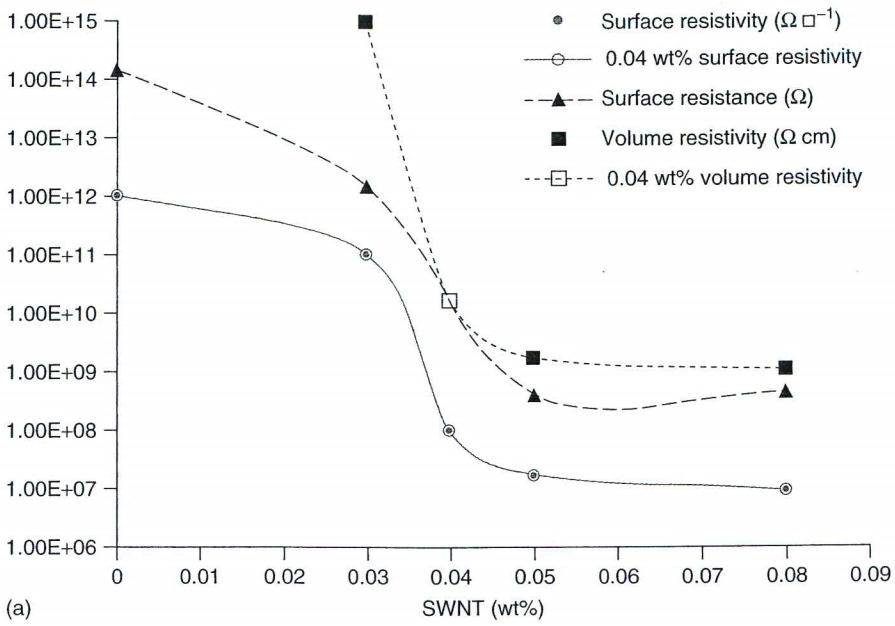

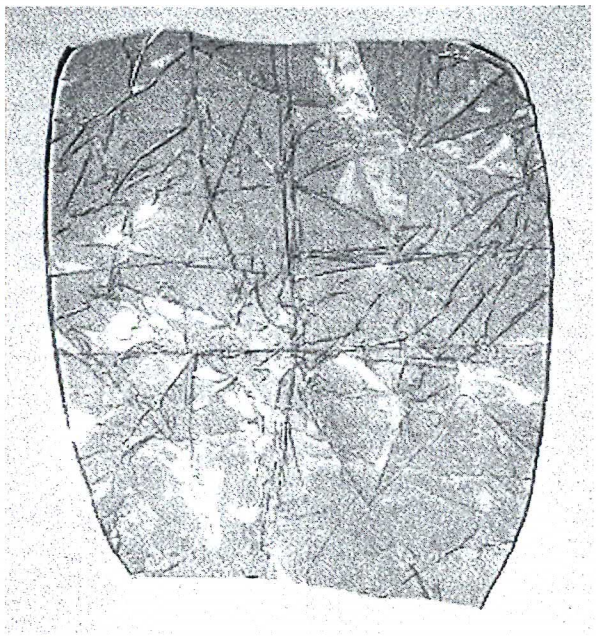

Figure 6 (a) Surface resistance and surface and volume resistivities of polyimide/functionalized-SWNT nanocomposites. (Reprinted from Smith *et al.*,[92] © 2004, with permission from Elsevier) and (b) the composite film after a crumple test showed no surface resistivity change. (Reprinted from Watson *et al.*,[72] © 2005, with permission from Elsevier)

for separation, though these methods are limited to very small quantities of nanotubes. In a more recent development, Arnold *et al.* reported the use of ultracentrifugation to separate single-strand DNA- or surfactant-wrapped SWNTs in solutions with density gradient media (Scheme 7).[100,101] The method represents an interesting improvement over others in the same category, but the limitation with the small amount of sample that could be processed remains.

Selective removal of either metallic or semiconducting SWNTs from their mixtures may be accomplished by current-induced electrical breakdown,[102] laser irradiation,[103,104] or specific chemical reactions.[105–113] In such reactions, metallic SWNTs are generally higher in reactivity than their semiconducting counterparts because of the higher electron density at the Fermi level. While most of reaction conditions favor metallic SWNTs, reversing the reactivity

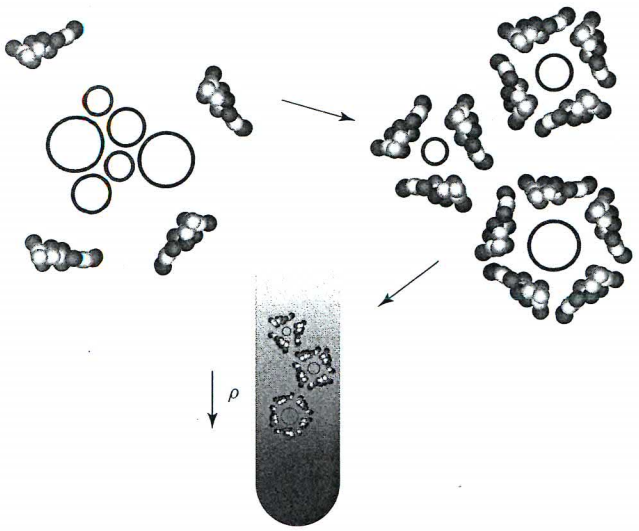

Scheme 7 A schematic illustration on the use of surfactant encapsulation and gradient density sorting for enriched metallic and semiconducting SWNTs. (From Ref. 97)

order was also possible by doping metallic SWNTs with hole-doping agents like H_2O_2.[113] As suggested by theoretical calculation, H_2O_2 would selectively shift the Fermi level to the first van Hove singularity band in semiconducting SWNTs, to result in their higher chemical reactivity.[113] Enriched metallic SWNTs could be recovered from the mixture with dopant by high-temperature annealing. It should be noted, however, that thermally annealed SWNT samples are generally so severely aggregated that their further processing or dispersion may become an extremely challenging task.

Bulk separation (on the order of milligram to gram quantity) is necessary for the evaluation of separated metallic and semiconducting SWNTs in polymeric nanocomposites. Several techniques amenable to bulk separation have been explored.[4,114–121] Papadimitrakopoulos and coworkers reported that the functionalization reaction of ODA with purified SWNTs under typical thermal reaction conditions preferred semiconducting ones over their metallic counterparts, thus allowing the recovery of enriched semiconducting and metallic SWNTs from the solubilized and precipitated fractions, respectively.[114–116] Maeda *et al.* found similar phenomenon in the use of smaller amine molecules including octylamine, propylamine, and isopropylamine to functionalize SWNTs,[117,118] though it is puzzling how these small amines were capable of solubilizing the nanotubes.

Sun and coworkers developed a bulk separation method by exploiting the selective interactions of relatively large planar aromatic molecules with semiconducting SWNTs for their solubilization in organic solvents.[4,119] The originally reported work was based on the use of a tetra-substituted free-base porphyrin, 5,10,15,20-tetrakis(hexadecyloxyphenyl)-21*H*,23*H*-porphine (THPP, Scheme 8).[4] In a relatively simple procedure, THPP was mixed with purified SWNTs (from arc-discharge or laser-ablation production) in an organic solvent.

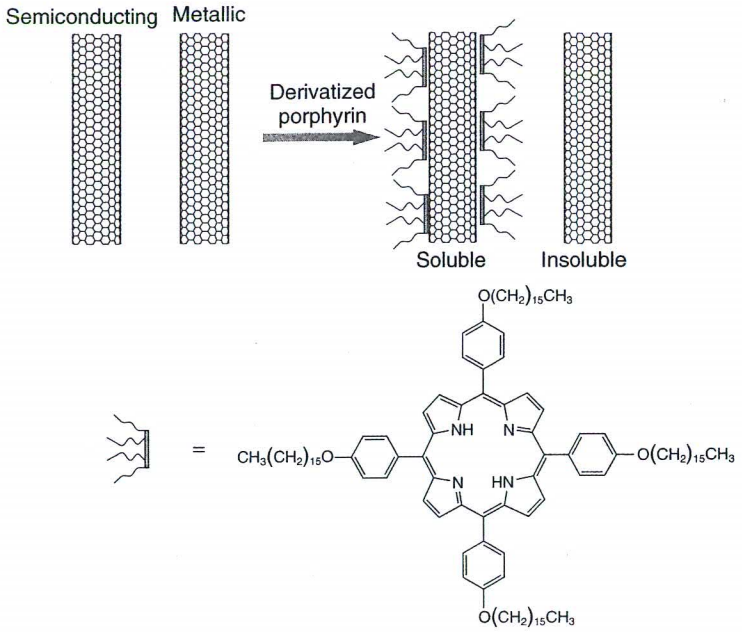

5,10,15,20-Tetrakis(hexadecyloxyphenyl)-21*H*,23*H*-porphine

Scheme 8 The separation of metallic and semiconducting SWNTs based on selective interactions of large aromatic molecules, as reported in Ref. 4

Upon sonication, the soluble fraction and insoluble residue were found to be enriched with semiconducting and metallic SWNTs, respectively.[4] Other planar aromatic molecules have been evaluated for the bulk separation, among which the pyrene derivative 1-docosyloxymethyl-pyrene (DomP) is particularly effective.[119–121] The separation is efficient and scalable (already at gram quantity). As for the quality of the separation, the metallic fraction can be enriched to contain at least 85% of metallic SWNTs (with reference to the starting population of one-third), while the other fraction reached a semiconducting purity beyond 95%.

The same group has demonstrated recently that the separated metallic SWNTs did offer much enhanced performance in nanocomposites with conductive polymers.[121] In a comparison of polythiophene carbon nanotube composites that are dispersed with the separated metallic SWNTs vs. those with preseparation purified SWNTs, the former consistently exhibited substantially better electrical conductivity.[121] The improvements were more significant at higher nanotube loadings, as shown in Figure 7, suggesting that the electrical conductivity in the nanocomposites was governed by available conductive channels, namely, the amount of metallic SWNTs. In fact, the relationship between the calculated actual concentrations of metallic SWNTs in the nanocomposites and their corresponding observed electrical conductivities adhered to the percolation theory.[121]

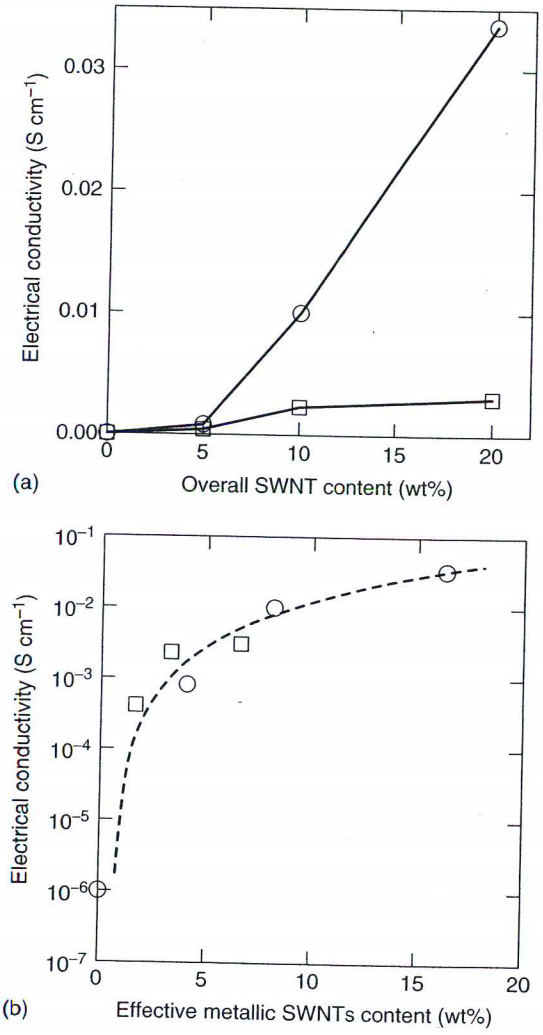

Figure 7 The electrical conductivity results of P3HT/SWNT composite films depending on (a) different amounts of preseparation (□) and separated metallic (○) nanotube samples and (b) their corresponding effective metallic SWNT contents in the films (dashed line: the best fit in terms of the percolation-theory equation). (Reprinted with permission from Wang *et al.*[121] © 2008 American Chemical Society)

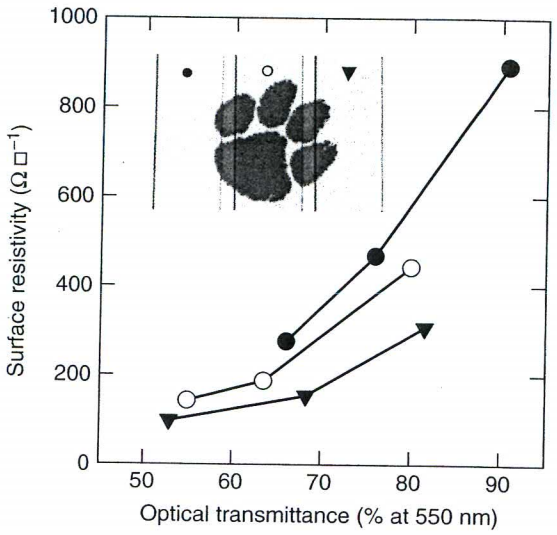

Figure 8 The surface resistivity results of PEDOT : PSS/SWNT films on glass substrate with the same 10 wt% nanotube content (○: preseparation purified sample and ▼: separated metallic SWNTs; and for comparison, ●: blank PEDOT : PSS without nanotubes), but different film thickness and optical transmittance at 550 nm. Shown in the inset are representative films photographed with tiger-paw print as background. (Reprinted with permission from Wang *et al.*[121] © 2008 American Chemical Society)

The potential of the bulk-separated metallic SWNTs in transparent conductive nanocomposite thin films was explored with poly(3,4-ethylene-dioxythiophene) : poly (styrene-sulfonate) (PEDOT : PSS) as the matrix polymer.[121] In the study, PEDOT : PSS was processed as an aqueous dispersion. For solvent compatibility, DMSO was used to disperse nanotubes. The suspension of the nanotubes in DMSO was mixed with the aqueous PEDOT : PSS solution, and the mixture was used for fabricating the transparent conductive coating on glass substrate via spraying. Two PEDOT : PSS/SWNT mixtures with one containing 10% (wt/wt) of the separated metallic fraction and the other 10% (wt/wt) of the preseparation purified nanotube sample were prepared, so was an aqueous solution of neat PEDOT : PSS (also containing the same amount of DMSO) as reference. Depending on the amount of solution or mixture sprayed, the coating thickness varies, as reflected by the variation in

optical transmittance at 550 nm. The surface resistivity results compared in Figure 8 demonstrate clearly the enhanced electrical conductivity with the separated metallic SWNTs in the transparent conductive films.

In the development for alternatives to the currently dominating indium tin oxide (ITO) technology,[122] PEDOT : PSS transparent conductive films have been demonstrated for some successful uses in organic optoelectronic devices.[123,124] For example, the organic photovoltaic cell with a PEDOT : PSS electrode was found to be only 15% less in efficiency when compared to the same cell with a classic ITO electrode.[124] A strategy already discussed in the literature on further improving the performance of transparent PEDOT : PSS electrode is the incorporation of SWNTs.[125–127] The results from the recent work by Wang *et al.*[121] suggest that the use of bulk-separated metallic SWNTs might offer the necessary conductivity enhancement without sacrificing the optical transparency to make the resulting PEDOT : PSS/SWNT composite films competitive with ITO coatings for transparent electrodes and other applications.

4 THERMAL CONDUCTIVE NANOCOMPOSITES

Carbon nanotubes are excellent thermal conductors,[17–19] but their uses as fillers in polymeric matrices have not yielded the kind of highly thermal conductive nanocomposites that one might expect. A key difference between polymeric carbon nanotube composites for enhanced electrical and thermal properties is that the latter is not governed by the percolation phenomenon.[128] Nevertheless, since polymers are usually poor thermal conductors, with thermal conductivity on the order of $0.1\,W\,m^{-1}\,K^{-1}$, the incorporation of carbon nanotubes still offers significant thermal-conductivity improvements in the resulting nanocomposites.

Several groups have prepared polymeric nanocomposites with carbon nanotubes for the investigation of their thermal conductive properties.[129,130] For example, Biercuk *et al.* dispersed SWNTs into epoxy to increase thermal conductivity.[129] At 1 wt% loading of nanotubes, the room-temperature thermal conductivity of the nanocomposite was about $0.5\,W\,m^{-1}\,K^{-1}$, more than doubling that of the neat epoxy. Significantly less improvement was observed in the epoxy composite with vapor-grown carbon fibers (VGCFs) at the same filler-loading level (Figure 9). Similarly, Kashiwagi *et al.* reported that the thermal conductivity of the polypropylene nanocomposite with 5 wt% MWNT was about $0.3\,W\,m^{-1}\,K^{-1}$ at room temperature, roughly 30% higher than that of pure polypropylene.[130] These seemingly unimpressive improvements in thermal conductivity have been typical in other polymeric nanocomposites with SWNTs or MWNTs at similar nanotube loadings.

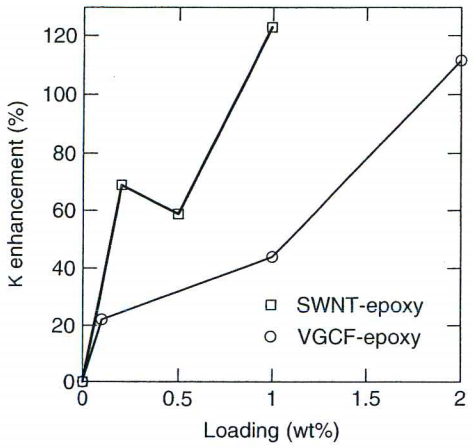

Figure 9 Thermal conductivity enhancements in epoxy/carbon nanocomposites with different SWNT or VGCF concentrations. (Reprinted with permission from Biercuk *et al.*[129]. *Applied Physics Letters*, **80**, 2767–2769. © 2002, American Institute of Physics)

Carbon nanotubes are pseudo-one-dimensional nanostructures, and their thermal properties are highly anisotropic, with much higher thermal conductivity along the nanotube axis. To take advantage of the anisotropically high thermal conductivity, Huang *et al.* fabricated composite films with aligned carbon nanotubes by in situ inject molding of silicone elastomers onto CVD-grown nanotube arrays (Figure 10).[131,132] The film with 0.3 wt% nanotube loading, upon reactive-ion etching treatment to expose nanotube tips, exhibited thermal conductivity of $1.21\,W\,m^{-1}\,K^{-1}$, 2.2 times that of the pure silicone elastomer. The thermal-conductivity enhancement was attributed entirely to the embedded nanotube arrays.

Mechanistically, the high interfacial thermal resistance in polymeric carbon nanotube composites is believed to be a limiting factor.[80] Since the heat transportation in the nanocomposites is carried out by phonons with different frequencies, the phonons slow down at the polymer–nanotube interface due to material characteristics such as the polymer being largely amorphous in nature, resulting in high interfacial thermal resistance. Huxtable *et al.* applied a picosecond transient absorption technique to estimate the interfacial thermal conductance in polymer–nanotube composites, with the estimated conductance as small as $12\,MW\,m^{-2}\,K^{-1}$.[133] Therefore, the development of highly thermal conductive polymeric carbon nanotube composites may be dependent on ways to reduce the high interfacial thermal resistance. One possible way is the chemical functionalization of carbon nanotubes, because the covalent bonding between carbons on the nanotube surface and polymers in the matrix could facilitate the phonon transportation at the interface.[55,134] However, the flip side of the covalent bonding on nanotube surface is that it may act as phonon scattering center to reduce the intrinsic thermal conductivity of the carbon nanotube. Therefore, the effect of chemical functionalization on thermal conductivity needs

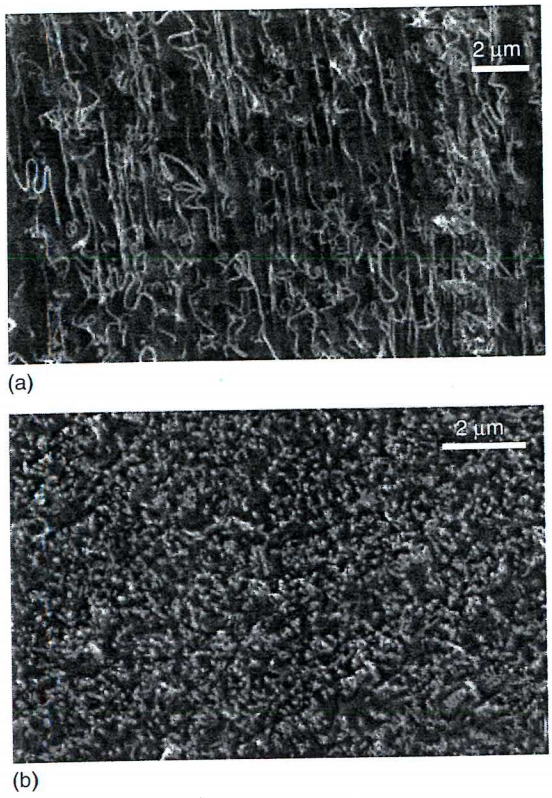

Figure 10 SEM images of aligned carbon nanotube composite films prepared by in situ inject-molding method: (a) side view and (b) top view. (Reprinted with permission from Huang *et al.*[131] © 2005 Wiley-VCH Verlag GmbH & Co. KGaA)

to be carefully investigated. According to the calculation by Padgett *et al.*, the random chemical functionalization of 1% of the carbon atoms on a nanotube with phenyl groups would reduce the thermal conductivity of the nanotube by more than a factor of 3.[135] The lower thermal conductivity was attributed to decreased phonon scattering length. As shown in Figure 11, there is a faster convergence for functionalized carbon nanotubes, implying that the phonon scattering length in a functionalized tube is shorter than in a pristine one.[135] Similarly, Shenogin *et al.* performed molecular dynamics simulation to examine the impact on thermal conductivity of carbon nanotubes upon their being chemically bound to the polymer matrix.[136,137] In their results, the thermal conductivity remained nearly constant at about 1700 $W m^{-1} K^{-1}$ as 1% of the nanotube carbons were functionalized, while the thermal interfacial resistance was reduced by three to four times as a result of the covalent functionalization. It was found that the net effect of functionalization on thermal conductivity was dependent on the nanotube aspect ratio. For aspect ratios in the range of 100–1000, the functionalization leaded to thermal conductivity of the nanotube higher by a factor of 2 (Figure 12).

On the issue of thermal conductivity enhancement in polymeric carbon nanotube composites, the experimental

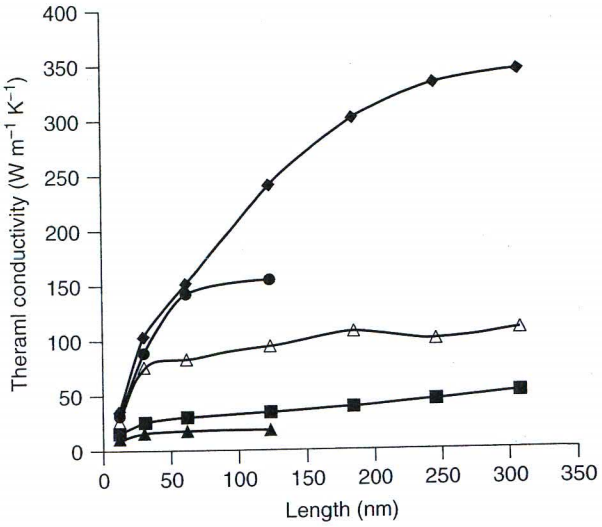

Figure 11 Thermal conductivity vs. nanotube length for various degrees of chemical functionalization (♦: 0%, •: 0.25%, △: 1%, ■: 5%, and ▲: 10% functionalized). (Reprinted with permission from Padgett and Brenner[135] © 2004 American Chemical Society)

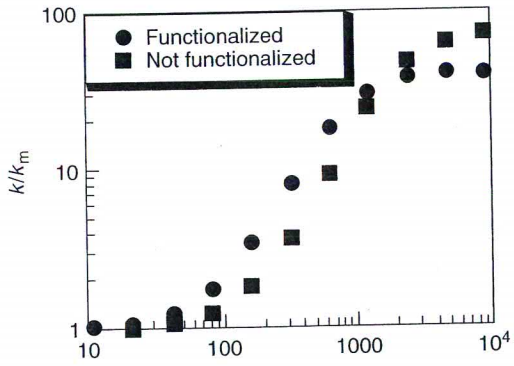

Figure 12 Calculated thermal conductivity of composite with 1% randomly oriented carbon nanotubes in low-conductivity organic matrix for unfunctionalized and highly functionalized carbon nanotubes. (Reprinted with permission from Shenogin *et al.*[136]. *Applied Physics Letters*, **85**, 2229–2231. © 2004, American Institute of Physics)

and simulation results discussed above seem to suggest the need for an optimal density of covalent links on the nanotube surface, at which the desired reduction in interfacial resistance could be realized without sacrificing too much the intrinsic thermal conductivity of the nanotubes. As for the effect of aspect ratio, longer nanotubes, and thus larger aspect ratios are always desirable for thermal-conductivity enhancement.[138–140] However, while SWNTs are each of a very large aspect ratio, they are often tangled and bundled, resulting in lower effective aspect ratios.[140] More rigid and straight MWNTs, such as those synthesized by aligned CVD method,[141] could be competitive as fillers for

thermal conductive nanocomposite materials. These principles seem easier to appreciate, but more difficult to evaluate and materialize, with only a limited number of relevant experimental investigations.[142,143]

Ghose *et al.* tested experimentally some of the strategies discussed above.[142] In their experiments, functionalized MWNTs were mixed with commercially available PI (Ultem™ 1000) in dimethylacetamide (DMAC) solution at various concentrations ranging from 5 to 20 wt% effective nanotube contents. The resulting blends were molded into pellets in which the nanotubes were randomly orientated. These pellets of nanocomposites with functionalized MWNTs exhibited higher thermal conductivity values than did those with pristine MWNTs. The performance was also dependent on the degree of surface functionalization in the functionalized nanotube samples. For nanocomposites with the same 20 wt% nanotube loading, the one from the functionalized MWNTs with surface functionalization density controlled at 6% had a thermal conductivity of 0.8 $W m^{-1} K^{-1}$, while the other with 15% functionalization density had a higher thermal conductivity of 1.1 $W m^{-1} K^{-1}$. This is more than double the thermal conductivity value of the composite with pristine MWNTs, and a more than 900% increase over that of the pure Ultem polymer.[142]

The same group also demonstrated the anisotropic thermal conductive properties in Ultem nanocomposites with aligned MWNTs (Figure 13), where the nanotube alignment was a result of the melt extrusion processing.[142] The observed thermal conductivity of the nanocomposite at 20 wt% nanotube loading was 2 $W m^{-1} K^{-1}$ in the direction of the nanotube alignment, higher than that of the same nanocomposite with randomly oriented MWNTs, but only 0.2 $W m^{-1} K^{-1}$ in the direction perpendicular to the alignment.

Functionalized carbon nanotubes are more readily aligned in polymeric nanocomposites because of their being well-exfoliated and dispersed. Therefore, as demonstrated by Wang *et al.*,[143] the nanocomposites could be mechanically stretched to align the embedded nanotubes for much enhanced thermal conductivity in the alignment direction. In the study,[143] PVA-functionalized SWNTs were used to prepare PVA nanocomposite films with different nanotube contents.[58] Then, the films were mechanically stretched to align the embedded nanotubes.[64,70] The nanotube alignment was characterized by polarized luminescence and electronic microscopy techniques (Figure 14a). According to results from the in-plane thermal diffusivity measurements, the PVA nanocomposite film with 10 wt% functionalized SWNTs had a poststretching increase of 3.4 times in thermal diffusivity along the stretching direction (Figure 14b).

As discussed in the beginning of this section, while much effort has been made, which has resulted in many valuable insights into the development of highly thermal conductive polymeric carbon nanocomposites, the use of carbon nanotubes through their chemical modification or various other manipulations or arrangements for the predicted ultimate performance still remains a significant challenge.

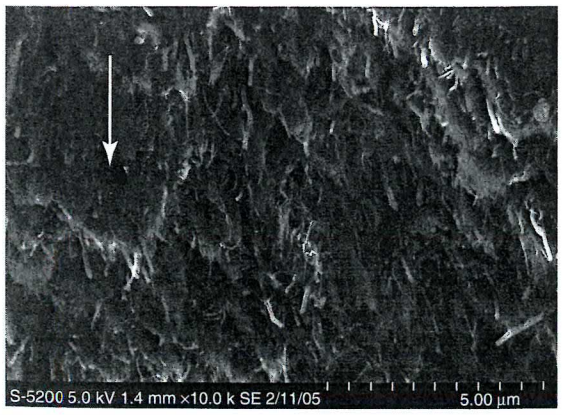

Figure 13 SEM image of melted press Ultem/MWNT at 20 wt% (the arrow indicating direction of nanotube alignment). (Reprinted from Ghose *et al.*[142] © 2006, with permission from Elsevier)

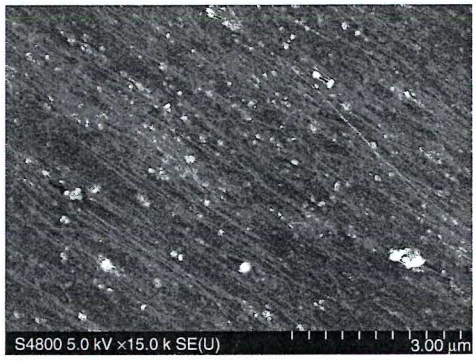

(a)

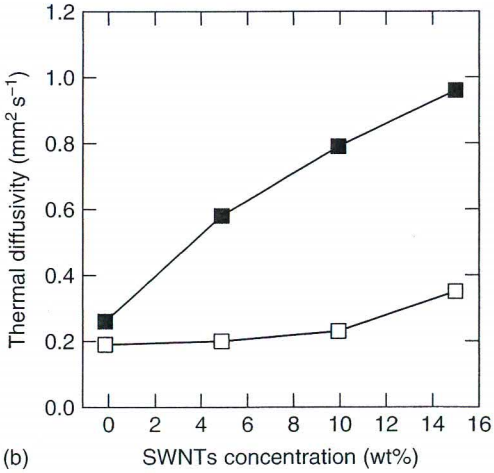

(b)

Figure 14 (a) SEM image of mechanically stretched PVA/functionalized-SWNT (10 wt%) nanocomposite film with a draw ratio of 5.5 and (b) the in-plane thermal diffusivity results of PVA/functionalized-SWNT nanocomposite films with different nanotube concentrations with (■) and without (□) the mechanical stretching

5 SUMMARY

The known electrical and thermal properties of carbon nanotubes have prompted many predictions on their extraordinary potentials for ultimately performing polymeric nanocomposites. However, the experimental materialization of these predictions has proved to be more complex in the development of nanocomposites for electrical properties and more challenging in those for high thermal conductivity. Nevertheless, chemical modification and functionalization of carbon nanotubes have been demonstrated as being effective for high-quality polymeric carbon nanotube composites, especially with the elegant approach of using polymers that are structurally identical or maximally similar to the matrix polymers in the nanotube functionalization. For desired electrical properties, the dispersion of carbon nanotubes in the polymer matrix is important to the performance, and the use of only metallic nanotubes may offer solutions in some of the more demanding applications (such as transparent conductive coatings or films). For highly thermal conductive polymeric nanocomposites, on the other hand, the feasibility of using carbon nanotubes to achieve the desired performance has yet to be convincingly demonstrated experimentally.

6 ACKNOWLEDGMENTS

We thank NASA, NSF, ONR, Center for Advanced Engineering Fibers and Films (NSF-ERC at Clemson University), South Carolina Space Grant, and our industrial partners for financial support.

7 ABBREVIATIONS AND ACRONYMS

AROP = anionic ring-opening polymerization; ATRP = atomic transfer radical polymerization; CVD = chemical vapor deposition; DMAC = dimethylacetamide; DMF = dimethylformamide; DMSO = dimethyl sulfoxide; DomP = 1-docosyloxymethyl-pyrene; DOS = density of states; DWNT = double-walled carbon nanotube; EMI = electromagnetic interference; EVOH = poly(ethylene-*co*-vinyl alcohol); ITO = indium tin oxide; MWNT = multiple-walled carbon nanotube; ODA = octadecylamine; PABS = poly(*m*-aminobenzensulfonic acid); PEDOT:PSS = poly(3,4-ethylene-dioxythiophene): poly(styrene-sulfonate); PHET = poly[3-(2-hydroxyethyl)-2,5-thienylene]; PI = polyimide; PPE = poly(phenylene ethylene); PPEI = poly(propionyl-ethylenimine); PPEI-EI = poly (propionylethylenimine-*co*-ethylenimine); PS = polystyrene; PVA = poly(vinyl alcohol); PVK = poly(*N*-vinyl carbazole); PVP = poly(vinyl pyrolidone); SDS = sodium dodecylsulfate; SWNT = single-walled carbon nanotube; THPP = 5,10,15,20-tetrakis-(hexadecyloxyphenyl)-21*H*,23*H*-porphine; VGCFs = vapor-grown carbon fibers.

8 REFERENCES

1. S. Iijima, *Nature*, 1991, **354**, 56.
2. P. M. Ajayan, *Chem. Rev.*, 1999, **99**, 1787.
3. M. S. Dresselhaus, G. Dresselhaus, and P. C. Eklund, 'Science of Fullerenes and Carbon Nanotubes', Academic Press, San Diego, 1996.
4. Y. Lin, K. A. S. Fernando, W. Wang, and Y.-P. Sun, in 'Carbon Nanotechnology: Recent Developments in Chemistry, Physics, Material Science and Device Applications', ed. L. Dai, Elsevier, Netherlands, 2006, p. 255.
5. H. Dai, *Acc. Chem. Res.*, 2002, **35**, 1035.
6. R. Saito, M. Fujita, G. Dresselhaus, and M. S. Dresselhaus, *Phys. Rev., B*, 1992, **46**, 1804.
7. C. Journet, W. K. Maser, P. Bernier, A. Loiseau, M. Lamy de la chapelle, S. Lefrant, P. Deniard, R. Lee, and J. E. Fischer, *Nature*, 1997, **388**, 756.
8. A. Thess, R. Lee, P. Nikolaev, H. Dai, P. Petit, J. Robert, C. Xu, Y. H. Lee, S. G. Kim, A. G. Rinzler, D. T. Colbert, G. E. Scuseria, D. Tomanek, J. E. Fisher, and R. E. Smalley, *Science*, 1996, **273**, 483.
9. B. Kitiyanan, W. E. Alvarez, J. H. Harwell, and D. E. Resasco, *Chem. Phys. Lett.*, 2000, **317**, 497.
10. H. Dai, A. Z. Rinzler, P. Nikolaev, A. Thess, D. T. Colbert, and R. E. Smalley, *Chem. Phys. Lett.*, 1996, **260**, 471.
11. C. A. Dyke and J. M. Tour, *J. Phys. Chem., A*, 2004, **108**, 11151.
12. M.-F. Yu, B. S. Files, S. Arepalli, and R. S. Ruoff, *Phys. Rev. Lett.*, 2000, **84**, 5552.
13. R. H. Baughman, A. A. Zakhidov, and W. A. de Heer, *Science*, 2002, **297**, 787.
14. S. J. Tans, A. R. M. Verschuern, and C. Dekker, *Nature*, 1998, **393**, 49.
15. P. L. McEuen and J.-Y. Park, *MRS Bull.*, 2004, **29**, 272.
16. J.-Y. Park, S. Rosenblatt, Y. Yaish, V. Sazonova, H. Ustunel, S. Braig, T. A. Arias, P. W. Brouwer, and P. L. McEuen, *Nano Lett.*, 2004, **4**, 517.
17. S. Berber, Y. K. Kwon, and D. Tomanek, *Phys. Rev. Lett.*, 2000, **84**, 4613.
18. J. Hone, M. Whitney, C. Piskoti, and A. Zettl, *Phys. Rev., B*, 1999, **59**, R2514.
19. P. Kim, L. Shi, A. Majumdar, and P. L. McEuen, *Phys. Rev. Lett.*, 2001, **87**, 215502.
20. E. T. Thostenson, Z. Ren, and T.-W. Chou, *Compos. Sci. Technol.*, 2001, **61**, 1899.
21. P. J. F. Harris, *Int. Mater. Rev.*, 2004, **49**, 31.

22. R. Andrews and M. C. Weisenberger, *Curr. Opin. Solid State Mater. Sci.*, 2004, **8**, 31.
23. J. N. Coleman, U. Khan, and Y. K. Gun'ko, *Adv. Mater.*, 2006, **18**, 689.
24. M. Moniruzzaman and K. I. Winey, *Macromolecules*, 2006, **39**, 5194.
25. P. M. Ajayan and J. M. Tour, *Nature*, 2007, **447**, 1066.
26. H. Xia, Q. Wang, K. Li, and G.-H. Hu, *J. Appl. Polym. Sci.*, 2004, **93**, 378.
27. O. Regev, P. N. B. Elkati, J. Loos, and C. E. Koning, *Adv. Mater.*, 2004, **16**, 258.
28. F. Du, J. E. Fischer, and K. I. Winey, *J. Polym. Sci., Part B: Polym. Phys.*, 2003, **41**, 3333.
29. B. Z. Tang and H. Xu, *Macromolecules*, 1999, **32**, 2569.
30. P. M. Ajayan, O. Stephan, C. Colliex, and D. Trauth, *Science*, 1994, **265**, 1212.
31. Y.-P. Sun, K. Fu, Y. Lin, and W. Huang, *Acc. Chem. Res.*, 2002, **35**, 1096.
32. S. Niyogi, M. A. Hamon, H. Hu, B. Zhao, P. Bhowmik, R. Sen, M. Itkis, and R. C. Haddon, *Acc. Chem. Res.*, 2002, **35**, 1105.
33. A. Hirsch, *Angew. Chem., Int. Ed.*, 2002, **41**, 1853.
34. J. L. Bahr and J. M. Tour, *J. Mater. Chem.*, 2002, **12**, 1952.
35. D. Tasis, N. Tagmatarchis, A. Bianco, and M. Prato, *Chem. Rev.*, 2006, **106**, 1105.
36. M. F. Islam, E. Rojas, D. M. Bergey, A. T. Johnson, and A. G. Yodh, *Nano Lett.*, 2003, **3**, 269.
37. V. C. Moore, M. S. Strano, E. H. Haroz, R. H. Hauge, and R. E. Smalley, *Nano Lett.*, 2003, **3**, 1379.
38. M. J. O'Connell, P. Boul, L. M. Ericson, C. Huffman, Y. H. Wang, E. Haroz, C. Kuper, J. Tour, K. D. Ausman, and R. E. Smalley, *Chem. Phys. Lett.*, 2001, **342**, 265.
39. R. J. Chen, Y. Zhang, D. Wang, and H. Dai, *J. Am. Chem. Soc.*, 2001, **123**, 3838.
40. J. Chen, H. Liu, W. A. Weimer, M. D. Halls, D. H. Waldeck, and G. C. Walker, *J. Am. Chem. Soc.*, 2002, **124**, 9034.
41. S. A. Curran, P. M. Ajayan, W. J. Blau, D. L. Carroll, J. N. Coleman, A. B. Dalton, A. P. Davey, A. Drury, B. McCarthy, S. Maier, and A. Strevens, *Adv. Mater.*, 1998, **10**, 1091.
42. A. Star, J. F. Stoddart, M. Diehl, A. Boukai, E. W. Wong, X. Yang, S. W. Chung, H. Choi, and J. R. Heath, *Angew. Chem., Int. Ed.*, 2001, **40**, 1721.
43. M. Zheng, A. Jagota, E. D. Semke, B. A. Diner, R. S. McLean, S. R. Lustig, R. E. Richardson, and N. G. Tassi, *Nat. Mater.*, 2003, **2**, 338.
44. V. N. Khabashesku, W. E. Billups, and J. L. Margrave, *Acc. Chem. Res.*, 2002, **35**, 1087.
45. M. Holzinger, J. Abraham, P. Whelan, R. Graupner, L. Ley, F. Hennrich, M. Kappes, and A. Hirsch, *J. Am. Chem. Soc.*, 2003, **125**, 8566.
46. N. Tagmatarchis and M. Prato, *J. Mater. Chem.*, 2004, **14**, 437.
47. J. Chen, M. A. Hamon, H. Hu, Y. Chen, A. M. Rao, P. C. Eklund, and R. C. Haddon, *Science*, 1998, **282**, 95.
48. Y.-P. Sun, W. Huang, Y. Lin, K. Fu, A. Kitaygorodskiy, L. A. Riddle, Y. J. Yu, and D. L. Carroll, *Chem. Mater.*, 2001, **13**, 2864.
49. B. P. Grady, F. Pompeo, R. Shambaugh, and D. E. Resasco, *J. Phys. Chem., B*, 2002, **106**, 5852.
50. W. Wu, S. Zhang, Y. Li, J. Li, L. Liu, Y. Qin, Z.-X. Guo, L. Dai, C. Ye, and D. Zhu, *Macromolecules*, 2003, **36**, 6286.
51. G. Viswanathan, N. Chakrapani, H. Yang, B. Wei, H. Chung, K. Cho, C. Y. Ryu, and P. M. Ajayan, *J. Am. Chem. Soc.*, 2003, **125**, 9258.
52. H. Kong, C. Gao, and D. Y. Yan, *J. Am. Chem. Soc.*, 2004, **126**, 412.
53. S. Qin, D. Qin, W. T. Ford, D. E. Resasco, and J. E. Herrera, *J. Am. Chem. Soc.*, 2004, **126**, 170.
54. Z. Yao, N. Braidy, G. A. Botton, and A. Adronov, *J. Am. Chem. Soc.*, 2003, **125**, 16015.
55. Y. Lin, M. J. Meziani, and Y.-P. Sun, *J. Mater. Chem.*, 2007, **17**, 1143.
56. D. E. Hill, Y. Lin, A. M. Rao, L. F. Allard, and Y.-P. Sun, *Macromolecules*, 2002, **35**, 9466.
57. D. E. Hill, Y. Lin, L. F. Allard, and Y.-P. Sun, *Int. J. Nanosci.*, 2002, **1**, 213.
58. Y. Lin, B. Zhou, K. A. S. Fernando, P. Liu, L. F. Allard, and Y.-P. Sun, *Macromolecules*, 2003, **36**, 7199.
59. L. Qu, Y. Lin, D. E. Hill, B. Zhou, W. Wang, X. Sun, A. Kitaygorodskiy, M. Suarez, J. W. Connell, L. F. Allard, and Y.-P. Sun, *Macromolecules*, 2004, **37**, 6055.
60. W. Wang, Y. Lin, and Y.-P. Sun, *Polymer*, 2005, **46**, 8634.
61. D. Hill, Y. Lin, L. Qu, A. Kitaygorodskiy, J. W. Connell, L. F. Allard, and Y.-P. Sun, *Macromolecules*, 2005, **38**, 7670.
62. L. Qu, L. M. Veca, Y. Lin, A. Kitaygorodskiy, B. Chen, A. M. McCall, J. W. Connell, and Y.-P. Sun, *Macromolecules*, 2005, **38**, 10328.
63. K. A. S. Fernando, Y. Lin, B. Zhou, M. Grah, R. Joseph, L. F. Allard, and Y.-P. Sun, *J. Nanosci. Nanotechnol.*, 2005, **5**, 1050.
64. Y. Lin, P. Liu, B. Zhou, K. A. S. Fernando, W. Wang, D. E. Hill, L. F. Allard, and Y.-P. Sun, *Composites Part B*, in press.
65. J. Gao, B. Zhao, M. E. Itkis, E. Bekyarova, H. Hu, V. Kranak, A. Yu, and R. C. Haddon, *J. Am. Chem. Soc.*, 2006, **128**, 7492.
66. J. E. Riggs, Z. Guo, D. L. Carroll, and Y.-P. Sun, *J. Am. Chem. Soc.*, 2000, **122**, 5879.
67. Y. Lin, A. M. Rao, B. Sadanadan, E. A. Kenik, and Y.-P. Sun, *J. Phys. Chem., B*, 2002, **106**, 1294.
68. W. Huang, Y. Lin, S. Taylor, J. Gaillard, A. M. Rao, and Y.-P. Sun, *Nano Lett.*, 2002, **2**, 231.

69. Y. Lin, D. E. Hill, J. Bentley, L. F. Allard, and Y.-P. Sun, *J. Phys. Chem., B*, 2003, **107**, 10453.

70. B. Zhou, Y. Lin, L. M. Veca, K. A. S. Fernando, B. A. Harruff, and Y.-P. Sun, *J. Phys. Chem., B*, 2006, **110**, 3001.

71. J. G. Smith Jr., J. W. Connell, D. M. Delozier, P. T. Lillehei, K. A. Watson, Y. Lin, B. Zhou, and Y.-P. Sun, *Polymer*, 2004, **45**, 825.

72. K. A. Watson, S. Ghose, D. M. Delozier, J. G. Smith Jr., and J. W. Connell, *Polymer*, 2005, **46**, 2076.

73. B. Zhou, Y. Lin, D. E. Hill, W. Wang, L. M. Veca, L. Qu, P. Pathak, M. J. Meziani, J. Diaz, J. W. Connell, K. A. Watson, L. F. Allard, and Y.-P. Sun, *Polymer*, 2006, **47**, 5323.

74. O. Lourie and H. D. Wagner, *J. Mater. Res.*, 1998, **13**, 2418.

75. V. G. Hadjiev, M. N. Iliev, S. Arepalli, P. Nikolaev, and B. S. Files, *Appl. Phys. Lett.*, 2001, **78**, 3193.

76. J. Liu, T. Liu, and S. Kumar, *Polymer*, 2005, **46**, 3419.

77. Y. Lin, B. Zhou, R. B. Martin, K. B. Henbest, B. A. Harruff, J. E. Riggs, Z.-X. Guo, L. F. Allard, and Y.-P. Sun, *J. Phys. Chem., B*, 2005, **109**, 14779.

78. L. Lacerda, G. Pastorin, W. Wu, M. Prato, A. Bianco, and K. Kostarelos, *Adv. Funct. Mater.*, 2006, **6**, 1839.

79. N. Grossiord, J. Loos, O. Regev, and C. E. Koning, *Chem. Mater.*, 2006, **18**, 1089.

80. K. I. Winey, T. Kashiwagi, and M. Mu, *MRS Bull.*, 2007, **32**, 348.

81. Z. Li, G. Luo, F. Wei, and Y. Huang, *Compos. Sci. Technol.*, 2006, **66**, 1022.

82. H. M. Kim, K. Kim, C. Y. Lee, J. Joo, S. J. Cho, H. S. Yoon, D. A. Pejackovic, J. W. Yoo, and A. J. Epstein, *Appl. Phys. Lett.*, 2004, **84**, 589.

83. Y. L. Yang, M. C. Gupta, K. L. Dudley, and R. W. Lawrence, *Nano Lett.*, 2005, **5**, 2131.

84. N. Li, Y. Huang, F. Du, X. He, X. Lin, H. Gao, Y. Ma, F. Li, Y. Chen, and P. C. Eklund, *Nano Lett.*, 2006, **6**, 1141.

85. R. Ramasubramaniam and J. Chen, *Appl. Phys. Lett.*, 2003, **83**, 2928.

86. S. Li, Y. Qin, J. Shi, Z.-X. Guo, Y. Li, and D. Zhu, *Chem. Mater.*, 2005, **17**, 130.

87. B. Philip, J. Xie, A. Chandrasekhar, J. Abraham, and V. K. Varadan, *Smart Mater. Struct.*, 2004, **13**, 295.

88. E. Bekyarova, M. E. Itkis, N. Cabrera, B. Zhao, A. Yu, J. Gao, and R. C. Haddon, *J. Am. Chem. Soc.*, 2005, **127**, 5990.

89. J. G. Smith, D. M. Delozier, J. W. Connell, and K. A. Watson, *Polymer*, 2004, **45**, 6133.

90. J. G. Smith, J. W. Connell, K. A. Watson, and P. M. Danehy, *Polymer*, 2005, **46**, 2276.

91. D. M. Delozier, K. A. Watson, J. G. Smith, and J. W. Connell, *Compos. Sci. Technol.*, 2005, **65**, 749.

92. G. Smith, Jr., J. W. Connell, D. M. Delozier, P. T. Lillehei, K. A. Watson, Y. Lin, B. Zhou, and Y.-P. Sun, *Polymer*, 2004, **45**, 825.

93. R. Krupke and F. Hennrich, *Adv. Eng. Mater.*, 2005, **7**, 111.

94. S. Banerjee, T. H. Benny, and S. S. Wong, *J. Nanosci. Nanotechnol.*, 2005, **5**, 841.

95. S. Campidelli, M. Meneghetti, and M. Prato, *Small*, 2007, **10**, 1672.

96. R. Krupke, F. Hennrich, H. von Lohneysen, and M. M. Kappes, *Science*, 2003, **301**, 344.

97. R. Krupke, S. Linden, M. Rapp, and F. Hennirch, *Adv. Mater.*, 2006, **18**, 1468.

98. M. Zheng, A. Jagota, M. S. Strano, A. P. Santos, P. Barone, S. G. Chou, B. A. Diner, M. S. Dresselhaus, R. S. Mclean, G. B. Onoa, G. G. Samsonidze, E. D. Semke, M. Usrey, and D. J. Walls, *Science*, 2003, **302**, 1545.

99. M. Zheng and E. D. Semke, *J. Am. Chem. Soc.*, 2007, **129**, 6084.

100. M. S. Arnold, S. I. Stupp, and M. C. Hersam, *Nano Lett.*, 2005, **5**, 713.

101. M. S. Arnold, A. A. Green, J. F. Huvat, S. I. Stupp, and M. C. Hersam, *Nat. Nanotechnol.*, 2006, **1**, 60.

102. P. G. Collins, M. S. Arnold, and P. Avouris, *Science*, 2001, **292**, 706.

103. K. Maehashi, Y. Ohno, K. Inoue, and K. Matsumoto, *Appl. Phys. Lett.*, 2004, **85**, 858.

104. H. Huang, R. Maruyama, K. Noda, H. Kajiura, and K. Kadono, *J. Phys. Chem., B*, 2006, **110**, 7316.

105. M. S. Strano, C. A. Dyke, M. L. Usrey, P. W. Barone, M. J. Allen, H. Shan, C. Kittrell, R. H. Hauge, J. M. Tour, and R. E. Smalley, *Science*, 2003, **301**, 1519.

106. M. L. Usrey, E. S. Lippman, and M. S. Strano, *J. Am. Chem. Soc.*, 2005, **127**, 16129.

107. N. Nair, W.-J. Kim, M. L. Usrey, and M. S. Strano, *J. Am. Chem. Soc.*, 2007, **129**, 3946.

108. W.-J. Kim, M. L. Usrey, and M. S. Strano, *Chem. Mater.*, 2007, **19**, 1571.

109. S. Toyoda, Y. Yamaguchi, M. Hiwatashi, Y. Tomonari, H. Murakami, and N. Nakashima, *Chem. Asian J.*, 2007, **2**, 145.

110. K. Seo, C. Kim, Y. S. Choi, K. A. Park, Y. H. Lee, and B. Kim, *J. Am. Chem. Soc.*, 2003, **125**, 13946.

111. G. Y. Zhang, P. F. Qi, X. R. Wang, Y. R. Lu, X. L. Li, R. Tu, S. Bangsaruntip, D. Mann, L. Zhang, and H. J. Dai, *Science*, 2006, **314**, 974.

112. Z. Chen, X. Du, M.-H. Du, D. Rancken, H.-P. Peng, and A. G. Rinzler, *Nano Lett.*, 2003, **3**, 1245.

113. Y. Miyata, Y. Maniwa, and H. Kataura, *J. Phys. Chem., B*, 2006, **110**, 25.

114. D. Chattopadhyay, I. Galeska, and F. Papadimitrakopoulos, *J. Am. Chem. Soc.*, 2003, **125**, 3370.

115. G. G. Samsonidze, S. G. Chou, A. P. Santos, V. W. Brar, G. Dresselhaus, M. S. Dresselhaus, A. Selbst, A. K. Swan, M. S. Unlu, B. B. Goldberg, D. Chattopadhyay, S. N. Kim, and F. Papadimitrakopoulos, *Appl. Phys. Lett.*, 2004, **85**, 1006.

116. K. A. S. Fernando, Y. Lin, W. Wang, L. Cao, M. J. Meziani, X. Wang, M. L. Veca, P. Zhang, R. A. Quinn, L. F. Allard, and Y.-P. Sun, *J. Phys. Chem. C*, 2007, **111**, 10254.

117. Y. Maeda, S.-I. Kimura, M. Kanda, Y. Hirashima, T. Hasegawa, T. Wakahara, Y. Lian, T. Nakahodo, T. Tsuchiya, T. Akasaka, J. Lu, X. Zang, H. Tokumoto, and R. Saito, *J. Am. Chem. Soc.*, 2005, **127**, 10287.

118. Y. Maeda, M. Kanda, M. Hashimoto, H. Tadashi, S.-I. Kimura, Y. Lian, T. Wakahara, T. Akasaka, S. Kazaoui, N. Minami, T. Okazaki, Y. Hayamizu, K. Hata, J. Lu, and S. Nagase, *J. Am. Chem. Soc.*, 2006, **128**, 12239.

119. H. Li, B. Zhou, Y. Lin, L. Gu, W. Wang, K. A. S. Fernando, S. Kumar, L. F. Allard, and Y.-P. Sun, *J. Am. Chem. Soc.*, 2004, **126**, 1014.

120. K. A. S. Fernando, Y. Lin, W. Wang, S. Kumar, B. Zhou, S.-Y. Xie, L. T. Cureton, and Y.-P. Sun, *J. Am. Chem. Soc.*, 2004, **126**, 10234.

121. W. Wang, K. A. S. Fernando, Y. Lin, M. J. Meziani, L. M. Veca, L. Cao, P. Zhang, M. M. Kimani, and Y.-P. Sun, *J. Am. Chem. Soc.*, 2008, **130**, 1415.

122. G. Gruner, *J. Mater. Chem.*, 2006, **16**, 3533.

123. W. Kim, L. C. Palilis, A. J. Makinen, H. Kim, M. Uchida, and Z. H. Kafai, *Mat. Res. Soc., Symp. Proc.*, 2004, **814**, 343.

124. G. P. Kushto, W. Kim, and Z. H. Kafai, *Appl. Phys. Lett.*, 2005, **86**, 093502.

125. D. L. Carroll, R. Czerw, and S. Webster, *Synth. Met.*, 2005, **155**, 694.

126. J. S. Moon, J. H. Park, T. Y. Lee, Y. W. Kim, J. B. Yoo, C. Y. Park, J. M. Kim, and K. W. Jin, *Diamond Relat. Mater.*, 2005, **14**, 1882.

127. E. Kymakis, G. Klapsis, E. Koudoumas, E. Stratakis, N. Kornilios, N. Vidakis, and Y. Franghiadakis, *Eur. Phys. J. Appl. Phys.*, 2007, **36**, 257.

128. N. Shenogin, S. Shenogin, L. Xue, and P. Keblinski, *Appl. Phys. Lett.*, 2005, **87**, 133106.

129. M. J. Biercuk, M. C. Llaguno, M. Radosavljevic, J. K. Hyun, A. T. Johnson, and J. E. Fischer, *Appl. Phys. Lett.*, 2002, **80**, 2767.

130. T. Kashiwagi, E. Grulke, J. Hilding, K. Groth, R. Harris, K. Butler, J. Shields, S. Kharchenko, and J. Douglas, *Polymer*, 2004, **45**, 4227.

131. H. Huang, C. Liu, Y. Wu, and S. S. Fan, *Adv. Mater.*, 2005, **17**, 1652.

132. Y. Wu, C. H. Liu, H. Huang, and S. S. Fan, *Appl. Phys. Lett.*, 2005, **87**, 213108.

133. S. T. Huxtable, D. G. Cahill, S. Shenogin, L. Xue, R. Ozisik, P. Barone, M. Usrey, M. S. Strano, G. Siddons, M. Shim, and P. Keblinski, *Nat. Mater.*, 2003, **2**, 731.

134. C. H. Liu and S. S. Fan, *Appl. Phys. Lett.*, 2004, **86**, 123106.

135. C. W. Padgett and D. W. Brenner, *Nano Lett.*, 2004, **4**, 1051.

136. S. Shenogin, A. Bodapati, L. Xue, R. Ozisik, and P. Keblinski, *Appl. Phys. Lett.*, 2004, **85**, 2229.

137. S. Shenogin, L. Xue, R. Ozisik, and P. Keblinski, *J. Appl. Phys.*, 2004, **95**, 8136.

138. F. H. Gojny, M. H. G. Wichmann, B. Fielder, I. A. Kinloch, W. Bauhofer, A. H. Windle, and K. Schulte, *Polymer*, 2006, **47**, 2036.

139. F. Deng, Q.-S. Zheng, L.-F. Wang, and C.-W. Nan, *Appl. Phys. Lett.*, 2007, **90**, 021914.

140. P. C. Song, C. H. Liu, and S. S. Fan, *Appl. Phys. Lett.*, 2006, **88**, 153111.

141. R. Andrews, D. Jacques, A. M. Rao, F. Derbyshire, D. Qian, X. Fan, E. C. Dickey, and J. Chen, *Chem. Phys. Lett.*, 1999, **33**, 467.

142. S. Ghose, D. C. Working, J. W. Connell, J. G. Smith, K. A. Watson, D. M. Delozier, Y.-P. Sun, and Y. Lin, *High Perform. Polym.*, 2006, **18**, 961.

143. W. Wang, L. M. Veca, and Y.-P. Sun, unpublished results.